Fabrication and investigation of III-V quantum structured solar cells with Fabry-Pérot cavity and nanophotonics in order to explore high-efficiency photovoltaic concepts : towards an intermediate band assisted hot carrier solar cell

Benoît Behaghel

Université Pierre et Marie Curie

Ecole doctorale de Physique et Chimie des Matériaux

Institut de Recherche et Développement sur l'Énergie Photovoltaïque (IRDEP, Chatou)

Centre de Nanosciences et de Nanotechnologies (C2N, Paris-Saclay)

Japanese-French Laboratory for Next generation Photovoltaic Cells (NextPV, Tokyo)

Fabrication and investigation of III-V quantum structured solar cells with Fabry-Pérot cavity and nanophotonics in order to explore high-efficiency photovoltaic concepts

Towards an intermediate band assisted hot carrier solar cell

Par Benoît Behaghel

Thèse de doctorat de Physique

Dirigée par Jean-François Guillemoles et Stéphane Collin

Présentée et soutenue publiquement le 18 décembre 2017

Devant un jury composé de :

Christian SEASSAL	Directeur de Recherche (INL, Lyon)	Rapporteur
Guilhem ALMUNEAU	Chargé de Recherche (LAAS, Toulouse)	Rapporteur
Christophe SAUVAN	Chargé de Recherche (LCF, Paris-Saclay)	Examinateur
Alexandra FRAGOLA	Maître de conférences (UPMC, Paris)	Examinateur
Yoshitaka OKADA	Professeur (RCAST, Tokyo)	Examinateur
Stéphane COLLIN	Chargé de Recherche (C2N, Paris-Saclay)	Directeur de thèse
Jean-François GUILLEMOLES	Directeur de Recherche (IRDEP, Chatou)	Directeur de thèse

To Paker, Fr. Bernard and Léon,
To all my family and friends,
So that we can use our energy better.

Our duty as men is to act as though there were no limit to our power.
— Pierre Teilhard de Chardin s.j.
('Science and Christ', 27 February 1921.)

Acknowledgements

This manuscript present the work of a scientific collaboration between Japan and France. Behind all collaborations there is the story of people interacting with each others. It is at the same time a challenge and a chance and I want to acknowledge all the people who helped to write this story.

First I want to thank my supervisors Stéphane Collin and Jean-François Guillemoles for their support and trust. They taught me that it is important to be rigorous and humble in your own work while being benevolent and patient towars others. Then I want to thank Professor Yoshitaka Okada who welcomed me very warmly in his lab and Pierre Destruel who triggered the creation of the Japanese-French laboratory "NextPV". In Japan I discovered a different way of doing research however I felt the same core feeling of respect and dedication towards science. This experience would not have been possible without the support of the Monbukagakusho scholarship I received from the Japanese Ministry of Education, Culture, Sports, Science and Technology (MEXT). I want to thank all the people from the Japanese embassy in France, especially Akiko Ishii-Foret for her kindness and all the staff from Tokyo University who made my stay confortable. For the French side, I thank my doctoral school (ED 397) and UPMC administration for their understanding of my specific situation between France and Japan. For the PhD defense, I want to thank Christian Seassal and Guilhem Almuneau for the reviewing of this work, the time they spent and their questions. I also thank the other jury members Alexandra Fragola and Christophe Sauvan for attending and judging my work. I am glad to have been accepted as a Doctor by the scientific community. I have learned to respect researchers and I think most of them have a good balance between their dreams, their science integrity and their duty towards our society. I thank them for giving me the opportunity to grow in this environment, learning and confronting ideas through conferences and publications.

I had the chance to work with three different laboratories. The first one was the C2N (ex-LPN). After all this time I realize how lucky I was to have been trained there. In term of clean room and nanofabrication it is a dream place. I want to thank Christophe Dupuis who is always ready to help anyone and does not hesitate to share his knowledge with a smile. He is (and will always be in my heart) a great soccer player. Throught soccer I met a lot of people and it was easier afterwards to interact because we shared playing under snow or heat waves. I want to thank Stéphane Guilet ninja and plasma warrior, Lorenzo Bernardi and Olivier Oria both being genius goal keepers and great support for IT. Kamel Merghem for his great audio sportcaster, dribbling and microbonding skills. Dominique Mailly as an endurant forward but also one of the coolest director I met. In the younger generation, Michaël Verdun, Juan Castro, Faycal Bai you were my greatest support on the soccer field and in the lab. Thanks for keeping up the positive attitude even under harsh situations that we all met at some point. In the PV team, I would like to thank first my sempai when I came in the group: Inès Massiot, Clément Colin and Nicolas Vandamme. I know I was sometime a bit annoying with my questions. You were exemplary for me with your kindness and patience. You gave me the motivation to give back to others and be tolerant to newcomers. In the second generation of sempai, I want to thank Alexandre Gaucher, Jérôme Michallon and especially Julie Goffard who helped me when I was in Ja-

pan. She also taught me a lot about the art of capoeira and the difficulty of being a young mum. Talking about mum, I would like to thank Nathalie Bardou, Emilie Steveler and Cécile Joulaud who were always ready for advice and discussions fueling my motivation. About daddy advices, I will remember the discussions with Gregory Vincent, Fabrice Oehler, Andrea Scaccabarozzi and especially Andrea Cattoni who helped me to grow as a nanoimprinter but also gave me tips about many other things. I won't forget also the BANG master Clément Tardieu and many participants like Christelle Tuambilangana, Ludivine Emeric, Jihene Zribi, Romaric de Lépinau, Louis Gouillart, Daniel Pelati, Ahmed Ben Slimane and Amadeo Michaud (also great soccer players). In the young generation, I want to thank particularly Hung-Ling Chen who helped a lot at C2N, IRDEP and with NextPV. I wish him good luck for his last year of PhD. I also wish the best to Thomas Bidaud who worked with NextPV and is now starting a PhD in C2N. The Japanese-French collaboration needs motivated students that can make the link between France and Japan. In this perspective, I also want to thank Maxime Giteau who has been working at C2N and is now starting his PhD in Japan at NextPV. I also want to thank Fabrice Pardo and Jean-Luc Pelouard for some coffee discussions. I thank Xavier Lafosse and Alan Durnez for their help in teaching me about dielectric deposition, ellipsometry and reflectometry measurements. Laetitia Leroy and Laurent Couraud for metal depositions, Abdelmounaim Harouri for UV lithography and Jean-Claude Esnault for his dedication to the clean room. I thank Alain Péan for his tireless energy to fix many issues in the 2nd floor of our building not only computer stuff. Also I want to thank Agnès Roux for helping me dealing with administrative papers. I don't forget the adorable twin combo from Klearia: Anne-Claire Louër and Guillaume Da Rold who helped me and entertained me a lot in the clean room. Finally I cannot name all people of C2N but I want to give a general thank to this exceptional research center and the great people I met there.

For my second year of PhD, I moved to Japan in NextPV on Komaba campus. There I found a new environment and I can say here again that I was very lucky. The diversity of scientific topics on this campus is almost unlimited. First I want to thank the Japanese professors who helped me get confortable in this new place: Masakazu Sugiyama, Yoshiaki Nakano and Takaya Kubo. In Okada lab, I was first welcomed by Hoshii-san. I thank him for always being keen to answer my numerous questions. Regarding the clean room environment and substrate removal, I want to thank Miyashita-san for Okada lab and Watanabe-san for Sugiyama lab. Both were patients and cautious with my training. In term of characterization, Tamaki-san introduced me to many setup. I want to thank him especially for his rigorous, tenacious and honest mind which was essential to improve my work and attitude towards science. I want to thank Shoji-san for his dedication in growing good samples for me and also for staying very late with me for discussion and sometimes playing games after hard work to release the stress. I thank Sogabe-san and Yoshida-san for advising me on the modelisation and simulation. I thank Ahsan-san for introducing me to the photoreflectance setup and for the good company everytime we had the chance to discuss. In Okada lab and Sugiyama lab, I also want to thank Ogura-san, Sodabanlu-san, Wang-san for the nice discussion and also the students Bern-san, Hung-san, Naito-san, Osawa-san, Shimomura-san, Mori-san, Yamashita-san and especially Inoue-san and Champ for their help in many aspects. I won't forget also Fujiki-san and Hosaka-san for their kind help, I thank them for being such good Japanese mama for me. In NextPV, I also had the opportunity to work with people from the French part of the collaboration. First I would like to thank Ludmila Cojocaru for being such a great example for us. I thank Amaury Delamarre for helping me getting installed in Tokyo and also on many scientific aspects. I also want to thank Zacharie Jehl for sharing his experience in Japan and in many field of science, especially the science of boxing and hiking. Last but not least, I want to thank Lea Tatry and Anatole Julian who did long internship with us and produced great results for the collaboration but also participated to the good mood in the lab.

After I returned to France, I was given the opportunity to work more closely with IRDEP laboratory and especially the advanced characterization team. First I want to thank Laurent Lombez for always welcoming me in his team with a positive mood and sometime great jokes. Big up to Pierre Rale for the great work and many debates we had together. I thank Myriam Paire for her wise advices. François Gibelli and Dac-Trung Nguyen for great discussions on PL fitting and hot carriers. Florian Proise, Jean Rodière, Sébastien Jutteau and Gilbert El-Hajje as PhD comrades. I thank Enrique Leite for helping with many things in the characterization room. I also thank Adrien Bercegol, Baptiste Bérenguier, Daniel Ory, Ombline Lafont and Jean Rousset for the numerous coffee breaks and discussions after lunch. I hope IPVF will be a great success for French PV research and industry. Finally I want to thank Daniel Lincot for accepting me in his lab and Claire Vialette for her continuous support all along my PhD.

My last thanks are for my friends and family who shared my joys and sometimes my frustrations. I want to thank my two sisters: Solène and Anne-Colombe, my three brothers: Amaury, Ghislain and Louis-Marie, my in-laws: Bruno, Anne-Laure, Astrid and Théau and of course their children: Corentin, Alix, Aurore, Klervie, Xavier, Nour-Marie, Maxime, Aliénor, Augustin and Victoire. I want to thank my parents for their unconditionnal support and my grandmother Magny for being an example of tenacity.

Abstract

In the past decade, photovoltaics (PV) has become a key player for the future of worldwide energy generation. Innovation in PV is likely to rely on high efficiency PV with flexible and lightweight thin films to enable PV deployement for mobile applications. In the framework of the Japanese-French laboratory “NextPV”, this thesis investigates the development of III-V quantum structured solar cells to explore high-efficiency photovoltaic concepts especially intermediate band solar cells (IBSC). Quantum structured IBSC have proven to be limited by thermal escape at room temperature and by low subbandgap light absorption. Following a consistent approach, we evaluate the topology, thermal escape mechanism, quantum structure and optical absorption of In(Ga)As quantum dots in a wide gap $Al_{0.2}GaAs$ host material. We also characterize quantitatively the device operation and improve the optical design. For a high irradiation, we evidence a hot carrier population in the quantum dots. At the same time, sequential two-photon absorption (S-TPA) is demonstrated both optically and electrically. We also show that S-TPA for both subbandgap transitions can be enhanced by a factor x5-10 with light management techniques, for example by implementation of Fabry-Perot cavities with the different epitaxial transfer methods that we developed. More advanced periodical nanostructures were also fabricated in the case of multi-quantum well solar cells using nanoimprint lithography techniques. Overall we discuss the possibility of realizing intermediate-band-assisted hot-carrier solar cells with light management to open the path for high-efficiency quantum structured IBSC.

Key words: photovoltaics, thin films, quantum structures, high efficiency, light management, nanofabrication

Résumé

Le photovoltaïque (PV) s'est imposé comme un acteur majeur de l'énergie. L'innovation dans ce domaine passera sans doute par le PV à haut rendement sur des couches minces flexibles et légères permettant son déploiement dans les applications mobiles. Cette thèse étudie le dévelopement de cellules solaires III-V à structures quantiques visant des concepts PV hauts rendements tels les cellules solaires à bande intermédiaire (IBSC). Ces IBSC se sont montrés limités du fait de l'échappement thermique des porteurs à température ambiante ainsi que la faible absorption optique sous le gap. Nous avons évalué la topologie, le mécanisme d'échappement thermique, la structure quantique ainsi que l'absorption de boites quantiques en In(Ga)As dans un matériau hôte en $Al_{0.2}GaAs$ à grand gap. Nous avons aussi caractérisé de manière quantitative comment opère ce système et avons amélioré son design optique. Sous une forte irradiation, nous avons mis en évidence l'apparition d'une population de porteurs chauds dans les boites quantiques. Par ailleurs, l'effet d'absorption sequentielle à deux photons (S-TPA) a été démontré. Nous avons observé une augmentation de ce S-TPA d'un facteur x5-10 grâce à du management de la lumière réalisé notamment avec des cavités de Fabry-Pérot. Des nanostructures périodiques ont aussi été fabriquées dans le cas de cellules solaires à multi-puits quantiques par l'utilisation de lithographie en nanoimpression. Dans l'ensemble cette étude vise à discuter la possibilité de réaliser des cellules solaires à porteurs chauds assistés d'une bande intermédiaire et améliorées par un management optique afin d'ouvrir la voie pour des cellules à hauts rendements.

Mots clés: photovoltaïque, couches minces, structures quantiques, haut rendement, management optique, nanofabrication

Dans ce travail de thèse nous explorons le domaine des nouveaux concepts pour le photovoltaïque, en particulier, pour le dévelopement d'une nouvelle génération de cellule solaire à haut rendement. Pour cela nous avons participé à la fabrication et à l'étude des hétérostructures III-V semiconductrices contenant des structures quantiques. Ce travail de thèse s'est déroulé dans le cadre du laboratoire international associé (LIA) « NextPV » hébergé au « Research Center for Advanced Science and Technology » (RCAST) de l'Université de Tokyo, en collaboration avec deux laboratoires du CNRS : le Centre de Nanosciences et de Nanotechnologies (C2N) ainsi que l'institut de recherche et développement sur l'énergie photovoltaïque (IRDEP) faisant maintenant partie de l'Institut Photovoltaïque d'Ile-de-France (IPVF).

Le chapitre 1 constitue une introduction sur le sujet du photovoltaïque ainsi que les possibilités pour le haut rendement, en particulier pour le domaine spécifique des cellules solaires à bandes intermédiaires (IBSC). L'apport du management de la lumière est précisé essentiellement pour promouvoir l'absorption, naturellement faible dans les nanostructures quantiques. En illustration de ce chapitre, il peut être intéressant de commenter la Fig. i ci-dessous qui résume les challenges clés liés à la fabrication de ces cellules. Ces challenges peuvent être séparés en trois parties. En premier lieu, ceux qui sont directement relatifs au fonctionnement d'une IBSC. D'un côté la préservation d'un voltage au même niveau qu'une cellule classique simple jonction doit être réalisée. Et de l'autre, un courant additionnel venant de l'absorption sequentielle de deux photons sous le gap doit être assuré via l'introduction de la bande intermédiare. Dans le cadre spécifique des cellules solaires à boites quantiques (QDSC), plusieurs problèmes interviennent relativement à ces deux challenges. D'un côté, l'échapement thermique des porteurs venant des boites ainsi que le fort taux de recombinaisons non-radiatives pénalisent la préservation du voltage. De l'autre, la faible densité volumique des boites dans les couches quantiques ainsi que le faible niveau de remplissage de la bande intermédiaire ne permettent pas une absorption efficace de photons sous le gap. Enfin toutes ces problématiques sont intrinséquement liées aux conditions de fabrication de ces boites. Nous citons en exemple deux procédés permettant d'améliorer les proprités de nos IBSC, la technique du « capping » ou recouvrement et la technique de dopage des boites quantiques.

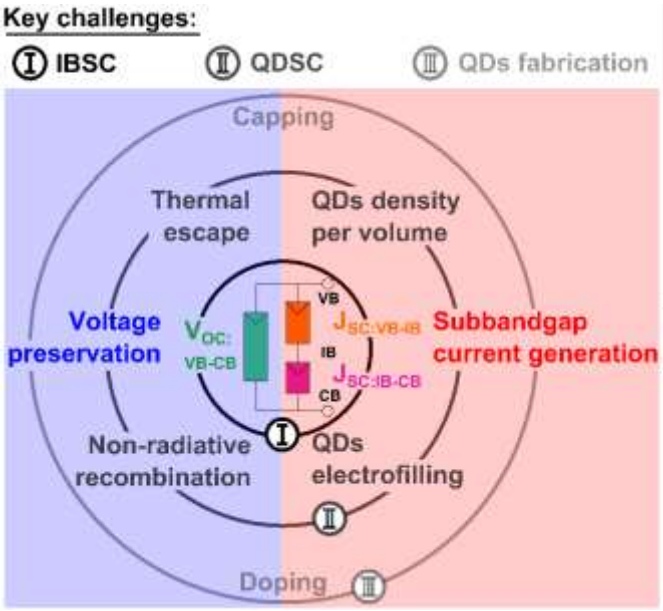

Fig. i: Schéma explicatif résumant les challenges clés liés à la fabrication de cellules solaires à bande intermédiaires fabriqués à l'aide de boites quantiques.

Dans le chapitre 2, nous introduisons les principales étapes technologiques nécessaires à la réalisation de nos cellules. Nous expliquons notamment les technologies de report sur substrat hôte que nous avons utilisé ainsi que les différentes étapes de nanostructuration. La Fig. ii, donne une vision d'ensemble du process flow.

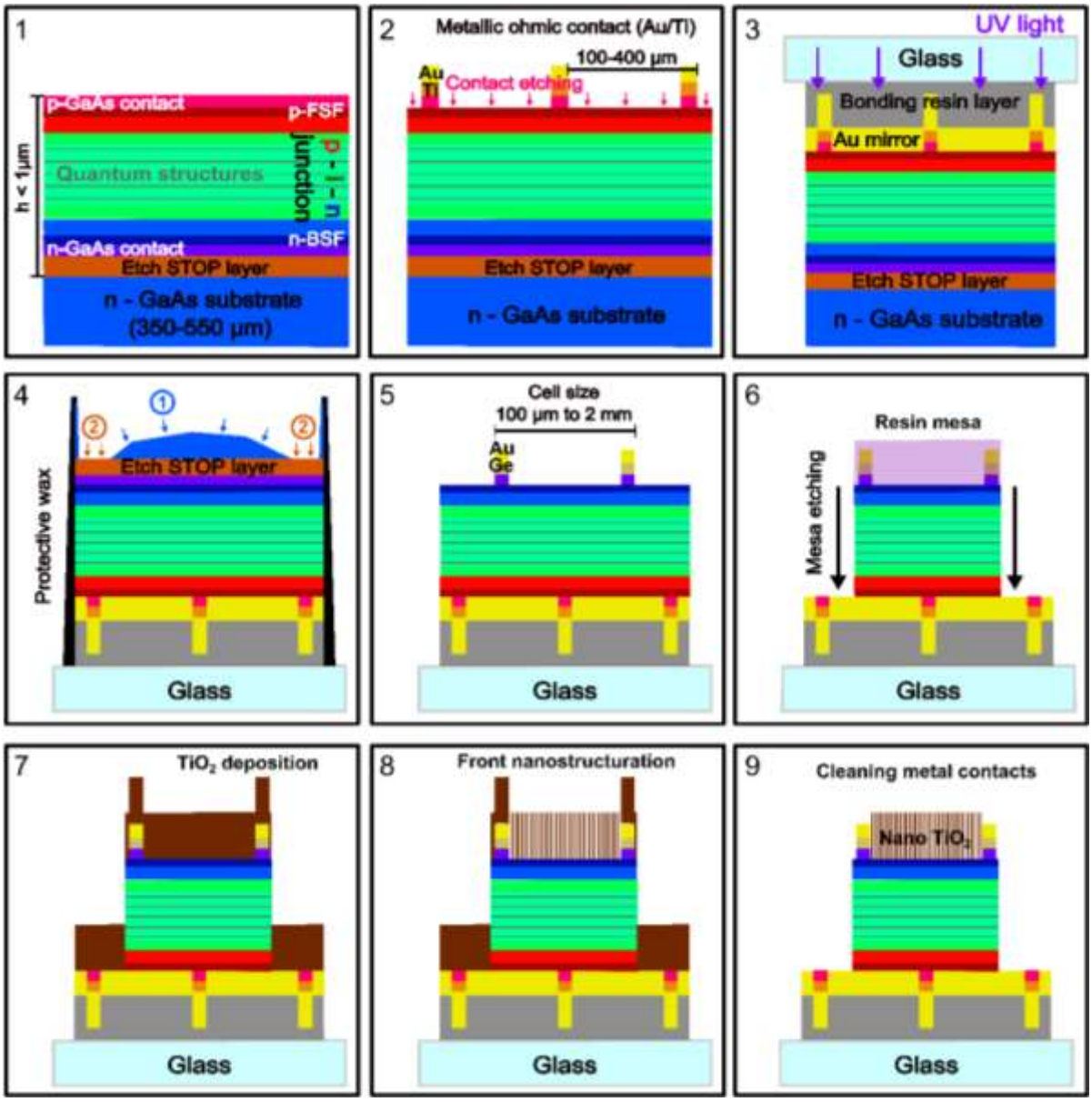

Fig. ii: Schéma du process flow résumant les différentes étapes de fabrication menant à la realisation d'une cellule solaire à boites quantiques avec nanostructuration (ici en face avant).

Tout d'abord, (1) la jonction *p-i-n* avec les structures quantiques est crû sur un substrat en GaAs dopé n avec une couche « etch STOP layer » pour la phase de transfert de substrat. En (2), les contacts métalliques localisés en face arrière sont effectués par enrésinement, lithographie UV, dépôt de métal et lift-off et la couche de contact en GaAs dopé p est gravée. En (3), un dépôt de mirroir est effectué puis un collage sur un substrat de verre est fait à l'aide d'une résine photosensible. En (4), le substrat en GaAs est gravé sélectivement sans que la couche « etch STOP » soit attaquée. Les bords de la couche epitaxiée sont protégés de la gravure latérale par une cire de protection. La couche « etch STOP » est ensuite gravée séléctivement sans que la couche de contact ne soit attaquée. En (5), l'étape de fabrication des contacts avant est effec-

tuée de la même manière que pour les contacts arrière. En (6), l'étape de « mesa » est réalisée qui consiste à isoler les cellules solaires les unes des autres en les protégeant avec de la résine et en gravant entre. En (7), une couche de TiO_2 est déposée. En (8), l'étape de nanostructuration en face avant est effectuée à l'aide de plusieurs étapes décrites au chapitre 2. Enfin en (9), le reste du TiO_2 déposé est retiré des contacts pour pouvoir effectuer la caractérisation éléctrique des cellules.

Dans le chapitre 3, le design et le fonctionnement des IBSC à boites quantiques semiconductrices sont introduits en particulier avec les matériaux constitués de boites quantiques d'In(Ga)As avec matrice en $Al_{0.2}Ga_{0.8}As$. Nous signalons aussi l'influence de facteurs comme la concentration en boites quantiques sur le mécanisme d'absorption séquentielle à deux photons et le rôle clé que peut jouer à cet égard la concentration du champ électromagnétique par piégeage optique. Les procédés de croissance épitaxiale sont brièvement décrits, ainsi que la topographie des nanostructures obtenues. Une étude plus approfondie sur les mécanismes d'échappement et de collecte des porteurs est ensuite présentée. Les mesures de photoluminescence résolue en température, présentées dans la Fig. iii, permettent notamment de mettre en évidence un régime d'échappement et de transfert par saut et relaxation vers les boîtes quantiques les plus grandes.

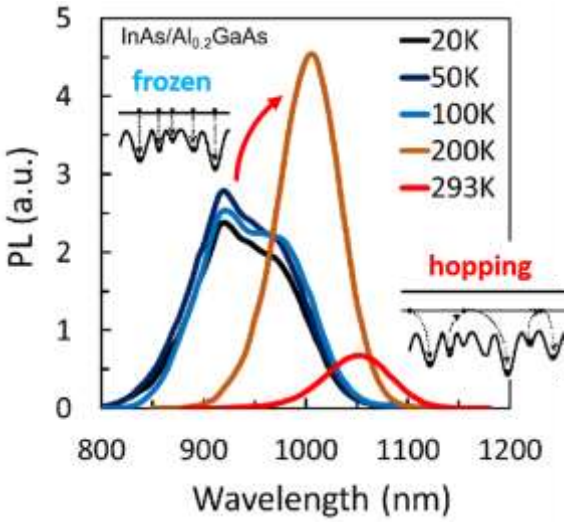

Fig. iii: Mesure de photoluminescence en temperature mettant en évidence une transition dans les boites à partir de T > 100 K. L'on passe d'un régime où les porteurs sont « gelés » à un régime où ils peuvent « sauter » de boites en boites.

Des mesures électriques ont par ailleurs mis en évidence l'impact des défauts dans la matrice d'AlGaAs sur les mécanismes de transport et d'échappement des porteurs. Enfin nous avons essayé d'étudier de manière précise l'absorption dans ces structures quantiques de plusieurs manières, notamment de manière expérimentale à l'aide d'une méthode interférentiel fondé sur l'utilisation de cavité de Fabry-Pérot à l'aide de différentes épaisseurs de diéléctriques positionnées en face avant comme réprésenté dans la Fig. iv. Des « marches » en diélectriques (SiN_x) sont effectuées sur le dessus de la surface des couches reportées sur miroir afin de créer des cavités de Fabry-Pérot d'épaisseur différentes comme cela est indiqué sur le schéma ainsi que la photo au microscope. Ces différentes épaisseurs de cavité induisent des résonances positionnées à différents endroits spectralement, que l'on remarque sur les spectres de réflectométrie. En fittant ces courbes on est en mesure de remonter à la valeur de l'absorption sur la plage du spectre balayé par le décalage de ces pics de résonances.

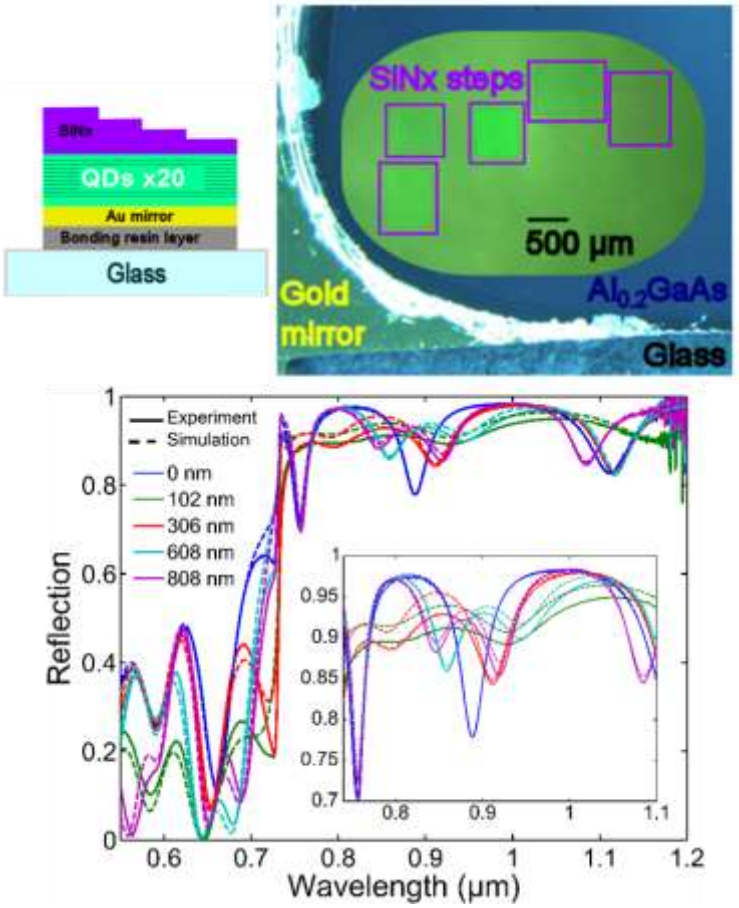

Fig. iv: Principe de l'interférométrie de Fabry-Pérot pour la caractérisation de l'absorption. Des « marches » en diélectriques (SiN_x) sont effectuées sur le dessus de la surface des couches reportées afin de créer différentes cavités de Fabry-Pérot d'épaisseur différentes comme cela est indiqué sur la photo au microscope. Ces différentes épaisseurs de cavité induisent des résonances positionnées à différents endroits spectrallement, que l'on remarque sur les spectres de réflectométrie. En fittant ces courbes on est en mesure de remonter à la valeur de l'absorption sur la plage du spectre balayé par le décalage de ces pics de résonances.

Le chapitre 4 présente une étude de la dynamique de la bande intermédiaire constitué par les états quantiques formés dans les boites. Un ensemble de caractérisations optiques est présenté, en vue d'évaluer les paramètres importants des cellules solaires à boites quantiques. Il s'agit notamment des facteurs d'idéalité, des effets de saturation des niveaux des boîtes, et de la mise en évidence de populations possiblement indépendantes entre boîtes et milieu hôte. Lorsque la concentration de porteurs dans les larges boites quantiques atteint le niveau de semiconducteurs dégénérés, un régime de porteurs chauds semble pouvoir apparaître. Cette population chaude semble avoir un effet thermoelectrique qui sépare le potentiel chimique dans le matériau hôte de celui dans les boites quantiques permettant ainsi d'isoler la bande intermédiaire lorsque celle-ci se retrouve à moitié remplie. Cette interprétation s'appuie notamment sur l'analyse de la Fig. v. Ces graphes représentent l'évolution de la température d'une part (gauche) et celle de la séparation des quasi niveaux de Fermi (QFL) d'autre part (droite) en fonction de l'excitation laser pour la population de porteurs dans les boites quantiques et celle dans la wetting layer (WL) et le matériau hôte. L'augmentation en température des porteurs dans les boites semblent suivre une loi d'Arrhénius avec une énergie d'activation (E_a) d'envrion 250 meV tandis que la température dans le matériau hôte semble rester à tempérautre ambiante. Cette différence en température semble conduire à la séparation des QFL jusqu'à une valeur de 140 meV.

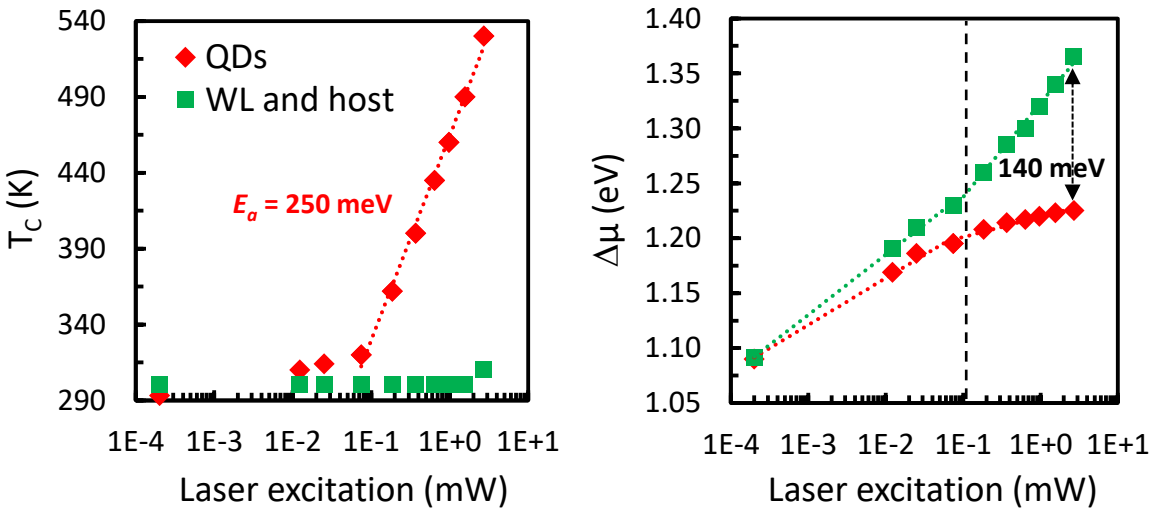

Fig. v: Graphes représentant l'évolution de la température d'une part (gauche) et celle de la séparation des quasi niveaux de Fermi (QFL) d'autre part (droite) en fonction de l'excitation laser pour la population de porteurs dans les boites quantiques et celle dans la wetting layer (WL) et le matériau hôte. L'augmentation en température des porteurs dans les boites semblent suivre une loi d'Arrhénius avec une énergie d'activation (E_a) d'envrion 250 meV tandis que la température dans le matériau hôte semble rester à tempérautre ambiante. Cette différence en température semble conduire à la séparation des QFL jusqu'à une valeur de 140 meV.

Dans ce chapitre, nous étudions par ailleurs les propriétés relatives à l'absorption sequentielle de deux photons qui sont indispensables au fonctionnement des cellules solaires à bande intermédiaire. Ainsi nous démontrons la possibilité pour ces cellules de combiner à la fois le concept de bande intermédiaire et de porteurs chauds sous le nom de cellules solaires à porteurs chauds assistées d'une bande intermediaire (IB-HCSC). Nous évaluons les performances et perspectives de telles cellules qui pourraient fonctionner comme cellule à haut rendement à condition de disposer d'un matériau hôte de qualité optimisée et de pré-remplir les niveaux des boîtes (par capping ou dopage).

Le cinquième et dernier chapitre concerne l'utilisation de résonances optiques, qu'elles soient simples comme dans le cas de Fabry-Pérot verticaux ou plus complexe comme avec des réseaux périodiques à deux dimensions réalisés à l'avant ou à l'arrière de la cellule. Ces effets sont étudiés dans le cas de matériaux à base de multi-puits quantiques et de matériaux à base de boites quantiques. On observe un effet de l'augmentation du courant de court-circuit, qui est reliée à l'absorption dans les structures quantiques. Les possibilités d'augmenter le rendement au-delà, au travers du positionnement optimal des structures quantiques est discuté pour la structure à puits et illustré dans la Fig. vi.

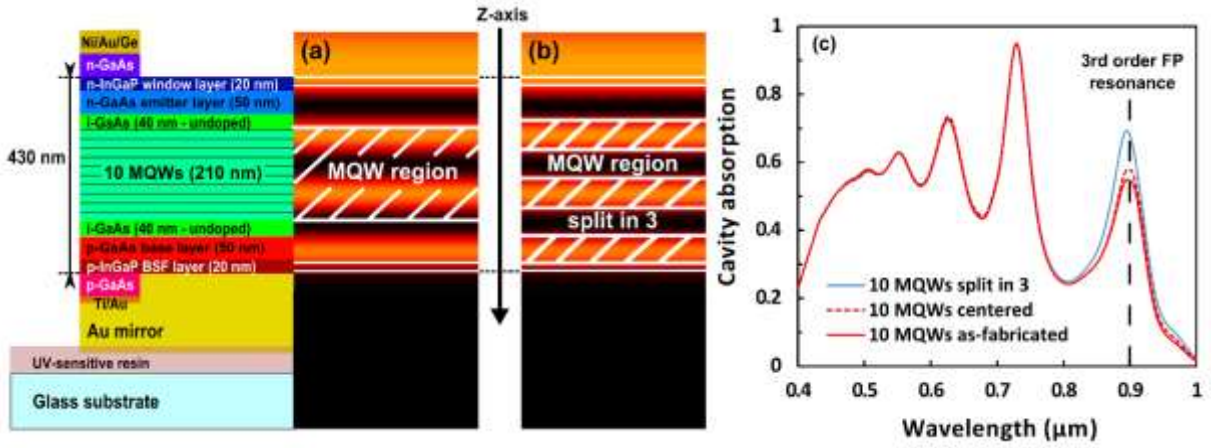

Fig. vi: Illustation de l'effet du positionnement des structures quantiques. Dans le cas (b), la zone des multi-puits est divisée en trois parties pour correspondre parfaitement aux maxima du champ éléctrique de la lumière incidente. Cela induit directement un gain dans l'absorption comme cela est illustré sur les spectres d'absorption.

Dans le cas des structures à boîtes quantiques, dont l'absorption initiale est très faible aux grandes longueurs d'onde, une stratégie exploitant des structures métal-isolant-métal (MIM) est proposée. Cette structure, présente une efficacité qui n'est pas suffisante au regard de l'augmentation nécessaire dans les présentes structures. Cette augmentation ne peut être obtenue qu'au travers d'une grande densité de résonances à fort facteur de qualité.

En conclusion de ce manuscrit, nous établissons un certain nombre d'idées et de perspectives pour le futur des ces cellules. Tout d'abord, nous pensons que l'effort devrait être en priorité porté sur l'aspect fabrication des boites quantiques notamment en essayant d'avoir un matériau hôte présentant moins de défauts afin d'avoir une efficacité radiative du même ordre qu'une cellule simple jonction III-V à l'état de l'art. En deuxième axe, l'étude du dopage des boites quantiques semblent être aussi important afin d'essayer de préremplir avec des porteurs dans l'optique d'avoir un niveau d'apparition des porteurs chauds pour des niveaux d'irradiation moins élevé. Il est aussi intéressant de noter qu'un fort dopage des boites pourrait peut-être conduire à réaliser des objets optiques exotiques intéressants de type « relai plasmonique » en utilisant des effets de couplage plasmonique dans le proche infrarouge. Enfin, niveau fabrication, il paraît essentiel de s'orienter vers des structures quantiques plus denses dans la direction de croissance afin de gagner sur le plan de l'absorption. En terme de dispositif optoéléctronique, l'idée d'aller vers une cellule sans jonction composée seulement de boites quantiques avec des contacts sélectifs couplé à une structure MIM paraît intéressante pour maximiser le ratio de structure quantique par rapport à l'épaisseur totale de la couche absorbante ainsi que dans l'idée d'avoir un photofilling pour le concept de cellules IBSC à porteurs chauds. Enfin, toutes ces approches doivent être étudiées dans le cadre du développement de cellules solaires flexibles, légères et bas coût. Ainsi le dévelopement des techniques de transfert déjà commencé dans ce sens doit être prolongé. En suivant un certain nombre des pous pensons que pour les dix prochaines années, il pourrait y avoir une cellule IBSC à porteurs chauds à simple junction qui dépasse la barrière symbolique des 30% de rendement.

Contents

General introduction

In the past decade, growth of photovoltaics (PV) has followed an exponential curve making it a key player for the future of worldwide energy generation. PV manufacturing companies have been consolidating and more money is being invested in research and development (R&D). Innovation in PV is blooming in three directions: (i) the cost of the device, (ii) the energy efficiency gain and (iii) the ease of deployment via new PV architectures. On one hand, industrials compete and invest a lot of efforts to reduce the cost of PV modules, and at the same time, research on new materials like Perovskite seems to be promising to reduce production cost of a solar cell. On the other hand, research on high-efficiency PV is still in an exploratory phase and needs proof of concept in order to attract more attention. Finally, new PV architectures are being developed thanks to flexible and lightweight thin-films. In the future, it is likely that high-efficiency PV with flexible and lightweight thin-films will become more conventional and unlock novel applications e.g. indoor PV, solar-powered vehicule, PV high altitude sky platforms, etc.

This thesis work is born thanks to the will of Japanese and French researchers to collaborate on PV upstream concepts throught the creation of an international joint laboratory called “NextPV”. From the Japanese side, Okada and Sugiyama laboratories from the Research Center for Advanced Science and Technology (RCAST) of the University of Tokyo have brought their expertise in the realization of quantum-structured materials necessary to achieve promising high-efficiency PV concepts. On the other side, the French National Center for Scientific Research (CNRS) has contributed on the topic of nanophotonics and nanofabrication for thin-films via the Centre for Nanoscience and Nanotechnology (C2N). The CNRS Institute of Research and Development on Photovoltaic Energy (IRDEP) was also involved for advanced characterization. In the framework of this collaboration, my time was divided evenly between France and Japan, in particular thanks to the Monbukagakusho scholarship from the Japanese Ministry of Education, Culture, Sports, Science and Technology (MEXT) and the involvement of the Embassy of Japan in France.

In this thesis, we investigate III-V quantum-structured solar cells with light management strategies and nanofabrication for the realization of high-efficiency PV concepts. This solution has great potential to reach high-efficiency PV and has the advantage of having a less complex device structure compared to nowadays high-efficiency PV solutions. We believe that in the future it could become an economically viable lightweight, flexible and high-efficiency solution and we want to work towards a proof-of-concept solar cell to validate the theory and open the path for future investments.

In chapter 1, we introduce our topic. We explain the basic principles of PV energy conversion, the main properties of solar cells and novel concepts to overcome the energy efficiency limit of conventional PV, for example in our case by using quantum-structured solar cells. We also discuss the need of light management

strategies in PV devices and especially we give examples of state-of-the-art investigations on quantum-structured solar cell.

In chapter 2, we describe the fabrication techniques that were involved all along our work. We cover the topic of the clean room microfabrication of PV devices and report on two epitaxial layer transfer methods that we developped and used in the framework of the “NextPV” collaboration. We also detail the technique that was used to implement nanophotonics at the C2N and we give a general process flow of a final solar cell fabricated during this thesis.

In chapter 3, we thoroughly investigate the physical properties of the main quantum-structured system that was used: the In(Ga)As / $Al_{0.2}Ga_{0.8}As$ quantum dot (QD) system designed especially for high-efficiency intermediate band solar cell (IBSC). We explain the target, design and material growth of such system that are being fabricated in Okada laboratory. We give details on basic characterization from a topological and morphological point of view. We also investigate thermal, electrical and optical properties by characterizations and simulations.

In chapter 4, we demonstrate the potential of such systems for the realization of high-efficiency PV, especially for the concept of intermediate band assisted hot carrier solar cells (IB-HCSCs). We use specific characterization techniques dedicated to the investigation of carrier and light dynamics and interactions in the In(Ga)As / $Al_{0.2}Ga_{0.8}As$ QD system.

Finally, in chapter 5, we investigate the light management strategies that were implemented on quantum-structured solar cell. We optimize optical design by numerical calculations and fabricate nanopatterned structures at the back or the front to induce a multi-resonant photonic effect inside PV layers. Nanopatterning was made only on multi-quantum well (MQW) solar cells fabricated in Sugiyama laboratory. Such quantum-structured solar cells are easier than QD solar cells in terms of growth control and physical interpretation. Fabrication, characterization, analysis and comparison of a simple Fabry-Pérot (FP) cavity effect is presented for QD solar cells.

This thesis presents results in many domains of experiments. Design and numerical simulations, material growth and fabrication in clean room, basic and advanced characterization and analytical or numerical fitting. I want to acknowledge here the different contributions to the work presented in this manuscript. The III-V quantum-structured layers were epitaxially grown at RCAST in Japan by Dr. Kentaroh Watanabe and Dr. Yasushi Shoji. Some of QDs AFM images were taken by Dr. Yasushi Shoji. PL at low temperature was done under the supervision of Dr. Ryo Tamaki. A special acknowledgment goes to Dr. Christophe Dupuis, Dr. Nicolas Vandamme and Dr. Naoya Miyashita, whose help and advice have been really appreciated along the different fabrication processes. I also had the pleasure to supervise and receive help from Lea Tatry during her 6-month Master’s internship on the development of epitaxial lift-off (ELO) transfer technique. All SEM images presented in this thesis have been taken at C2N by coworkers (Dr. Christophe Dupuis, Dr. Juan Castro, Dr. Alexandre Gaucher and Dr. Julie Goffard). The process of transfer using UV reticulation polymer glue was proposed by Dr. Andrea Cattoni. He also trained me to the nanoimprint lithography. The sol-gel TiO2 was provided by Dr. David Grosso and his team (LCMCP, Collège de France, Paris). The deposition of dielectric coatings on samples were supervised by Dr. Xavier Lafosse and Dr. Alan Durnez. Regarding characterization, the current-voltage (I-V) and external quantum efficiency (EQE) characterizations were made in RCAST, C2N or IRDEP. I-V at low temperature were done under the supervision of Dr. Zacharie Jehl. The calibrated PL and two-color excitation characterization presented in chapter 4 have been performed at

IRDEP by Dr. Pierre Rale and Hung-Ling Chen. Data analysis, PL numerical fitting and interpretations have been done with the help of Dr. Pierre Rale, Hung-Ling Chen, Dr. Laurent Lombez, Dr. François Gibelli and Dr. Dac-Trung Nguyen. Optical numerical calculations have been performed using transfer matrix or Rouard's method for simple FP cavity. In chapter 5, I used the Reticolo software provided by Dr. Philippe Lalanne and Dr. Christophe Sauvan (Institut d'Optique, Palaiseau) in order to investigate the effect of nanostructuration. Dr. Katsuhisa Yoshida and Dr. Tomah Sogabe helped me to better understand the 8-band k·p calculations made using nextnano software provided by Dr. Stefan Birner. I finally want to acknowledge the fruitful discussions that we had with Dr. Amaury Delamarre, Dr. Nazmul Ahsan, Dr. Stéphane Guillet and Dr. Takuya Hoshii.

Chapter 1 Introduction to photovoltaics and light management

Photovoltaic technologies are becoming essential to the development of renewable energy production at world scale. Nowadays most of photovoltaics revolve around one economical and competitive solution, which has ensured a fast deployment of solar energy in the last decade. For many reasons, it is strategic and reasonable to keep pushing the research and development (R&D) towards other solutions that can offer more flexibility in the use of solar energy for the market. In this perspective, we propose to focus on the challenge of high-efficiency solar cells. In a first part, we describe the basic principle of photovoltaics with the coming of novel concepts. We describe in particular the solution of an intermediate band solar cell (IBSC) based on III-V quantum-structured materials. All along the manuscript, we will see the many advantages and disadvantages of these materials. The development and emergence of new PV technologies often necessitate the control of three phases: (1) control over the material fabrication and properties, (2) control over the device fabrication and characterization, and finally (3) the control over optical or light management. For this reason, in a second part, we introduce and discuss the application of light management for PV applications and especially for quantum-structured solar cells.

1.1 Photovoltaics: towards high-efficiency solar cells

In this first part, we introduce the origin and principle of PV in order to discuss the possibility of increasing its efficiency. We report on various innovative paths that are being investigated worldwide. In the framework of the French-Japanese International Joint Laboratory “NextPV”, we chose to focus on intermediate band solar cell (IBSC) concept based on III-V quantum-structured materials. We describe the core concept and underline the advantages and disadvantages of this approach.

1.1.1 Principle of photovoltaic conversion of solar energy

The photovoltaic effect has been first observed by French physicist Edmond Becquerel in 1839 throught his work on electrochemical cell [1]. It is defined as the creation of voltage or electric current in a material upon exposure to light. Later in 1940, with the advance of solid-state devices, semiconductor researchers at Bell Labs paved the route towards the nowadays-dominant silicon *p-n* junction technology. In 1954, they demonstrated the first practical silicon solar cell with about 6% efficiency at converting sunlight energy into electricity. In the sixties, Shockley and Queisser proposed a model to determine the theoretical efficiency limit [2]. At the same time as the rest of the scientific community, they evidenced the future routes towards higher efficiency [3].

1.1.1.1 Basic principle of PV conversion

i). Electron-hole pair generation in a two-level system

The photovoltaic effect is a fundamental effect that can be seen as the response of an ensemble of atoms under irradiation. As represented in Figure 1.1-1 (a), the representation of atoms by Bohr introduce the idea that positively charged atomic nucleus possess electrons jumping between orbits by emitting or absorbing electromagnetic energy: $\Delta E = h\nu$ with h the Planck constant and ν the irradiation frequency. More precisely, quantum mechanics band theory has been successfully used in solid-state physics to model the electronic structure of ensemble of atoms. It is especially true for periodic organization like crystals, which have specific electronic band structures.

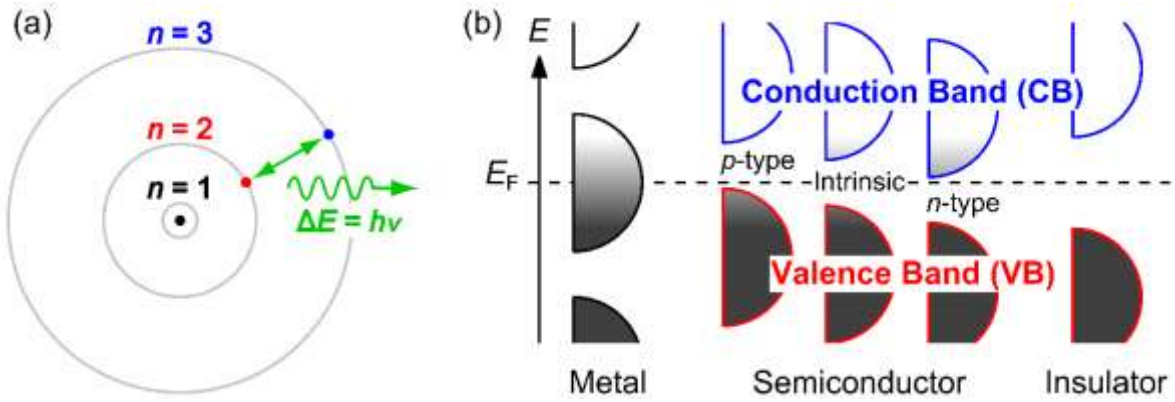

Figure 1.1-1: (a) Bohr model of the hydrogen atom where the negatively charged electron confined to an atomic shell encircles a small positively charged atomic nucleus. Electron jump between orbits is accompanied by an emitted or absorbed amount of electromagnetic energy (hv). The orbits in which the electron may travel are shown as grey circles. (b) Filling of the electronic states in various types of materials at equilibrium. Here, height is energy while width is the density of available states for a certain energy in the material listed. The shade follows the Fermi-Dirac distribution (black = all states filled, white = no state filled). In metals, the Fermi level E_F lies inside at least one band. In insulators and semiconductors, the Fermi level is inside a band gap between the valence and conduction bands. Adapted from Wikipedia.

As represented in Figure 1.1-1 (b), in the case of semiconductor materials, a two-level system is usually used to model the electronic band structure with carrier filling of the electronic states following a Fermi-Dirac distribution, represented with the shades (black = all states filled, white = no state filled). The bottom level is the valence band (VB) and is defined as the highest range of electron energies in which electrons are normally present at absolute zero temperature. The upper level is the conduction band (CB) and is defined as the lowest range of vacant electronic states. In PV, the energy band gap between the two bands is used to absorb the electromagnetic energy irradiation to promote an electron from VB to CB. This phenomenon creates an electron-hole pair harvesting a potential energy corresponding to the bandgap energy. The hole in the VB is seen as a positive charge like an electronic vacancy in chemistry. The PV conversion is successful if the electron in the CB becomes a free electron that can be extracted in the form of an electric power for the system: $P_{elec} = I \times V$ with I the electric current and V the electric potential.

The Fermi level can be considered to be a hypothetical energy level, such that at thermodynamic equilibrium this energy level would have a 50% probability of being occupied at any given time. Quasi-Fermi levels (QFLs) are used to describe electrons and holes populations respectively in the CB and VB when they are displaced from equilibrium and reach a quasi-equilibrium. For example in the case of photon flux generating continuous electron transitions from VB to CB, it is possible to describe the two populations of carriers using Fermi-dirac distribution. In this case, the difference

between the two QFLs is called QFL splitting (QFLS) expressed with notation $\Delta\mu$. It represents the electrochemical potential when a solar cell absorbs a photon flux.

Current extraction is favored by an efficient spatial charge separation of photogenerated carriers (electrons and holes) before they recombine. To optimize the separation of the generated free carriers we differentiate electron and hole using various schemes. At least two types of strategies are often used and combined: implementation of a junction and implementation of selective contacts. Both techniques are used in our devices and will be described in chapter 2 when discussing the fabrication of PV devices.

ii). Electric equivalent circuit and I-V characteristics

In order to characterize and compare solar cells, an electrically equivalent model is often used as shown in Figure 1.1-2 (a). The generated photocurrent I_L for an applied voltage V is modeled as an ideal current generator. PV conversion process is limited by several sources of losses that are taken into account by the following electric components. (1) Electron-hole recombination losses are represented as a dark current I_D modeled by a diode in parallel. (2) Leakage currents are modeled by a shunt resistance R_{SH} that is in parallel with the current generator. (3) The semiconductor resistance and contact resistance are modeled by a serie resistance R_S. Series resistance is particularly important in the case of high injection levels, as for concentrated light. For the study of our solar cells, to take into account different recombination mechanisms, we used a two-diode model fitting of dark I-V curves measured at forward bias using Equation 1.1-1 with q the electron charge, k_B the Boltzmann constant and T the temperature [4].

$$I = I_{dark\ (n=2)} \exp\left(\frac{q(V+IR_S)}{2k_BT}\right) + I_{dark\ (n=1)} \exp\left(\frac{q(V+IR_S)}{k_BT}\right) + \frac{V+IR_S}{R_{SH}}$$

Equation 1.1-1: Two-diode equation of a solar cell in dark condition (I_L=0)

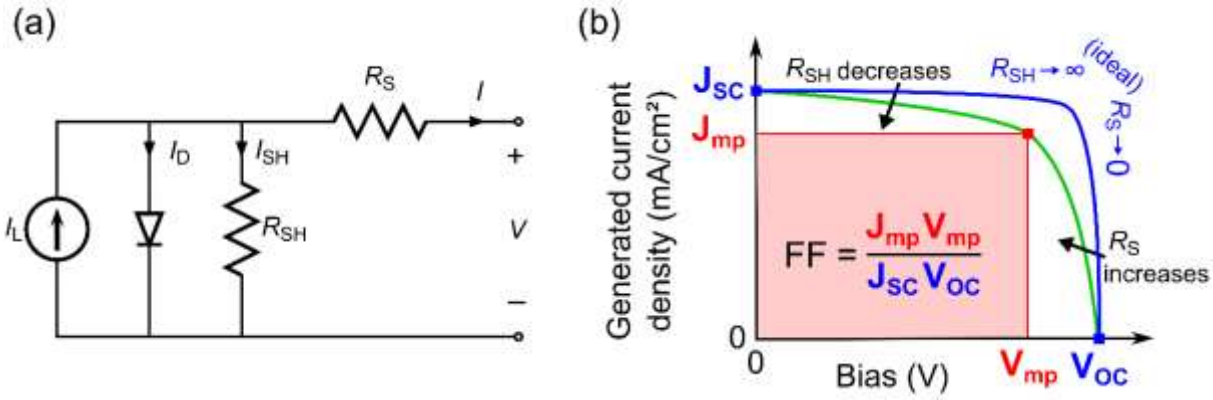

Figure 1.1-2: (a) Electric equivalent circuit (taken from Wikipedia) and (b) schematic of I-V curve characteristics.

A standard characterization often found is the current-voltage (*I-V*) curve as represented (green line) in Figure 1.1-2 (b). As the generated photocurrent depends on the irradiated area, it is common to use the current density (*J*), usually expressed in *mA/cm²*. J_{SC} is the short-circuit current density and corresponds to the current that can be extracted from the cell at zero bias (V = 0). V_{OC} is the open-circuit voltage and corresponds to the potential of the cell for zero current (J = 0). It is equivalent to the quasi-Fermi level splitting (QFLS) or electrochemical potential of a solar cell.

Between these two points (J_{SC} and V_{OC}), there is a point where the solar cell can achieve a maximum electrical power: $P_{max} = J_{mp} \times V_{mp}$ (red square). The fill factor (*FF*), as defined in Figure 1.1-2 (b), gives a useful indication of the deviation between an ideal solar cell and the actual device.

1.1.1.2 Solar energy and Shockley-Queisser limit

i). Solar spectral irradiance

In order to calculate the efficiency of a solar cell, the output maximum electrical power is divided by the incident light power. For PV application, the solar spectral irradiance is taken as a reference to calculate solar cell efficiencies. In Figure 1.1-3, we represent the solar spectral irradiance in photons flux (mA/cm²) per photon energy in electron-volt (eV) unit. The solar spectral irradiance outside the atmosphere, also called air mass zero (black line AM0), is very close to the one of a black body at 6000 K. The Sun behaves like a black body whose emission follows the Planck's law. PV industry uses American standards for solar spectral irradiance with a 1.5 atmosphere thickness due to the latitude of the USA (AM1.5G). The presence of absorption bands can be noticed, due to atmosphere elements such as dioxygen, water vapor and carbon dioxyde. On Earth surface, the global irradiance integrated over all photon energies is close to 100 m*W/cm²*, which is defined as the irradiance used in standard testing conditions (STC) and is often used to rescale power density in "suns" value for example in the case of concentration application.

In Figure 1.1-3, we indicate and represent the energy bandgap of $Al_{0.2}GaAs$ semiconductor material that will be a reference material in this study. We see that in the case where the photon energy is lower than the bandgap energy, the photon can pass through the material without being absorbed. In other cases, the photon can be absorbed, promoting an electron to an excited state within the CB resulting in the creation of an electron-hole pair as discussed earlier.

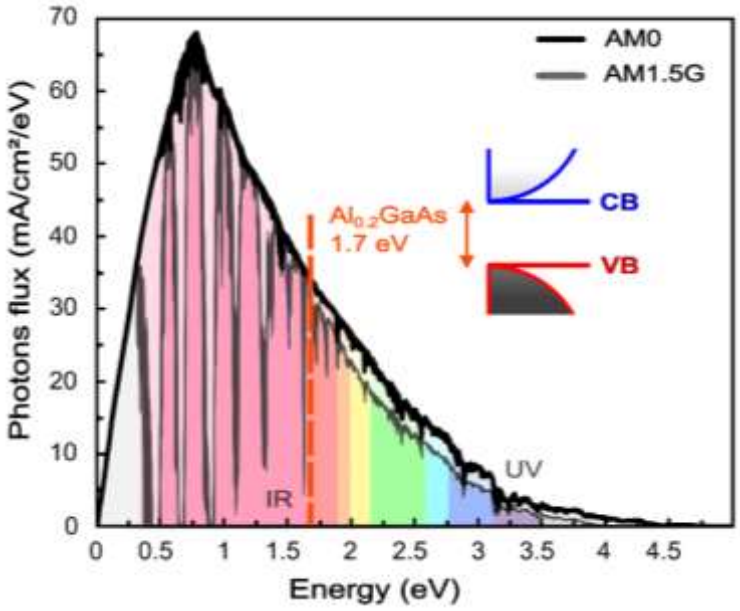

Figure 1.1-3: Solar spectral irradiance in photons flux (mA/cm²) per photon energy in eV outside the atmosphere (black line AM0) and on earth surface (AM1.5G). Energy position of $Al_{0.2}GaAs$ bandgap is shown to indicate absorbed photons with higher energies (on the right: UV and visible light) and non-absorbed photons with lower energies (on the left: IR light).

For electrons (or holes) in excited states with energy higher than the CB minimum (lower than the VB maximum) also called "hot carriers", there is a relaxation of the excess energy so that both car-

rier populations reach a quasi-equilibrium at band edges. There are three mechanisms that can dissipate the excess energy: (1) carrier-carrier scattering (Auger effect, impact ionization), (2) phonon emission (thermalization) or (3) photon emission (intra-band emission of a thermal photon). These processes are competing with each other but thermalization is usually considered as the dominant mechanism for a bulk material. These dissipation mechanisms are limiting the PV efficiency of a solar cell based on a two-level material. In the case of a semiconductor with a low-energy bandgap, most photons will be absorbed but the extracted electrons will have a low energy due to thermalization. On the contrary for a semiconductor with a high-energy bandgap, electrons with high-energy will be extracted but a reduced ratio of solar spectrum will be absorbed. We see that a trade-off on the bandgap energy is needed in order to get a maximum output electrical power from the solar spectral irradiance.

ii). Shockley-Queisser limit for a single-junction solar cell

This trade-off has been investigated by Shockley and Queisser in 1961 [2]. They were the first to express the efficiency limit of a single-junction solar cell as a function of its bandgap. Shockley-Queisser (SQ) analysis was based on the following assumptions. (1) One electron-hole pair excited per incoming photon. (2) Thermal relaxation of the electron-hole pair energy in excess of the band gap. (3) QFLs are constant in the cell. (4) Perfect absorption of photons with energy higher than the bandgap. They considered a solar cell at 300 K under the AM1.5G illumination, only impacted by radiative recombination. Combining altogether the different loss contributions due to blackbody radiation, radiative recombination and spectral losses (hot carriers relaxation and non-absorbed below bandgap photons), they calculated the maximal conversion efficiency as a function of the material bandgap. In Figure 1.1-4, we represent a graph where the causes of the SQ limit are attributed to the different mechanisms. The black zone represents energy that can be extracted as useful electrical power. The pink and green zones represent different spectral losses, respectively the energy of non-absorbed below-bandgap photons and the “excess energy” lost by relaxation of hot carriers to band edges. The blue zone is the energy lost in the trade-off between low radiative recombination versus high operating voltage. The SQ limit curve gives a maximal efficiency of 33.7% under 1 sun illumination for bandgaps close to 1.4 eV.

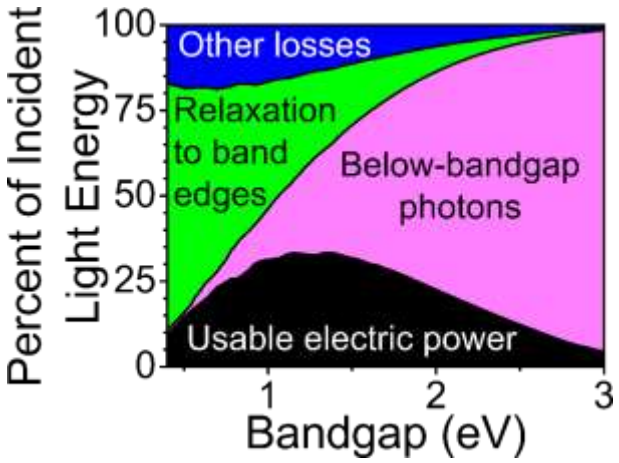

Figure 1.1-4: SQ limit and the origin of losses. The black zone represent energy that can be extracted as useful electrical power. The pink and green zones represent spectral losses, respectively the energy of non-absorbed below-bandgap photons and the energy lost by relaxation of hot carriers to band edges. The blue zone is energy lost in the trade-off between low radiative recombination versus high operating voltage. Taken from Wikipedia.

In Table 1.1-1, we summarize recent world record efficiencies for different PV devices compared with the SQ limit of single-junction with Silicon and GaAs semiconductor materials. Publications of efficiency results can be found on the websites of the different companies and are usually summarized by Professor Martin A. Green in its biannual *Solar cell efficiency tables* [5]. On one hand, we see that the world best single-junction solar cells are made of thin-film crystalline GaAs (bandgap energy of 1.42 eV) grown by metalorganic chemical vapor deposition (MOCVD) with record efficiency of 28.8% under 1 sun achieved in 2012 by Alta Devices in their lab and certified by the National Renewable Energy Laboratory (NREL). Flexible small size commercial solar cells (8.5 cm²) have an efficiency of about 26% using industrial processes and they advertise their PV modules to have 24.8% efficiency. On the other hand, Silicon (bandgap energy of 1.11 eV) solar cell industry has been dominating the market for the past sixty years. A highest efficiency record of 26.7% under 1 sun was achieved in 2017 by Kaneka in practical size (79 cm²) solar cells and 26.6% for large size (180 cm²). In 2016, Kaneka had already taken over the crown for module efficiency from SunPower builduing a PV module that was verified by the Japanese National Institute of Advanced Industrial Science and Technology (AIST) to be 24.4 percent efficient, the highest among manufacturers of silicon panels catching up with GaAs solar cell technology.

Table 1.1-1: Recent world record efficiency for different PV devices compared with SQ limit of single-junction with Silicon and GaAs semiconductor materials (updated in 2017).

PV devices / Efficiencies (%)	Silicon – 1.11 eV	GaAs – 1.42 eV
SQ limit	33	33
Solar cells (lab record)	26.7 (Kaneka)	28.8 (Alta Devices)
Solar cells (industry size)	26.6 (Kaneka)	~26 (Alta Devices)
Modules (commercial)	24.4 (Kaneka)	24.8 (Alta Devices)

iii). Importance of the external radiative efficiency (ERE)

Three losses can be categorized as causes for the experimental performance to fall below the SQ limits [6]: (1) photon collection losses, (2) non-radiative recombination (R_{nr}) versus radiative (R_{rad}) represented by the external radiative efficiency (ERE) [7] and (3) electrical losses.

ERE, also called external luminescent efficiency (η_{ext}) represents the fraction of electron-hole pairs that recombine radiatively to yield a photon that ultimately escapes the cell [8]. It depends on both the quality of the material throught the internal radiative efficiency (IRE), as well as the optical design, also called light management [9]. IRE, also called internal luminescent efficiency (η_{int}) represents the fraction of electron-hole pairs that recombine radiatively inside the material. On thermodynamic grounds [10], it has been shown that the V_{OC} would be penalized by poor ERE [8], [9]. In Equation 1.1-2, we summarize the different relations between the V_{OC}, η_{ext} and η_{int}. $V_{OC-ideal}$ is the value of V_{OC} in the ideal, detailed-balance limit where there are no non-thermodynamic losses. $\overline{P_{esc}}$ and $\overline{P_{abs}}$ are the energy-, solid-angle-, and volume-averaged probabilities that a photon emitted either escapes directly or is reabsorbed. This expression of η_{ext} is only valid assuming η_{int} is uniformly distributed over the cell volume, which is often the case for very high quality solar cells. For cells that are dominated by non-radiative recombination, whether in the bulk or in the depletion region, the influence of the optical design seems to be negligible [8].

$$V_{OC} = V_{OC-ideal} - \frac{k_B T}{q} \ln\left(\frac{1}{\eta_{ext}}\right); \qquad \eta_{ext} = \frac{\eta_{int}\overline{P_{esc}}}{1 - \eta_{int}\overline{P_{abs}}}; \qquad \eta_{int} = \frac{R_{rad}}{R_{rad} + R_{nr}}$$

Equation 1.1-2: Expression of V_{OC}, η_{ext} and η_{int} showing the importance of ERE over a solar cell efficiency

We notice that the three categorized losses respond to the three phases described in the introduction. On one hand, control on the material is essential to have a high ERE by increasing the IRE. On the other hand, control over devices fabrication and light management can address losses (3) and (1). Finally, in the case when IRE is high enough, light management can also be used as a refinement to increase ERE for example using photon recycling (increasing $\overline{P_{abs}}$).

Solar cells from laboratories have the best control over all losses especially for loss (1) and (3) compared with industrial cells or even commercial modules. Therefore, they show the best performances. SQ theory assumes 100% ERE, therefore the ERE ratio determines how we can get close to an ideal solar cell. We notice that laboratories' Silicon solar cells have lower efficiencies than GaAs solar cells. For Silicon, ERE is lower (0.1-2.2%) and constrained to values well below 100%, as intrinsic non-radiative Auger recombination is stronger than radiative recombination [7]. By considering this factor, a specific limit of 29.4% was predicted for Silicon solar cells by Glunz's group from the Fraunhofer Institute for Solar Energy (ISE) systems [11]. For crystalline III-V materials, ERE can be higher. GaAs is an example of one of the very few material systems that can reach IRE close to 100% [12]. In the case of the record 28.8%-efficient GaAs cell, it is interesting to notice that not only high quality material but also light management was used to achieve 32.3% ERE.

Overall, we see that record single-junction solar cells are about 4% below their ideal limits. Therefore, PV R&D on single-junction technology will likely reach a maximum limit in the next five years. In Figure 1.1-4, we notice that for the maximum efficiency around 1.4 eV, losses are almost evenly splitted between the two spectral losses (non-absorbed and excess energy) with about 26% for each zones (respectively pink and green zones). Therefore, we see that actual PV solar cell might potentially increase their efficiency by a factor x3 if they can convert the spectral losses in usable electric power.

1.1.2 Novel concepts for high-efficiency PV conversion of solar energy

In the first part, we have seen the basic principle of PV conversion of solar energy using single-junction technologies and we have seen the potential efficiency gain by overcoming the SQ limit. In this second part, we show that various innovative paths are being investigated worldwide. We focus on the intermediate band solar cell (IBSC) concept describing the theoretical limit and different methods to create an intermediate band (IB). Finally, we explain the main reasons for choosing a system based on III-V quantum-structured materials and the many challenges to fabricate proper high-efficiency IBSCs.

1.1.2.1 Overcoming SQ limit

In order to overcome the SQ limit, two options are considered: (i) the use of photonics application in order to concentrate sunlight or to restrict the cell acceptance angles and (ii) the development of novel solar cell design to convert the spectral losses in usable electric power.

i). Photonics implementation: concentrated sunlight and restriction of cell acceptance angles

One way to exceed the SQ limits by using photonics application is to focus sunlight from the outside using concentrator PV (CPV). The J_{SC} increases linearly with photon flux, whereas V_{OC} increases logarithmically with concentration (C), thus giving a superlinear increase in power [6]. A maximum concentration limit of 46,200 suns is determined by Sun's acceptance half-angle with Earth's surface [13] and a maximum efficiency around 45% is calculated for direct sunlight (AM1.5D) on single-junction solar cell material with energy bandgap close to 1.1 eV like Silicon [6]. Concentrators like Fresnel lens array need to be used with Sun trackers to optimize the concentrating system. For bad weather, the diffuse fraction of light becomes more important and CPV becomes less interesting. Additionally, optical and resistive losses are more significant under concentration. However, concentration reduces the importance of cell costs by reducing cell area, which is an important factor for the large deployment of pricy materials for example like III-V semiconductors.

The other way around, it is also possible to overcome the SQ limit by restricting cell acceptance angles, by a an angular selectivity factor (s) [14], so that cells convert light only from a limited directional range [6]. Recently, the impact of light management was thoroughly studied by Yablonovitch's group and NREL [15]. As an example of the importance of this technique, efficiencies above the SQ limit have been calculated by Polman and Atwater for Auger-limited Silicon (33.4%) and GaAs (35.4%) solar cells with maximum angle restriction of about 3°, a perfect back reflector and considering only the direct portion of the spectrum [16], [17].

If we compare the concentration (C) and angular selectivity (s) techniques, we see that in both case, the objective is to increase the density of photons inside the cell. In the first case, an increase of the density is achieved by reducing the absorber area with CPV. In the second case, the increase of the density is obtained throught the reduction of the photon losses betting on photon recycling increase by angular restriction. As explained earlier, in the case of photon recycling, the impact of non-radiative recombination is significant. The V_{OC} gain (ΔV_{OC}) for both techniques is summarized in Equation 1.1-3 for a solar cell depending if the total electron-hole pair recombinations are dominated by radiative (R_{rad}: n=1) or non-radiative recombinations (R_{nr}: n=2).

$$V_{OC-rad} \sim \frac{k_B T}{q} \ln\left(\frac{J_{SC} \times C}{\frac{J_{dark-rad}}{s}}\right) \quad \Rightarrow \quad \Delta V_{OC-rad} = \frac{k_B T}{q} \ln(C) + \frac{k_B T}{q} \ln(s)$$

$$V_{OC-nr} \sim \frac{2k_B T}{q} \ln\left(\frac{J_{SC} \times C}{J_{dark-nr}}\right) \quad \Rightarrow \quad \Delta V_{OC-nr} = \frac{2k_B T}{q} \ln(C)$$

Equation 1.1-3: V_{OC} gain (ΔV_{OC}) for concentration (C) and angular selectivity (s) techniques for radiatively (ΔV_{OC-rad}) or non-radiatively (ΔV_{OC-nr}) dominated cases.

We see that in the radiatively dominated case (ΔV_{OC-rad}), both concentration and selectivity can contribute equally to the V_{OC} gain. However, in the non-radiatively dominated case, only the concentration effect can contribute because the selectivity factor has a neglible impact on non-radiative dark current. Here again, we understand that for low internal radiative efficiency (IRE) materials, the influence of optical design seems to be not so important to overcome SQ limit throught a V_{OC} gain.

ii). Solar cell strategies to deal with the non-absorbed and excess energy

Many solutions have been suggested to convert the spectral losses in usable electric power. Figure 1.1-5 summarizes the different propositions [18]. First, we present two concepts using spectral splitting to cover different parts of the solar spectrum and then we discuss solutions that focus on using the “excess energy” for example when working from a low-energy bandgap material.

Multi-junction solar cells (MJSCs): It is the most used and steadiest solution, which consists in using numerous absorbers with different bandgaps. Nowadays the solar cell world record efficiency is held by MJSC technology for a four-junction solar cell [19] with 46% efficiency under concentration fabricated by the Fraunhofer ISE / Soitec French-German cooperation in 2014. They were also able to demonstrate a 43.4 % efficiency for mini-modules using the same technology. Under 1-sun illumination, the highest efficiency was achieved with a five-junction solar cell at 38.8% by Boeing-Spectrolab. However, the complicated multilayered structures needed for MJSCs is a big issue. In 2015, even with the best technology, Soitec had to give up on solar CPV because they could not compete on the PV market. Nevertheless, these solutions are usually considered economically profitable for space applications thanks to their high power-per-weight ratio.

Intermediate band solar cells (IBSCs): Another idea using spectral splitting is the intermediate band solar cell (IBSC) concept that uses an absorber with an intermediate band (IB) in its fundamental bandgap [20]–[23]. In an IBSC, photons of low energies excite electrons from the VB to the IB and then from the IB to the CB. In the literature, this effect is called the “two-step two-photon absorption” (TSTPA), “resonant TPA”, "sequential TPA" (S-TPA), or "1+1 absorption". For S-TPA, the absorption for each transition is a first order (linear) process. It should not be confused with “nonresonant TPA” which is a third order (nonlinear) optical process occurring via a "virtual" state created by the interaction of multiple photons. The “nonresonant TPA” is several orders of magnitude weaker than linear absorption. This concept of two low-energy particles generating one high-energy particle follow the same principle as spectral up-conversion [24]. However, IBSCs involve various issues that will be detailed in the next part.

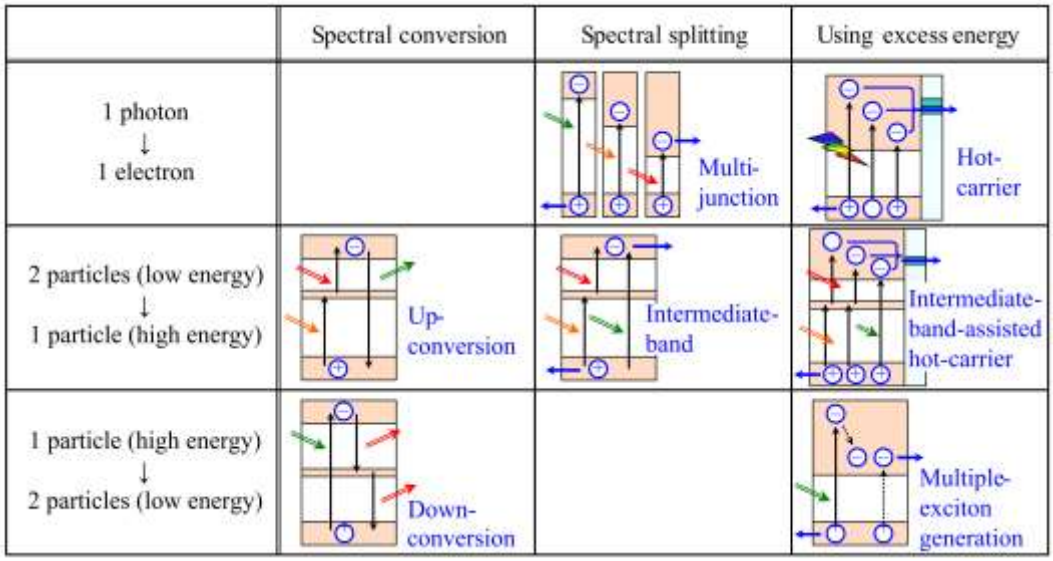

Figure 1.1-5: Solar cell concepts to exceed the SQ limit. Taken from [18].

In parallel of spectral splitting, other solutions are being studied which are dedicated to converting the "excess energy". As discussed earlier, three mechanisms can dissipate the excess energy: (1) carrier-carrier scattering (Auger effect, impact ionization), (2) phonon emission (thermalization) or (3) photon emission (intra-band emission of a thermal photon). The "excess energy" solutions are focused on dealing with these mechanisms so that they do not impair but on the contrary favors the current generation [18] throught the development of (1) multiple-exciton generation (MEG) solar cells, (2) hot carrier solar cells (HCSCs) and (3) intermediate band assisted hot carrier solar cells (IB-HCSCs). It is interesting to notice that for all these solutions thermalization mechanism (2) leads to irreversible losses and should be avoided.

MEG solar cells: The basic principle is that a high-energy photon can generate two or more carriers for example throught impact ionization as described in Figure 1.1-5 [25]–[28]. Although previously reported quantum yields are not sufficiently high to boost the conversion efficiency [29]. This process is similar to that in spectral down-converters [30] because one high-energy particle is converted to two (or more) low-energy particles.

Hot carrier solar cells (HCSCs): In contrast with MEG solar cells, carriers of high energies are directly extracted from HCSCs [31]–[34]. The most essential requisite for HCSCs to realize high conversion efficiency is to suppress thermalization because it is often the fastest relaxation process and represents an irreversible loss for the hot carrier population. This technology is conceptually attractive as a long-term photovoltaic solution but is facing many challenges [35].

Intermediate band assisted hot carrier solar cells (IB-HCSCs): An intermediate band assisted hot carrier solar cell (IB-HCSC) has been proposed recently in order to help the extraction of hot carriers from an absorber that has an IB [18], [36]–[39]. It provides a higher limiting efficiency and enables to work on all relaxation mechanisms. For example, in this configuration, MEG can be used to fill the IB with more carriers.

Among all the novel concepts, we see that the use of an IB provides an attractive way of achieving high-efficiency keeping a relatively simpler design than MJSCs. In the next part, we discuss in detail the theory and challenges to realize an IBSC.

1.1.2.2 IBSC theory and challenges

First, we describe the historical evolution of the IBSC concept and its limits starting with the theory of "impurity PV". Then we discuss the different paths to engineer an intermediate band.

i). IBSC rules and limits

The concept of using mid-gap states for two-step absorption process was first proposed by Wolf in 1960 [3]. Using intentional mid-gap defects or impurities, this concept is often called "impurity PV" as represented in Figure 1.1-6 (a). In 1970 Güttler and Queisser confirmed the previous finding of SQ [2] that "impurity PV" could not improve SQ limit of single-junction solar cells [40].

In 1990, a new proposal of a related multiple-absorption-threshold device was proposed by Barnham (Blackett Laboratory) and Duggan using multi-quantum well (MQW) solar cells [41] as represented in Figure 1.1-6 (b). The carrier photogeneration in lower-bandgap quantum-well regions and subsequent thermal escape to the higher-bandgap host material, stimulated work that clarified the basic thermodynamics of the two-step absorption process.

In 1997, associated thermodynamic constraints were resolved by extending SQ concepts to introduce the idea of IBSC throught Luque and Marti's study (Instituto de Energia Solar) [20]. Three assumptions were made when calculating the detailed balance limit of IBSC: (i) non-radiative transitions are forbidden, (ii) no carriers should be extracted from the IB and (iii) no overlapping between absorption coefficients for each interband transition. In practice, at room temperature, none of these assumptions was proven to be true for IBSC materials at the moment.

Green *et al.* refined the model by considering "relaxation" of IB carriers in a state that does not communicate with the VB [42], [43], which was recently envisioned in the term of a photon "ratchet band" by the Blackett Laboratory [44], [45] as described in Figure 1.1-6 (c).

In Figure 1.1-6 (d), we show an electric equivalent circuit that is common to IBSC approach. The boxes indicate SQ-like cells, with box length representing the value of the cell's energy absorption threshold. The circuit illustrates that non-radiative communications between IB and edge bands can short-circuit the system, which will be equivalent to a C2 or C3 SQ-like cell. In Figure 1.1-6 (e), we show the calculated limiting efficiency under unconcentrated AM1.5G sunlight (solid lines) with and without the energy relaxation towards a "ratchet band". The dashed line shows results under maximally concentrated direct (D) AM1.5D radiation, where relaxation makes no significant difference.

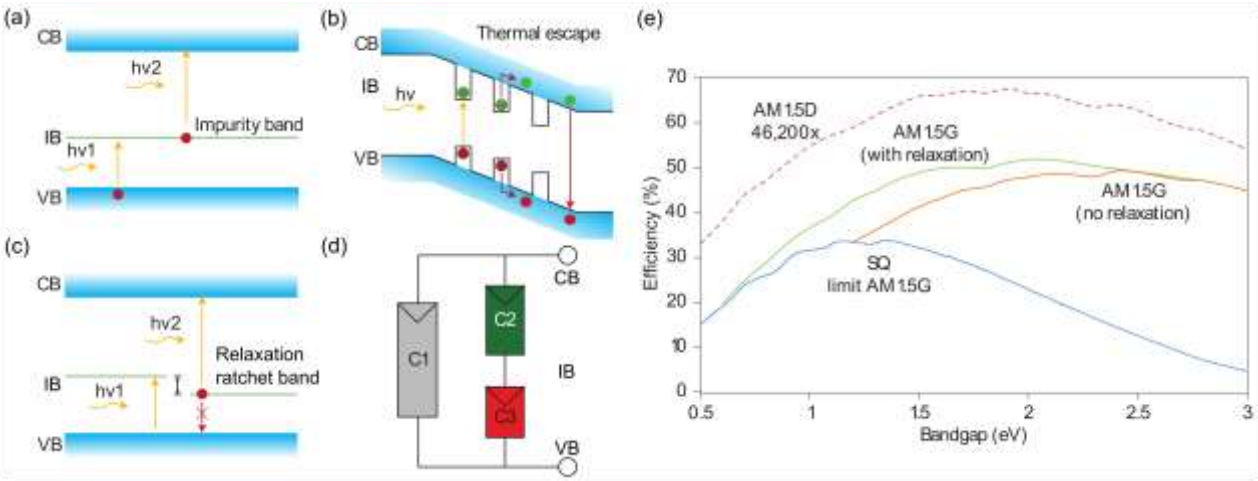

Figure 1.1-6: (a) Solar cell in which an intermediate band (IB) is present, such as when impurities are present in sufficient quantities to cause overlapping between isolated states. (b) MQW solar cell showing carrier generation by low-energy photons in quantum wells, with subsequent thermal escape to the higher-bandgap host material. (c) Excitation from the valence band (VB) to the conduction band (CB) through an IB with energy relaxation using a photon "ratchet band", which does not communicate with the VB. (d) Electric equivalent circuit that is common to IBSC approach. The boxes indicate SQ-like cells, with box length representing the value of the cell's energy absorption threshold. (e) Limiting efficiency under unconcentrated AM1.5G sunlight (solid lines) with and without the energy relaxation towards a "ratchet band" [44]. The dashed line shows results under maximally concentrated AM1.5D radiation, where relaxation makes no significant difference. Adapted from [6].

In Figure 1.1-7, we show the unconcentrated AM1.5G sunlight (1-sun) and maximally concentrated limits calculated by varying the CB-VB (C1) and CB-IB (C2 or C3) energy gaps [46] indicating the maximum points. Optimal energy positions of the IB is calculated to be at 1/3 to 2/5 of the CB-VB bandgap.

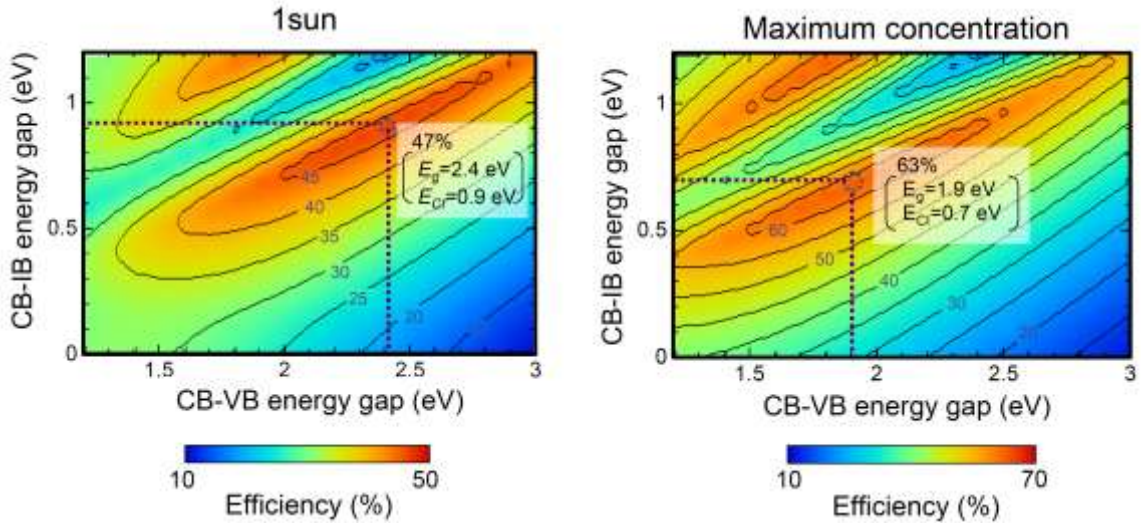

Figure 1.1-7: Limiting efficiency under unconcentrated AM1.5G sunlight (1sun) and maximally concentrated sunlight varying the CB-VB (C1) and CB-IB (C2 or C3) energy gaps [46].

ii). Intermediate band engineering

In the academic world, three solutions using different materials properties are being investigated to achieve IBSCs.

(1) Impurity PV: Historically, the oldest solution envisioned with the aim of extending cell response by excitations through energy states due to controlled defects. For example, this solution is being studied at the Massachusetts Institute of Technology (MIT) for hyperdoped Silicon (HD-Si) [47], [48].

(2) Quantum-structured solar cells: The most studied solution in the world nowadays for IBSC's purpose. Excitation in the lower bandgap regions provides a different energy threshold compared to the wider bandgap. For reference, we can cite two leading groups. The Blackett Laboratory (Imperial College London) for MQW solar cells [49] and the Okada laboratory (University of Tokyo) for quantum dots solar cells (QDSCs) [50].

(3) Highly mismatched alloys: This solution especially emerged with the topic of nitride-based semiconductor alloys. It appears that some alloys have a CB splitting predicted by the band anticrossing model [51]. For example, this solution is being studied at Lawrence Berkeley National Laboratory by Walukiewicz's group [52]–[54].

The different attempts to implement an IB have not been particularly successful [55]. Introducing an IB greatly increases non-radiative recombination mechanisms. Additionally, the IB needs to be partially filled to allow for carrier movement to and from the IB. This often requires donor carriers. The second solution that uses quantum structures is the one we will use during our study. It is the most promising solution because these structures are supposed to be better controlled. They were initially developed and are already used for other applications in the semiconductor industry (e.g. high-speed optical switches, high-gain amplifiers).

1.1.2.3 III-V quantum-structured solar cells

The quantum-structured IBSC system that we study relies on the combination of III-V materials well known and used in the semiconductor science and industry. Unfortunately, quantum structures have several issues that hinders IBSCs to work properly. The chapter 3 is dedicated to the study of QD-IBSCs from an ideal quantum-structured IBSC system to a realistic experimental device. In Figure 1.1-8, we represent the key challenges for realizing a proper QD-IBSC. The two important things that need to be considered from an IBSC point of view are the voltage preservation of the high-energy material bandgap ($V_{OC:\ VB\text{-}CB}$) and the subbangap current generation from the sequential-TPA process ($J_{SC:\ VB\text{-}IB}$ and $J_{SC:\ IB\text{-}CB}$).

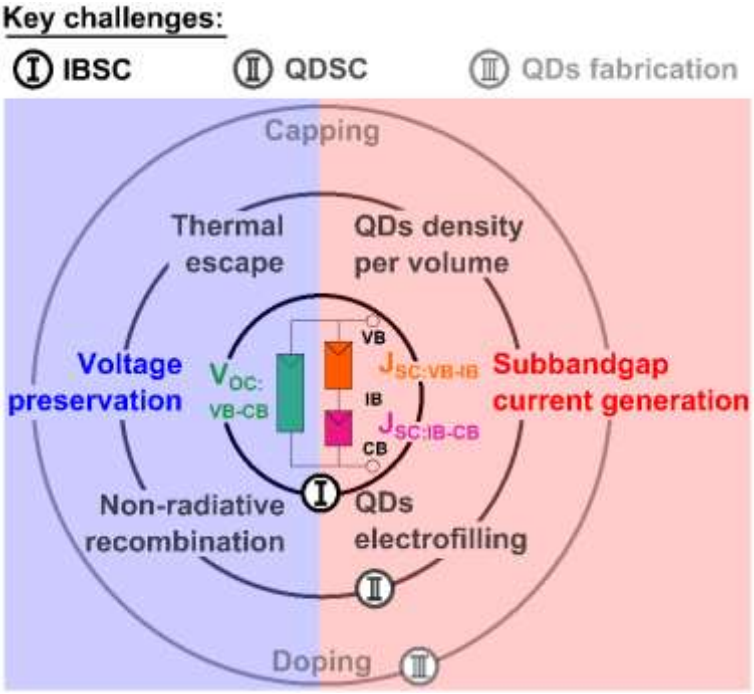

Figure 1.1-8: QD-IBSC key challenges at different level to achieve voltage preservation (blue) and subbandgap current generation (red). Inside the first circle (I), is represented the IBSC equivalent system with on the left the $V_{OC:\ VB\text{-}CB}$ (green) from the higher-energy bandgap material and on the right $J_{SC:\ VB\text{-}IB}$ (orange) and $J_{SC:\ IB\text{-}CB}$ (purple) are the subbandgap current from sequential two-photon absorption (S-TPA). The second circle represents major challenges for QDSCs (II) that are sometime codependent. All contribute to both voltage preservation and subbandgap current generation. However, the limitation of thermal escape and non-radiative recombinations (on the left) are more likely to preserve voltage while an increase of QDs density and electrofilling (on the right) contribute more to subbandgap current generation. The last circle represents QDs fabrication challenges (III). Two important issues are indicated as examples: capping and doping that are both studied in the literature.

From a quantum dot solar cell (QDSC) point of view, these two things are confronted with four key challenges that are sometime codependent: thermal escape, non-radiative recombinations, the QDs density per volume and the QDs electrofilling.

Thermal escape: Devices are often found to be only effective at low temperature as they are prone to thermal escape. It has the effect of short-circuiting the higher-bandgap host material in the equivalent circuit representation of an IBSC. This phenomenon has been investigated by *I-V* measurements for QDSCs under concentration by varying temperature. It was found that at low temperature there is a "voltage recovery" effect meaning that QDSCs with lower-bandgap QD regions have an equivalent V_{OC} compared to reference high-energy host material single-junction solar cells without QDs [56]. From a thermodynamic point of view, the limitation of thermal escape has been stud-

ied for MQW solar cell [57]. Fundamental improvements are only possible if carrier excitation from wells involves particles that are not in equilibrium with the lattice, for example like in the case of hot carriers. Therefore, IB-HCSCs might be a good option for quantum-structured materials. Recently, different studies seem to indicate that the thermal escape would be reduced by the use of higher-energy material [58], capping [59], [60] and doping [61]–[64] techniques. Capping and doping techniques are also used to decrease non-radiative recombinations and increase QDs electrofilling.

Non-radiative recombinations: First, the use of numerous quantum structures increases non-radiative recombination even though it is necessary to increases subbandgap absorption (QDs density per volume). In order to compensate this phenomenon, high quality materials need to be grown. However, quantum heterostructures usually have a lot of interfaces and strains which might induce defects [65]–[70] and low internal radiative efficiency (IRE). In addition, in the case of material like InAs QDs, the use of Indium gives a limit on the temperature growth because of Indium diffusion. Therefore, low-temperature capping layers are used, which often result in a high density of defects. In some cases, annealing is used after the growth. Recently, different studies seem to indicate that capping techniques might reduce non-radiative recombination and doping techniques might have a passivation effect on defects or simply might fill the QDs, which can also reduce non-radiative recombinations [61]–[64].

QDs density per volume: Quantum-structured solar cells exhibit poor absorption for below-bandgap-energy photons. The QD surface density and number of QD layers need to be increased for that purpose. Using closely stacked structures can help to reach a higher level of light absorption. In the case of QDs, even for a very dense material, only 10% will be made of QD absorbing elements. In the case of superlattices, the ratio can exceed 50%. However, a higher surface density of QDs might induce an increase of non-radiative recombinations. In addition, the growth of numerous quantum layers can impede the carrier transport and increases the lattice strain on the device. Superlattices [71], [72], closely stacked QDs [73], type-II QDs [50] and wire-on-well (WoW) [74] fabrication techniques with strain release or strain balancing layers have been proposed to alleviate this constraint.

QDs electrofilling: In the IBSC theory, an electrofilled intermediate band (IB) or metal-like IB is needed [75]. It is especially important for the subbandgap absorption of photon for the transition between the IB and the CB. Indirect and direct doping of QDs have demonstrated a positive effect for IBSC, both numerically [64] and experimentally [61]–[64]. It seems doping can pre-fill QDs excited states, which might help to reach a higher electron density in quantum structures necessary to trigger hot carrier effects.

As we have seen, all of these four key challenges influence the voltage preservation and subbandgap current generations. However, to simplify we can say that thermal escape and non-radiative recombinations are more essential for the voltage preservation while QDs density per volume and QDs electrofilling is more important for subbandgap absorption and current generation as indicated in Figure 1.1-8.

1.2 Light management for quantum-structured IBSCs

In the first part, we introduced high efficiency PV solutions and more precisely, we focused on intermediate band solar cells (IBSCs) fabricated using III-V quantum structured materials. We have seen that the challenges are mostly on the control of material and device fabrication (phase 1 and 2). In this second part, we will discuss the use of light management for PV applications and especially for quantum-structured IBSCs. In the discussion on the importance of external radiative efficiency (ERE), we discussed that light management can be used to increase the photon recycling inside the absorber. We reckon this effect would be interesting for IBSCs. However, due to very low internal radiative efficiency (IRE) in quantum-structured materials, we believe that such application of light management is not of primary importance. Nevertheless, there are at least two reasons why light management can be attractive for quantum-structured IBSCs: (1) to have a thinner quantum structured region and (2) to enhance absorption in specific spectral regions.

Light management is often used in PV for light trapping in order to enhance the light path in a PV absorber. For thin-film PV, it is especially interesting to reduce the thickness of the grown PV layers, which is of the greatest importance for quantum-structured materials. From a fabrication point of view, we saw that it is easier to grow a limited number of quantum layers, for example to reduce the risk of dislocations and limit non-radiative recombinations. In term of device, a limited number of layers is also interesting to have a better separation and collection of photogenerated carriers. In term of QD density, a high density of QDs is not an essential condition if the light trapping can be localized directly in the quantum absorbing elements where the subbandgap absorption takes place. In term of QDs electrofilling, by enhancing light absorption for thinner structure, a higher concentration of photons but also a higher electron density inside QD layers can be achieved offering an alternative solution to electrofilling called “photofilling” [76]. Finally, it is theoretically possible to change the emission of a quantum structure by inserting it into an optical resonator. In our case, we will only study optical cavity where light is weakly coupled, however it is theoretically possible that light management has a direct effect on the dynamics of carriers inside the intermediate band (IB).

In all cases, we see that the goal of light management for QD-IBSCs is usually (i) primary to increase the J_{SC} contribution from subbangap absorption. (ii) Secondary, to fabricate innovating device structures more compact and more efficient. (iii) Third, investigate the effect on the IB dynamic.

In this part, we first introduce the topic of optimal light trapping for PV in the case of Lambertian scattering. Then, we discuss its application to quantum-structured material and we present another approach using multiresonant effects. Finally, we give some examples of recent results for light management in quantum structured IBSCs.

1.2.1 Lambertian scattering PV light trapping

Research on light-trapping strategies for PV application has been a hot topic in the past few years. It is theoretically possible to calculate a maximum enhancement due to optimal light trapping. In the early 1980s, almost simultaneously, Goetzberger [77] and Yablonovitch [78] described schemes based on randomising light directions in solar cells by the use of diffusely scattering (Lambertian) surface textures. Their models work with two assumptions: (i) ray optics regime which means that the typical size R of the structure is larger than the wavelength of light ($R >> \lambda$) and (ii) weakly absorbing materials. Recently, Martin A. Green from the University of New South Wales (UNSW) ex-

tended their studies by describing an analytical solutions that applies to both weakly and strongly absorbed light [79].

1.2.1.1 Principle

For thick films, light is not coherent over the thickness of the film and light trapping can be described with ray optics. For an absorbing layer of thickness *t* without light trapping, the intensity of light decreases exponentially with the traveled distance, according to Beer-Lambert's law. Single-pass absorption is given by Equation 1.2-1 assuming no reflection on the front and back surface. The absorption coefficient α is wavelength-dependent (λ) and related to the imaginary part of the refractive index of the material (κ or sometime expressed by variable *k* in this manuscript).

$$Abs(\lambda) = 1 - \exp(-\alpha(\lambda)t) \quad with \quad \alpha(\lambda) = \frac{4\pi\kappa(\lambda)}{\lambda}$$

Equation 1.2-1: Single-pass absorption assuming no reflection on the front and back surfaces

Standard light-trapping schemes rely on scatterers disposed at the front or at the back surface of a solar cell in order to increase the light path in the absorbing media. In Figure 1.2-1, we show three possible Lambertian texturing approaches usually represented [79].

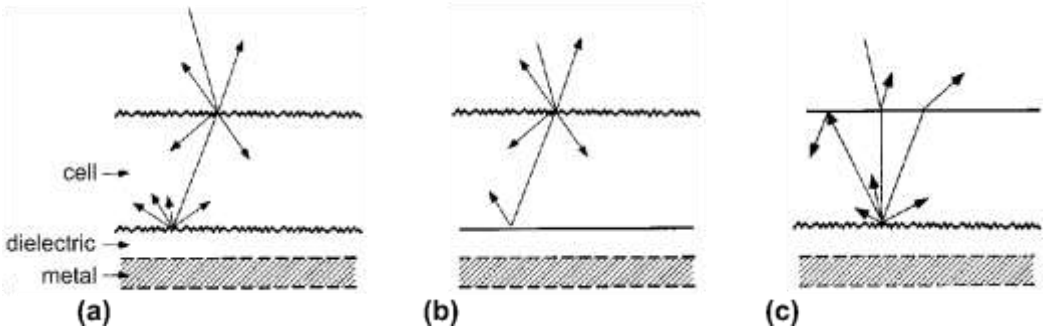

Figure 1.2-1: Three possible Lambertian texturing approaches. Taken from [79].

A Lambertian surface is a perfectly randomising surface that scatters light isotropically, which means that all reflected angles have the same probability. We consider incident light hitting a flat front surface as described in the case of Figure 1.2-1 (c). After reflection on the rear surface, if the ray strikes the front surface with an angle wider than the critical angle, it is internally reflected for another double pass within the cell. Only rays that are reflected within the escape cone come out of the cell.

1.2.1.2 Yablonovitch or Lambertian limit

We find the average path length due to Lambertian scattering $l_{sc}(\lambda)$ following Equation 1.2-2 [78], where a factor of 2 is related to the back mirror, another factor of 2 is related to the increased effective thickness of oblique rays. The n² term is due to the increased portion of light traveling outside the light cone with $n(\lambda)$ the refractive index of the absorbing material.

$$\overline{l_{sc}(\lambda)} = 4n(\lambda)^2 t$$

Equation 1.2-2: Average path length due to Lambertian scattering.

It is well known as the Yablonovitch or Lambertian limit and it represents a light path enhancement factor $F = 4n^2$ with respect to single-path absorption. Total absorptivity is expressed by Equation 1.2-3 [79].

$$Abs(\lambda) = \frac{1 - \exp(-4\alpha(\lambda)t)}{1 - (1 - \frac{1}{n(\lambda)^2})\exp(-4\alpha(\lambda)t)} \quad or \quad Abs(\lambda) = \frac{F\alpha(\lambda)t}{1 + F\alpha(\lambda)t} \quad for\ "low"\ \alpha(\lambda)t$$

Equation 1.2-3: Total absorptivity for a Lambertian texturing (left expression) simplified for weakly absorbing materials with low and intermediate values of the product $\alpha(\lambda)t$ (right expression) and F the light path enhancement factor.

The simplified expression is a good approximation in practice for weakly absorbing materials with low and intermediate values of the product "$\alpha(\lambda)t$".

1.2.2 Application to quantum-structured solar cells

In this part, we describe the application of light management to quantum-structured solar cells. First, we discuss the specificity of these materials in term of absorption, and then we introduce the use of cumulated resonant effects in the multi-resonant approach. Finally, we give examples of recent achievements.

1.2.2.1 Absorption for quantum structured materials

In Figure 1.2-2, we represent a slab of a quantum structured material with a Lambertian scatterer at the back. In the case of quantum structured IBSCs, we are focusing on enhancing light absorption in the subbandgap region of the high-energy material ($\lambda > \lambda_{high-energy}$). For this region, only quantum structures are absorbing the light, therefore the effective medium absorption coefficient for the total solar cell can be written as: $\alpha(\lambda) = \alpha_{quantum\ structures}(\lambda) \times t_{quantum\ structures}/t$.

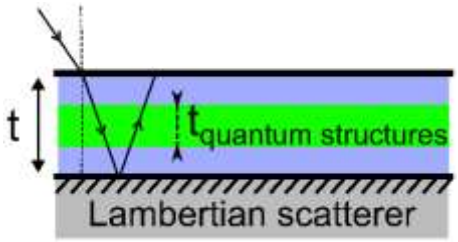

Figure 1.2-2: Schematic of Lambertian light-trapping for a quantum structured material of thickness *t* with quantum structured layer of thickness $t_{quantum\ structures}$

It means that in order to have maximum subbandgap light absorption, using a Lambertian scattering approach, we need to have: $t_{quantum\ structures} = t$. In other term, the part of the solar cell with no quantum structures need to be reduced at the minimum if we want to focus on helping subbandgap absorption. This might be obvious but in practice, it is generally not taken into consideration because solar cells are usually designed to maximize the generated current that is often more important for the high-energy bandgap region. However, if we strictly consider the IBSC equivalent circuit as represented in Figure 1.1-8, attention should be paid to the fact that the current generated by an IBSC should follow condition described by Equation 1.2-4.

$$J_{SC:\,VB-CB} = J_{SC:\,VB-IB} + J_{SC:\,IB-CB}$$

Equation 1.2-4: IBSC condition on current generation

In this sense, QD-IBSCs design should be made almost only with quantum structures. This conclusion is true for spectrally homogeneous light trapping. However, by using specific resonant effect, we are able to enhance only specific part of the spectral region, which is particularly interesting for subbandgap absorption by low absorbing quantum structures.

1.2.2.2 Multi-resonant approach using nanophotonics

We have seen that the Lambertian approach work in ray optics regime for relatively "thick" absorbers ($R >> \lambda$). The apparition of resonant mechanisms is usually considered for wave optics regime for dimensions of the same order as the wavelength ($R \sim \lambda$). In the case of PV application, solar spectrum wavelength range is roughly between 300 nm and 3 µm. Therefore, we see that nanophotonic objects can be used to induce resonant effects in solar cells of wavelength dimensions. In the wave-optics domain, a solar cell can support a great diversity of optical modes [80], [81].

The multi-resonant approach is achieved by juxtaposing different resonant mechanisms at different wavelengths. Collin's group at C2N laboratory has extensively studied this effect for PV application in different PV materials [81]–[84]. The basic idea is to maximize the number of resonant modes, and to optimize the absorption maxima at resonance wavelengths. Upon the penetration of light inside a PV layer, we want to excite optical modes whose energy remains trapped inside the material. These modes are often called guided or trap modes. It was originally proposed to combine vertical Fabry-Pérot resonances and guided modes in very thin solar cells with absorber thickness of hundred of nanometers [83].

In order to achieve light trapping and coupling to guided modes a typical structure with front or back nano-grating is used. The scattering, or diffractive, nanostructures bring the additional momentum required to couple bound modes to free space. Different PV groups in the world have studied this topic extensively [85]–[91]. The use of such structures offer a combination of resonant optical modes to enhance the light path for a certain spectral domain. We can make use of at least three different optical effects:

- Periodic resonances in the vertical direction as Fabry-Pérot (FP) modes or in the horizontal direction as waveguide modes by coupling incident light with a nanostructured optical grating.
- Localized Mie resonance induced by the geometry of a nanostructures.
- Near-field resonant effect for example due to plasmonic resonances.

In Figure 1.2-3, we reproduce a figure from [92], which illustrates the origin of the resonant effects in a front nanostructured solar cell with a metallic back mirror and an a front dielectric layer that acts as an anti-reflection coating. The numbers 1–4 label four distinct coupling mechanisms. In Figure 1.2-3b, simulated absorption is shown as a function of the illumination wavelength and angle of incidence for a 1-µm-thick c-Si cell with a light-trapping layer consisting of a periodic array of c-Si nanowires. The numbers 1–4 label four specific illumination wavelength-angle pairs at which the coupling mechanisms illustrated in Figure 1.2-3a are active. In Figure 1.2-3 c–f, a side views of the electric-field-intensity distribution inside the cell are represented for the four different illumination conditions (1–4) shown in Figure 1.2-3b. The Figure 1.2-3c, shows the excitation of a mixture of a hexapolar-symmetry Mie resonance in the nanowires with a guided resonance at λ = 880 nm and for normal incidence conditions. Figure 1.2-3d, shows the excitation of a low-quality-factor Fabry-Pérot resonance at λ = 1031 nm and 28° incident angle. Figure 1.2-3e shows the excitation of a guided resonance in the Si layer at λ = 946 nm and normal incidence. Finally, Figure 1.2-3f shows a

diffracted resonance by which a laterally propagating wave is excited in the light-trapping layer at λ = 1011 nm and normal incidence.

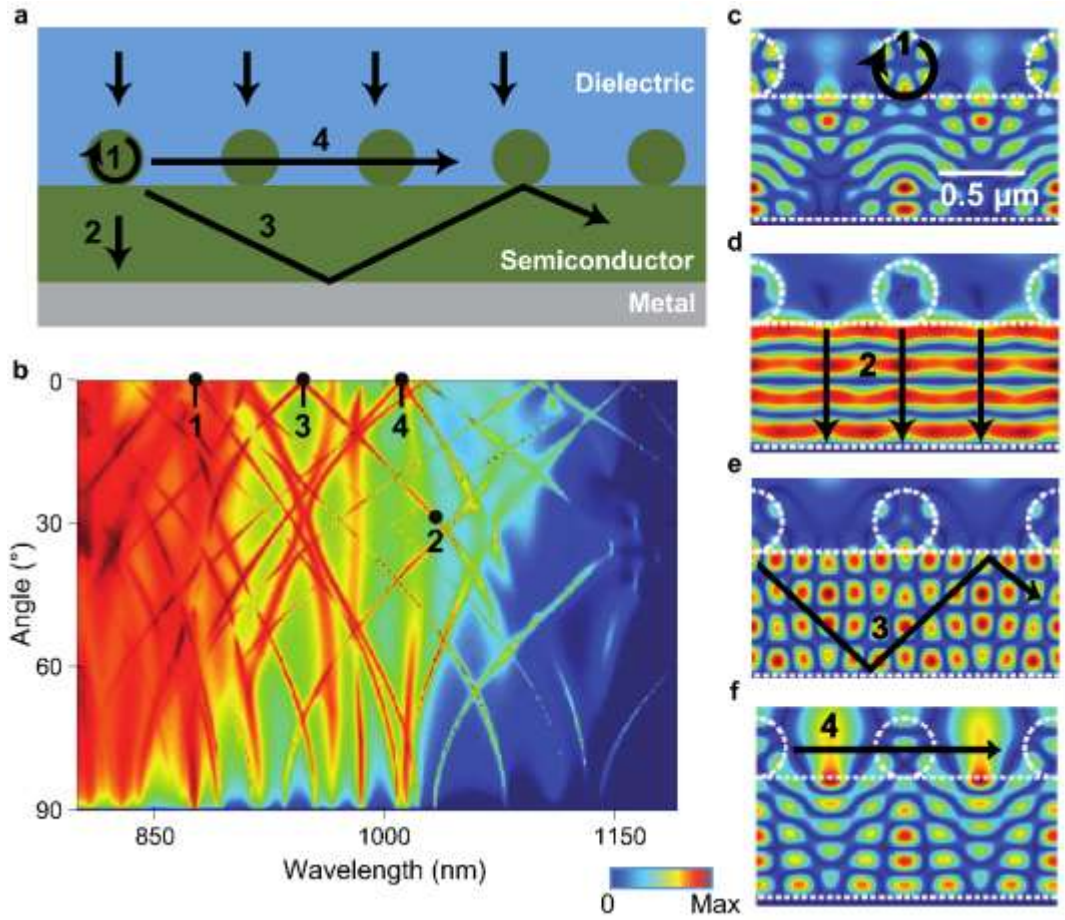

Figure 1.2-3: Absorption enhancement caused by the excitation of optical resonances in a thin PV cell. a, Schematic showing how various optical resonances supported by a model cell structure can be excited to enhance light absorption in the active semiconductor material (green). The numbers 1–4 label four distinct coupling mechanisms. b, Simulated absorption as a function of the illumination wavelength and angle of incidence for a 1-μm-thick c-Si cell with a light-trapping layer consisting of a periodic array of c-Si nanowires. The numbers 1–4 label four specific illumination wavelength-angle pairs at which the coupling mechanisms illustrated in a are active. c–f, Electric-field-intensity distribution inside the cell for the four different illumination conditions (1–4) shown in b. The dashed white lines outline the c-Si structure. c, λ = 880 nm, normal incidence, showing the excitation of a mixture of a Mie resonance with a guided resonance. d, λ = 1,031 nm, 28° angle of incidence, showing the excitation of a Fabry-Pérot resonance. e, λ = 946 nm, normal incidence, showing the excitation of a guided resonance in the Si layer. f, λ = 1,011 nm, normal incidence, showing a diffracted resonance by which a laterally propagating wave is excited in the light-trapping layer. Adapted from [92].

It is possible to assess the maximal light trapping enhancement due to the multi-resonant absorption approach with the help of the temporal coupled-mode theory that will be used in some part of this manuscript [80], [81]. Overall absorption is considered as a set of overlapping independent resonant optical modes in the critical coupling condition, for which the total absorption of the structure reaches 100% and radiative and non-radiative decay rates are perfectly balanced [82]. Its average value depends on the density of modes and resonance bandwidth of each mode. Considering the density of optical states (DOS) of bulk material, a light-trapping limit has been calculated as a function of absorber thickness by Collin's group [93]. In the literature, the use of nanophotonic structures that enhance the density of optical modes over a broadband range of wavelengths have

proven that a light-trapping enhancement ratio significantly beyond the conventional limit can be achieved [94]–[96].

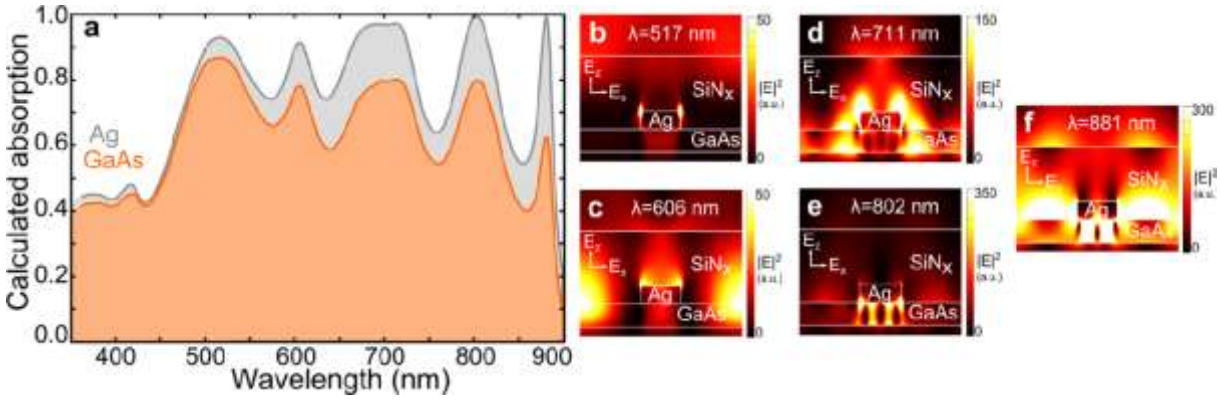

Figure 1.2-4: (a) Calculated absorption fraction in the GaAs layer (orange) and silver (top grid + back mirror; gray) at normal incidence. (b–f) Maps of the electric field intensity |E2| at λ = 517, 606, 711, 802, and 881 nm for an excitation at normal incidence. All the intensity maps have the same unit. Taken from [97].

In Figure 1.2-4, we present an example of broadband juxtaposition of multiple resonances for a design that consists in a metal-semiconductor-metal (MSM) structure. This design also called metal-insulator-metal (MIM) has been previously explored for new types of photodetectors [98] with the absorbing layer in-between a back silver mirror and a top metal layer nanopatterned as a 2D silver nanogrid as represented in Figure 1.2-5. The grid is embedded in a top dielectric layer made of 80 nm of silicon nitride (SiNx) with an ultrathin 25 nm-thick unintentionally doped GaAs layer as the absorber. The absorption in these structures has been calculated using rigorous coupled wave analysis (RCWA) calculations.

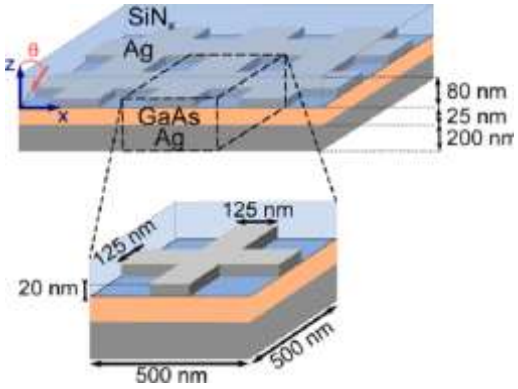

Figure 1.2-5: (Top) Schematic of an ultrathin MIM structure with a two-dimensional metal nanogrid. (Bottom) Schematic of the unit cell made of two crossed gratings: length = 500 nm, width = 125 nm, thickness = 20 nm. Taken from [97].

In Figure 1.2-4, we see that the coupling of the metal grid to the ultrathin GaAs layer and the metal mirror leads to a multiresonant absorption spectrum with five main absorption peaks at λ = 517, 606, 650–710, 802, and 881 nm. The total absorption is higher than 0.9 at each resonance wavelength in particular, for the long wavelength resonances (802 and 881 nm) where critical coupling condition is nearly fulfilled. As in Figure 1.2-3, electric field intensity maps allow to better identify resonant effects, however here we benefit from near-field resonant effect due to plasmonic resonances originating from the metallic interfaces. For example, we recognize a localized plasmonic resonance under the silver nanostructure for 802 nm. Coupling between SPPs at the two met-

al/semiconductor interfaces leads to an horizontal oscillation of the electric field with very high enhancement factors (>100) [97].

1.2.2.3 State of the art investigations

In order to perform light management in quantum structured solar cells, different approaches have been proposed using a simple epitaxial transfer on a metallic mirror [99]–[102], distributed Bragg reflectors [103], diffractive gratings with nanostructures [104]–[111] and near-field enhancement [112]–[114]. In this part first, we discuss recent numerical simulations of Lambertian light-trapping in QDSCs [115]. Then we focus on the work of McPheeters who calculated and fabricated ~800 nm-thin MQW solar cells and QDSCs transferred with a 2D metallic back grating [108].

i). Example of a numerical simulation of Lambertian light-trapping

In Figure 1.2-6, is shown recent numerical simulations of Lambertian light-trapping (LT) in QDSCs [115].

Layer	Thickness [nm]
cap layer, p^+ (10^{19} cm^{-3}) GaAs	20
FSF, p^+ (5×10^{18} cm^{-3}) $Al_{0.8}Ga_{0.2}As$	30
emitter, p^+ (10^{18} cm^{-3}) GaAs	200
QD region, i-GaAs	1000
base, n-GaAs (2×10^{17} cm^{-3})	1500
BSF, p^+ (5×10^{18} cm^{-3}) $Al_{0.2}Ga_{0.8}As$	50
buffer, n^+ (5×10^{18} cm^{-3}) GaAs	50
substrate, n^+ (5×10^{18} cm^{-3}) GaAs	300

Parameter definition	Value
Number of layers, N_L	20
QD density, N_{QD}, [cm^{-2}]	6×10^{10}
QD thickness, t_{QD}, [nm]	4
E_g^{WL}, E_g^{ES}, E_g^{GS}, [eV]	1.33, 1.22, 1.14
Peak optical absorption, α_{WL}, α_{ES}, α_{GS}, [cm^{-1}]	2×10^4, 1800, 800
$\tau_{n,cap}^{B\text{-}WL}$, $\tau_{n,cap}^{WL\text{-}ES}$, $\tau_{n,cap}^{ES\text{-}GS}$, [ps]	0.3, 1, 1
$\tau_{p,cap}^{B\text{-}WL}$, $\tau_{p,cap}^{WL\text{-}ES}$, $\tau_{p,cap}^{ES\text{-}GS}$, [ps]	0.1, 0.1, 0.1
$\Delta E_n^{B\text{-}WL}$, $\Delta E_n^{WL\text{-}ES}$, $\Delta E_n^{ES\text{-}GS}$, [meV]	63, 139, 70
$\Delta E_p^{B\text{-}WL}$, $\Delta E_p^{WL\text{-}ES}$, $\Delta E_p^{ES\text{-}GS}$, [meV]	28, 16, 16

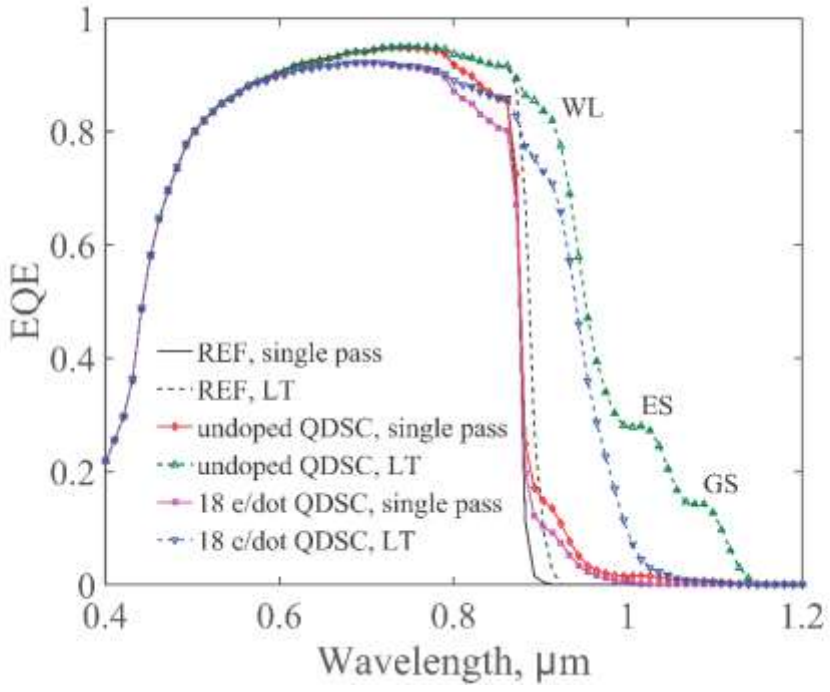

Figure 1.2-6: (Table left) Cell structure parameters. (Table right) QDs parameters. (bottom figure) EQE spectra of undoped reference cell, undoped QDSC, and directly doped 18 e/dot QDSC for single pass and Lambertian light-trapping configuration. Taken from [115].

A Jsc gain of 4.3 mA/cm² (+17%) is found and we see how the doping has a negative effect on the absorption because of the bandfilling that will be discussed in chapter 4.

ii). Example of an experimental realization of quantum structured solar cells with nanophotonics

In Figure 1.2-7, we summarized results from McPheeters work [108]. In Figure 1.2-7 (a), we see that he fabricated a cavity with SiO_2 anti-reflection coating (ARC) at the front and a back grating with SiO_2 and Pd metal as a reflector at the back. There are numerous types of solar cells with quantum structures based on the combination of GaAs/InGaAs: ('GaAs-p') *p-i-n* GaAs with planar metal backside; ('QW-p') quantum-well solar cell with planar metal backside; ('QD-p') quantum-dot-in-well solar cell with planar metal backside; and ('QD-g') quantum-dot-in-well solar cell with a backside diffraction grating. Overall for the subbandgap part of the spectrum (850-1250 nm), he finds average enhancement of about x4 due to the diffraction grating which is on the same level as his simulations. However, we notice that the level of spectral response for the QD-p (red) is about on the same level as the noise level that we see for a spectral response at 1500 nm which is far below QDs PL emission.

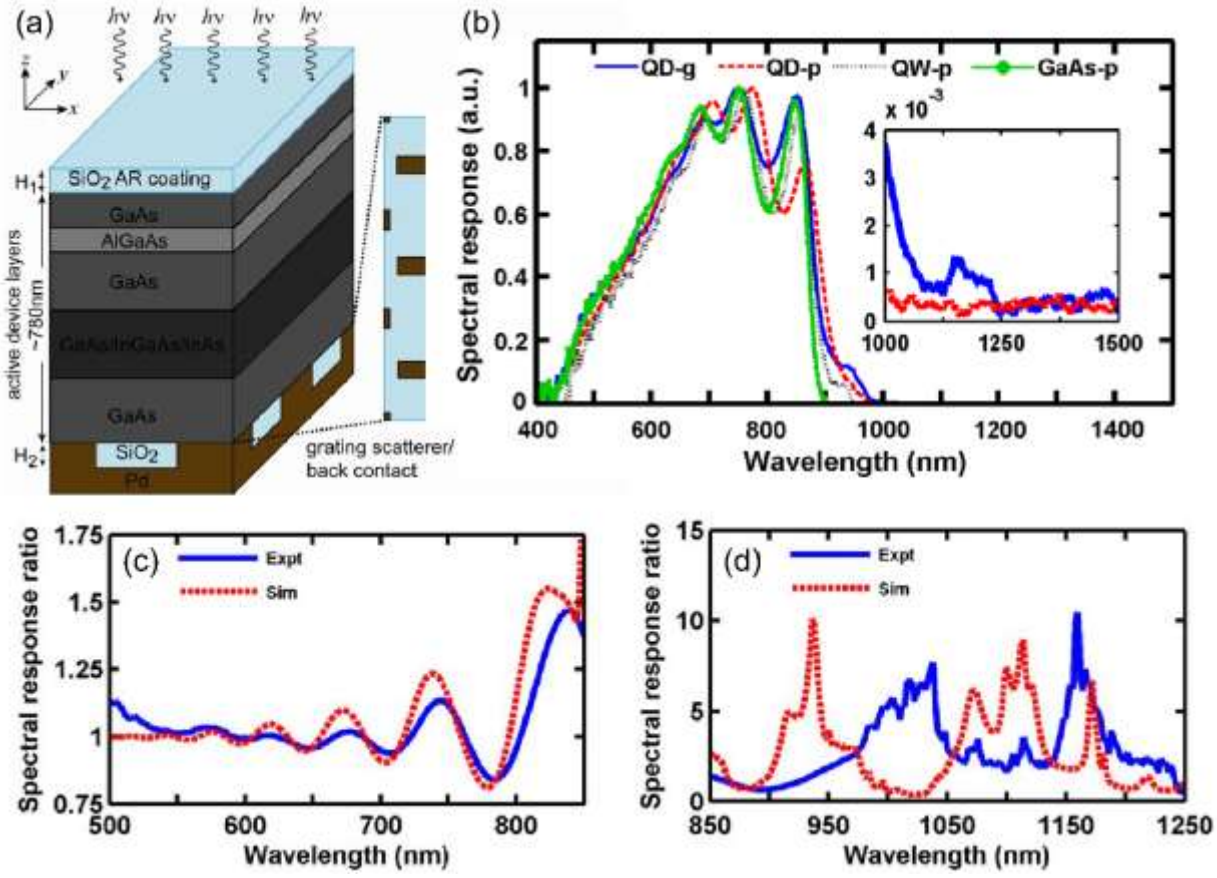

Figure 1.2-7: (a) Diagram of the simulated device, which is equivalent in semiconductor layer structure to the experimental quantum-well solar cell shown in figure 1, and, additionally, has a broadband, two-dimensional grating located on its rear with dimensions W1 = 184 nm, L1 = 474 nm, W2 = 168 nm, L2 = 356 nm, D1 = 900 nm, D2 = 1.13 µm. (b) Normalized spectral response of thin-film devices: ('GaAs-p') *p-i-n* GaAs with planar metal backside; ('QW-p') quantum-well solar cell with planar metal backside; ('QD-p') quantum-dot-in-well solar cell with planar metal backside; and ('QD-g') quantum-dot-in-well solar cell with a backside diffraction grating. Inset: the response of the grating-equipped and planar metal backside quantum-dot-in-well devices at wavelengths longer than the quantum-well absorption edge. Ratios of ('Expt') measured spectral response and ('Sim') simulated absorption in a thin-film quantum-dot-in-well solar cell to devices with planar metal backsides at wavelengths (c) shorter and (d) longer than the GaAs band edge, respectively.

From the analysis of these two papers, we understand that light management is still a new topic for quantum-structured solar cells and especially for QD solar cells. We see the potential gain for the cell and the limitation in term of subbandgap absorption. This aspect will be investigated in chapter 5 after careful investigation of our system in chapter 3 and 4.

Conclusion

In this chapter, we have introduced the topic, motivations and challenges of our work on high-efficiency photovoltaic concepts. We would like to summarize and underline some messages that we think are important for our study:

- Mass production of single-junction PV technologies with lower cost has enabled PV industry and market to bloom and become steady but it is now reaching a limit in efficiency. The future of PV will be in economically viable light-weight, flexible and high-efficiency solutions. The solution we propose to study rely on PV thin-films that can theoretically fulfill all these conditions but we need proof-of-concept experimental results to validate the theory and open the path for future investments.

- In PV, three improvement paths need to be followed when investigating a new solution: (1) control over the material fabrication and properties, (2) control over the device fabrication and characterization, and finally (3) the control over optical or light management. It is best to follow them in this order but practically they can be intricately linked. In the following chapters, we will present the research work that has been made to investigate our solution following this procedure: (1) chapter 3: fabrication and material properties, (2) chapter 2 and 4: device fabrication and characterization, and (3) chapter 2 and 5: implementation of light management and results.

- Our solution rely on three cornerstones: (1) quantum-structured materials, (2) high-efficiency concepts, and (3) multi-resonant light management solutions.

- We noticed that, for high-efficiency concepts like multi-exciton generation solar cells (MEG-SCs), hot carrier solar cells (HCSCs) or intermediate band solar cells (IBSCs), the main question is how we can retrieve the excess energy that is usually lost through three channels of loss: (i) carrier-carrier scattering (Auger effect, impact ionization), (ii) phonon emission (thermalization) or (iii) photon emission (intraband emission of a thermal photon). The intermediate band assisted hot carrier solar cell (IB-HCSC) concept seems to encompass all the high-efficiency concepts.

- We proposed to focus on quantum-structured materials because they seem to be good candidates to investigate IBSCs, HCSCs and eventually IB-HCSCs that will be discussed in chapter 4. We underlined the different challenges to fabricate quantum dot solar cells (QDSCs) that will be detailed in chapter 3 and especially the importance of balancing subbandgap generation with voltage preservation for IBSCs.

- Finally, we discussed the potential gain of using light management on quantum-structured materials: (i) primary to increase the J_{SC} contribution from subbangap absorption, (ii) secondary to fabricate more compact and more efficient devices, and (iii) third to investigate the effect on the intermediate band dynamic. We underlined the fact that in most case, QD-IBSCs design should be made almost only with quantum structures and we presented the main idea of multi-resonant light management strategy that we will use in our study (chapter 2 and 5).

Chapter 2 Fabrication and nanofabrication for quantum structured solar cells

In the study of new concepts for photovoltaics, we need stability and control of the fabrication steps. In the case of this study, we deal with nanostructures for electronic and photonic applications. In this chapter, we will discuss about the fabrication of the devices we use and we will focus especially on two important steps: the transfer process of semiconductor layers on a host substrate and the surface nanopatterning.

2.1 Sample fabrication

In this part, we detail the different steps that are necessary to fabricate the solar cells that are used in our study. First, we will discuss about the important parameters to take into consideration before the epitaxial growth. Then we will cover the main fabrication steps and finally some additive steps that are sometimes used to improve the device. A scheme of the protocol is detailed in Figure 2.1-1. It is a general simple method but we want to underline the fact that characterizations are necessary as milestones to monitor the evolution of the sample.

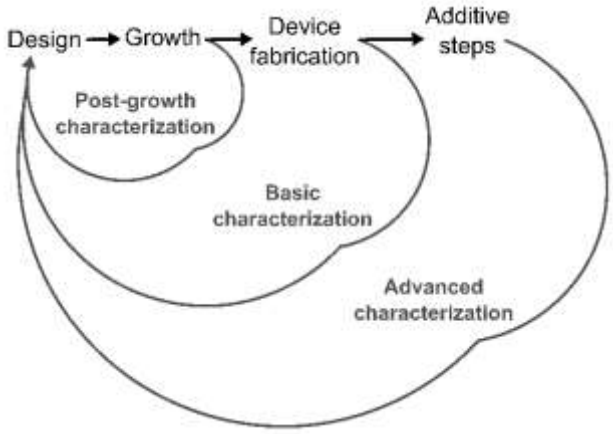

Figure 2.1-1: Sample fabrication protocol

2.1.1 Stacking design and growth

In our study, we wish to combine new concepts based on nanostructures for photovoltaic application. On the side of electronics, we want to use quantum nanostructured heterostructures that are implemented during the growth step. On the side of photonics, we want to use nanophotonic strategies that are usually implemented after the growth of the material. In both cases, we need to developp specific designs that are different from those employed in conventional solar cell.

2.1.1.1 Solar cell design

The principle of a solar cell is to harvest the optical power from the sun. The photon flux is converted into an electric current by absorption while the energy of photons is collected as an electrochemical potential that depends on the cell structure. The main goal is to separate and collect photogenerated electrons and holes before they recombine. To optimize the separation of the generated free carriers we differentiate electrons and holes using different strategies.

At least two types of strategies are often used: implementation of a junction and implementation of selective contacts.

i). Junction implementation

The implementation of a junction is usually thought as an upstream solution for the separation of carriers. The juxtaposition of two inversely doped semiconductors leads to the creation of a depletion region dedicated to carriers separation [116]. In a way, the *p-n* junction secures the carrier separation and enable to control the position where the electric field is important. It is the most used solution nowadays for PV applications. In some cases, like in most quantum-structured solar cells, the depletion region is increased by the insertion of a non intentionnaly doped layer also called intrinsic region *i*.

ii). Selective contacts implementation

On the other hand, implementation of selective contacts (or selective barriers) is a downstream solution to filter carriers before they are taken out of the cell. This solution is used especially for organic PV where it is more difficult to make use of high quality junctions. In the case of III-V semiconductors, selective barriers are often used to support the junction like in the case of front or back surface field (BSF) layers. These layers are especially usefull to decrease the probability of recombinations at sensitive spots such as metal or air interfaces with the semiconductor. The front surface field layer (FSF) is also called a window layer as it plays the same role as in a house letting the light through while maintaining a controled flow of energy inside.

In Figure 2.1-2, the energy band diagram scheme summarizes the typical strategies of solar cells that will be used in our study. The slope in the *n-i-p* junction highlights the effect of the electric field that is neglected in the other parts of the energy band diagram.

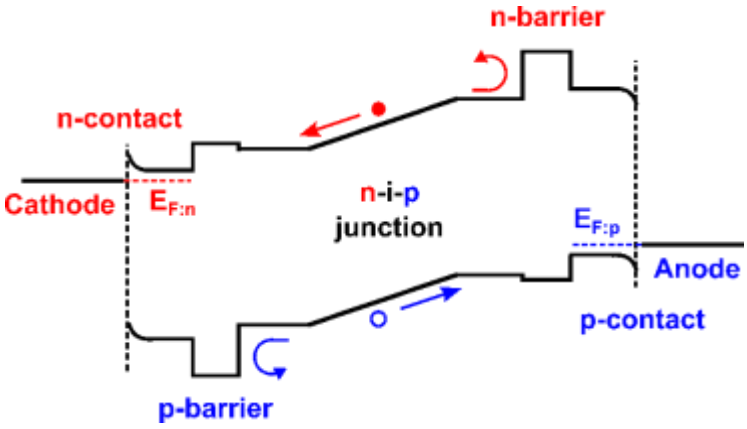

Figure 2.1-2: Energy band diagram scheme to summarize the strategies used for our solar cells. Electrons (red) and holes (blue) are separated by the combined action of *n-i-p* junction and selective contacts with barriers to enhance the filtering effect. $E_{F:n}$ and $E_{F:p}$ represent the quasi-Fermi level for population of electrons and holes. The difference is equal to the electrochemical potential of the cell.

Electrons (red) and holes (blue) are separated by the combined action of *n-i-p* junction and selective contacts with barriers to enhance the filtering effect. $E_{F:\,n}$ and $E_{F:\,p}$ represent the quasi-Fermi level for population of electrons and holes. The difference is equal to the electrochemical potential of the cell. We also want to point out that barriers and contacts are not always perfect. For example, in some cases, the *p*-barriers might also induce a small barrier for electrons. In addition, the contact with metal electrode has to be controlled in order to avoid the formation of a Schottky barrier, which can decrease the performance of the cell. For this reason, highly doped semiconductor layers (> 1e18 cm^{-3}) are usually used as contact layers.

2.1.1.2 Quantum-structured materials

For the development of novel PV concepts, we want to use quantum-nanostructured heterostructures that are especially important for bandgap engineering of the absorbing material. For III-V materials, the implementation of these nanostructures usually takes place during the growth step.

Two methods are considered in our study for growing III-V semiconductor thin films: molecular beam epitaxy (MBE) and metalorganic vapor phase epitaxy (MOVPE). The latter is also known as metalorganic chemical vapor deposition (MOCVD).

i). Quantum nanostructured heterostructures for bandgap engineering

The main goal behind the growth of quantum heterostructures is to confine the electrical wave and trigger new properties inside the absorbing material. The difficulty is to obtain a monolayer precision with the same interface quality as in typical heterostructures. Confinement can be implemented in:

- One-direction, as it is the case for quantum wells (QWs).
- Two-direction, as it is the case for quantum wires (QWRs).
- Three-direction, as it is the case for quantum dots (QDs).

Usually the confining material with the highest bandgap energy is called the “barrier” for QWs and “host” material in the case of QDs.

ii). Multi-quantum well layers grown by MOCVD

In the framework of NextPV collaboration with RCAST, we were able to work with multi-quantum well (MQW) layers grown by MOCVD in Sugiyama Laboratory [71], [74], [117], [118]. A special care was taken to balance the strain induced by wells that have some lattice mismatch with GaAs. In Figure 2.1-3, we detail the basic scheme of the QW solar cell structure. The quantum-nanostructured zone is sandwiched inside the *n-i-p* junction, the well material is $In_{0.18}Ga_{0.82}As$ and strain compensation barriers are made of $GaAs_{0.78}P_{0.22}$. Two excitonic energy levels are shown for electrons (red) and holes (blue).

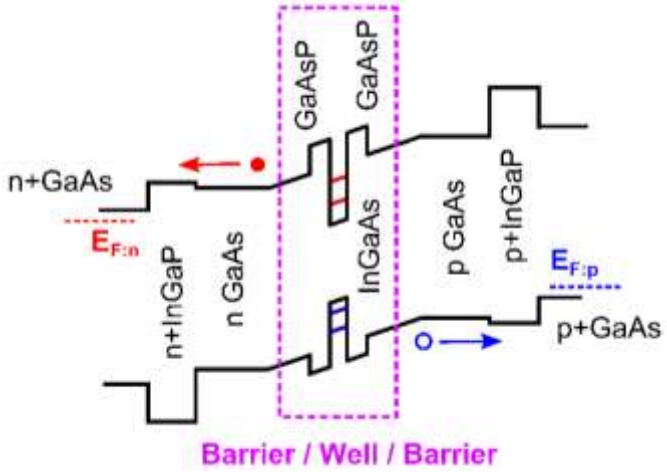

Figure 2.1-3: Energy band diagram of a QW solar cell in our study. The band structure is based on GaAs with window and BSF layers in InGaP. Well material is $In_{0.18}Ga_{0.82}As$ and strain compensation barriers are made of $GaAs_{0.78}P_{0.22}$. Two excitonic energy levels are shown for electrons (red) and holes (blue).

Such system offers a first step to apprehend the physics of quantum-structured solar cell as discussed in the first chapter with the possibility of absorbing subbandgap photons in QW levels. They are well-controlled and less complex than QDs solar cells.

iii). Multi-stacked quantum dot layers grown by MBE

We were also able to work with multi-stacked QD layers grown by MBE in Okada Laboratory [22], [46], [50]. In theory, QDs have a higher potential for the development of novel concepts because they offer a higher confinement and more versatility. However, they are also more challenging than QWs both in terms of fabrication and in terms of physical interpretation. In the framework of a French-Japanese exchange supported by the Japanese Ministry of Education, Culture, Sports, Science and Technology (MEXT), we were able to closely investigate QDs solar cells grown in Okada Laboratory. Chapter 3 is dedicated to the description of such system.

We used multi-quantum well (MQW) solar cells as a first system because the fabrication was better controlled and it was easier to understand the effect of light management strategies, as it will be discussed in chapter 5. The QD system was investigated to highlight the potential of quantum-structured solar cells in the realization of novel concepts especially for example in the discussion of intermediate band assisted hot carrier solar cell (IB-HCSC) in chapter 4.

2.1.1.3 Light management constraint on thickness and epitaxial transfer

In order to achieve light management in quantum-structured solar cells, we decided to focus on the multi-resonant approach discussed earlier using nanophotonics. In this approach, we wish to use a combination of resonant optical modes to enhance the light path for a certain spectral domain. We can make use of at least four different optical effects:

- Fabry-Pérot (FP) resonances corresponding to round-trips of light between the front and back surface of the cell.
- Guided mode resonances induced by periodical nanopatterns allowing incident light to couple to waveguide modes.
- Localized Mie resonance induced by the geometry of nanostructures.
- Near-field resonant effect (plasmonic resonances) in metallic nanostructures.

i). Thin FP cavity as a first step

For subwavelength thicknesses, the vertical confinement can be properly tuned to induce broad resonances in the structure thanks to FP vertical cavity. Afterwards, other resonant effects can be added by implementing dielectric or metallic nanostructures. The addition of different resonant effects contribute to the realization of a multi-resonant light management strategy.

Accordingly, a special care has to be taken to design, control and check the thickness of the layer stacking in the PV device in order to tune FP resonances in the spectral range of interest. In our study, we worked with samples having a FP cavity thickness below or equal to 500 nm. The constraint of having to work with very thin films is another difficulty for the fabrication of our device. We need precise control on the growth and fabrication processes.

ii). Back mirror implementation

In Figure 2.1-4, we summarize two different ways of implementing a back mirror for solar cells by epitaxial growth or by epitaxial transfer. In both cases, we need to use a "target layer" that is grown between the substrate and PV active layers.

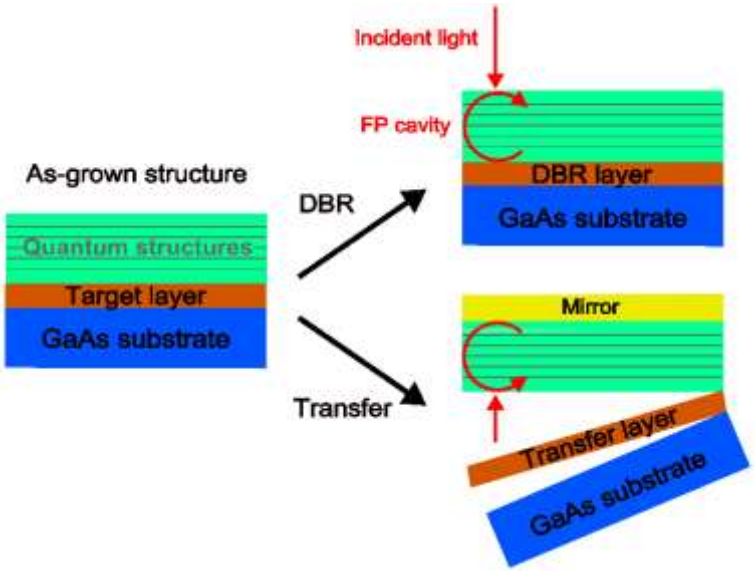

Figure 2.1-4: Description of two methods to implement a back mirror on quantum-structured solar cells using a target layer positioned between the substrate and PV active layers. In the first method, the target layer is a grown DBR acting as an internal back mirror creating a FP cavity in the PV active layers. The fabrication of solar cells is on the front side of the device. In the second method, the target layer is a transfer layer that enables the removal of the substrate. It becomes possible to deposit a mirror on the front surface to create a FP cavity for the PV active layers and fabricate solar cells from the rear side of the sample.

In the first method, the target layer is a grown distributed Bragg reflector (DBR) acting as an internal back mirror. It is a structure formed from multiple layers of alternating materials with varying refractive index. The DBR creates a FP cavity between the PV active layers and the top interface and enables the fabrication of solar cells from the front side of the device. In the case of GaAs-based III-V semiconductors, DBR are often made by alternating growth of $Al_xGa_{1-x}As$ layers with different concentrations of Aluminium. This path has been thoroughly investigated by the Blackett Laboratory for light management in MQWs [119], [103], [120].

In the second method, the target layer is a transfer layer that enables the removal of the substrate and keeps the PV active layers intact. It becomes possible to deposit a mirror on the front surface to create a FP cavity for the PV active layers and fabricate solar cells from the rear side of the sample upon substrate removal.

During our study, we used the epitaxial transfer strategy and explored two ways of achieving epitaxial transfer that will be detailed next. Anyhow, if the transfer step is a success, the fabrication of solar cells will be more or less the same. We will discuss it now.

2.1.2 Device fabrication

After the growth of the adequate structure, we follow the protocol detailed in Figure 2.1-1. If the post-growth characterizations are satisfactory, we can move on to the fabrication of the device starting with wafer cutting. In our study, we usually worked with samples taken from 2 inches wafer in the case of MQWs by MOCVD and 3 inches wafer for QDs solar cells grown by MBE. Samples were usually cut manually using a diamond scriber to graze the sample and then using a needle as a lever to cleave. For device fabrication, sample size were usually chosen at maximum around 1.5 x 1.5 cm² and at minimum around 0.7 x 0.7 cm² depending on which kind of mask were chosen for micro-patterning and in order to create dozens of solar cells on each sample. In Figure 2.1-5, we summarize the main fabrication processes that are used to fabricate the device. UV-lithography, metal deposition, lift-off and chemical etching processes are often combined to contribute at each steps.

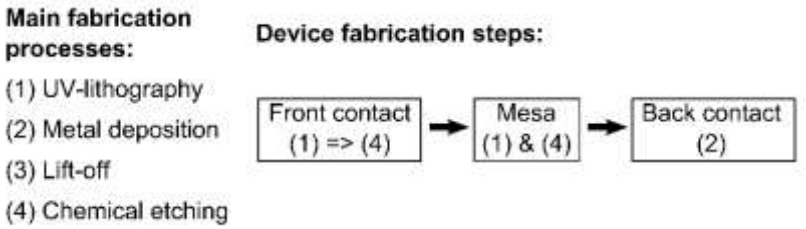

Figure 2.1-5: Main fabrication processes and device fabrication steps

In the case of the "back contact" step, the simplest is to deposit metal directly on the rear side of the wafer. In some cases, we have to fetch the back contact layer from the front side. Therefore, we need to combine mesa step in order to etch the epitaxial layers and reach the contact layer. In the next paragraphs, we detail the fabrication processes that are used. As an example, a detailed process for a simple as-grown (non-transferred) solar cell is described in appendice ***A-1***.

2.1.2.1 Micro-patterning

Combining UV-lithography, deposition techniques, lift-off and etching is essential to control the fabrication of patterns at a micrometer level.

i). UV-lithography process

The UV-lithography process has at least four steps:

- Resin spin-coating
- Thermal curing
- UV insolation with a mask
- Chemical development

In our study, three different UV-machines were used but they mostly function the same way. In Figure 2.1-6, we present an MJB4 machine with a microscope for alignement and a chrome mask for micro-patterning. Over all, every steps need to be precisely controlled and sometimes has to be adjusted when using a new mask.

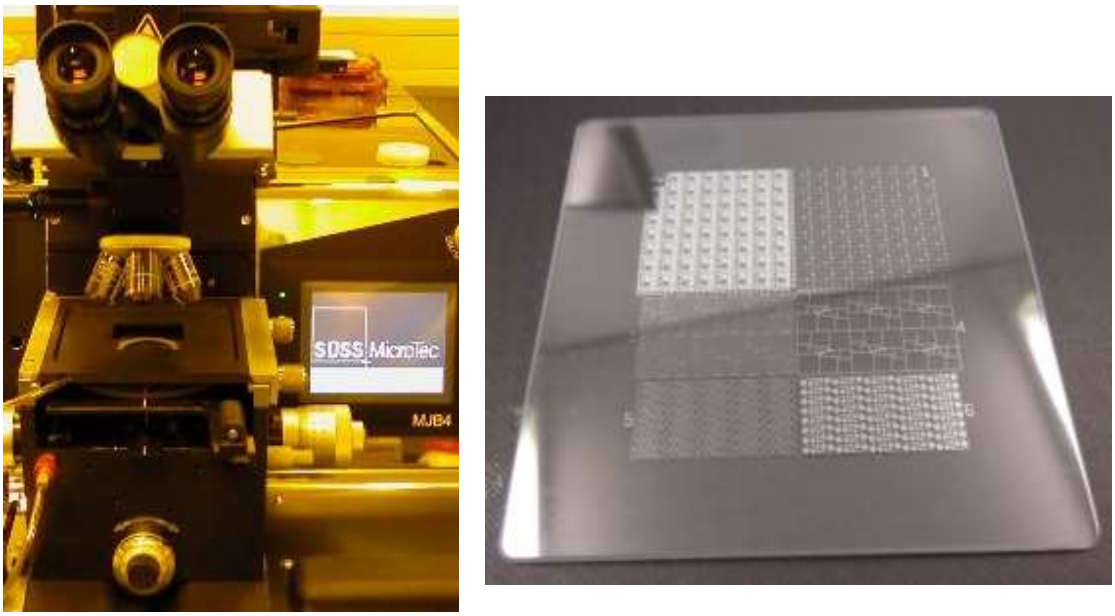

Figure 2.1-6: UV-lithography MJB4 machine with a microscope for alignment (left) and chrome mask (right) to design solar cells. For the round-shaped solar cells, pattern #5 is used in the front contact step and pattern #6 for mesa fabrication.

In our study, we used different masks dedicated to the fabrication of our solar cells but also for testing samples dedicated to other purposes (e.g. chemical etching tests, transmission line measurement tests, etc). For the fabrication of the solar cells we used two different masks. The one for MQWs sample is presented in Figure 2.1-6 with annular contacts (#5) and round-shaped mesa (#6). The typical diameter size vary from 150 µm to 1 mm. The width of the contact is around 70 µm for the largest solar cells which makes it almost impossible to contact by eyes and usually necessitates the use of a particular setup with a microscope and microprobing.

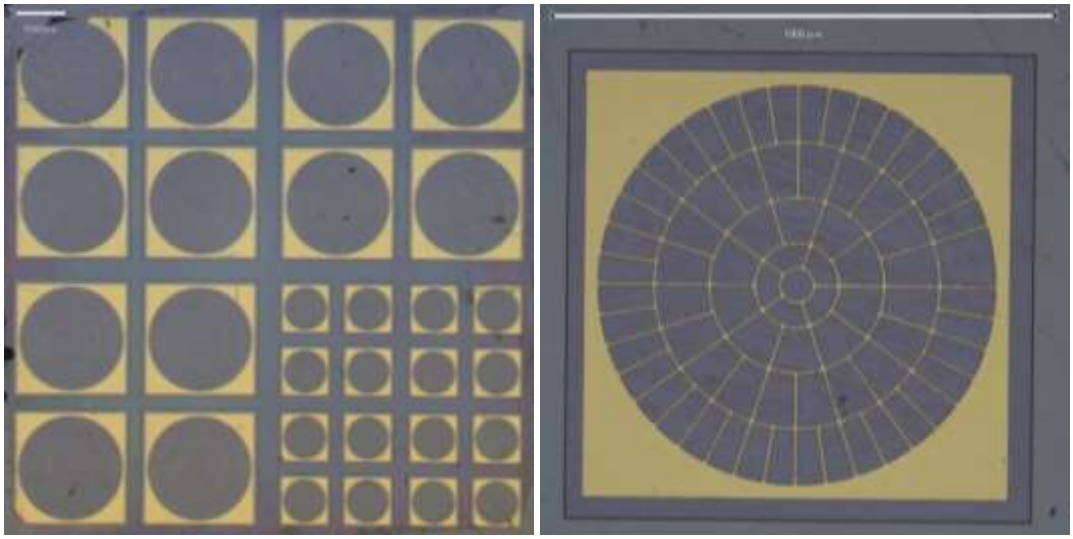

Figure 2.1-7: Photos of a typical 1 cm² sample with QDSCs (left) and zoom on a 1 mm² small cell with inner grid optimized for solar concentration and 15% shading ratio. White bar scale represents 1 mm.

For QDSCs, we fabricated solar cells as shown in Figure 2.1-7 with median size and small solar cells. We usually study the 1x1 mm² small diodes as they are more robust to our fabrication process especially in the case of transferred sample with a back mirror. Such small diodes have a 150 µm contact pad which is large enough for contacting by eyes with spring-probe. We notice small damages at the surface of the contact but no degradation of the electrical properties.

ii). Metal deposition and lift-off

For metal deposition, we used three different types of machines: sputtering, thermal evaporation and electron-beam evaporation. We notice that the thermal evaporation machine we used could heat our samples up to 200°C, which damaged a serie of our transferred sample. The adhesion of metallic gold mirror on semiconductor surface was always checked (e.g. using commercial Kapton® tape) and we tried different techniques to enhance such adhesion. The best one we could find was to use a 5-10 minutes deoxidation bath with 37%-HCl commercial solution diluted at 20% in deionized water just before putting our samples in the vacuum chamber.

After metal deposition, we used a lift-off process as described in Figure 2.1-8. We used acetone to dissolve AZ5214 resist.

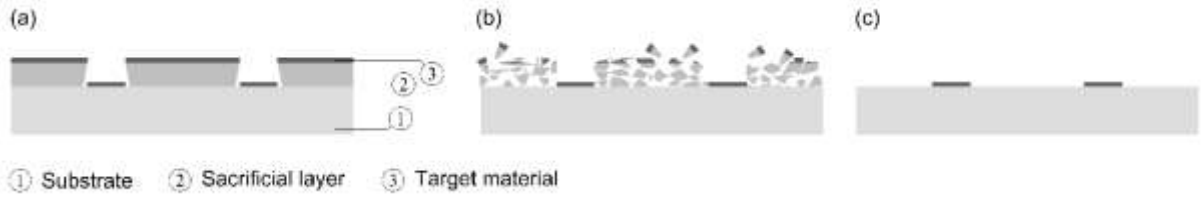

Figure 2.1-8: Lift-off general process for patterning of a target material on a substrate with the use of a sacrificial layer. In our case, after the metal has been deposited (a), the acetone bath will dissolve the remaining resist entering from the sides (b) and then only the metal remains on the surface (c). Adapted from Wikipedia.

iii). Chemical etching

Chemical etching is especially important for mesa step to isolate solar cells from each other. The "mesa" term refers to the geographical mesa in some deserted area and it is illustrated in Figure 2.1-9 by the depiction of an unsuccessful and succesful mesa.

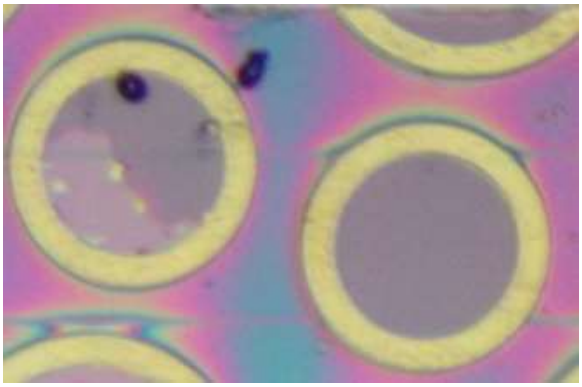

Figure 2.1-9: Photos of unsuccessful and successful resist protection for mesa etching. In this sample, the chemical etching is non-selective and is stopped in the intrinsic zone of the *nip* junction. This sample has been transferred on a gold mirror. Color change is due to FP interferences and indicates different etched thicknesses due to inhomogeneous etching of the chemical solution.

There are two types of chemical solutions: selective and non-selective. By definition, the selective etching solution only attacks some type of material and stops at the interface with other. For example, in the case of MQW samples the interface between GaAs and InGaP material enables the selective etching of contact layers after deposition of metal contact. A non-selective solution in contrary is blind and can prove to be useful in the case of etching difficult interfaces for example. In Table 2.1-1, we detail the main chemical solutions that were used or adapted from the literature [121]–[123].

Table 2.1-1: Main etching solutions that were used for the fabrication of our solar cells

Composition	Etched materials	Etch stop	Etching speed	Purpose
$H_2O_2/H_3PO_4/H_20$ (1/3/80)	GaAs and AlGaAs	InGaP	50 nm/min	Precise etching
Citric acid based	GaAs and $Al_{x<0.35}GaAs$	$Al_{x>0.35}GaAs$	300 nm/min	Long etching
$NH_3/H_2O_2/H_20$ (1/1/2)	GaAs and $Al_{x<0.45}GaAs$	$Al_{x>0.45}GaAs$	> 3 µm/min	Long etching
37%-HCl non diluted	InGaP and $Al_{x>0.45}GaAs$	GaAs and $Al_{x<0.45}GaAs$	> 1 µm/min	Flash etching
HF solution	$Al_{x>0.45}GaAs$, TiO_2, SiO_2	GaAs and $Al_{x<0.45}GaAs$	> 1 µm/min	Flash etching
Bromure based	All	No	> 1 µm/min	Flash etching

We will see in chapter 3.4.2.2 that the depositon of dielectric layer, the use of UV-lithography and dry etching (for example using reactive ion etching) can also lead to micro-patterning.

2.1.2.2 Control characterization tools

During the fabrication process, the use of characterization tools is important to control or even adapt the process. We list different techniques that were used all along our study.

i). Microscope and visual observation

It is an essential tool to evaluate directly and quickly the impact of a process on the sample. It is also important to notice every little things happening during each steps. For example bubbles during chemical etching, melting of metal source during thermal evaporation, resist thermal or UV curing, etc.

ii). Profilometer analysis

The mechanical profilometer enables to know the vertical profile of a surface. By repeating measurements at a precise location on the sample, the accuracy can be of about 10 nm.

iii). Reflectometer analysis

We used it in order to have a more precise idea of the thickness of the layer stacking for a transferred cell on a mirror. It is a very accurate technique but some assumptions are needed for the fitting. More details on reflectometry fitting will be given in chapter 3.4.2.2.

iv). SEM analysis

Finally, scanning electron microscope (SEM) offers a nanometer resolution in vertical and horizontal directions as illustrated in Figure 2.1-10.

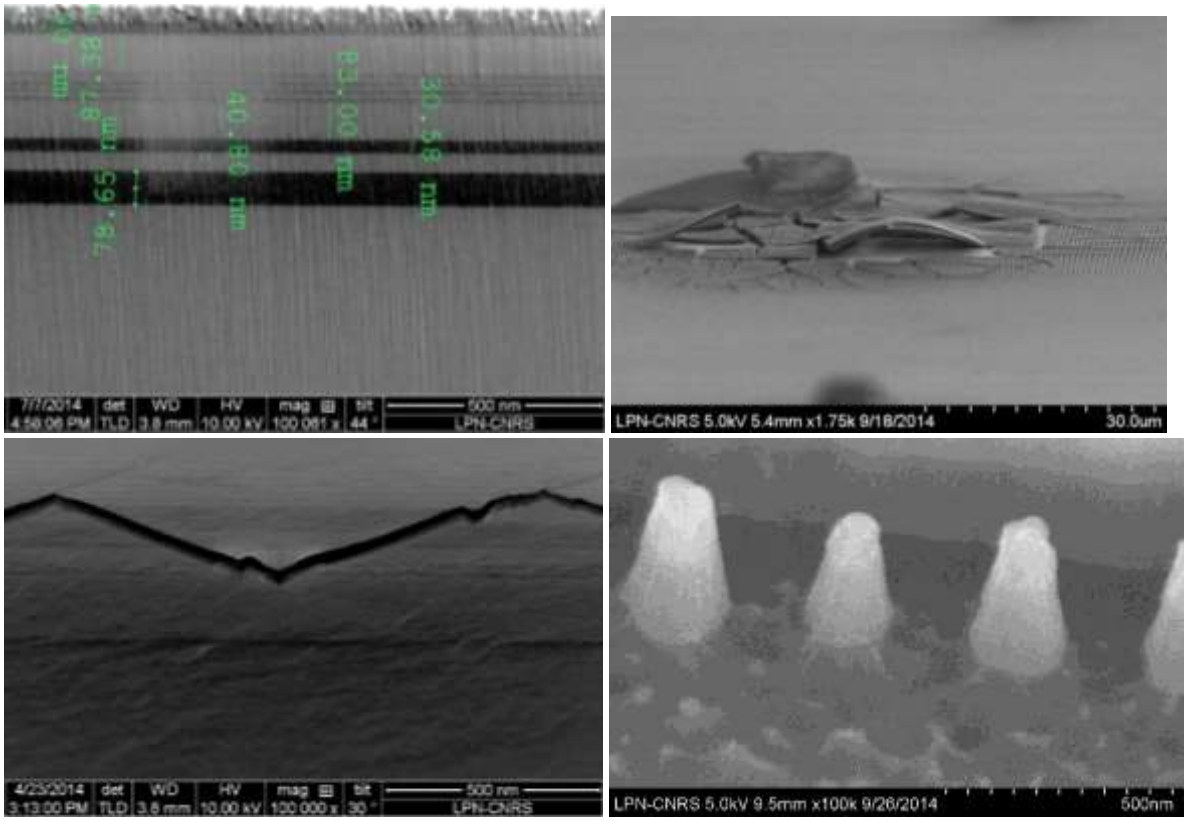

Figure 2.1-10: SEM images for different purposes. Top left shows the cross-section of a MQW solar cell stacking layers from the side. Top right show cracks due to uncontrolled strains in a patterned dielectric front layer. Bottom left shows quantum dot solar cell (QDSC) stacks with a crack attributed to uncontrolled strains at the position of the etch stop layer. Bottom right show TiO_2 nanocones for front patterning.

It can be used as a way to check layer stacking from the side of a sample as we show for a MQWs solar cell in Figure 2.1-10 top left. It can also be used to better understand a problem as in the case of cracks due to uncontrolled strain (top right and bottom left). Finally, it enables to assess the dimensions of nanopatterned structure (bottom right).

2.1.3 Additional processes

After fabrication of the samples, additional processes can be used to optimize the efficiency of our solar cells. These additional processes have the same problematic as other processes, we need to adapt recipes to find optimal parameters.

2.1.3.1 Rapid thermal annealing

Rapid thermal annealing (RTA) is used as a heat treatment for example in order to activate dopants, change interfaces, densify deposited films or change states of grown films. The annealing duration can range from a few seconds to several minutes. In our case, the RTA is made by an oven with lamp-based heating under reduced pressure with an argon-hydrogen flow. Heating results from the temperature conduction to graphite sample holder and protecting cap, which absorb the lamps radiation.

During the course of our work we tested RTA to try to get better ohmic contacts. However, we did not obtain any enhancement and even in some cases, we noticed a decrease in the performance of our cells. This decrease was attributed to defaults induced by metallic atom diffusion with heat. The

metal diffusion length is thought to be non-negligible for our thin junctions. The RTA process is a difficulty that needs to be considered especially for solar cells transferred on a metallic mirror. The increase in temperature can have an effect on the interdiffusion of metal atoms in the semiconductor and induces defects or even be an issue for the adhesion of the epitaxial layers on the supporting substrate.

For simplicity, we decided to stop using RTA for all of our samples (non-transferred and transferred). For 1-sun or low concentration PV irradiation conditions, annealing is thought to be unnecessary if the doping level of contact layers is high enough.

2.1.3.2 Anti-reflection coating

The goal of anti-reflection coating (ARC) is to increase the coupling between the incident light and the absorbing layers and therefore reduce the reflection. Many coatings consist of transparent thin film structures with alternating layers of contrasting refractive index. In our study, we used three different types of machines to deposit SiO_2, SiN_x and TiO_2 layers: sputtering, e-beam evaporation and ion beam assisted deposition (IBAD). These deposition methods imply different temperatures but also different qualities for the deposited material or surface. As we showed in Figure 2.1-10 top right, the deposition of layers can induce strains and even damage the solar cell.

2.1.3.3 Wire-bonding

In the case of a collaboration, laboratories do not all have the same setup for characterizing solar cells sample. For electrical characterization, wire bonding can help to facilitate the connection and use of a sample. We used three different machines with ball bonding technique where the wire is attached using a combination of downward pressure, ultrasonic energy and heat. For non-transferred samples, this technique was well-controled. However, in the case of transferred solar cells even after optimization of different parameters we found a success ratio less than one out of five. We consider the failure is because of the very thin transferred layers. Another way of connecting wires to the cell was attempted with epitaxy glue. However, after the solidification, the glue seems to induce strain that also damage the very thin layers.

Finally, we consider that wire-bonding needs to be better optimized and should be reduced to its minimum use. Therefore, we advice that during the fabrication metal contacts should be made large enough so that it is not a limitation for the characterization. We reckon that a 200 µm metal pad is large enough for spring probing by eyes and can be easily found in many laboratories.

2.2 Epitaxial transfer processes

In order to implement light management strategies, we choose to use FP-based strategies with a back mirror. We consider to use transfer process strategies instead of an internal grown DBR. The practical reasons are because DBR takes time to be grown and necessitates a particular strain-balance control. The growth of quantum structures and especially QDs growth is very time consuming and also induces strain in the epitaxial layers. There is also an industrial reason. Optimized transfer process can be cost effective especially if the substrate can be reused for a few more growths.

In our study, we investigated two different transfer methods. In both methods, we use selective chemical etching to separate the substrate from the PV active layers. In the first method, the transfer layer is used as an etch stop layer during the chemical etching of the substrate as described in [99]. In the second method, it is used as a sacrificial layer etched in order to lift-off the active layers without substrate etching as in [100].

2.2.1 Etch stop layer technique

This method has been developed and has proven to work relatively well for PV application in the French PV CNRS collaboration [82]. First, we describe the basic principle to make use of this technique and we discuss about the main obstacles and difficulties that we had to face. As an example, a detailed protocol for the etch-stop layer transfer process is shown in appendice ***A-2*** including the fabrication of back contacts.

2.2.1.1 Principle

In Figure 2.2-1, we summarize the main steps necessary for the epitaxial transfer technique with an etch stop layer. First, during the growth step, an etch stop layer is grown and positioned in-between the GaAs substrate and the PV active layers with quantum structures. For MQWs solar cells the etch stop layer is a 50 nm InGaP layer while in the case of QDSCs it is an Al_xGaAs whose Al composition and thickness had to be optimized. Second, during the back mirror step, there are two phases. Back contacts (not depicted in this figure) are made on the front surface following the main fabrication steps detailed in Figure 2.1-5. Afterwards, a gold layer ≥ 200 nm is deposited. Third, during the bonding step on a host substrate, a UV-sensitive resin (ORMOSTAMP) is spin-coated on the gold mirror surface and then bonded to a 1 mm soda-lime glass substrate by UV curing during 20 minutes. Fourth, during the wafer substrate removal step, we use a selective chemical attack of GaAs substrate followed by a selective chemical attack of the etch stop layer.

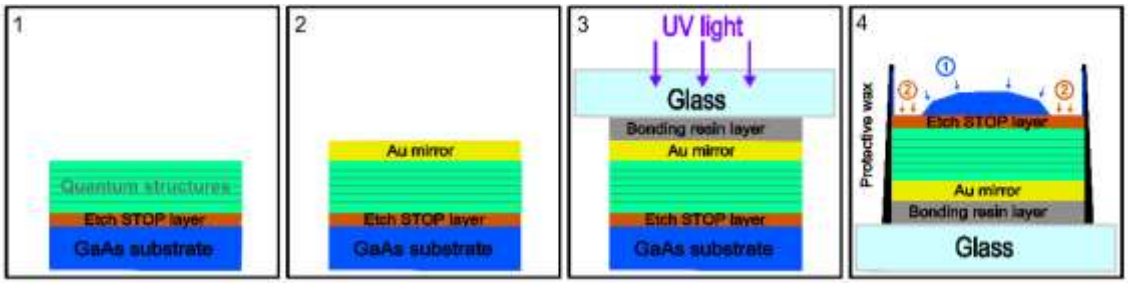

Figure 2.2-1: Schematic of epitaxial transfer technique with an etch stop layer. (1) Growth step: etch stop layer is grown and positioned in-between GaAs substrate and the PV active layers with quantum structures. (2) Back mirror step: contact fabrication is made on the front surface by gold deposition. (3) Support bonding: UV-sensitive resin is spin-coated on the gold mirror surface and bonded to a 1 mm glass substrate by UV curing. (4) Wafer substrate removal: 1/. Selective chemical etching of the GaAs substrate followed by 2/. Selective chemical etching of the etch stop layer.

All steps are equally important but it is usually during the fourth step that we can judge of the success of the transfer process which is why this fabrication process is delicate and time-consuming. In Figure 2.2-2, we show a comparison of successful non-transferred and transferred QDSCs. The transferred sample is cut smaller to save material because in this case the process was only optimized for small diodes because of fabrication issues that we are going to discuss.

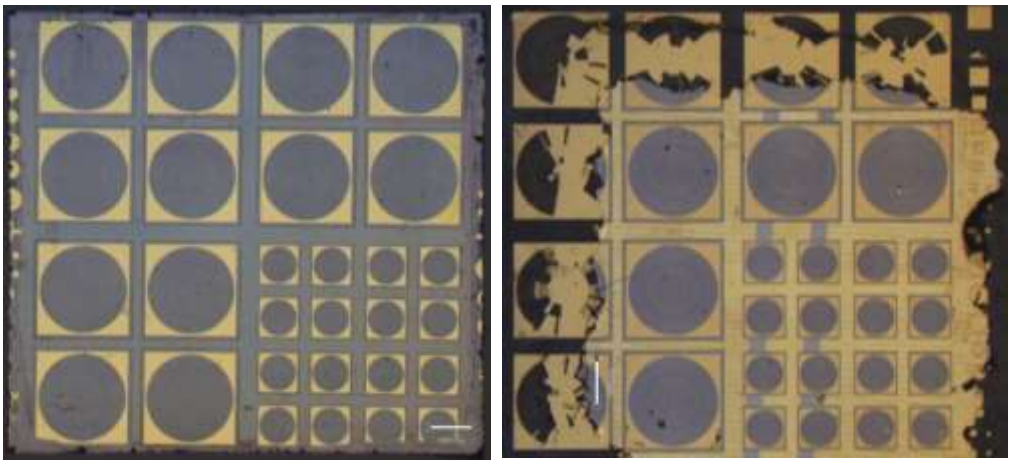

Figure 2.2-2: Comparison of non-transferred (left) and transferred (right) samples with QDSCs. The transferred sample was cut smaller on purpose to save material. We can see the back mirror and back contacts with small lines (10 µm-thick grid) and large bands (300 µm-thick busbars) of remaining GaAs contact layer.

2.2.1.2 Difficulties

In the development of transferred MQW solar cells, Sugiyama laboratory had already worked on an optimized epitaxial transfer process therefore we only had to follow and adapt the same recipe in the French laboratory. However, for QDSCs, the path was more complicated. First, we noticed that in the case of MBE growth from Okada laboratory, the $NH_3/H_2O_2/H_20$ (1/1/2) solution presented in Table 2.1-1, is also etching the AlAs etch stop layer while it is not the case for MOVPE growth from Sugiyama laboratory. Therefore, we used a citric acid based solution with a slow etching time as in [99], [124]. Overall, the duration of the substrate removal step became four times longer but we were able to process four samples at the same time so overall this long time did not weight too much on our fabrication process. Other issues had a more damageable impact.

<u>i). Strains in the epitaxial layers</u>

Strain related problems were found in Okd-1 and Okd-4 growths, as detailed in Table 3.2-1. For Okd-1, we used a 50 nm-thick AlAs etch stop layer. However, we noticed cracks near the etch stop layer as shown in Figure 2.1-10 bottom left SEM image. It resulted in the lift-off of the etch stop layer along with the GaAs contact layer that is etched by the chemical solution used for substrate removal as shown in Figure 2.2-3. The etching stops on the $Al_{0.8}GaAs$ window layer (yellow-white part).

For Okd-1, replacing AlAs etch stop layer by an $Al_{0.8}GaAs$ etch stop layer seemed to solve the cracks problems in the etch stop layer.

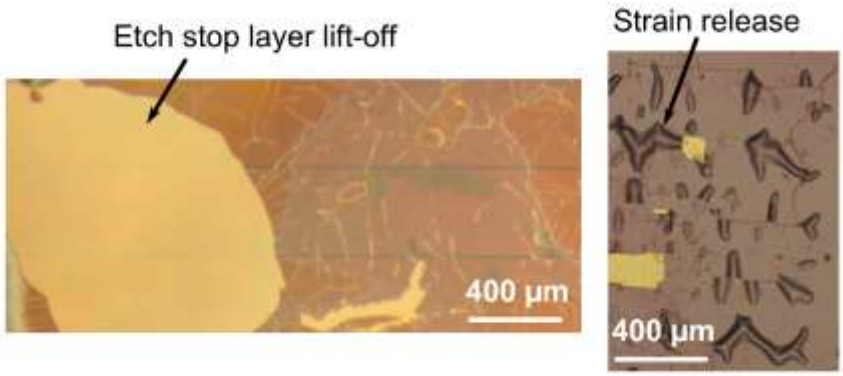

Figure 2.2-3: Illustration of strain problems. For Okd-1 (left), cracks in AlAs etch stop layer induces the layer lift-off with GaAs contact layer. For Okd-4 (right), substrate removal induce strain release that is too strong for the bonding glue.

For Okd-4 the problem was a bit different. The growth of a 3 µm thick epitaxial layer with many QDs layers resulted in strain accumulation in the epitaxial stacks. By removing the GaAs substrate, the strain is released in the resin bonding glue, which is not strong enough to resist, and therefore the epilayers separates from the supporting substrate. This is also happening in the case of samples heated at temperatures above 200°C. We show an illustration in Figure 2.2-3. To solve this issue, it is better to have a strain-controlled epilayer and use a sufficiently strong glue.

ii). MBE growth defects

In Figure 2.2-4, we summarize one issue related to MBE growth defects. Microscope and Dektak profile measurements reveal holes with deep trenches all throught the epitaxial layer just after MBE growth. During substrate removal, it results in an inefficient etch stop layer (bottom figures) with square-shaped lateral etching and lift-off resulting in the apparition of the back gold mirror.

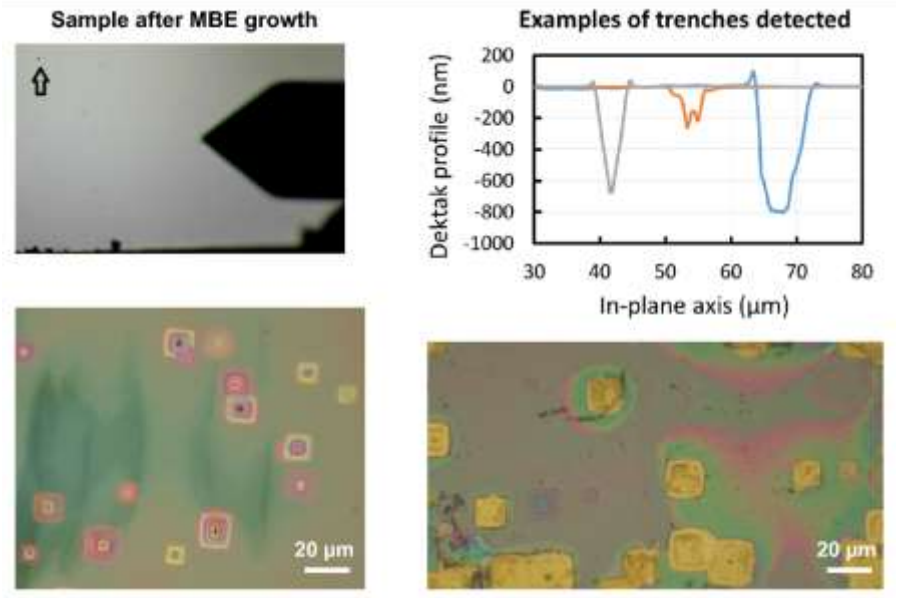

Figure 2.2-4: Illustration of growth defects. Microscope and Dektak profile measurements reveal holes with deep trenches all throught the epitaxial layer. During substrate removal, it results in an inefficient etch stop layer (bottom figures) with lateral etching and lift-off resulting in the apparition of the back gold mirror.

In the literature, we find that oval defects or polyhedral pits defects are often encountered in MBE growth. In order to reduce the density of such defects, many parameters can be used like the

growth temperature, growth rate, gas pressure and pollution free MBE chamber. By reducing the growth rate by half we were able to significantly reduce the defect density and therefore succeeded in the etch stop layer transfer process.

2.2.2 Sacrificial layer technique

This method may offer a way to reuse the substrate and enable low cost III-V PV with high efficiency. The technique is usually associated with flexible substrates, which offer a broader range of application than typical PV module. It has been investigated during the past four decades by renown academic groups [125], [126]. It lead to the creation of industrial projects with companies like IBM [127], MicroLink Devices [128] or Alta Devices, which today is a leading company for high-efficient III-V solar cells with numerous patents and world records. First, we describe the basic principle of the method we chose and then discuss about the main obstacles and challenges.

2.2.2.1 Principle

In the case of the sacrificial technique, the principle is to separate the epitaxial PV layers from the supporting substrate by destroying a sacrificial layer that is grown in-between. The layer can be destroyed by different means for example by mechanical, thermal treatments or chemical etching. Chemical etching is a common technique used for PV layers with GaAs substrate. However, it is usually a slow technique because the etching is perpendiculat to the growth direction. It is especially difficult for the reactants and products of the chemical reaction to penetrate far in the perpendicular direction. To speed up the process different lift-off techniques have been investigated, where the use of a flexible substrate facilitates the penetration of the chemical solution.

In Figure 2.2-5, we describe the basic steps to realize a successful transfer with the sacrificial layer technique by chemical etching. First, we need to choose a supporting substrate that is flexible and resistant to the chemical solution that will be used. And we need to find a way to bond the PV sample to the supporting substrate. In our case, we used a commercial plastic tape. Second, we need to think about the right etchant solution. In our case, we used diluted hydrofluoric acid (HF) to etch selectively the AlAs sacrificial layer. The solution needs to be inert for the PV layers therefore $Al_{0.4}GaAs$ windows and BSF layers have to be grown instead of $Al_{0.8}GaAs$ because of the etching selectivity. Third, we need to choose an epitaxial lift-off process (ELO). In our case, we studied many different options but I will only discuss about the option that showed the best results which is the weight-induced (WI) ELO technique that was extensively studied by Schermer's group [126]. Fourth, the substrate reuse and process optimization have to be taken into account if we want to make full profit of this transfer process.

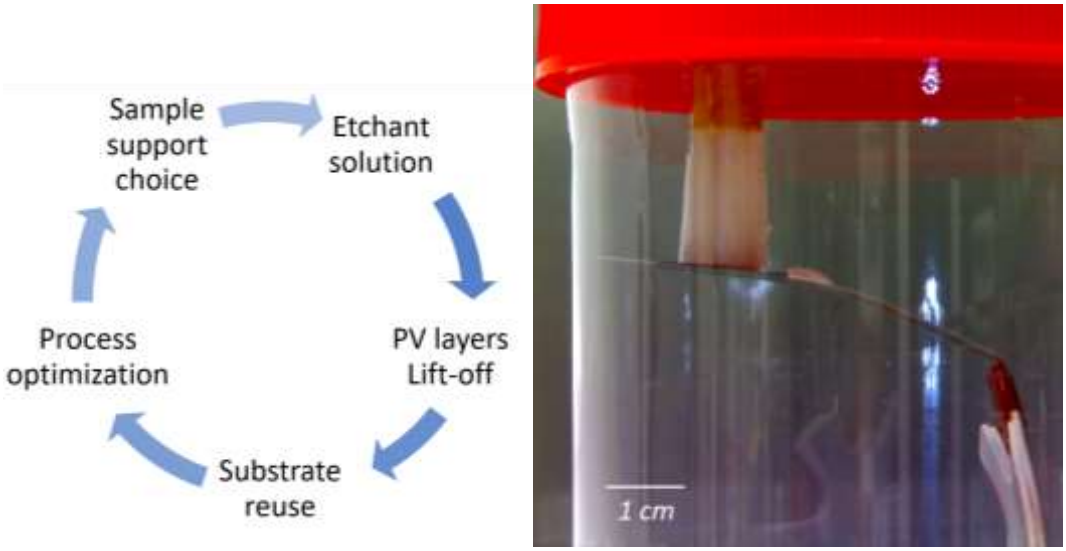

Figure 2.2-5: Basic steps to realize a successful transfer with the sacrificial layer technique (left). Photos of weight-induced epitaxial lift-off (ELO) process that we used (right). We can see the HF droplet attacking the edge of the sample to detach the epitaxial layers from the GaAs substrate. A close P.E.T. beaker resistant to HF is used to avoid evaporation of HF.

2.2.2.2 Challenges of the WI-ELO process

In Figure 2.2-5, we show a photo of our WI-ELO setup. A weight is bending the flexible supporting substrate while we see the HF droplet etching the edge of the sample to detach the epitaxial layers from the GaAs substrate. A close P.E.T. beaker resistant to HF is used to avoid evaporation of HF. Many parameters need to be optimized to have a fast and succesfull WI-ELO process for example the thickness of the sacrificial layer, the weight, the HF volume and concentration of the droplet. After careful investigation, we found that the sacrificial layer thickness should be around a dozen of nanometers. This result is coherent with Schermer's group findings. For hundreds of nanometers the sacrificial layer is not etched homogeneously and some cracks are appearing that are damageable for the fabrication of solar cells as shown in Figure 2.2-6.

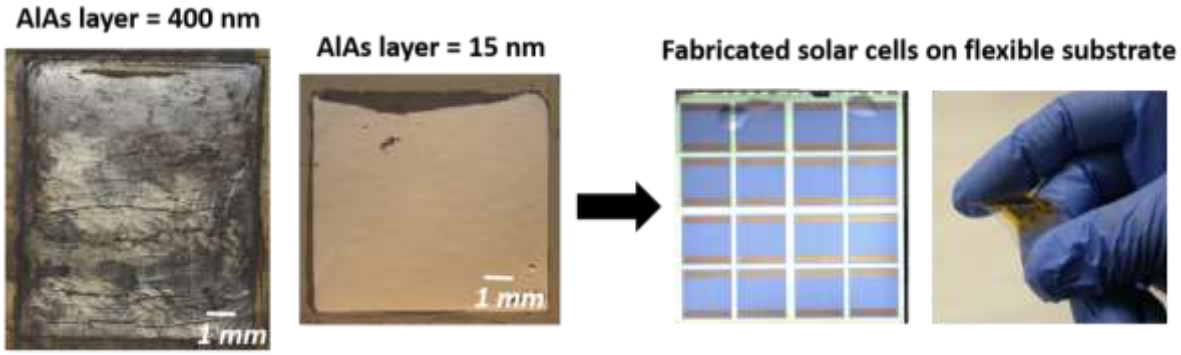

Figure 2.2-6: PV epitaxial layers after WI-ELO process for AlAs sacrificial layer of different thicknesses. The successful WI-ELO lead to the fabrication of solar cells on flexible substrate in Okada Lab. As illustrated in the right photos taken from [129].

In Figure 2.2-6, we show an illustration of solar cells fabricated using the WI-ELO technique that we developed in Okada Lab. Because of time issues, we could not apply this technique for quantum structured solar cells but it was recently successfully used in Okada Lab. for GaInNAsSb solar cells [129].

2.3 Nanofabrication

In this final part, we discuss the different fabrication of nanopatterns we investigated in our study for quantum-structured solar cells. First, we introduce the nanoimprint lithography that was used, and then we detail the process for the fabrication of back structured and front structured cells.

2.3.1 Soft nanoimprint lithography

Many techniques can be used in order to realize the nanofabrication of patterns. Nanoimprint lithography consists in reproducing a nanopattern by printing a stamp on a resist deposited on a targeted substrate. In C2N laboratory, a specific degassing assisted patterning (DAP) technique has been developed in the recent years by Andrea Cattoni [130].

In Figure 2.3-1, we detail the main steps necessary to the realization of the technique. First, a nanopattern is reproduced from a master mold onto a PDMS stamp. In our case, the master mold was usually a Silicon wafer nanostructured by electron beam lithography. Second, the PDMS stamp is degassed in a dessicator for 10 minutes. Third, the stamp is deposited on the target surface with spin-coated resist. During this step, the degassed stamp is sucking the resist inside the nanostructures and air bubbles trapped between the substrate and the stamp are removed. Fourth, we proceed to UV or thermal curing to solidify the resist, and we carefully remove the mold, thereby achieving the nanopatterning of the target surface. For this final step, a residual layer might remain on the target surface, in-between the nanostructures but it can be easily removed for example by anisotropic reactive ion etching.

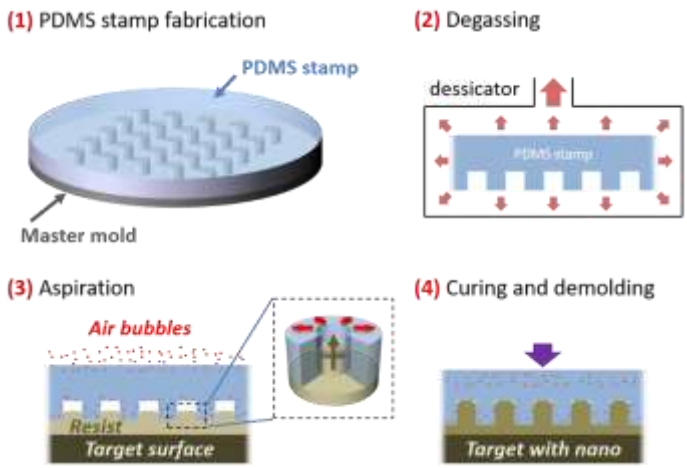

Figure 2.3-1: Main steps for the realization of soft nanoimprint lithography. (1): a nanopattern is reproduced from a master mold onto a PDMS stamp. (2): degassing of the stamp in a dessicator for 10 minutes. (3): Deposition of the stamp on the target surface with spin-coated resist. (4): UV or thermal curing and demolding to achieve the nanopatterning of the target surface. A residual layer might remains on the target surface, in-between the nanostructures. Courtesy of A. Cattoni.

For the fabrication of solar cells, we have seen that UV-lithography plays an import role for the micropatterning of our samples. The soft nanoimprint lithography enables to realize patterning at the nanometer scale for pitches as small as 40 nm [130]. In the next part, we will show how we used this technique for our quantum-structured solar cells. For the application to solar cells, we focused on using and developing nanoimprint with TiO_2 sol-gel resist because we wanted to benefit from its higher refractive index.

2.3.2 Application to solar cells

In this part, we will detail the application of soft nanoimprint lithography to solar cells for light management purpose. In all cases, we build our light management strategy from existing Fabry-Pérot cavity devices that we developed by achieving a good control over the epitaxial transfer process. First, we will discuss about metallic structured patterns and then dielectric structured patterns.

2.3.2.1 Metallic structured nanopatterns

Metallic structured nanopatterns can be used for the structuration of a back mirror or on the front side. For the deposition of metallic nanostructures, we make use of the soft nanoimprint lithography on a TiO_2 sol-gel layer with subsequent metal deposition. In Figure 2.3-2, we show two examples for solar cell application that we developed for quantum-structured solar cells. Results and simulation will be shown and commented in chapter 5.

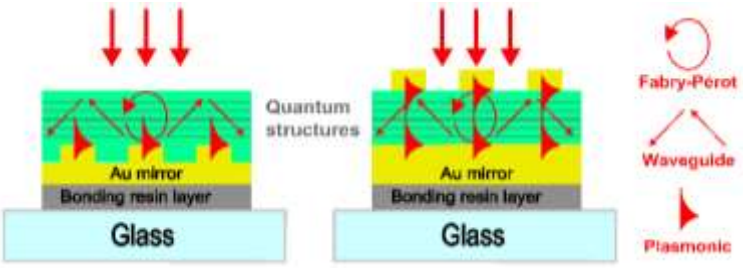

Figure 2.3-2: Two examples of metallic nanopatterns for light management in quantum-structured solar cells. In the left figure, gold nanopatterns are positioned at the back acting as a back grating while in the right figure they are positioned at the front in the metal-insulator-metal (MIM) configuration. In both case, Fabry-Pérot, waveguide and plasmonic resonant effects will span over the solar cell junction. In the case of the MIM configuration we notice that plasmonic effects from the front and the back might be coupled throught the absorbing layer for very thin junction.

In the left figure, gold nanopatterns are positioned at the back acting as a back grating while in the right figure they are positioned at the front in the metal-insulator-metal (MIM) configuration. In both cases, Fabry-Pérot, waveguide and plasmonic resonant effects will span over the solar cell junction and enhance the light path. In the case of the MIM configuration, we notice that plasmonic effects from the front and the back might be coupled throught the absorbing layer for very thin junctions. In Figure 2.3-3, we show SEM images of a nanoimprint grid that can be used for back structured mirror or front nanopatterning. Pitch is of 700 nm in the left SEM image and height is around 100 nm in the side-view SEM image (middle). The photo on the right shows the back mirror of a MQWs solar cell sample with nanostructures of different pitches (700 nm and 800 nm).

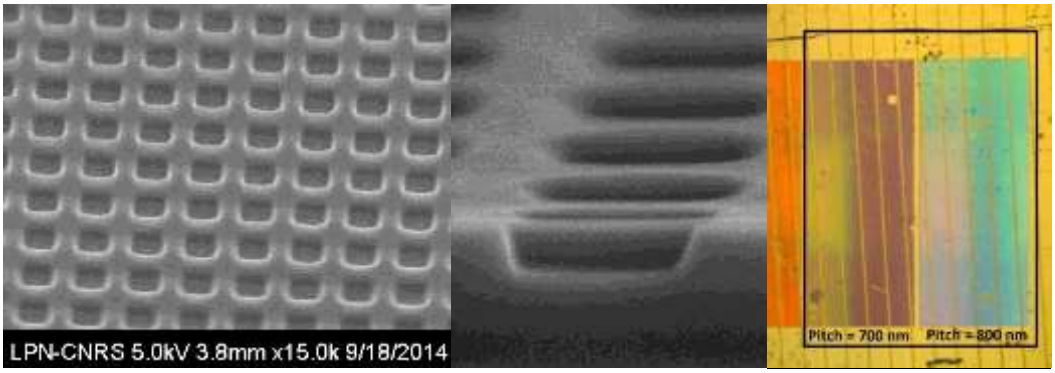

Figure 2.3-3: SEM images of a nanoimprint $Ti0_2$ sol-gel grid for back structured mirror or front nanopatterns. Pitch is of 700 nm in the left image and height is around 100 nm in the middle image. Photo on the right shows the back mirror of a MQWs solar cell with nanostructures of different pitches (700 and 800 nm).

2.3.2.2 Dielectric structured nanopatterns

Dielectric structured nanopatterns are especially interesting to avoid plasmonic losses. However, contrary to metallic patterns it often needs to be thicker to have a higher aspect ratio and use the benefit of localized Mie resonance. It is also usually necessary to use transparent dielectric with high refractive index [131], [92].

In Figure 2.3-4, we describe the process we used for the fabrication of TiO_2 front nanopatterns on transferred quantum structured solar cells. First, after the deposition of a 200 nm-thick high-index TiO_2 layer by ion beam assisted deposition (IBAD), we use soft nanoimprint lithography with adequate PDMS stamp: squared-shape nanopatterns of 200 x 200 nm with period of 400 nm.

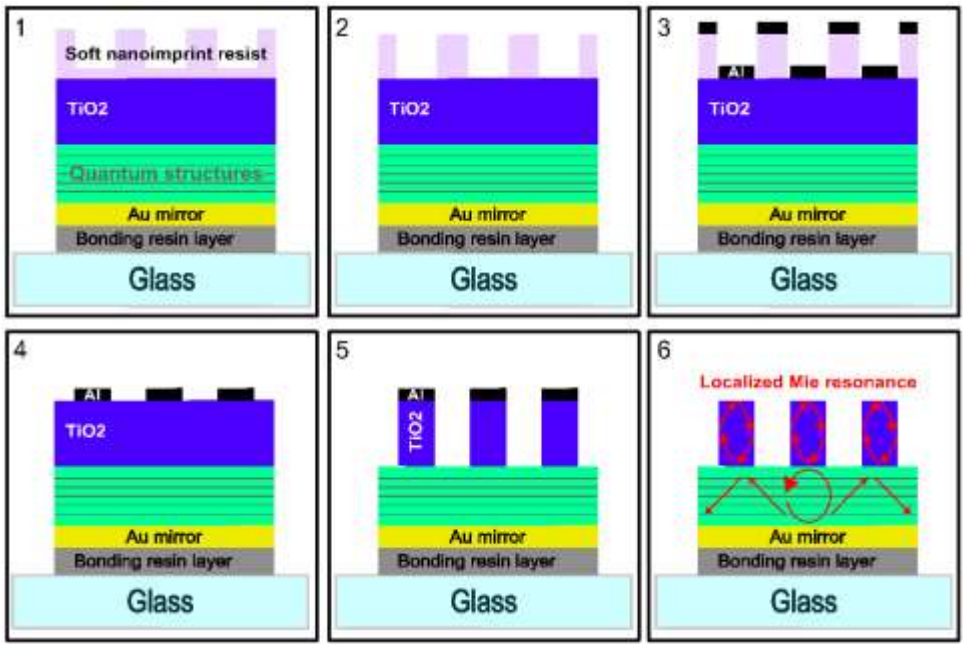

Figure 2.3-4: TiO_2 front nanopatterns on quantum-structured solar cell. (1): after the deposition of a 200 nm-thick high-index TiO_2 layer by ion beam assisted deposition, we use soft nanoimprint lithography with adequate PDMS stamp and a bi-layer "soft nanoimprint resist" made of a sol-gel TiO_2 layer deposited on a 100 nm-thick PMMA layer (for the lift-off step). (2): removal of remaining nanoimprint resist by reactive ion etching. (3): deposition of 20 nm-thick layer of aluminium. (4): lift-off step, only aluminium nanopatterns remain to mask TiO_2 layer. (5): reactive ion etching of the TiO_2 dielectric layer. (6): aluminium nanopatterns removal in a NaOH bath. Fabry-Pérot and waveguide effects are represented as in Figure 2.3-2 but also localized Mie resonant effect originating from the high aspect ratio and shape of the TiO_2 dielectric nanopatterns.

Prior to the deposition of the sol-gel TiO_2 nanoimprint resist, a 100 nm-thick PMMA resist is deposited by spin-coating and annealed at 110°C. Second, we remove the remaining nanoimprint resist and PMMA by reactive ion etching (RIE). Specific RIE programs were developed: we use a "RIE TiO_2" program during 40 seconds and a "RIE NIMPR" during 90 seconds for the PMMA. Third, after checking with SEM, we deposit a 20 nm-thick layer of aluminium by electron beam evaporation. Fourth, we lift-off the PMMA and the sol-gel TiO_2 nanoimprint resist with trichloroethylene so that aluminium nanopatterns remain to mask the 200 nm-thick TiO_2 layer deposited by IBAD. Fifth, we use reactive ion etching on the TiO_2 dielectric layer: "GEJ10" program for about 15 minutes. Sixth, aluminium nanopatterns are removed in a NaOH bath (40 g/L) for 1 minute.

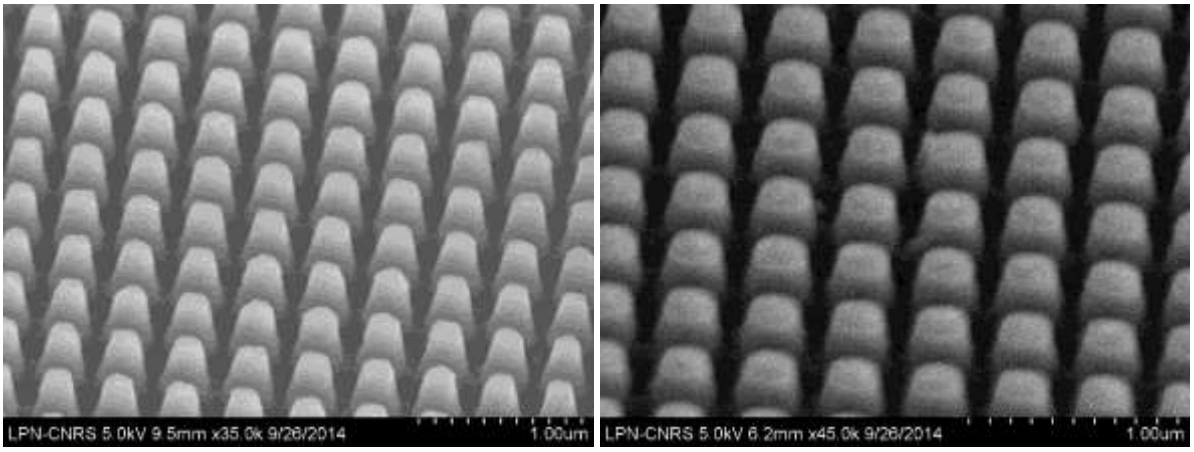

Figure 2.3-5: SEM images of 200 nm cubic TiO_2 nanostrucutres before (left) and after removal of aluminium mask (right).

At the end of the process, we notice Fabry-Pérot and waveguide effects as in Figure 2.3-2 but we also have localized Mie resonant effect originating from the high aspect ratio and shape of the TiO_2 dielectric nanopatterns. In Figure 2.3-5, we show SEM images of 200 nm-size cubic TiO_2 nanostrucutres before (left) and after removal of aluminium mask (right).

In Figure 2.3-6, the general process flow to fabricate a transferred quantum-structured solar cell with front nanopatterned TiO_2 is detailed. First, we show the stacking structure of the grown *p-i-n* junction with quantum structures on an n-doped GaAs substrate with an etch stop layer. Back-surface field (BSF) and front-surface-field (FSF) layers are 20 nm-thick and highly doped GaAs contact layers are 50 nm-thick. Total growth is less than 1 µm-thick. Second, back contacts are fabricated by: UV lithography, Ti/Au metal deposition, lift-off and selective chemical etching of the p-doped GaAs contact layer as explained earlier. Spacing between contacts vary between 100 and 400 µm depending on the mask used. Third, we show the transfer process with UV photoresist bonding layer after gold mirror deposition. Fourth step shows the substrate removal after protection of edges by wax and then the etch stop removal. Fith step shows the fabrication of front contact for the cells the same way as the back contacts. Cell size vary between 100 µm and 2 mm depending on the mask used. In the sixth step, mesa are made to isolate cells from each other. Seventh, TiO_2 is deposited by IBAD. Eight we show the front nanostructuration by the process described in Figure 2.3-4. Finally, in the ninth step we need to remove the residual TiO_2 layer on contacts by RIE after UV lithography.

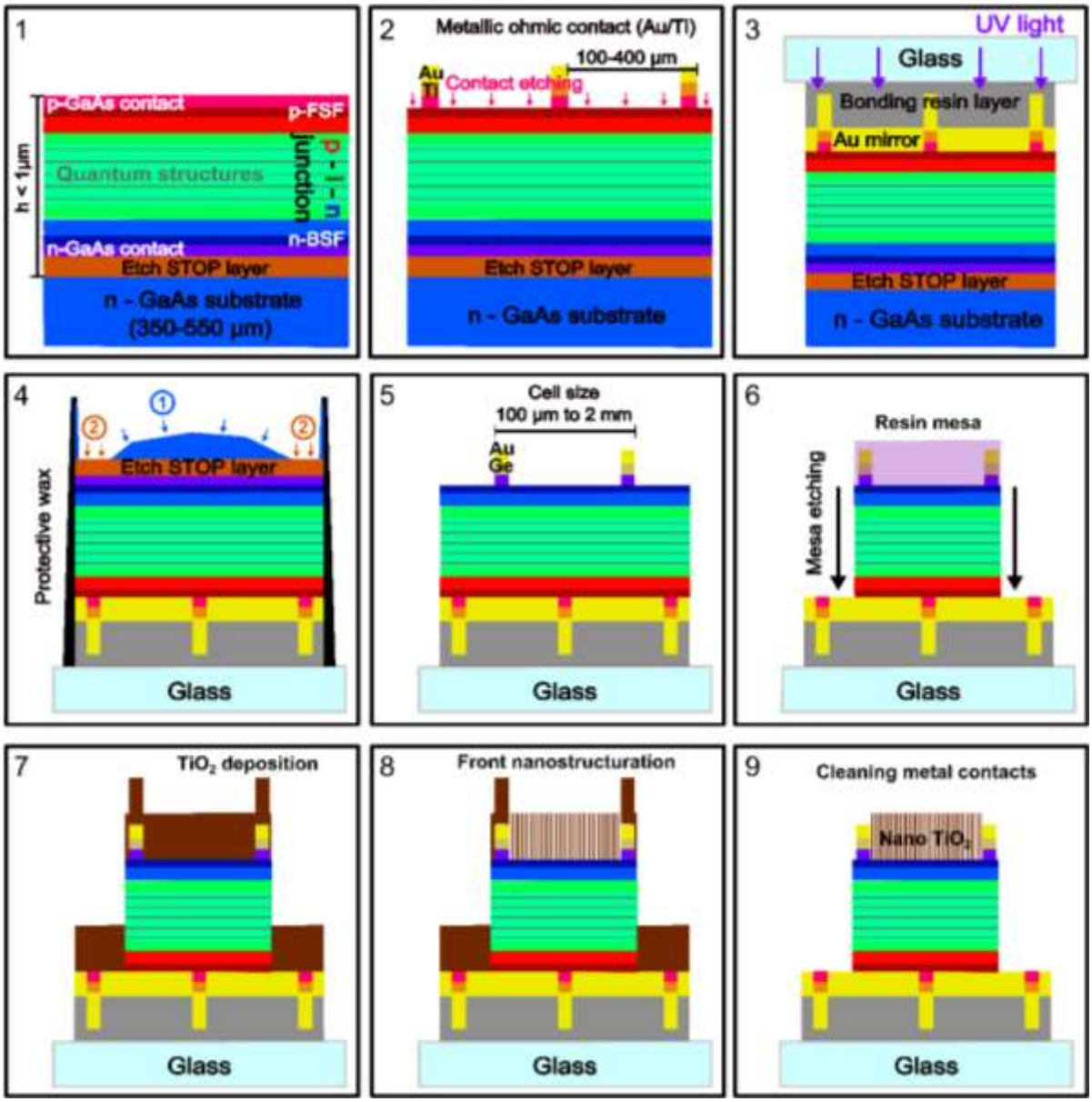

Figure 2.3-6: General process flow to fabricate a transferred quantum-structured solar cell with front nanopatterned TiO_2. (1): Growth of a *p-i-n* junction with quantum structures on a n-doped GaAs substrate with an etch stop layer. Back-surface field (BSF) and front-surface-field (FSF) layers are 20 nm-thick and highly doped GaAs contact layers are 50 nm-thick. Total growth is less than 1 µm-thick. (2): Back contacts are fabricated by: UV lithography, Ti/Au metal deposition, lift-off and selective chemical etching of the p-doped GaAs contact layer. Spacing between contacts vary between 100 and 400 µm depending on the mask used. (3): Transfer process with UV photoresist bonding layer after gold mirror deposition. (4): Substrate removal after protection of edges by wax and then etch stop removal. (5): Front contact fabrication the same way as the back contacts. Cell size vary between 100 nm and 2 µm depending on the mask used. (6): Mesa to isolate cells from each other. (7): TiO_2 deposition by IBAD. (8): Front nanostructuration by process described in Figure 2.3-4. (9): Remove residual TiO_2 layer by RIE after UV lithography.

The general process flow illustrates the numerous steps and level of complexity to realize such object from a fabrication point of view. In the next part, we will see that the growth of quantum structures is maybe even more challenging.

Conclusion

In this chapter, we have described the key processes used and developed for the fabrication of our devices. We emphasized the fact that our work uses basic patterning technology at micrometer level but also more advanced one at the nanometer level. We also showed the difficulty of adapting and controlling the epitaxial transfer of semiconductor layers. We would like to underline some points that seem important for our study and highlight our achievements:

- Our work needed precision, stability and control using a clean room environment and high-level technological advisers. The work procedure has many feedback loops in order to evaluate and improve our design and fabrication step by step. The conventional fabrication of a solar cell was relatively smooth with some technological adaptation related to etching solutions, rapid thermal annealing (RTA) or wire-bonding.

- In order to combine high-efficiency PV concepts using quantum-structured materials and light management techniques, we had to think about an original strategy for the design of our structure: (1) the spectral range for the light absorption enhancement needs to be defined according to the material and PV concepts, (2) the thickness of the Fabry-Pérot cavity has to be chosen accordingly before the growth, and (3) the use of more complex nanophotonics can be implemented afterwards during the device fabrication. More details about light management strategy will be given in chapter 5.

- In both cases, for quantum-structured materials and light management implementation, we chose to start with basic concepts that could be achieved more easily. On one side, we used multi-quantum wells (MQWs) structures that are well understood and better controlled and on the other, we transferred on a flat mirror to create a simple Fabry-Pérot cavity with low-quality resonances. After validation of each step, we were able to move on to a higher level of complexity using quantum dot (QD) structures on the side of quantum-structured materials and multi-resonant nanopatterns on the side of light management.

- In term of achievements, we were able to work successfully on the development of two methods to transfer very thin (subwavelength) epitaxial layers. First, the development of the “etch stop layer” technique on QD layers was laborious and it took time to identify the origin of each problem in order to adapt the device fabrication recipe to the epitaxial growth recipe. For this reason, we also started to work on the “sacrificial layer” technique also called epitaxial lift-off (ELO) technique. It has many advantages like the possibility of fabricating light-weight flexible solar cells and reuse the substrate to lower the material cost. Therefore it should be very interesting to pursue the development of this technique in order to achieve the economically viable light-weight, flexible and high-efficiency solution discussed in chapter 1.

- We were also able to work successfully on the development of two different nanopatterning strategies: a metallic nanostructured back mirror and a dielectric nanostructured front grating. In both cases, we used degassed-assisted nanoimprint lithography technique that is low cost compared to conventional nanolithography techniques. Overall, these steps were quite simple to realize because we could benefit from an extraordinary clean room environment and assistance. In the future, more complex nanostructures could be patterned, like assymetric or even 3D structures.

Chapter 3 QD-IBSC system: from ideal to experimental PV material

The actual completion of an ideal quantum dot intermediate band solar cell (QD-IBSC) is difficult from a technological point of view but also because of material considerations related to quantum structures that will be investigated in this chapter. It is important to know from where we start before thinking about proof of concept characterizations that will be made in chapter 4 or light management strategies proposed in chapter 5. In a first part, we discuss about the system description, on one side the choice of material and on the other the designed stacking structure for the device. In a second part, fabrication issues are considered from a nanoscopic to a macroscopic point of view for the realization of quantum dot solar cells (QDSCs). In a third part, characterization of the QDs is proposed by the analysis of temperature-dependent photoluminescence (PL), current-voltage (I-V) and reverse bias current spectral photoresponse. QD assembly properties are also investigated via the calculation of energy states and electron wave probability related to the quantum physics of self-assembled In(Ga)As QDs. Finally, in a fourth part, QDs absorption is discussed from a simulation and an experimental approach.

3.1 Description of QD-IBSCs system for light management implementation

Following chapter 1 describing the numerous systems of IBSCs and the different techniques for light management, the aim of this first part is to describe the basic system on which we have worked. We want to explain the reasons why we chose this system in the first place and the path for improvement that can be found in the literature. We try to consider it especially in the perspective of our work for the implementation of light management strategies in IBSCs.

3.1.1 Choice of material: In(Ga)As QDs in Al0.2GaAs host material

In this part we will show that In(Ga)As/AlGaAs system is a suitable candidate for the realization of high efficiency IBSCs from a material point of view. It offers a good compromise, to overcome some of the difficulties encountered in IBSCs and still keep a system that is not completely new and on which we can hope to demonstrate proof of concepts in the near future [132].

3.1.1.1 III-V materials

First, the system relies on the combination of III-V materials well-known and used in the semiconductor science and industry as illustrated in Figure 3.1-1. III-V material lattice constants are plotted with respect to their bandgap energies on the left axis colored scale. On the right axis, we show the irradiation wavelengths of the majority of the solar spectrum from ultra-violet (UV) to infrared (IR) representing respectively 99% and 92.7% of AM1.5G and AM0 photon flux.

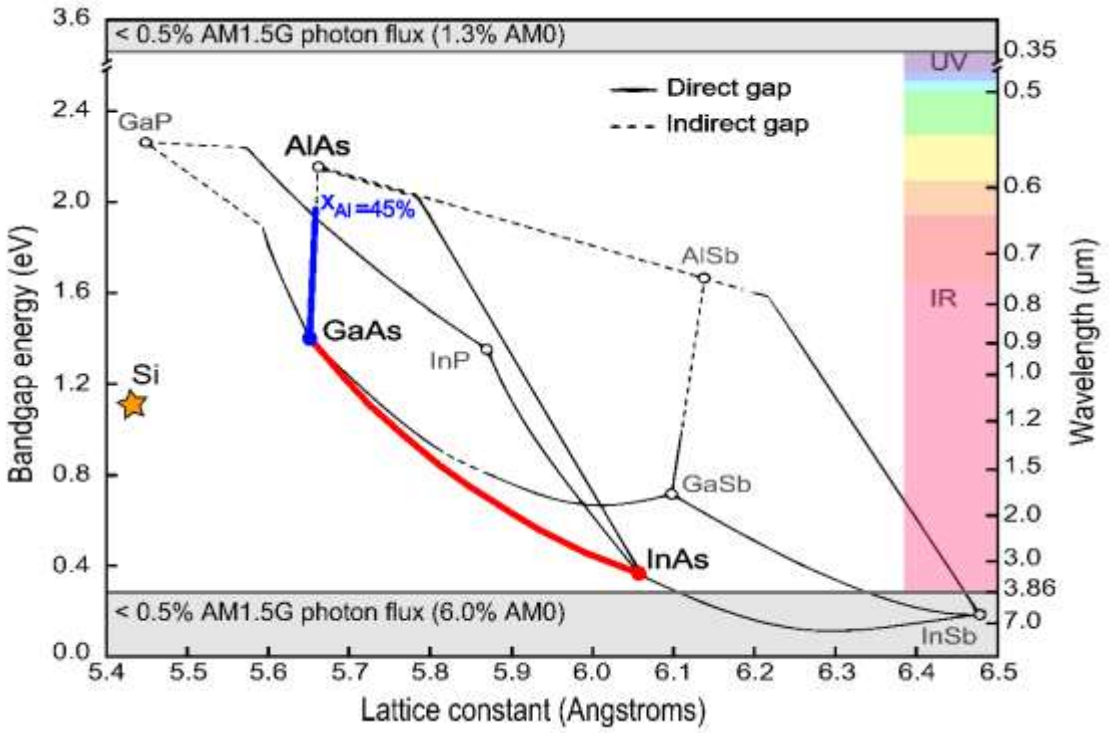

Figure 3.1-1: III-V lattice constant vs bandgap energy

3.1.1.2 GaAs based system

As reported in chapter 1, the world best single-junction solar cells are made of thin-film crystalline GaAs grown by metalorganic chemical vapor deposition (MOCVD) with record efficiency of 28.8% under 1 sun achieved in 2012. GaAs semiconductor has the advantage of having a direct bandgap of 1.42eV at 300K. This value is an optimum for the so called Shockley Queisser efficiency limit under 1 sun of illumination [2]. GaAs material has also the advantage of being well-known and widely used in the semiconductor industry. This advantage makes it easier to explore new concepts because the right recipe or tools have already been developed for its growth and characterization.

3.1.1.3 InAs/GaAs combination

Nevertheless, Figure 3.1-1 shows that most infrared (IR) photons from the solar spectrum have energies lower than the GaAs bandgap and thus pass through solar cells and are lost for PV conversion as explained in chapter 1. For this reason, high efficiency GaAs-based solar cells need to host materials with lower bandgap energies.

As previously discussed in chapter 1, the strategy used for QD-IBSCs is to grow QDs inside a host material. In Figure 3.1-1, two paths can be chosen in the perspective of growing a lower bandgap energy material inside a GaAs host material: the path towards InAs (in red) and the path toward GaSb. The dotted part around 0.8 eV stands for $GaAs_{1-x}Sb_x$ alloy miscibility gap for $0.3 < x < 0.6$. Both alloys are lattice-mismatched on GaAs and can be grown in the form of QD structures. For the past 3 decades, GaSb QDs have been less studied in the literature than InAs QDs. Recently GaSb type II QDs have attracted attention and even hybrid structure with type-I InAs/GaAs plus type-II GaSb/GaAs quantum dot structure have been tested with success [133]. Nevertheless, in the scope of QD-IBSCs, it is usually considered that InAs/GaAs system offers a safer combination for proof of concepts applications.

3.1.1.4 In(Ga)As: InAs or InGaAs QDs

Once the choice of the lower bandgap material has been made, the question is: in what proportion is it possible to make In(Ga)As/GaAs QD layers and stack them on top of each other? One difficulty is strain control but also the creation of defects, the wetting layer, the shape of the QDs and In/Ga interdiffusion.

The technical points and problems related to the growth of QDs layers are discussed in part 3.2.1. Still, without going into details, it is important to understand that expressions like "InAs QDs" and "InGaAs QDs" are just ways for QDs grower to report about one parameter of their growth conditions, which is the number of elements they try to incorporate during the QDs growth. In reality it is difficult to certify what is the concentration of Indium and that is why many authors prefer to use the expression In(Ga)As. For example, in 2004, A. Lemaitre, et al. [134] have checked the concentration of Indium in $In_xGa_{1-x}As$ material using cross-sectional transmission electron microscopy (TEM) as described in Figure 3.1-2. In the case of a 2.4 ML InAs QDs MBE growth, they found a maximum of 55% indium only at specific part of the QDs around the apex. In average the concentration is more around 30-40% with a specific profile called inverted trumpet-shaped gradient profile as shown in Figure 3.1-2 [135].

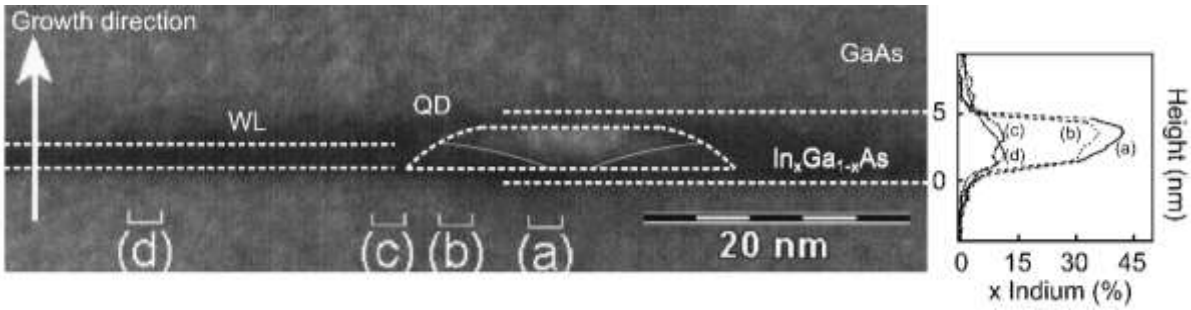

Figure 3.1-2: 002 TEM DF images of InAs/GaAs QDs capped with GaAs. Letters indicate locations of composition profiles plotted on the right side with respect to the height. Adapted from reference [134].

This factor is important for designing QD-IBSCs to potentially know which $In_xGa_{1-x}As$ alloy can be used as a low bandgap energy material for the fabrication of QDs. In the case of a 30-40% Indium-rich $In_xGa_{1-x}As$ material, the bandgap energy is around 1 eV. This energy sets a limit for the VB-IB transition that can only be between 1 eV and the bandgap of the host material depending on geometrical parameters of the QDs. In the literature, In(Ga)As usually have a photoluminescence (PL) emission between 1.1 eV and 1.3 eV. In addition, the influence of the wetting layer (WL) and capping will be discussed later.

3.1.1.5 Optimal IB energy position: choice of $Al_xGa_{1-x}As$ host material

In chapter 1, it is shown that an optimal IBSC with highest efficiency can be determined for a host material bandgap energy around 2 eV and a VB-IB transition around 1.3 eV [50]. In Figure 3.1-1, it is shown that using Al incorporation in GaAs, following blue line it is possible to increase host material bandgap up to 2 eV for x=45% with nearly no lattice mismatch and keeping direct bandgap for the host material. AlGaAs/GaAs is also a well-known couple that was highly investigated over the past decades. Unfortunately, AlGaAs suffers from growth problems related to oxygen incorporation inducing deep donor levels [136], [137]. Usually it is found that the higher the concentration of aluminium, the more difficult it is to get a good quality material. For an aluminium concentration high-

er than 45%, the semiconductor has an indirect bandgap energy and many properties close to GaAs material are shifting to AlAs system due to reverse Γ–L–X valley ordering [138].

Considering these growth issues, it is judged safer to move smoothly in Al concentration from GaAs to $Al_{0.45}GaAs$ host material. First step is to work with a realistic system where it is possible to put together piece by piece all elements needed for fabricating a working QD-IBSCs. Recent results have shown that it is possible to obtain high quality AlGaAs solar cells with 20% of Al [139]. In this perspective In(Ga)As/$Al_{0.2}GaAs$ system, as described in Figure 3.1-3, seems to be a good candidate for making a high efficient solar cell. Bandgap of $Al_{0.2}GaAs$ is around 1.7 eV [138], therefore photons of higher energies can be absorbed via the valence band (VB) to conduction band (CB) transition. Moreover, for a QDs PL emission around 1.2 eV, we have an intermediate band (IB) positioned in such way that VB to IB transition can absorb photons of energies higher than 1.2 eV and IB to CB transition can absorb photons of energies higher than 0.5 eV. This way, the system can theoretically absorb most of the solar spectrum and reach 40% under 1 sun and 60% at full concentration [46]. In comparison, nowadays four-junction solar cells world record obtained in laboratories are of 39% under 1 sun and 46% under 300 suns [5].

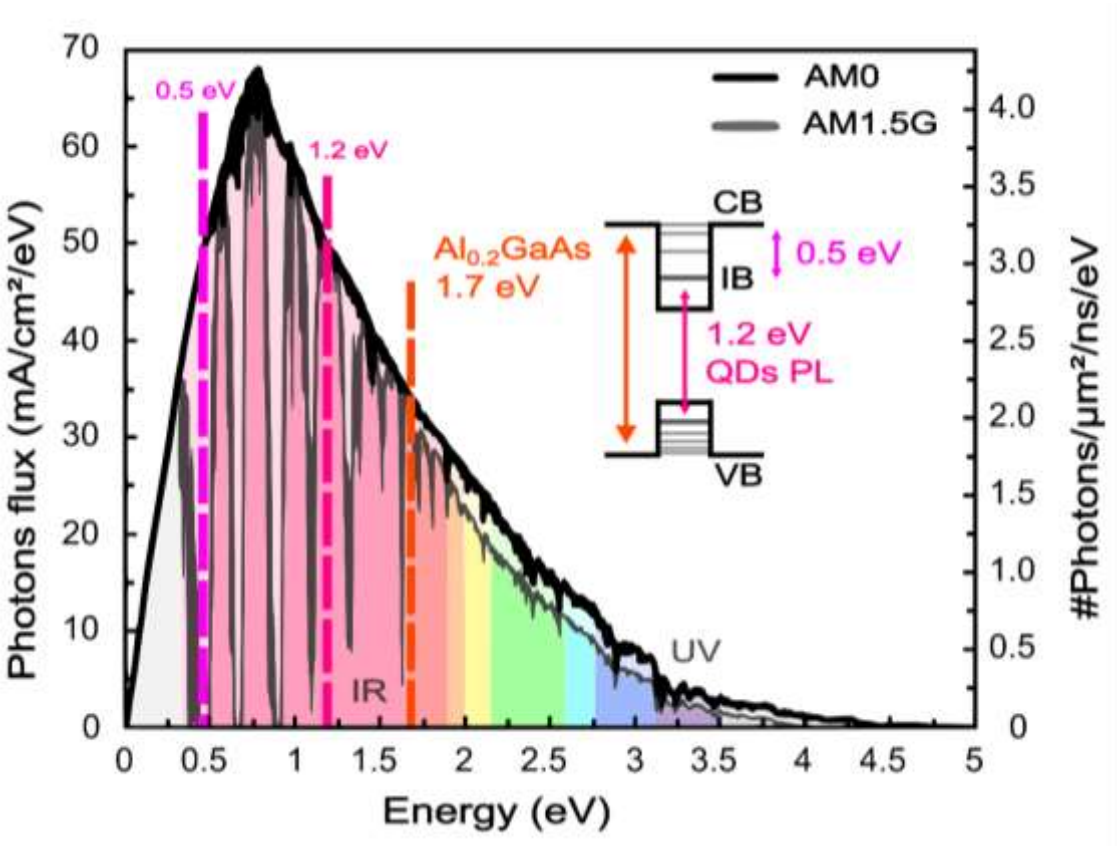

Figure 3.1-3: AM0 (black) and AM1.5G (grey) solar spectrum in photon flux per eV. In(Ga)As/Al0.2GaAs QD system is shown and interband energy levels are positioned with solar spectrum. Left axis shows the photon flux value in terms of photons per µm² and nano seconds.

Figure 3.1-3 right axis shows the photon flux value in terms of photons per µm², per nano seconds and per eV to appreciate the balance of photons in such system. The usual PL recombination time in a QD assembly is of the order of 1 ns and the usual scanning method for QDs are made by atom force microscopy (AFM) characterization which gives an estimate of the number of QDs on mi-

crometer-size areas. For the present system that we investigated, the order is usually of 400 QDs/µm² (4e10 cm^{-2}) for a single layer.

In our study, we are especially focused on light management in IBSCs. Thus, for the In(Ga)As/$Al_{0.2}$GaAs system that we present in Figure 3.1-3, it is especially interesting to investigate the balance of photons for an optimal IB positioned as a stepping stone configuration to perform sequential two-photon absorption (S-TPA). As discussed in chapter 1, in theory, we would like to have the same photon flux for the VB to IB transition and for the IB to CB transition. With AM0 solar spectrum, we integrate the photon flux over the different spectral range of interest. For $E_{VB\text{-}CB}$ transition by integrating for energies higher than the host material (1.7 eV) we see that we can absorb a maximum of 1.8 photon/µm²/ns. For the $E_{VB\text{-}IB}$ and $E_{IB\text{-}CB}$ transitions we can get respectively 1.3 and 3.5 photon/µm²/ns. For AM1.5G, $E_{VB\text{-}CB}$ can get 1.4 photons/µm²/ns, while $E_{VB\text{-}IB}$ can get 1.1 and $E_{IB\text{-}CB}$ 1.8. These values show that the balance of photons is good enough for the stepping stone effect to take place. Under AM1.5G, over 1-µm², there is at least 1 photon available for the VB to IB transition and almost 2 photons for the IB to CB transition. If we consider that electrons are localized in the IB, it means that the ideal configuration would be to have one QD making 100% of an absorber layer over a 1-µm² area. However, this would mean that QDs would not be confined in the surface plane. In reality there is a compromise between the number of QDs and the electron flux taking place in the IB. Increasing the photon flux (photofilling) or increasing directly the number of free electrons (electrofilling) by doping are two ways to balance the number of QDs to achieve successful S-TPA.

3.1.1.6 Photofilling of IB

It is possible to consider the number of photons per QDs following Equation 3.1-1 where Φ_{ph} represents the photon flux directly dependent on the illumination for an array area, Abs represents the absorptance of a QDs layer for such array area and N_{QDs} the number of QDs in the array area.

$$N_{ph/QD} = \Phi_{\mathrm{ph}} \times \frac{Abs}{N_{QDs}}$$

Equation 3.1-1: Number of photons per QDs

For simplicity, we consider a periodic array of square-shaped QDs with diameter size $\boldsymbol{d}$ and lateral interdot spacing $\boldsymbol{l}$ as illustrated in Figure 3.1-4.

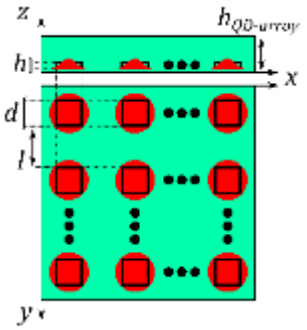

Figure 3.1-4: Schematic representation of a QD array: *x*-*z* side view (top) and *x*-*y* top view (bottom). QD diameter (*d*), height (*h*) and lateral interdot spacing (*l*) are shown. Delocalized nature of light (green) compared to localized electron wavefunction in QDs (red).

QDs usually represent only 10-25% of a QDs layer surface because of this interdot lateral spacing. This percentage is usually directly reflected in the absorption calculation of a QDs layer if we approximate it by considering it as an effective medium. Thus, as an approximation, we can write the following Equation 3.1-2 with Abs_{QD} the absorptance of a single QD that can only be 1 at maximum considering no resonant or scattering photonic effect from the QD array.

$$N_{ph/QD} = \Phi_{\mathrm{ph}} \times \frac{Abs_{QD} \times \left(\frac{d}{d+l}\right)^2}{\frac{array\ area}{(d+l)^2}} = \Phi_{\mathrm{ph}} \times Abs_{QD} \times \frac{d^2}{array\ area}$$

Equation 3.1-2: Number of photons per QD considering QDs as an effective medium

Abs_{QD} can also be seen as a ratio between the QD absorption and geometrical cross-section. It shows that the number of photons per QD can be directly proportional to its QD surface (d^2) no matter the arrangement of QD arrays area and it is maximum if the array is only made of a QD. A typical In(Ga)As QD arrays is described in Table 3.1-1.

Table 3.1-1: Typical InAs QDs array

	***d* (QD size)**	***l* (interdot spacing)**	**N_{QDs} (QDs density)**
Typical In(Ga)As QDs array	20 nm	30 nm	400 QDs/µm²

Under 1-sun illumination, for $\Phi_{\mathrm{ph}} \sim 1$ photon/µm²/ns with a typical In(Ga)As QDs array, we find $N_{ph/QD} \sim 5.10^{-4}$ photons/ns. This is a limitation for an IBSCs system. As illustrated in Figure 3.1-4, contrary to the delocalized nature of the light (green) propagating in all the QD layer, the electron wavefunction (red) remains localized inside one QD. A very low value of $N_{ph/QD}$ per nanosecond is bad news for the S-TPA process. It means that the process will be less probable and also that many QDs are useless which naturally will induce traps. This topic has been recently investigated by Tex et al. and their experimental results seem to confirm that low-density QD layer largely outperforms the high-density layers [140]. In our calculation, the value of $N_{ph/QD}$ per nanosecond does not take into account non-radiative loss and assumes a maximum absorptance for each QD ($Abs_{QD} = 1$). In reality, the value is much lower because of host material defect and the intrinsic low value of QD absorptance that will be discussed later.

To overcome this limitation from a photofilling point of view [76], the easiest way is first to increase directly the photon flux for example using concentration PV (CPV). In this case, only high CPV (HCPV) of 2000 suns or more can give a proper balance of $N_{photons/QD} \sim 1$ photons/ns for S-TPA. Using medium CPV concentration of 300 suns we can calculate that only large QD of size $d \geq 60$ nm can give a good balance. The problem is that such QDs are too large to be considered as QDs in the perspective of IBSCs rules established by Luque and Marti.

Second, if we consider efficient light management techniques we might be able to achieve 100% absorption inside the QD absorber layer by introducing specific photonic effect such as scattering and resonant effects with the localization of the electric field of light around the QDs for the spectral range of interest. Assuming we are capable of 100% absorption inside the absorber layer ($Abs = 1$), the number of photons per QD can be rewritten as in Equation 3.1-3.

$$N_{ph/QD} = \Phi_{\mathrm{ph}} \times \frac{1}{N_{QDs}} = \Phi_{\mathrm{ph}} \times \frac{(d+l)^2}{array\ area}$$

Equation 3.1-3: Number of photons per QD considering 100% absorption in QDs layer

Thanks to light management techniques, we see that any QD size (d) can be considered because in this case it is only the QDs density that matters (N_{QDs}). For a typical In(Ga)As QDs array as de-

scribed in Table 3.1-1, we can calculate that for medium CPV a good balance for the stepping stone effect would be achieved for QDs with density of 250 QDs/µm². For low CPV (LCPV) systems this value falls to about 50 QDs/µm². We understand that this way, we would have to force the localization of light to match the localization of the electron by some kind of near-field light management technique. One difficulty in term of light management is that for QD-IBSC, the localization for both transitions in the S-TPA process has to be precisely at the QD position. This constraint can be relaxed if QD assembly share the electron population for example by tunnelling or if QDs are thermally activated with the host material. In chapter 1, we also see that "relaxation" is being recently investigated in order to decouple both transitions for example by engineering a "photon ratchet" band [44], [141].

Third, light management technique with strong light-matter interactions could be used in order to tune the radiative recombination time inside QDs. In our study, we consider weakly coupled resonant effects and we don't expect to see a direct effect of our optical design on the IB dynamic. In chapter 5, we will try to investigate this effect.

3.1.1.7 Electrofilling of IB

An alternative to IB photofilling is electrofilling of the IB. For the past 5 years many papers have been published to cover this possibility either by direct doping of QDs or indirect δ-doping of a nearby layer [61], [142]–[144]. The addition of electrons into QDs is believed to reduce the rate of electron trapping in the host material due to partial occupation of the QD states and repulsive electrostatic interactions. It can also increase the probability of absorption of a photon that can promote an electron from the intermediate state to the host CB but at the same time reduce absorption cross section for photons that promote electrons into the QDs [145]. Other drawbacks can be that more of the QDs are located in a flat-band potential due to doping. Also doping during growth, doping might induce more defects or on the contrary in some case it can have a passivation effect [146], [147]. This field of study is still under development but it seems overall that a level of doping around 8 Si atoms per QDs might be beneficial for the electrofilling of In(Ga)As self-assembled QD-IBSCs without degrading the crystal quality of QDs and interfaces [144].

Sellers et al have recently proven with their InAs/GaAs IBSCs system that doping does not help optical interband transitions [148]. Doping can be used to slightly increase the total photocurrent from IBSC devices however, increased doping does not increase the relative contribution of optically driven escape mechanisms. Optically driven processes, which are critical to efficient harvesting of solar energy, are responsible for less than 5% of the total carrier escape even under photon irradiances equivalent to extreme solar concentration, regardless of doping. These results therefore suggest that future efforts to improve the net efficiency of IBSC devices should focus on methods other than doping in order to suppress carrier trapping processes. The escape process will be discussed later.

3.1.2 Position of QD layers

In this part, we will discuss about QDs-IBSCs from a device stacking design point of view. We especially want to discuss about the position of QD layers inside a solar cell structure and the possibility of making some adjustement for light management in the case of very thin structures that could maybe escape the classical picture of a *p-i-n* solar cell.

3.1.2.1 QDs layer sandwiched in p-i-n

Traditionally QDSCs have been thought to be fabricated with QDs layers sandwiched in the *i*-region of a *p-i-n* junction. The main purpose of *p-i-n* against *p-n* is to increase the space charge region (SCR) inside the material. It is a "default" location for QDs layers in optoelectronic field of application. Especially when the interest is in the investigation of electric field over QDs region and generation of light by recombination of electron-hole pairs. It has been maintained also because it seems more challenging in term of growth to have the QDs layers in a *n*- or *p*-doped region [149].

Nevertheless, in the past 5 years, this tradition has been challenged in many ways. Zhou et al [149], have published an experimental investigation of QD layers outside the intrinsic region of a solar cell. Their results show that the Voc is almost recovered when QD layers are outside the *i*-region compared to QD layers inside *i*-region that usually have lower V_{OC} than reference cells with no QDs. On the other hand, the Jsc and FF suffer more and it was attributed to the fact that there can be more recombination via QDs or maybe more defects due to fabrication. In this perspective, Kechiantz et al, have suggested by using simulation that QD layers should be positioned in the p-region of a GaSb/GaAs QDSC [150].

Also very recently, Driscoll et al [151] have investigated the shift of QD layers inside the intrinsic region and they noticed that the best position for their cells was not where they expected because of unintentional *n*-doping of the intrinsic region (UID). Indeed, recombination in the intrinsic region is higher when electrons and holes population are equal which is in the center of intrinsic region in a symmetrical structure. Because of unintentional doping, the equality of electrons and holes population happens much closer to the p-type region and thus the junction becomes a *n+np* junction as shown on Figure 3.1-5.

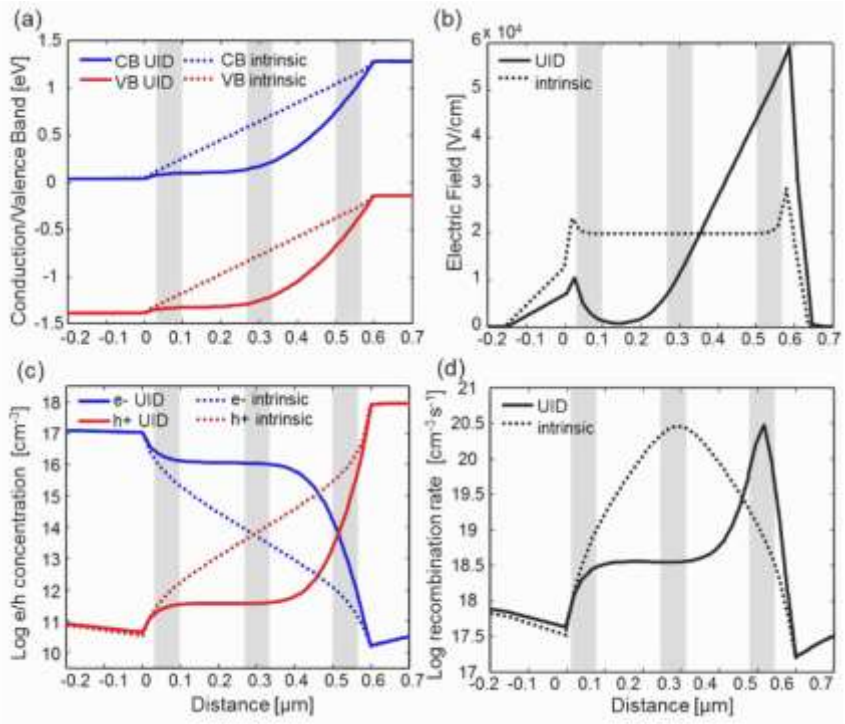

Figure 3.1-5: Simulated: (a) conduction and valence band diagram, (b) electric field magnitude, (c) electron and hole densities, and (d) SRH recombination rate versus position for a purely intrinsic and unintentional doped (UID) n-type intrinsic region under 0V bias ((a) and (b)) and 0.5V bias ((c) and (d)). The shaded regions correspond to the position of the QDs in the base-shifted, centered, and emitter-shifted devices. The origin along the growth axis corresponds to the base-intrinsic interface. Taken from reference [151].

We see in Figure (a) that the "intrinsic" case looks more like a *p-n* energy band diagram at 0 V bias. In Figure (b) is shown the electric field at 0 V bias, we see that is almost equal to zero in the *n*-doped region for the UID case. Figures (c) and (d) illustrates the fact that at 0.5 V forward bias, recombination is higher in the *i*-region for normal *p-i-n* junction and is higher in the *p*-doped region for UID *n*-doped solar cells that becomes like a *n+np* junction.

In the case of light management for our project this UID giving an *n+np* junction would be favourable. It is better to have *p*-region at the top of the cell to avoid holes generated by UV light to go throught QD layers region because their mobility is lower than electrons. In addition, we would have no problem in having QDs layers at the bottom of our cells because QDs layers are mostly interesting to consider for the absorption of infrared light that usually have a longer penetration into the cell.

3.1.2.2 Electric field and damping layer: toward pn junction

The *n-p* structure has also been investigated in the purpose of field damping [152]. In the IBSCs theory, it is considered important to have an almost flat band condition in the QD layers at voltage bias where we obtain the maximum power point on the I-V curve. Figure 3.1-6 illustrates the effect of the electric field on the filling of multi-stacked QD layers. We can see that the filling is not homogeneous and tunneling process out of QD layers is enhanced. It is the same for QWs solar cells where it was found that the optimization of QWs location depends upon accurate information on the background doping level. Moreover it is found that the advantage of strategic location of the QWs is greater for devices containing one or a few QWs than for multi-QW devices [153]. This point is important in the perspective of realizing very thin devices with a limited number of quantum structured layers.

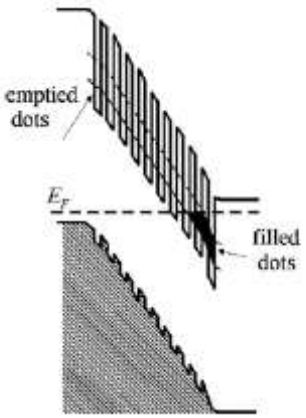

Figure 3.1-6: Simplified bandgap diagram of a QD-IBSC with the QD layers fully immersed in the depletion region. Taken from reference [152].

From a simulation point of view this phenomenon has also been investigated in 2012 by Gu et al [154]. They found that the position of QDs layers is especially important if inter-band absorption is high enough. If it is not, QDs only act as recombination centers and it is better to keep them outside of the depletion region so that V_{OC} is preserved.

3.1.2.3 Towards new device stacking design with the use of light management strategies

Here we want to summarize some of the findings of this first part on In(Ga)As / $Al_{0.2}GaAs$ IBSC system. First, we have seen that having a minimum number of QDs layers can only be beneficial from an electrical point of view. In fact, the balance of photon indicates that only one QD/µm² would be enough to do two-step generation if it could absorb in the same place all photons coming on 1-µm² area. It means that very thin devices with a minimum number of QD layers but a high absorption enhancement could prove to be interesting for the development of novel IBSCs. In this sense, ultra-thin QDSCs with nanophotonics enhancement strategies seems to go in the right direction.

Second, QDs absorbing layers have to be positioned properly in term of carrier distribution but also in term of the electric field of light originated by incident photons. It is especially important for ultrathin solar cells. We reckon that junction are not really needed for ultra-thin QDSCs, therefore junctionless solar cells with very thin selective contacts are considered as in hot carrier solar cells (HCSCs).

In the rest of our study we will always use QDSCs designed using quantum structures positioned inside the *i*-region of a *p*-*i*-*n*. We decided to keep this parameter for growth simplicity because we did not have enough time to check another structure and because we wanted to compare our solar cells with previous structures developed in our group. Nevertheless, we should keep in mind that we not only have some degrees of freedom over the device stacking design (when thinking about light management strategies) but these light management strategies might offer a new road to achieve high efficiency solar cell. These considerations will be discussed again in chapter 5.

3.2 Fabrication of QDs absorber suitable for IBSCs

In recent years, control on the fabrication of QDs materials has improved especially in order to get higher density of QDs. However, there are still some issues to fulfill completely the IBSC's assumptions. First, we will focus on the description of QDs MBE growth mechanism. It needs atomic scale or at least monolayer scale control with many parameters influencing the growth conditions like: temperature, material flux, timing, surface, capping, and morphology limitation. Understanding how QDs are formed is the first condition to improve QDs material. Then we will consider nanoscopic scale to investigate QD shape, microscopic scale to study QDs assembly formation and finally macroscopic scale for the realization of working device IBSCs. We start by discussing the literature and then we present our samples, basic characterization and improvements.

3.2.1 Growth of QDs by MBE

A high level of understanding of QDs growth is necessary to achieve the fabrication of suitable QDs absorber. Not only the user needs to understand and master the use of MBE system but he also needs to understand the physics behind the formation of QDs assembly step by step, monolayer by monolayer with the right tool to control the growth in-situ.

3.2.1.1 MBE system

Molecular beam epitaxy (MBE) is an epitaxy method for thin-film deposition of single crystals. It takes place in high vacuum or ultra-high vacuum chamber as shown in Figure 3.2-1.

For our study, the deposition rate is always less than 1-µm/h. During operation, reflection high energy electron diffraction (RHEED) is used for monitoring the growth of crystal layers. A computer controls shutters in front of each effusion cells, allowing precise control of the thickness of each layer, down to a single layer of atoms. Intricate structures of layers of different materials may be fabricated this way. Such control allows the development of structures where the electrons can be confined in space like QDs. The wafers on which the crystals are grown are mounted on a rotating wafer holder that can be heated to several hundred degrees Celsius during operation.

The Asaro-Tiller-Grinfeld (ATG) instability is an elastic instability often encountered during MBE. If there is a mismatch between the lattice sizes of the growing film and the supporting crystal, elastic energy will be accumulated in the growing film. At some critical height, the free energy of the film can be lowered if the film breaks into isolated islands, where the tension can be relaxed laterally. The critical height depends on the Young's modulus, lattice mismatch, and surface tension [155]. Applications for this instability have been researched, such as the self-assembly of QDs. This community uses the name of Stranski-Krastanov (S-K) growth [156] for the ATG instability and it will be detailed next.

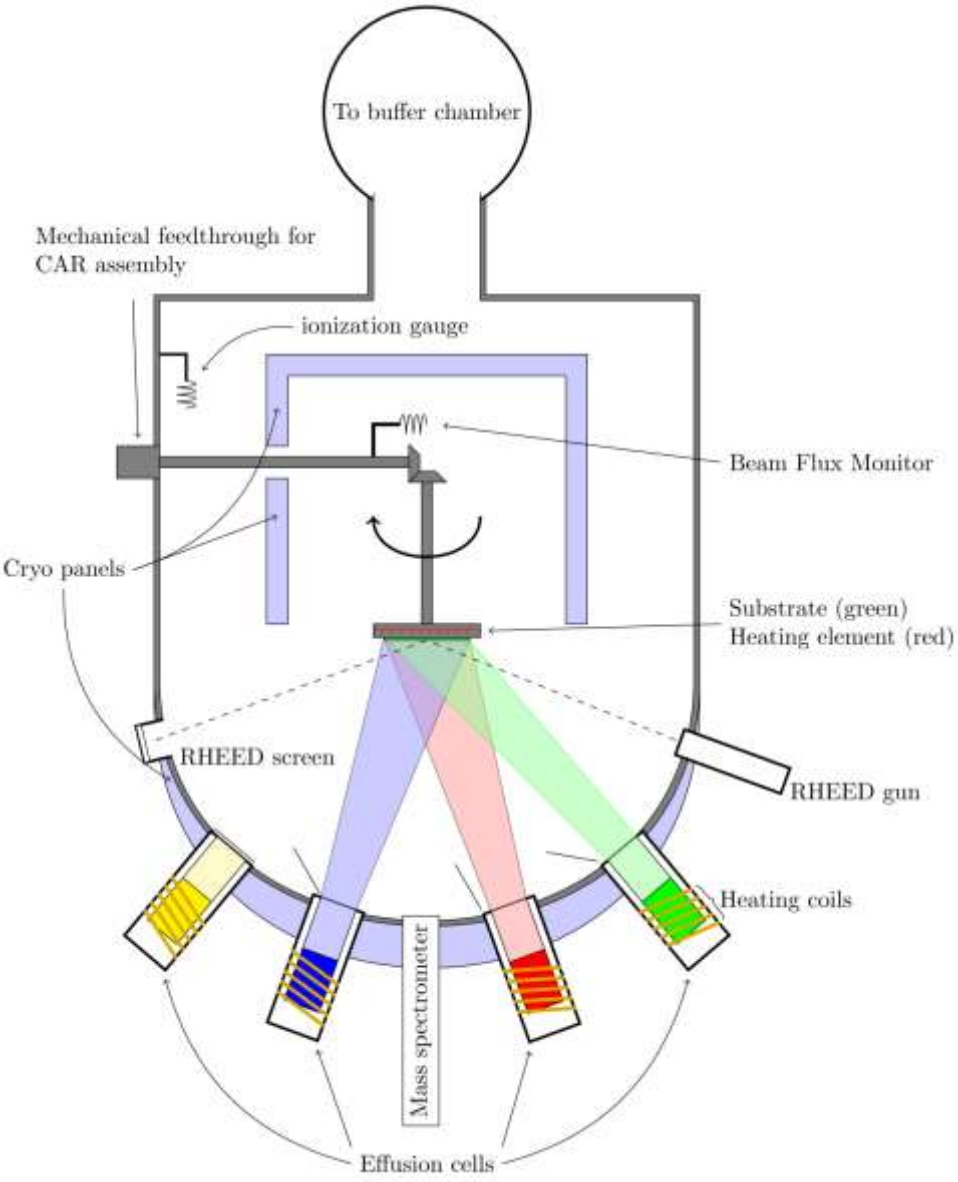

Figure 3.2-1: Sketch of a molecular beam epitaxy (MBE) reaction chamber. Taken from Wikipedia.

3.2.1.2 Stranski–Krastanov QDs growth steps

Also known as “layer-plus-island growth”, the S-K growth follows a two-step process: initially, complete films of adsorbates, up to several monolayers thick, grow in a layer-by-layer fashion on a crystal substrate, it is the growth step of the wetting layer (WL) as shown in Figure 3.1-2. Beyond a critical layer thickness, which depends on strain and chemical potential of the deposited film, growth continues through the nucleation and coalescence of adsorbate 'islands'. The thickness of this WL is strongly dependent on the lattice mismatch between the film and substrate, with a greater mismatch leading to smaller critical thicknesses. For large island densities, curvature effects from neighboring clusters will cause defected island creation, which is why defects-free high-density QDs layers are extremely difficult to grow. In the case of InAs on GaAs, the island growth usually starts after the deposition of 1.5 ML. If we assume WL is flat, the height will be around 0.45 nm. In reality,

WL may form randomly and QDs may start before the whole GaAs surface is covered as we will see in part 3.2.2.1 where we present AFM measurements from our samples growth investigation. Usually in the literature the height is considered around 0.5 nm but because of In/Ga inter-diffusion there might be a formation of a thicker InGaAs alloy layer of more than 1 nm as shown on Figure 3.1-2.

Real-time probing of the self-assembling process is usually performed by using conventional RHEED equipped with the MBE. The RHEED pattern shows quite highly sensitive changes depending on the S-K growth. As reported in many articles, the InAs deposition changes a streak pattern of the initial GaAs surface into a diffused pattern of the InGaAs WL and then a chevron pattern representing the three-dimensional island formation. After the island formation, the chevron pattern keeps changing, while the islands are growing up. In the literature [157], it has been understood from the dynamic evolution of the chevron structure that the QD growth consists of four significant steps. According to the feature observed in each growth step, these steps can be called: nucleation step, assembling step, self-limited step, and dissolving step. These four steps appear, even when the growth conditions are changed and they reflect changes in the facets of the surface as described on Figure 3.2-2.

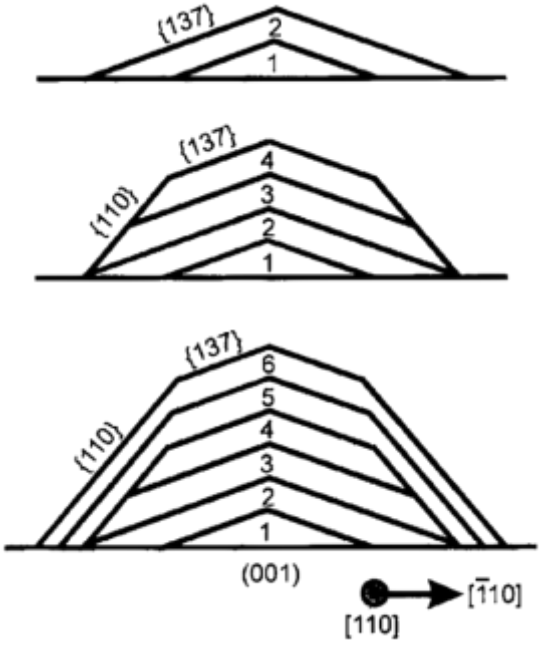

Figure 3.2-2: Schematic growth model of InAs QD's grown on the GaAs001 surface. Taken from reference [158].

Nucleation step happens just after the diffused pattern of the WL. The RHEED chevron signature for this step corresponds to a multifaceted surface with no clear orientation. Because island formation is triggered by a certain level of strain, this step starts with some geometrical multifacet structures that evolves towards QDs with high-index facets, such as {137}, as shown in Figure 3.2-2. From this point, the assembling step starts and QDs transition into their final shape with low-index facets, such as {110}. Moreover, the incorporation of Indium (In) atoms becomes easier. The third step is the self-limitation of QDs growth because of the more stable nature of low-index facets [158]. This step enables more homogeneous growth of a QD population. The dissolving step is not wanted because it corresponds to the coalescing or dissolution of QDs.

3.2.1.3 Temperature, flux dependence and $Al_xGa_{1-x}As$ growth surface

QD growth can be engineered by controlling the growth parameters such as deposition rate, growth temperature, and Arsenic (As) pressure. All these parameters affect the Indium (In) migration length, and so this is a key factor in the island formation. An increase of As pressure and a decrease of temperature gives a shorter In migration length that causes a less uniform size distribution.

Maxwell et al. have investigated the dependence of QDs density, size, composition and homogeneity on Al_xGaAs by varying these parameters [159]. For $Al_{0.15}GaAs$:

- Lower InAs growth rate induces lower QDs density.
- From 490°C, a 30°C increase on growth temperature induces a QD density reduction by four but almost constant QD height.
- Temperature higher than 520°C might induce high inhomogeneity and evaporation of In atoms.
- Between 490°C and 510°C, InAs volume fraction incorporated into QDs is lowered from 55% to 35%.

In the perspective of QD-IBSCs, it is usually thought important to have a high density and height with the largest InAs volume fraction because of the low optical absorption of QD layers. The dependence to the growth parameters show that growth of QDs is not easy and some tricks have to be used like closely stacking of QDs or the use of special capping techniques.

3.2.1.4 Capping process

Since the capping layer growth on InAs QDs is also lattice mismatched, it gives rise to significant In segregation and In/Ga intermixing. These phenomena dramatically change the island shape and size, as depicted in Figure 3.2-3.

<u>i). Real-time evolution following RHEED patterns</u>

When GaAs starts to deposit on the QD, an unfaceted surface is formed. Detailed structure of the unfaceted surface is not clear as in Figure 3.2-3(b).

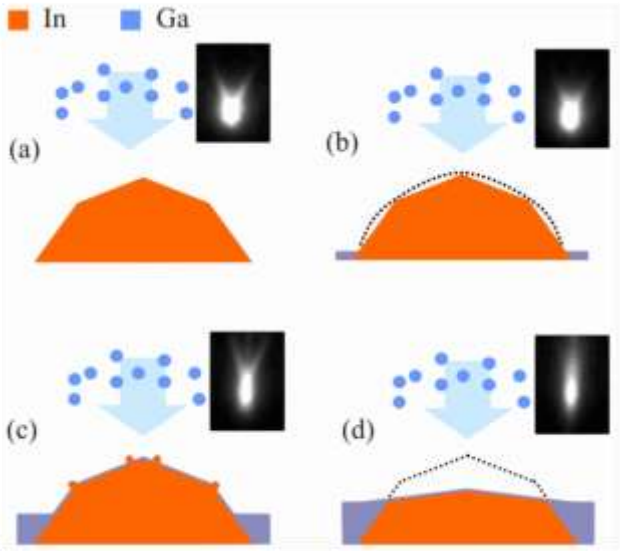

Figure 3.2-3: Model of the island shape transition during the GaAs capping layer growth. (a) chevron in the inset show a faceted surface, (b) chevron signal is fading because of an unfaceted surface, (c) unfaceted surface comes off , faceted chevron signal recovered but thinner, (d) In atoms have migrated and chevron signature completely disappears. Taken from reference [157].

Soon this unfaceted surface comes off the islands, there is a tendency for the Ga adatoms to migrate away from the top of the dots and then, the faceted surface appears again. The initial GaAs layers cover the region between InAs QDs as in Figure 3.2-3(c). This leads to an increase in the strain at the edge of the QDs. The increase in strain causes In atoms to migrate from the QDs to the WL region and hence the reduction in QD size as in Figure 3.2-3(d). A gradual shift of the chevron angle was confirmed [157]. The angle approaches zero when the deposited thickness approaches about 1.7 nm. This thickness is very thin as compared to the as-deposited QD height. Therefore, the top of the QD is considered to be truncated as mentioned by Lemaitre, et al. [134].To prevent this collapse in QDs shape, three parameters were investigated in the literature: material capping and especially the use of aluminum, capping temperature and growth interruption time.

ii). Restrain surface diffusion by AlAs capping and reduce WL effect

To restrain surface diffusion, capping by Aluminum (Al) was investigated by Lemaitre, et al., as shown on Figure 3.2-4 [134]. The bright AlAs layer is clearly visible, covering the substrate itself capped by the WL, and the lower flanks of the QD, but not its top. Accumulation of Al atoms on the lower flanks occurs at the very early stages of the capping process and indicates an energetically favorable location. Indium segregation preferentially occurs in the directions with relatively low surface energies. The resulting AlAs layer forms a blocking barrier. On the contrary, Al does not accumulate at the top of the QD, an elastically unfavorable region because of its In-rich content.

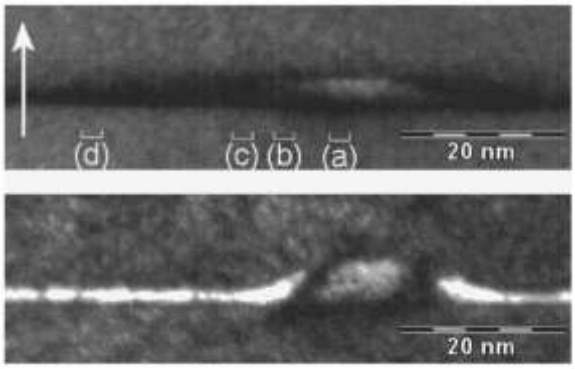

Figure 3.2-4: 002 TEM DF images of InAs/GaAs QDs capped with GaAs (top figure) and covered with 1 nm of AlAs before capping with GaAs (bottom figure). Taken from reference [134].

When the InAs QDs are capped by GaAs, In usually diffuses in the WL and In/Ga intermix, leading to QD collapse. In the case of $Al_xGa_{1-x}As$ capping, the lowly migrating Al adatoms bonding to In atoms in the QDs slow down the In migration and suppress the QD collapse as shown in Figure 3.2-5 [160].

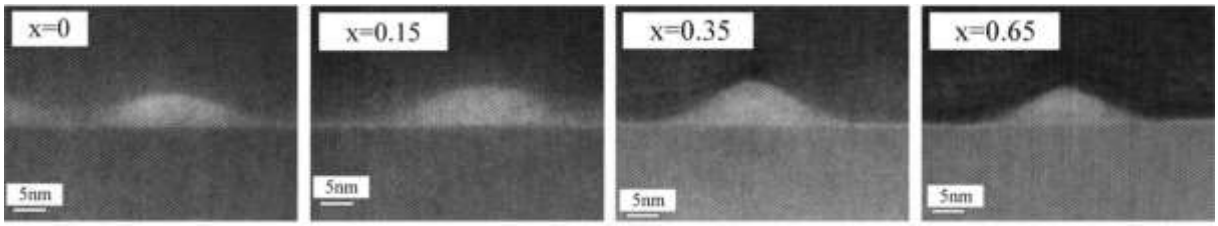

Figure 3.2-5: single-dot scanning TEM images of InAs/GaAs QDs capped by GaAs or AlxGa1−xAs. Note that the selected single dots for scanning TEM do not exactly reflect the average QD sizes. Taken from reference [160].

Another positive effect of AlAs capping is the disintegration of InGaAs WL. Segregation of In atoms leads to alloy intermixing and formation of InGaAs in the region between dots. When InAs QDs are capped by AlAs, there is the creation of an InAlAs alloy layer at the place of the InGaAs WL as it can be seen in Figure 3.2-4 (bright white layer). In the literature, 2ML [59], [60] to 3.5ML [134], [161], deposition of AlAs have been used for pre-capping. Comparing with 1.5ML of InAs critical thickness before QD nucleation step, it means that the ratio of Indium in InAlAs will be roughly equal or less than x=0.43. Hence, the newly formed alloy WL will have a bandgap energy higher or equal to 1.66 eV following Figure 3.1-1. Therefore in InAs/$Al_{0.2}$GaAs system, a 2ML AlAs capping seems to remove the S-K WL traditional issue of having a WL energy position in-between QDs ground states energy and host material [59], [60]. Other capping materials have also been tested as strain-balancing layers like GaAsN [22].

iii). Temperature and growth interruption time

Growth temperature and growth interruption time have also been investigated [162]. As expected, low-temperature capping at 300°C helps to maintain QD shape and size. On the contrary, growth interruption of 20 seconds is enough to trigger the collapse and leveling of QDs as shown in Figure 3.2-6.

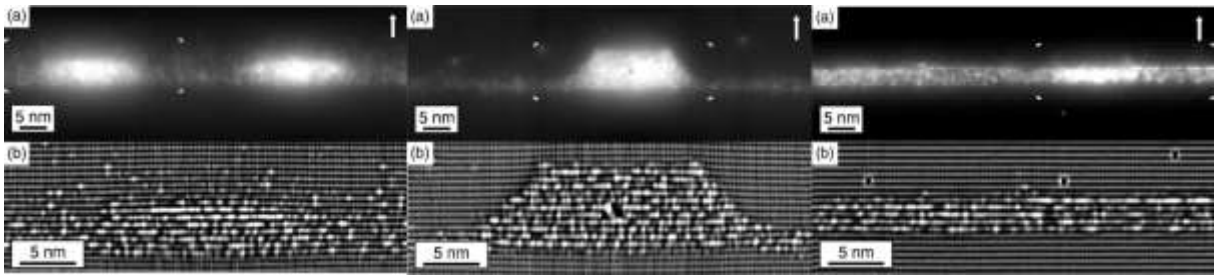

Figure 3.2-6: (a) Filled states topography X-STM image InAs QD for capping at 500°C (left), 300°C (center) and with growth interruption time (right). Part of the image (a) marked by four corners is treated by a local mean equalization filter and shown in (b). In (a) the arrow indicates the growth direction. Adapted from reference [162].

iv). Morphology limitation

In a recent study, Gonzalez et al. [163], have tried to estimate the effect of the capping process on the morphology of InAs/GaAs QDs by using different GaAs-based capping layers, ranging from strain reduction layers (e.g. GaAsSb) to strain compensating layers (e.g. GaAsN). Their results indicate that the QDs evolve during the capping process. Both the lateral and vertical dimensions seem to vary in order to adopt a similar spherical dome shape (aspect ratio *r*) for different sizes, independently of the predominant capping layer induced mechanism. A particularly stable shape for each size exists that should therefore result in a minimized strain and interface energy.

This process seems to occur regardless of the QDs/capping layer mismatch, the different compositions, and the different growth conditions of the capping layer. In this process, the capping layer features such as the presence of Sb and/or N have an influence on the scale of the QD size changes but not on the average aspect ratio, which is maintained around 0.208. This results is thought to be indicative of a universal behavior of the overgrowth processes in self-organized InAs QDs. This conclusion helps to understand that self-organized InAs QDs have intrinsic limitations that might not be overcome simply by changing the capping material.

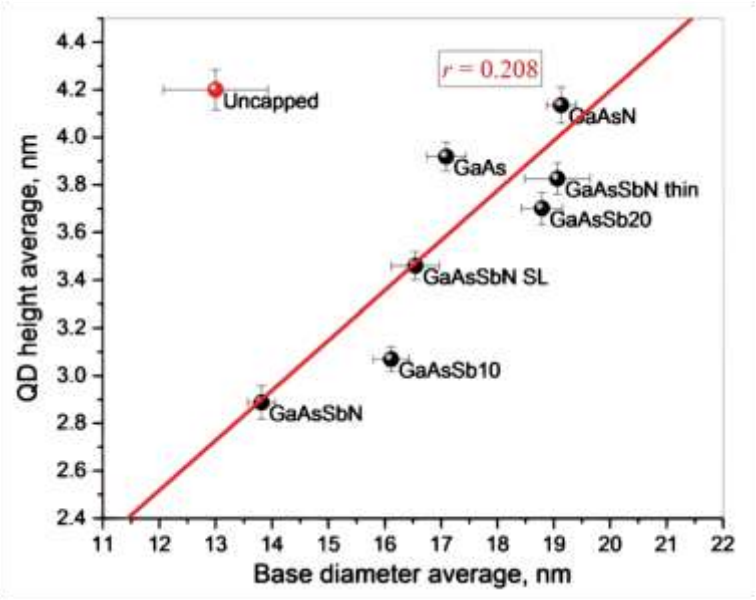

Figure 3.2-7: Average QD height vs base diameter for different capping layers. Error bars are the standard error of the measurements. The red line represents the fitted aspect ratio r=0.208. Taken from reference [163].

Thus, to keep a reasonable QD size but at the same time have a non-negligible absorption, complementary strategies might be needed like closely stacked QDs [73] or the so called quantum-dot superlattice (QDSL) [164].

3.2.2 Control and improvement of QDs growth

In the previous part, we focused on global investigations that we found in the literature on the topic of self-assembled In(Ga)As QDs grown by MBE. In this part, we focus on the MBE setup and samples that were fabricated in Okada Lab. by Dr. Yasushi Shoji. Using MBE requires control tools and techniques to have information on the grown layers. In the course of our project, five different growth conditions have been tested for different samples as summarized in Table 3.2-1. For every sample name, at least two more test samples have been made for different types of characterization techniques.

Table 3.2-1: Five different growth conditions for In(Ga)As/AlGaAs system

Name	QDs	Growth temperature	Capping	Spacer	QDs doping	# QDs layers	MBE setup
Okd-1	2.0 MLs InAs	500°C	$Al_{0.2}GaAs$	25 nm $Al_{0.2}GaAs$	No	10	Version 1
Okd-2	2.0 MLs InAs	450°C	$Al_{0.2}GaAs$	20 nm $Al_{0.2}GaAs$	No	10	Version 1
Okd-3	1.9 MLs InAs	480°C	$Al_{0.2}GaAs$	23 nm $Al_{0.2}GaAs$	No	10	Version 1
Okd-4	9 MLs InGaAs	520°C	2 MLs AlAs	25 nm $Al_{0.3}GaAs$	4 Si/QDs (8e17 Si/cm^3)	40	Version 1
Okd-5	1.9 MLs InAs	480°C	2 MLs AlAs	25 nm $Al_{0.2}GaAs$	4 Si/QDs (8e17 Si/cm^3)	20	Version 2

Each of these growths had different purposes that we will explain. They helped to get knowledge on our QD growth and also to improve the MBE setup.

3.2.2.1 AFM and STEM characterizations from micron to atomic scale

Atomic-force microscopy (AFM) is a type of scanning probe microscopy that provides a three-dimensional surface profile with a resolution of less than one nanometer. This tool is especially useful to assess diameter, height, shape and density of QDs before capping.

i). Investigation of growth condition

As an illustration, Figure 3.2-8 shows different 1-µm² AFM images for Okd-1 and Okd-3 MBE growth conditions. Two different parts of the wafer are characterized: center and edge. By decreasing the temperature from 500°C to 480°C and decreasing the number of deposited monolayers (MLs) from 2.0 to 1.9 MLs, we observed that we are able to increase both QDs homogeneity (in diameter) and density.

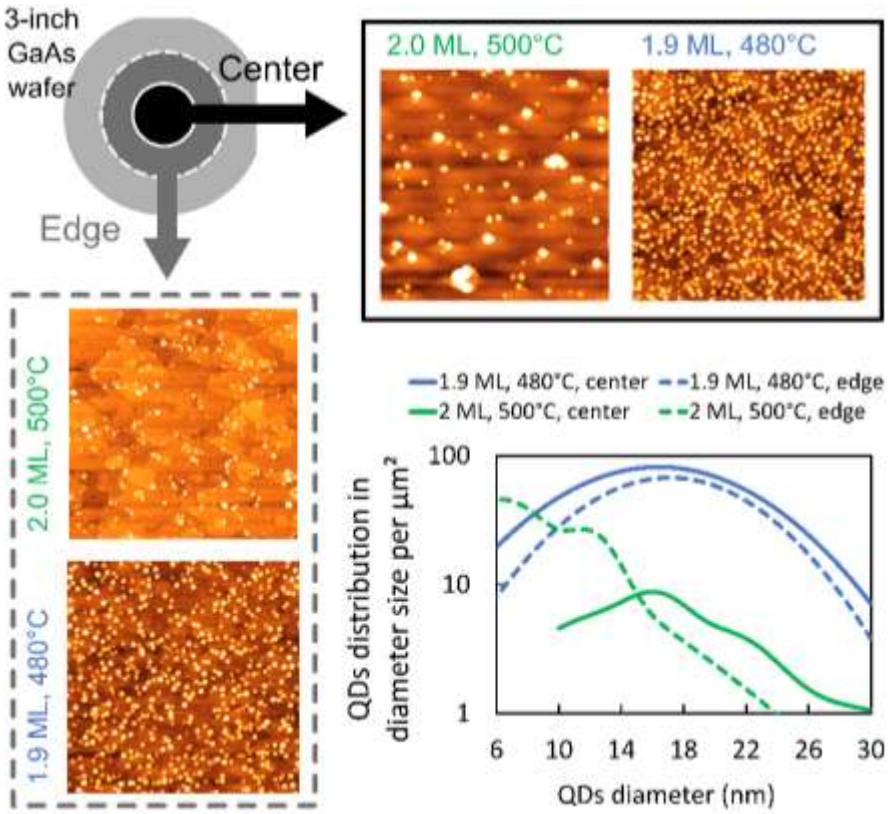

Figure 3.2-8: AFM images performed on 4 samples over 1x1 µm²: for 2 different MBE growth conditions (Okd-1 and Okd-3) and 2 different locations on the 3-inch wafer: center and edge. Graph shows the QD size distribution per µm² as a function of the diameter for these 4 samples.

ii). Investigation of QDs shape and WL

AFM is also very useful to investigate the shape and topography of QD growth. Figure 3.2-9 to Figure 3.2-12 show three AFM colored images of the same measurement over 1-µm² considering different z-planes as references for height. The AFM measurement is done on an Okd-3 type of growth in the middle zone of a 3-inch wafer.

Figure 3.2-9 shows the AFM image with a reference plane at the position of $Al_{0.2}GaAs$ layer. We assume that the lowest height is the $Al_{0.2}GaAs$ layer because when we integrate the z-profile we find about the same order of MLs as deposited during 1.9 MLs QDs growth. This AFM image illustrates very well the S-K growth process described earlier. For a critical amount of InAs deposited there is the apparition of a landscape with peaks (QDs islands in red) and valleys ($Al_{0.2}GaAs$ in dark blue). The maximal difference in height is around 5 nm which shows the potentiality of having 5 nm-high InAs QDs. Top view inset shows an almost xy spherical symmetry for QDs. Side view inset shows that at least 1 nm-thick InGaAs WL links almost all QDs together.

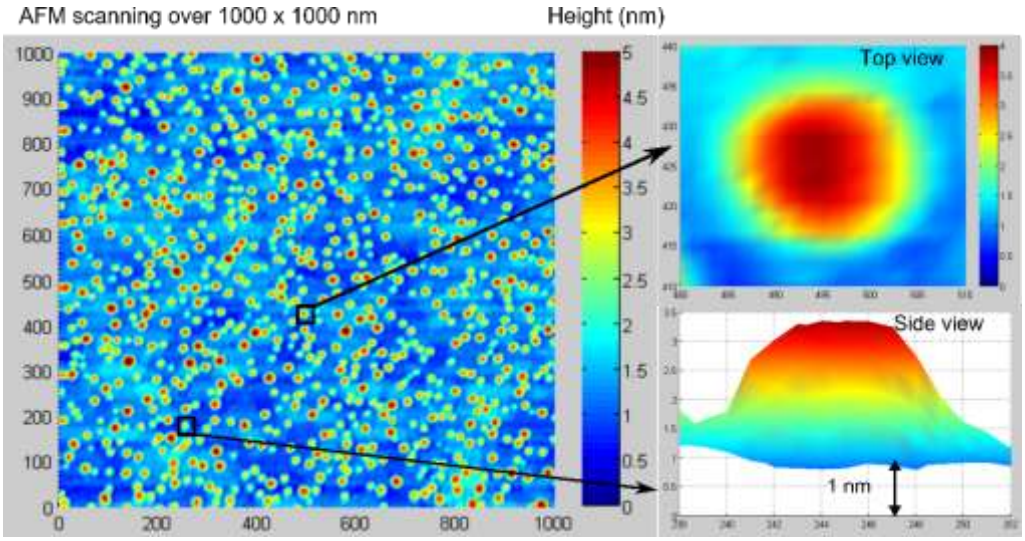

Figure 3.2-9: AFM color image with z-profile reference at $Al_{0.2}GaAs$ base layer. 1.9MLs InAs QDs growth at 480°C.

In certain case, this WL is 2 nm-thick as it can be seen on the whole 1 µm² area looking at colorbar height up to 2 nm (turquoise color). In the literature, these zones with thicker WL are referred as "nanodisks" or "quantum-well islands" (QWIs) [140], [165]–[167] as represented in Figure 3.2-10 [166].

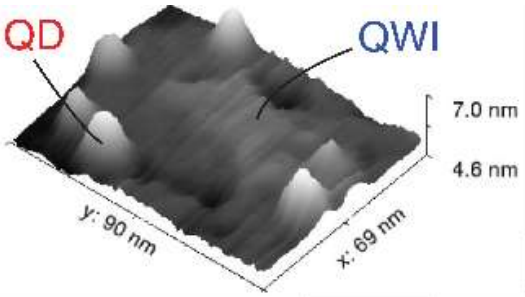

Figure 3.2-10: 3D AFM image with QDs and a QWI on the WL of an InAs/AlGaAs layer without capping. Taken from [166].

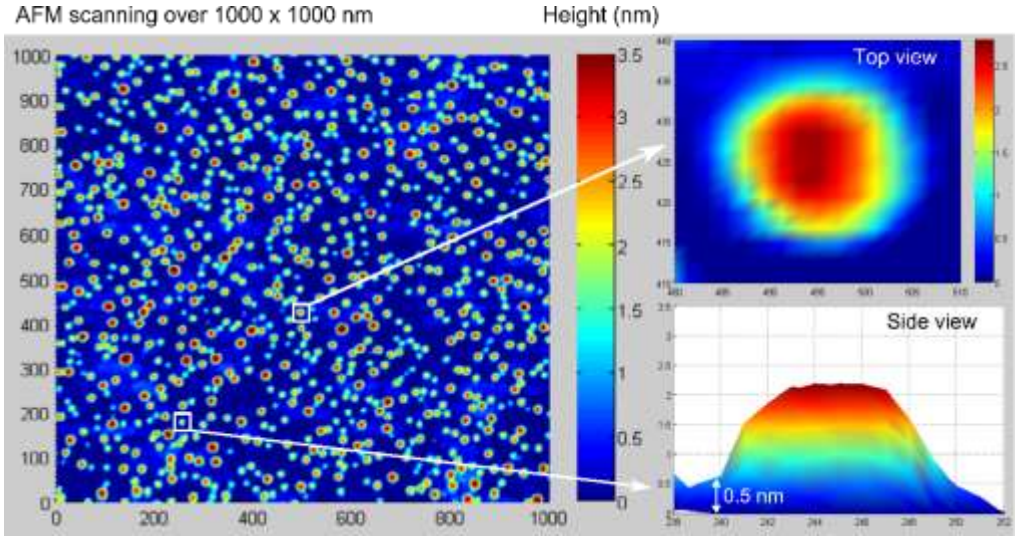

Figure 3.2-11: AFM color image with z-profile reference at WL critical thickness for 1.9MLs InAs QDs growth at 480°C.

Figure 3.2-11 shows the same image for a z-reference around the WL level. This height position is defined by integrating the whole area to find the 1.5 MLs critical WL thickness value that triggers QDs growth as discussed previously. We notice that almost all QDs are separated for this z-reference. Nevertheless, we can also notice a pyramidal “WL halo” or “WL tail” surounding QDs and still offering a footbridge in-between QDs because of the “nanodisks” or “QWIs”.

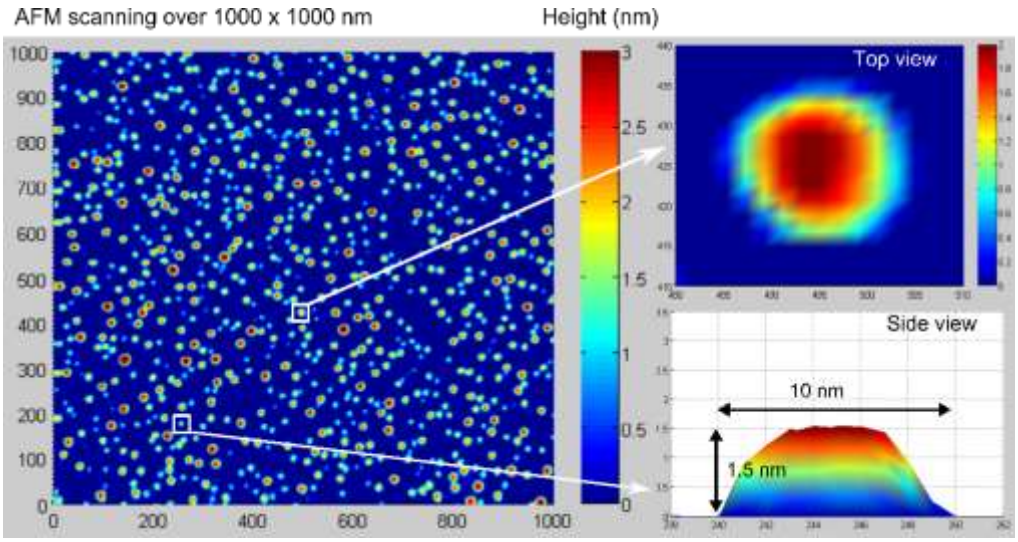

Figure 3.2-12: AFM color image with z-profile reference at position where all QDs are separated and have a lens shape.

Figure 3.2-12 is shown for a z-reference where all QDs are separated from each others without the “WL tail”. This image is especially interesting to investigate the lens shape of QDs as seen on the side view inset.

Overall, this investigation of QDs shape and decomposition between the $Al_{0.2}GaAs$, WL, QWIs and QDs is useful to understand and remodel by simulation the quantum properties and interactions of those nano-objects.

iii). Investigation of QDs population

By considering Figure 3.2-11 and Figure 3.2-12 as representatives of QDs geometrical shapes, we can estimate QDs height and diameter as summarized on the histograms in Figure 3.2-13.

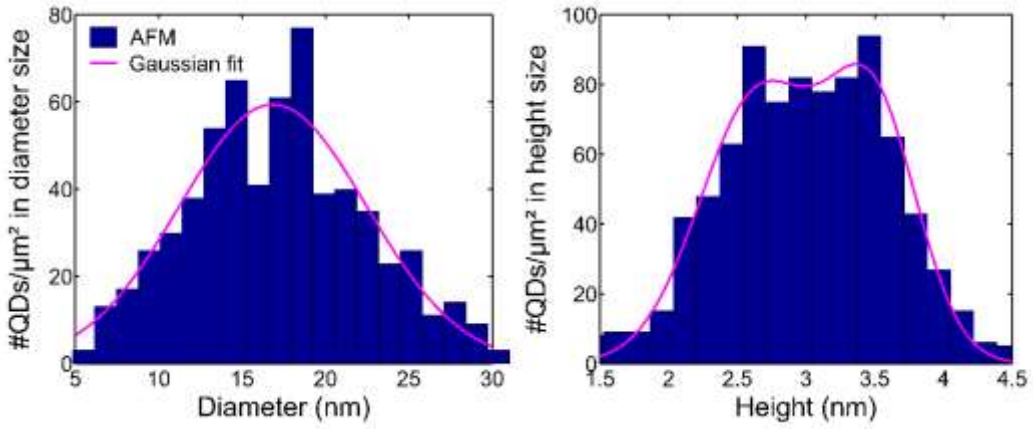

Figure 3.2-13: Histograms representing QD height and diameter distribution of Figure 3.2-9 AFM measurements.

Figure 3.2-13 shows an almost gaussian distribution with QD diameters centered at 17 nm. Diameter are detected using ImageJ particle analysis software. The analysis method will mostly consider diameters as shown in Figure 3.2-12 which means that these diameter values neglect the lateral contribution of "WL tail". The resolution of AFM is limited by the sharpness and shape of the tip whose normal radius of curvature is 10 to 60 nm so there is a lack of precision in AFM measurements of nanometer-sized samples in the lateral dimension. In order to obtain trustworthy spatial measurements of QD diameters, cross sectional TEM images can give a complementary view [163].

In Figure 3.2-13, for the height we see a bimodal shape centered respectively at 2.5 nm and 3.5 nm. These values of height are including the WL and QWIs thicknesses that are estimated to be around 1-2 nm as revealed by Figure 3.2-9 and Figure 3.2-11. We have to keep in mind that uncapped QDs should have a different shape than capped QDs but we also know that $Al_{0.2}GaAs$ capping can almost preserve QDs from collapsing as illustrated earlier in Figure 3.2-5.

iv). STEM measurement confirmation

In Figure 3.2-14, we present a STEM image of an InAs/$Al_{0.2}GaAs$ stacked layers of QDs with Okd-2 type of growth.

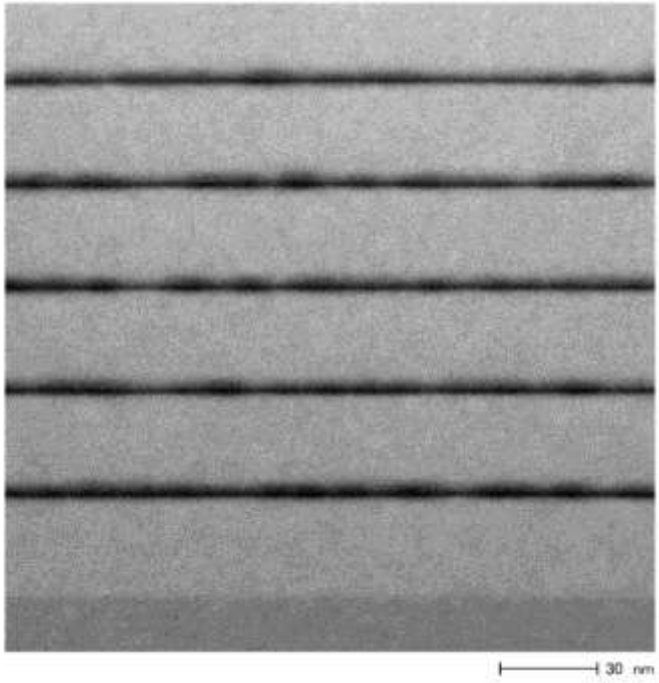

Figure 3.2-14: bright-field-STEM images: InAs QDs of 15-20 nm diameter with $Al_{0.2}GaAs$ capping layers

For this QDs system, AFM images show that the average diameter is around 15-20 nm. We cannot clearly distinguish the WL height because all QDs in the plane contribute to electron transmission. However, we can give an estimation of the maximum QDs heights that seem to be around 3 nm. This image seems to confirm AFM measurements and the shape is close to a lens-shape about the same kind as in Figure 3.2-5 for a 15% aluminium concentration. The aspect ratio of our QDs are in the range of 0.15-0.24 depending on how thick WL is considered. This value is in the range of the previously discussed universal behavior found by Gonzalez et al. [163] and illustrated in Figure 3.2-7.

In conclusion, it seems our InAs/$Al_{0.2}$GaAs QDs are comparable with usual self-organized InAs QDs found in the literature. As explained earlier, it should be possible to have an estimation of In concentration for example by quantitative analysis of dark field image contrast. We did not perform the experiment in our case due to a lack of time. We will assume the concentration to be in the better case of an average of 55% [134]. This is useful to estimate the QD energy state levels and to get a more precise picture of our system.

3.2.2.2 PL mapping from centimeter to micron scale

Photoluminescence (PL) mapping techniques is a fast non-destructive technique that gives a lot of basic information on the optical properties of direct bandgap semiconductor material. In our case, the PL characterization is made using a HORIBA Jobin-Yvon scientific PL mapping system that can also be used for Raman spectroscopy. The sweeping step in *xy*-direction is 200 µm. PL excitation is achieved with a 532 nm wavelength laser and x10 objective. The excitation spot diameter should be less than 10 µm in usual configuration. Two different types of detector are usually used. Charge coupled device (CCD) Silicon detector for the visible and NIR part of the spectrum up to 1.1 µm and IR detector for longer wavelengths (e.g. PbS or InGaAs detectors). In the following, it is used to control and improve QD growth on a wafer scale.

i). PL mapping of AlGaAs host material

We can use this PL mapping setup to estimate the aluminium content of the AlGaAs host material over a 3-inch wafer. Figure 3.2-15 shows the PL mapping characterization of the Okd-5 type of growth sample (MBE setup version 2). Mapping shows that PL peak of AlGaAs is around 734-738 nm at room temperature as shown by the color bar on the right of the graph. We clearly see a 2-inch homogeneous zone of AlGaAs with PL peak at 734 nm which represents a bandgap energy of 1.69 eV. Following Adachi experimental equation for AlGaAs materials [168] we find that it corresponds to an Al concentration of 21.3%. On the edge for 738 nm, energy bandgap is 1.68 eV thus we find an Al concentration of 20.5%. In conclusion we have less than 1% difference in Al concentration for the 3-inch wafer and almost completely homogeneous for 2-inch zone. We suspect this 2-inch zone might be due to the size of effusion cell crucible that were initially designed for 2-inch wafers in this MBE machine.

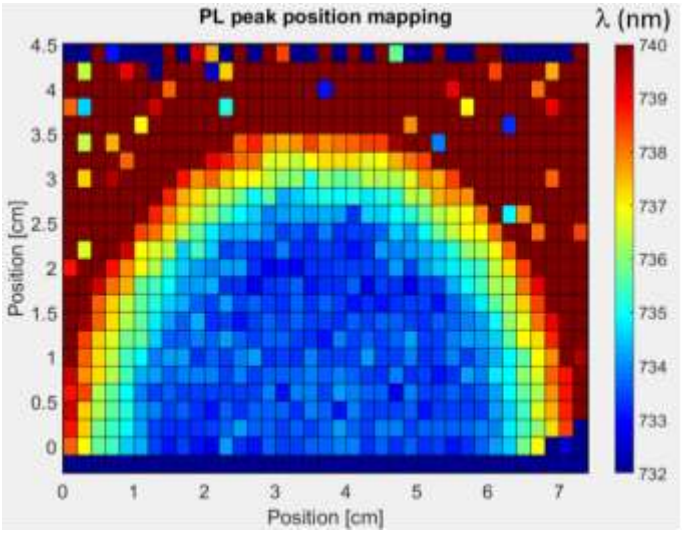

Figure 3.2-15: AlGaAs PL mapping for half of the Okd-5 type of growth 3-inch wafer sample. Wavelength peak position is shown in colorscale. Sweeping step is 200 µm with a 532 nm laser with spot diameter less than 10 µm.

ii). PL mapping of InAs QDs: PL peak shift and PL intensity decrease on 3-inch wafer

For InAs QDs, in Figure 3.2-8, we noticed by AFM that Okd-1 showed large inhomogeneity in the growth of QDs between the edge and the center of a 3-inch wafer. Okd-3 seems to offer a better homogeneity according to AFM images in terms of diameters and densities. The PL map of its QD PL wavelength peak is shown in Figure 3.2-16. We see that the QD emission peak is much less homogeneous in comparison to the homogeneity showed by growth of the AlGaAs host material.

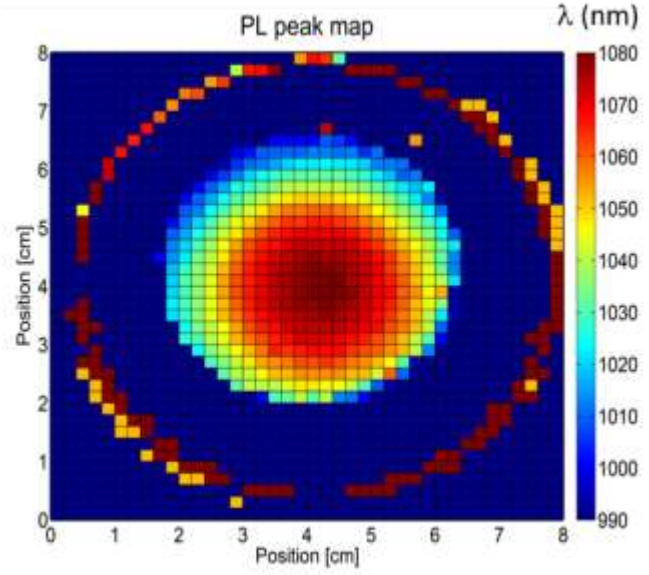

Figure 3.2-16: QDs PL mapping for Okd-3 type of growth 3-inch wafer sample. Wavelength peak position is shown in colorscale. Sweeping step is 200 µm with 532 nm laser

In Figure 3.2-16, we see only a 1-inch diameter area in the center that has an almost homogeneous QD PL peak around 1060-1080 nm which corresponds to a bandgap energy of 1.15-1.17 eV. The position of PL peaks can be related to QD size and especially the height. Larger QDs will have lower bandgap energy and thus a higher PL peak in wavelength.

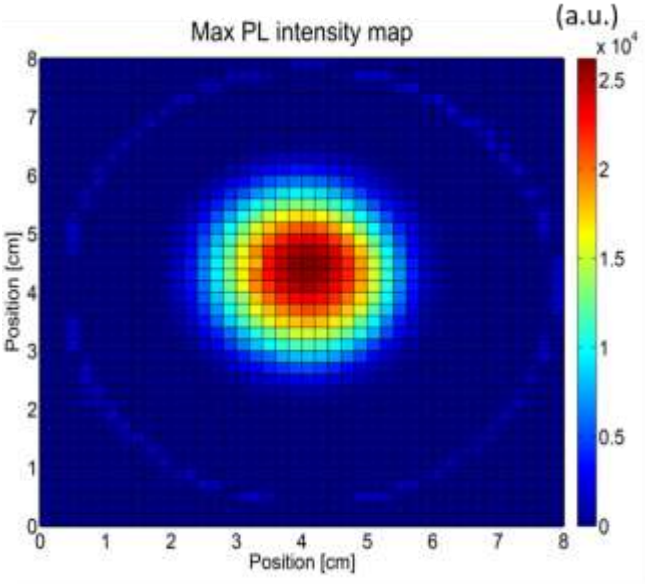

Figure 3.2-17: QDs PL mapping for Okd-3 type of growth 3-inch wafer sample as in Figure 3.2-16. PL peak maximum intensity is shown in colorscale in arbitrary units. The ratio between the highest detected peak and the lowest is about x30.

On the edge of the 3-inch wafer we see no signal from PL QDs which can mean that the density of QDs is too low or non-radiative recombination are too high compared to PL. In Figure 3.2-17, a map of the PL peak intensity is shown, and we see that the 1-inch center zone has a x2.5 ratio difference between the highest and lowest peak and for the 2-inch area it goes up to x30. PL peak intensity can be related to QD size, QD density or non-radiative trap concentration.

AFM images show that the density of QDs is higher in the center of the wafer as shown in Figure 3.2-18. We have seen earlier that at least over the 1-inch center zone, QDs have about the same size due to the PL peak position that is almost not shifting. Therefore, it seems that the density of QDs might be responsible for the decrease of the intensity at least for this center area. There might be another explanation if we think about the dynamic of PL at room temperature and relate it to the bimodal distribution of QDs underlined in Figure 3.2-13.

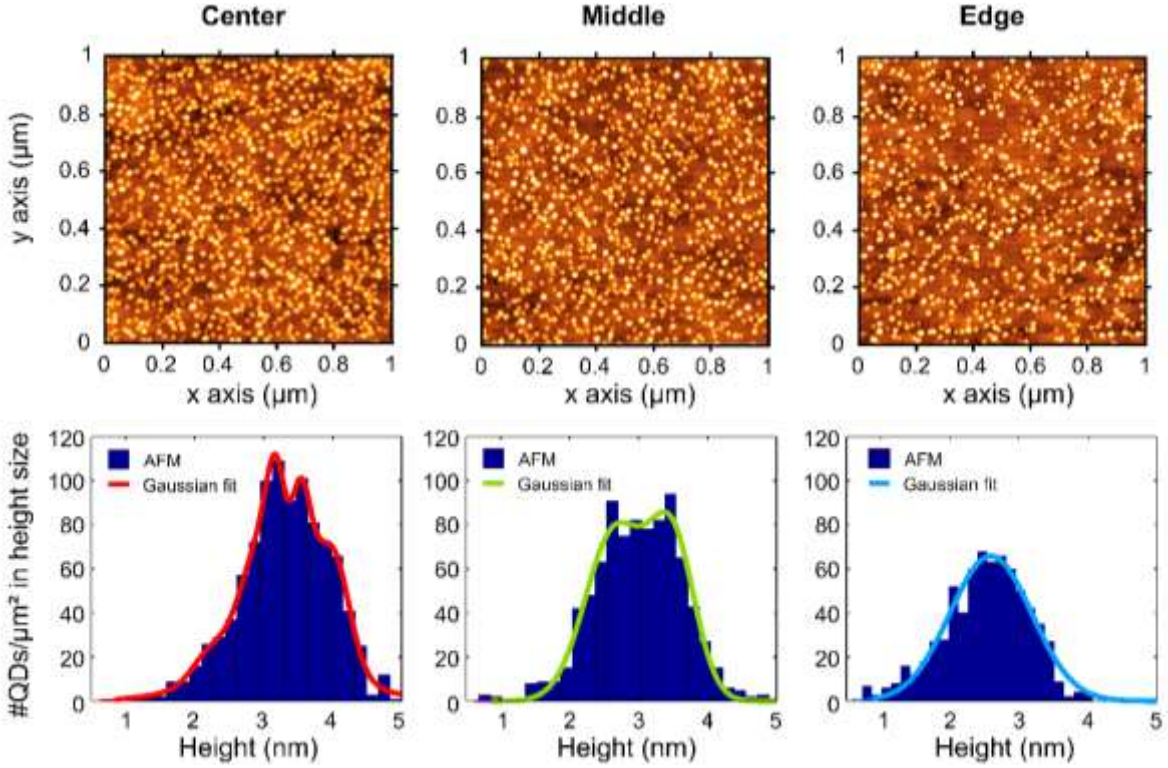

Figure 3.2-18: AFM images taken from 3-inch wafer Okd-3 growth condition, in the center, middle, and edge zones. Histograms of heights are presented for these measurements, which reveals different type of Gaussian distributions: multimodal, bimodal and single-modal.

In Figure 3.2-18, not only the density but we also notice the change in QDs heights distribution going from a single-modal distribution for edge AFM measurements to bimodal for middle and multimodal in the center zone. In Figure 3.2-19, we compare the changes in heights distribution, diamerer distributions and PL zones. We can separate the 3-inch Okd-3 wafer in 4 zones: center, middle, edge and off-beam. We use the “off-beam” expression because we detect no QDs PL signal for this zone and we think it might be due to the fact that this zone is outside of the beam flux of indium. This was taken care of in the MBE setup version 2 that will be discussed later.

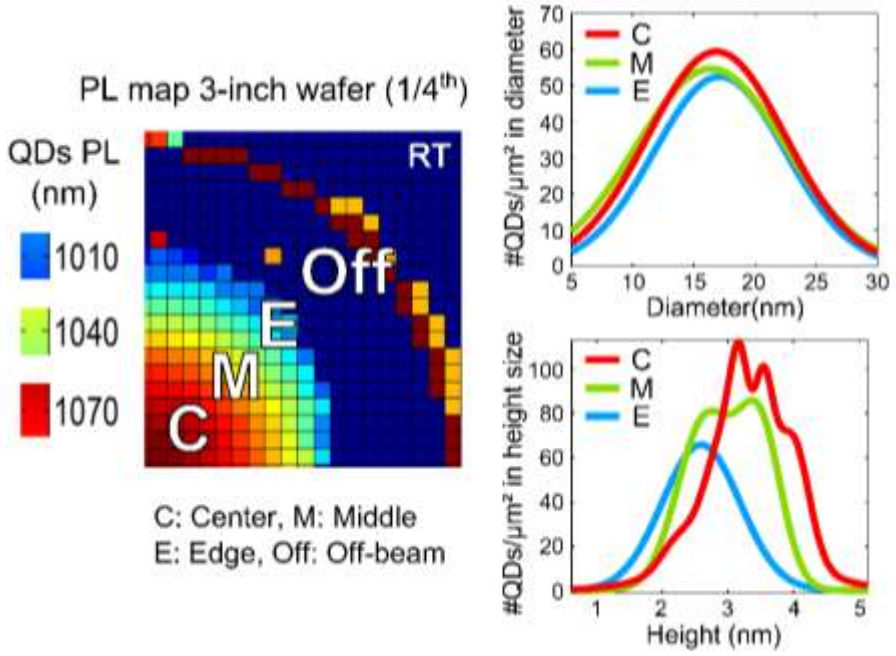

Figure 3.2-19: 4 QDs zones are detected on 3-inch wafer with Okd-3 type of growth. The 4 zones are indicated on the PL map at room temperature (RT). Colors indicate PL peak in wavelength. AFM gives indication on the diameter and height distribution.

iii). PL mapping of InAs QDs: PL gaussian fitting

Figure 3.2-18 indicates a multi-modal and bimodal distribution of QDs in height but Figure 3.2-20 indicates a nearly perfect Gaussian fit for PL curve taken from the center of the wafer to the edge zone. This seems to be a contradiction but we will see later by studying temperature-dependent PL that this gaussian PL is due to a trapping/detrapping effect that favors "large QDs" over smaller ones for PL emission. This effect has been refered as a kind of "Stokes shift" effect in the literature [169].

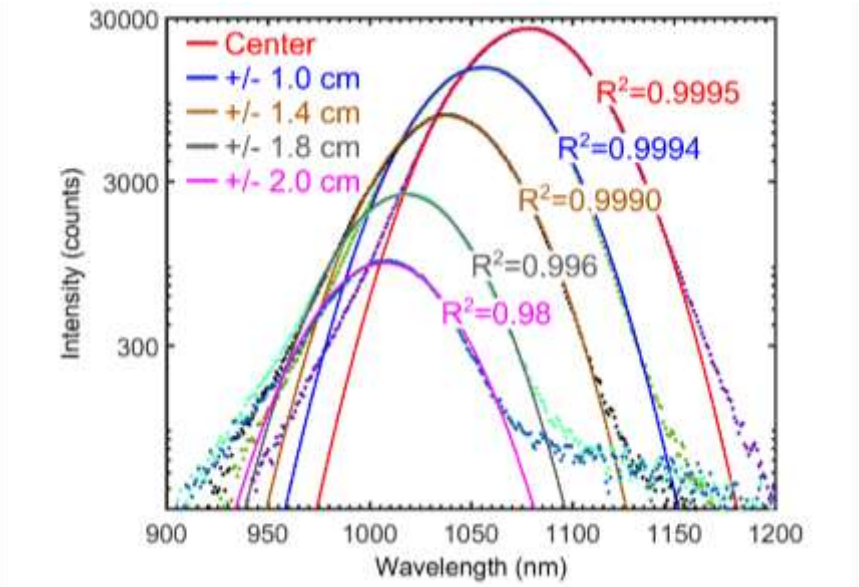

Figure 3.2-20: PL in log scale (dotted line) from QDs at different positions starting from the center of the 3-inch wafer (Okd-3 sample). The one-gaussian fitting is shown with the coefficient of determination r-square for each position.

iv). PL mapping of InAs QDs: PL FWHM

Thanks to almost perfect Gaussian fitting of PL we can easily have a mapping of the full width at half maximum (FWHM) for each PL measurement on the Okd-3 3-inch wafer. We see almost the same FWHM around 65 nm in average. If we consider doing gaussian fitting of PL with energy instead of wavelength, we find a value of FWHM of 70 meV +/- 6eV. We can consider Okd-3 sample to be almost homogeneous in term of FWHM which means that the broadening in term of QDs population for the "large QDs" is almost the same even when QDs size is changing. Comparing to the literature, such value is expected for a typical population of QDs.

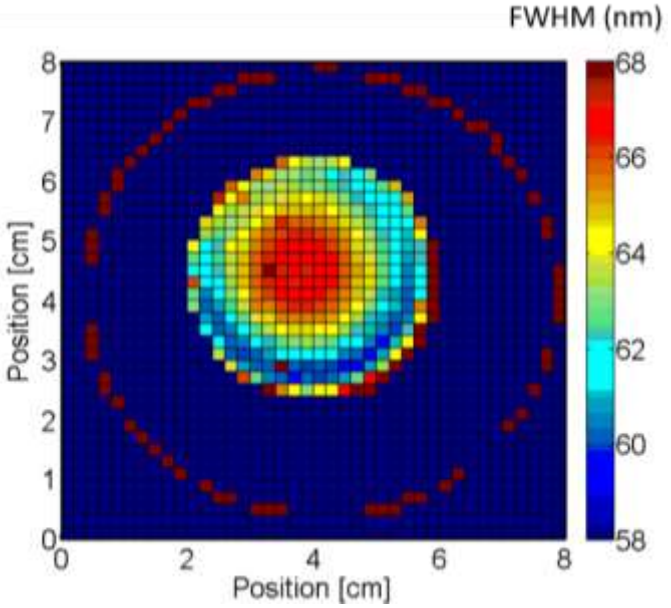

Figure 3.2-21: FWHM mapping extracted from Okd-3 3-inch wafer sample QD PL mapping. FWHM is shown in colorscale.

v). Inhomogeneity of QDs: hypothesis and improvements

Inhomogeneity of QD growth can be interesting in some cases. For example, it can offer a low cost way to investigate different types of QDs in one growth as we will see later. Nevertheless it is also very time consuming because we need to assess the properties of each sample individually. Moreover, in some cases, even on the same 1-cm² sample, one can find large differences for solar cells fabricated at different positions. Ideally, homogeneity of QD growth on 3-inch wafer is better from an experimental point of view so that each solar cell shares almost the same optical and electrical properties.

Considering the PL peak shift from the center that we relate to the QD size, we think the change might be explained by an inhomogeneity from the substrate heater. For a single heater system, we found that there can be a 20°C temperature difference between the center and the edge of the wafer. On the other hand the PL peak intensity decrease that we relate to the QDs density might be explained by the Indium flux and the size of the Indium effusion cell that is of 2-inch for Okd-3 with MBE setup version 1.

For Okd-5 growth, we were able to change to an MBE setup version 2 with a 3-inch Indium effusion cell and improve the substrate heater homogeneity by using a two-zone heater system. Compared to Okd-3, growth conditions were almost the same but the number of QD layers in Okd-5 is doubled because it was grown for a different purpose where we wanted to increase the overall subbandgap

absorption. In Figure 3.2-22, we see that the change made on the MBE system really increased the homogeneity of QDs growth for our sample in term of QD size. Colorbar scale spreading is the same for both images but red on Okd-5 corresponds to a 1020 nm PL peak in wavelength.

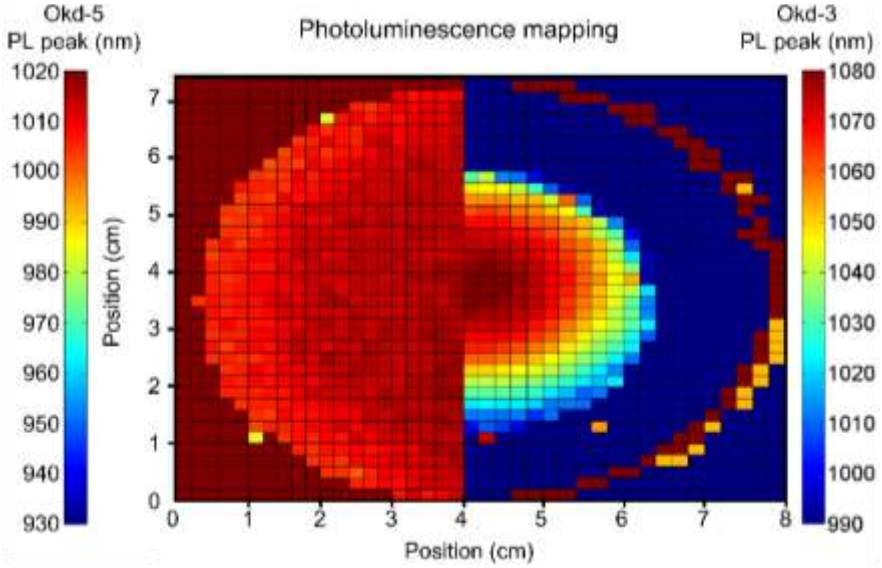

Figure 3.2-22: PL mapping of QDs peak position for Okd-5 (left) and Okd-3 (right). Same growth conditions (1.9 MLs InAs, 480°C) but MBE setup is improved for Okd-5 (version 2). Colorbar scale spreading is the same for both images but red on Okd-5 corresponds to a 1020 nm PL peak in wavelength because of heater change.

The PL peak intensity is also improved as shown in Figure 3.2-23. We still have some differences between the center and the edges but the center zone is about ten times larger which enable to have ten times more homogeneous samples per growth.

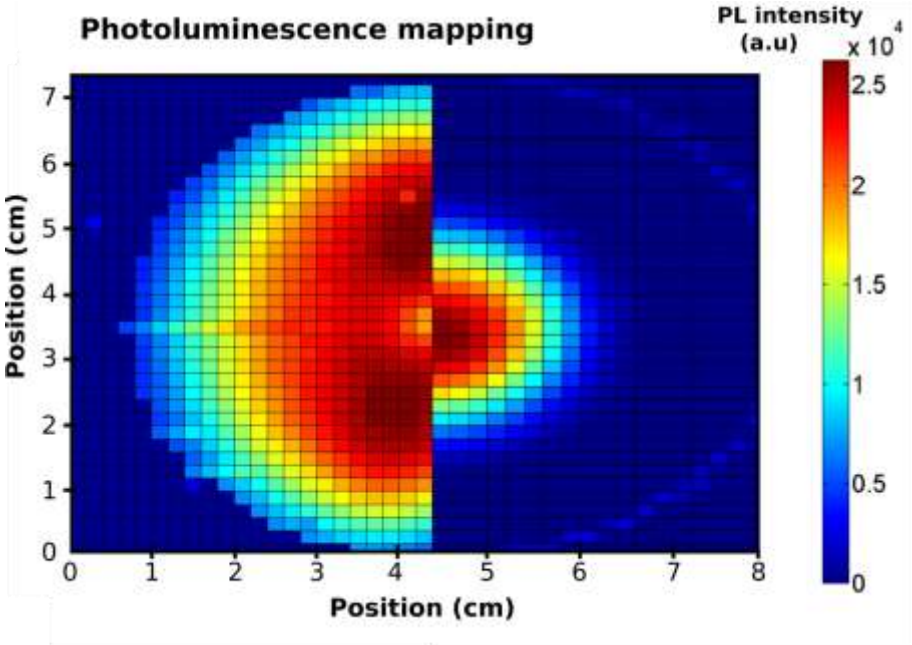

Figure 3.2-23: PL intensity mapping for Okd-5 (left) and Okd-3 (right). Same growth conditions (1.9 MLs InAs, 480°C) but MBE setup is improved for Okd-5 (version 2).

Table 3.2-2 summarizes the differences of the results obtained with the MBE setup version 1 and version 2 used for Okd-3 and Okd-5 growths, respectively.

Table 3.2-2: comparison between MBE setup version 1 and 2

	Qkd-3 MBE version 1	Okd-5 MBE version 2
Use of 3-inch wafer	2-inch zone	all
Homogeneous zone	3 cm²	30 cm²
Peak position range	[1000-1080 nm]	[1000-1015nm]
FWHM	65 nm	85 nm
Goodness of gaussian fit	2-inch zone	Almost everywhere

Almost all parameters are improved except FWHM that has increased by 20 nm in Okd-5 but this could be due to the fact that Okd-5 has twice more QDs layers than Okd-3.

3.2.2.3 Investigation of InGaAs vs InAs QD growth

In the perspective of In(Ga)As QDs, we have mentioned earlier that expressions like “InAs QDs” and “InGaAs QDs” are just ways for QDs grower to report about one parameter of their growth conditions, which is the number of elements they try to incorporate during the QD growth. We report here about our investigation on these two different types of growths.

i). Comparison between InAs and InGaAs QDs growth

In Table 3.2-3 are summarized the main advantages and drawbacks that we usually relate to InAs or InGaAs QD growth. First, InGaAs QD growth usually have a higher PL wavelength. Therefore they offer deeper QDs which is better because it will increase the intermediate band (IB) to conduction band (CB) transition. Thanks to k·p calculation that will be presented later, we understand that it is related to the InGaAs QD height that is higher compared with what can be obtained with InAs QD growth. This is due to the lattice mismatch that is reduced in the case of InGaAs QD growth. On the other hand, we will have a thicker wetting layer (WL) in the case of InGaAs QD growth because of the lower lattice mismatch compared with InAs QD growth. For the same reason, it is easier to grow closely stacked InGaAs QDs and also have host material with a higher percentage of Aluminium which also enables a higher separation of IB and CB. Finally, InGaAs QD growth gives larger QDs. It is good in term of light absorption but the larger diameter and lower Indium concentration goes in the direction of QDs with quasi-continuunm of quantum states which should be in theory detrimental for the separation of the IB.

Table 3.2-3: comparison between InAs and InGaAs QDs growth

QDs	InAs growth	InGaAs growth
Deep QDs	☹ : min 1.15 eV	☺ : min 1.05 eV
Host material Al %	☹ : max 22 % (1.70 eV)	☺ : max 40 % (1.90 eV)
Closely stacked	☹ : min spacer layer ≈ 20 nm	☺ : min spacer layer ≈ 7 nm
Absorption	☹ : QDs volume ≈ 2.0 MLs	☺ : QDs volume ≈ 9 MLs
Thin wetting layer	☺ : < 2 nm-thick	☹ : thicker
Small QDs	☺ : min 15 nm diameter	☹ : min 30 nm diameter
Indium concentration	☺ : max 55%	☹ : lower
Discrete levels	☺ : ≈ 60 electron states, intraband energy separation ≤ 60 meV	☹ : more states, closer states in energy

Initially we decided to work with InAs QD growth to have more discrete levels because InAs QDs are smaller and are supposed to have a higher Indium concentration. In that sense, we hoped to have a

better separation of the IB energy level with the CB. However, thanks to k·p calculation that will be presented in part 3.3.2, we found that even with InAs QDs growth we have a quasi-continuum of electron states. For a typical Okd-3 InAs QD growth, there are 60 electron states between QD ground state and the wetting layer. Moreover, the intraband energy separation is very low, around 60 meV between the QD ground state and the first excited states for electrons and then it is always below 30 meV in energy. One solution might be to try to get even smaller InAs QDs. However, if we believe that there is a universal law on the aspect ratio for self-assembled In(Ga)As QDs, it means that smaller InAs QDs in diameter will have smaller height and shallower energy level. Therefore it might not help to have better QD-IBSC system with a discrete IB.

On the other hand, InGaAs growth offers many advantages such as the possibility of having host material with higher energy bandgap and deeper QDs in energy that would offer a better-optimized system for IBSCs. In addition, it is possible to have closely stacked QDs and higher absorption because of a higher volume of QDs.

ii). Wetting layer problem

The main remaining problem for InGaAs is the WL thickness that is thicker for InGaAs system and would be counter-productive for the separation of the IB from continuum states. To overcome this issue, in Okd-4 and Okd-5, we tested capping with 2MLs of AlAs. In both cases we did not have any PL signal from the WL at high PL excitation. In Figure 3.2-24, a comparison of Okd-3 and Okd-5 PL at different excitation intensities is shown. For both of these growths almost all parameters related to the QDs are the same except the WL PL that can be seen at 800 nm for Okd-3 but is strongly reduced and can hardly be seen in Okd-5.

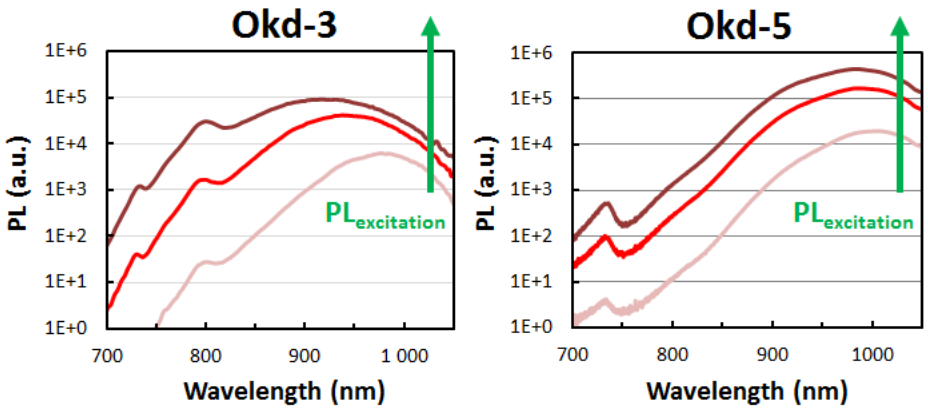

Figure 3.2-24: Comparison PL at different excitation for Okd-3 and Okd-5 growth. WL PL at 800 nm can hardly be seen for Okd-5 while AlGaAs host material PL can be seen around 740 nm.

iii). Problem related to InGaAs QD growth

By considering that the WL thickness is not an issue anymore, and by considering that InAs QDs do not have sufficient discrete states because of their sizes and low Indium concentration, there is no more obstacle to move to an InGaAs QDs growth. Okd-4 growth conditions were optimized to integrate all the advantages detailed earlier with a higher energy bandgap AlGaAs material of 30% in aluminium, 2MLs AlAs capping and 9 MLs of InGaAs. QDs PL target is kept at a reasonable energy of 1.1 eV because we want to avoid too large QDs. Spacers are also kept at a safe value of 25 nm in order to avoid too much strain because we wanted to grow a high number of layers.

In appendice **A**, we detail the investigation of InGaAs growth that we made in Okada Laboratory with Dr. Yasushi Shoji. We notice that growing InGaAs QDs poses serious homogeneity challenges that might be due to the very fast growth. One solution could be to increase the time of InGaAs QDs growth by reducing Gallium (Ga) flux. This flux is controlled by the temperature of Ga effusion cell that is fixed for the purpose of AlGaAs growth. If there is a free port in the MBE chamber it could be equipped with another Ga effusion cell.

3.3 Investigation and modeling of QDs properties

In addition to AFM and PL mapping, other characterization techniques are needed to get a better picture of QDs absorber behavior. In this third part, we will focus more on the intermediate band (IB) characterization by investigating QDs electrical and thermal properties. First by photoluminescence with temperature, external quantum efficiency and current-voltage measurements with temperature, we will show how the IB interact with the host material. Then in a second section we will use k·p calculation with the software nextnano to try to explain such behavior in term of QD energy state distribution and localization of the electron wave inside the In(Ga)As / $Al_{0.2}$GaAs system described in part 1 and 2 of this chapter.

3.3.1 QDs interactions with host material: thermal and electrical properties

Using photoluminescence temperature-dependent characterizations we investigate the dynamic of QDs trapping and detrapping of carriers with temperature. Electrical characterization like reverse bias external quantum efficiency at room temperature show the influence of the electric field for different excitation wavelength. Finally, current-voltage temperature-dependent measurements reveal the evolution of the electric field influence with temperature. These characterizations give information on the QDs interactions with host material, which is necessary to understand the basic working mechanism that involves our QD-IB.

3.3.1.1 Low temperature PL and Stokes shift

Low temperature PL is usefull in order to apprehend the effect of temperature-activated processes in direct bandgap semiconductors. In the case of In(Ga)As QDs in AlGaAs host material, it is especially important to understand the nature of trapping/detrapping processes inside QDs and the relation between absorption and emission of light.

i). Low temperature PL and AFM height distribution

The sample we used for this low temperature characterization comes from the center zone of a 3-inch wafer Okd-3 type of growth. In Figure 3.3-1, following previous AFM investigations, we compare height distribution with low temperature PL spectrum plotted in energy. The bimodal PL shape at low temperature (20 K) is superposed with the QD distribution in height for the center zone (C).

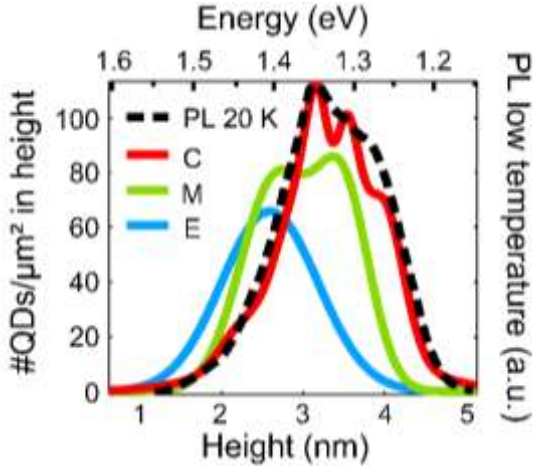

Figure 3.3-1: Superposition of PL measurements characterization for a center-zone sample with AFM measurements as previously studied and shown in Figure 3.2-18 and Figure 3.2-19.

ii). PL evolution with temperature

Figure 3.3-2, reports PL measurements from 20 K to 293 K (RT: room temperature). In the top left graph, we can see a bimodal PL shape at low temperature (20-100K) evolving to a gaussian shape above 200 K, and with a strong decrease of PL at RT.

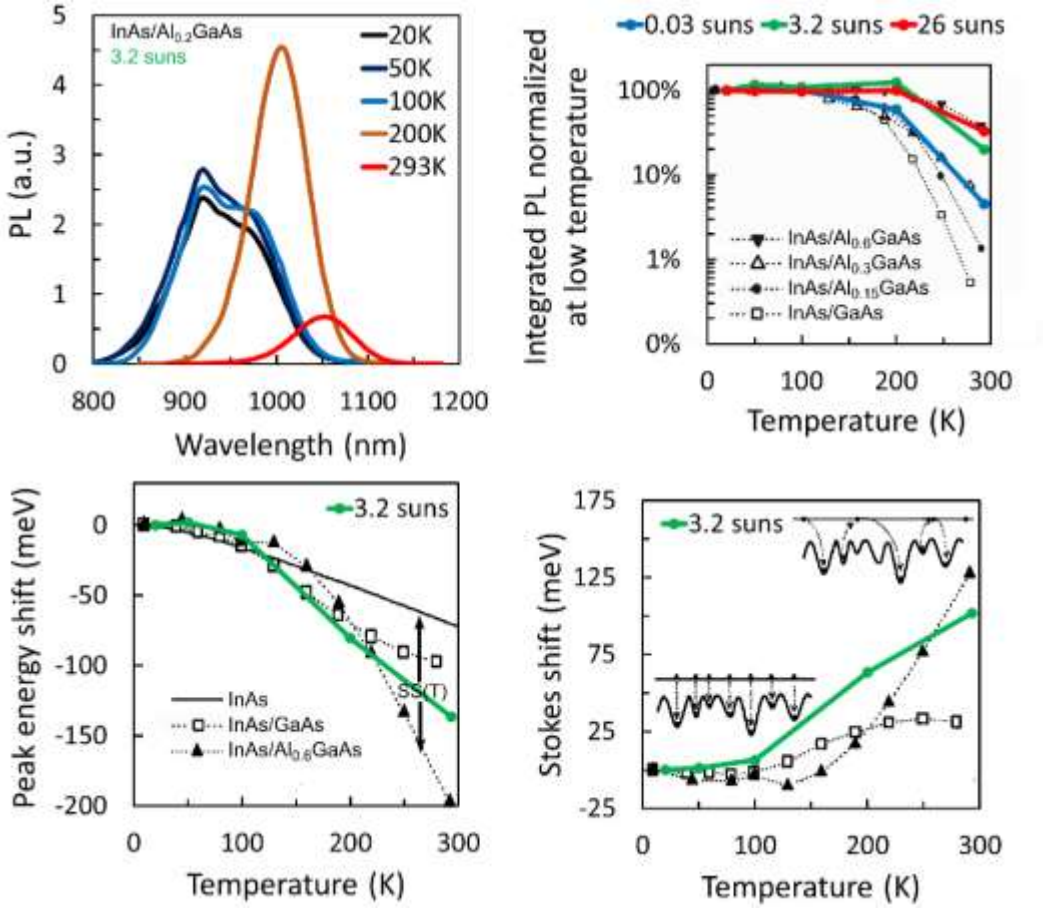

Figure 3.3-2: Photoluminescence measurements as a function of the temperature at 3.2 suns laser excitation λ=532 nm (top left). Integrated PL at different excitations compared for different AlGaAs host materials (top right), PL peak shift (bottom left) and Stokes shift (bottom right) for "frozen" and "hopping" regimes. We compare with characterization performed by Polimeni et al with different aluminium concentration for the host material [169].

In Figure 3.3-2, we also show, in the top right graph, the integrated value of PL normalized at low temperature for different temperatures and under different excitations (0.03 suns to 26 suns). Our experimental measurements are compared to Polimeni et al. measurements with different aluminium concentration for the host material [169].

At least three general remarks can be made:

- From 20 K to 100 K, PL shape and intensity is almost the same.
- From 100 K to 200 K, PL shape is changing but the integrated PL is almost the same.
- From 200 K to room temperature, PL quenching with temperature is less pronounced for higher excitation (3.2 and 26 suns) or for higher aluminium AlGaAs material (Al0.3GaAs or Al0.6GaAs) as shown by Polimeni et al.

These remarks are hint to the fact that there are at least three different types of temperature regimes that are well known in the literature [169], [170], [171], [172]:

1/. Frozen randomly regime for low-temperature range: $T_1 \leq 100$ K.
Carriers are “frozen” randomly into QDs and PL reflects the absorption of the QD ensemble with multi-modal shape as illustrated in Figure 3.3-1.

2/. Stokes shift via carriers hopping for middle-temperature range: $100\ K < T_2 \leq 200$ K.
Carriers may be thermally activated outside the QDs into the WL or the $Al_{0.2}GaAs$ host material and then relax into different QDs. Carrier hopping between QDs favors a drift of carriers toward QDs having a higher binding energy. Among the bimodal population of QDs, “large” QDs are the more favourables for PL emission therefore they end up as the new signature of PL. This is known in the QDs literature as a sort of “Stokes shift” effect [169] because emission from “large QDs” is shifted compared to the average absorption threshold that is given by the entire QDs ensemble comprising “large” and “small” QDs.

3/. Temperature PL quenching for high-temperature range: $200\ K < T_3$.
Carriers not only can detrap but they also can transfer to shallow or deep defects from AlGaAs host material. These traps are less active with higher Aluminium concentration in AlGaAs host material or can be saturated under higher light bias. In the literature, shallow and deep defect investigations have been performed for GaAs or AlGaAs systems grown by MBE [136], [137]. Deep-level transient spectroscopy (DLTS) has been performed on GaAs layers grown in our lab and we found trap densities in the order of 5e14 cm^{-3} for well-known EL4-types of defects [136], [173]. The EL4 defect is known to be a Ga vacancy defect, which has been suggested for the observed 0.8 eV PL band in GaAs. For our $Al_{0.2}GaAs$ host material, the activation energy would be above 0.5 eV and active for temperature above 200 K. Further investigations would be needed to quantify the impact and importance of such defects in our In(Ga)As / $Al_{0.2}GaAs$ system as it can be found in the literature [65]–[70].

In Figure 3.3-2 the two bottoms figures are plotted following Polimeni et al understanding of the PL peak shift as a kind of “Stokes shift” effect. In the bottom left, the full line represents the shift in bandgap energy for InAs semiconductor following Varshni equation determined experimentally [174]. By calculating the difference between InAs bandgap energy shift we have an estimation of our Stokes shift that amount to about 100 meV at room temperature as shown on the bottom right figure.

iii). QDs carriers escape natures

Such temperature-activated processes depend on the nature of the carrier escape from QDs. Three differents dynamics are usually considered [172], [175]:

- Excitonic escape for fully correlated electron-hole pairs.
- Ambipolar escape for which the faster carrier (hole or electron) induces the escape of the slower one in such a way that both carrier are thermally emitted from QDs on average in pairs.
- Unipolar escape for which single-carrier escape is dominated by the less confined carrier. It is usually considered to be holes for self-assembled In(Ga)As QDs.

Thermal escape lifetimes are often calculated following Equation 3.3-1 [175].

$$\tau_{th-escape:\, i\to f} = \frac{DOS_i}{DOS_f} \times \tau_{th-capture:\, i\to f} \times \exp(-\frac{E_{a:\, i\to f}}{k_B T})$$

Equation 3.3-1: thermal escape time expression for initial state *i* to final state *f*.

For an initial state *i* to a final state *f*, $\tau_{th-capture:\, i\to f}$ is the lifetime for QDs to capture a carrier in the initial state *i*. *DOS* is the density of states and $E_{a:\, i\to f}$ the activation energy of the transition between the initial and final level. The activation energy depends on the escape nature. For excitonic escape, it will be equal to the optical energy gap between the QD bound states and the higher levels. In other terms, it is given by the sum of the conduction and valence band discontinuities between the initial and the final states. For ambipolar escape, half of this energy gap value is considered due to weak correlation of the carriers. Finally, in the case of unipolar escape, the activation energy is equal to the energy difference for the less confined carrier.

To uncover the escape nature, Arrhenius fitting of the PL quenching with temperature is often found in the literature to reveal the activation energy for different QD states. We did not investigate precisely the activation energy with temperature-dependent PL. Nevertheless, in the top right graph of Figure 3.3-2, it seems that the slope factor is decreasing with increasing excitation. This decrease of the activation energy could be an indication that the escape nature becomes less excitonic for higher excitation. The change of escape behavior for higher excitation is also encountered in the literature [176]. We will discuss about it in chapter 4 when studying "optical I-V" with a calibrated PL setup.

In the case of PV devices, not only thermal but also tunneling effect can play a role in the carrier exctraction by an electric field. We will investigate it in the next sections thanks to electrical characterization.

iv). QDs carriers thermal-assisted escape mechanisms

In the case of thermal-assisted escape, the nature of the escape gives an indication on the binding energy of the carrier at a certain energy inside QDs. It gives an information on the radiation nature of the electron-hole interaction but not on the mechanism of escape. However, both the nature and mechanism can be related. At least three different energies can contribute to the thermal-escape phenomenon via different mechanisms:

i). Phonon energy escape via multi-phonon-carrier scattering.

ii). Photon energy escape via radiative transition with IR radiation also called thermal photons.

iii). Carrier energy escape via carrier-carrier scattering.

As we discussed in chapter 1, these three different mechanisms and energies are currently being investigated in order to be beneficial to PV high-efficiency concepts:

i). Hot carrier solar cells (HCSCs).

ii). Intermediate band solar cells (IBSCs).

iii). Multi-exciton generation solar cells (MEGSCs).

Therefore, we see that quantum structured solar cells offer a high potential but we do not know yet which path will lead to the realization of high-efficiency solar cells.

3.3.1.2 Carrier collection efficiency

In the previous part, we have studied the temperature-dependence of PL for non-connected samples (open-circuit voltage conditions). In this part we want to assess the influence of bias on the extraction of photocarriers from In(Ga)As QDs. In order to investigate this effect we will use the carrier collection efficiency (CCE) measurements as proposed by Fuji et al. in the case of multi quantum wells (MQWs) [71]. CCE is calculated by normalizing the current enhancement induced by light illumination to its saturation value at reverse bias. The derivation of the CCE is based on several assumptions:

1) The bias dependency of light absorption is negligible.
2) 100% of photogenerated carriers are collected from a "saturation" reverse bias.
3) Behavior of the photo-generated carriers does not change for monochromatic illumination and AM1.5 illumination.
4) Effects of series and shunt resistance are negligible.

For the moment, it is still not clear if QDSCs can fulfill all of these conditions, nevertheless we will present CCE as if the system can fulfill such conditions.

As detailed in the fabrication chapter, we have two types of samples: (1) non-transferred (NT) samples that are as-grown *p-i-n* junctions on n-doped GaAs substrate and (2) transferred-on-mirror (M) samples that are few hundreds of nanometers thick nip-junction on a gold mirror. In this part, we will focus on samples fabricated with the Okd-3 growth conditions. The QDs PL mapping method detailed earlier is used to give an indication on QDs nature for different samples.

<u>i). External quantum efficiency measurements</u>

As a first fulfillment of CCE, we need to investigate external quantum efficiency (EQE). First, we fabricated samples at different locations on the wafer.

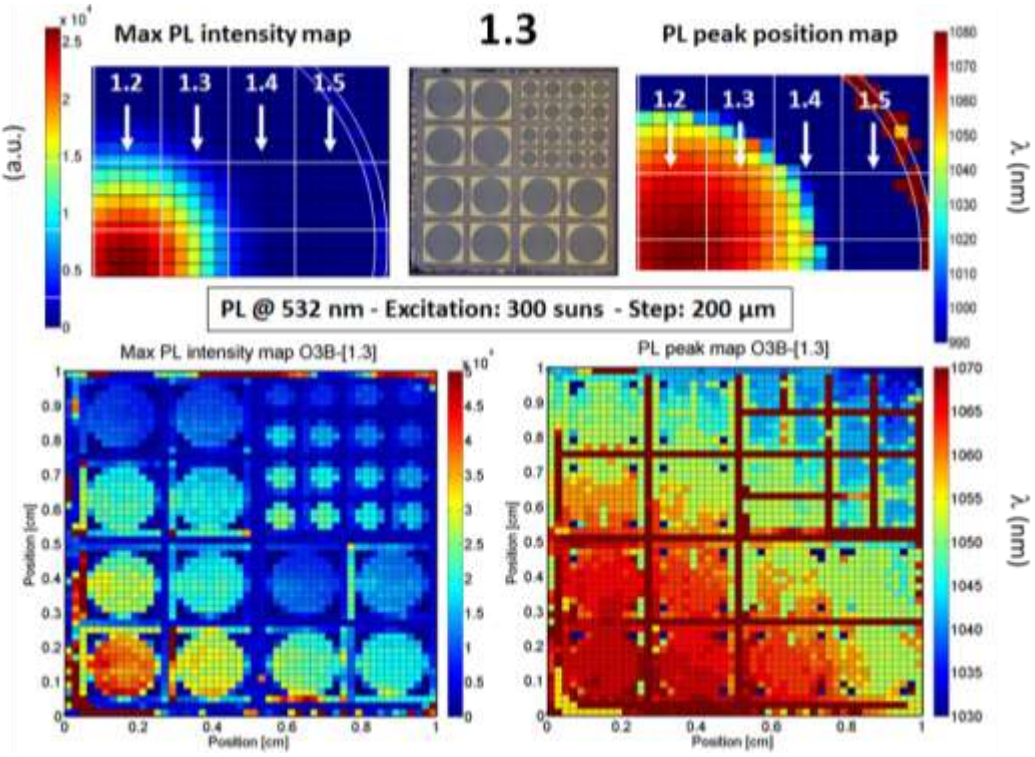

Figure 3.3-3: Non-transferred (NT) samples fabricated and their positions on wafer Okd-3. Sample 1.2NT is in the center and sample 1.5NT on the edge. As an example detailed PL mapping of 1.3NT sample is given. Colorbar scale are not the same for top and bottom figures.

On each sample, we performed PL mapping again so that we can get information of what kind of QDs we deal with. For example, Figure 3.3-3 gives a description of the samples investigated and PL mapping for sample Okd-3-1.3NT. Sample mapping enables to confirm high inhomogeneity even for a 1 cm² sample. As we can see on sample Okd-3-1.3NT, the QDs PL peak wavelength goes from 1070 nm (left bottom corner) to 1030 nm (right top corner).

EQE measurements confirm this phenomenon as it can be seen on Figure 3.3-4. $Al_{0.2}GaAs$ sample is a reference sample with no QDs, we see a strong EQE decrease around 740 nm corresponding to the $Al_{0.2}GaAs$ bandgap wavelength.

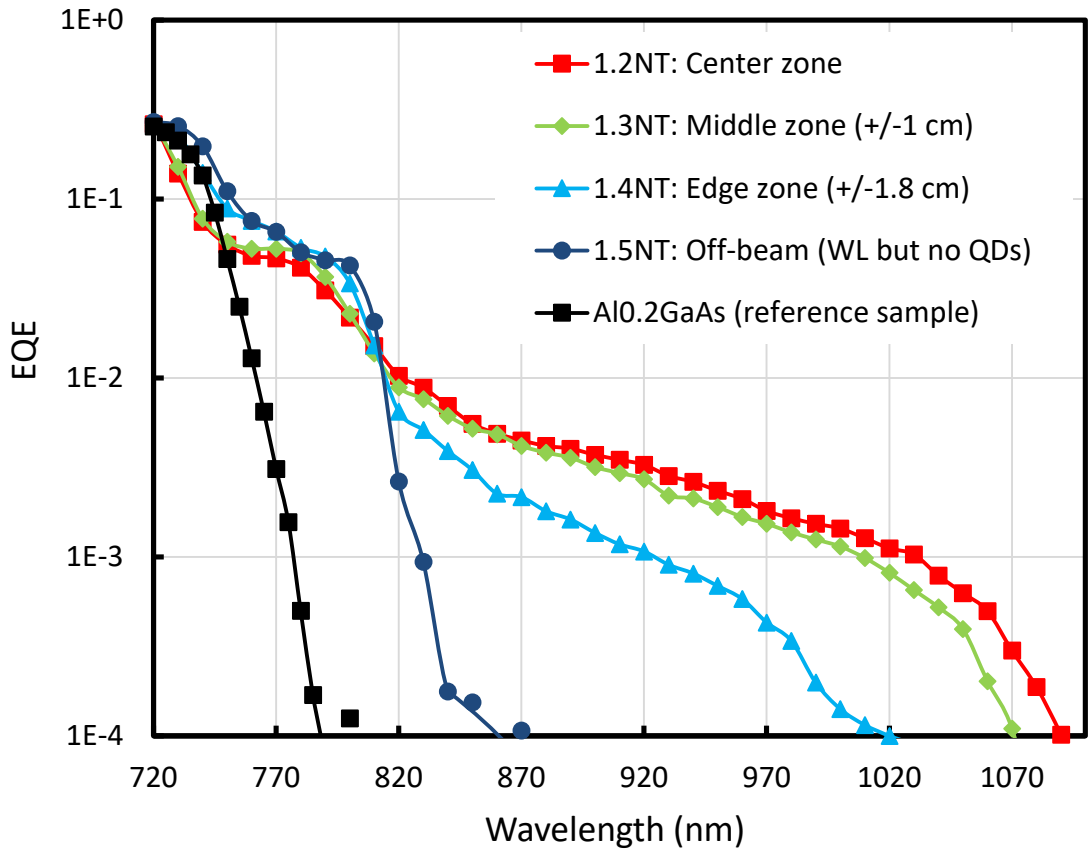

Figure 3.3-4: EQE in log scale of solar cells from different samples taken with respect to their position from the center of Okd-3B wafer and EQE of an $Al_{0.2}GaAs$ reference solar cell shown as a comparison.

1.5NT sample is taken in the off-beam zone described previously on the 3-inch wafer. We have seen earlier that no QDs PL emission can be detected for such samples. Thus only the WL can be seen with a strong decrease of EQE around 800 nm. We also see a higher EQE in the WL spectral region 740-800 nm for this sample that we can relate to the fact that the QDs coverage is reduced to the benefit of WL absorption. As in the low-temperature PL study, we compare EQE measurements of samples 1.4NT (edge), 1.3NT (middle) and 1.2NT (center) with AFM height distribution of QDs. In Figure 3.3-5, we show a good agreement between AFM measurements and EQE for the three different zones that are considered: center, middle and edge. EQE measurements, in log scale, are following the height distribution increase up to a maximum point defining a bandgap energy slope. We also show the superposition of low temperature PL measurement for the center zone. The en-

ergy scale between the two figures is the same if we consider Varshni equation [168]. In the case of $Al_{0.2}GaAs$ material, we find a Varshni shift of 95 meV. For 1.4NT, 1.3NT and 1.2NT the strong EQE decreases takes place respectively around 1.30 eV, 1.25 eV and 1.23 eV. For these samples, PL peak emission with PL mapping is respectively around 1030 nm (1.20 eV), 1050 nm (1.18 eV) and 1070 nm (1.16 eV). Therefore we find a Stokes shift between absorption and emission that is respectively of 100 meV for 1.4NT, 70 meV for 1.3NT and 70 meV for 1.2NT. This value is a little below the value found with temperature PL study (100 meV) but PL excitation is around 300 suns, x100 compared to the temperature PL study thus a blueshift of PL can be expected to occur due to the filling of QDs energy states which will reduce the Stokes shift.

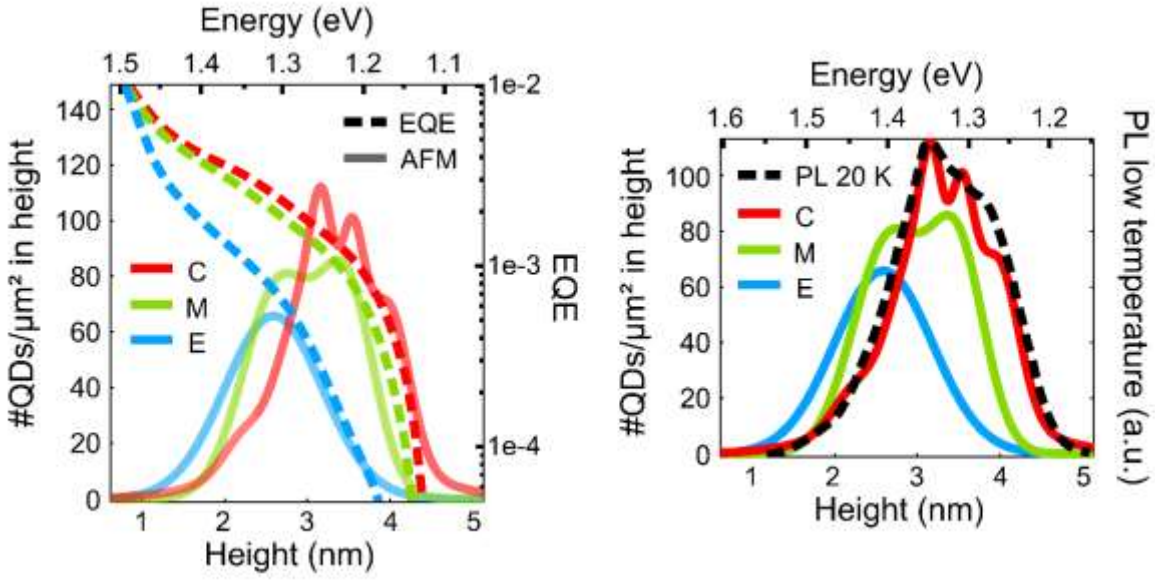

Figure 3.3-5: Superposition of EQE measurements characterization for a center-zone sample with AFM measurements as previously studied (left figure). Figure 3.3-1 is also shown as a comparison. Energy scale between the two figures is the same if we use Varshni equation to reproduce the equivalent PL spectrum at room temperature. Varshni shift is around 95 meV.

ii). Reverse bias EQE

In the perspective of studying carrier collection efficiency (CCE), it is crucial to study EQE over a large bias range. Especially at reverse bias, if we want to evaluate the impact of tunnelling extraction over carriers localized inside QDs or through the WL region. Figure 3.3-6 shows $\Delta J = J_{1sun} - J_{dark}$ curves for QDSCs on Okd-3 non-transferred sample (Okd-3-1.3NT) and sample transferred on a gold mirror (Okd-3-1.1M) that have comparable distributions of QDs. Curves are normalized at short-circuit current for comparison because transferred solar cells have higher current due to an increase of light absorption. We see three different regions with increasing reverse bias for transferred sample. First for bias between 0V and -6V there is a regular linear increase of the current, then between -6V and -14V, the current remains flat and for reverse bias higher than -14V there is an increase with an exponential behavior. The non-transferred solar cell only show a regular increase of the current with also an exponential behavior for high reverse bias. The exponential behavior arises when breakdown voltage regime starts, the electric field is estimated to be around 400-600 kV/cm in the devices for reverse bias between -14 V and -20 V.

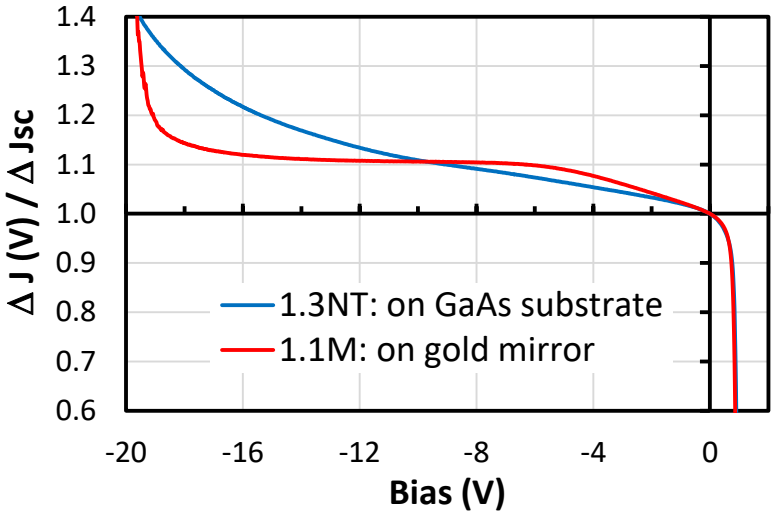

Figure 3.3-6: ΔJ curve under 1 sun: J(1sun) – J(dark) for transferred sample Okd-3-1.1M (red) and non-transferred sample Okd-3-1.3NT (blue) normalized by ΔJsc (short-circuit condition, bias = 0 V).

In order to better understand the difference between the two samples, in Figure 3.3-7 and Figure 3.3-8 are plotted EQE for different reverse biases. In addition, absorption calculation of the corresponding $Al_{0.2}GaAs$ pin structure is plotted for both case (dashed flashy green).

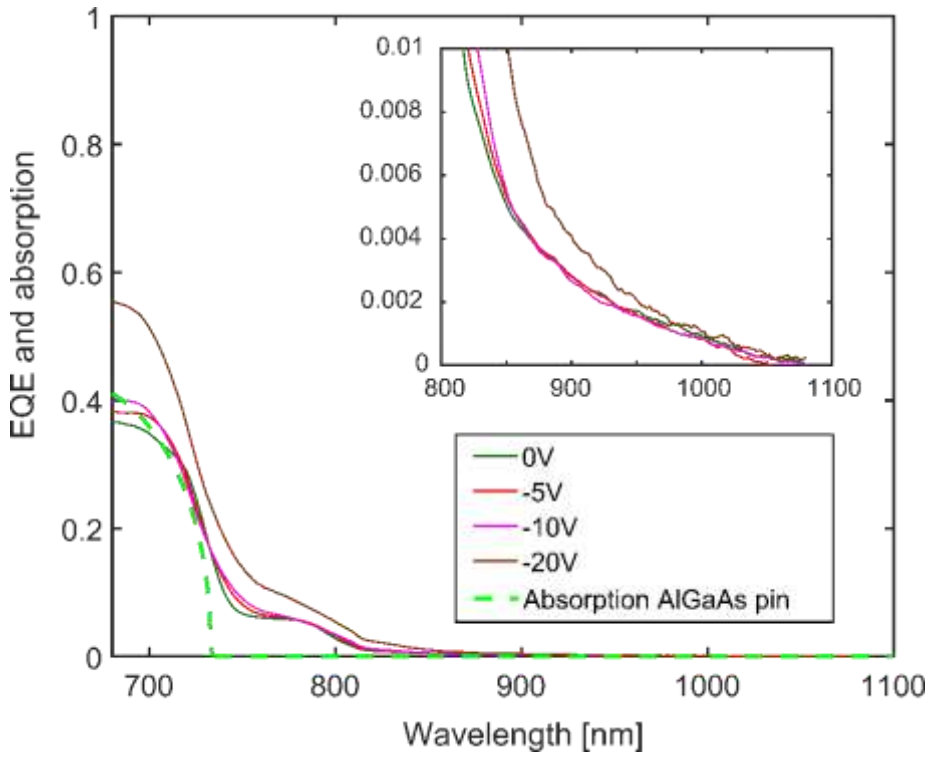

Figure 3.3-7: EQE for non-transferred (NT) sample Okd-3-1.3NT under different bias and calculated optical absorption of an $Al_{0.2}GaAs$ *p-i-n* plotted in dashed line. Inset shows a closed view of the spectral region where only QDs are absorbing.

In Figure 3.3-7, we see that there is a continuous increase of current with reverse bias. At -5V it is equal to the total absorption of light and it increases a lot for for -20V reverse bias. In the case of the transferred solar cell in Figure 3.3-8, we see no increase of current after -6V reverse bias and the value of the EQE is significantly lower than the calculated absorption or even the reflectome-

try (R) measurements performed on this cell. Therefore, it seems that the GaAs substrate is responsible for the increase of current in the non-transferred cell while the transferred cell has no substrate and thus the current is limited until breakdown voltage point is reached for very high reverse bias.

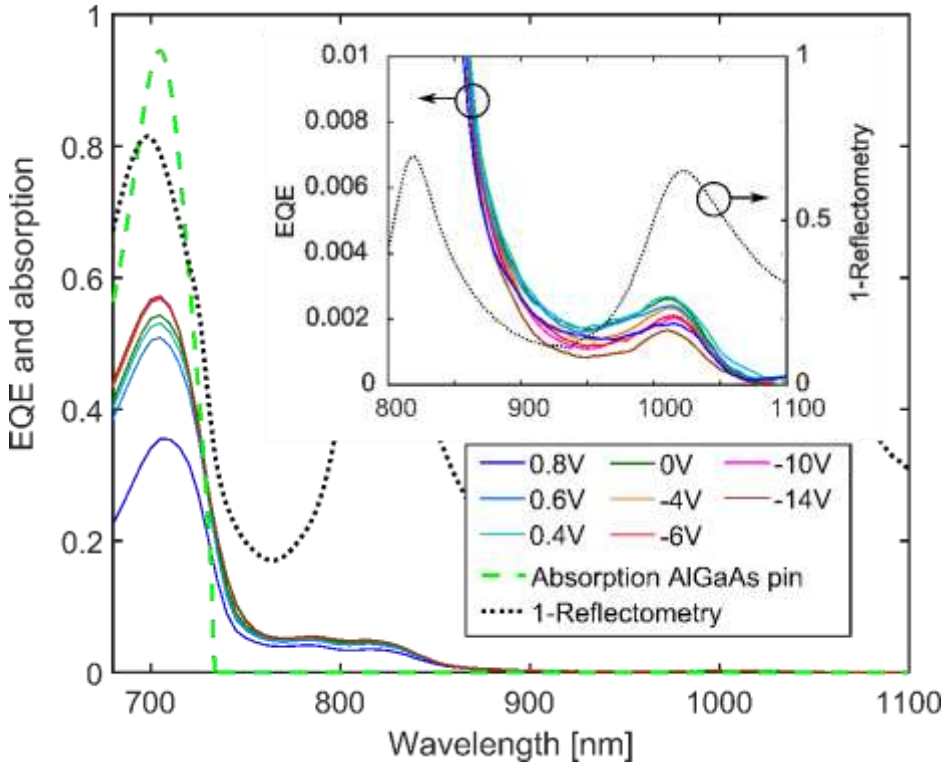

Figure 3.3-8: EQE for transferred sample on mirror (M) 1.1M under different biases and calculated optical absorption of an $Al_{0.2}GaAs$ pin plot in dashed line. 1-R is plotted in dotted line. Inset shows spectral region where only QDs are absorbing, 1-R is plotted on a different scale on the right axis.

iii). Carrier collection efficiency

Following this interpretation, we will only consider transferred solar cells for estimating CCE because we believe the flat zone (between -6V and -14V) corresponds to a kind of saturation current. We calculate CCE following Equation 3.3-2. The CCE depends on the ratio of the difference of generated and dark current under bias over the difference that is reached at a saturation regime. It is also important to consider CCE integrated over different spectral region to investigate the possibility of tunnelling to extract carriers directly absorbed inside the WL and QDs.

$$CCE\ (V) = \frac{\Delta J(V)}{\Delta J_{sat}}$$

Equation 3.3-2: Carrier collection efficiency depends on the ratio of the difference of extracted photogenerated and dark current under bias over the difference for a saturation regime.

Figure 3.3-9, represents the CCE obtained by integrating EQE measured with no light bias over different spectral regions: All=350-1100nm, WL=750-800nm, QDs=850-1000nm and normalizing with different voltage saturation points: All=-10V, WL=-10V but QDs=0.4V. We see a strange non-monotonous behavior for the QDs spectral region. For an increase of the reverse bias, the current collected from the QDs is decreasing.

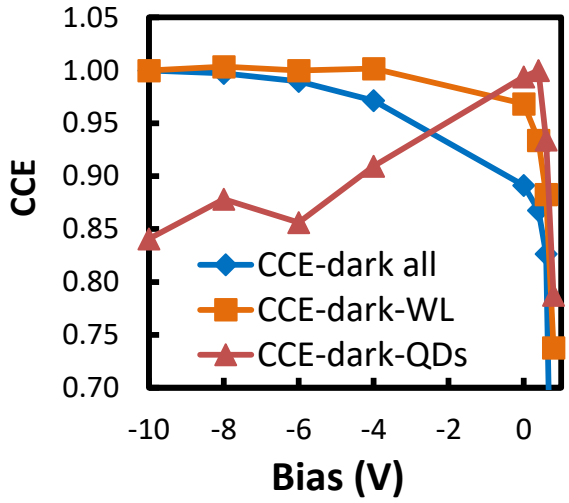

Figure 3.3-9: Carrier collection efficiency (CCE) obtained by integrating EQE with no light bias over different spectral regions: All=350-1100nm, WL=750-800nm, QDs=850-1000nm and normalizing with different saturation points: All=-10V, WL=-10V but QDs=0.4V.

In Figure 3.3-10, we compare these reverse bias EQE measurements with light bias and we see that the strange behavior from QDs is recovered. This might be an indication of a tunnelling mechanism between QDs energy states and deep level defects that would become inactivated under light bias (for example EL4-type discussed earlier with the temperature-dependent PL study).

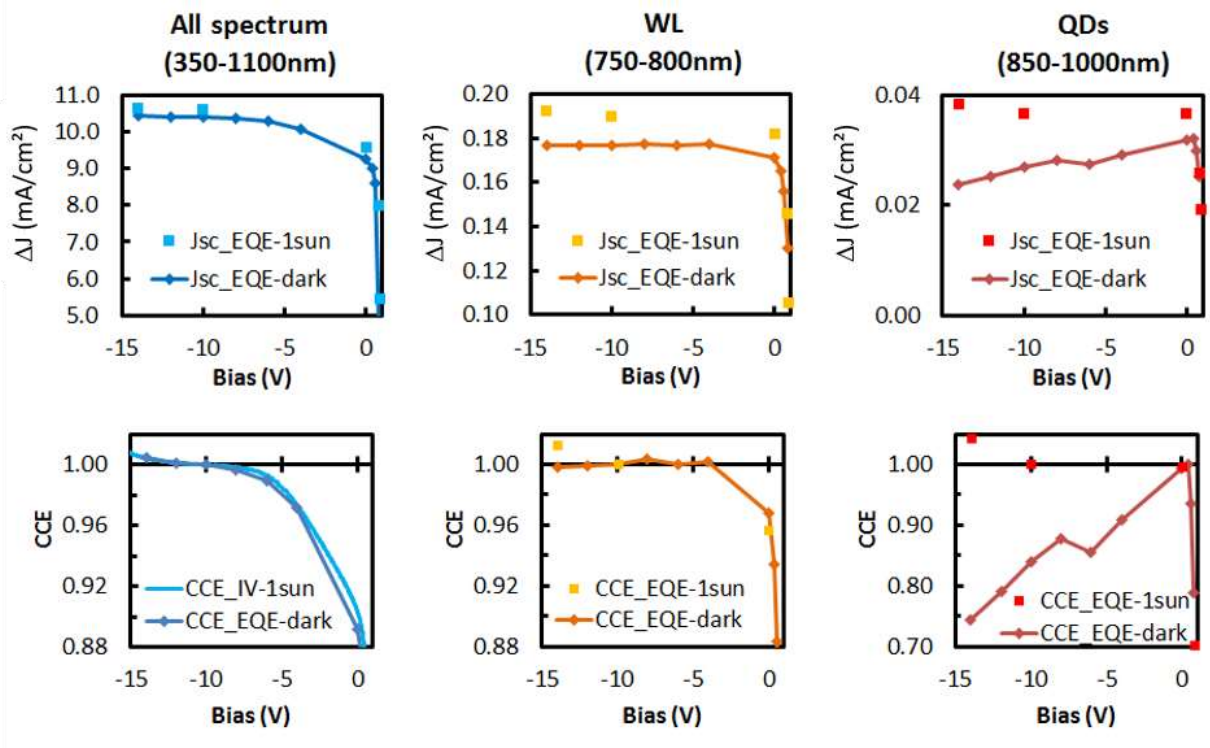

Figure 3.3-10: (top) ΔJ non-normalized curve integrated for dark and 1-sun EQE on three spectral regions: All spectrum (350-1100 nm), WL (750-800 nm) and QDs (850-1000 nm). (Bottom) Comparison with calculated CCE in dark and 1-sun bias on the same spectral regions.

Finally, in Figure 3.3-11, we compare the CCE measurements at 1 sun bias for all spectral regions and we normalize all CCE for the same value of reverse bias at -10 V. It seems that for this value we

reach a certain saturation regime. Nevertheless, it does not mean that we collect all charge photo-generated inside QDs. Especially in the case of QDs, some carriers might recombine before being extracted. It is important to remember that almost all assumptions from Fuji et al. [71] were not checked precisely but still our characterization show the appearance of a saturation regime from increased collection at reverse bias.

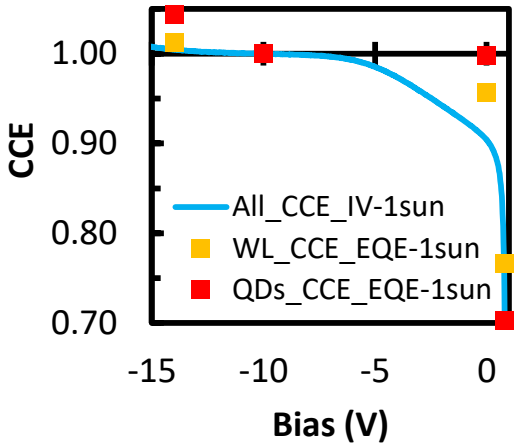

Figure 3.3-11: Carrier collection efficiency (CCE) obtained under 1 sun bias over different spectral regions: "All" is taken from I-V measurements, WL=750-800nm, and QDs=850-1000nm from EQE and they are normalized at bias = -10V.

In the literature, Hubbard et al. have recently investigated thoroughly the effect of the electric field on carrier escape mechanism in InAs/GaAs and InAs/AlGaAs QD-IBSC grown by MOVPE [177], [178]. For their InAs/AlGaAs QD-IBSC, the CCE at 1000 nm in wavelength is stable for a reverse bias starting around -1 V. They attribute it to the fact that almost all carriers generated from subbandgap absorption are collected under short circuit conditions. In our case, we make the same observation for the CCE from our QDs. Their CCE at 500 nm in wavelength does not change a lot compared to their CCE at 1000 nm. However, in our case, reverse bias up to -10 V is needed to get a stable CCE considering the integration of EQE over all the spectrum. Moreover, our *p-i-n* junction is rather thin, therefore the built-in field in the QDs layers intrinsic region should be relatively higher than in other structures. This high saturation reverse bias might indicate that our InAs/AlGaAs QD-IBSC grown by MBE has a higher defect density compared to their solar cell. Creti et al. have also very recently investigated InAs/$Al_{0.17}$GaAs QD-IBSC grown by MBE at reverse bias [179]. The EQE in their host material seems also stable for a lower reverse bias value (-2 V). It is interesting to notice that both groups have developed a specific growth process to minimize defects during the growth. For example, Creti et al. have grown $Al_{0.17}$GaAs layers at a higher temperature of 620°C compared to our MBE growth at 480°C.

iv). Reverse bias dark I-V

Figure 3.3-12 is showed as an introduction to next part where we will consider current-voltage (I-V) temperature-dependent measurements. We show dark and 1 sun I-V measurements for Okd-3-1.1M transferred sample that was investigated for CCE.

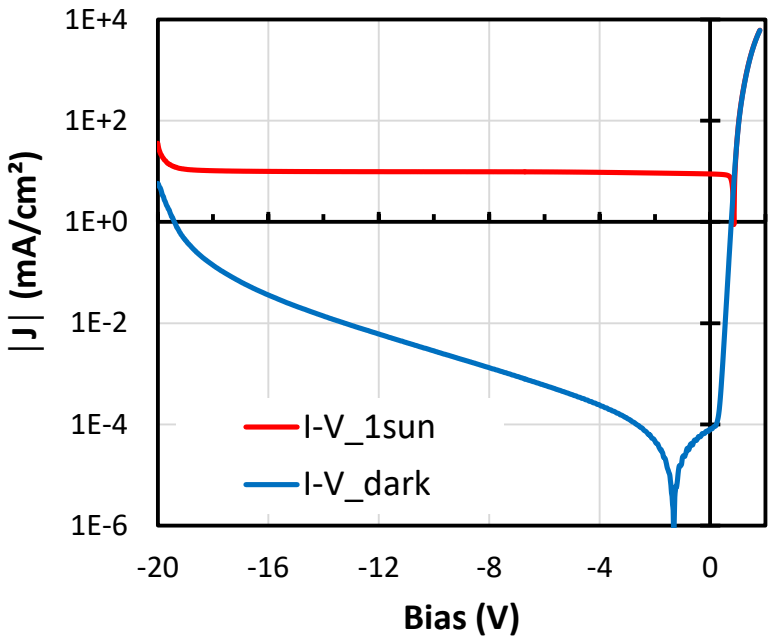

Figure 3.3-12: J-V curves under 1 sun and dark conditions for transferred sample 1.1M.

For the dark I-V, we notice that the logarithmic evolution of the absolute value of the current density $|J|$ linearly depends on the bias at reverse bias. It is usually interpreted as a tunneling transport mechanism in the literature (either band-to-band or trap-assisted tunneling) [180]. We will see that this tunneling transport mechanism is not trivial and could come from deep-level trap states or surface states that would be induced by process etching or damages during the fabrication process or characterization by hard probing.

3.3.1.3 IV measurements at low temperature

In this part, we investigate the temperature dependence of I-V measurements especially at forward bias for two different non-transferred samples: QDSC (Okd-3) and $Al_{0.2}GaAs$ reference cell with no QDs. One difficulty of these measurements is that the cryostat setup we used had metallic probes that were moving slightly when temperature reached about 200 K. For this temperature, in the vacuum condition, there is the formation of ice that we could see throught the glass. We noticed that everytime we pass by this temperature our cells were slightly degraded. Especially fitting with a one-diode model we noticed that the shunt resistance was reduced in the low forward bias region and serie resistance in the high forward bias region was a little increased. This shows that the surface and contacts were slightly damaged by the probes. Nevertheless, dark current saturation level in the intermediate forward bias region were not degraded, which is the region corresponding to the volume recombination that is of most interest for PV devices.

i). Local ideality factor

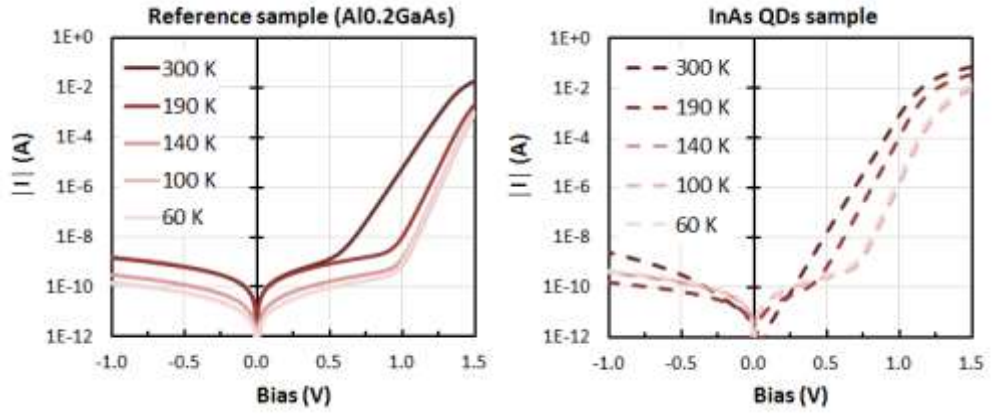

Figure 3.3-13: I-V curves from low (60K) to room temperature (300K) on 2 types of samples: Okd-3 In(Ga)As QDs in $Al_{0.2}GaAs$ sample (dashed lines) and a reference sample with no QDs (solid lines).

From measurements in Figure 3.3-13, we deduce the local ideality factor expressed by Equation 3.3-3 for different temperatures.

$$\frac{1}{n_{Local\ ideality\ factor}} = \frac{k_B T}{q}\frac{d(\ln(I))}{d(V)}$$

Equation 3.3-3: Equation giving the local ideality factor

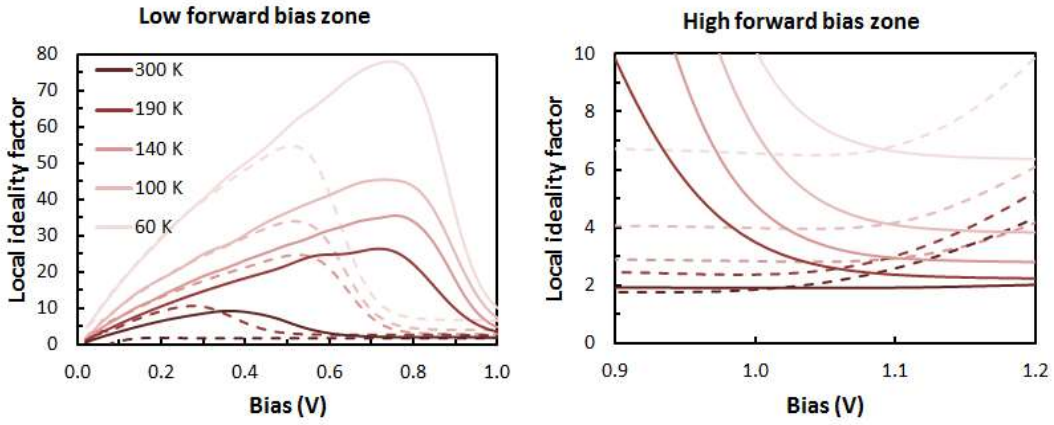

Figure 3.3-14: Local ideality factors for the two types of samples: In(Ga)As QDs in $Al_{0.2}GaAs$ sample (dashed lines) and a reference sample with no QDs (solid lines). Two different regions are investigated: low forward bias zone (0V < V < 1V) and a high forward bias zone (0.9V < V < 1.2V).

Non-ideal behavior of the dark current–voltage (I–V) characteristics of typical solar cells is characterized by an unexpectedly large recombination current, often characterized by an ideality factor larger than 2 and an ohmic characteristic at low reverse bias. Generally, an ideality factor larger than two means that, with increasing forward bias, the recombination rate increases slower than the *p*–*n* product. Hence, the recombination should be limited by any kind of saturation effect. Several proposals have been made to explain large ideality factors, such as trap-assisted tunneling. The unexpectedly large magnitude and the unexpectedly large ideality factor of the recombination current can both be explained by taking into account that this current is not flowing homogeneously, as assumed in classic diode theory, but flows locally in the position of extended defects crossing the

junction [181]. The most important defect of this type is the edge of the cell, where the surface crosses the junction and in our case we noticed during experiments that scratches induced by the probe will increase this local ideality factor at low bias.

Therefore, in both case samples, we cannot distinguish major differences in term of I-V characteristics. Even at high forward bias zone, the local ideality changes with temperatures are almost the same.

ii). Thermoionic-field emission

It is interesting to investigate the increase in the ideality factor with the decrease of temperature in order to know which mechanism dominates. If Shockley-Read-Hall recombination occurs via a single trap level in the space charge region, the ideality factor should be independent of temperature, with a value of 1-2. In contrast, tunneling-mediated recombination will cause a temperature dependence of the ideality factor. As it was seen previously with low-bias, tunnelling-mediated recombination can be found at the interface and are sensitive to the quality of the cell for example the number of dislocations [182].

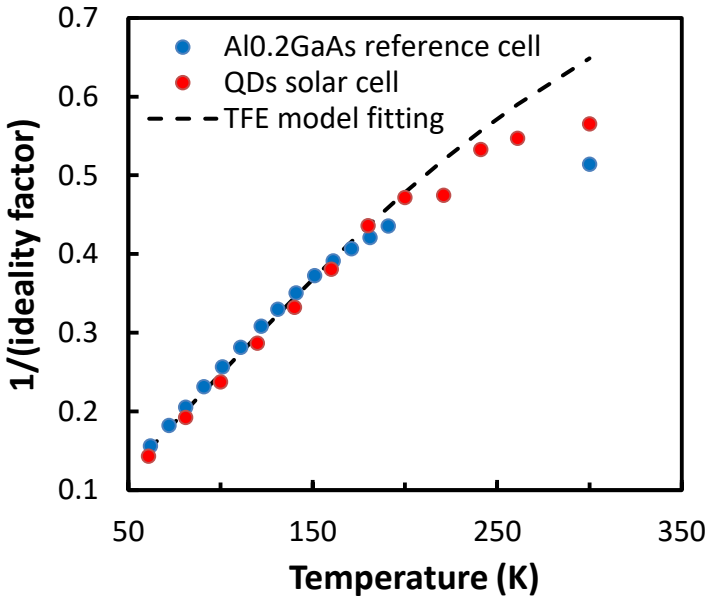

Figure 3.3-15: Inverse of ideality factor plotted with respect to temperature of the sample and TFE model fitting following Equation 3.3-4.

In Figure 3.3-15, is plotted the variation of the inverse ideality with temperature and the fitting with Equation 3.3-4 originated from *Padovani and Stratton* [183] theory's of thermoionic emission (TE) and especially thermoionic-field emission (TFE) regime that introduces E_{00} the tunnelling parameter characteristic energy. Ideality factor have been obtained by using a one-diode model fitting over all the forward bias region. It also corresponds to local idealities values shown in high-bias region around +1V in Figure 3.3-14. In the Okd-3 studied solar cell, the built-in field is around 40 kV/cm for the QDs layers intrinsic region. At forward bias around +1V, the built-in field is reduced to 15 kV/cm. This is still a high value that can lead to tunneling of electrons outside the QDs [184] or outside of deep-level defects in the case of the reference sample.

$$\frac{1}{n_{TFE\ ideality\ factor}} = \frac{k_B T/q}{E_{00}} \tanh\left(\frac{E_{00}}{k_B T/q}\right)$$

Equation 3.3-4: Ideality factor equation from TFE model [183].

The tunnelling parameter characteristic energy E_{00} can be obtained by fitting using Equation 3.3-5 with N_D the donor density in the investigated material, m_e^* the electron mass for the investigated material and ε_s the dielectric constant.

$$E_{00} = q\frac{\hbar}{2}\sqrt{\frac{N_D}{m_e^* \varepsilon_s}}$$

Equation 3.3-5: Tunnelling parameter characteristic energy E_{00}.

The fitting is relatively good for both the QDSC and reference sample with a characteristic energy $E_{00} = 37\ meV$. In the case of AlGaAs or InAs semiconductors with defects or traps (like QDs), such value corresponds to a donor density $N_D = 2e18\ cm^{-3}$. Electron density inside QDs or trap defects can be easily high due to their dimensionality, low energy level attracting free carriers and also considering background *n*-doping in undoped layers grown by MBE. Anyhow, this value of E_{00} is considered sufficiently high so that TFE dominates up to a certain temperatures where TE takes over. In our case, this temperature is around 200 K where we can see that the fitting becomes unreliable. The fact that TE regime would take over from temperatures around 200 K seems coherent with the carrier thermal escape and PL quenching detected for low temperature PL measurements reported earlier. Regarding the reference sample with no QDs, this measurement could be an indication that there is a high concentration of deep-level defects acting as carrier traps. In a sense, the reference sample could be seen as a kind of "impurity PV" solar cell, as discussed in chapter 1. This is not surprising because $Al_{0.2}GaAs$ reference sample is grown at the same temperature as QD sample. The temperature is low (480°C) to avoid the diffusion of Indium atoms and collapsing of In(Ga)As QDs. In the literature of GaAs, such low temperature can induce a hundred time more defects than a high-quality GaAs growth. These defects would induce the same TFE mechanism as in QDs sample and might even be dominant in regard to the QD density.

iii). Thermoionic emission: Richardson constant

To investigate the TE regime, we plot in Figure 3.3-16 the saturation current fitted from I-V measurement following Equation 3.3-6 [185] in function of the temperature to show the dependence with a barrier energy from a certain temperature.

$$J_s = A^{**}\mathrm{T}^2 \exp\left(-\frac{\mathrm{q}\Phi_b}{k_B T}\right)$$

Equation 3.3-6: Saturation current according to Richardson's law.

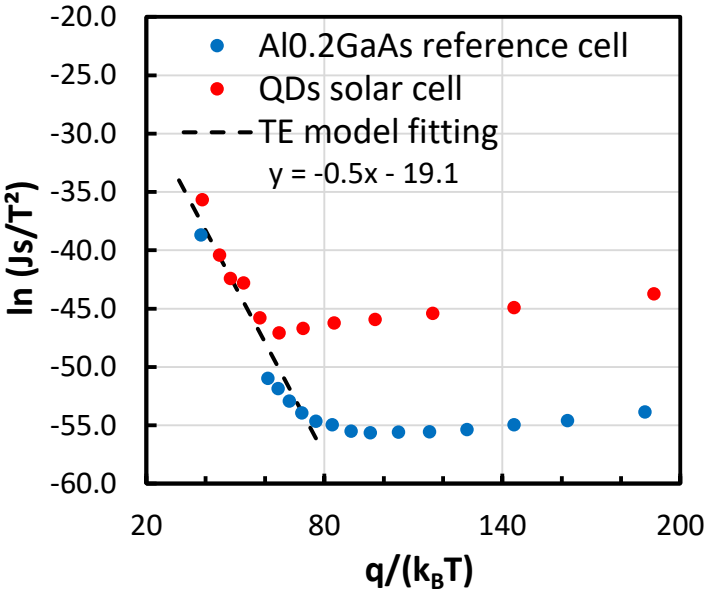

Figure 3.3-16: Plot showing saturation current follows a Richardson law from temperature T>200K ($q/k_BT<70$).

TE model fitting of current saturation gives a Richardson constant of $A^{**} = 5e-9\ A.cm^{-2}.K^{-2}$ far from realistic values but we still see the effect of a strong increase of Js that is following a Richardson law starting from temperatures around 200 K and we know that from these range of temperature we also have strong PL decrease.

TFE analysis shows that we have tunnelling-mediated recombinations that are relatively low at low temperature. For T > 200 K, recombination current increases following a Richardson law. Thus we can postulate that inside the space charge region (SCR), in AlGaAs reference and QDs solar cells, there are some trap states that can tunnel or at least communicate all together by trapping/detrapping of some sort. At some point they are sufficiently thermally activated to become more important. This approach from temperature-dependent electrical characterization goes in the same direction as the temperature-dependent PL analysis detailed earlier.

In recent literature, a new model called extended thermionic trap-assisted tunneling (ETTAT) has been proposed to explain the thermal droop in an InGaN-based single QW light-emitting diode [186]. This model is described in Figure 3.3-17. It consists of a two-step zero bias extended phonon-assisted tunneling from the quantum well to the trap, which acts as an intermediate reservoir of electrons, and from the traps to the border of the conduction band. In the case of In(Ga)As / $Al_{0.2}$GaAs solar cells, it is still difficult to know the exact nature of the exctraction mechanism but we believe it might be close to an ETTAT model with a combination of tunneling and thermal extraction. In the literature, this phenomenon of defect mediated extraction has been recently reported in InAs/GaAs QDSCs [187], [188].

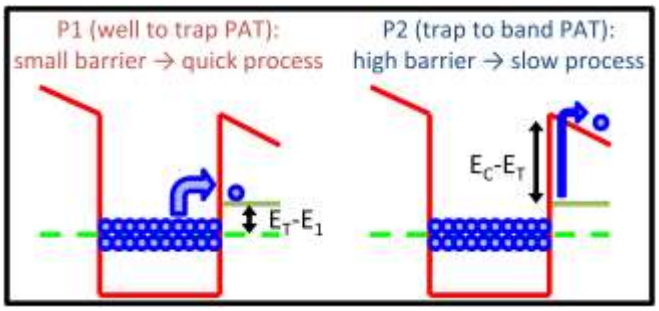

Figure 3.3-17: Sketch of the extended thermionic trap-assisted tunneling (ETTAT) escape process taken from [186].

3.3.2 Simulation of different QDs: shape, aspect ratio, QWIs, WL, In content

Following the characterization of QDs thermal and electrical interaction with the host material we consider using k·p calculation with nextnano software to investigate the energy states distribution and localization of the electron wave inside QDs.

3.3.2.1 k·p calculation using nextnano software

i). k·p method

In(Ga)As QDs in $Al_{0.2}GaAs$ host material is a system composed of direct bandgap semiconductors. Each semiconductor has a periodic structure that form a bandstructure commonly known as the dispersion curve of the material. The highest points in the valence band and the lowest points in the conduction band, which occurs at the same point for direct bandgap semiconductors, determine many properties of semiconductors. Conduction band and valence band are usually considered using Bloch theorem with electron wavefunctions satisfying Schrödinger equation. The k·p perturbation theory is an approximation method that uses perturbation theory and takes into account symmetry properties of the Bloch lattice functions to simplify and calculate the band structure and optical properties of a semiconductor. In the case of heterostructures with different lattice constants, like in the case self-assembled S-K grown QDs, strain induced by lattice mismatch is calculated based on elasticity theory [189]. In the recent years, this method has been often used by different groups to consider In(Ga)As QDs for IBSCs [190], [191], [192], [193], [194], [195], [196], [197], [198].

ii). Nextnano software

The 3D nanometer device project *nextnano* is a simulation tool that aims at providing global insight into the basic physical properties of realistic three-dimensional mesoscopic semiconductor structures [199], [200]. Since 2012, it has evolved into a commercial software distributed by the *nextnano GmbH* with tutorials dedicated to many fields of application in semiconductor physics including In(Ga)As QDs with a tutorial called: *Energy levels in a pyramidal shaped InAs/GaAs quantum dot including strain and piezoelectric fields* that can be found easily online. The tutorial is based on a paper by Craig Pyror [201] that uses an eight-band strain-dependent k·p hamiltonian for pyramidal shaped QD. Dr. Stefan Birner managing the nextnano team has been kind enough to authorize the use and adaptation of this tutorial in the perspective of a student investigation to better understand how different parameters of a QDs layer will impact energy states discretization and electron wavefunction localization. For simplification of use, we were adviced to use the nextnano++ version that is the latest version. Details about the software can be found online and especially in the recent PhD thesis of Dr. T. Andlauer who also investigated self-assembled In(Ga)As QDs [202].

3.3.2.2 Energy distribution with shape and aspect ratio

The first investigation is on the QDs geometrical parameters and shape impact on energy states.

i). Rectangular box and lateral confinement approximation

The simplest shape is the rectangular box with dimensions (L_x, L_y, L_z). By assuming that there are infinite potential barriers at the edges of the box, the energy levels are given by Equation 3.3-7 where (n_x, n_y, n_z) are the quantum number integers specifying the quantized levels in each direction [203].

$$E(n_x, n_y, n_z) = \frac{\pi^2 \hbar^2}{2m^*}\left(\frac{n_x^2}{L_x^2} + \frac{n_y^2}{L_y^2} + \frac{n_z^2}{L_z^2}\right)$$

Equation 3.3-7: Energy for a rectangular box QDs of dimension (L_x, L_y, L_z).

Therefore if we consider a rectangular InAs QDs, with very small aspect ratio (*z* << *x* and *y*), ground state energy will be dominated by the vertical dimension (along *z*) while most of excited states will arise due to lateral confinement (along *xy*-plane). In the same way, it is possible to calculate lens-shaped QDs energy states with very small aspect ratio by assuming cylindrical symmetry and separate Shrödinger equations for vertical and lateral confinements [203].

ii). Self-assembled InAs QDs shapes

Nevertheless, in the case of self-assembled InAs QDs, such considerations on the lateral confinement are not valid because lateral dimensions also influence the energy position of the ground states (GS). Therefore we use k·p calculation and consider different type of shapes. Starting from the pyramidal shaped QDs tutorial, we can modify the code to investigate different kind of shape and compare with our experimental PL and AFM results. As an illustration, Table 3.3-1 gives ground state energies at low temperatures for typical "small" and "large" QDs calculated for four different shapes: pyramid, truncated pyramid, semi-ellipsoid and lens-shape as shown in Figure 3.3-18. These typical sizes are taken from AFM histograms half-maximum values shown in Figure 3.2-13. For the heights, we consider values without the 1-2 nm-thick WL because it gives values of vertical confinement that are more dependent on the shape. For diameters, we increase the value by 20% to take into consideration the "WL tail" that we previously identified to "nanodisks" or quantum-well islands (QWIs). Therefore, we consider typical "small" QDs have heights h=1.1 nm and diameters d=12 nm. On the other side "large" QDs have heights h=2.3 nm and diameters d=26 nm. These two extrema give an estimation of the dispersion of QDs in size and in ground states energy thus it should corresponds to low temperature PL FWHM that is around 200 meV.

Table 3.3-1: Ground states in eV for typical "small" and "large" QDs for different shapes

Shape	Small QDs d=12 nm, h=1.1 nm	Large QDs d=26 nm, h=2.3 nm	Δ(Small-Large)
Truncated pyramid	1.33 eV	0.94 eV	0.39 eV
Semi-ellipsoid	1.40 eV	1.01 eV	0.39 eV
Lens-shape	1.44 eV	1.05 eV	0.39 eV
Pyramid	1.51 eV	1.11 eV	0.40 eV

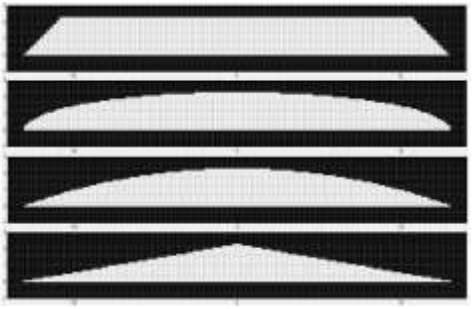

Figure 3.3-18: Different QDs side shapes that can be calculated with nextnano++ software (from top to bottom): truncated pyramid, semi-ellipsoid, lens-shape, pyramidal shape.

Table 3.3-1 shows that the larger the volume, the lower GS will be in energy thus energy of pyramidal GS > lens-shape GS > semi-ellipsoid GS > truncated-pyramid GS. For all shapes, we have the same difference in energy between small and large QDs. It shows that even though lateral confinement influence the energy position of GS, vertical confinement in the center is dominant and the difference of energy for large and small QDs will remain the same independently of the shape. Finally, we notice that the difference in energy between small and large QDs is around 400 meV, which is twice the FWHM for PL at low temperature. This high dispersion can be understood by the fact that, in our calculations, we consider InAs QDs with 100% indium concentration while we saw previously, in part 3.1.1.4 that in reality QDs indium concentration is about half this value in average. By considering this along with the impact of the WL we are able to fit the PL dispersion and AFM measurements with k·p calculation.

3.3.2.3 Including Indium profile composition, QWIs and WL

i). Final designed structure for In(Ga)As QDs in $Al_{0.2}GaAs$

In order to consider this gradient of Indium composition we use a trumpet-shaped gradient, as mentionned previously in part 3.1.1.4, with indium composition ranging from 30% to 100% inside a lens-shape In(Ga)As QD as described in Figure 3.3-19 (for y = 0 nm). Then, to model the impact of the quantum-well islands (QWIs) that was noticed from AFM measurements in part 3.2.2.1, we first use a truncated-pyramid below the QDs between z=0 nm and z=-0.8 nm with an inverted trumpet-shaped gradient concentration of Indium between 30% and 100%. This gradient is to consider the fact that indium is pushed in the center and is mixing with the already grown WL that was grown before the nucleation step. As described in Figure 3.3-19 (for y = 10 nm), this truncated-pyramid has a limited size that is +20% wider on both side following AFM analysis. Moreover, as described in Figure 3.3-19 (for y = 14 nm), we include a 0.8 nm-thick InGaAs WL with a linear indium gradient composition along the vertical axis from 0% to 100% starting at z=-0.8 nm and going in both direction (+0.4 nm toward the top and -0.4 nm towards the bottom). This linear indium gradient is used to take into account observations from AFM and TEM images that often give an image of a thickness between 1 and 2 nm while PL emission energy corresponds to a 0.3 nm-thick InAs QW. Figure 3.3-19 illustrates the different parts of the designed structure by showing *xz*-plane cut at different positions along *y*-axis.

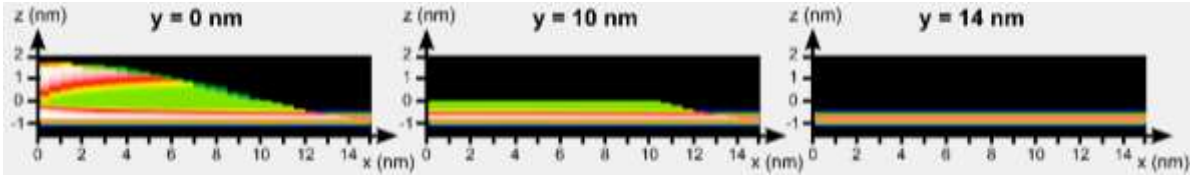

Figure 3.3-19: Final design structure for k·p calculation. Different cut are shown for y=0 nm (QDs center), y=10 nm (QDs edge showing QWI) and y=14 nm (QWI edge showing the flat WL). Colors reflect Indium composition as shown in Figure 3.3-20.

By tuning these different parameters, we are able to respect at the same time topological considerations, AFM histograms, TEM images and PL measurements at low temperature. We find a typical "medium" size QDs with ground state energy around 1.3 eV at low temperature (~950 nm in wavelength) and geometrical parameters as described in Figure 3.3-20. The height for the lens shape part is ~2 nm, the truncated-pyramid part representing the QWIs is ~0.5 nm and the continuous WL acting as a footbridge between QDs is ~1 nm thick. QD diameter is ~20 nm.

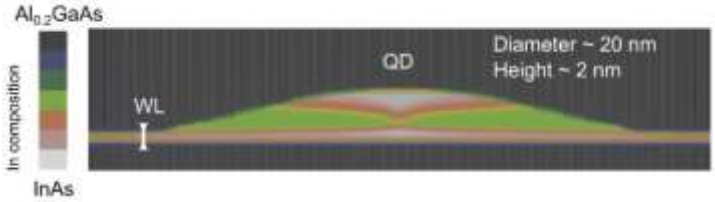

Figure 3.3-20: Example of "medium" size QDs side structure (y=0, middle of QD) calculated using k·p calculation with nextnano++ software

The chosen parameters for the final design are in good agreement with other typical dimensions found in the literature. For example, Dr. T. Andlauer, who developed nextnano++ version, investigated self-assembled InAs QDs using truncated-pyramidal shape QDs as shown in Figure 3.3-21. Aspect ratio is ~0.17 with 15 nm diameter, 2.5 nm height and inverted indium gradient concentration from 40% to 100%. On each side of the QDs there is a 50% indium InGaAs WL of thickness 0.5 nm. In our case, in Figure 3.3-20, indium concentration is between 30% and 100% with a total QDs+WL height ~3.5 nm for ~20 nm diameter and aspect ratio ~0.17.

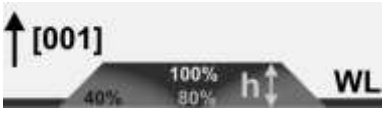

Figure 3.3-21: Truncated pyramid QDs with Indium inverted Indium gradient concentration adapted from [202].

The aim of designing precisely QDs final structure is so that energy diagram and electron wave function probabilities are considered to be more realistic. It can help to understand the dynamic of electrons inside the QDs.

ii). Energy diagram and electron wave function probability

Using the final designed structure, with k·p model we calculate the number of states with their energy positions and wavefunction inside a certain volume decided by a quantum grid. For a typical "medium" size QDs as represented in Figure 3.3-20, we have *xy*-quantum-grid step of 0.8 nm and a *z*-quantum-grid step of 0.1 nm. We only calculate for one isolated QD with an extension of the quantum volume inside $Al_{0.2}GaAs$ host material of +/-5 nm in all directions. Conditions at limit are

set as periodic boundary conditions and it is safe to assume that for 10 nm spacing (5 nm x2) there is no coupling between QDs, as we will discuss later. In Figure 3.3-22, we represent the energy diagram for a "medium" size typical QD of Okd-3 type of growth. It has been calculated at low temperature and Varshni equation for $Al_{0.2}GaAs$ was used on the conduction band energy states to reposition the energy states at 300K.

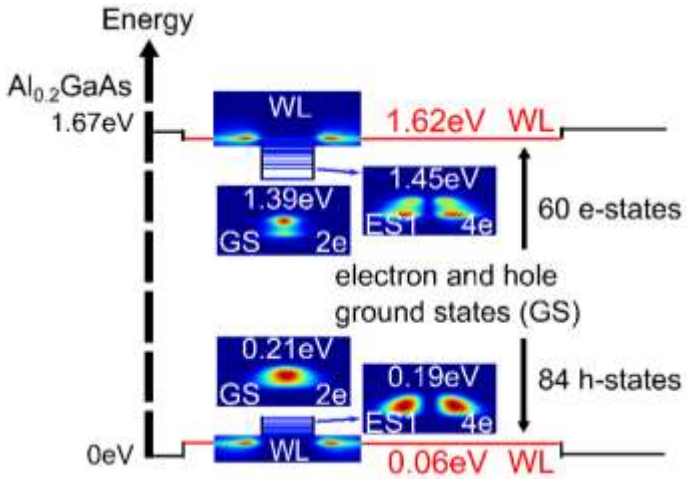

Figure 3.3-22: Energy diagram of a "medium" size typical In(Ga)As QD with $Al_{0.2}GaAs$ host material in black lines, InGaAs WL in red lines and ground state (GS) with excited states (ES) in blue lines. There are about 60 electron states and 84 hole states from GS to WL energies. Also electron wavefunction probability color plots side cuts (y=0, middle of QD) are shown for electron and hole GS, ES and also WL state.

This repositioning method is used because most of parameters used in k·p model are found for low temperatures [204]. Varshni equation is an empirical temperature-dependent expression that has proven to be reliable [168]. Usually in k·p calculations, valence band energy states are considered to be nearly temperature-independent. It is an approximation to help visualize the band energy diagram at room temperature, which is the usual operating temperature for a solar cell. We find ground states (GS) energies of 1.39 eV for electrons and 0.21 eV for holes, which means that PL emission is around 1.18 eV at room temperature (1050 nm in wavelength).

As shown in Figure 3.3-23, electron wavefunction probability for GS show one maximum. There seems to be a relatively good coupling of electron and hole states but we see in the side cut that the maxima for electron states tend to be localized at the two positions where the indium concentration is the highest: at the apex of the QD and at the bottom of the QD mixing with the WL. This behavior can be seen also for excited states (ES). As shown in Figure 3.3-24, the first excited states (ES1) show two maxima and have an occupancy of four electrons. In this case, we can guess that these first excited states are more related to the *xy*-plane lateral confinement following the idea of the lateral confinement approximation detailed earlier.

The energy separation for GS and ES1 is around 60 meV for electrons and 20 meV for holes. These values are too small to consider that these levels are well separated at room temperature. Looking at electron wavefunction probability color plots we see that the coupling between GS and ES1 seems limited which mean that the transition dipole moment is weak and radiative recombination would be unlikely.

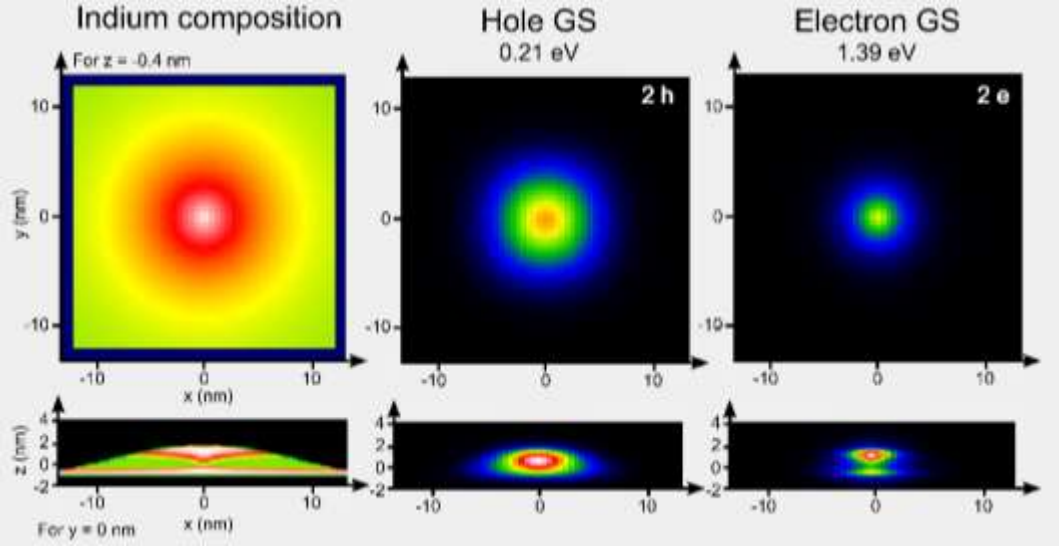

Figure 3.3-23: Ground state (GS) electron wavefunction probability for states in the *P*-type valence band for holes and the *S*-type Γ-band for electrons. Color plot are shown for the xy-plane at position z=-0.4 nm at the intersection of the bottom of the QDs and the beginning of the WL. In addition, *xz*-plane cut is shown at center position (y=0 nm).

iii). Coupling of QDs with QWIs and WL

Over all the excited states electron wavefunction probability-plots that are shown in Figure 3.3-24, it is interesting to notice that the electron wavefunction is often localized near the edge of the QDs and even at a position overlapping with the quantum-well islands (QWIs) and WL region. In Figure 3.3-22, electron wavefunction probability-plot is shown for a pure WL energy state to give an idea. The footbridge continuous WL connecting QDs starts for $x > 13$ nm. If we are to consider that coupling starts for a distance inferior to 5 nm, we see that ES1 is just at the limit of overlapping with the WL, inside the QWI. $ES2_B$, $ES2_C$, $ES3_B$ electron wavefunctions are clearly localized on the edge in the QWI region therefore the overlapping with the continuous WL is high. It means that over the 18 first ES, almost half of them overlap with the WL region.

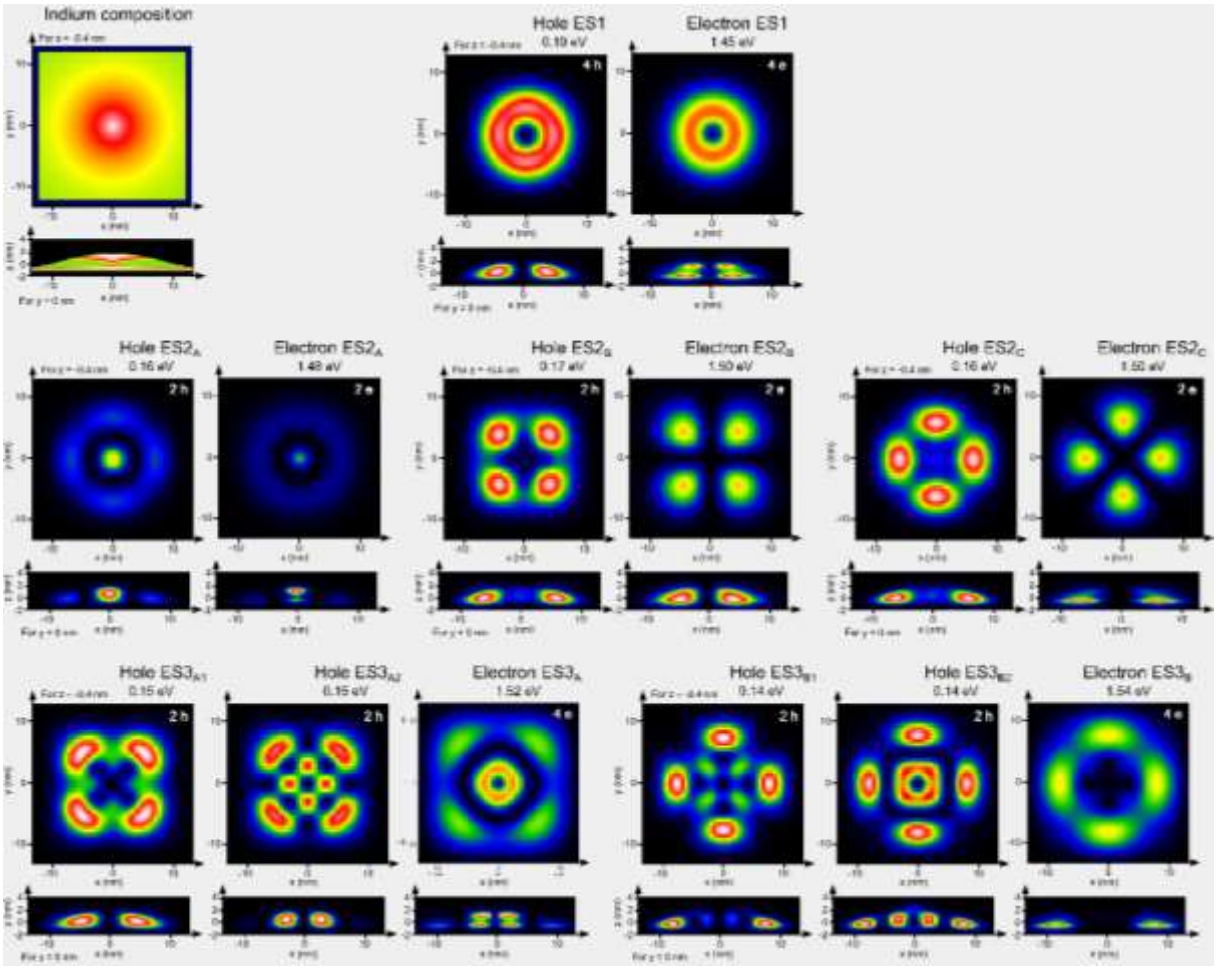

Figure 3.3-24: Electron wavefunction probability for the first 18 electron and hole excited states. They are regrouped according to their main transition energies around 1.26 eV for ES1, 1.33 eV for ES2 and 1.38 eV for ES3.

In ideal QDs, the WL should not have a big impact on the extraction of electrons from excited states because the WL region would be beside the QDs as schematically represented in Figure 3.3-21. From this figure, it would be considered that electron wavefunction from energy states localized inside the QD would have relatively small coupling with the electron wavefunction of energy states in the WL. In our case for the lens-shaped QD design with QWI and WL, that we present here, the QD wavefunction is localized in the center of the confined area but also in the QWI, near the WL part, thus coupling with the WL is highly probable. In this case, it may allow radiative thermal photons to extract more easily electrons outside of the QD confined region. This approach of thermal photons is well-known in the litterature [205]. Also the impact of the coupling with virtual bound states (VBS) that have energies higher than the WL or barriers may play a role [206].

3.3.2.4 Coupling distance for adjacent QDs

Finally to conclude this study over the use of k·p calculation for self-assembled In(Ga)As QD-IBSCs, we present the calculation in Figure 3.3-25 from reference [198], a paper from Dr. Teruhisa Kotani and Dr. Stefan Birner related to the study of closely stacked one-dimensional InAs QDs supperlattices. They studied the impact of inter-dot spacing between QDs as described on the right figure. By looking at Figure 3.3-25 on the right figure (c) and (f), we see that even for 5 nm spacing, QDs are not coupled vertically. Lateral coupling seems even less probable except via quantum-well islands (QWIs) or WL energy states as we discussed previously. Figure 3.3-25 illustrates the fact that for a

reduced spacing distance in the vertical direction, coupled QDs will shift from a QD-like density of states (DOS), as shown in Figure 3.3-25(c) and (f) (L_z = 5 nm), towards a quantum-wire-like DOS, as shown in Figure 3.3-25(a) and (d) (L_z = 1 nm). For an intermediate spacing Figure 3.3-25(b) and (e) (L_z = 3 nm), we are in the case of QD superlattices (QDSLs). The intermediate band (IB) is separated from the energy continuum but is wider in energy and has a higher DOS compared to QDs due to QD coupling.

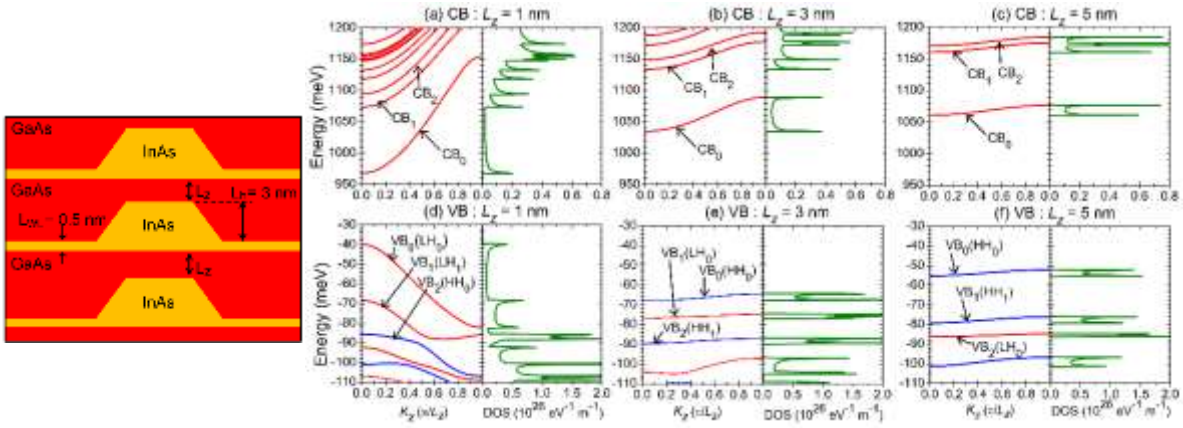

Figure 3.3-25: Left figure: cross-sectional shape of a truncated pyramidal InAs/GaAs 1D-QD superlattice. The height L_h and the base length L_b of the QDs are 3.0 nm and 10.0 nm, respectively. The WL thickness L_{WL} is 0.5 nm. The inter-dot spacing L_z varied from 0.5 to 10 nm. Right figure: Subband dispersions (left) and density of states (DOS) (right) of the conduction and valence bands for different inter-dot spacing. The DOS in these figures have been convoluted with a Gaussian broadening function with a full width at half maximum of 0.5 meV. Adapted from [198].

Overall in this part, photoluminescence temperature-dependent characterization evidence a mechanism of thermal escape and hopping for QDs with the apparition of a the so-called “Stokes shift” effect. Electrical characterization like reverse bias external quantum efficiency at room temperature seems to indicate tunneling effects also maybe with defects for QDs. Current-voltage temperature dependent measurements for QDs and reference solar cells indicate thermoionic field emission to thermoionic emission dependence supposedly due to a high density of deep level defects in $Al_{0.2}GaAs$ host material. Finally, our work with k·p calculation conjugated with the AFM analysis indicate one explanation for thermal escape due to the coupling of QDs with QWIs, then QWIs to WL and WL to host material. In the next section, we also use the k·p calculation tool to investigate the optical absorption of our QDs and compare with experimental findings.

3.4 QDs absorption: simulation and experimental determination

In the last part of this chapter, we study QDs absorption with both a simulation and experimental approach. In the first section using k·p calculation, we are able to understand more closely the interaction of light with our QDs. It is very useful to apprehend the intermediate band (IB) filling behavior that will be challenged in chapter 4. In the second section, experimental characterizations enable to confirm and validate a very small value of absorption from our QD layers. We also present a novel approach for the characterization of low-absorption materials with the help of FP interferometry.

3.4.1 Absorption from k.p calculation

In this part we use k·p calculation to investigate absorption for the designed QDs structure described in the previous part considering different sizes of QDs, different polarizations of light and implementing a broadening to simulate the distribution of QDs in size, which was noticed in previous part by precise analysis of the self-assembled In(Ga)As QDs.

3.4.1.1 Theory

Absorption calculation using the k·p model is based on the calculation of the integral of the coupled electromagnetic field of light with the transition dipole moment also called the momentum matrix element for optical transitions. The transition dipole moment (TDM) is the electric dipole moment $\boldsymbol{\mu}_{i-f}$ associated with the transition between an initial state *i* and a final state *f*. The absorption coefficient can be expressed following Equation 3.4-1 [189].

$$\alpha(\hbar\varpi) = \frac{\pi\varpi}{n_r c\varepsilon_0}\frac{2}{V}\sum_{k_i}\sum_{k_f}\left|\hat{\boldsymbol{e}}\cdot\boldsymbol{\mu}_{i-f}\right|^2\delta(E_f - E_i - \hbar\varpi)(f_i - f_f)$$

Equation 3.4-1: Absorption coefficient expressed with the TDM due to transition rate in semiconductor.

In Equation 3.4-1, n_r is the real part of the refractive index, ε_0 the dielectric permittivity of vacuum, *c* the speed of light, V the volume of the structure and $\hat{\boldsymbol{e}}$ the unit vector of light polarisation. The initial and final state energies are E_i and E_f. $\hbar\varpi$ is the photon energy and f_i and f_f are the initial and final states Fermi–Dirac distribution functions, respectively.

From the nextnano++ software it is possible to calculate the 3D-wavefunction envelope amplitudes inside the chosen quantum volume for the calculated 8 bands. The basis functions are *S*-like for the Γ-band of the electrons and *P*-like for the valence band with an orthogonal basis. All states are twice spin degenerated and can be written as: $S\uparrow\rangle, X\uparrow\rangle, Y\uparrow\rangle, Z\uparrow\rangle, S\downarrow\rangle, X\downarrow\rangle, Y\downarrow\rangle, Z\downarrow\rangle$.

Due to symmetry considerations and using the Kane matrix element energy $E_p = 25eV$, the momentum matrix elements for optical transitions can be calculated with the overlap of the wavefunction envelope of holes φ_i^{hl} and electrons φ_f^{el} in the initial and final states. Using information provided by nextnano documentation, we are able to find the absorption formula described by Equation 3.4-2.

$$\alpha(E) = \frac{q^2 \hbar E_p}{\pi c \varepsilon_0 m_0 n_r} \times \frac{1}{E} \times \frac{1}{V} \sum_a \sum_b \left| \int \hat{\boldsymbol{e}} \cdot (\boldsymbol{\varphi}_a^{el} \times \boldsymbol{\varphi}_b^{hl}) dV \right|^2 \times \frac{\Gamma}{\Gamma^2 + \left((E_b - E_a) - E\right)^2} \times (f_a - f_b)$$

Equation 3.4-2: Absorption coefficient calculated by integration of the overlap of wavefunctions for different initial and final states.

Compared with Equation 3.4-1, the energy conservation criteria is relaxed by Lorentzian Γ broadening as it is often found in the literature [193]. We checked that this formulation is valid by calculating the absorption for simple structures like for example using the example of an InGaAs QW inside $Al_{0.2}GaAs$ host material and comparing the calculated absorption in the energy continuum part with the experimental absorption measured by ellipsometry.

Due to QDs symmetries and growth direction, calculation of absorption is often made by integrating the projected TDM along two different polarizations of light represented by the directions: along z-axis (TM mode for example electric field polarization along [001]) and along xy-plane (TE mode: for example electric field polarization along [110]).

3.4.1.2 Absorption calculation over 3 different kind of QDs

In the previous discussion of k.p calculations, we have considered three typical QDs with different sizes as shown by their PL emission wavelengths represented in Figure 3.4-1: small (QD1), medium (QD2) and large (QD3).

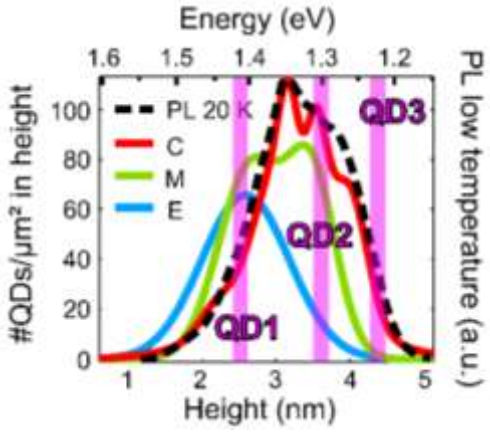

Table 3.4-1: Three typical QD sizes encountered in Okd-3 MBE growth. Figure 3.4-1 show their energy in comparison of AFM and low-temperature PL measurements.

Shape	Small (QD1)	Medium (QD2)	Large (QD3)
Diameter (QDs+WL)	> 10 nm	20 nm	< 30 nm
Height (QDs+WL)	> 2 nm	3.5 nm	< 4.5 nm
PL emission at RT	1.32 eV	1.18 eV	1.11 eV

Figure 3.4-1: (left) Reminder of Figure 3.3-1: Superposition of PL measurements characterization for a center-zone sample with AFM measurements as previously studied and shown in Figure 3.2-18 and Figure 3.2-19. Indication in pink are given to show the different types of QDs that we calculate in this study: small (QD1), medium (QD2) and large (QD3). Energy scale is for low temperature PL. A -95 meV Varshni shift can be used to compare with energy transition at room temperature.

In Figure 3.4-2, we have plotted the result of absorption calculations for each QD scaled by their own volume. Each calculation is made by taking a certain number of transitions from hole (h) states in the valence and electron (e) states in the conduction band. For each QD type we have calculated the transitions between 400 h and 300 e states. In the case of medium and large QDs, this number of states is not enough to cover all transitions below the host material energy bandgap (1.67 eV) but it is enough to give an estimation of the absorption profile at least up to about 1.5 eV. This value of absorption represents a hypothetical maximum limit for the absorption of a very closely stacked QD layer.

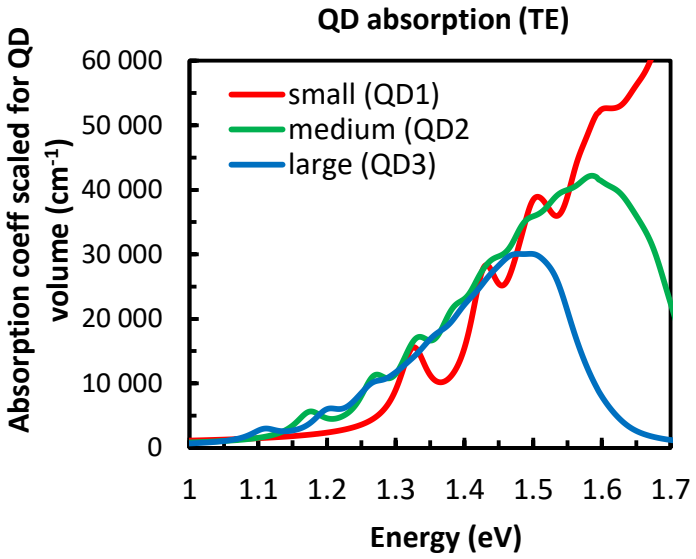

Figure 3.4-2: Calculated absorption coefficient for the three types of QD. Lorentzian inhomogeneous broadening is plotted for Γ=25 meV (room temperature). Only TE modes are shown for simplicity. Absorption coefficients are normalized by their QD volume.

We see that the envelope is about the same for each QD but larger QDs have more energy states and therefore in the same spectral range their absorption profile is more step-like as in the case of QWs. If we take an average value around 1e4 cm^{-1}, using simple path approximation of light absorption with perfect antireflection coating it means that 1 µm-thick of such absorbing layer would be needed to absorb 2/3 of light and 5 µm for almost 100% which is about as good as GaAs material.

Considering these different QDs, we present in Figure 3.4-3 the calculated absorption for different layers that are not closely stacked but more like Okd-3 type of growth. They have these types of QDs with same inter-dot spacing length of 25 nm and same spacing layer of 25 nm in the vertical direction. The volume filling fractions are the following: ~0.6% for QD1 layer, ~2.4% for QD2 layer, and ~4.5% for QD3 layer. We also show Lorentzian inhomogeneous broadening of Γ=5 meV (low temperature) to better see the energy position corresponding to the transition dipole moment (TDM) that have a high transition rate.

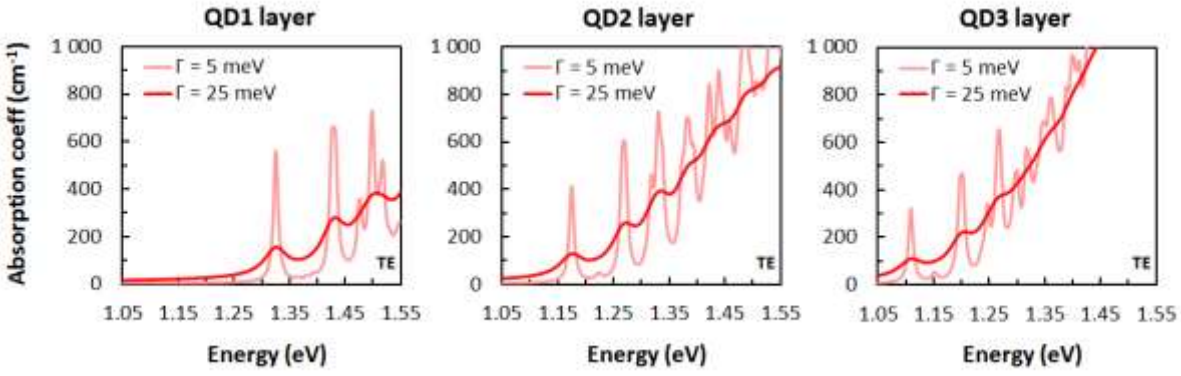

Figure 3.4-3: Calculated absorption coefficient for the 3 types of QD layers. Lorentzian inhomogeneous broadening is plotted for Γ=5 meV (low temperature) and Γ=25 meV (room temperature). Only TE modes are shown for simplicity.

We notice that the absorption coefficient is higher for large QD layers because they have a higher volume ratio of QDs. Nevertheless, for the ground states levels and first excited states, we notice that all QDs have about the same absorption coefficient of about 100-250 cm^{-1}. By mixing the 3 types of QDs with a simple pyramidal distribution in diameter following AFM measurements, we get the mixed profiled as shown in Figure 3.4-4. Both TE and TM modes are represented and also the absorption coefficient for intraband transitions inside the conduction band. For IBSCs, it can be associated with the IB to CB transitions if we consider that IB states are filled, which is rarely the case for low concentration illumination. Two important comments can be made and are also usually verified in the literature:

- For VB to QD energy states (IB), TE absorption dominates by a ratio about proportional to the aspect ratio of the QDs (0.15-0.20).
- For QD energy states (IB) to CB, TM absorption is spectrally shifted compared to TE and it is more favourable for the sequential two-photon absorption (S-TPA) phenomenon. In reality, the TE [XY] optical absorption will be negligible because the energy is too low.

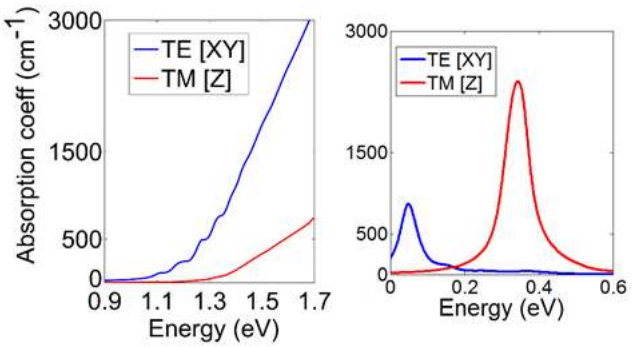

Figure 3.4-4: Calculated absorption coefficient for a mixing of the 3 types of QDs presented earlier. TE and TM modes are presented for interband absorption of VB to CB (left figure) and for intraband absorption inside the CB for QDs energy states that would be filled up to the WL energy.

3.4.1.3 Gaussian broadening due to the gaussian distribution of QDs

In the next part, we will try to compare the calculated absorption with experimental measurements. In the previous part, we considered the mixing of three types of QDs following a pyramidal distribution for simplicity. It is also possible to consider that QDs have monotoneous shifts of energy states depending on their size. Thus, we can use gaussian broadening to describe the whole population of QDs. This broadening can be done by using a Voigt function that uses the convolution of a Lorentzian (for inhomogeneous broadening from temperature) with a Gaussian (homogeneous broadening from QDs size distribution) [207]. In Figure 3.4-5 we present the TE projected transition dipole moment (TDM) of a "medium size" QD for different types of broadening: Lorentzian with Γ=25 meV, Gaussian with FWHM of 63 meV (that is the smallest one-Gaussian distribution by fitting low temperature PL with a bimodal expression to get "large QDs" distribution) and the Voigt function for those two distributions. We notice the Voigt profile to be a lot smoother than the other profiles, we almost don't recognize the energy position of the TDM from the medium size QD.

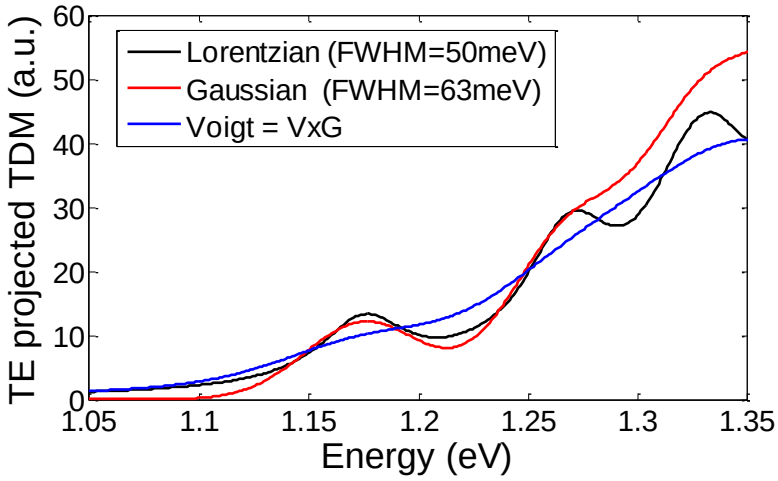

Figure 3.4-5: TE projected TDM of a medium size QD for different types of broadening: Lorentzian with Γ=25 meV, Gaussian with FWHM of 63 meV and the Voigt function for those two distributions.

FWHM of Voigt function can be written as a function of the FWHM of the associated Gaussian and Lorentzian profiles following Equation 3.4-3 [208].

$$FWHM_{Voigt} = 0.5346 \times FWHM_{Lorentzian} + \sqrt{0.2166 \times FWHM_{Lorentzian}^2 + FWHM_{Gaussian}^2}$$

Equation 3.4-3: FWHM Voigt profile as a function of FWHM Gaussian and Lorentzian functions

Following Equation 3.4-3, at room temperature for Lorentzian with Γ=25 meV and Gaussian with FWHM of 63 meV we have a Voigt FWHM of 94 meV. We noticed earlier in section 3.2.2.2 that PL at room temperature can be relatively well fitted by a Gaussian and the corresponding FWHM is around 90 meV.

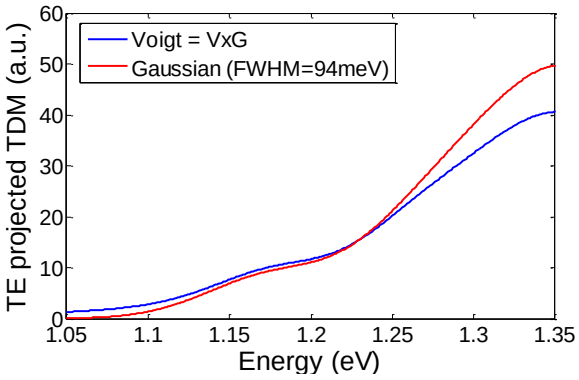

Figure 3.4-6: Comparison of previous Voigt profile in Figure 3.4-5 with a Gaussian broadening with FWHM of 94 meV

Figure 3.4-6 shows that the TE projected TDM with Gaussian distribution of FWHM at 94 meV is almost equal in term of profile to the previous calculated Voigt FWHM. Voigt functions are not convenient to use in numerical calculation. For simplicity in the next parts of this study, we will use a Gaussian function when considering QDs absorption as an approximation of a Voigt function. For example, we will use the Gaussian approximation when fitting the PL at room temperature instead of using a Voigt function.

3.4.2 Absorption measurements

The optical properties of self-assembled In(Ga)As QDs in $Al_{0.2}GaAs$ host material requires more investigations especially if we wish to combine it with light management techniques that requires accurate knowledge of the complex optical index ($\tilde{n}=n+i\kappa$).

The refractive index of bulk materials or thin films is generally determined by ellipsometry. However it is not well-developped for quantum-structured materials. A few studies have shown that the optical index can also be obtained using Fabry-Perot (FP) interferometry [209], [210], [211]. At normal incidence, this technique is particularly suitable for anisotropic materials, such as QDs, as it provides the optical index in the plane of the QD layers. Transmission measurements can also be performed, but thick epitaxial layers (several microns) are required, which is very difficult for QDs materials because of strain accumulation and inhomogeneity of QDs layers.

3.4.2.1 Comparison of different absorption characterization method

In order to determine experimentally the optical absorption of quantum structured materials, many approaches can be found in the literature. Table 3.4-2 summarizes different techniques that are used with their advantages and disadvantages.

i). Ellipsometry method

First, ellipsometry method measures the change of polarization upon reflection or transmission and compares it to a fitting model. In the case of classical bulk material, many studies and models have been developed in order to relate the change of polarization with dielectric properties of the material. For quantum-structured material, it is difficult to find such model so a specific model needs to be developed and tested. Moreover, from a technical point of view, the usual characterization set-up requires to have an incident light with 70 degree angle from the direction normal to the surface. As we saw previously QDs are anisotropic objects and absorption for TM polarization is a lot lower than for TE polarization. Finally, QD absorption of light is very small and it is difficult to detect with no enhancement of light absorption.

ii). Reflection and transmission method

This method is the most basic method to investigate the absorption from any material. The principle is to measure the reflected and transmitted light in order to find the ratio of light absorbed. First problem is that QD absorption is very low and only a limited thickness of QD layers can be grown because of strain constraints, typically less than 1-µm thick. On the other hand, GaAs substrate can be more than 400 µm-thick and will induce parasitic absorption up to its bandgap energy level and even below due to free carrier absorption. Therefore, this technique can be used in our case only if GaAs substrate is removed but even in this case light path enhancement might be needed.

iii). Carrier collection efficiency

Following CCE characterization principle discussed earlier, it is an easy method to perform on any electrical diode under reasonable CCE approximation. Assuming that all carriers are collected at reverse bias, we approximate the EQE at saturation reverse bias to be equal to the absorption inside the electrical device. Using the transfer matrix method, fitting of the absorption can be related to the effective medium absorption coefficient of QDs layers.

An advanced variation of this method can be performed to investigate IB to CB transition with sequential two-photon absorption (S-TPA). For example, bandfilling of IB can be performed with a light source with energy higher than IB while current originated from IB to CB photons is collected using a Fourier transform infrared (FTIR) source with a photocurrent spectroscopy (FTPS) setup. In the literature, different groups [212], [58], have successfully investigated IB to CB optical transitions for InAs/AlGaAs systems at low temperature but no exact value of absorption has been measured directly. For example, in Figure 3.4-7b, Tamaki et al. have shown that the maximum absorption for the IB to CB transition in the IR region arises at an energy around 0.35 eV for the InAs/$Al_{0.2}$GaAs system. This value was also confirmed by Luque group [212] for the same kind of sample grown by Dr. Y. Shoji who is also the grower for our samples. In our k·p calculation at room temperature, we find an increase of the absorption coefficient around 0.3 eV for the IB to CB transition with TM [Z] polarization as shown in Figure 3.4-4. We see that we are in good agreement with the experimental results performed by these groups at low temperature. We would like to point out that the characterization setup from Tamaki et al. and Luque group mainly excite the TE [XY] part of the absorption coefficient. Indeed the IR source incident light is hitting the semiconductor surface with an incident angle of 25° at maximum which gives an internal angle of 7° at maximum. Therefore, the TM [Z] part represents 12% of IR light at maximum for such characterization setup. This might contribute to the fact that IB to CB optical detection is difficult.

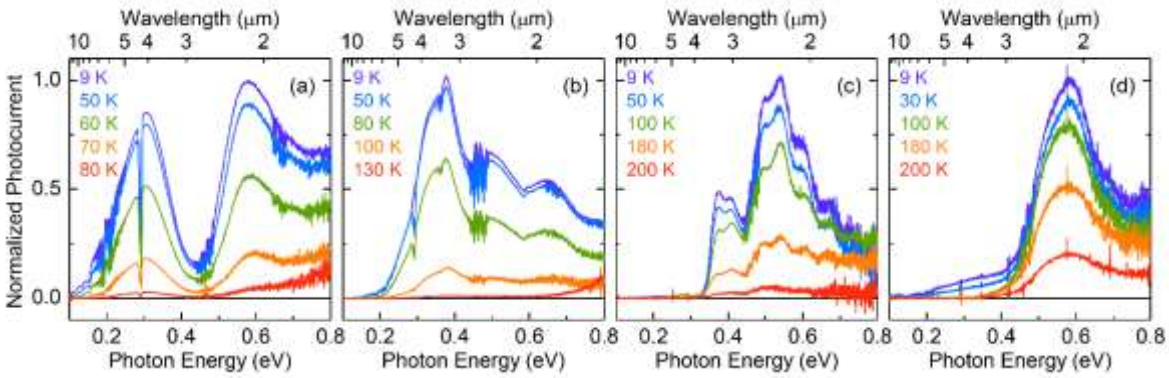

Figure 3.4-7: Temperature dependence of normalized FTIR photocurrent spectra via two-step photon absorption under white-light bias irradiation on (a) InAs/GaAs, (b) InAs/Al0.2Ga0.8As, (c) InGaAs/Al0.3Ga0.7As, (d) InGaAs/GaAs/InGaP QDSCs at short-circuit conditions. The dip and noisy fringes, respectively, at 0.30 and 0.47 eV are atmospheric absorption of CO2 and H2O. Taken from reference [58].

iv).Photoluminescence excitation method

Photoluminescence excitation (PLE) consists in recording the PL signal while varying the excitation wavelength. Dr. P. Rale who contributed to extensive spectroscopy analysis of these QDSCs samples suggested the use of this method for characterization of QD layers absorption [213]. Indeed, considering PL is linear with the excitation intensity, if PL intensity is changing with wavelength for a fixed excitation intensity, it means that the absorption coefficient is also changing. Moreover, as the luminescence is layer selective, this method gives access to the absorbance of a particular layer in a stack. The excitation source he used was a Fianium supercontinuum laser, the variation of luminescence intensity obtained has to be corrected by the incident power, and quantitatively calibrated. The complexity in this setup characterization consists in recording the luminescence without being disturbed by the laser reflexion. There are also at least two obstacle from a PL point of

view. First PL intensity has to be linear with excitation intensity and second PL peak should be stable in the same spectral region along the variation of excitation wavelength.

These two conditions are often not met for the QDSCs samples we study. In such samples, the absorption varies more than two orders of magnitude from the spectral region where absorption from host material dominates (λ ≤ 740 nm) to the spectral region where only QDs layers are absorbing. These variations imply different bandfilling dynamic for PLE. In a worst-case scenario, the PLE of host material region (λ ≤ 740 nm) might be in a saturation regime for the lower energy QDs states ("large" QDs). This saturation might induce a non-linear saturation regime with PL peak shifting due to the filling of higher energy states.

Qualitatively this situation can be solved if we consider to investigate separately spectral regions with about the same order of magnitude for absorption. In the case of Dr. P. Rale thesis, results are shown for the characterization of samples with Okd-1 type of growth, which is higly inhomogeneous in QDs size as shown by AFM measurements in Figure 3.2-8. QDs layers are transferred on mirror by etch stop transfer layer process detailed in chapter 2. It induces a FP cavity as shown by FP resonances in reflectometry experimental measurements (1-R orange line) in the left graph of Figure 3.4-8 taken from [213].

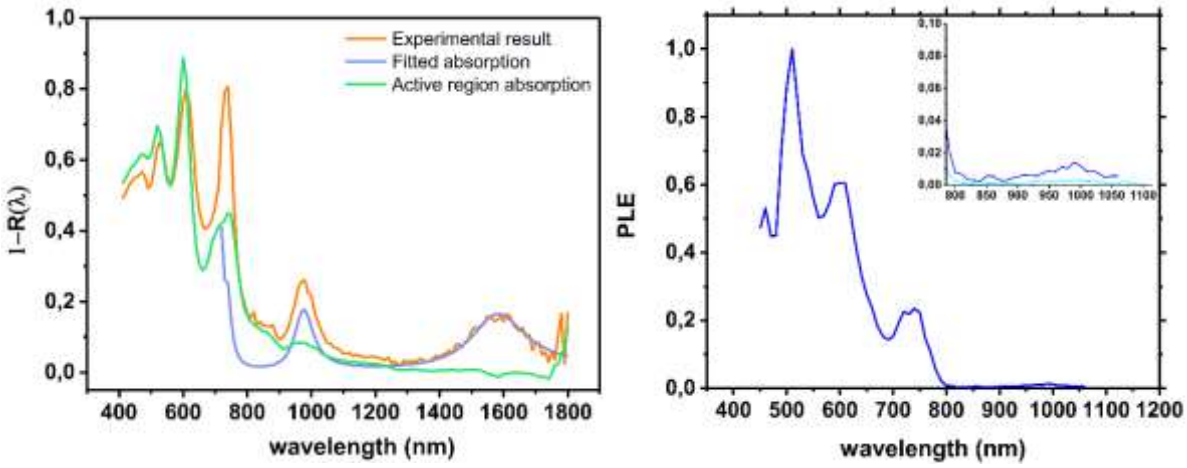

Figure 3.4-8: Absorptivity obtained from reflectometry measurements (left graph). The uncertainty of this reflectometry measurement is high especially for the region where absorptivity is low because the measurement is more sensitive to parasitic losses like light scattering. In this regard, PLE measurements (right graph) gives a more direct information of absorption inside QDs layers. Taken from [213].

In the right graph of Figure 3.4-8, a PLE spectrum is shown for the integration of PL over low energy QDs or "large" QDs that will be filled first. Therefore we can consider that this integration reflects the variation for the lowest absorptive region that is the spectral region where only QDs are absorbing.

We can see the impact of FP resonance from the cavity on the absorptivity measurement that is reflected in the inset of the PLE characterization with an increase around 1000 nm in wavelength. For calibration, we use reflectometry measurements but the scaling needs to be done for a spectral region where we are sure that most of light is absorbed by the absorber and contribute to PL. In low absorption region, mirror absorption is high, therefore, calibration is done for the host material absorption region. Thus, we are faced with an incertainty because we are dealing with two different

regimes of bandfilling. Still, if we consider PLE in this region to be equal to the absorptivity of the FP cavity we can relate it to an absorption coefficient around 400 cm^{-1} at 1.45 eV which is coherent with the k.p calculation in part 3.4.1.2.

v). Multipass waveguide method

This method is detailed in Figure 3.4-9 taken from [214]. The incident light is coupled from the side through a wedge. West and Eglash [215] suggested to use this method for QWs in order to investigate the intersubband transition, which can only be excited by mid-IR light polarised in the quantum well direction.

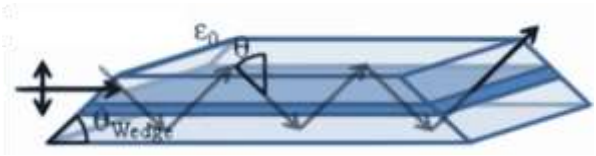

Figure 3.4-9: Sketch of a multipass waveguide. Light coming from the side through a wedge with angle θ that determines reflection angle inside the waveguide. Taken from reference [214].

In the case of QDs, k·p calculation also predict TM [Z] modes to be the only ones that can excite IB to CB transitions. Experimentally, we can have some results even when we use light that is not highly polarized in the QDs layer direction as shown with the S-TPA characterization from Okada and Luque's groups [58], [212]. One reason might be because some part of the WL and QDs are tilted and thus their vertical axis is not always aligned with growth direction contrary to QWs. Nevertheless, using the multipass waveguide method is also a good way to have an increased light path for absorption characterization. It can be a complementary characterization method for the FP interferometry approach that will be detailed next but it also necessitates a specific process that was not developed in the course of this work.

Table 3.4-2: Advantages and disadvantages for different QDs absorption characterization method

QDs absorbtion characterization method	Advantages	Disadvantages
Ellipsometry	Well-known method	• 70 degree angle for incident light • Need a particular model • Low signal, large spot
1 – (Reflection+Transmission)	Basic method	• Absorption from substrate • Low signal
CCE	Easy to test on an electrical diode	• Need valid CCE approximation
PLE	Easy to test on any sample	• Difficulty to calibrate, not absolute • PL peak shift uncertainty
Multipass waveguide	Enable light path enhancement Investigation of TM modes (eventually TE also)	• Specific fabrication process
FP interferometry	Enable light path enhancement Investigation of TE mode (eventually TM also)	• Specific fabrication process

3.4.2.2 Fabry-Pérot interferometry

i). Principle and theory

The idea behind FP interferometry is to enhance light path using FP resonances that are tuned by different cavity thicknesses so that the spectral region of interest is modulated by these different FP resonances. Then by using reflectometry measurements, it is possible to fit the different curves and have a good estimation of the optical properties of the investigated material inside the optical cavity.

There are different ways to consider the tuning of the thickness of the cavity. It is possible to make steps by etching the cavity material as in reference [211]. We thought about this solution and it is one reason we decided to fabricate Okd-4 type of design. Ideally, it was designed to be highly absorbing (InGaAs QDs), with 3 µm-thick of epitaxial layers, homogeneous in QDs and with a certain number of etch stop layers positioned inside the stack. Unfortunately, the Okd-4 growth showed very high inhomogeneity as we discussed previously in section 3.2.2.3 and the appendice **A**. In addition, there was another technical problem. When removing the GaAs substrate with chemical etching, we noticed that the epitaxial layer was detaching itself from the glass substrate at the end of the process. This was encountered by other people from our group and it is usually attributed to high strain in the epitaxial layer as discussed in chapter 2. The UV-glue is not strong enough to absorb the strain that was before absorbed by the GaAs substrate.

Since we could not obtain results on Okd-4, we decided to use another method and instead of etching the absorbing layer, we thought about adding thickness in the form of non-absorbing dielectric layers with well-controlled optical properties. We also decided to come back to a simpler stacking structure with Okd-5.

ii). Fabrication

In chapter 2, we discussed in details about the different steps needed for fabricating the electrical devices and nanophotonic structures used along our project. In this part, we discuss about the fabrication process of SiN_x staircase FP cavity for QDs light absorption Fabry-Pérot (FP) interferometry characterization.

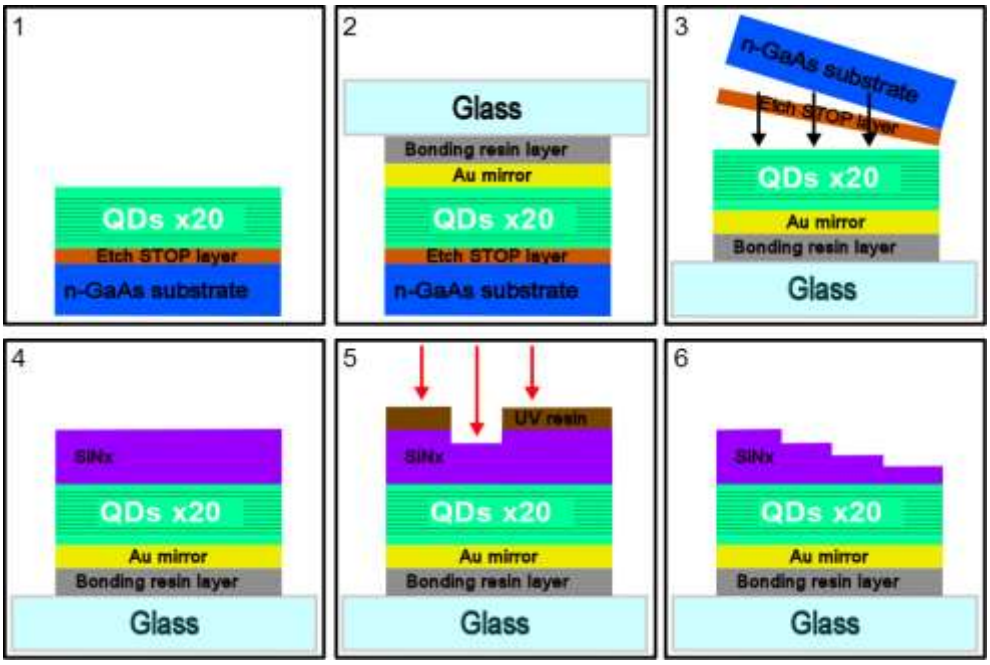

Figure 3.4-10: Fabrication process of the SiNx staircase Fabry-Pérot (FP) cavity with gold mirror at the back. 1: 20 layers of 1.9 MLs InAs QDs with Al0.2GaAs spacing layers have been grown by MBE both at 480°C. QDs have been Si doped at about 4 Si/QDs (8e17 Si/cm^3). 2MLs AlAs capping has been used to reduce the wetting layer (WL).Etch stop layer is in Al0.8GaAs. 2: Gold mirror deposited by e-beam evaporation, UV bonding resin is used with 1mm glass as a supporting substrate. 3: Etch stop step is realized by different type of chemical etchings. 4: 800 nm of SiNx is deposited by sputtering. 5: Staircase steps are done by reactive ion etching (RIE) with UV lithography to protect outside the step. 6: Process is repeated many times, until obtention of sufficient staircase steps.

For the experimental investigation of QDs absorption we use Okd-5 type of growth. We decided to come back to In(Ga)As / $Al_{0.2}GaAs$ system that was the main system we studied along the project contrary to Okd-4 attempt. That is why Okd-5 growth conditions are more or less the same as Okd-3, but with three main changes: (i) AlAs capping to investigate the reduction of the WL, (ii) 4 Si/QDs doping (8e17 Si/cm^3) to have sufficient prefilling of QDs for characterization of intersubband transition and (iii) MBE setup version 2 that was discussed earlier to investigate QDs homogeneity improvement. The thickness of the total absorber is around 560 nm with 20 layers of 1.9 MLs In(Ga)As QDs with $Al_{0.2}GaAs$ spacing layers both grown by MBE at 480°C. An $Al_{0.2}GaAs$ sample was also grown in the same conditions with no QDs to use as a reference.

In Figure 3.4-10, the three first steps are the same as the transfer process with etch stop layer as described previously in chapter 2. During step 4, 800 nm of SiN_x is deposited by sputtering. During step 5, staircase steps are done by reactive ion etching (RIE) with UV lithography to protect the region outside of the staircase step. The process is repeated many times to fabricate a staircase with enough steps for FP interferometry.

In Figure 3.4-11, is shown a microscope photography of the sample and an inset (in green) to evidence the etching steps. On the photo, we can see the gold mirror transferred on the glass substrate and the 560 nm-thick $Al_{0.2}GaAs$ absorbing layer with or without QDs in the case of the reference sample. In the green image are shown five SiNx steps that have different thickness and all of them have an area of about 500 x 500 μm^2.

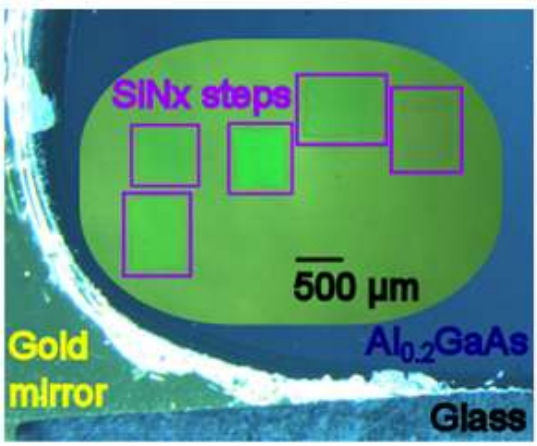

Figure 3.4-11: Sample structure top view, five SiNx steps are shown and different part of the sample are shown: SiNx in green, $Al_{0.2}GaAs$ in blue, gold mirror in left corner and glass at the bottom of the picture.

iii). Reflectometry fitting

Upon the fabrication of both samples, we can make reflectometry measurements using the gold mirror as a background and reference for the calibration. Figure 3.4-12 shows the reflectometry measurements for reference and QDs samples using Fourier-transform infrared (FTIR) spectrometry. A microscope objective x10 was used and aperture angle is less than 25°. We calculated that the angle is negligible for the fitting of the FP cavity reflectometry. Spot size is less than 300 µm in diameter for squared steps of more than 500 µm in size as shown in Figure 3.4-11. $Al_{0.2}GaAs$ sample with no QDs was used as a reference. A -8% decrease in reflectometry is attributed to QDs absorption for FP resonance around 0.9 µm in wavelength.

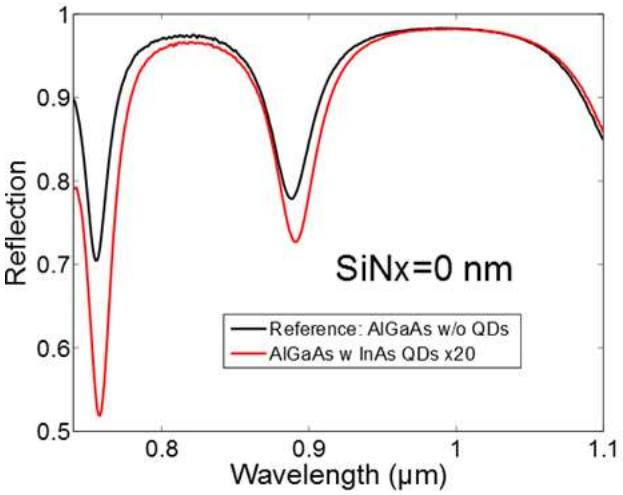

Figure 3.4-12: Reflectometry measurements using Fourier-transform infrared (FTIR) spectrometry. x10 microscope objective was used and aperture angle was taken into account. Spot size is <300 µm in diameter for squared steps >500 µm in size as shown in Figure 3.4-11. Al0.2GaAs sample with no QDs was used as a reference. A -8% decrease in reflectometry attributed to QDs absorption can be seen at FP resonance around 0.9 µm.

For the fitting of those reflectometry measurements, we use the analytical formula of reflection *R* shown in Figure 3.4-13 following the application of Rouard's method for a double layer Fabry-Pérot (DLFP) cavity [216]. Following the description in Figure 3.4-13, $r_{a\to b}$ are the Fresnel coefficients between *a* and *b* media for the four different media considered here: Air, SiNx, QDs layers and Gold mirror. r_3 represents the wave that is reflected from QDs media. The round trip wave propagation in medium *a* is expressed with $p_a = \exp(i2\tilde{n}_a t_a k_0 \cos(\theta_a))$ where $\tilde{n}_a = n_a + i\kappa_a$ and t_a are respectively the refractive index and thickness of the *a*-media. θ_a represents the angle for the direction of propagation with k_0 the wavevector.

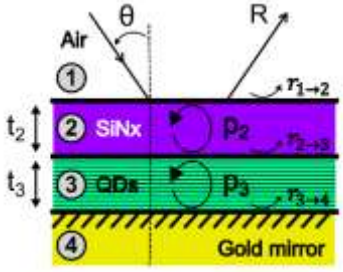

$$R = \left|\frac{r_{1\to2} + r_3 p_2}{1 + r_{1\to2} r_3 p_2}\right|^2$$

$$r_3 = \frac{r_{2\to3} + r_{3\to4} p_3}{1 + r_{2\to3} r_{3\to4} p_3}$$

Figure 3.4-13: Schematic drawing of the structure for the calculation of the reflection in a double layer Fabry-Pérot (DLFP) structure following Rouard's method with the analytical expression of reflection in function of Fresnel coefficients, wave propagation and reflection.

Thicknesses of the different layers are known by fabrication, profilometry characterization, reflectometry and ellipsometry measurements. Position of resonant peaks are mainly due to the product of the thickness with the real part of the refractive index and we consider that the real part of the refractive indices are well-known in our case. The only unknown values are the imaginary part κ of the refractive indices in the case of the reference $Al_{0.2}GaAs$ layer with no QDs and the sample with QDs layers. Figure 3.4-14, shows the reflectometry fitting (dashed lines) in the case of the reference sample with no QDs. To fit at the best we tried to change the $n\&\kappa$ optical parameters of the gold mirror in-between different well-known values found in the literature (for example: Palik, Johnson&Christy, Babar, Rakic, Hagemann). The fitting is almost good but unfortunately, there are still

some differences. They can be attributed to parasitic loss like surface roughness or subbandgap absorption from $Al_{0.2}GaAs$ material.

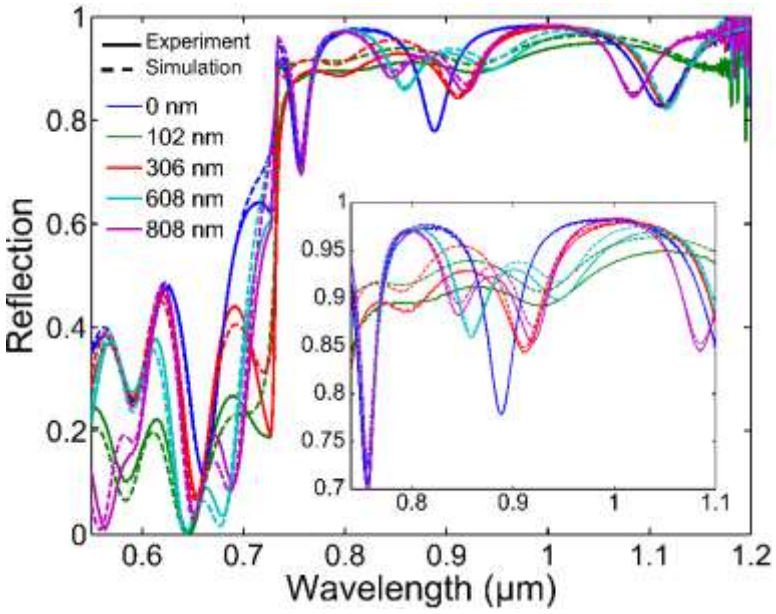

Figure 3.4-14: FTIR Reflectometry measurements. 5 colors curves correspond to measurement on steps region with different thickness of SiNx (from 0 to 800 nm). Background/reference calibration for FTIR is done on gold mirror in left corner as shown in Figure 3.4-11. Simulations using Rouard's method are shown in dashed lines. Al0.2GaAs sample with no QDs is used as a reference with the exact same structure to fit at best the simulation with experiment assuming no subbandgap absorption and finding an optimum n&k value for gold mirror. Inset shows that some parasitic loss remains and will be evaluated and taken into consideration for the calculation of QDs absorption.

To fit at best over all the spectrum for different thicknesses t_k, we use the same algorithm as in reference [211]. It computes the calculated reflectometry across the whole spectrum for a wide range of κ values. It then calculates the root mean square deviation (RMSD) between the calculated and measured curves for successive intervals of width $\Delta\lambda$ from Equation 3.4-4 where N_t and $\delta\lambda$ are the number of dielectric thicknesses and the step width for each interval $\Delta\lambda$, respectively. For each interval $\Delta\lambda$, the smallest value of RMSD gives the best approximation for $\kappa(\lambda)$.

$$RMSD(\kappa) = \sqrt{\frac{1}{N_h(\frac{\Delta\lambda}{\delta\lambda})}\sum_{t_k}\sum_{\lambda_j}[R_{\text{meas}}(t_k,\lambda_j) - R_{calc}(\kappa,t_k,\lambda_j)]^2}$$

Equation 3.4-4: Root mean square deviation formula to find the best approximation of the imaginary part of the refractive index κ along the whole spectrum for different SiNx dielectric thicknesses.

In Figure 3.4-15, we represent the calculated κ values for the fitting of reflectometry measurements with SiNx steps for the reference sample expressed as parasitic loss (magenta line with blue error bars) and the QDs sample (black line with red error bars). By substracting the parasitic loss we get an estimation of the imaginary value κ for the 20 QDs layers (green line). Errors bars are calculated for +/-50% on the root mean square error between the measurement and the simulation with the calculated κ values. Error bars for the reflectometry measurement are even less due to very small fluctuation in the reflectometry measurements that are precise at +/-0.2%.

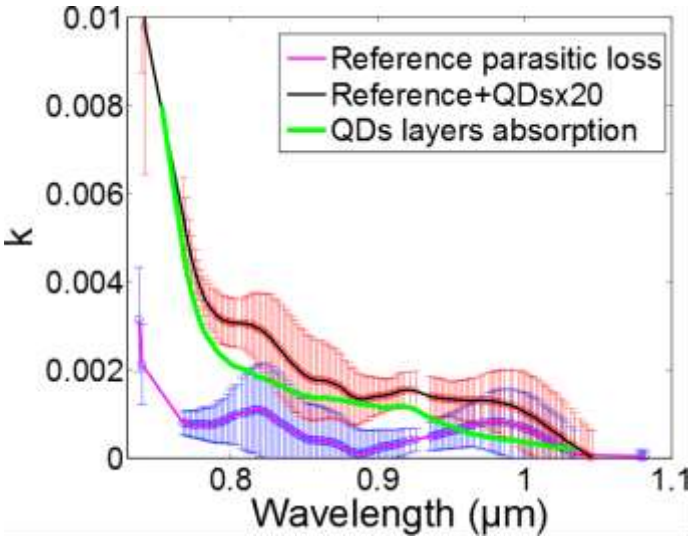

Figure 3.4-15: Complex optical index calculated for reference sample and sample with InAs QDs. Error bars are calculated for +/-50% on the root mean square error (RMSE) between the measurement and the simulation with the calculated κ values. Error bars for the reflectometry measurement are even less due to very small fluctuation in the reflectometry measurements, only +/-0.2%.

Parasitic absorption from the reference sample seems to be around 100 cm^{-1} which is close to the value we find for the QDs absorption near PL emission. It would be interesting to understand further from where it might come from. We tried to consider different scenarii but it seems like the most probable source for the parasitic loss would be because of $Al_{0.2}GaAs$ subbandgap absorption via trap states defects. Along all the investigation of In(Ga)As QDs / $Al_{0.2}GaAs$ system in this chapter, we noticed that our $Al_{0.2}GaAs$ material has a high level of trap defects. We know from the literature that low trap defects density (< 1e14 cm^{-3}) $Al_{0.2}GaAs$ solar cells are grown by MOVPE at temperature of 640°C [139], while in our case we grow by MBE at 480°C. For high quality $Al_{0.2}GaAs$ material with low density of traps, we found in the literature that the value of the absorption coefficient is around 10 cm^{-1} [217]. We also found that trap defect density can increase of 2 order of magnitude by changing the growth temperature [136]. Therefore, in our case, if we have a density of trap defects on the order of 1e15 cm^{-3}, an absorption coefficient around 100 cm^{-1} would not be absurd. In our lab, deep level transient spectroscopy (DLTS) measurements were done on GaAs samples grown at low temperature as QDs host material. Trap density of 5e14cm^{-3} was observed for EL4 type of defects with activation energy around 0.5 eV. In the future, it would be interesting to check the trap defects density also for AlGaAs host materials.

<u>iv). Absorption coefficient comparison with k.p calculation and reverse bias EQE fitting</u>

From the characterization of the imaginary part of the refractive index κ for QDs layers, we can deduce their absorption coefficient following Equation 3.4-5 and compare with other values discussed previously as shown in Figure 3.4-16.

$$\alpha(\lambda) = \frac{4\pi\kappa}{\lambda}$$

Equation 3.4-5: Absorption coefficient in function of the imaginary part of the refractive index κ and wavelength

From Okd-5 PL measurement at room temperature, we deduce the ground state (GS) in the QDs layers to be close to 1.24 eV in energy. In Figure 3.4-16, we show the k·p calculation for QDs with

such GS using a Gaussian broadening to take in consideration temperature and size effect as explained previously. From room temperature PL fitting, we find a Gaussian broadening of 110 meV at FWHM that we attribute to “large QDs”. In reality, the distribution of QDs might be larger but we did not measure PL at low temperature on Okd-5 QDs layers. From Okd-3 carrier collection efficiency (CCE) results obtained on transferred or non-transferred devices, and by assuming that 100% of collected electrons come from absorbed photons, we can fit and find different values of absorption. For example, the QDs absorbtion from CCE fit showed in Figure 3.4-16 comes from the reverse bias EQE measurement of Okd-3-1.3NT sample at -10V. We also performed reflection plus transmission method on transferred sample on glass without gold mirror. Values of absorption are found to be on the same order as FP interferometry method. Nevertheless, the certainty of the measures can only be assumed for some spectral positions at FP resonant peaks (due to glass cavity) and the signal is lower than in the gold cavity structure because light path enhancement is very limited.

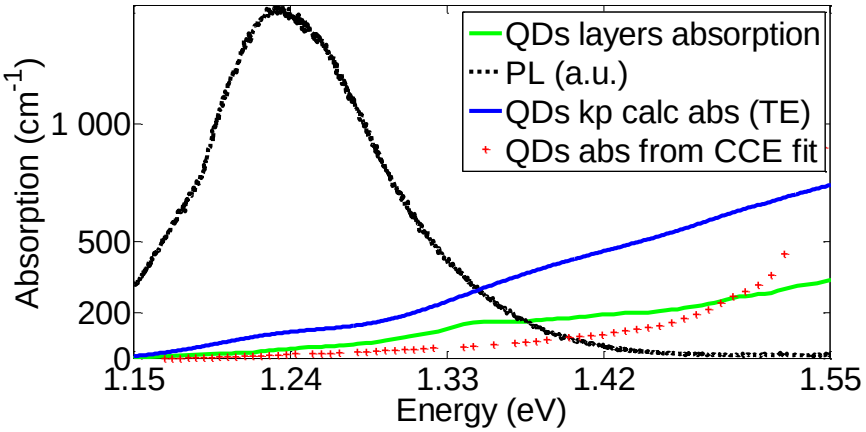

Figure 3.4-16: Comparison of the experimental value of absorption with k.p calculations. We find the same order of magnitude as for TE. Absorption is around 200 cm^{-1} for QDs GS with energies around 1.24 eV confirmed by PL measurement. Also as a comparison, the value of absorption is showed for fitting of CCE measurement from an Okd-3 sample.

Other CCE fits are shown in Figure 3.4-17 for solar cells in different zones of the 3-inch wafer. The positions of the solar cells are shown in Figure 3.4-18 with PL mapping. QDSCs with higher PL intensity also have larger absorption from excited states following EQE measurements presented earlier. By comparing these CCE results with QDs layers absorption experimental FP interferometry measurement of Okd-5 type of growth (green line), we see that absorption is at least twice or three times less around the GS (or PL emission). This might be explained by the fact that electrons at this energy might have a CCE of 50% or less because of the competition with PL recombination.

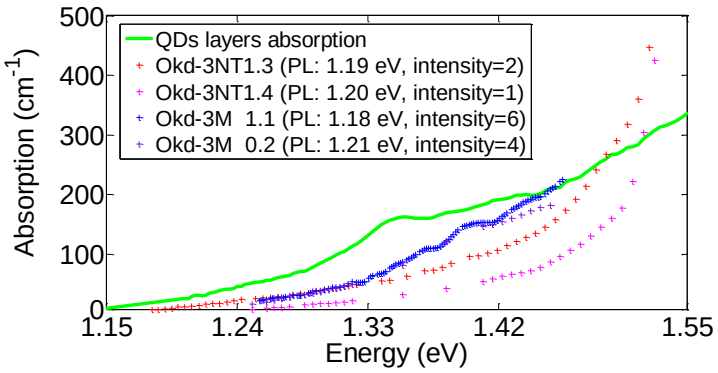

Figure 3.4-17: Comparison of absorption from CCE fitting of different solar cells. We see that QDSCs that have the higher PL intensity also have the larger absorption from excited states.

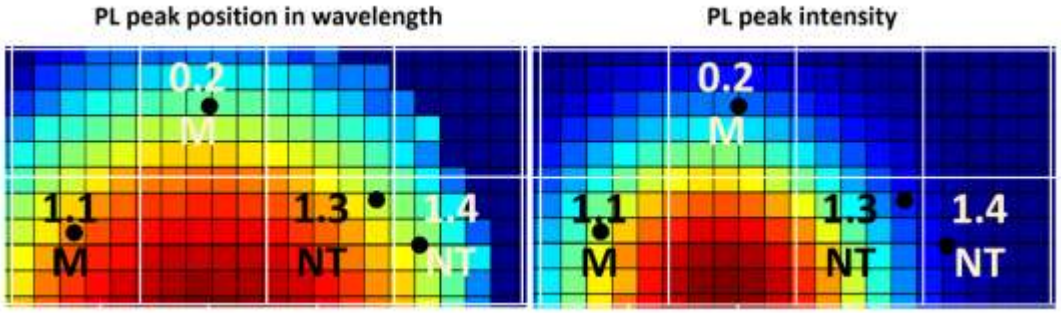

Figure 3.4-18: Color map from PL mapping of Okd-3 with different samples for CCE and the position of the measured cells.

Finally, Table 3.4-3 summarizes absorption values found with different method, type of growth and spectral position. For the wetting layer (WL) region at 1.55 eV, we notice that for the k·p calculation value, the CCE (Okd-3) value and the PLE (Okd-1) value, we find almost the same absorption coefficient around 750 cm^{-1}. This value is twice less in the case of FP interferometry method (Okd-5). This might be due to the reduction of the wetting layer (WL) by AlAs capping. For the excited states spectral region (1.30-1.45 eV), we find a lower value for CCE that we think might be explained by not so efficient CCE. Overall, we can estimate that we have an absorption coefficient around [100-400] cm^{-1} for this excited state region.

Table 3.4-3: Comparison of absorption values with different method, for different type of growth and at different spectral positions

Spectral region of interest	FP interferometry (Okd-5)	k.p calculation (Okd-3)	CCE (Okd-3)	PLE (Okd-1)
Wetting layer[>1.55 eV]	> 340 cm^{-1}	> 740 cm^{-1}	> 700 cm^{-1}	> 800 cm^{-1}
Excited states [1.30-1.45 eV]	[100-200] cm^{-1}	[200-500] cm^{-1}	[50-200] cm^{-1}	[200-400] cm^{-1}
Ground states [<1.24 eV]	< 50 cm^{-1}	< 100 cm^{-1}	< 25 cm^{-1}	< 100 cm^{-1}

This table and interpretation of QDs absorption is necessary, in the next chapters, to consider light interaction with QDs and especially the possibility of implementing efficient strategy for light trapping.

Conclusion

In this chapter, we wanted to show that QDs-IBSCs are far from being an "ideal" IBSCs system. After careful investigation and characterization, it is possible to get a better knowledge of such system. We would like to underline some points that seem important for our study and highlight our achievements:

- In the first part, we showed that In(Ga)As/AlGaAs is theoretically a promising system for IBSCs. GaAs is a well-known material for the industry of semiconductor and high quality $Al_{0.2}GaAs$ solar cells have been achieved recently. In(Ga)As/GaAs QD material, and its use for IBSCs, is well-documented in the literature. Nevertheless, in the field of IBSCs, the combination of In(Ga)As QDs with a wide bandgap material like $Al_{0.2}GaAs$ has only recently attracted attention and is still under investigation. All along this chapter, we were able to confirm that In(Ga)As/$Al_{0.2}GaAs$ system has a lot in common with In(Ga)As/GaAs system used in conventional QD-IBSCs:
    1. In term of growth, AFM investigation seems to indicate the same issues of wetting layer (WL), quantum-well islands (QWIs), and morphology limitation.
    2. The temperature dependent PL characterization gave us information on "frozen" and "hopping" regimes where carriers thermal escape induce a so-called "Stokes shift" effect (relaxation in "large" QDs).
    3. Carrier collection efficiency (CCE) characterization and temperature dependent current-voltage (I-V) characterization tell us about the influence of the electric field on carrier escape and the possible presence of a high defects density in $Al_{0.2}GaAs$ host material.
    4. The use of k·p calculations indicates that thermal escape might be facilitated by the low confinement of holes with a continuum of quantum states: 84 holes states for 150 meV energy separation with the wetting layer. For electrons, ground states and the first excited states have a 60 meV energy separation but afterwards there is a quasi-continuum of electron states: in total 60 electron states for a 230 meV energy separation. Moreover, the investigation of the wavefunction localization seems to indicate a possible coupling, tunneling and escape through QWIs and the WL.

  In summary, it seems likely that, at room temperature, the In(Ga)As QD intermediate band (IB) interaction with the $Al_{0.2}GaAs$ host material is ruled by a kind of thermionic trap-assisted tunneling escape process with a unipolar escape nature dominated by holes. These conclusions are important to understand the device operation that will be discussed in chapter 4.

- In the first part, we also discussed a QD-IBSC conundrum about sequential two-photon absorption (S-TPA):
    1. In term of photon balance, under 1 sun illumination, only 1 QD/µm² is suited to make sub-bandgap absorption with S-TPA via QD states. Indeed, too many QDs will hinder the S-TPA process because of the localization nature of the electron wavefunction inside QDs compared to the delocalized nature of the incident light in the QD layer.
    2. However, QDs are low absorption material, therefore people usually want to increase their numbers to increase light absorption. In this way, they also increase the trap density and reduce the probability of S-TPA.
    3. We considered that a solution would be to use photofilling via light concentration or using localized light management techniques along prefilling of quantum dot states with direct or indirect doping techniques.

4. We considered using higher absorption QD material for example InGaAs QDs that have a larger volume or using closely stacked QDs also called QD superlattices where QDs are coupled in the growth direction which enable the electron wavefunction to be delocalized in one direction.
5. We also discussed the position of QD layers that from our point of view should not be in the center of the junction's intrinsic region. In term of design, we consider that a new design of ultrathin junctionless QDSCs with selective contacts could be investigated in the future. The idea would be to have a maximum ratio of QD material and therefore benefiting at maximum from light management as discussed in chapter 1.

These remarks could be interesting for a next generation of ultrathin IB-HCSCs specifically designed for the implementation of advanced light management techniques.

- In term of achievements, we were able to show the many improvements that were made and are still to be implemented for the growth of QDs-IBSCs. We discussed the disadvantage of having a disparate growth of QDs on a 3-inch wafer that can become an advantage offering a low cost way to investigate different types of QDs in one growth. We also showed the effect of AlAs capping which decreased the influence of the WL as indicated by PL characterization and absorption characterization when comparing AlAs-capped Okd-5 growth with Okd-1 and Okd-3 initial growths.

- Finally, the last part helped us to understand what we can expect from an absorption point of view. The k·p calculation confirmed the difference in absorption between TE and TM polarization and we noticed that for our QD assembles, "small", "medium" and "large" QDs have the same effective absorption per volume because of the quasi-continuum nature of the density of states along with temperature broadening. Experimentally, we proposed an innovative method to investigate low absorption materials using Fabry-Pérot interferometry with the addition of a dielectric staircase. This method was applied to the characterization of our QD material and confronted with absorption taken from CCE characterization, photoluminescence excitation (PLE) method and k·p calculation. We confirmed that In(Ga)As/$Al_{0.2}$GaAs QD material has a low light absorption (hundreds per cm) on the same order as what is found in the literature for conventional In(Ga)As/GaAs QD system. This information is important for the analysis of the device operation in chapter 4 and also optical modelisation presented in chapter 5.

Chapter 4 Intermediate band dynamic study to evidence novel PV concept

In this chapter, we focus on the study of the intermediate band dynamic for our quantum dot solar cells (QDSCs) that we thoroughly investigated in chapter 3. At first, we study the effect of laser excitation on photoluminescence (PL) at room temperature under different regimes of excitation in order to get an insight into the bandfilling dynamic of QDs. Then, we study the effect of a second laser excitation to investigate sequential two-photon absorption (S-TPA), which is essential for intermediate band solar cell (IBSC). Finally, we summarize our results and put them in perspective with simple junction solar cells based on the wide bandgap $Al_{0.2}GaAs$ host material but also with the concept of intermediate band assisted hot carrier solar cell (IB-HCSC).

4.1 Calibrated photoluminescence

In this part, at first, a description of the setup is given, then we discuss about the balance of photons in such system and we present a method to evaluate the quasi-Fermi level splitting (QFLS) arising from two different carrier populations in the QDs and in the host material. In this part, all measurements are done at open-circuit voltage for a simple non-transferred solar cell from Okd-3 type of growth in the "edge zone" of the 3-inch wafer that we defined in the chapter 3 (3.2.2.2).

4.1.1 Characterization setup

For the purpose of calibrated PL at room temperature, a hyperspectral imaging system has been used where luminescence emission is imaged for different wavelengths. A calibration method allows to obtain absolute intensity of luminescence. The hyperspectral imager system used in this study, has been developed by Photon etc. Inc. in collaboration with IRDEP during Dr. Delamarre's theses for photovoltaics applications [218]. All characterization measurements presented here have been done by Hung-Ling Chen during his six-month internship at IRDEP under the supervision of Dr. Pierre Rale and Dr. Laurent Lombez in the framework of the Japanese-French "NextPV" collaboration [219].

4.1.1.1 Hyperspectral imager experimental setup

A schematic illustration of the experimental setup is shown in Figure 4.1-1. A collimated green laser of 532 nm has been used as the excitation source (coherent Genesis 6W CX355-6000STM). The laser is partly reflected by a beam splitter (BSW26: 50:50 UV fused Silica plate, coating 350-1100 nm), and enters a microscope objective (Nikon Plan Fluor 0.8/50x) in order to be focused on the sample. Luminescence emitted by the sample is collected by the same microscope objective and passes through the beam splitter. An additional filter (FEL650: long-pass filter, cutoff 650 nm) is used to

stop residual laser light. Luminescence then passes through the hyperspectral imager, and is finally recorded by a digital CCD (Charge-Coupled Device) camera.

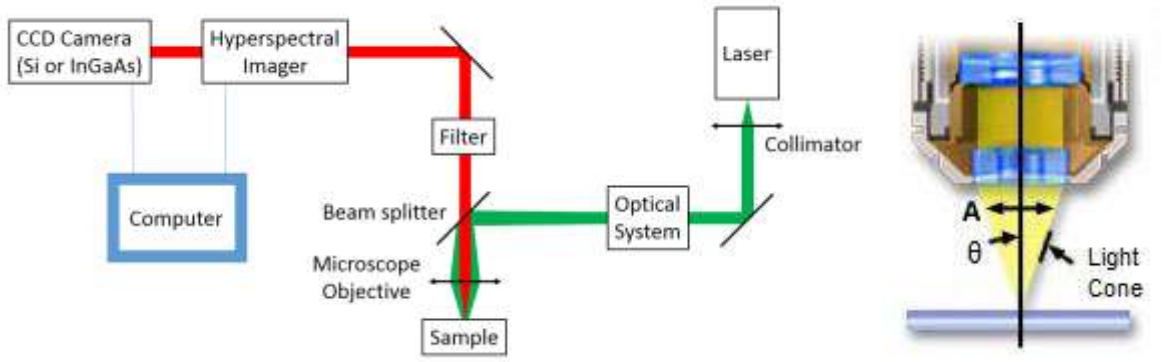

Figure 4.1-1: Schematic illustration of the experimental hyperspectral imager setup taken from [219].

4.1.1.2 Detection system

The detection system consists of two volume Bragg gratings whose angular positions are being controlled precisely. Luminescence can be filtered and recorded as in typical grating spectrophotometer but in this case contrary to typical grating spectrophotometer, an image of the photoluminescence is recorded with a pixel size resolution depending on the objective that is used and diffraction limited. Depending on the spectral range of luminescence, Tucsen Si-CCD camera (TCH-1.4ICE-II, 1360x1024 pixels) or Xenics InGaAs camera (Xeva-1.7-320, 320x256 pixels) can be used. The sensitivity of Si is ranged from the visible to 1100 nm, while InGaAs is sensitive to infrared region (900 nm to 1700 nm).

4.1.1.3 Calibration of the system

The system needs calibration from a spectral and spatial point of view. For the wavelength calibration of the gratings, two external sources are used to calibrate the central pixels of the image. Other pixels are deduced from the transfer function of the system. Then a relative calibration of the system is performed with a calibrated halogen lamp coupled with an integrating sphere in order to generate spatially homogeneous light input to the system. Finally, absolute calibration in photons/s/m²/nm is done since the output of the digital camera is linear to the incident photon flux. We can confirm the spatial calibration of our system by imaging an object of well-known size. For example in Figure 4.1-2, we show the image of a grating of 2-µm period. We have a pixel resolution of 0.27 µm with an estimated error of less than 2%.

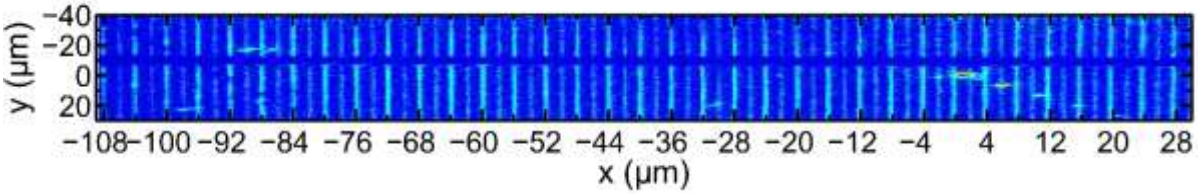

Figure 4.1-2: Image of a 2-µm grating by our hyperspectral imager system to calibrate spatially our system. PL intensity is shown in colorscale arbitrary unit.

4.1.1.4 Excitation spot

For typical use of laser in optical setup as described in Figure 4.1-1, excitation spot is limited by diffraction from the objective. The diameter can be calculate following the first Airy disk formula using the numerical aperture (NA) of the objective. In our case, for the 532 nm laser and NA of 0.8, the Airy spot size radius limit would be of 0.4 µm. In Figure 4.1-3, we show the typical configuration for our characterization of a 1-mm² solar cell. Photos #1 and #2 show the global design and center of the cell with a 60-µm diameter for the central circle. Photos #3 and #4 are taken with the setup to show the position of the laser spot. Photo #3 is taken without the 650 nm long-pass filter, we can see the laser spot has an ellipsoidal shape. Photo #4 is taken with filter so the detected spot comes only from the PL of the sample. The spatial distribution of the laser intensity is a two-dimensional Gaussian therefore 58% of its power is concentrated inside the full width at half-maximum (FWHM). The laser spot radius at half-maximum is measured using images taken without the long-pass filter on a silver mirror and other types of surface like the grating used for calibration. In all cases we find that the laser spot area has an averaged radius of 0.6 µm at half-maximum. Laser excitation power is changed using different neutral density thus we consider this spot size to be constant with the excitation power.

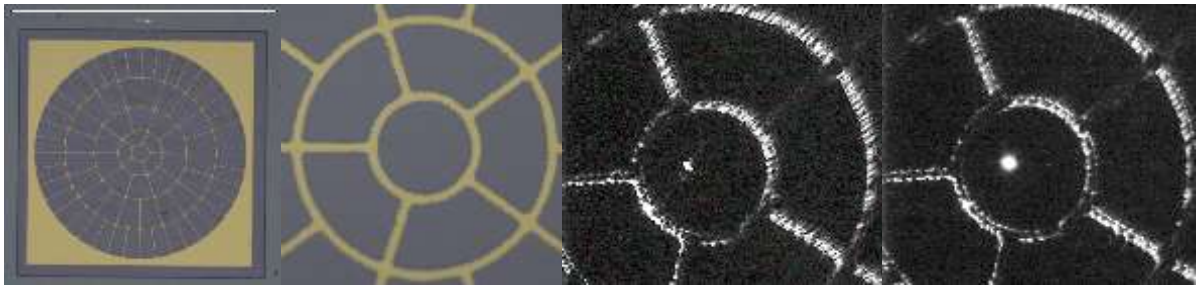

Figure 4.1-3: From left to right: photos #1 and #2 are taken with optical microscope for 1 mm² small diodes type described previously. The central circle has a 60 µm diameter. Photos #3 and #4 are taken with calibrated PL setup to show the position of the laser spot. Photo #3 is without the 650 nm long-pass filter we can see the laser spot has an ellipsoidal shape. Photo #4 is taken with filter so the detected spot comes only for the PL of the sample.

4.1.2 Balance of photons

Using the absolute calibrated PL setup, we can investigate the balance of photons in the QD-IBSCs system that was introduced in chapter 3. At first, we simply discuss the radiative dynamic spectrally and spatially for different laser excitations. Then a simple model evaluating the PL of QDs energy states with the increase of bandfilling is described and we compare it with experimental data. Finally, by fitting the PL high-energy tail we discuss the occupancy of high-energy states and the role of the activation energy barrier with the wetting layer (WL) and host material.

4.1.2.1 Radiative dynamic balance

In the previous chapter, we saw that QDs systems were first investigated for optoelectronics considerations where the main goal was to emit light. In our case, using the calibrated hyperspectral imager PL setup, we are able to know the intensity of light injected and emited from the system both spectrally and spatially and thus calculate the radiative ratio of our In(Ga)As / $Al_{0.2}GaAs$ QD-IBSC.

i). Three spectral domains of interest

Hyperspectral images, as described in Figure 4.1-6, are taken for different detection wavelengths of PL representing transition energies from the system. For In(Ga)As self-assembled QDs in $Al_{0.2}GaAs$ host material, we have seen in chapter 3 that, for our Okd-3 sample, there are three PL peaks corresponding to the ground states (GS) of QDs (E_{QDs}~$1.15 - 1.25\ eV$), the InGaAs wetting layer (E_{WL}~$1.55\ eV$) and the $Al_{0.2}GaAs$ host material (E_{host}~$1.69\ eV$). Therefore, three different energy (E) spectral domains are considered for the study of PL and absorption:

- $E \geq E_{host}$~$1.69\ eV$ ($Al_{0.2}GaAs$ host material PL).
- $E_{host} > E \geq E_{WL}$~$1.55\ eV$ (InGaAs wetting layer PL).
- $E_{WL} > E \geq E_{QDs}$~$1.15 - 1.25\ eV$ (ground states for In(Ga)As QDs).

In Figure 4.1-4, we show the calibrated PL spectrum, in photons/s/m²/eV with log scale (black curve left axis) and with linear scale (dashed black curve right axis), under a 0.37 mW power excitation with a 532 nm laser, measured at room temperature. The three spectral domains of interest are shown in color. The PL spectrum from Figure 4.1-4 is extracted from the hyperspectral images by integrating spatially over a "centered area zone" that will be defined next.

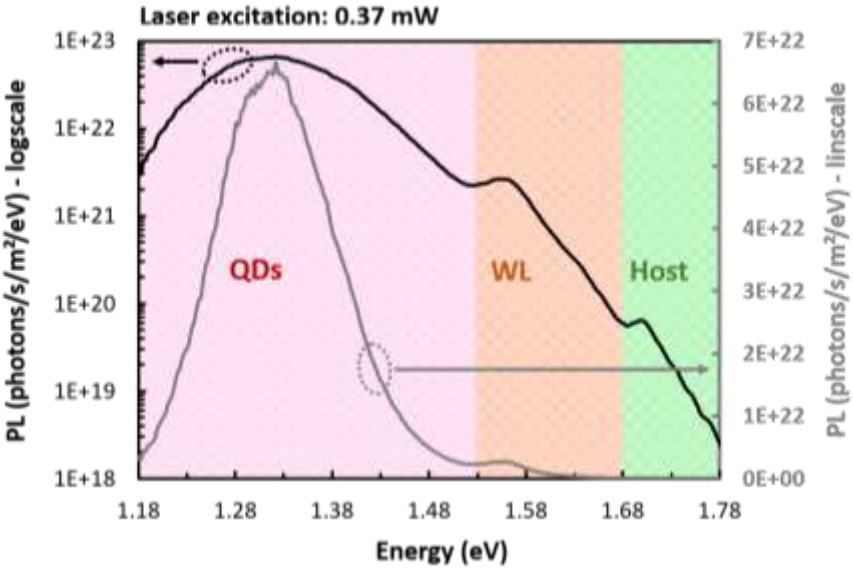

Figure 4.1-4: Calibrated PL spectrum in photons/s/m²/eV with log scale (black curve left axis) and with linear scale (dashed black curve right axis). Caption gives the excitation power (0.37 mW) for a 532 nm laser excitation. The three spectral domains of interest are shown in color: QDs (1.18-1.53 eV in pink), WL (1.53-1.68 eV in orange), and host material $Al_{0.2}GaAs$ (1.68-1.78 eV in green). Measured at room temperature.

ii). Power density considering laser absorption or photoluminescence emission

In this paragraph, we want to explain why it is not trivial to consider the power density for PL excitation characterization with a focused-spot setup:

- First, as we saw the source of the excitation is not homogeneous but Gaussian-like with 58% of power at FWHM.
- Second, purely "optical" power density from the absorption of the incident laser spot and "electrical" power density generating PL emission inside the semiconductor might be different because of carrier absorption and diffusion.

As summarized in Table 4.1-1, for different laser power excitation, we calculate the equivalent "optical" and "electrical" average power density at FWHM by considering either the incident laser spot ("optical") or the PL emission spot ("electrical").

Average "optical" power density from absorption of the incident laser spot at half-maximum: on one hand, for a 0.37 mW excitation, considering a Gaussian laser beam with spot size of 0.6-µm average radius at half-maximum (HM) and 58% of power at HM, we find an average absorbed "optical" power density of 10 kW/cm² at HM (surface normalization of power by the laser spot at HM). We calculate the absorbed flux by considering an absorptivity of 53%. This value is deduced from EQE measurements under reverse bias considering that all photogenerated carriers are collected at 532 nm in wavelength.

Average "electrical" power density from PL emission spot at half-maximum: On the other hand, the hyperspectral images show that QDs PL is Gaussian-like with spot size of 2.2-µm average radius at half-maximum (HM) under a 0.37 mW laser excitation and 58% of power at HM. Assuming that the QDs PL echoes the electron density, we calculate an average "electrical" power density of 0.75 kW/cm² at HM (surface normalization of power by PL spot at HM).

We can relate these densities to equivalent sun power densities. By integrating the number of photons in the solar spectrum up to QDs ground state (GS), we find that one sun is equivalent to 75 mW/cm² for AM 1.5G. Therefore, for a 0.37 mW laser power excitation we have an average "optical" power density corresponding to a concentration of 130 k suns and an average "electrical" power density corresponding to the concentration of 10 k suns. The maximum theoretical sun concentration is x46200, so our regime of excitation is far from being realistic for normal PV applications.

Table 4.1-1: Laser excitation average "optical" and "electrical" power density at half-maximum (HM)

Laser excitation	Average "optical" power density at HM	Average "electrical" power density at HM
0.01 mW	0.26 kW/cm² (4 k suns)	0.08 kW/cm² (1 k suns)
0.37 mW	10 kW/cm² (130 k suns)	0.75 kW/cm² (10 k suns)
2.71 mW	74 kW/cm² (1 M suns)	4.4 kW/cm² (58 k suns)

iii). PL evolution with power density

The shape of the PL over the entire QDs domain gives an indication on the occupation of QDs energy states.

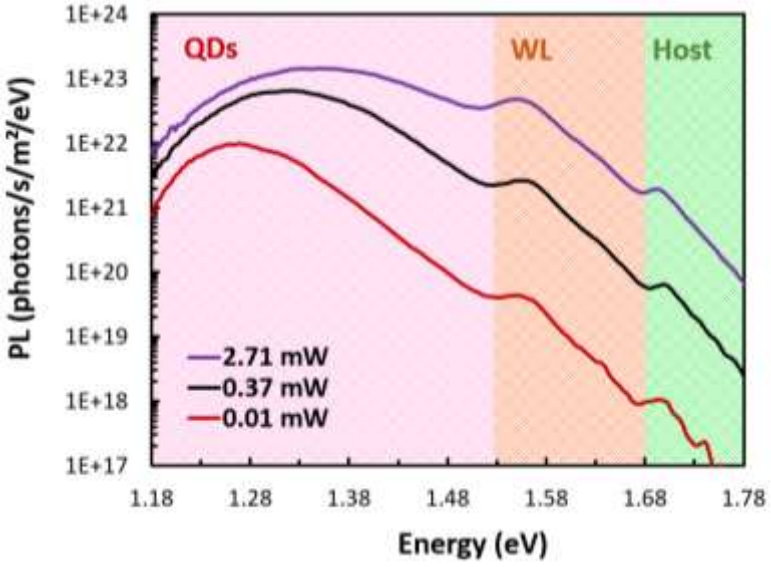

Figure 4.1-5: Calibrated PL spectrum in photons/s/m²/eV with log scale for three laser excitations power integrated spatially for over the same "centered area zone". Measured at room temperature.

In Figure 4.1-5, we compare PL spectrum for three different laser excitations following the same method. We notice the followings:

- Emission increases differently depending on the energy position which makes PL peak from QDs domains to shift towards high-energy. This effect is attributed to bandfilling of QDs energy states either because of the filling of excited states (ES) or because of QDs of smaller size with higher ground states (GS) energy.

- A shift of 10 meV can be seen on wetting layer (WL) and host PL peaks for the highest excitation regime (2.71 mW). It is attributed to lattice heating and would amount to a +10°C increase in temperature that seems understandable considering the high power density from laser excitation.

To model properly the bandfilling dynamic of QDs we have to take into consideration the so-called "Stokes shift" effect (relaxation in "large" QDs), recombination time changes and non-radiative losses. We will try to model it in this chapter but first we want to investigate hyperspectral images to better explain our setup and consider spatial repartition of PL in our QDSC system.

iv). Hyperspectral images

In Figure 4.1-6 we present the calibrated PL images integrated over the three types of spectral domains in linear scale for the three different excitation discussed earlier.

The PL from the laser spot is Gaussian-like and has an ellipsoidal shape as we already noticed in photo #3 of Figure 4.1-3 for the laser excitation spot without the long-pass filter. Overall, the PL spot integrated for the QDs spectral domain is larger than the PL spot from the WL domain. Both of them increase with increasing excitation. For the lowest excitation power at 0.01 mW, we can see that the PL of $Al_{0.2}GaAs$ host material is low and we barely distinguish the laser spot excitation from the rest of the image. The PL spot from the host material spectral domain starts to have a Gaussian spatial distribution for an excitation around 0.2 mW. At low excitation, the halo is barely larger than the WL PL spot but at high excitation it is clearly larger than the QDs spot. This effect might be a first observation of the apparition of a separated carrier population in the host material that will be discussed later.

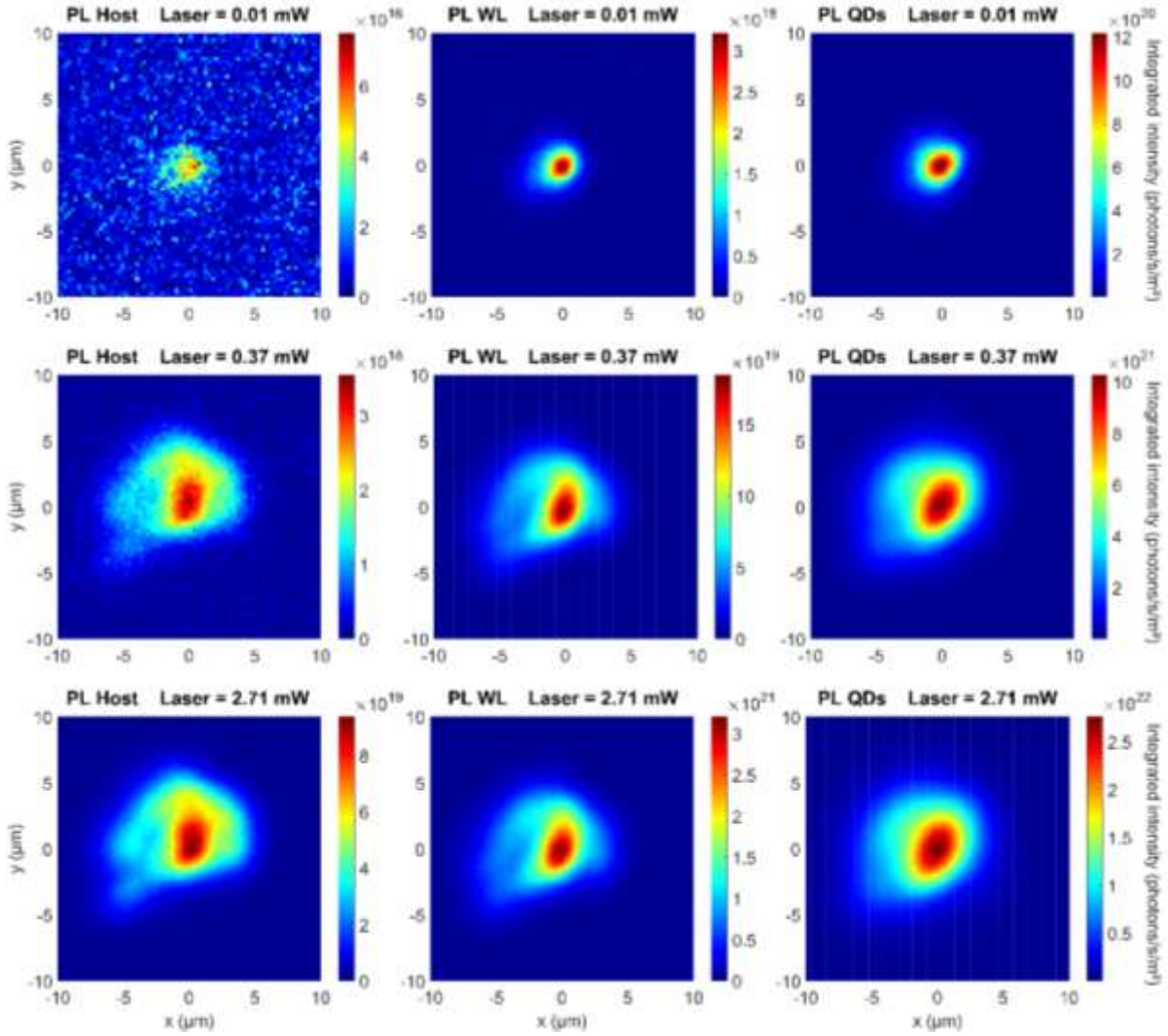

Figure 4.1-6: Calibrated hyperspectral images over a 20 x 20 µm² area in linear scale for three different laser excitation and spectrally integrated over the three domains of interest: QDs (1.18-1.49 eV), WL (1.52-1.59 eV), host (1.68-1.73 eV).

v). Carrier diffusion

From the spatial analysis presented in Figure 4.1-6, it is possible to investigate the carrier diffusion for different types of radiative recombinations by considering the enlargement of PL spots at half-maximum (HM).

In Figure 4.1-6, for each spectral domain of interest, we consider only pixels that have a PL intensity equal or higher than the half-maximum (HM) value of the maximum pixels at the center of the spot. After summation of these pixels, we deduce an “average” radius from this area and we compare it with the 0.6 µm spot radius of laser excitation as shown in Figure 4.1-7.

In all cases, these “average” spot radii are increasing with excitation as noticed in Figure 4.1-6. The radius of the wetting layer (WL) PL spot at HM is always smaller than the radius of QD PL while the radius from host material is always higher except for the lowest excitation.

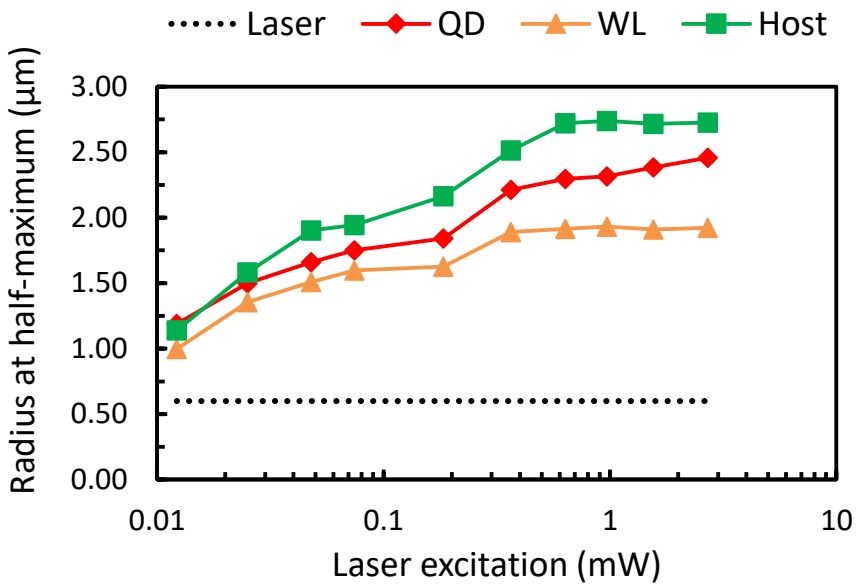

Figure 4.1-7: Radius for an averaged area at half-maximum of PL intensity for the three domains of interest and for the measured spot of laser excitation.

Our interpretations are the following, on one hand, for the host material PL, most of the pixels superior or equal to the half-maximum (HM) value are the result of a delocalized electron wave with a larger diffusion length. It could be seen as the manifestation of an electron that did not encounter a QD or was able to detrap successfully. On the contrary, in the case of the WL PL, electron wave is not delocalized as we saw with AFM measurements in chapter 3. The WL is not continuously homogeneous and is generally coupled laterally with QDs via quantum-well islands (QWIs), as we saw in chapter 3. An electron trapped at WL energy level will most probably recombine into a nearby QD. Because of this coupling, most of PL signal from the WL might result from the localized electron wave inside QDs that is leaking out into the WL. If we consider this approach, the filling of QDs might non-linearly influence the WL PL and it could exaplain the difference in radius at half-maximum.

At high excitation, we notice that all radii are converging towards threshold limits that would be close to 3 µm for the host, 2.5 µm for QDs and 2 µm for the WL. From the literature, we found a typical diffusion coefficient *D* of 100 cm²/s for electrons inside $Al_{0.2}GaAs$ material meaning that a typical diffusion length would be in the range of 3 to 10 µm depending on the recombination time (1 to 10 ns in AlGaAs materials). A QD layer can be seen as an effective medium with $Al_{0.2}GaAs$ material, InGaAs WL, QWIs and In(Ga)As QDs. A typical capture time for In(Ga)As QDs is estimated to be on the order of hundred of picoseconds in the literature [220]. If we assume a diffusion coefficient *D* of 100 cm²/s for electrons in the QD layers, as in $Al_{0.2}GaAs$ material, we calculate a diffusion length in the QD layers of about 1 µm. Experimentally, if we take the value from the QDs PL radius at half-maximum (HM) and substract by the laser spot we find a carrier diffusion length in the QDs of 600 nm at low excitation and almost 2 µm at high excitation. If we imagine that the diffusion length in QD material will increase with the filling of QDs, we find that our experimental diffusion length is in good agreement with the calculated diffusion length.

Now we want to discuss specifically about vertical carrier diffusion from one layer to another. Hyperspectral images cannot give us depth information. First, we want to know where the generation

of electrons takes place in our device. In Okd-3 type of growth, the total device thickness is 515 nm and there are 10 QDs layers over a 200 nm range in the vertical direction. For the non-transferred solar cells, with laser excitation at 532 nm in wavelength, it is safe to assume that almost all the generated electrons come from the absorption of photons by the $Al_{0.2}GaAs$ host material. In Figure 4.1-8, we calculate the percentage of absorbed photon flux for each layers in the stacked device. About half of the electrons are generated directly nearby the QDs layers but the other half comes from the absorption of the top layer (42%) and the bottom layer (11%).

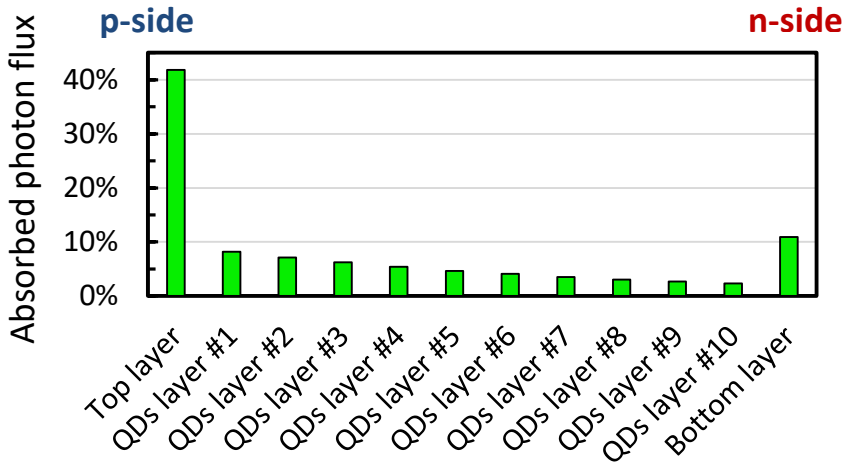

Figure 4.1-8: Percentage of absorbed photon flux at 532 nm in wavelength, for each layers of the 515 nm-thick QDSC device using RCWA code. It gives an idea of the electron generation position in depth.

If we assume that vertical and horizontal carrier diffusion are either equal or superior to 600 nm we will have a rather homogeneous distribution of electrons inside the QDs layers. However, if QDs layers limit the vertical carrier diffusion, the top and bottom QDs layers will have respectively 50% and 13% of the total absorbed photon flux.

Moreover, when considering vertical diffusion it is important to evaluate the impact of the built-in field. Experimentally, under 1 sun, V_{oc} is of 0.87 V while the calculated built-in field in our structure is of 1.57 V. Therefore, the remaining electric field at Voc under 1 sun will be around 18 kV/cm for the 380 nm-thick intrinsic region. For high excitation, if we consider that V_{oc} follows a logarithmic law with ideality of 1.7 (dark I-V fit), the electric field could fall to 5 kV/cm. In the case, of a dominant effect of the electric field, bottom QDs layers on n-side will be filled first as illustrated in Figure 3.1-6.

For simplicity, in the next parts of our study, we will consider the carriers to be homogeneously distributed over the QDs layers but we will discuss our results also considering the possibility of inhomogeneous distribution of carriers inside the device.

vi). Optical I-V curve

The absorbed photon current can be seen as equivalent to an injection of electrical current in that both change the carrier concentration, the electric field and the open-circuit voltage. PL intensity in logarithmic scale is proportional to the open-circuit voltage of the solar cell via the generalized Planck's law that will be introduced later. Thus, plotting PL intensity in function of laser power in logarithmic scale makes an "optical I-V curve" and we can deduce an ideality factor *n* linked to the

recombination dynamic as in the case of electrical I-V curve following Equation 4.1-1 [221], [222]. This law is independent of the temperature of carriers.

$$PL_{intensity} \propto {P_{exc}}^{n}$$

Equation 4.1-1: PL intensity is proportional to laser excitation to the n^{th}-power, *n* being an ideality factor for the investigated diode considering optical I-V curve formalism developed in [221] or [222].

As already discussed in chapter 3, the ideality factor *n* depends on the dominant recombination mechanism of a diode. If radiative recombination is the dominant mechanism, only photons takes the recombination energy. Therefore, the splitting of the quasi Fermi levels of hole and electron populations equals the applied bias voltage and *n* = 1 (linear dependence). In the case of defects related recombination, it depends on the energy position of the defect. Deep defects are impacting hole and electron populations, both population evenly take on the recombination energy, therefore *n* = 2 (quadratic dependence). Shallow defects located close to one of the band edges are almost inactive because they are far from the energy region of efficient recombination.

In the case of QDSCs, QDs are intermediate levels, meaning that they can be considered in-between deep and shallow defects. Diodes with such intermediate defect-states continuously change their I-V slope with increasing voltage bias. Indeed, in the space charge region (SCR), the energy region of efficient recombination widens and finally envelopes the intermediate defect energy position [4]. Finally, other mechanisms involving more than two particles may arise for high carrier density. For example, in the case of Auger recombination, three particles are involved and *n* = 2/3 [223], [224].

In Figure 4.1-9, we show the PL intensity integrated spatially over the “centered area zone” for the three different spectral domains in function of the laser excitation power. We consider two different excitation regimes following previous observations: low-excitation (P_{exc}< 0.2 mW) and high-excitation (P_{exc}> 0.2 mW). We find very good agreements with Equation 4.1-1. Ideality from QDs PL is constant near a 0.6 value close to Auger-type recombination showing a saturation behavior maybe due to high electron density. For low-excitation regime, WL and host PL idealities are around 1.1 near radiative-related ideality while for high-excitation, WL has an ideality of 1.5 and host PL has a 1.7 ideality closer to defect-related ideality. This change of behavior between low and high excitation might be explained by the fact that for low-excitation most of the population is directly related to the population inside QDs which is radiative or even Auger-limited. At high excitation, there is sufficient electron injection so that population in the WL and host show independent behavior.

We can relate this interpretation with the temperature-dependent study in the previous chapter where we discussed about the escape nature of carriers. In QDs literature, linear (*n* = 1), superlinear (*n* > 1) and sublinear (*n* < 1) behaviors are often associated to escape and capture dynamics of carriers. Linear behavior indicates that carriers are captured into QD states in the form of correlated electron-hole pairs or excitons. Superlinear dependence reflects the capture of independent electrons and holes into QD states. Sublinear dependence is attributed to an excitation regime where states filling of the QDs occurs [176].

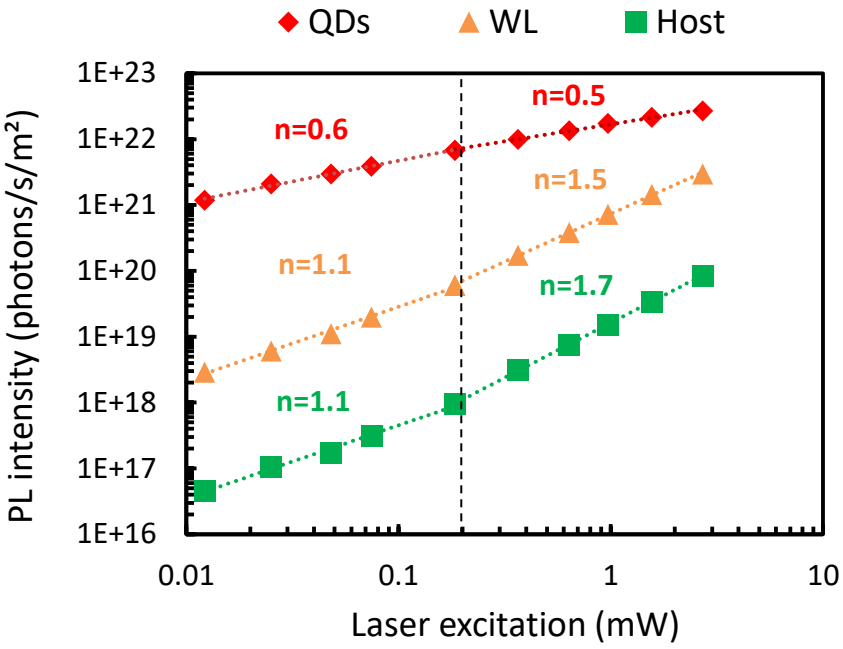

Figure 4.1-9: Optical I-V curve for the three spectral domains of interest following Equation 4.1-1. We consider two regimes for low and high excitation separated at 0.2 mW. Slopes corresponds to different idealities fitting.

vii). Radiative ratio

In Figure 4.1-6 we have seen that even for high sun concentration, the PL of $Al_{0.2}GaAs$ host material is low. As a comparison, we show in Figure 4.1-10, the integrated PL intensity hyperspectral image for a 220 nm-thick *p-i-n* GaAs solar cell transferred on a silver back mirror. The sample has 50 nm-thick AlGaAs barrier layers and was grown by MBE in the framework of Dr. Nicolas Vandamme's PhD thesis [225]. Whatever the thickness of the grown junction these samples revealed the presence of growth-related oval defects with density on the order of 1000 cm^{-2} [82]. PL measurement of the sample is performed with the same characterization setup with a homogeneous 150 µm-diameter excitation spot from a 532 nm laser using a diffuser and optical lens. For this cell, the absorptivity at 532 nm is ~90% and the averaged power density is of 0.024 W/cm² (x300 suns). In terms of absorbed photon flux density, it amounts to about 5.8e23 photons/s/m² for the solar cell.

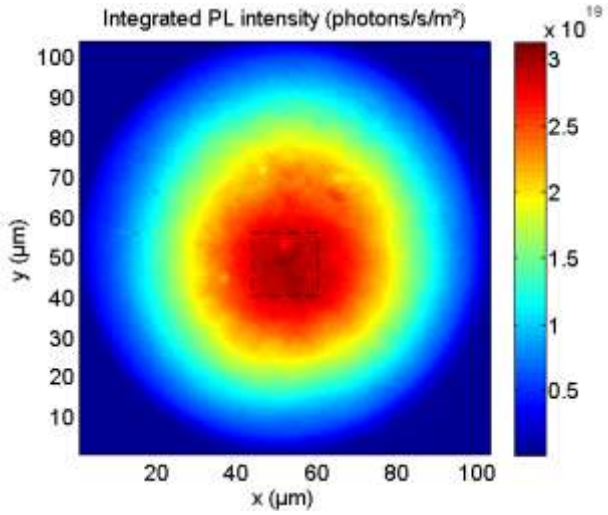

Figure 4.1-10: Hyperspectral image of PL spot for a GaAs solar cell over *xy*-square zone of 100 µm² with integrated PL intensity in colorbar and squared center-zone showed in dashed line. Taken from [219].

We also compare with measurements performed on a standard GaAs solar cell from the Fraunhofer Institute for Solar Energy Systems (ISE) using the same characterization setup [226]. The solar cell is a 4 µm-thick *n-i-p* junction with respectively 30 nm-thick *n*-AlGaInP and 50 nm-thick *p*-GaInP barrier layers. Absorptivity at 532 nm is ~90%.

Table 4.1-2 gives a comparison of theses PL hyperspectral measurements in term of radiative ratios and compare them with radiative ratios integrated over the three different spectral domains of interest in the case of our QDSC. We give the value in power density to compare with the other data. In order to normalize the laser power, in both case for excitation and emission we use the same assumptions as for the calculation of "electrical" power density. Four our QDSC, we have an absorptivity of 53% and the average radius of the PL emission considered in the carrier diffusion study is assumed to be Gaussian-like with 58% of power at FWHM.

Table 4.1-2: Comparison of hyperspectral measurement on GaAs SCs and In(Ga)As / $Al_{0.2}GaAs$ QDSC

Sample / PL domain	Absorbed photon flux (photons/s/m²)	Emitted photon flux (photons/s/m²)	Radiative ratio (Emitted/Absorbed)
4 µm nip SC / GaAs	1.5 e23	1.5 e21	1 e-2
220 nm *pin* SC / GaAs	5.8 e23	2.3 e19	4 e-5
515 nm *pin QDSC* / $Al_{0.2}GaAs$	2.3 e24	3.5 e17	2 e-7
515 nm *pin QDSC* / WL	2.3 e24	3.7 e18	2 e-6
515 nm *pin QDSC* / QDs	2.3 e24	1.6 e21	7 e-4

The calculated radiative ratio can be seen as an approximation of radiative efficiency for the investigated samples. GaAs solar cell from the Fraunhofer ISE (GaAs ISE) show the best radiative ratio which is in good agreement with results already reported in the literature with radiative efficiency for GaAs ISE of 1.26% [7]. The MBE grown GaAs solar cell show a degraded radiative ratio which is not surprising considering the defect issue we discussed. PL of QDs also show a bad radiative ratio on the same order as CdTe solar cells in reference [7]. This might be due to the high defects we suspect in our system as discussed in the previous chapter. PL of WL and host material are even worse on the same order as dye or organic PV cells [7] likely because of QDs that act as supplementary traps.

From our investigation in chapter 3, we know trapping/detrapping happens very fast. In the literature, characterization measurements at low temperature for In(Ga)As QDs system have estimated a CB to QD recombination time of 0.3 ns [227] for a PL radiative recombination time of 0.9 ns. At room temperature, PL radiative recombination times up to 10 ns have been found [228], [229]. Taking this value into consideration, at room temperature, an electron inside QDs may have time to detrap and trap more than 10 times before it recombines radiatively. If QD ground state (GS) is filled, the recombination time will be longer therefore non-radiative loss or radiative probability for other states like excited state (ES), WL or host will increase.

In Figure 4.1-11, we present the evolution of these radiative ratios with laser excitation for our investigated QDSC.

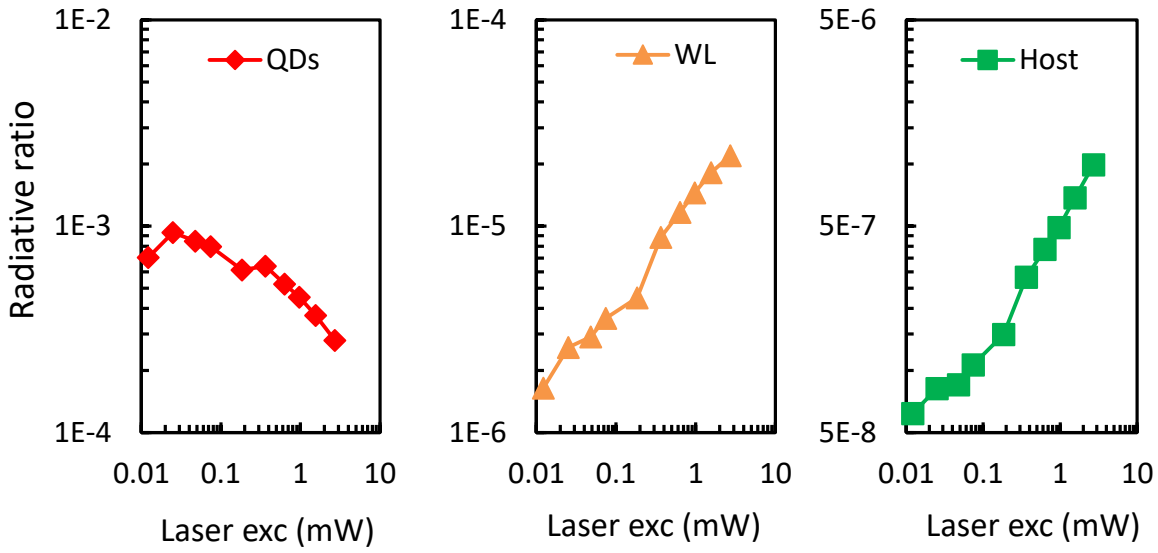

Figure 4.1-11: Radiative ratio integrated for the three spectral domains of interest with increase laser excitation.

For QD PL, at first there is an increase of the radiative ratio. We know from electrical current-voltage measurements under dark conditions that ideality factor is around *n*=1.8 while optical I-V curve gives a linear or sublinear ideality factor for low laser excitation. This might indicates that QDs defects are being passivated by light illumination. Then we see a rather monotoneous logarithmic decrease that might be because of electron filling of QDs and eventually saturation. On the contrary, the WL radiative ratio increases linearly up to about 0.2 mW and then we see an increase with logarithmic slow-down. From the investigation of carrier diffusion, we have seen how WL and QDs PL seem related. Here we see both logarithmic decrease and increase respectively for the radiative ratio of QDs and WL starting around 0.2 mW. Finally, for the host material we see a slow evolution and then a linear increase. This triggering effect also observed with hyperspectral image happens for about 0.2 mW at the same time as QD PL show saturation effect. We will discuss more about this triggering effect when investigating fitting of high-energy PL tail with carrier temperature and the activation energy barrier.

For a 0.2 mW laser excitation, we can consider that there will be an averaged power density of about 1.4e25 absorbed photons/s/m². We can translate this value in term of "electrical" power density considering all the absorbed photons are converted into electrons. Therefore we will have an average "electrical" power density of 1.4e4 electrons/ns/µm². In Okd-3 type of growth we have 10 layers of QDs with surface density of 700 QDs/µm², thus it amounts to an average value of 2 electrons/ns/QD. To evaluate the occupancy of QDs by electrons that will radiatively transition towards the valence band, we need to know the recombination time. In the literature, the usual recombination time at low temperature is around 1 ns but can go up to 10 ns at room temperature or even more. In our system, we consider a recombination time of 8 ns following investigations that will be presented later. Therefore, it means there is an average occupancy of 16 electrons/QD at half-maximum for a 0.2 mW laser excitation. As shown in Figure 4.1-4, the PL peak is around 1.33 eV. This energy level corresponds to ES2 level for medium size QDs in the previous chapter calculation shows that there can be a maximum occupation of 12 electrons/QD up to this energy level. Nervetheless, because of QDs distribution in size and "Stokes shift" effect (relaxation in "large" QDs), each QDs will have a different occupation depending on its size.

viii). Spatial investigation of calibrated PL images

Using calibrated PL images, we are able to get an insight on the spatial distribution of the electron gas responsible for the PL emission in our material.

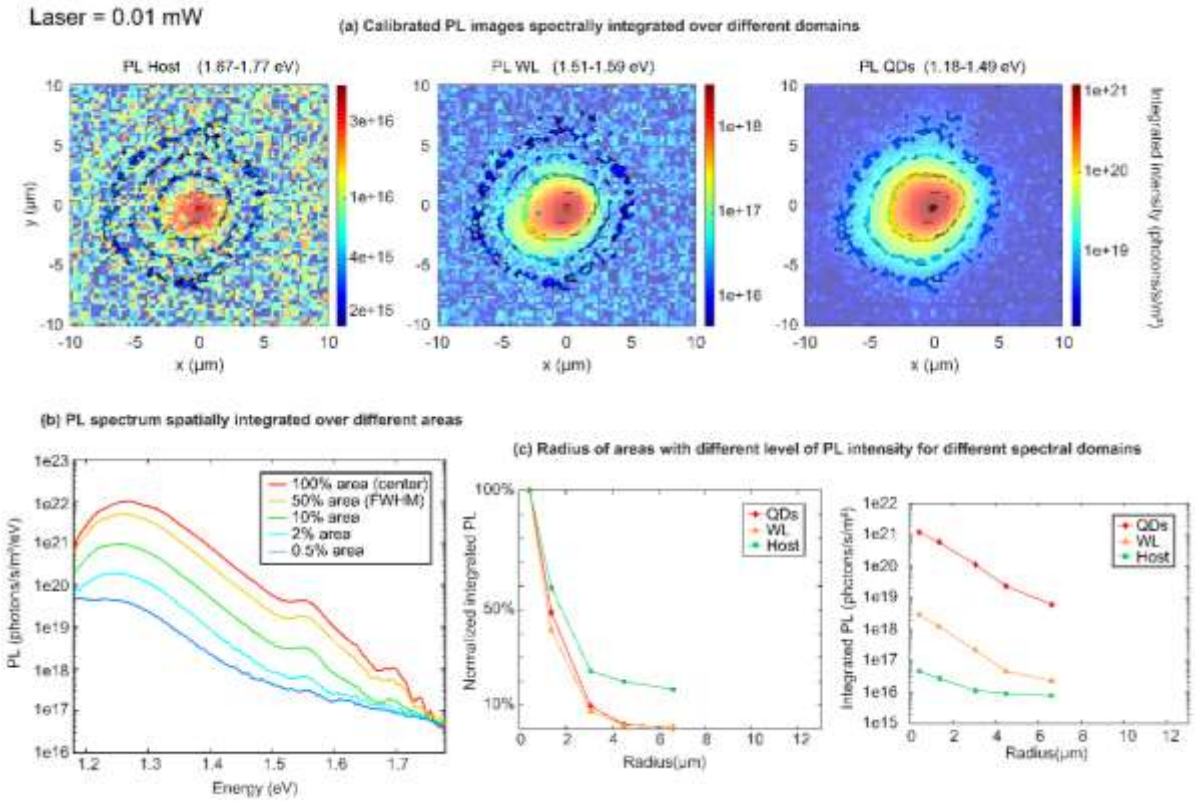

Figure 4.1-12: Spatial investigation of calibrated PL images for 0.01 mW laser excitation. (a) calibrated PL images are shown in log scale with different spectral domains integration to see the contribution from QDs, WL and host energy levels. Five differents contours are shown: center corresponding to the maximum of Gaussian laser excitation (100%), at FWHM (50%), in the middle (10%), on the border (2%) and outside the spot (0.5%). (b) PL spectrum spatially integrated inside the contours are shown for the different investigated areas. (c) Radius of areas versus their integrated level of PL intensity are shown normalized and in log scale for QDs, WL and host spectral domain regin.

As shown in Figure 4.1-12 and Figure 4.1-13, we define five different spatial zone of interests on the calibrated PL images for different averaged laser excitations: 0.01 mW, 0.37 mW and 2.71 mW. The five different zones are defined to cover at best different parts of the Gaussian PL spot using QDs PL as the reference spot. Center zone (100% area) is defined for pixels with intensity equal or superior to 95% of maximum of QDs PL spot. The second zone is the FWHM zone (50% area) for pixels at +/- 6% from the half value. Third zone (10% area) is a middle zone for pixels at +/- 3% of the 10% value. Fourth zone is an edged zone (2% area) for pixels at +/- 0.4% of the 2% value. Finally, fifth zone is considered as a kind of off-spot zone (0.5% area) for pixels at +/- 0.2% of the 0.5% value. Color maps with contours are shown in the (a) part, PL spectrum in (b) and in (c) we show PL intensity in function of the averaged radius for each zone.

This averaged radius represents a typical distance to the center of the laser excitation. We notice for each excitation an exponential evolution of QDs PL intensity with the averaged radius. Typical Gaussian intensity distribution of a laser as described in Equation 4.1-2 is used.

$$I_{PL}(r) = I_0 \exp(-\frac{2r^2}{\omega_0^2})$$

Equation 4.1-2: Typical Gaussian intensity distribution of a laser with ω_0 the Gaussian beam radius and I_0 the intensity at the center.

The spot of QDs PL fits quite well up to the edge zone (2% area). Overall, a simple exponential fitting reproduces the evolution of PL intensity with the averaged radius. Following Equation 4.1-3, we use the simple exponential fitting to calculate a local "electrical" power density (LEP) for the different zones assuming that QDs PL spot echoes the "electrical" power density distribution inside the device.

$$LEP(r) = \frac{P_\infty[\exp\left(-\frac{2(r-\frac{\delta r}{2})}{\omega_{exc}}\right) - \exp\left(-\frac{2(r+\frac{\delta r}{2})}{\omega_{exc}}\right)]}{\pi(r+\frac{\delta r}{2})^2 - \pi(r-\frac{\delta r}{2})^2}$$

Equation 4.1-3: Local electrical power density (LEP) calculated for the countour areas.

P_∞ is the laser excitation, ω_{exc} the fitting parameter for each excitations and δr the thickness of the defined zone expressed in radius using Equation 4.1-2. Table 4.1-3 summarizes the considered fitting.

Table 4.1-3: Fitting parameters for Gaussian and simple exponential fitting of PL intensity.

Laser excitations	ω_0 (µm)	ω_{exc} (µm)
0.01 mW	2.7	2.3
0.37 mW	5.1	3.6
2.71 mW	5.6	4.1

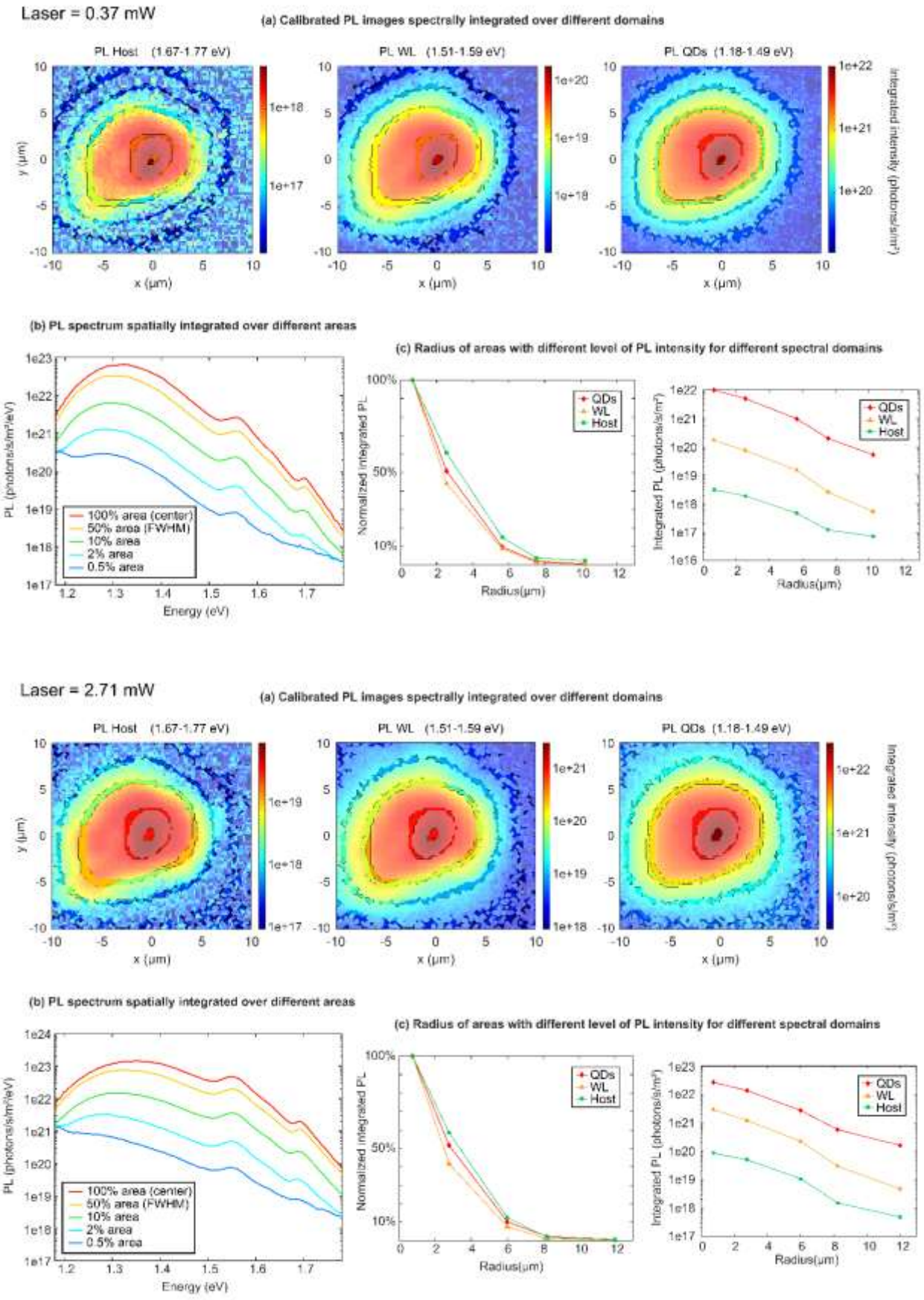

Figure 4.1-13: Same as Figure 4.1-12, for 0.37 mW and 2.71 mW laser excitations

LEP values are converted in electrons/QD using the same method explain before considering the 10 layers of QDs are homogeneously filled, each of them has a surface density of 700 QDs/µm² and a recombination time of 8 ns. This value is given to estimate the potential concentration of electrons per QD relatively to the different zone and for different excitation. LEP in electrons/QD are shown in insets of Figure 4.1-14.

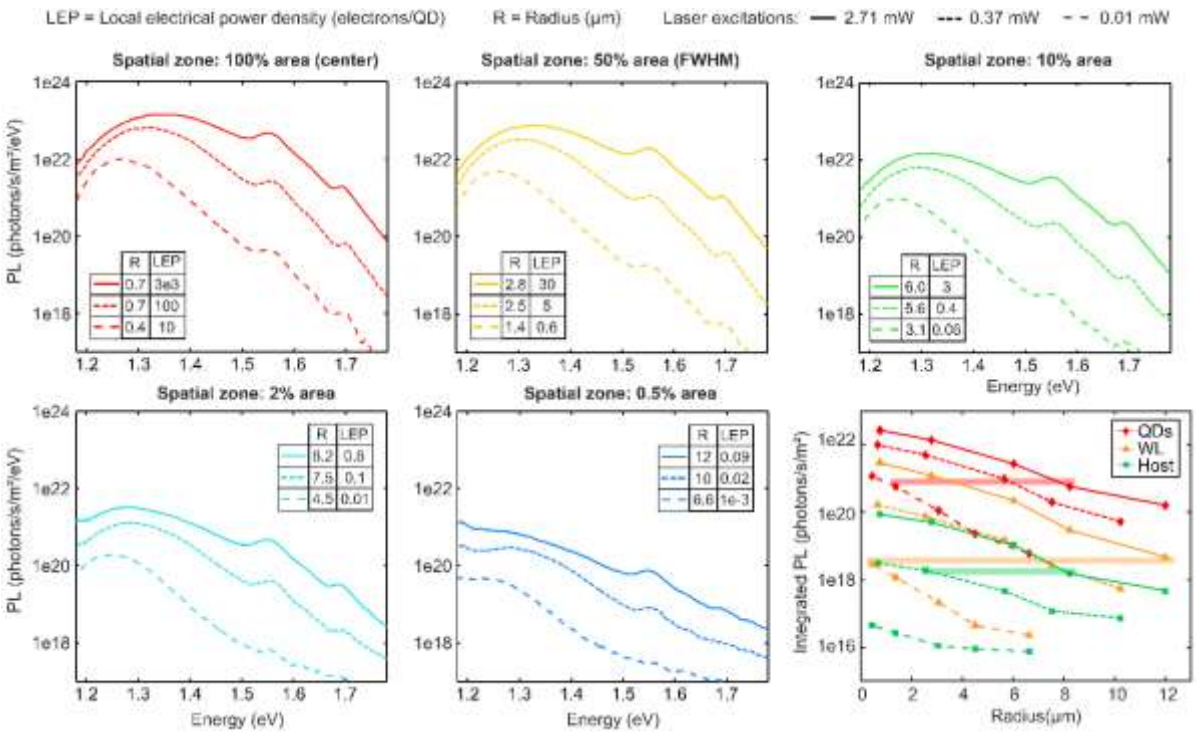

Figure 4.1-14: Comparison of PL spectrum of same zones for different laser excitation. Integrated PL plot show that some zones have the same PL intensity integrated for QDs, WL or host domains.

In Figure 4.1-14, we compare PL spectrum from same areas but with different laser excitation. High-energy tails from WL and host PL peak become less and less visible when shifting to the outside of the PL spot. It seems that the high-energy tail from the QDs PL dominates WL and host spectral domains for spatial zones far from the laser spot. This trend is common for all excitations, and it can be related to the evolution of integrated PL intensity for the WL and host material shown in the bottom right corner of the figure. At the lowest excitation (0.01 mW, dashed lines), a constant threshold for host PL intensity (dashed green line) is obtained for a radius around 4 µm and around 5 µm in the case of the WL (dashed orange line). At medium excitation (0.37 mW, dotted lines), the threshold radius is around 9 µm for host (dotted green line) and 10 µm for WL (dotted orange line). Finally at high excitation (2.71 mW, solid lines), it is around 12 µm for both. These increases of radius follow the increase of radius due to carrier diffusion showing that PL intensity levels of WL and host material also spatially depend on the filling of QDs as it was noticed for the radiative ratio study.

Integrated PL plots, in Figure 4.1-14, shows that some zones have the same PL intensity integrated for QDs (red bar, ~8e20 photons/s/m²), WL (orange bar, ~2e18 photons/s/m²) or host domains (green bar, ~1e18 photons/s/m²). In Figure 4.1-15, we compare directly the PL spectrums that have almost equal PL flux respectively for QDs, WL and host spectral domains.

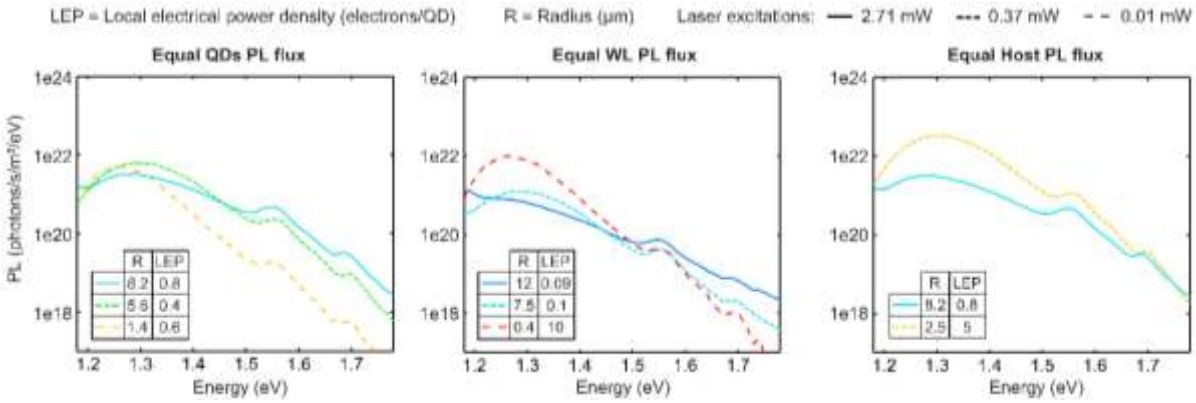

Figure 4.1-15: Comparison of PL spectrum of equal intensity from different zones.

In the case of equal QDs PL flux, the local electrical power density (LEP) is almost the same for all spatial zones but we notice that the PL intensity flux for WL and host domains increase following the increase of laser excitation. In the case of equal WL PL flux, we notice a comparable phenomenon. To achieve the same level of WL PL flux, the lowest laser excitation regime (0.01 mW) needs higher LEP and higher PL from QDs energy states. Finally, the equal host PL flux also follow the same rule. With the highest laser excitation regime (2.71 mW), a LEP of 0.8 electrons/QD is enough to have the same host PL flux as a LEP of 5 electrons/QD in the case of lower excitation regime (0.34 mW).

Finally, to further investigate the spatial effect, in Figure 4.1-16, we present optical IV curves for the five different PL spot areas: 100% area (center), 50% area (FWHM), 10% area (middle), 2% area (edge) and 0.5% area (off-spot). We consider low and high excitation regimes as in Figure 4.1-9 for laser power lower or higher than 0.2 mW. The slopes show the fitting using Equation 4.1-1 from which we can deduce different values of optical IV ideality factor.

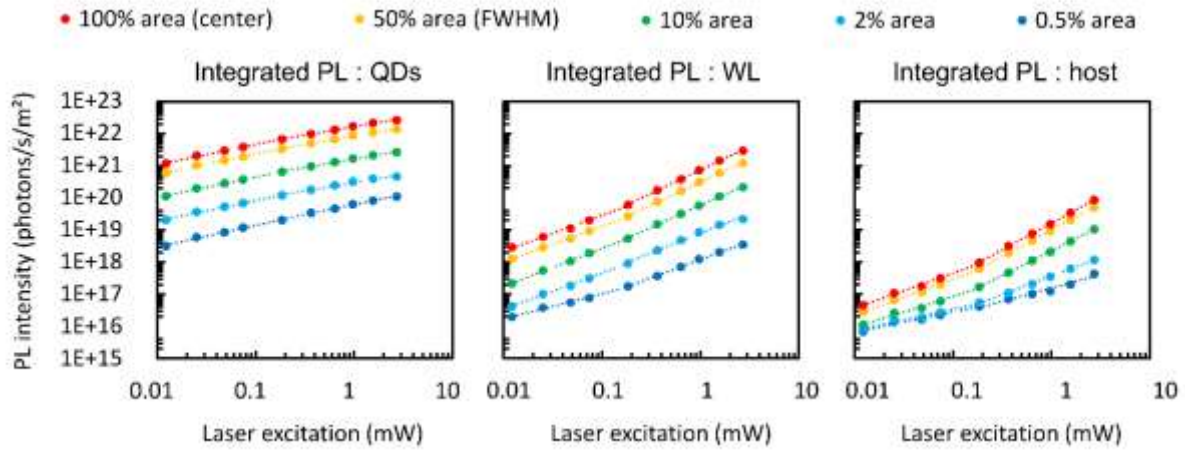

Figure 4.1-16: Optical I-V curve for the three spectral domains of interest following Equation 4.1-1 as in Figure 4.1-9. We consider five different spatial zones: 100% area (center), 50% area (FWHM), 10% area (middle), 2% area (edge) and 0.5% area (off-spot). We consider two regimes for low and high excitation separated at 0.2 mW. Slopes corresponds to different idealities fitting.

In Figure 4.1-17, we summarize the evolution of optical ideality factor over different spatial zone for low and high excitation regimes. For low excitation regime, we see that off-spot area PL for WL and

host energy domains have the same ideality as PL from QDs energy domain. It is a strong indication that the PL entirely comes from QDs and not the WL or host material. For FWHM and center area we see the same behavior as explained before with an ideality close to radiative-limited recombination (n~1) for WL and host. At high excitation, it is interesting to notice the evolution of ideality factor for host energy domains that is crossing with WL starting at 10% area. This seems to indicate the existence of an independent carrier population in the host material.

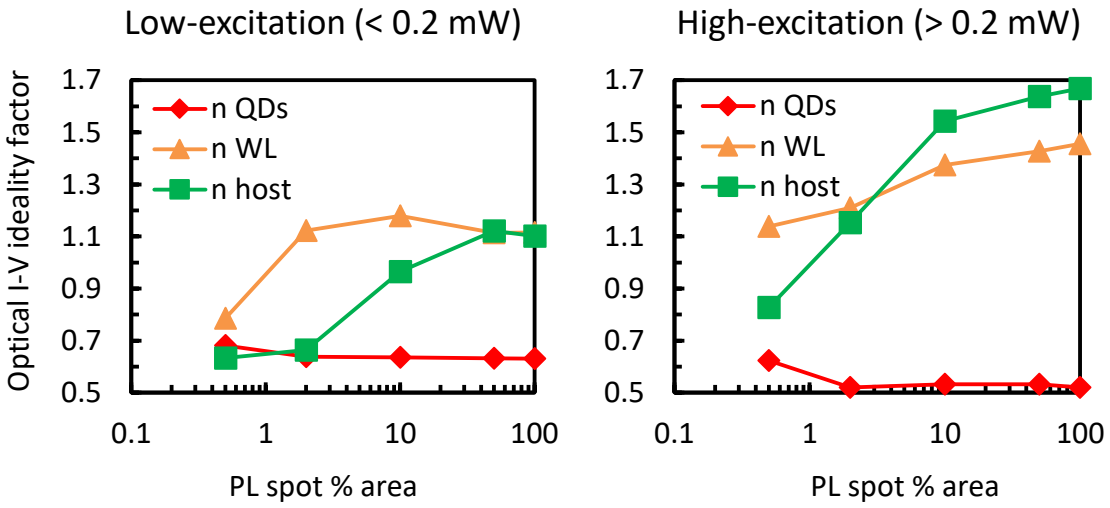

Figure 4.1-17: Optical I-V ideality factors are plotted with respect with the PL spot area for low excitation and high excitation following fitting of curves presented in Figure 4.1-16.

The spatial investigation in this part show that laser excitation not only has a role on the bandfilling but also on the nature of the whole electron gas in our device. The nature of this electron gas is usually defined in term of temperature and we will see how we can extract one in this chapter. For a fixed laser excitation, there seems to be a decreasing of the overall PL intensity when moving outside the center of the PL spot. However the high-energy PL tail for QDs seems to be almost the same wherever we are on the PL spot and depends on the laser excitation, as shown in Figure 4.1-12 and Figure 4.1-13. In the second part of this chapter, we will discuss more about this phenomenon when comparing focused and defocused laser spot. It seems that it could be due to the different behavior between holes and electrons.

4.1.2.2 Energy bandfilling dynamic

After investigating about the radiative dynamic balance of the QDSC system, we want to properly look at the bandfilling in term of energy levels. First, we will discuss about a simple model to reproduce the PL profile with increasing filling of QDs energy states. Then we will compare with our measurements and conclude on the bandfilling dynamic.

i). Simple PL model: description

Considering the previous chapter investigation on the In(Ga)As / $Al_{0.2}GaAs$ QD system, we want to develop a simple model to reproduce the evolution of PL with increasing filling of energy states. There are three important steps in this model. First, we need to define the energy levels for holes in the valence band (VB) and electrons in the conduction band (CB). Second, we need to calculate all possible transitions from different continuous wave (CW) PL regimes of excitation. Third, we need to estimate the emitted photon flux from filled states.

ii). Simple PL model: energy states from QDs distribution

To reproduce the QD system, first we define a number of energy states available in the conduction band and valence band. From the PL and AFM QDs height distribution profile found in the previous chapter for an "edge zone" sample, we can consider the distribution of QDs described in Figure 4.1-18. Total number of QDs is around 700 for an area of 1 µm² derived from AFM measurement with histogram of Figure 3.2-18. The Gaussian-fitting curve with diamonds represents different types of QDs with different ground states (GS) energy transitions that are following PL at low temperature as in Figure 3.3-1. The QDs population is sampled by discretizing their PL peak every 25 meV, which is the considered temperature broadening so the discretization seems to be enough to describe PL dynamic.

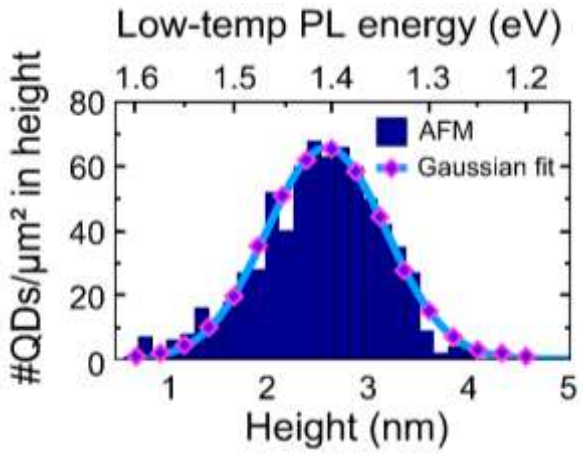

Figure 4.1-18: "Edge zone" QDs distribution from AFM (histogram in blue) superpositionned with low temperature PL.

Using k·p calculation we find that, different types of energy states for holes or electrons have linear evolution in energy with their size.

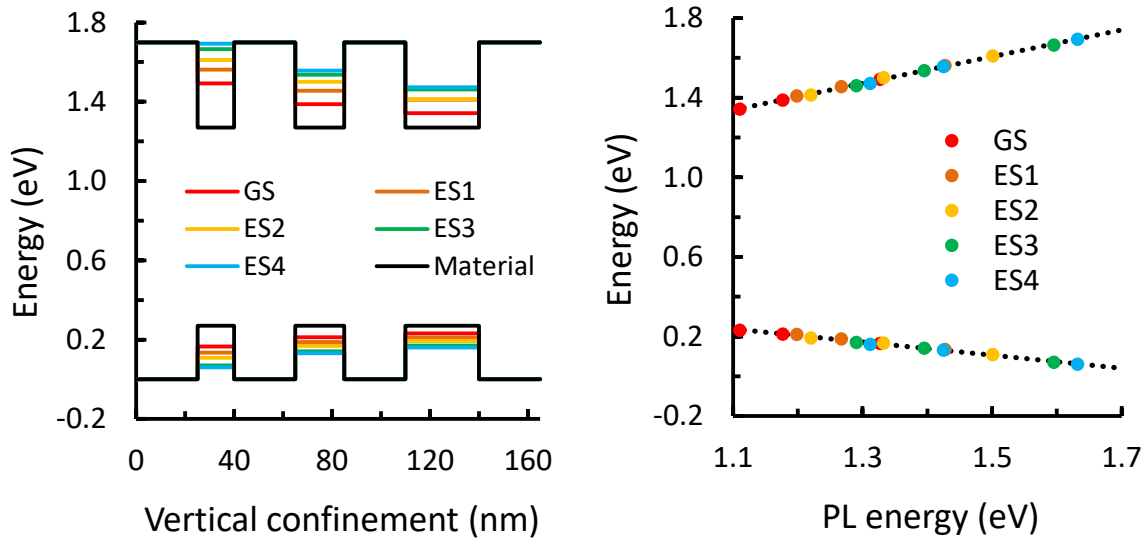

Figure 4.1-19: Three types of QDs with different confinement and energy states (left figure), electron and hole energy states are plotted versus their respectives main PL energy transition revealing linear behavior (right figure).

In Figure 4.1-19, we show an example for the three types of QDs described in chapter 3 (QD1, QD2, and QD3) for the GS and the four first excited states (ES) energy levels. Overall, they amount to about 25 electrons or holes energy states and we see their shift in transition energy follow the same linear law. Therefore, starting from k·p calculation of a medium size QD as described in the previous chapter, it is possible to estimate the energy states distribution for the QD Gaussian distribution described in Figure 4.1-18 following this linear law.

In other words, in Figure 4.1-18, each energy transition corresponds to a QD with a particular size and energy states distribution. The energy state distribution is weighted considering the number of QDs per µm². For bandfilling of our system, we need to multiply this value by ten because we have ten layers of QDs for a 1-µm² illumination coming onto the surface of the device and we consider a homogenous repartition of carriers over the ten layers.

Electron-hole pairs generation and bandfilling are dependent on the excitation regime as we explained earlier. The filling of QDs will start for low energy states meaning for "large QDs" with highest wavelength PL transition. For example in the QDs distribution profile of Figure 4.1-18, there is about one "large QDs" per µm² at 1.2 eV low-temperature PL energy. For 10 layers of QDs it means that the first 20 energy states of our system are related to this "large QD". If we want all these "large QDs" to be filled with one electron it means that we need at least 10 electrons/µm² at all time. Considering a recombination time of 8 ns, it means that an absorbed flux of 1.3 photons/ns/µm² is a minimum value to fill with one electron the ground state (GS) from these "large QDs". In our system for 53% absorptivity, this absorbed flux is equivalent to x1.3 suns concentration. In fact, we will see later that the filling does not takes place for one large QD at a time. It seems that energy states that are close to each other are all being filled at the same time. This might be due to the effect of QDs distribution and temperature broadening.

iii). Simple PL model: transition possibilities

For different levels of excitation, we consider that electron-hole pairs generation will induce different possible combinations of transitions for electrons in the CB and holes in the VB. The transitions probabilities are related to the coupling of transition dipole moments (TDM) that can be calculated using k·p model as we explained in chapter 3.

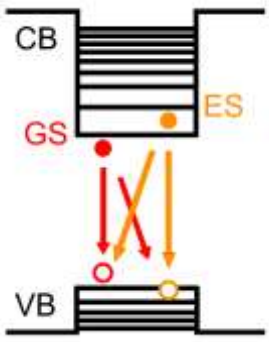

Figure 4.1-20: Possible transition combinations for 2 electron-hole generated pairs.

It is referred as the oscillator strength (F_{osc}) of a transition, and it is inversely proportional to the radiative recombination time of a transition (τ_{rad}) following Equation 4.1-4 [230]. Therefore, for each level of laser excitation, all possible transitions are being calculated with their respective oscillator strengths as depicted in Figure 4.1-20.

$$F_{osc} = \frac{\left|\left\langle \boldsymbol{\varphi_a^{el}} \right| \boldsymbol{\varphi_b^{hl}} \right\rangle\right|^2 E_K}{2\,E_{PL}} \quad \text{and} \quad \frac{1}{\tau_{rad}} = \frac{2\,n_r \pi q^2}{3\lambda_{PL}\varepsilon_0 c m_0} F_{osc}$$

Equation 4.1-4: Relation between TDM coupling, Fosc and τ_{rad}.

iii). Simple PL model: emitted photon flux

To estimate the PL flux, we decide to consider the following logic. For radiative recombinations to happen, electrons need to occupy a certain level of energy for a certain time. Filling is done from low energy states to high energy states. Thus, each electron state is considered one by one in increasing order. When considering the emission of an electron from the considered electron state, we evaluate all channels of recombination possible with hole states but also from +/- 25 meV neighbouring electron states to take into account the temperature broadening as described in Figure 4.1-21.

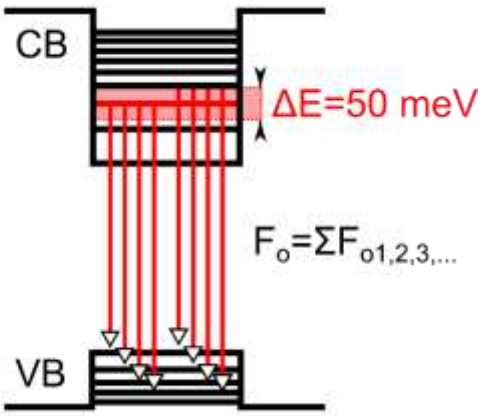

Figure 4.1-21: PL emission flux depending on oscillator strength. From electron energy state considered (in red) and neighboring state in a +/- 25 meV zone.

In Figure 4.1-22, we show PL characterization measurements performed at low laser excitation between 1e-2 and 100 suns at room temperature with the Raman/PL HORIBA Jobin-Yvon system that was used for PL mapping. The sample used is a “center zone” sample on which we did PL measurement at low temperature (black dashed line). At room temperature for low excitation up to hundreds of sun, we see that the shift of PL peak is relatively small (red triangles). The PL emission corresponds to an emission from “large QDs” (pink and red solid lines). FWHM is about 90 meV. This value of FWHM corresponds to a Voigt distribution of Gaussian and Lorentzian both with FWHM of 50 meV. Therefore, it corresponds well to a typical room temperature Lorentzian broadening convoluted with a homogeneous broadening due to QD Gaussian distribution of “large QDs”. That is why we consider that the PL emission from an occupied state is influenced by +/- 25 meV neighbouring electron states.

Oscillator strengths for each transition are used to evaluate the probability of emission for each channel compared to all the channel of emission. Finally, we take into consideration the emission flux by attributing a time recombination for each electron state by summing the oscillator strengths for all channels of emission following the description of Figure 4.1-21. To reproduce the PL spectrum we sum all transitions represented by Gaussian with FWHM of 90 meV illustrating homogeneous and inhomogeneours broadening and following Figure 4.1-22 characterizations.

Recombination time is calculated using Equation 4.1-4, and we find that ground states (GS) have a 4 ns recombination time. In the literature of QDSCs, this value was discussed recently to be even possibly on the order of milliseconds [231]. In time-resolved PL (TRPL) for In(Ga)As self-assembled QDs, it is usually found that the long lifetime related to the GS radiative transition of QDs is around 1 ns at low temperature [220]. Nevertheless it was shown that this lifetime changes at room temperature with sometimes a square-root dependence with temperature as in the case of quantum wire (QWR) or closely stacked QDs [73]. Our TRPL experiment revealed lifetime of 8 ns and recent studies show the same trend [228], [229]. The increase in the radiative lifetime of GS QDs with increasing temperature has been equally attributed to carrier transfer between QDs, to carrier escape and recapture and to reduction of the nonradiative decay.

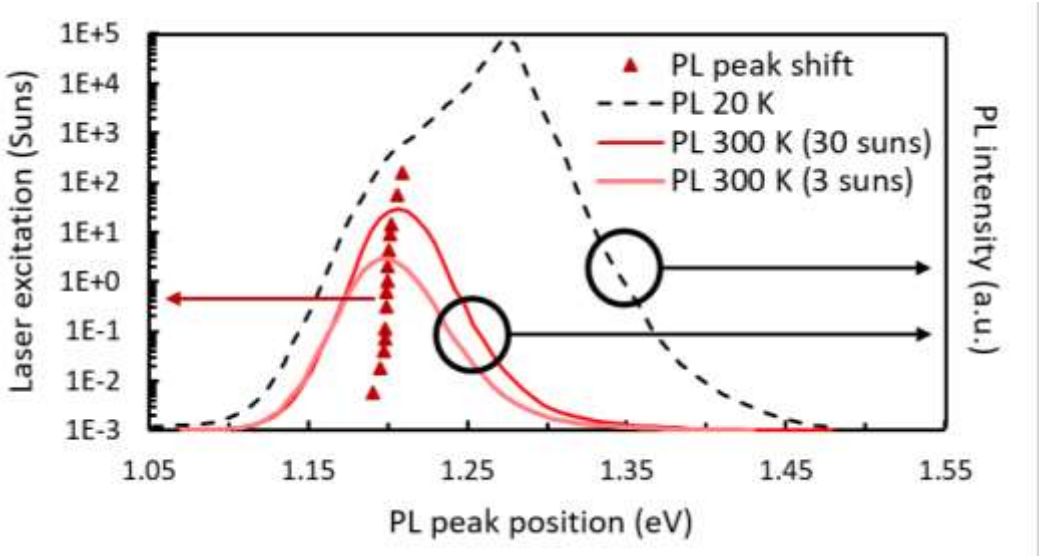

Figure 4.1-22: PL peak shift of PL measured at low excitation with laser power on left axis. PL at room temperature (300K) are shown for different excitation compared to the multi-modal PL at low temperature that is Varshni shifted (dashed line) in order to see that only "large QDs" contribute to PL for very low-excitation at room temperature.

In TRPL, the oscillator strength from a higher energy state is dominated by the intraband non-radiative transition to lower energy states [232]. In the case of continuum-wave (CW) PL we make the assumption that the intraband transition from higher to lower energy states is limited due to the constant absorbed photon flux.

Interaction with the wetting layer (WL) and host material is not taken into account, as we do not really know how energy states will interact with them. Moreover, we do not consider other effects like interaction of carriers between them, as we want to keep this model relatively simple. Nevertheless, there should be some carrier-carrier effects arising from bandfilling like Auger or impact ionization. These effects are usually considered when discussing about low-dimensionnal quantum structures solar cells for hot carrier solar cells (HCSCs) or multi-exciton generation (MEG) solar cells [233]. Following these considerations, we can predict two things that are not taken into account by our model but might happen for the filling of high-energy states:

- Coupling with WL and host energy states should increase with filling of higher energy states, which will decrease the radiative emission of photons compared to our model.

- High density of carriers means higher non-radiative interactions and so it will also decrease emission of photons compared to our model.

To compare the simple model calculation with experimental PL we considered radiative recombination ratio inside the QDs from our investigation presented in Figure 4.1-11.

iv). Comparison with calibrated PL experimental measurements

In order to compare our model's results with calibrated PL experimental measurements, we are especially interested in considering how PL peak is blueshifting and how the global intensity level increases with bandfilling. We will consider the distribution presented in Figure 4.1-18 for "edge zone" samples with specific QD distribution on Okd-3 wafer. Different levels of filling of energy states are taken into account by reproducing same position of PL peak as in the experimental data.

Table 4.1-4: Calculated values of emitted PL photon flux for "edge zone" QDs distribution. Calculations are shown for different PL peak positions representing different fillings of QDs. Filling percentages are shown for GS, ES1 and ES2.

Position #	PL peak (eV)	Emitted photon flux (photons/s/m²)	GS (%)	ES1 (%)	ES2 (%)
0	1.20	1.3 e22	6	0	0
1	1.26	9.4 e23	29	0	0
2	1.30	9.0 e24	35	12	6
3	1.32	1.1 e25	41	18	12
4	1.35	5.6 e25	47	24	18

Table 4.1-4 summarizes several calculated values of emitted PL photon flux and filling percentages are shown for different energy levels (GS, ES1 and ES2) for the QDs distribution. For example in the case of a PL peak maximum at 1.30 eV, 35% of QDs have their GS filled, 12% have ES1 filled and 6% have ES2 filled.

In Figure 4.1-23, we show a comparison between the previous calculation and experimental calibrated PL measurements for different laser excitation. To recalibrate in term of intensity, the photon flux is multiplied by the decreasing radiative ratio as presented in Figure 4.1-11.

We notice that we are able to reproduce PL emission following the same shift in PL peak and also in intensity for different level of filling. Peak positions #2 and #3 would correspond to a 0.18 mW and 0.37 mW laser excitation respectively at the starting point of the high-excitation regime (≥ 0.2 mW) defined previously. From this point, we notice that more than 1/3 of QD population GS are filled with 2 electrons and a portion of excited states (ES1 and ES2) are also starting to be filled. In our model, we assume that each energy level below the PL peak has to be filled with 2 electrons. In reality this constraint might be relaxed especially when a QD starts to see his excited states being filled.

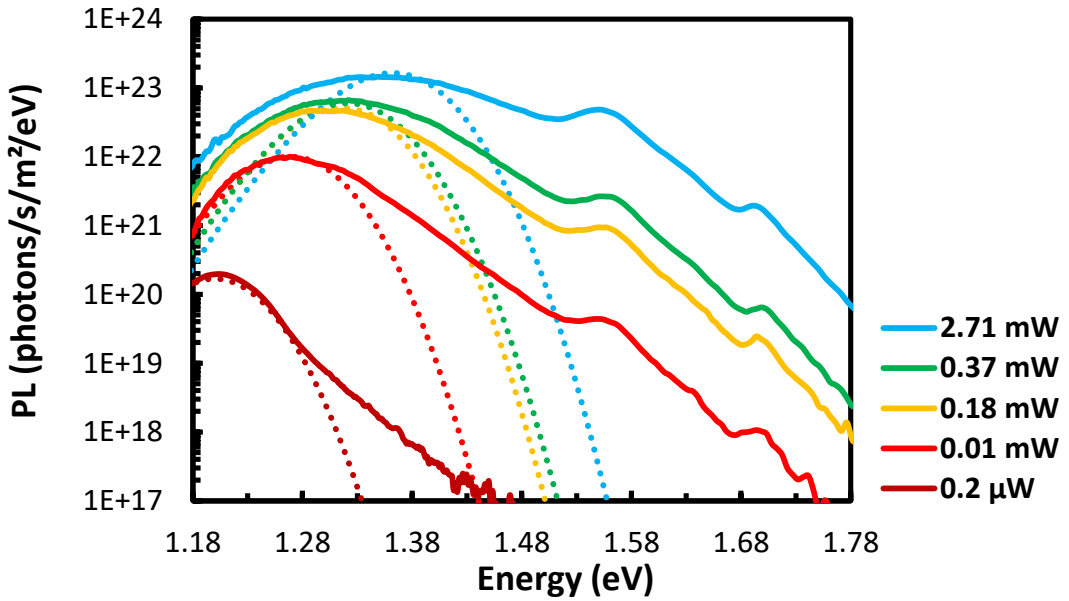

Figure 4.1-23: Calculated PL with radiative ratio following Figure 4.1-11 (dotted lines) compared with experimental values from calibrated PL with integrated hyperspectral images in the center spot area. Laser excitation are varied from 0.01 mW to 2.71 mW. The low excitation spectrum at 0.2 µW of excitation comes from HORIBA PL system and is recalibrated in intensity by assuming a linear increase of PL intensity for low excitation to show the evolution of the shape and blueshift of PL peaks from 1.2 eV to 1.35 eV.

For example, in our model at peak position #2, 6% of the QD population (the larger QD) would have 12 electrons per QD (GS, ES1 and ES2 filled). If we consider roughly 12 electrons for the volume of a pyramidal "large" QD (30x30 nm² base and 4.5 nm height), we find an electron concentration of about 1e19 cm^{-3}, which makes it a metal-like or degenerately doped semiconductor. In chapter 3, AFM investigation shows that "small" and "large" QDs are mixed and often next to each other in some sort of aggregates. It is likely that such a high local carrier concentration in a "large" QD would escape and leak into an adjacent empty QD even if it has a higher GS energy. This effect could be compared to a kind of "spatial smearing effect" that has been reported in QDs and will be discussed later [176].

In Figure 4.1-23, we see that two parts of the spectrum are not well fitted. For the lower energy part, we notice that our modeled photon flux is lower than the experimental values. This might be due to the fact that, in our model, we consider low energy states to fill first, meaning that a spin-degenerated energy level is fully filled. In the real case, Coulomb repulsion might be an obstacle for complete filling of states that have the same energies especially if they have low level of occupancy. Typically, ground states (GS) can only host two electrons of opposite spins. To take into account this effect, carrier-carrier interaction should be considered.

We also see that we are not able to fit correctly the high-energy tail for calibrated PL spectrum. As we discussed previously, this high-energy tail is a signature of the electron gas inside our QDSC. In this model, we do not consider the effect of a gas therefore we cannot fit properly this part of PL spectrum. We will explain in the next part that we can consider a Maxwel-Boltzmann distribution to fit the PL for carriers in this high-energy region.

In conclusion, this bandfilling study shows that PL from QDs states has a complex dynamics. It cannot be simply explained by the luminescence of excitonic states transitioning at different energies. For the low-energy part, we can suppose that after one electron per QD is achieved, a saturation dynamic takes place with Coulomb repulsion, more carrier-carrier interaction like inter, intra Auger recombination or carrier-phonon interaction. For the high-energy part, the contribution of a photon gas needs to be considered. This photon gas might be impacted by the low-energy saturation that might induce a different energy distribution for high-energy states. Overall we notice that for the high-excitation regime (≥ 0.2 mW), at least 1/3 of the QD population is filled and maybe more because of a "spatial smearing effect". Therefore we can say that we are approaching a "half-filled" metal-like intermediate band (IB) condition suitable for IBSCs.

4.1.2.3 Activation energy

In the previous part, we considered bandfilling effect with a simple model. The spatial and spectral investigation of calibrated PL measurements show that the high-energy PL tail is somehow independent from the bandfilling effect and is changing with laser excitation regime. We will try to explain the meaning and relation of this high-energy PL tail.

i). Maxwell-Boltzmann distribution

When trying to estimate a distribution of classical particles, Maxwell-Boltzmann (MB) distribution is often encountered as an approximation of two well-known more realistic distributions: Fermi-Dirac (FD) and Bose-Einstein (BE) distributions as represented in Figure 4.1-24.

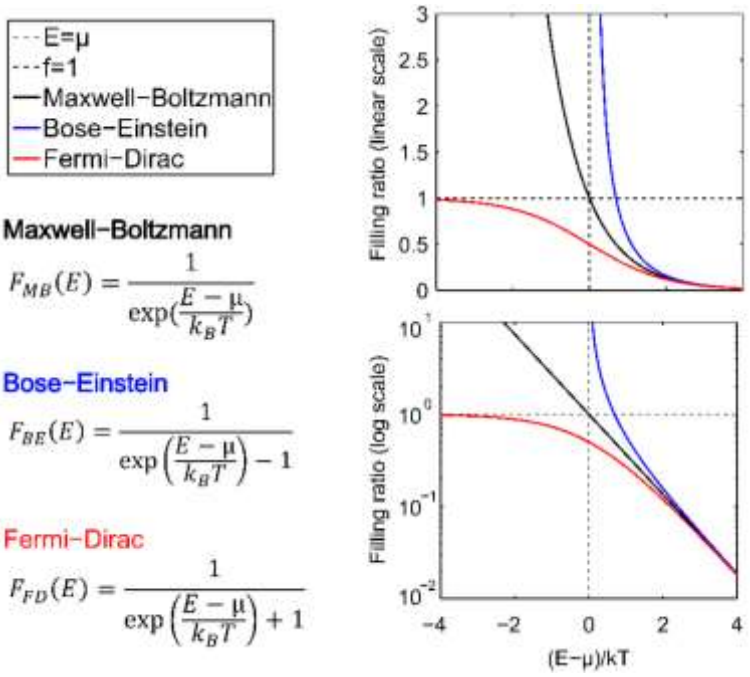

Figure 4.1-24: Comparison of Maxwell-Boltzmann, Bose-Einstein and Fermi-Dirac distributions

FD distribution is used for fermions governed by the Fermi exclusion principle: indistinguishable particles cannot be together in the same state. BE distribution is used for bosons that follow the opposite trend, it is often said that “the more the merrier” is their motto. Fermions are sometimes said to be the constituents of matter, while bosons are said to be the constituents of radiation. In our case study, carriers like electrons or holes are fermions while photons or even phonons and excitons are considered as bosons. From a mathematical point of view these three distributions expressions are close to each other but filling of states behavior change dramatically when considering low energy levels. Starting for $E - \mu \geq 2k_B T$, we see that FD and BE distributions are converging towards a MB distribution.

In our case, when we consider the fitting of PL, we can relate to the Generalized Planck’s law following Equation 4.1-6. This expression will be detailed later. We can already see that PL flux is proportional to the absorptivity $A(E)$, the square of the energy and a BE distribution regarding photons with a chemical potential written $\Delta\mu$ that will be explained later. In the absorptivity is also hidden the distribution of carriers. We will see in the next section how we consider this distribution.

$$\phi_{PL}(E) \propto A(E) \times E^2 \times \frac{1}{\exp\left(\frac{E-\Delta\mu}{k_B T}\right) - 1}$$

Equation 4.1-5: PL flux is proportional to absorptivity, square of the energy and a BE distribution representing the photons with a certain chemical potential written $\Delta\mu$ following the Generalized Planck’s law.

Anyhow, in the case of high-energy tail for $E - \Delta\mu \geq 2k_B T$, we can assume a MB distribution for carriers in the high-energy tail of PL that are far from the chemical potential of the photon gas that should be below PL peaks. Following Equation 4.1-6, the high-energy tail can be fitted by an exponential law with photon energy E and T the temperature of the photon gas that should also correspond to the temperature of carriers and therefore probing a certain occupancy of high-energy states.

$$\frac{\phi_{PL}(E)}{A(E)E^2} \propto \exp(-\frac{E}{k_B T_C})$$

Equation 4.1-6: Equation showing dependence of high-energy PL tail with carriers' temperature T_C.

ii). Absorptivity calculation

To use this expression, we see that it is important to have an idea of the absorptivity inside our device and its dependence with energy. It will be especially important when we consider the use of light management structure for example with Fabry-Pérot (FP) cavity. As in the previous chapter, we will use Rouard's method to give a simple analytical formula of the absorptivity in a simple cavity: Air/Absorber/Back-layer. The absorber (*Abs*) can be seen as an effective medium comprising all the layers in the stacked device. The back-layer (*BL*) can be the as-grown substrate or a mirror as in the case of transferred samples. As in chapter 3, using Fresnel coefficients, we can calculate the reflection R and transmission T and deduce the absorptivity $A(E)$ following Equation 4.1-7 for incident light perpendiculat to the cavity ($\theta = 0$).

$$R = \left| \frac{r_{Air\to Abs} + r_{Abs\to BL}\, p_{Abs}}{1 + r_{Air\to Abs}\, r_{Abs\to BL}\, p_{Abs}} \right|^2$$

$$T = \left| \frac{t_{Air\to Abs}\, t_{Abs\to BL}\, p_{Abs}}{1 + r_{Air\to Abs}\, r_{Abs\to BL}\, p_{Abs}} \right|^2 \Re(\frac{n_{BL}}{n_{Air}})$$

$$A(E) = 1 - \big(R(E) + T(E)\big)$$

Equation 4.1-7: Analytical formula expressing the absorptivity of a simple cavity.

The round trip wave propagation in the absorber is expressed with $p_{Abs} = \exp(i2\tilde{n}_{Abs} t_{Abs} k_0)$ where $\tilde{n}_{Abs} = n_{Abs} + i\kappa_{Abs}$ and t_{Abs} are respectively the refractive index and thickness of the absorber layer.

In our case, for the fitting of the high-energy tail PL, the spectral domain of interest is around 1.35 eV and 1.5 eV. In this region, only QDs layers are absorbing. Therefore, we need to consider absorption coefficient as studied in chapter 3. We will use two types of absorption profile.

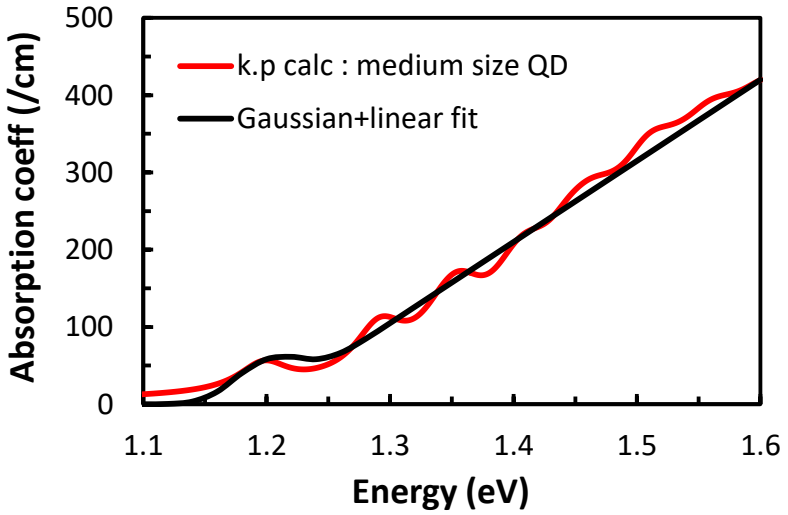

Figure 4.1-25: Absorption coefficient deduce from k·p calculation (in red) for medium size QDs with GS at 1.2 eV and same QDs density as in O3BNT1.4 sample which means 10 layers of QDs with about 700 QDs/µm² for a 515 nm-thick solar cell absorber thickness. Gaussian fit plus linear (in black) to estimate absorption profile trend for a Gaussian distribution.

First, thanks to the k·p calculation study, and considering Gaussian distribution of QDs, we can estimate that the profile of absorption for a typical size of QD is following a Gaussian expression for the ground states (GS) and a linear distribution in energy for the following excited states as shown in Figure 4.1-25. The use of a Gaussian expression is justified by our previous investigation on the Gaussian distribution of QDs. In Figure 4.1-19, we saw that QDs of different sizes and excited states (ES) all seem to follow a linear law in function of their transition energy. Therefore, in the case of QDs having almost the same GS energy E_{GS_i}, we can write the absorption coefficient as in Equation 4.1-8. We consider the following fixed parameters to fit the k·p calculation of absorption: $\sigma = 25$ meV (FWHM = 60 meV), $A_{quasi\text{-}continuum}/A_{GS}$ = 18 and $\gamma = 10$ meV. The denominator expression of the quasi-continuum states originates from the sigmoidal expression of the subandgap absorption coefficient [234].

$$\alpha_{QDs_i}(E, A_{QDs_i}, E_{GS_i}) = A_{QDs_i} \times [\mathrm{A}_{GS} \times \exp\left(-\frac{\left(E - E_{GS_i}\right)^2}{2\sigma^2}\right) + A_{quasi-continuum} \times \frac{E - E_{GS_i}}{1 + \exp\left(-\frac{E - E_{GS_i}}{\gamma}\right)}]$$

Equation 4.1-8: Absorption coefficient formula for QDs having almost the same GS energy E_{GS_i} following k·p calculation.

A second piece of information on subbandgap absorption in this sample is given by CCE fitting that was explained in chapter 3. We consider a subbandgap tail of Equation 4.1-9, as described in Figure 4.1-26.

$$\alpha(E) = \alpha_{host}\exp(-\left(\frac{E - E_{host}}{\gamma_{gauss}}\right)^2)$$

Equation 4.1-9: Gaussian fitting of subbandgap tail absorption due to QDs in $Al_{0.2}GaAs$ host material of bandgap energy $E_{host} = 1.69$ eV with a characteristic energy $\gamma_{gauss} = 240$ meV and $\alpha_{host} = 220$ cm^{-1}.

This functional form is often found to describe subbandgap tail states [235], with E_g the bandgap energy of the $Al_{0.2}GaAs$ host material and γ_{gauss} a characteristic energy called the Urbach energy for a linear exponential dependence. A square dependence has been found for example by Morgan using Thomas-Fermi method for the study of impurity bands [236]. In our case, this square dependence or Gaussian statistic can be explained by the fact that we have different size of QDs with Gaussian distribution. The summation of these Gaussian distribution regularly spaced amounts to a Gaussian tail. Nevertheless, we notice that when the number of states increases for WL and host energy levels ($E > 1.5\ eV$), the behaviors follow a square-root tendency as in the case of bulk materials.

In Figure 4.1-26, we show the absorption coefficient and we see a Gaussian dependence for QDs states with another tail coming from WL states.

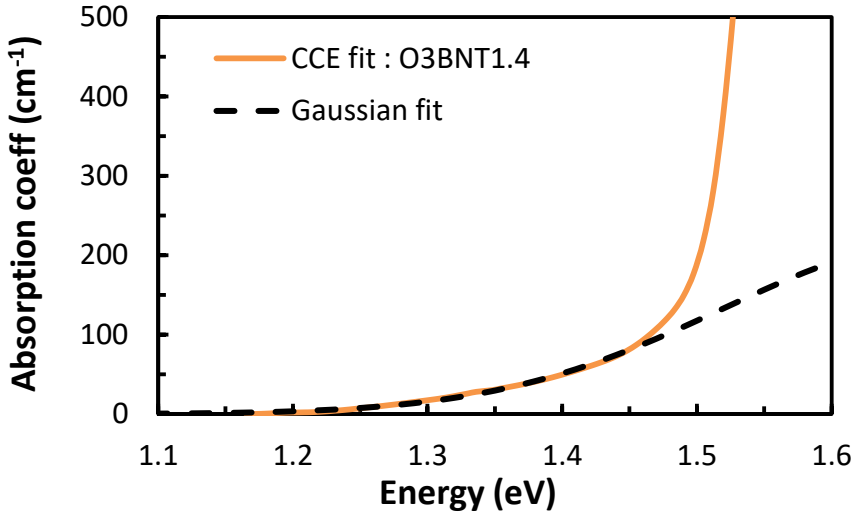

Figure 4.1-26: Absorption coefficient deduce CCE fitting (in orange) for O3BNT1.4 sample. Gaussian fit (in dashed black) to estimate absorption profile trend for a Gaussian distribution: $E_{host} = 1.69$ eV, $\gamma = 240$ meV and $\alpha_{host} = 220$ cm^{-1}.

It is interesting to notice that this tail is high compared with k·p calculation. This might be because the WL volume would be underestimated in k·p calculation. It can also be because carrier collection is more efficient for photons absorbed at WL energy states transitions compared to QDs energy states.

iii). “Hot” carriers

Using Equation 4.1-6, we present in Figure 4.1-27 the fitted temperatures for different level of laser excitation considering absorption from carrier collection efficiency (CCE) fitting. The high-energy tail fitting is very sensitive to the slope and is not always accurate especially near PL peak. A better fitting will be performed in the next part considering both low-energy and high-energy part of the PL from QDs. Nevertheless, this method has been commonly used. Therefore, it is interesting to explain the physical meaning behind it and compare with other experimental findings.

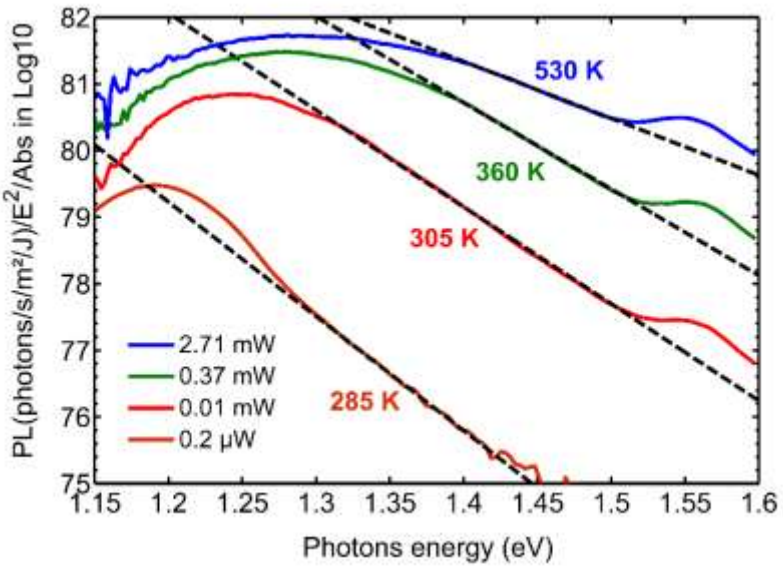

Figure 4.1-27: High-energy tail PL fitting for increasing laser excitation using absorption from CCE fitting.

In Figure 4.1-28, we compare fitting with the two absorption profiles that were assumed using k.p calculation (Equation 4.1-8) and CCE fitting (Equation 4.1-9). Spectrum at 0.2 µW laser excitation is again shown as a comparison but it was taken with a different setup with a different type of detector as explained before.

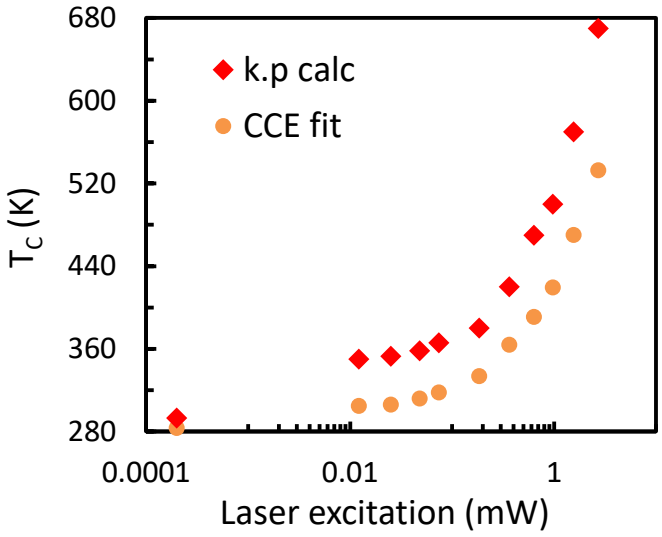

Figure 4.1-28: Fitted temperature from PL characterization presented previously at different excitation and at room temperature, using absorption from k.p calculation and from CCE fitting.

In both case we notice an increase of the carrier temperature for laser excitation around 0.2 mW. At maximum excitation, we find “hot” carriers with temperature around 600 K +/-70 K.

The term “hot carriers” was originally introduced to describe non-equilibrium electrons or holes that have an elevated effective temperature [237]. It illustrates a correlation between power dissipated, the electron gas temperature and overheating. In simpler terms, when electrons carry current in normal conductors, they heat up. At low temperatures, but also at ordinary temperatures in nanoscale devices, their ability to dissipate this heat can be significantly impaired.

In chapter 3, we discussed that the capture and emission of charge carriers into or outside of QDs can be related to different mechanisms such as pure tunneling, thermoionic emission (TE) or thermoionic field emission (TFE). For a carrier to fall in a lower energy level it has to dissipate the excess energy. As explained before, inside the QDs, numerous mechanisms can dissipate the energy like carrier-carrier scattering (Auger effect, impact ionization) or phonon emission (thermalization). These processes are competing with each other. For photovoltaic application, the beneficial effects are the extraction of multiple carriers to increase the current or local storage to increase the chemical potential and therefore the V_{oc}. These mechanisms are considered in advanced concepts like MEG-SCs (carrier-carrier scattering) or HCSCs (thermalization) [32].

In early investigation of QDs, a “phonon-bottleneck” was predicted due to the lower dimensionality of the QDs and quenching of longitudinal phonons [238]. The “phonon-bottleneck” effect describe a situation when the spacing between size-quantized energy levels is larger than the vibrational energy. In the case of the In(Ga)As self-assembled QDs system, we saw that the assumption of ideal zero-dimensionality is not true because of QDs having a rather large lateral sizes. Nevertheless, the separated discrete electron energy levels may lead to the requisite of multi-phonon emission for

thermalizing. Multi-phonon emission proceeds at a slower rate compared to single phonon assisted relaxation processes which could potentially slow down the carrier cooling rate in nanostructures compared with their bulk counterparts [239]. This phenomenon was observed in QWs despite having an even higher dimensionality [240]. A good HCSC must have an electrical transport path between the absorber and collector that allows transfer of electrons at a rate faster than the electrons can interact with the lattice. In our case, a difference in carrier cooling rate between QDs (absorber) and the bulk host material (collector) might create the condition for a HCSC at high laser excitation.

This “phonon-bottleneck” effect is sill debated for QDs, on the other side Nozik *et al*, have demonstrated the existence of “multiple exciton generation” (MEG) in QDs [233]. They showed ultrafast rate of carrier-carrier scattering compared with bulk material and which should be even higher than hot exciton cooling. They use the term exciton instead of carriers because theoretically for QDs, the electron-hole pairs become correlated due to spatial confinement. In our case, for a self-assembled In(Ga)As QDs / $Al_{0.2}GaAs$ solar cell operated at room temperature, we saw that it is not obvious to determine if the carriers behave as excitons or free carriers. Especially thermal, electric field and filling effects might break the typical Coulomb interaction of excitons. Therefore we cannot conclude on the origin of this “hot carrier” effect.

From an experimental point of view, we have a “hot” carrier distribution. For PV applications, we do not need to explain if it is related to slow thermalisation or enhanced exciton generation. Since there is no electric power extracted, the absorbed power can only be lost as heat towards the lattice or by radiative recombinations. In other words, carriers lose their energy by interaction with phonons or photons.

The power lost by thermalisation can then be expressed as the difference between the absorbed power and the radiatively emitted power. The radiative emission is neglected compared to the incident power as we saw previously. The power lost by thermalisation can then be written as an Arrhenius’ equation with an activation energy E_a as we discussed previously in chapter 3.

$$P_{abs} = P_{th} \Leftrightarrow k_{rate} = C_{pre-exp} \times \exp(-\frac{E_a}{k_B T_H})$$

Equation 4.1-10: Absorbed power equals power lost by thermalisation can be written as an Arrhenius’equation

The Arrhenius’ equation gives the relationship between the activation energy and the rate at which a reaction proceeds where k_B is the Boltzmann constant, assuming a Maxwell-Boltzmann (MB) distribution. For continuous wave (CW) PL, the reaction rate coefficient k_{rate} is equivalent to the power absorption rate. The pre-exponential factor $C_{pre-exp}$ is a constant that defines the rate due to the frequency of collisions for carriers. Most simply, k_{rate} is the number of collisions that result in a reaction per second, $C_{pre-exp}$ is the number of collisions and the exponential factor with energy E_a is the probability that any given collision will result in a reaction. In our case, it seems reasonable to approximate the activation energy as being independent of the temperature. Similarly, the weak temperature dependence of the pre-exponential factor is often negligible compared to the temperature dependence of the exponential factor. Except in the case of "barrierless" diffusion-limited reactions, in which case the pre-exponential factor is dominant and is directly observable. In

such case, a modified Arrhenius' equation can be used as in the case of the linear law found by A. Le Bris [241] or the squared dependence in Richardson's law that we discussed in part 3.3.1.3.

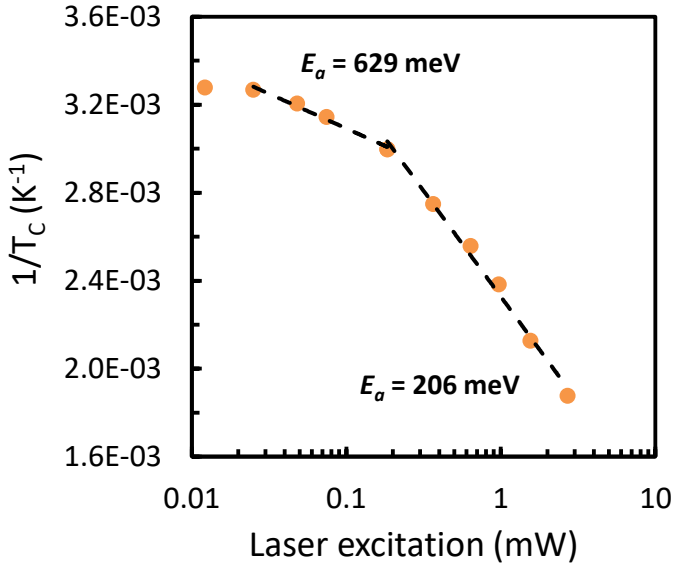

Figure 4.1-29: Fitted temperature using k.p calculation follows an Arrhenius'law with energy activation of 206 meV.

In our case, we consider the prefactor $C_{pre-exp}$ to be independent of carriers's temperature. We find good fitting with two different activation energy for the low-excitation (< 0.2 mW) and high-excitation (> 0.2 mW) regimes discussed previously. For low-excitation, $E_a = 629\, meV$ and at high-excitation $E_a = 206\, meV$ as shown in Figure 4.1-29. This PL fitting represents the evolution of high-energy QDs states. Following chapter 3 consideration on the carrier escape nature, we see that the two different regimes of activation energy might corresponds to excitonic and non-excitonic behaviors of the high-energy carriers inside the QDs. At low excitation (< 0.2 mW) the activation energy is closer to the energy gap between QDs states and the host material which would indicate an excitonic behavior. At high-excitation, the value is closer to the energy separation between QDs energy states and the host material (especially holes) as we saw previously in chapter 3. This would indicate a non-excitonic behavior. In the literature, the non-excitonic behavior of carrier escape has been confirmed for an increased excitation [176]. Host material acts as a barrier that control the evolution of the carrier gas's temperature.

As we show in Figure 4.1-30, we investigated QDs system that have other typical sizes of QDs from growth of Okd-1 (Okd-1 M10 sample) and Okd-3 (Okd-3 M0.2 sample). At high-excitation regime, we find that activation energy is larger for "large" QDs investigated via PL and AFM height characterization (Okd-1 M10 sample: green diamonds, E_a~250 meV). It is coherent with the fact that "large" QDs have a larger energy separation between QDs energy states and WL.

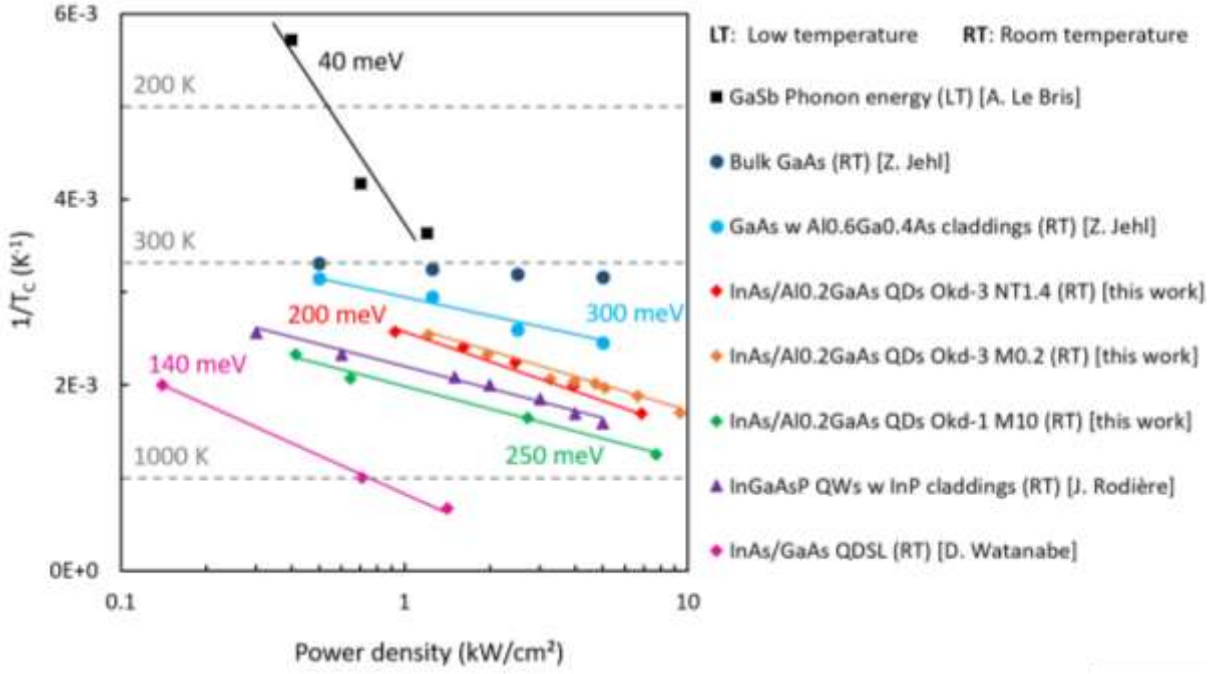

Figure 4.1-30: Comparison of high-energy tail carrier temperature fitting of PL measurements performed at low temperature (LT) and room temperature (RT) for different samples at high-excitation. Focus on the PL fitting for carrier temperature range between 175 K and 1500 K.

We also compare with data from other investigations of PL high-energy tail temperature's fitting. In Figure 4.1-30, all fitting showed are from PL at room temperature (RT) except the first value (black square) from a GaSb-based heterostructure investigation of hot carrier solar cells (HCSCs) at low temperature (LT) by A. Le Bris. An activation energy value E_a~40 meV is found and is attributed to longitudinal phonon energy that is the limiting mechanism at low temperature [241].

We compare other quantum-structured material, for example InAs/GaAs quantum dot superlattice (QDSL) solar cells (pink diamonds) investigated by D. Watanabe at room temperature [207]. The PL of QDs is around 1.1 eV and around 1.42 eV for GaAs host material. The measurement was performed by Professor Takashi Kita's group from Kobe University using time-resolved PL (TRPL) excitation therefore the comparison with continuous-wave (CW) PL may not be direct. We converted nJ/cm² in kW/cm² considering a 0.2 ns constant duration time before the thermalization of carriers that they investigated. From their QDSL solar cell, if we assume an ambipolar escape mechanism for carriers inside QDs, the activation energy will be equal to the energy gap divided by two (160 meV). This value will be even reduced in the case of unipolar escape via holes. Anyhow, the activation energy found by fitting with Arrhenius' equation is close (E_a~140 meV).

At room temperature (RT), we also show the results of $In_{0.8}Ga_{0.2}As_{0.44}P_{0.56}/In_{0.78}Ga_{0.22}As_{0.81}P_{0.19}$ QWs structure with InP cladding (purple triangles) [240]. PL characterization was performed using the same setup system as in this work. We find an energy activation E_a~260 meV wich is again coherent with the energy separation between the low energy material (here the wells) and the barriers.

We also show activation energy from PL characterization performed at room temperature (RT) by Dr. Zacharie Jehl on a thin layer of bulk GaAs sample (dark blue full circle) and on a thin GaAs layer with $Al_{0.6}Ga_{0.4}As$ cladding layers grown in order to confine the carriers (light blue circle). We notice almost no high-energy PL tail heating for the sample without claddings and E_a~300 meV energy ac-

tivation for the sample with claddings. Bandgap energy between GaAs and $Al_{0.6}Ga_{0.4}As$ is ~600 meV, therefore it would seem coherent with an ambipolar or unipolar escape mechanism.

Finally, in Figure 4.1-31 we compare our results with results published recently by Kita's group (Y. Harada) [242], where they investigated low and room temperature TRPL for their InAs/GaAs QDSL solar cells but also for InAs/GaAs MQWs solar cells grown in their lab. TRPL measurement at low temperature (LT) for QDSL seems to show two behaviors (dark blue diamonds). For carriers's temperatures between 160 K and 360 K, the activation energy would be very low (E_a ≤40 meV) while it goes up to E_a~200 meV for the carriers's temperatures above 360 K following the same trend as room temperature (RT) TRPL or PL measured by them (light blue diamonds), D. Watanabe (pink diamonds) or from our work on In(Ga)As QDs (red diamonds). This phenomenon might be explained by the fact that for carriers's temperature around 200 K, the thermal escape throught the host material becomes a dominant mechanism compared to thermalization via phonon energy inside QDs.

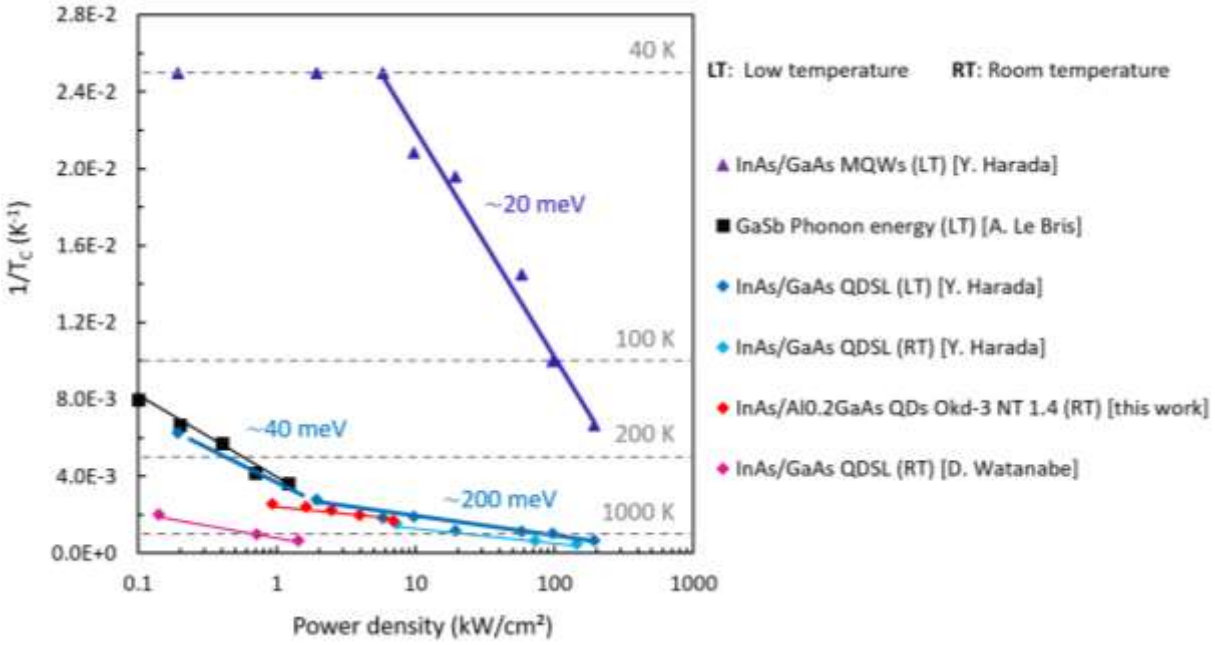

Figure 4.1-31 Comparison of high-energy tail carrier temperature fitting of PL measurements performed at low temperature (LT) and room temperature (RT) for different samples at high-excitation. PL fitting for carrier temperature range between 40 K and 1500 K.

For low temperature (LT) TRPL measurement on InAs/GaAs MQWs (Indigo triangles), we notice that carrier heating happens for a very high power density (~10 kW/cm²) compared with QDSL sample. It follows a low activation energy (E_a~20 meV) close to a typical longitudinal-optical (LO) phonon energy [170], [243]–[245]. The carriers's temperature does not reach 200 K, therefore it is possible that the thermal escape via GaAs barriers is limited.

In conclusion, the comparison of all these measurements seem to indicate that for a certain temperature, thermal escape from host material becomes a dominant mechanism with a certain activation energy that represents the probability that a carrier escapes the QD ensemble to thermalize in the host material. For continuous bandfilling, the carrier density inside QDs increases, also increasing the electron gas temperature following an Arrhenius' equation dominated by the thermal escape activation energy. For high-energy levels, the electron gas distribution follows a Maxwell-

Boltzmann (MB) distribution with an equilibrium temperature that will be the temperature of radiation obtained by fitting the PL high-energy tail.

To conclude on the bandfilling and balance of photons, we consider that a quantum structure can be seen as an electron bathtub. The emitted photon flux increases linearly until it becomes limited by radiative recombination flux from the bottom and non-radiative thermal escape from the top. A QDs ensemble share a carrier population that behaves differently than in the host material because of quantum confinement. Therefore, with increasing bandfilling for QDs ensemble, carriers will distribute following a certain "hot" distribution different from the distribution in the host material. In the next part, we want to investigate quasi-Fermi level splitting (QFLS), for the population localized in the QDs ensemble and compare with the host material population.

4.1.3 Quasi-fermi level splitting

The concept of quasi-Fermi level (QFL) is used to describe electrons and holes populations respectively in the conduction band (CB) and valence band (VB) when they are displaced from equilibrium and reach a quasi-equilibrium. For example in the case of photon flux generating a continuous electrons transition from VB to CB, it is possible to describe the two populations of carriers using Fermi-dirac (FD) distribution. In this case, the difference between the two QFL is called QFL splitting (QFLS) expressed with notation $\Delta\mu$ and thus it represents the electrochemical potential when a solar cell absorbs a photon flux. Therefore, it is also equivalent to the open-circuit voltage of a solar cell. In bulk material, energy states are close to each other with a high density of states and radiative limit is difficult to reach. Thus, QFLS is usually not increasing directly due to bandfilling but due to passivation of leakage channels. It follows a logarithmic law with ratio of generated current over the dark current with ideality factor of 2 in the case of dominant defect-related recombination. In the case of a QDs ensemble, we saw that the bandfilling dynamic and evolution in energy is closely related with radiative recombination. In addition, evolution of PL intensity with excitation has an ideality factor inferior or equal to one indicating a radiative or even Auger limited regime.

4.1.3.1 Generalized Planck's law

To evaluate the relation between photoluminescence and QFLS we will make use of the generalized Planck's law also called generalized Kirchhoff's law. In the domain of luminescent diode, this law has been formulated by Würfel in 1982 [246]. The application of this law to consider the reciprocity relation between electron generation, QFLS and luminescence has also been extensively investigated for solar cells by Rau [247]. Recently it was explicitely investigated with our hyperspectral calibrated PL setup to confirm the equivalence between QFLS and V_{oc} in GaAs and CIGS solar cells [218]. Equation 4.1-11, gives the usual formulation of this equation for normal incident angle with $\phi_{PL}(E)$, the photons flux at different energy E, and $A(E)$, the absorptivity of the luminescent material inside the device of interest [235].

$$\phi_{PL}(E) = A(E)\frac{2\pi}{h^3c^2}\frac{E^2}{\exp\left(\frac{E-\Delta\mu}{kT}\right)-1}$$

Equation 4.1-11: Generalized Planck's law also called generalized Kirchhoff's law or more recently called the Lasher-Stern-Würfel equation [235].

In the perspective of new PV material, this equation has been challenged especially in the case of subbandgap material because there is no general expression to consider subbandgap absorption. We will make use of Equation 4.1-7 to consider absorptivity. As we saw previously, the coefficient of absorption accounts for a part, which depends on the filling of energy states, and another part independent of the filling only representing the coupling of TDM written α_0 as expressed in Equation 4.1-12.

$$\alpha(E) = \alpha_0(E) \times (f_{VB}(E) - f_{CB}(E))$$

Equation 4.1-12: Absorption coefficient dependence to bandfilling

$f_{VB}\ and\ f_{CB}$ are the occupation probabilities of the valence band (VB) and conduction band (CB) for holes and electrons respectively. It is possible to express these occupation probabilities in terms of a single QFLS $\Delta\mu$ and the energy of the optical transition E. If we consider the case where the electron and hole effective masses are equal and the material is intrinsic, then the quasi-Fermi energies will split symmetrically about the intrinsic equilibrium Fermi energy at mid-gap. While this is not a good approximation for a doped semiconductor at low injection, it becomes a good approximation even for doped semiconductors at high injection. Since it is at high injection where we expect effects from occupation, this is generally a reasonable assumption. Therefore in the case of Fermi-Dirac (FD) distribution, we can write $f_{VB}\ and\ f_{CB}$ as in Equation 4.1-13.

$$f_{VB} = \frac{1}{\exp\left(-\frac{E-\Delta\mu}{2kT}\right)+1} \qquad and \qquad f_{CB} = \frac{1}{\exp\left(\frac{E-\Delta\mu}{2kT}\right)+1}$$

Equation 4.1-13: FD distributions for the VB and CB considering symmetrical energy splitting.

Following Equation 4.1-13, we express Equation 4.1-12 in terms of $\Delta\mu$ and T as shown in Equation 4.1-14 which represents the bandfilling dependence [235].

$$\alpha(E) = \alpha_0(E) \times (1 - \frac{2}{\exp\left(\frac{E-\Delta\mu}{2kT}\right)+1})$$

Equation 4.1-14: Absorption coefficient dependence to $\Delta\mu$ and T.

4.1.3.2 Validity for the InAs QDs ensemble system

It is common to accept the validity of the generalized Planck's law if a chemical and thermal equilibrium is set. This question is not obvious for QDs that are usually considered as isolated and confined structures.

i). Equilibrium of carrier populations: from "Stokes" shift to spatial smearing effect

As we saw in chapter 3 with temperature-dependent PL investigation, for very low excitation (e.g. 0.2 µW using HORIBA Jobin Yvon PL detection setup), the PL at room temperature only represents the PL from "large QDs". This so-called "Stokes shift" effect (relaxation in "large" QDs) is well known in the literature. It is considered that a local equilibrium distribution is achieved for these "large QDs" however, thermal induced escape of carriers does not lead to the formation of a position-independent Fermi level [170].

Nevertheless, the increase of excitation leads to a non-excitonic behavior of carriers inside the QDs. At first, we demonstrated it with "optical I-V" investigation where we found a saturation behavior

in the QDs even for the low-excitation regime (< 0.2 mW). And then we noticed the non-excitonic behavior from the investigation of activation energy using the Arrhenius's equation and temperature obtained from PL fitting of high-energy states inside the QDs. In the literature, using cathodoluminescence, it has been reported that high excitation result in a "spatial smearing effect". This effect is likely to be the result of an equilibration of carrier populations in adjacent groups of QDs. Figure 4.1-32 is a schematic illustration of this "spatial smearing effect" taken from [176].

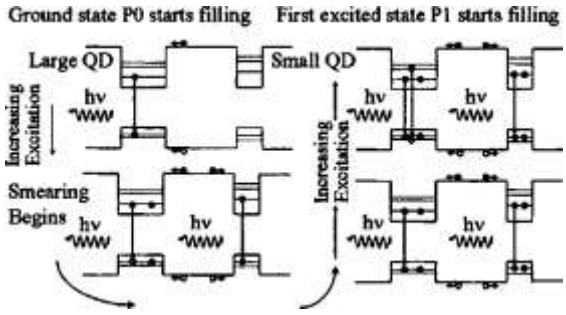

Figure 4.1-32: Schematic illustration of successive state filling in adjacent groups of QDs resulting in an equilibration of carrier populations and an excitation dependent "spatial smearing effect". Taken from [176].

Therefore, we will consider in the rest of our study that for the very low excitation PL measurements (0.2 µW) performed using HORIBA Jobin Yvon PL mapper, the QDs are not in equilibrium. However, in the case of the calibrated hyperspectral PL measurements, even for the low excitation laser of 0.01 mW we consider it is sufficient to have an equilibrium because we notice a saturation effect in the QDs reflecting state-filling that should be linked to a "spatial smearing effect". This could be checked in the future by using cathodoluminescence characterization measurements.

ii). Absorption coefficient

Therefore, we will consider the fitting of PL from QDs using the generalized Planck's law for the calibrated hyperspectral PL measurements. We fit the PL considering the coefficient of absorption as the sum of absorption coefficients from six different groups of QDs with different ground states (GS) energies following Equation 4.1-8. The six groups of QDs are separated by 50 meV so that $E_{GS_1} = 1.21$ eV, $E_{GS_2} = 1.26$ eV, $E_{GS_3} = 1.31$ eV, $E_{GS_4} = 1.36$ eV, $E_{GS_5} = 1.41$ eV,and $E_{GS_6} = 1.46$ eV. Therefore, we can write the absorption coefficient as represented in Equation 4.1-15 with A_{QDs_i} that represents the weight of each population in the absorption coefficient.

$$\alpha_0(E) = \sum_{i=1}^{6} \alpha_{QDs_i}\left(E, A_{QDs_i}, E_{GS_i}\right)$$

Equation 4.1-15: Coefficient of absorption for a QDs ensemble inside a host material with α_{QDs_i} calculated using Equation 4.1-8.

In the generalized Planck's law, a precise value of absorption is especially important for energies in the range: $E - \Delta\mu < 2k_BT$. Therefore, when increasing the excitation, $\Delta\mu$ also increases and PL spectrum will give information on the absorption from QDs that have a higher GS energy. In other words, at low excitation starting at 0.01 mW, PL peak is around 1.26 eV. It means that absorption coefficient contributions from QDs_6 (sixth group of QDs) with GS energy, $E_{GS_6} = 1.46$ eV, will have a very low impact on the PL because their energies is far from $\Delta\mu$. For the highest excitation, PL

peak is around 1.35 eV and the value of the absorption coefficient from this group will have a significant impact.

iii). Generalized Planck's law PL fitting

We present in this part the fitting of PL with the generalized Planck's law. The detailed method is explained in appendice **C**. By using this method, we can find large sets of values for A_{QDs_i} that fit well PL spectrum for different $[\Delta\mu, T]$ at each level of excitation. We keep the fitting values that have the best root mean square deviation (RMSD) with experimental values for the spectral range between 1.17 eV and 1.49 eV. Finally, we consider the median of the best values of A_{QDs_i}, which therefore offer a relatively good fitting and is statistically more probable. In Figure 4.1-33, we present the result of fitting for these median values of A_{QDs_i} (red in the center). We also present the fitting when we force a higher value of absorption (purple on the left) and when we fix temperature of carriers to be constant at 310 K for all excitations (pink on the right).

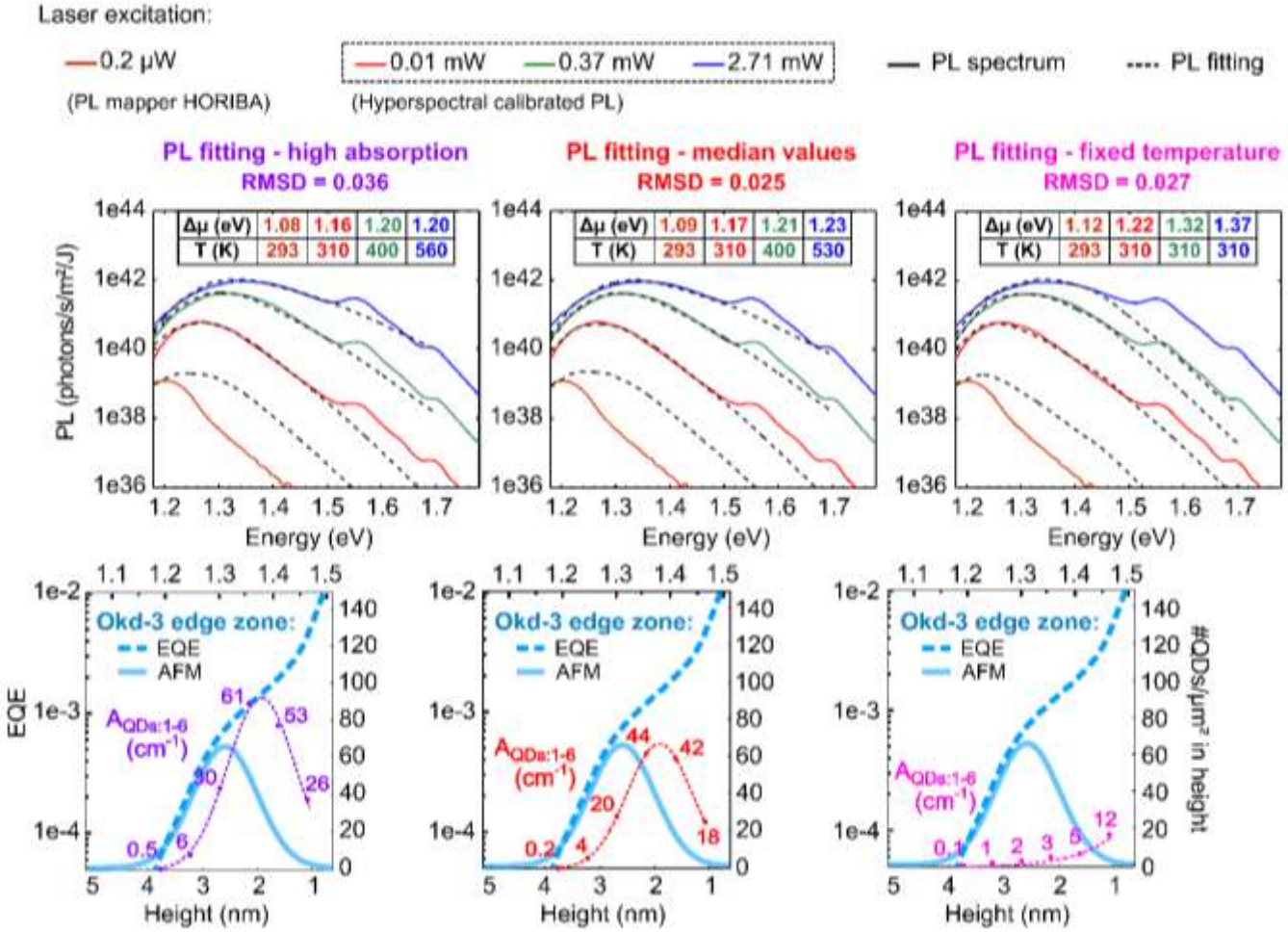

Figure 4.1-33: PL fitting using the generalized Planck's law for different laser excitations. The 0.2 µW value is a very low excitation regime that is obtained with PL mapper HORIBA and recalibrated in intensity as a comparison. PL spectrum with excitations between 0.01 mW and 2.71 mW are performed using hyperspectral imager and integrated in the center area. Three different absorption values are considered for the fitting: high absorption (purple on the left), median values (red in the center), fixed temperature (pink on the right). They have different RMSD values. $[\Delta\mu, T]$ are shown in table for each PL fitting. Colors are matched with curves and excitation regimes. Below each PL fitting graph are shown superposition of EQE from the considered O3BNT1.4 solar cell with AFM heights investigation on the "edge zone" following investigation presented in Figure 3.3-5. We compare with A_{QDs_i} prefactors for the six groups of QDs considered that have different GS energies (1.21 eV, 1.26 eV, 1.31 eV, 1.36 eV, 1.41 eV and 1.46 eV). Vertical axis is the same for the prefactors A_{QDs_i} with the three different absorption that are considered and presented as a comparison. Values are in cm^{-1}. Prefactors distribution in energy are Gaussian-like for high absorption and median values but exponential for fixed temperature.

In Figure 4.1-33, below each PL fitting are shown superposition of EQE from the considered O3BNT1.4 solar cell with AFM heights investigation on the "edge zone" following investigation presented in Figure 3.3-5. We compare with A_{QDs_i}prefactors for the six groups of QDs considered that have different GS energies (1.21 eV, 1.26 eV, 1.31 eV, 1.36 eV, 1.41 eV and 1.46 eV). Vertical axis is the same for the prefactors A_{QDs_i} with the three different absorption that are considered and presented as a comparison. Values are in cm^{-1}. Prefactors distribution are Gaussian for high absorption and median value but exponential for fixed temperature.

We also show the recalibrated very low excitation data (0.2 µW) from HORIBA Jobin-Yvon PL mapper. We notice that we cannot fit with values of absorption considered with hyperspectral PL data.

Finally, we show the absorption coefficient resulting from the PL fitting which is the summation of absorption coefficients from the six different QDs population with prefactors A_{QDs_i}. In Figure 4.1-34, we compare with the absorption coefficient from CCE fitting and the Okd-5 absorption coefficient experimentally measured using FP interferometry as presented in chapter 3.

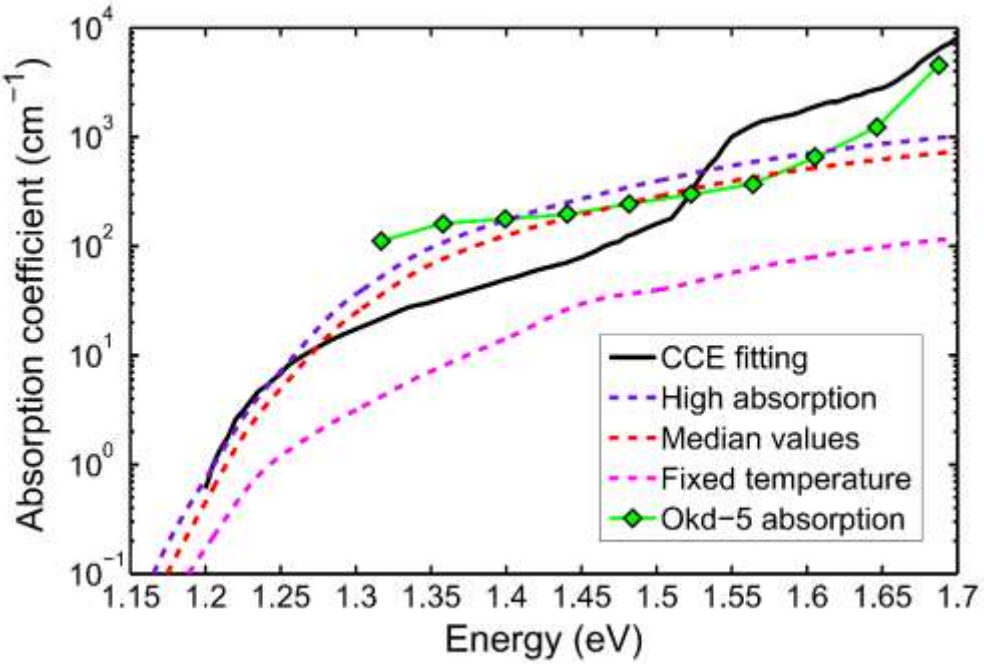

Figure 4.1-34: Absorption coefficient from CCE fitting (black solid line). It is compared with different absorption coefficients (dashed lines) used for PL fitting calculated with prefactors from Figure 4.1-33 and Equation 4.1-15: high absorption (purple), median values (red) and fixed temperature (pink). We also compare with experimental absorption measurements using FP interferometry on Okd-5 sample that was presented in chapter 3.

Overall, we think median values are a good compromise. They offer relatively good fitting backed by a statistical analysis of RMSD values. Prefactors follow Gaussian-like distribution as it is the case for AFM heights distribution. Absorption coefficient is close to the CCE fitting value and close to the Okd-5 absorption coefficient.

We think the different behavior of very low excitation data (0.2 µW) might be because, for such excitation, carriers have an excitonic nature with low binding energy. Thermal induced escape of carriers is enough to enable the delocalization from small to large QDs but does not lead to the formation of a position-independent Fermi-level as it is assumed in the case of higher excitation re-

gime. Therefore, high-energy PL would only be the result of the contribution of "large QDs" but not the result of the whole QDs ensemble as it is considered for hyperspectral data at higher excitation regime.

This assumption of local contribution could be also given if we consider the fixed temperature case. For fixed temperature at 310 K, the absorption coefficient of QDs is ten times less than what is expected. However, if we consider that only one layer is luminescing then it would be valid for the PL fitting. Also the non-Gaussian prefactors distribution (A_{QDs_i}) could be because of the fact that the density of states in one QD layer is the contribution of QDs (Gaussian) but also adjacent "quantum-well islands" (QWIs) that are in-between QDs and the wetting layer (WL) energy states. However, due to high QD density in our sample, it seems unlikely that these adjacents QWIs would contribute so much to the absorption as to change the Gaussian prefactors distribution into an exponential one. In proportion, if we look at our AFM measurements in chapter 3, the population of adjacent QWIs seems to be at least twice less than the QD population.

In the next parts of our study, we consider median values fitting to be the most accurate. Therefore, we suppose that luminescence is homogeneous in all the ten layers (vertical diffusion) and that the change of slope in high-energy PL is due to an increase of the carriers's temperature as discussed earlier.

4.1.3.3 Energy separation of carrier populations

Using absorption coefficient from previous analysis with median values, we investigate $[\Delta\mu, T]$ evolution with excitation for QDs. We compare with $[\Delta\mu, T]$ fitted from the spectral region of WL and host material PL using generalized Planck's law with a constant temperature of 300 K. In Figure 4.1-35, we present the evolution of the difference of $[\Delta\mu, T]$ for the carrier population inside QDs and the carrier population in the WL and $Al_{0.2}GaAs$ host material.

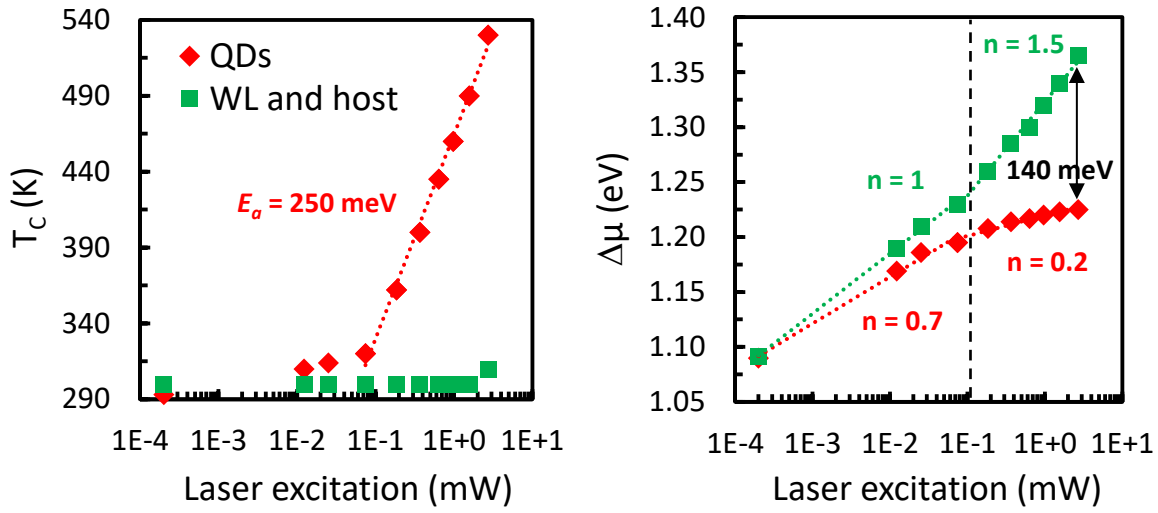

Figure 4.1-35: Evolution of temperatures T_c (left) and QFLS ≡ Δμ (right) for carrier populations inside QDs (red) in comparison with population in the WL and $Al_{0.2}GaAs$ host material. An activation energy of 250 meV is found related to temperature increase inside QDs. Different behavior of QFLS are noticed for low-excitation (< 0.2 mW) and high-excitation regimes (> 0.2 mW). For WL and host material we find same idealities of n=1 and n=1.5 as in the optical I-V investigation. For QDs, we find about the same ideality for the low-excitation regime, n=0.7 as in the optical I-V investigation. However, for high-excitation it is very reduced (n=0.2). A maximum difference of 140 meV is found between QFLS for the highest laser excitation.

An activation energy of 250 meV is found related to temperature increase inside QDs, which is close to the previous 206 meV value found with a simple fitting. Different behaviors of quasi-Fermi level splitting (QFLS) are noticed for low-excitation (< 0.2 mW) and high-excitation regime (> 0.2 mW). For wetting layer (WL) and host material we find same idealities of n = 1 and n = 1.5 as in the optical I-V investigation described in Figure 4.1-9. For QDs, we find about the same ideality (n = 0.7) for the low-excitation regime as in the optical I-V investigation. However, for high-excitation it is very reduced, here we find n = 0.2, to be compared with n = 0.5 for the "optical I-V" investigation. In the case of optical I-V, we represent the evolution of the integrated intensity which means the increase of photon radiation due to filling of QDs states. In the case of QFLS PL Planck's law fitting, we consider not only the filling but also the distribution in energy as indicated by the temperature in the Fermi-Dirac (FD) distribution in Equation 4.1-14. In other term, for the high-excitation regime, the QFLS inside the QDs is almost stable and the increase in electron filling is converted into an increase of the carrier temperature revealing a broadening of the energy distribution of electrons inside QDs. At the same time, the carrier population inside WL and host material becomes independent from QDs carriers's population and we see the apparition of a splitting in energy. A maximum difference of 140 meV is found between both QFLS for the highest laser excitation.

4.2 Two-color excitation photoluminescence

In the previous part, we investigated the behavior of carriers in QDs states with increased filling. We demonstrated that for a high-excitation regime, an independent carrier population is created in the host material. From an IBSC point of view, it represents the electrochemical potential of the cell. In this part, we want to get an insight on the sequential two-photon absorption (S-TPA) that is a fundamental piece to convert solar spectrum IR photons. First, we will describe the characterization setup that we used and then present our observations. In a third part, we will discuss about a simple steady-state rate equation model.

4.2.1 Characterization setup

In the calibrated PL setup described previously, the 532 nm laser makes all transitions between the valence band (VB), the intermediate band (IB) and the conduction band (CB) possible. We observed that PL is dominated by the recombination from QDs states (or IB) to VB, whereas recombination from the host material (or CB) appears at strong excitation. We used a second continuous wave (CW) laser at 1550 nm (0.8 eV) to excite exclusively the carriers from confined QDs states to continuous CB. In order to achieve this end, we used the same hyperspectral imager system with a two-stage optical setup (visible and IR excitation) to implement a dual-beam excitation on our solar cell. The reflection of IR laser beam and transmission of PL signal was fulfilled using a DMSP1180 short-pass dichroic mirror. The laser beams were defocalized in the focal plan of the objective in order to facilitate the overlap of the two laser spots. We did not directly observe the 1550 nm laser spot because of the spectral range of the detector. We used a 975 nm laser with specifications close to the 1550 nm laser to estimate the laser spot originating from the IR optical setup.

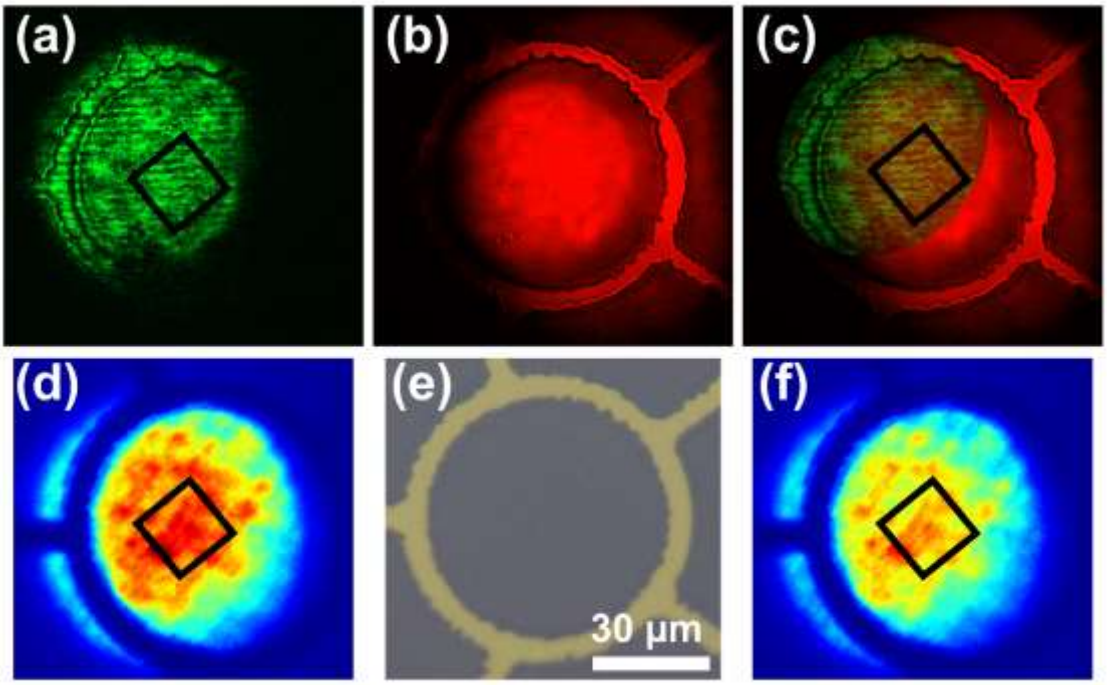

Figure 4.2-1: Two-color spot images taken with hyperspectral camera: (a) 532 nm laser reflection with no filter, (b) 975 nm laser reflection almost equal to the 1550 nm spot and (c) superposition of both spots. (d) PL spot intensity IR:OFF, (f) PL spot intensity IR:ON. Black square of 30 µm size indicates the zone of interest for our study. Photo of the center of the cell (inner circle: 60 µm) is also shown in image (e) as an indication.

We confirmed 975 nm and 1550 nm laser spots have about the same size with the optical setup by imaging on a Thorlabs fluorescing alignment disk. The observation of the 532 nm and 975 nm spots is shown in Figure 4.2-1 (a) and (b). A photo of the center of the solar cell (inner circle: 60 µm) is shown in image (e). Imaging the reflection of the beams, spot size diameter at FWHM for both lasers was estimated to be around 50 µm. The spot profile is not Gaussian and we estimate about 85% of the energy is inside the HM spot diameter. A superposition of the 532 nm and 975 nm spots is shown on image (c). The hyperspectral images are shown in image (d) for PL without 1550 nm laser (IR: OFF) and in image (f) for PL with 1550 nm laser (IR: ON). The color maps are drawn in the same color scale in order to see the global decrease in PL intensity when IR laser is ON. The spectra retrieved in each pixel of the black square area of the hyperspectral images are integrated and will be considered in the next part.

4.2.2 IR pump effect on photoluminescence

After having presented the characterization setup, we present the one-color and two-color PL excitation schematics in Figure 4.2-2. In this part, we investigate the same cell from sample O3B-NT-1.4 presented earlier in the calibrated PL study. First, we present the PL characterization for one-color excitation with 532 nm laser (G channel). Then, we present the effect of the second excitation with IR laser at 1550 nm (P channel). Finally we show the ratio of PL flux (channel F) between the two dynamics IR:OFF and IR:ON.

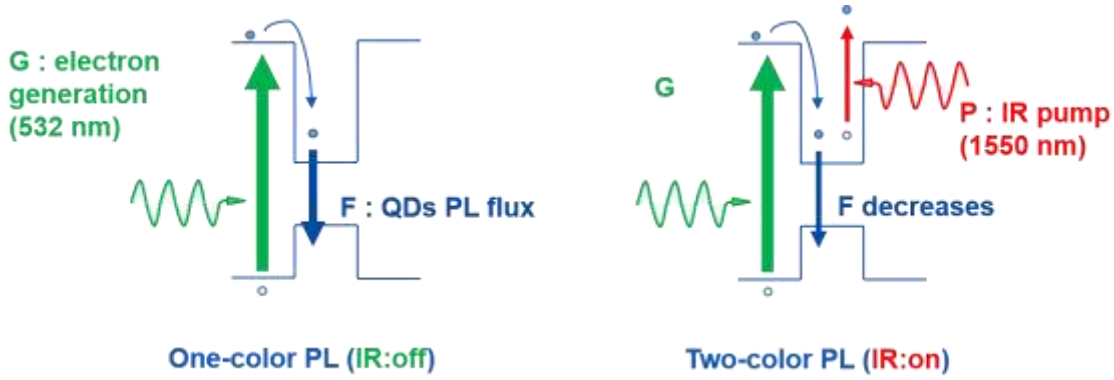

Figure 4.2-2: Schematic of one-color and two-color PL in the In(Ga)As / $Al_{0.2}GaAs$ QDs system. The G channel represents the generation of electrons induces by VB to CB transition due to absorption of 532 nm laser flux. F channel represents the radiative recombination flux from QDs states. P channel represents the IR pump effect on the re-generation of electrons inside QDs states to higher energy states.

4.2.2.1 One-color excitation photoluminescence

In contrast to the previous calibrated PL study, in this case the 532 nm laser excitation is defocused and the power density is less. In order to know in which kind of regime we find ourselves, we compare the defocused and focused PL spectrum for minimum, medium and maximum laser excitation as shown in Figure 4.2-3. We also show images of PL spots and tables summarizing information regarding the excitation and PL peak for the focused and defocused characterizations. In the defocused case, we find that the half-maximum (HM) diameter of the PL spot is around 45 µm for laser excitation of 0.81 mW (minimum) and 60 µm for 25.7 mW (maximum). It is difficult to estimate precisely the HM diameter because of the annular gold contacts that can be seen in Figure 4.2-1. Therefore, it is also difficult to estimate the carrier diffusion with the same method as before but since we are working on the same cell it is not so important to investigate it again. Overall, we will consider that in the case of defocalized excitation, the carrier diffusion is negligible compared to

the excitation spot size. Therefore, we suppose that the HM diameter of the PL follows the same profile and has the same size as the 50-µm optical spot from 532 nm laser excitation. In the tables of Figure 4.2-3, we calculate an "electrical" power density as in the previous part by normalizing with PL area at half-maximum (HM) considering 58% and 85% power respectively for Gaussian and defocused spot.

In Figure 4.2-3, we see that both focused and defocused PL spectrum have about the same peak intensity (ph/s/m²/eV) for minimum, medium and maximum excitations whereas they have different "electrical" power density (kW/cm²). However, for comparable "electrical" power density excitations, we find a good agreement in term of PL peak shift and high-energy tail.

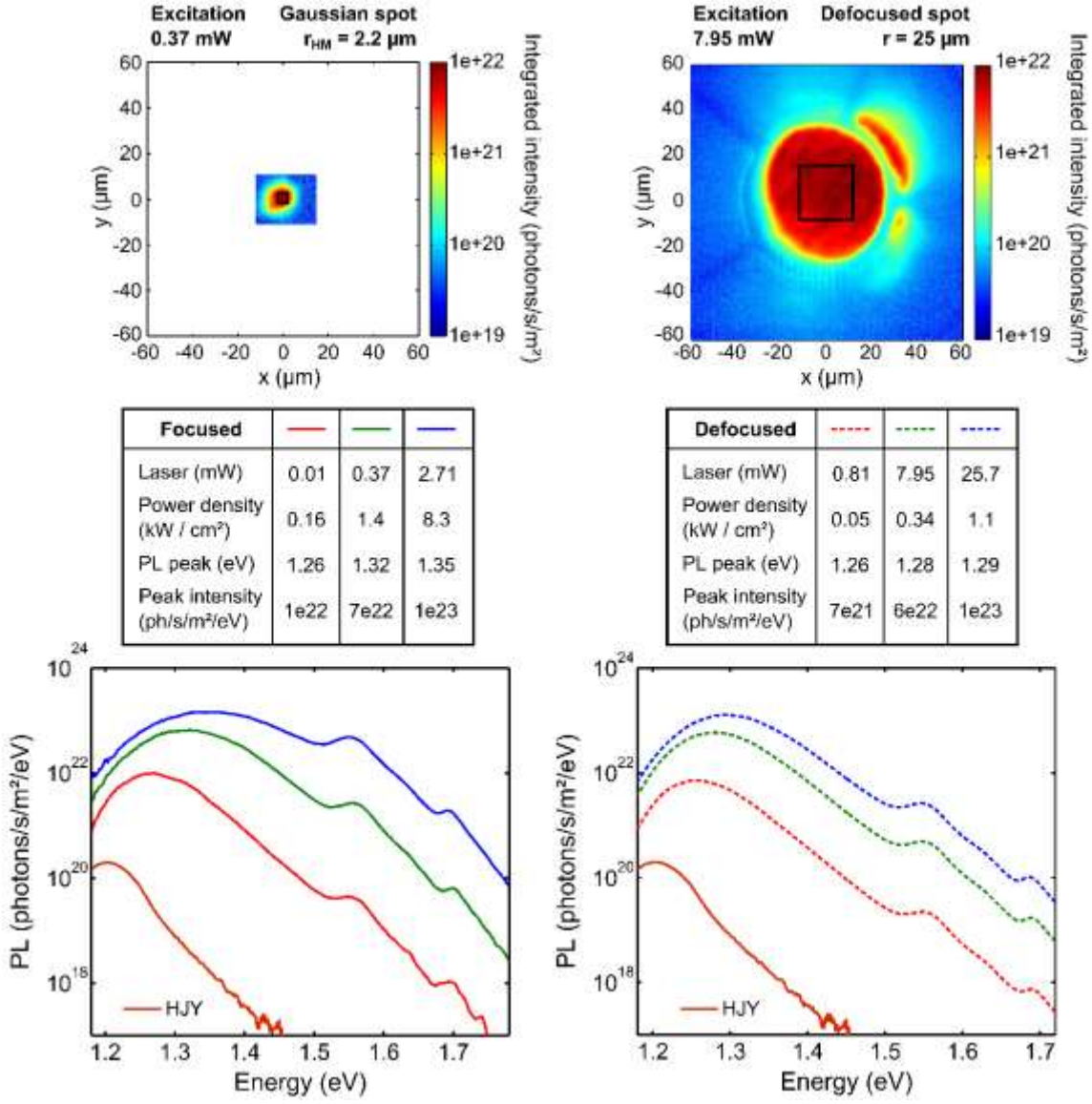

Figure 4.2-3: Comparison of hyperspectral imager calibrated PL characterization for two different settings. Focused laser excitation (left) as in the case of the previous investigation. Defocused laser excitation (right) as in the dual-beam study that we investigated here. PL spot images are shown for medium excitation: (left) focused laser excitation of 0.37 mW with half-maximum PL radius of 2.2 µm and (right) defocused laser excitation of 7.95 mW with half-maximum PL radius of 25 µm. Both images have the same *xy* scale and same color bar representing the spectrally integrated PL intensity. Tables summarize information regarding the excitation regime and PL peak position and intensity for PL spectrum that are taken by spatially integrating pixels from the black square area in the center of each spot. Very low excitation PL obtained with the Horiba Jobin-Yvon (HJY) setup is shown as a comparison.

Overall, it means that in the case of defocused characterization, the radiative ratio is improved as illustrated in Figure 4.2-5. This is understandable because for defocused spot, the spot area is more than a hundred time larger. If we consider an electron diffusion length *L* of 3 µm, it means that for the focused spot (r=2.2 µm at 0.37 mW excitation), 100% of the illuminated area can diffuse to an off-spot region which is in the dark and presents a high source of recombination rate. In the case of the defocused spot (r=25 µm), about 20% (five times less) of the illuminated area can diffuse to an off-spot region ($1-[1-L/r]^2$). In this sense, it seems logical that the radiative ratio is improved with a larger illumination spot.

However we notice that the QDs filling of energy states follows the excitation regime indicated by the global "electrical" power density independently from the PL peak intensity. We also observed the same phenomenon previously when analysing different areas of the focused spot. In other words, it means that PL intensity flux can be different for the same carrier occupation of QDs in energy.

It might be understandable if we think that the radiation is the result of two populations of carriers: electrons and holes. As we explained before, in self-assembled In(Ga)As QDs, holes are less confined and are assumed to play a dominant role in the carrier escape from QDs. Therefore, holes might be extracted faster than electrons. In the literature of In(Ga)As self-assembled QDs for IBSCs, the different roles of holes and electrons have been discussed [179], [188], [245]. For their InAs/$GaAs_{1-x}Sb_x$ QD-IBSC, Sellers et al. notice two different activation energies by Arrhenius fitting of temperature dependent PL. They associate them to the binding energy of the exciton (25 meV) and the strong electron confinement in the conduction band (141 meV) [188]. The rapid decrease in PL intensity is attributed to the breaking of the exciton and hole delocalization along with electron tunneling via Fowle-Nordhiem (FN) [248] or defect mediated processes [187]. Creti et al. investigation of InAs/GaAs system seems to indicate that hole escape via phonon assisted tunneling might start for temperature higher than 60 K while electron escape will start from 200 K [245]. They also notice two different activation energies depending on temperature. They consider that smaller QD activation energy value (a dozen of meV close to LO phonon energy) at a low temperature might be attributed to the thermally assisted escape of the less confined holes. The larger QD activation energy (hundreds of meV) is believed to correspond to the electron barrier. Very recently, they have also investigated InAs/$Al_{0.17}GaAs$ system confirming the different roles of carriers. They found that QDs do not contribute to the photocurrent generation up to 100 K since carriers are better confined and spectral structuring of the photocurrent contribution from QD states becomes relevant starting from 150 K [179]. It is interesting to notice that these values in temperature corresponds well with the results we present in chapter 3 for the PL temperature dependent characterization (3.3.1.1).

In addition, for $Al_{0.2}GaAs$ material, the mobility and diffusion of holes is usually reduced compared to electrons. It means that the local density of holes will decrease faster than the local density of electrons as illustrated in Figure 4.2-4. In this case, PL spot would be limited by the diffusion of holes. This trend would indicate the absence of an ambipolar diffusion. In most crystalline semiconductors, photoexcited electron-hole pairs tend to diffuse together with an intermediate diffusivity due to the Coulombic interaction between them. Here, instead, the charge separation and the emergence of a spatial distribution of net charges have been predicted to happen in so-called "relaxation semiconductors" [249], [250], including most wide-gap crystalline semiconductors and

amorphous semiconductors as demonstrated recently by scanning ultrafast electron microscopy [251]. In this sense, QDs from the center to the edge of the PL spot would have about the same occupation rate for electrons but occupation rate for holes would decrease faster inducing more non-radiative recombination, especially for example in the case of QDs near the edge.

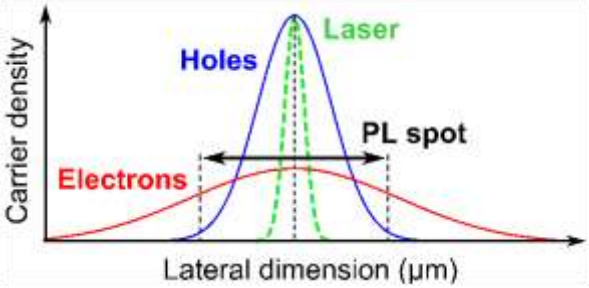

Figure 4.2-4: Schematic representation of lateral carrier density for holes (blue) and electrons (red) in our QDSC from a Gaussian laser excitation (green). The PL spot follows the hole profile for which the electron density is almost constant.

In the generalised Planck's law, there are two terms related to quasi-Fermi level (QFL) of electrons and holes. The Bose-Einstein (BE) distribution reflecting the radiation and the Fermi-Dirac (FD) distribution reflecting the carrier occupation. In the FD distribution, if we assume that most of the transition energy is due to the occupation of electron states (holes are less confined) we can neglect the occupation of holes. Thus, the variation of holes QFL will have a negligible impact on the PL peak shift. However, even a small variation of the QFL of holes will have a non-negligible impact on the PL intensity because of the exponential dependence in the BE distribution of the radiation. Previously we saw that the high-energy tail variation is mostly due to the increase of carrier temperature. We consider this temperature increase to be due to high carrier density. This approach of two populations would makes us consider that electrons alone are responsible for this temperature increase.

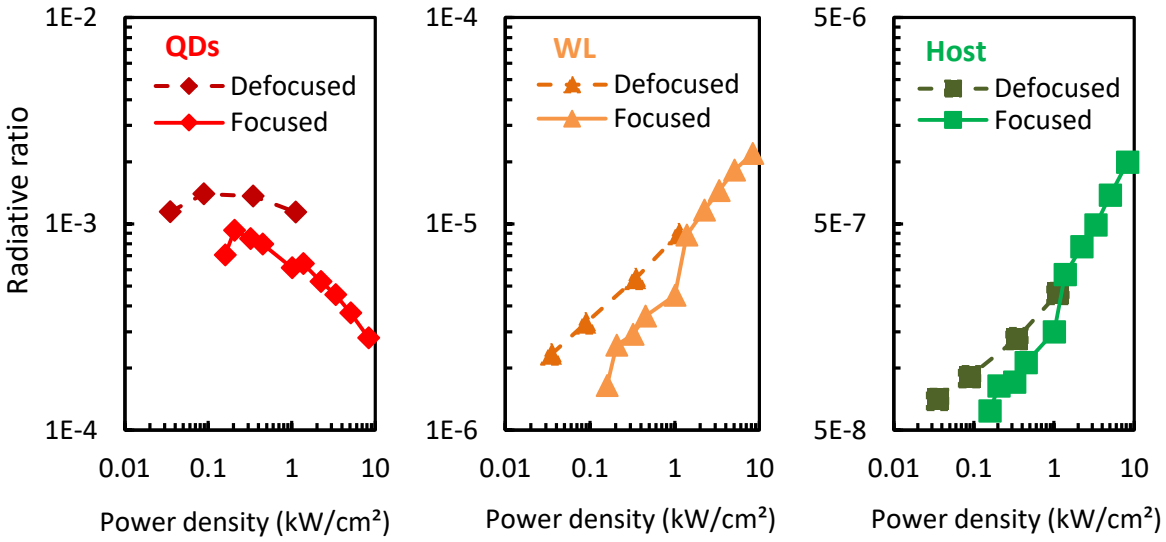

Figure 4.2-5: Comparison of radiative ratio for calibrated PL with focused (solid lines) and defocused (dashed lines) configuration for the three spectral domain of interest: QDs, WL and host material.

Anyhow, in the case of defocused characterization, power density of 0.05-1.1 kW/cm² are studied. In term of excitation power density, we are in the same regime as the low-excitation regime

(< 0.2 mW) studied earlier with the focused spot. For this regime, QDs ensemble is in equilibrium, carrier temperature is close to room temperature and the carrier populations in the wetting layer (WL) and host material are still much linked to the filling of QDs states.

In Figure 4.2-6, we show the optical I-V curve for the defocused characterization. We find a slight sublinear trend for QDs indicating saturation behavior. For WL and host material, both have the same ideality of 1.4 indicating that the population is transitioning from a linear to a superlinear behavior. However, carrier population density in the host material is not enough to show a higher ideality than WL as in the high-excitation case for defocused study.

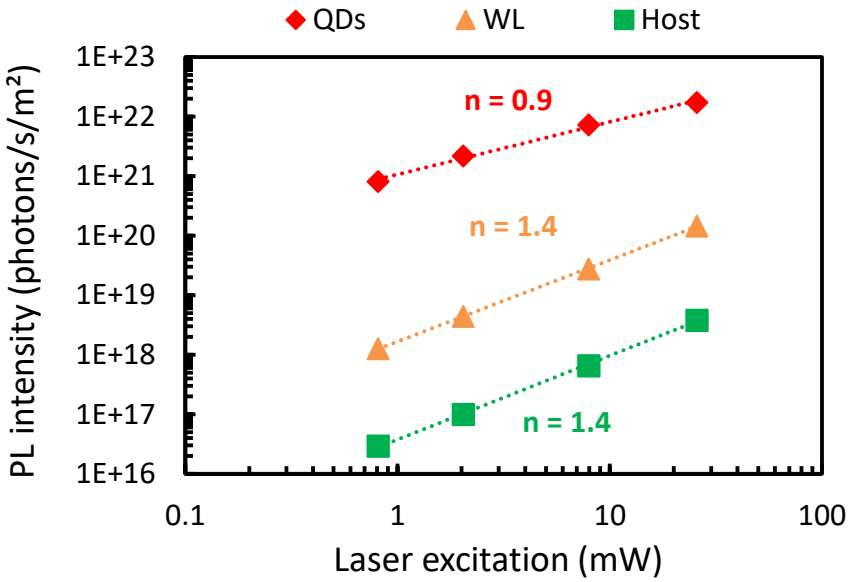

Figure 4.2-6: Optical I-V curve for defocused PL calibrated characterization. PL intensity is spatially integrated in the center black square zone, and the PL is spectrally integrated for the three spectral domains of interest (QDs, WL and host material). From the slopes we find idealities of 0.9 for QDs and 1.4 for WL and host material.

4.2.2.2 Two-color excitation photoluminescence

Now that we know better about the 532 nm laser excitation regime, we investigate the effect of the second 1550 nm laser excitation. In Figure 4.2-7 top left, we present the log-scale PL spectrum for a minimum excitation of 532 nm laser (0.81 mW) with IR : OFF and IR : ON with two different excitations for the 1550 nm laser: 14.3 mW and 48.6 mW. PL is also shown in linear plot for the three spectral domains of interest: QDs, WL and host material. We can see two different kinds of behavior. For QDs and WL domains, there is a quenching of PL by IR pump while in the case of the host material, there seems to be a slight increase in PL.

We also notice QDs, WL and host material PL peak are slightly shifted to lower energy for IR : ON. We attribute this shift to heating induce by the IR pump. For the host material PL peak, the shift is of about -0.3 meV for 14.3 mW excitation and -1 meV for 48.6 mW. Using Varshni equation, we find that it is equivalent to respectively +0.7°C and +2.3°C increase of the temperature for $Al_{0.2}GaAs$. It would amount to a thermal resistivity of about 0.05 °C/mW. In the literature, we find that $Al_{0.2}GaAs$ thermal conductivity is around 20 mW/mm/°C. Therefore, in term of heat dissipation, we calculate a ratio of the cross-sectional area over the length of the material (in the heat flux direction) of about 1 mm, which is a typical length for our solar cell in term of diameter and total thickness including the GaAs substrate. A more detailed investigation would be needed but a shift in energy due to IR heating is not unrealistic.

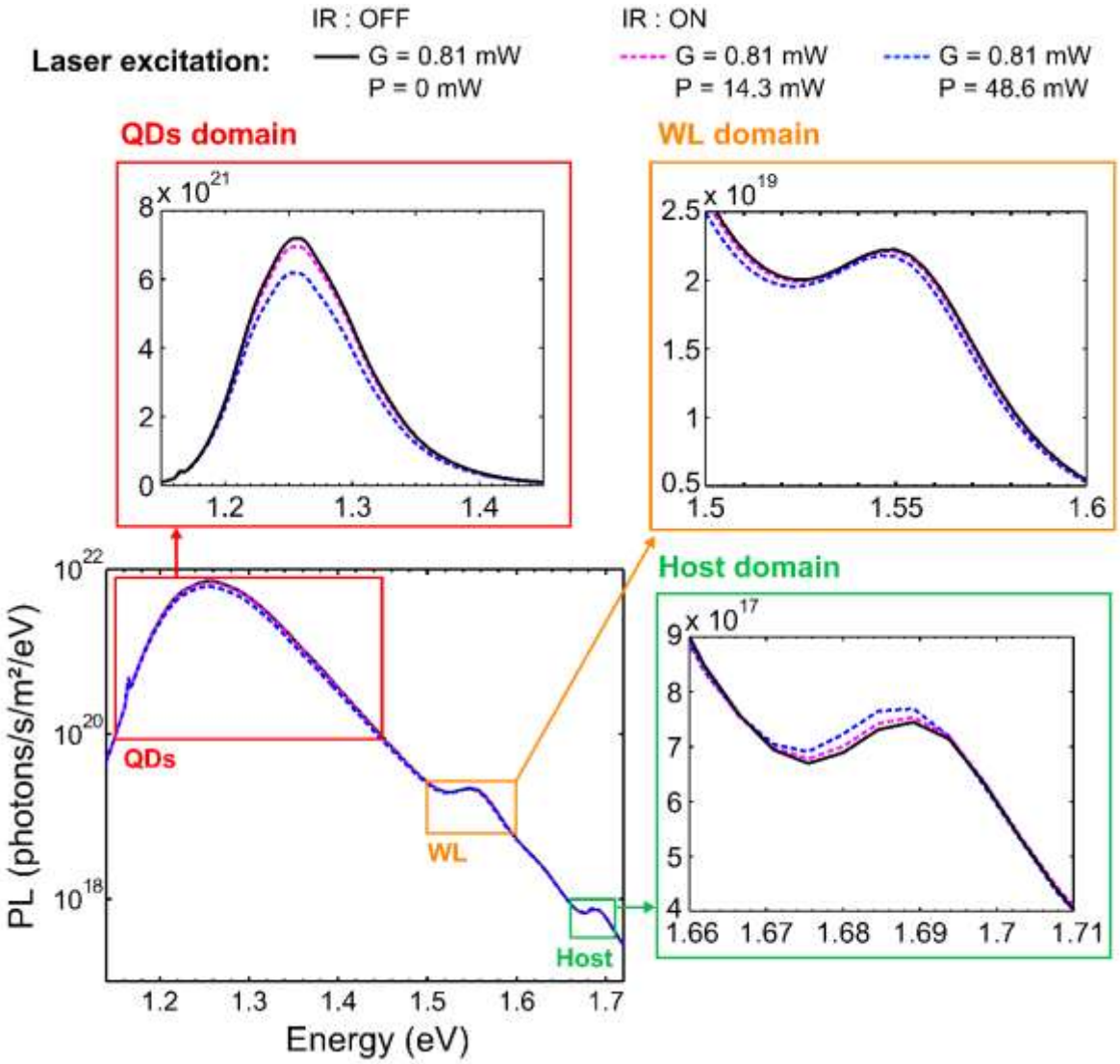

Figure 4.2-7: PL spectrum log plot for a 532 nm laser excitation (G) of 0.81 mW with three different values of IR pump: P = 0 mW (black solid line), P = 14.3 mW (pink dashed line) and P = 48.6 mW (blue dashed line). Zoom are shown in linear plot for QDs domain (red), WL domain (orange) and host material domain (green).

4.2.2.3 Photoluminescence IR pump ON/OFF ratio

We express the PL quenching or increase using Equation 4.2-1.

$$\frac{\Delta PL}{PL} = \frac{PL_{IR:ON} - PL_{IR:OFF}}{PL_{IR:OFF}}$$

Equation 4.2-1: Expression of the photoluminescence ON/OFF ratio

First, we investigate the ΔPL ratio evolution with increasing the 532 nm laser excitation (G) for a fixed IR pump as illustrated in Figure 4.2-8. On the left, we present the ΔPL ratio for the PL raw data. On the right, we express the same ratio but with a +1 meV shift correction on PL IR : ON that was attributed to IR laser heating.

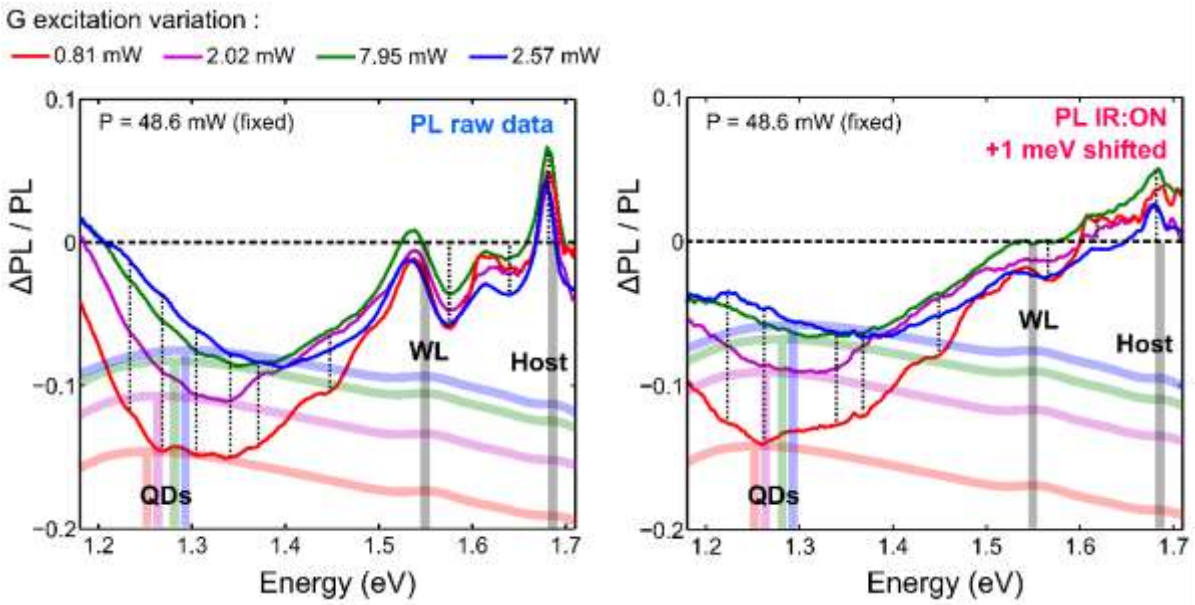

Figure 4.2-8: ΔPL ratio evolution with increasing the 532 nm laser excitation (G) for a fixed IR pump (P). On the left, the ratio is presented for PL raw data and on the right with a +1 meV shift correction on PL IR : ON that is attributed to IR laser heating. PL spectrul IR : OFF are arbitrarly positioned in the background as an guide for the eye. Different bands of colors represent the position of QDs PL peaks for different excitation regimes. Grey bands are also positioned at WL and host material PL peaks energy positions. Dotted black lines are underlining local maxima.

For the PL raw data on the left, we clearly notice the three spectral domains: QDs, WL and host material. Overall, PL quenching in the QDs decreases for higher G. However, it becomes more pronounced for QDs high-energy states and in the WL region. For all excitations, we notice an increase of PL in the host material domain and in low-energy QDs for high excitation.

For the ΔPL ratio with +1 meV shift correction on PL IR : ON, we see that the ratio is more flat for low-energy QDs and curves are smoother between the different spectral domains. It is difficult to find an optimum way to correct the PL data because the PL peak shift is not exactly the same for QDs, WL and host material. Anyhow we see the same trend with a decrease of PL quenching for higher excitation and a PL increase for host material domain.

In Figure 4.2-9, we also present the variation with an increase of IR excitation from 14.3 mW to 48.6 mW for different G: 0.81 mW on the left and 2.02 mW on the right. Data are presented with PL shift correction of +1 meV for 48.6 mW and +0.3 meV for 14.3 mW.

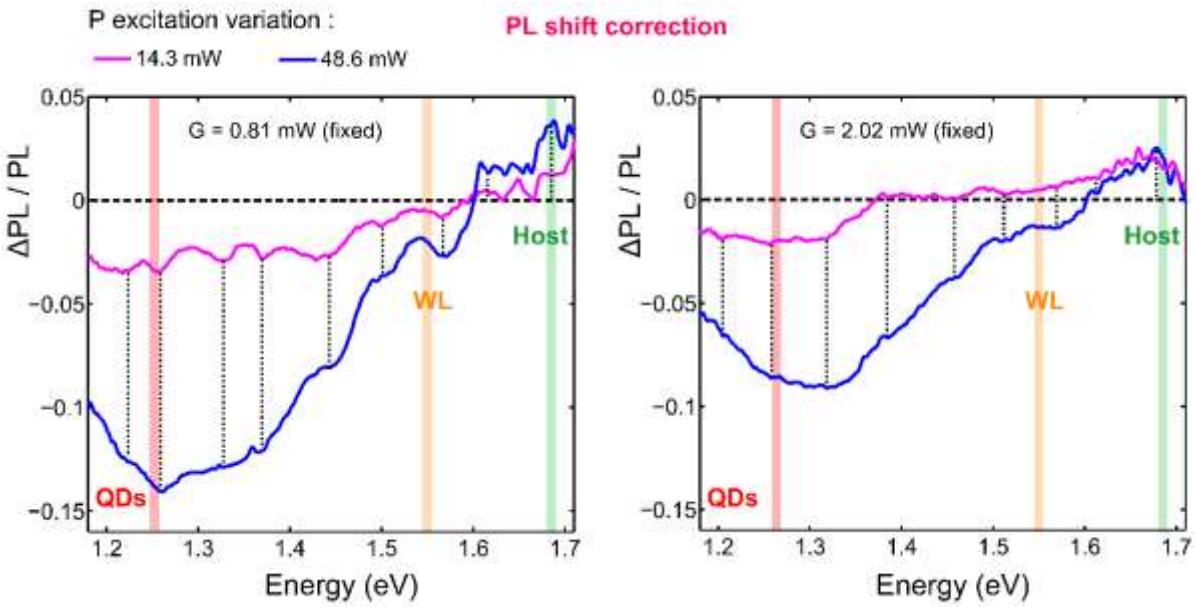

Figure 4.2-9: ΔPL ratio evolution with increasing IR excitation for fixed G excitation of 0.81 mW (left) and 2.02 mW (right). Color bands show PL peaks for the three spectral domains: QDs (red), WL (orange) and host material (green). Data are presented with PL shift correction for IR : ON PL with +1 meV in the case of 48.6 mW and +0.3 meV for 14.3 mW. Dotted black lines are underlining local maxima.

We notice that PL quenching in QDs and WL is increasing with IR excitation. For 0.81 mW G excitation, we observe a host material PL increases with IR excitation but for 2.02 mW, it is not so clear. Overall, in the host material domain, we clearly see an increase of PL but we find it difficult to detect a trend with variation of G or P. It might be because PL signal is low and noisy for energies higher than 1.72 eV. In addition, the effect of the shift with IR pump is pertubating the analysis.

Anyhow, we believe the two-color excitation characterization is proving that sequential two-photon absorption (S-TPA) would be possible for a large domain in energy for QDs and WL states. We see this measurement as a way to probe the electrical filling of energy states. In Figure 4.2-8 and in Figure 4.2-9, we see that the maximum of PL quenching in the QDs is always at an energy a slightly higher than the PL peak position. It might be due to the fact that it is the energy position with the highest density of carriers inside the QDs. At best, we observe a decrease of 15% of the PL inside QDs and an increase of 5% in the host material domain.

By integrating experimental PL spectrum in the host material spectral domain (1.67-1.72 eV), we obtain an increase of 3% with the addition of the IR laser. This increase could corresponds to an increase of the photogenerated current that would be collected directly from the host material (ΔJ_{sc}). By applying Equation 4.2-2, for an ideality in the host material of 1.4, we find that a +3% (x1.03) on current amount to +1 mV on the V_{oc}.

$$\Delta V_{oc} = n_{host} k_B T \ln(\Delta J_{sc})$$

Equation 4.2-2: Gain on the V_{oc} in function of the gain on the current J_{sc} and ideality n_{host}

Using generalized Planck's law, by fitting PL spectrum IR : OFF and IR : ON we also estimate that the difference in PL intensity amounts to a gain of +1 meV on the QFLS.

In Figure 4.2-10, we summarize the ΔPL ratio that are calculated by integrating experimental PL spectra in the QDs-WL (1.18-1.67 eV) and host material (1.67-1.72 eV) spectral domains for different excitations of the 532 nm laser. We also plot the mean values of ΔPL ratio for QDs-WL and host material specral domains. In the next part, we will present a simple method to model the dynamic for an intermediate band (IB).

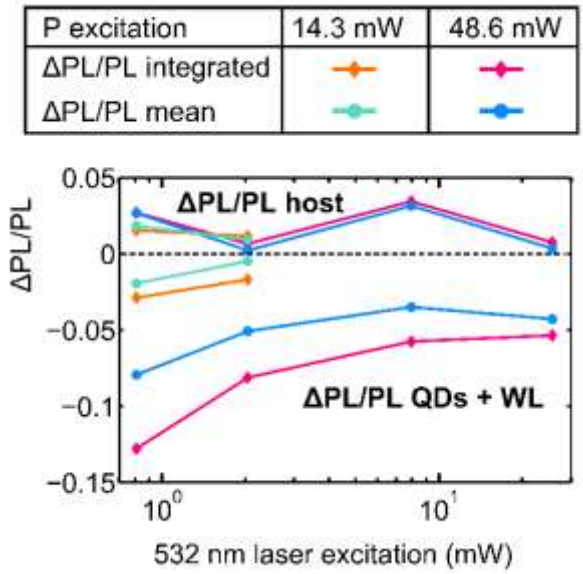

Figure 4.2-10: ΔPL ratio that are calculated by integrating experimental PL spectrum (diamonds) or taking the mean value (full circle) in the QDs-WL (1.18-1.67 eV) and host material (1.67-1.72 eV) spectral domains for different excitation of the 532 nm laser in the *x*-axis and for P excitation of 14.3 mW (orange and turquoise) or 48.6 mW (blue and pink).

4.2.3 Steady-state rate equation model

In the previous part, we showed that a second step absorption effect is possible for QDs or WL energy states due to IR excitation pumping with a 1550 nm laser. In this part, we will describe a simple steady-state rate equation model and use it to compare with our experimental results. In a last part, we will discuss about the impact of non-radiative recombination in our system.

4.2.3.1 Description

We consider a classic IBSC system with an intermediate band (IB) in-between a valence band (VB) and a conduction band (CB) as described in Figure 4.2-11. Electron filling of the system is ensured by G channel expressing the generated electrons originated from VB to CB by absorption of high-energy photons (532 nm laser). Different time constants are considered to represent the exchange of population between CB and VB (τ_C), between CB and IB (τ_{CI}) and between IB and VB (τ_I). Finally, the IR pump (P) allows the second generation of electrons from IB to CB.

To model this dynamic system, phenomenological rate equations can be used to describe the populations of electrons in CB (n_C) and IB (n_I), as expressed in Equation 4.2-3 [220], [252]. We suppose electron population of VB does not play an important role and is assumed to be non-limitative. It is consistent with the approach of holes being less confined than electrons in In(Ga)As self-assembled QD systems. These equations include the slowing of intermediate states filling by considering a maximum density of states D_I expressed in the same way as a Pauli blocking factor. In addition, we underline that the second step absorption of IR photons also depends on the filling of the IB. P ex-

presses the channel of electrons generated by the absorption of IR photons from the IB with P_{max} representing a maximum generation in case of total filling. We suppose that the hole population in CB is infinite. Finally, for continuous-wave (CW) PL we consider that populations reach a certain equilibrium and therefore the system is in a steady state and the partial derivative with respect to time is zero.

$$\textbf{\textit{CB balance}}: \quad \frac{\partial n_C}{\partial t} = G + P - \left[\frac{n_C}{\tau_C} + \frac{n_C}{\tau_{CI}}\left(1 - \frac{n_I}{D_I}\right)\right] = 0$$

$$\textbf{\textit{IB balance}}: \quad \frac{\partial n_I}{\partial t} = \frac{n_C}{\tau_{CI}}\left(1 - \frac{n_I}{D_I}\right) - \left[\frac{n_I}{\tau_I} + P\right] = 0$$

$$with \qquad P = P_{max}\frac{n_I}{D_I}$$

Equation 4.2-3: CB and IB balance define steady-state rate equations ruling the dynamic of two-color excitation PL

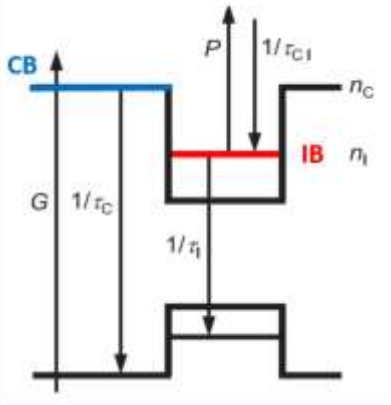

Figure 4.2-11: Schematic of rate equation model adapted from [220].

Time constants are supposed constants between IR : OFF and IR : ON. G and P_{max}, expressed in number of electrons per second and per unit of volume are calculated following Equation 4.2-4.

$$G = \frac{\phi_{532nm}}{t} Abs_{532nm}$$

$$P_{max} = \frac{\phi_{1550nm}}{t} Abs_{1550nm}$$

Equation 4.2-4: Electron generation per seconds and per unit of volume for the two channels of electron generations. G and P_{max} depend on the laser flux and the absorptivity at each considered wavelength normalized by the thickness t.

G and P_{max} depend on the laser flux ϕ_i and the absorptivity Abs_i at each considered wavelength normalized by the thickness t of the semiconductor junction. In Table 3.1-1, we present the parameters that are used in our model.

Table 4.2-1: Parameters used in the steady-state rate equation model

Fixed parameters	Values from exp	Fixed parameters	Values from exp	Variables	Fitted
ϕ_{532nm} (photons/s/m²)	[1e24 → 4e25]	Abs_{532nm} (%)	53	Abs_{1550nm} (%)	0.1
ϕ_{1550nm}(photons/s/m²)	[6e25 → 2e26]	D_I (electrons/m³)	2e22	τ_C (ps)	20
t (nm)	475	τ_I (ns)	8	τ_{IC} (ps)	100

4.2.3.2 Comparison with experiment

Nine parameters are needed in our simulation but six are fixed and taken from experimental findings. For the two photons fluxes, we use laser excitations powers measured and normalized by the PL spots areas. We consider a 475 nm thickness (t) that is equal to the junction without the two 20 nm-thick $Al_{0.4}GaAs$ front and back surface field layers. Value of absorptivity at 532 nm is taken from EQE measured at reverse bias and confirmed by calculation. The density of states D_I of 2e22 electrons/m^3 is calculated by considering 2 electrons per QDs for 10 layers with QDs surface density

of 700 QDs/µm² measured by AFM for the considered thickness of 475 nm. The τ_I time constant was measured by TRPL and is typically around 8 ns at room temperature. The three other parameters are fixed at reasonable values to fit our experimental findings.

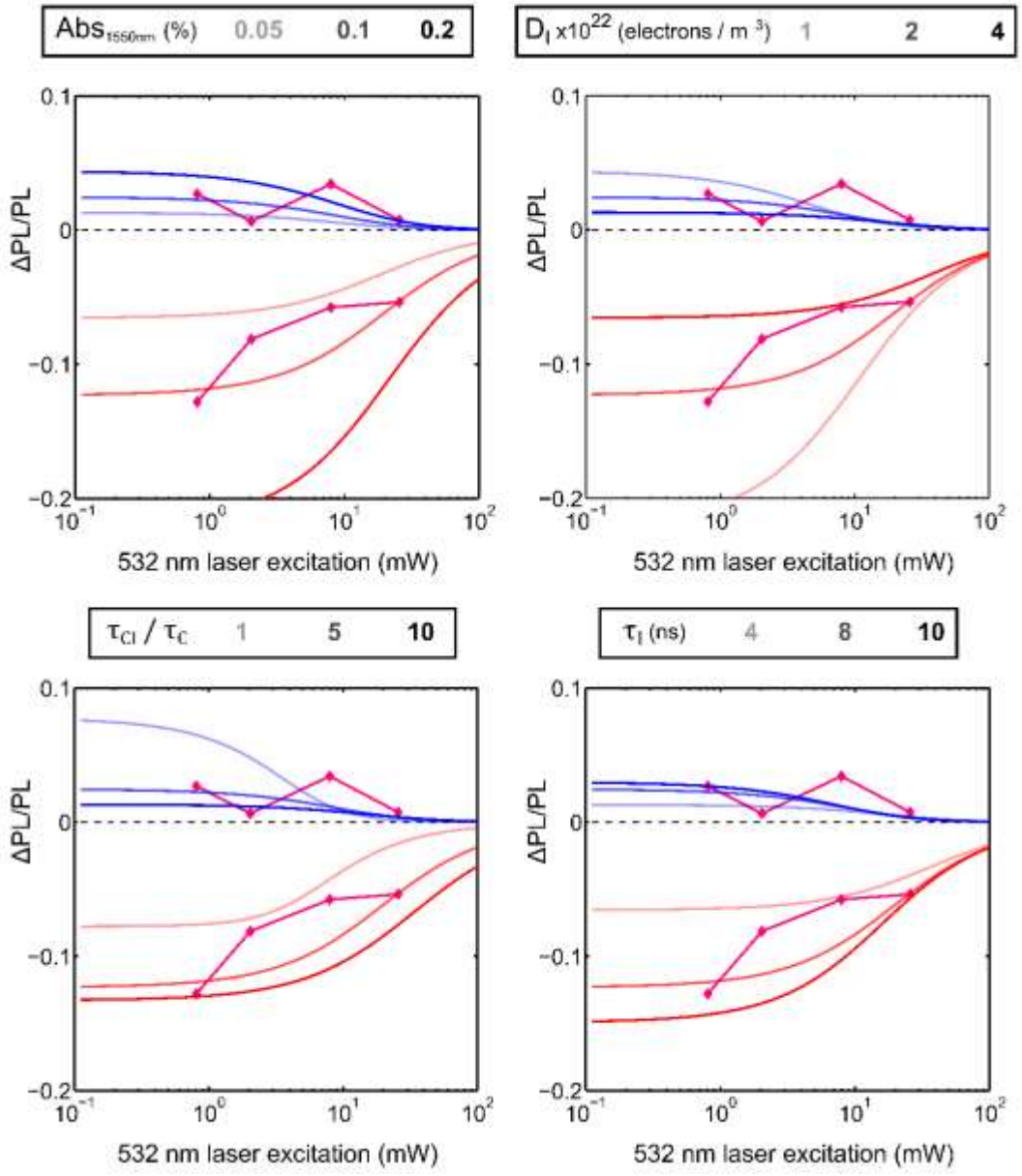

Figure 4.2-12: Comparison of ΔPL ratio integrated from experiment (pink diamonds) with our model. ΔPL ratio for QDs-WL domain are presented in red while ΔPL ratio for host materia domain are in blue. We show the variation of four parameters around the fixed values presented in Table 4.2-1. Only one parameter is changed at a time: Abs_{1550nm}, D_I, τ_I and the ratio of τ_{CI} over τ_C. For increased value of the parameter the color intensity is increased.

We simulate the ΔPL ratio using expressions of Equation 4.2-5 and compare with our experiment. We make the assumption that radiative time constant are the same for IR : OFF and IR : ON excitations.

$$\left(\frac{\Delta PL}{PL}\right)_{model:\,QDs+WL} = \frac{n_{I-IR:ON} - n_{I-IR:OFF}}{n_{I-IR:OFF}}$$
$$\left(\frac{\Delta PL}{PL}\right)_{model:\,host} = \frac{n_{C-IR:ON} - n_{C-IR:OFF}}{n_{C-IR:OFF}}$$

Equation 4.2-5: Expression used to calculate ΔPL ratio from our model

An absorptivity of 0.1% at 1550 nm is of the same order of magnitude as the VB to IB absorption measured by EQE. In k·p calculation we found a lower value but we did not calculate all possible transitions with electron states in the continuum. By optical characterization, at 1550 nm in wavelength, using Fabry-Pérot interferometry technique, we could not detect a difference in absorption for Okd-5 sample with 20 QDs layers and the Al0.2GaAs reference samples. However, we performed the measurement with a very low excitation compared to the ΔPL study. We used a halogen source that is at best around 1-sun excitation. It would be interesting to measure the absorption in this energy region for a higher excitation and therefore a higher level of filling of QDs states. The τ_C and τ_{CI} time constants are found to be respectively of 20 ps and 100 ps, which is about x100 faster than QDs to VB transition (τ_I). In the literature, values on the order of the hundreds of picoseconds are often estimated for the τ_{CI} time constants [220]. The very fast τ_C time constant is due to non-radiative recombinations that would mostly be the result of a high defects density that we already pointed out in many parts of our study.

In Figure 4.2-12, we compare our model with the integrated ΔPL ratio for different G excitations as already presented in Figure 4.2-10. The modeled ratio with fixed parameters of Table 4.2-1 are presented with some variations. We find that an increase of absorptivity at 1550 nm and equivalently an increase of P excitation lead to an increase of the ΔPL ratio in absolute value both for QDs-WL domain and host material domain. On the other hand, increasing the density of states or increasing the filling through an increase of G results in a decrease of the ΔPL effect. Regarding time constants, we find that the variation of τ_{CI} and τ_C are linked. Only the ratio of both constants matters. Both time constants correspond to loss channels for the CB carrier population. For a longer τ_{CI}, we notice that the ΔPL quenching is more important in the QDs but ΔPL increase is reduced in the CB. On the contrary, for a longer τ_C, ΔPL quenching is reduced in the QDs but increase for the CB. Finally, we also notice that a higher time constant for IB to VB (τ_I) is favorable to ΔPL quenching and increase in the CB.

Overall, the model does not allow us to find a very good agreement with our experimental values. This might be because we consider only one level while there are many levels with different densities of states and different time constants. They all communicate with each other with different steady-state rate equations. A more detailed model would be needed but we did not want to go further in this direction due to the rapid complexification related to the introduction of numerous parameters for each level.

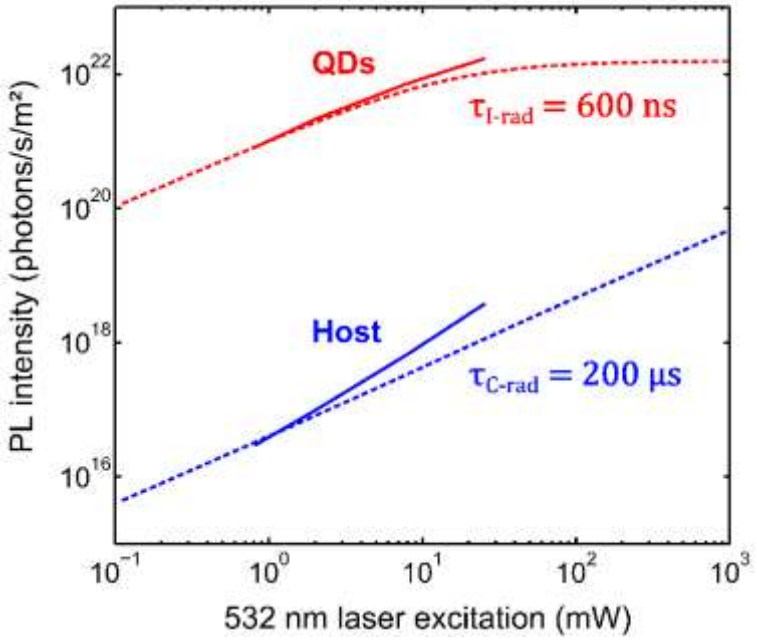

Figure 4.2-13: Comparison of experimental variation of PL intensity for variying 532 nm laser excitation (solid lines) with modeled PL intensity (dashed lines) calculated using radiative time constans indicated in the figure for the different spectral domain or bands of interest respectively QDs or IB (red) and host or CB (blue).

The model enables us to find the density of carriers for each population wether in the CB or the IB. We can therefore relate with PL intensity measurements presented in Figure 4.2-6. In Figure 4.2-13, we show a comparison with our model using fixed parameters from Table 4.2-1. To adjust the level of intensity we suppose a time constant of 600 ns for IB to VB radiative recombination and 200 µs for CB to VB radiative recombination. These radiative time constants can also be found by using radiative ratio calculated earlier.

This model allows us to explain qualitatively the ΔPL effect that we observe experimentally. We understand the dynamic of the IB and we see how important it is to have a high quality host material with low non-radiative recombinations. Most of the PL quenching does not participate in an increase of carrier population in the host material because of non-radiative recombination. For the same order of non-radiative recombination in the QDs and host material, the quenching of QDs PL would amount to a large increase of the V_{oc}. We see that this is a big issue for quantum dot solar cells (QDSCs), we suppose it might be because of the limitation of growing low temperature (480°C) $Al_{0.2}GaAs$ spacing layers to prevent the collapse of In(Ga)As QDs.

4.3 Potential of a hot carrier thermally activated QD-IBSC or IB-HCSC

In this part, we summarize the result that we found in this chapter on the dynamic of the intermediate band (IB) and we put them in perspective for achieving high-efficiency quantum dot intermediate band solar cells (QD-IBSCs). At first, we demonstrated a hot carrier effect triggering the apparition of separated QFLs for the thermally activated IB population (quantum states) and the conduction band (CB) population (host material). In a second part, we demonstrated that IR photons can enhance the CB population by second step generation of carriers from the IB.

As we discussed earlier, the hot carrier effect in quantum dot solar cells (QDSCs) has been discussed in the literature over the last decade. The principle of low-dimensional hot carrier solar cells (LD-HCSCs) using In(Ga)As QDs has been recently underlined by Kita Laboratory [207] with the idea of evaluating the potential of converting efficiently the solar spectrum for PV application. In the same sense, an intermediate band assisted hot carrier solar cell (IB-HCSC) has been proposed recently in order to help the extraction of hot carriers from an absorber that has an IB [18].

4.3.1 IB-CB QFL splittings

In the first part of this chapter, we were able to demonstrate that, under certain conditions of illumination, a hot carrier effect triggers the apparition of separated quasi-Fermi levels (QFLs) for the IB population and CB population. For simplification, we assume that the hole population in the IB and VB have the same QFL because QDs confinement is limited in the VB. The activation energy is a barrier energy of $E_a \sim 250$ meV. Hole is a limitative population for PL as we explained by spatial investigation study of PL spot and comparison of focused and defocused PL. In Figure 4.3-1, we schematize the results that were presented in Figure 4.1-35. We plot the evolution of temperatures (left) and QFL (right) for carrier populations inside the IB (red) and CB (blue) for increasing illumination concentration in number of suns. Activation energy of 250 meV is related to temperature increase in the IB starting around 10k suns. For the same illumination and beyond, the CB has an ideality of n=1.5 while the IB QFL remains almost flat.

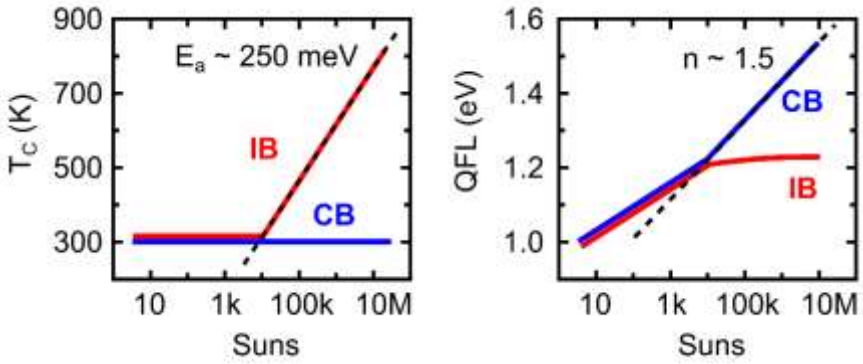

Figure 4.3-1: Scheme of Figure 4.1-35. Evolution of temperatures (left) and QFL (right) for carrier populations inside the IB (red) and CB (blue) for increasing illumination concentration in number of suns. Activation energy of 250 meV is related to temperature increase in the IB starting around 10k suns. For the same illumination and beyond, the CB has an ideality of n=1.5 while the IB QFL remains almost flat.

In the literature, demonstration of the operation principles of intermediate band solar cells at room temperature are made for low concentration PV operation, for example 390 suns in a recent paper

from Luque's group [23]. Li and Dagenais have recently developed a method to investigate the optical saturation of the on-resonance first photon transition to the intermediate band in InAs/GaAs QDs with ground state (GS) energy around 1.17 eV [253]. They found a QD saturation intensity as high as 10^6 W/cm² (about 1 M suns) for a sample with 40 QD layers and in-plane QD density around 3.8 10^{10}/cm², which is about the same as for Okd-3 samples. If we consider that our Okd-3 non-transferred sample (10 QD layer) has four times less QDs, the QD saturation intensity will be also four times less: around 250 k suns. This value seems not too far from Figure 4.3-1 schematic representation of the evolution of IB QFLs with incident power density.

The QFL behavior follows electron population but the energy value takes in consideration the QFL from hole population as we did not calculate separately QFL for electrons and holes during PL fitting with the generalized Planck's law.

4.3.2 Fermi-Dirac distribution inside QDs

In Figure 4.3-2, we represent the evolution of QFL FD distribution in LD-HCSCs. In (a) we represent a Fermi-Dirac (FD) distribution in energy with filling ratio in log scale. Logarithmic plot also evidences the change of slope due to temperature increase. From (b) to (d), we represent the evolution of FD distribution for increasing illumination. IB is formed by the juxtaposition of QDs with different sizes. The ground state (GS) and the electron filling are shown in red. The CB start with the wetting layer (WL) around 1.55 eV in blue and continue with the host material.

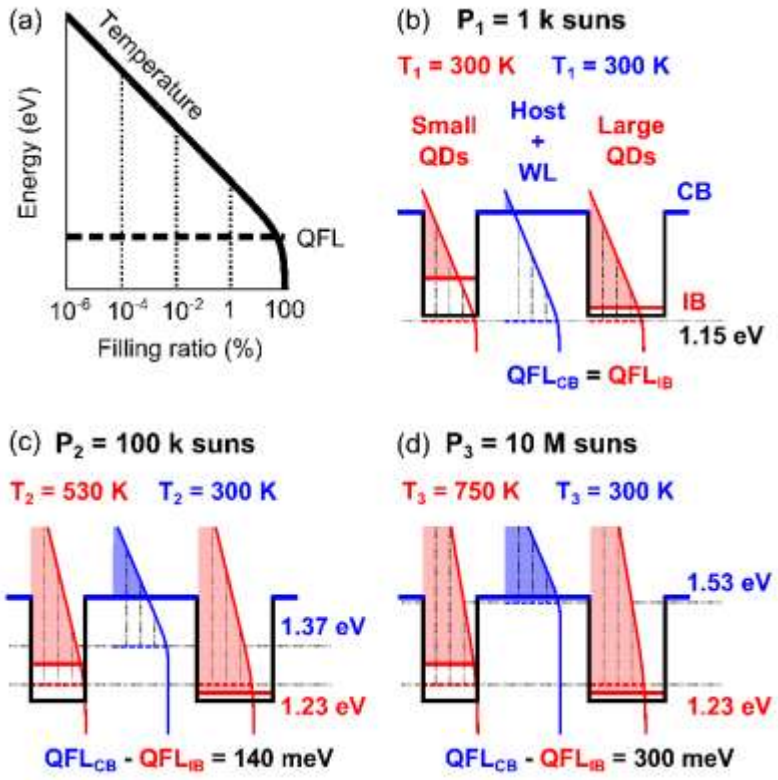

Figure 4.3-2: Scheme representing QFL distribution in LD-HCSCs. In (a) we represent a FD distribution in energy with filling ratio in log scale. From (b) to (d) we represent the evolution of FD distribution for increasing illumination. IB is formed by the juxtaposition of QDs with different sizes. The GS and the electron filling are shown in red. The CB start with the WL around 1.55 eV in blue and continue with the host material. In (b), for 1k suns, QFLs in the CB and IB are equal and carriers have the same temperature. Filling inside QDs is around 1% but it is less than 1e-6 % in the CB. In (c) and (d), we show the effect of hot carrier with a constant QFLs in the IB but an increasing QFL in the CB.

In (b), for 1 k suns, QFLs in the CB and IB are equal and carriers have the same temperature. Filling inside QDs is around 1% but it is less than 1e-6 % in the CB. In (c) and (d), we show the effect of bandfilling and hot carrier with a constant QFLs in the IB but an increasing QFL in the CB

4.3.3 Potential efficiency of a thermally activated QD-IBSC

We see that a LD-HCSC is equivalent to a thermally activated QD-IBSC with a hot carrier population. If we assume that most of the carrier population inside QDs can contribute to the extracted current, we can calculate the efficiency of such a solar cell for different illuminations like in reference [207]. In our case, in order to measure the potential of thermally activated QD-IBSC, we compare such QDSCs with the reference cell with no QDs. In Figure 4.3-3a, we show the evolution of QFLS with increase irradiation for our studied QDSC. Comparison (VOC@1 sun, ideality n) with low-quality reference solar cell without QDs (our lab, n=2) and high-quality Al0.2Ga0.8As solar cell (Fraunhofer ISE in 2015 [139], n=1) are shown. The arrows (i) and (ii) show possible improvements, for example by capping or doping. Insets show the evolution of carriers's temperature (T_C) following an Arrhenius' equation with activation energy (E_a) related to the barrier energy of holes (unipolar escape).

In Figure 4.3-3b, we show the impact of bandfilling on QDs absorptivity. The carrier Fermi-Dirac distributions are logarithmically plotted, as in Figure 4.3-2, to evidence the change of slope due to temperature. For a "cold" carrier population at an excitation of 100 k sun, we see that subbandgap absorption below 1.37 eV becomes impossible for VB to QD states due to bandfilling.

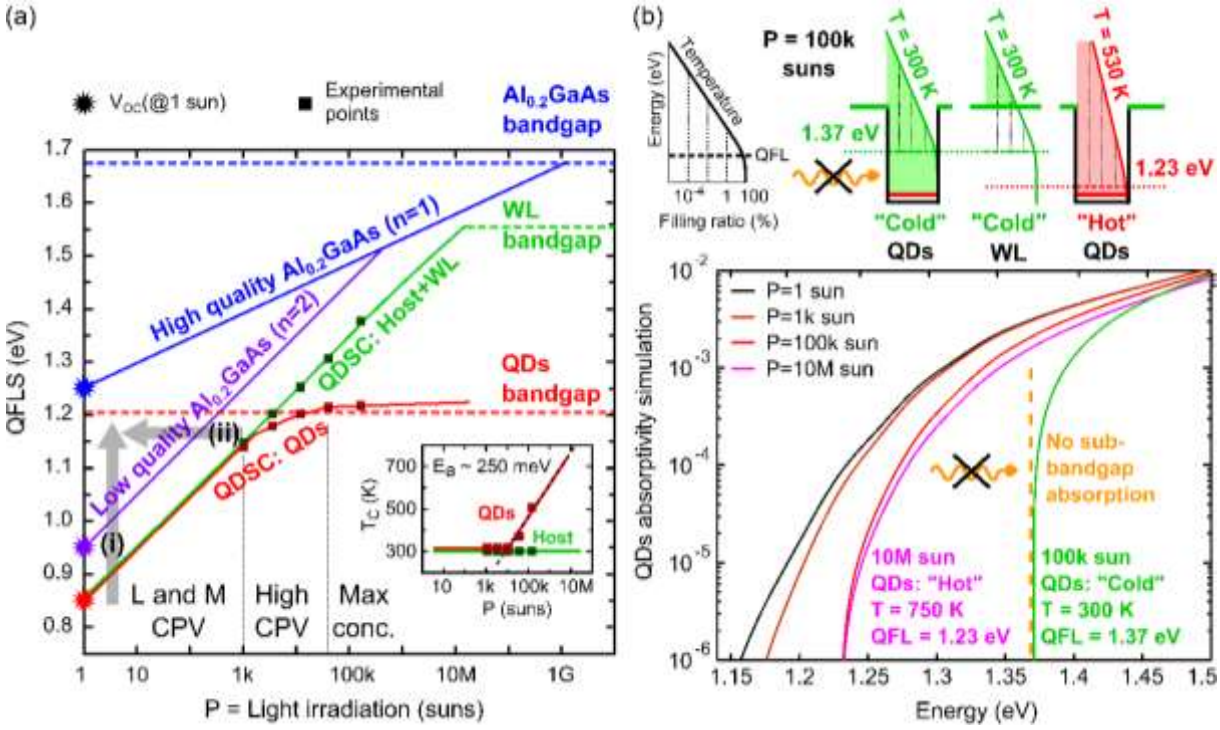

Figure 4.3-3: (a) Evolution of QFLS with increase irradiation for our studied QDSC. Comparison (VOC@1 sun, ideality n) with low-quality reference solar cell without QDs (our lab, n=2) and high-quality Al0.2Ga0.8As solar cell (Fraunhofer ISE in 2015, n=1) are shown. Arrows (i) and (ii) show possible improvements e.g. by capping or doping. Insets show the evolution of carrier temperature (TC) following an Arrhenius' equation with activation energy (E_a) related to barrier energy of holes (unipolar escape). (b) Impact of bandfilling on QDs absorptivity. Carrier Fermi-Dirac distributions are logarithmically plotted to evidence the change of slope due to temperature. For a "cold" carrier population at 100k sun, we see that subbandgap absorption below 1.37 eV becomes impossible for VB to QD states due to bandfilling.

From an IBSC point of view, the splitting in energy for IB QFL and CB QFL is fundamental and we see here that for "hot carriers" we can have such splitting and at the same time our two-color excitation experiment shows a high ratio of sequential two-photon absorption (S-TPA). In order to have high efficiency PV, we need to account for the intrinsic loss of V_{OC} compared with a single junction solar cell. We need to balance this loss with the gain in J_{SC} from S-TPA so that we can overcome SQ limit. By doing this calculation, we should be able to estimate the level of subbandgap absorption that is needed and therefore what type of QD structures we should grow or what level of light management we should reach.

In order to approach this issue, in Figure 4.3-4, we make a simple absorptivity calculation for Okd-3 (10 QD layers) non-transferred structure (red) for 300 K temperature and QFLS of 0.85 eV. We also show what it would be like for x10 (magenta), x20 (blue) or x40 (black) increase of absorptivity.

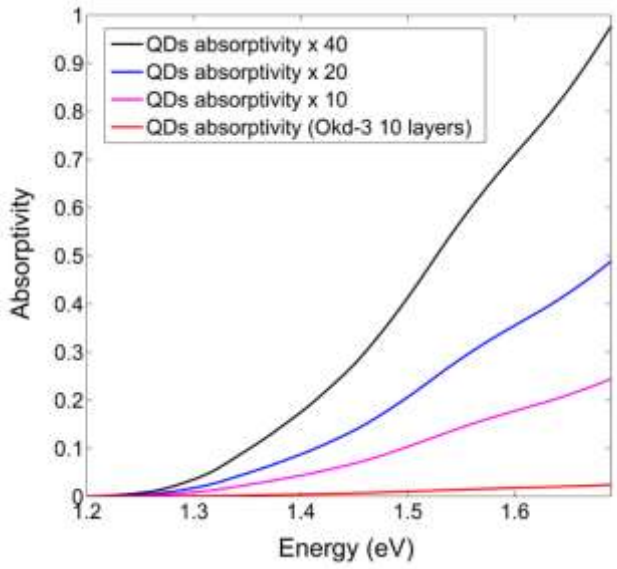

Figure 4.3-4: Absorptivity calculation for Okd-3 (10 QD layers) non-transferred structure (red) for 300 K temperature and QFLS of 0.85 eV. We also show what it would be like for x10 (magenta), x20 (blue) or x40 (black) increase of absorptivity.

From the absorptivity calculations, we make the approximation that all photogenerated carriers are extracted and contribute to the collected current. This way, we can calculate the short-circuit current obtained from QDs absorption for different temperatures and QFLS: $J_{SC-QDs}(T, \Delta\mu)$.

In order to compare the results in terms of PV efficiency, we calculate efficiencies and consider $Al_{0.2}GaAs$ Fraunhofer ISE 2015 simple junction solar cell record electrical parameters as a reference of a high-quality (Ref_HQ, blue) $Al_{0.2}GaAs$ solar cell: V_{OC}=1.25 V J_{SC}=15.8 mA/cm², *FF*=0.86 (1 sun illumination) [139]. For simplicity, we keep the same short-circuit current (J_{SC}) and fill factor (*FF*) parameters as ideal parameters for our low-quality laboratory $Al_{0.2}GaAs$ reference solar cell with no QDs and V_{OC}@1sun=0.95 V (Ref_LQ, purple). We also use the same J_{SC} and *FF* parameters for our QD-IBSC but we add the short-circuit current contribution from the QDs: $J_{SC-QDs}(T, \Delta\mu)$. In Figure 4.3-5, we distinguish the case of a "hot" (QD-IBSC_hot, red) or "cold" (QD-IBSC_300K, dashed green) carrier population which result in the energy splitting or no splitting of QFLs between IB and CB. We also show the influence of an increase of QDs absorptivity (x10, x20, and x40) to obtain higher efficiencies. The variation of efficiencies with illumination is calculated by taking the values

of V_{OC} from the values of QFLS as reported in Figure 4.3-3a, considering J_{SC} and *FF* are constants for Ref_HQ and Ref_LQ. *FF* is also supposed constant for QD-IBSC_hot and QD-IBSC_300K but $J_{SC-QDs}(T, \Delta\mu)$ is different in the case of "hot" and "cold" carriers as discussed in Figure 4.3-3b.

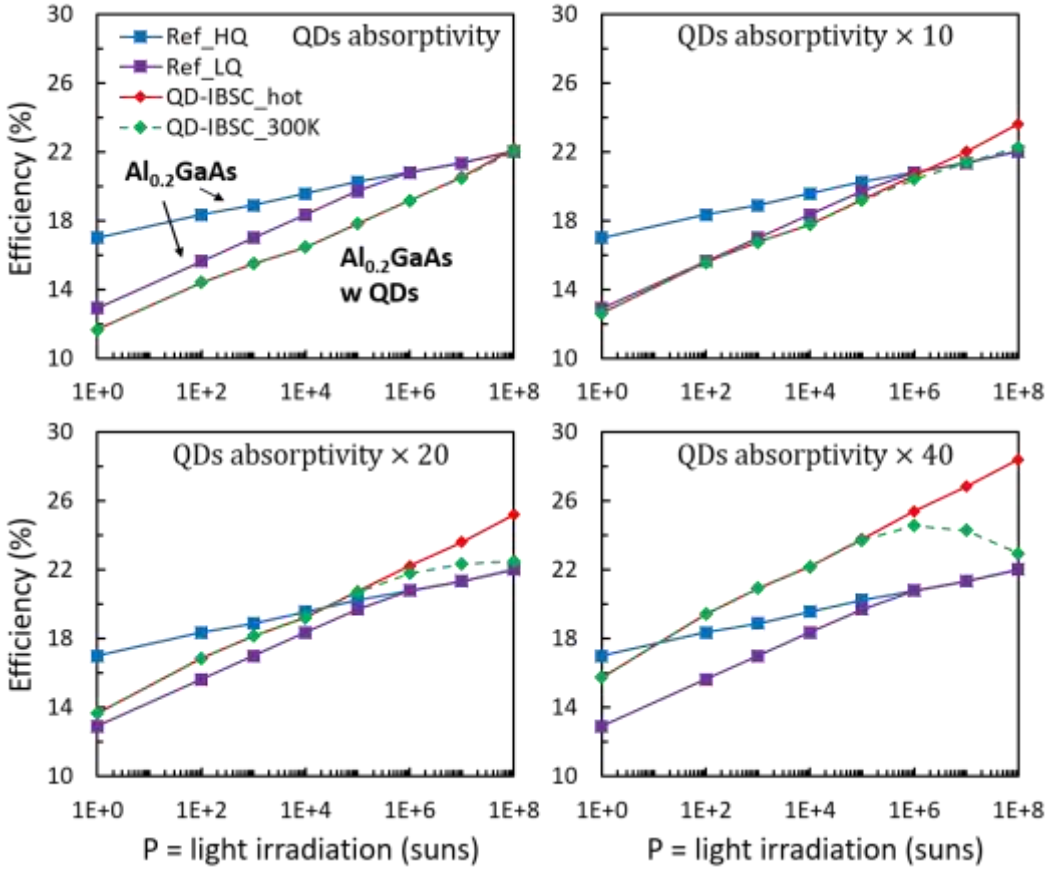

Figure 4.3-5: Schematic and simplistic representation of the evolution of solar cells efficiencies for QD-IBSCs ($Al_{0.2}GaAs$ with In(Ga)As QDs) compared with high-quality reference (Ref_HQ, blue) and low-quality reference (Ref_LQ, purple) simple-junction $Al_{0.2}GaAs$ solar cell. We distinguish the case of a "hot" (red) or "cold" (dashed green) carrier population which result in the energy splitting or no splitting of QFLs between IB and CB. We also show the influence of an increase of QDs absorptivity (x10, x20, and x40) to obtain higher efficiencies.

In Figure 4.3-5, we notice that for the present absorptivity of QDs in Okd-3 (10 QD layers), QD-IBSC efficiency can not overcome the reference cells efficiencies even for 100 M suns. For x10, we see that we could get close to low-quality reference cells. For x20 to x40, QD-IBSC could overcome high-quality reference cells starting at 10 k suns (x20) to 20 suns (x40). This is true for the enhancement of absorptivity using light management. If the absorptivity of QD layers is increased by increasing the number of QD states, it could lead to a decrease of V_{OC}. However, doping and capping techniques might help to avoid this issue. Finally, we notice the splitting of "hot" (red) and "cold-300K" (dashed green) QD-IBSC efficiencies due to the difference in temperature and separation of QFLs between the IB (QD states) and the CB (WL and host material). At very high illumination, the "cold" QD-IBSC is converging towards the HQ and LQ simple-junction $Al_{0.2}GaAs$ solar cells due to the fact that $J_{SC-QDs-cold} \rightarrow 0$ because of bandfilling and all V_{OC} are converging towards the radiative limit for $Al_{0.2}GaAs$ material.

The calculation of efficiencies in Figure 4.3-5 is very simplistic and makes rough assumptions especially because we do not really know how our cells would behave under very high illumination con-

ditions. However, we can conclude about two things. First, we see that the level of absorptivity from our QDs is too low and would need to be increase by at least x20 if we want to overcome high-quality reference cells. Second, we see that only with a “hot” population we can hope to overcome Shockley-Queisser limit in order to walk towards high-efficiency solar cells.

Conclusion

In this chapter, we focus on the investigation of the IB dynamics. We identify the different regimes of bandfilling and find that a "hot" carrier population appears for a certain bandfilling. Absolute calibrated photoluminescence (PL) spectroscopy indicates that the triggering mechanism happens when the QD ensemble is almost half-filled behaving as a metal-like IB. This is interesting for thermally activated QD-IBSCs because it proves the existence of a splitting of QFLs for a certain "hot" regime and at the same time we evidence the advantage of a "hot" population to maintain subbandgap absorption and walk towards the realization of simple-junction high-efficiency solar cells that could potentially overcome the Shockley-Queisser limit. We would like to underline some points that seem important for our study and highlight our achievements:

- During our study we were faced with fabrication issues that at some point prevented us to achieve electrical measurements to test the operating conditions of our solar cells. For this reason, we thought about relying on all optical characterization techniques that were specifically adapted to test IBSC PV device operation. In previous chapters, we saw that voltage preservation and subbandgap current generation are key factors for IBSC operation. The calibrated PL characterization was proposed to have an information on the voltage operation of our cell while the two-color excitation PL characterization was thought to test the sequential two-photon absorption (S-TPA). In the literature, we found that Kita Laboratory are working on the same kind of characterization techniques on their QDSCs. They use time-resolved PL (TRPL) while we work with continuous-wave PL (CW-PL). Our results are complementary to theirs, we do not have time-resolved information but we have a spatial and calibrated information enabling us to have a quantitative analysis of the dynamics in our cell.

- In order, to test different operating conditions of our solar cells, we used different laser excitations. One important point we discussed is how to link a laser excitation power density with "suns" illumination. It matters especially in the case of a focused spot excitation where carrier diffusion length is on the same order as the laser spot size. In the end, we chose to use the "electrical" power density normalizing by PL spot size. By varying the laser excitation we were able to plot "optical I-V" curves and get an idea on the ideality factors from the PL of QDs, the WL and the host material spectral domains. On one hand, linear to sublinear evolution of ideality factors with laser excitation in QDs indicate a saturation effect. On the other hand, linear to superlinear evolution in the WL and host material indicate the emergence of an independend carrier population in regards to carriers inside QDs.

- Working with calibrated characterization, we were able to calculate the evolution of the radiative ratio from the PL of QDs, the WL and the host material and compare with other materials. For QDs, we found a radiative ratio of 0.07% for thousands of suns. For WL and the host material it is at least two or three orders of magnitude below. These values give another indication that our cell is impacted by a high level of defects inducing non-radiative recombination as was discussed previously in chapter 3.

- Working with spatial and calibrated characterizations, we were able to get many information on the dynamics of carriers in our system. We showed a method to investigate the carrier lateral diffusion, with different behaviors from the PL from QDs, the WL and the host material spectral domains. We noticed a carrier diffusion around 600 nm for thousands of suns up to almost 3 µm for the highest excitation. This 3 µm value is on the range of what we expect to find in conventional $Al_{0.2}GaAs$ host material. The carrier diffusion from the host material PL seems to be always higher than for QDs PL but it is the opposite for the carrier diffusion in the WL PL. We considered that the host material PL echoes the car-

rier diffusion in host material where carriers may diffuse without encountering a QD while carriers in the WL will very likely diffuse in quantum-well islands (QWIs) and fall in QDs. Combining spatial and "optical I-V" curves we were able to identify that, for certain PL off-spot regions, the PL from host material behaves like QDs PL indicating an extension of the QDs carrier Fermi-Dirac distribution into neighboring host material that will therefore have a luminescence directly related to QDs. The spatial investigation along with the comparison of focused and defocused spot investigation also brought into light the possible different behavior of electrons and holes. We identified that for a fixed laser excitation, on most of PL spot surface area there was no change in the bandfilling profile but the PL intensity could be strongly reduced depending on the position from the center of the excitation. We supposed it is due to the fact that the local density of holes will decrease faster than the local density of electrons.

- In our attempt to understand the bandfilling dynamic, we tried to develop a simple model and found that the triggering of the "hot" regime might happen when the carrier concentration in "large" QDs becomes as high as in degenerately doped semiconductor (1e19 cm^{-3}). We also evidenced the fact that two regions of PL curves cannot be explained simply by a bandfilling effect: (i) For the low-energy part, there are saturation effects with supposedly carrier-carrier scattering effects. We did not try to investigate closely this topic but it could be interesting in the future and it has already been an important topic for other research groups, for example Nozik's group at the NREL. (ii) For the high-energy part, the luminescence comes from the Fermi-Dirac distribution of the carrier gas with a temperature equal or superior to the crystal lattice's temperature. We decided to investigate the evolution of this temperature and we found that the power lost by thermalisation can be written as an Arrhenius' equation with an activation energy E_a. For our QD system, we find a 200-250 meV value for the activation energy and we confronted our analysis with the literature on hot carrier solar cells (HCSCs). Thanks to the investigation on material properties performed in chapter 3 we can elaborate a hypothesis. For low temperature measurements, this activation energy seems to be linked to a phonon energy or an exciton energy in the case of QDs explained by a "frozen" regime with excitonic behavior in QDs. At higher temperature, this activation energy seems to be linked to a thermoionic barrier energy explained by a "hopping" regime with unipolar escape behavior of free carriers in In(Ga)As QDs.

- This "hopping" regime with a thermoionic barrier energy acting as an activation energy for the unipolar escape of carriers would enable us to consider that there could be a kind of common quasi-Fermi level (QFL) for all QDs at least in one QD layer throught the WL inducing a spatial smearing effect. Understanding this we develop an original PL fitting method in order to fit QDs PL using the generalized Planck's law and get a more precise estimation of QFL splitting (QFLS) and the temperature of carriers. The investigation of absorption in chapter 3 is essential to analyze our results. Overall we find statistically that best fitting parameters correspond to value of absorption that are the closest from our experiments, with temperature indicating a hot carrier effect and a QFLS because of a saturation effect inside the QDs. On the contrary, we tried to force a PL fitting for a "cold" carrier population fixed at the material lattice temperature which is the room temperature. We found no saturation of QFL inside QDs, a ten times less absorption compared with our experimental results, and a QD distribution with an exponential profile. It seems unrealistic because, in term of absorption, it would mean that only one QD layer (among the ten QD layers) is participating to the PL. From a QD distribution point of view, an exponential profile would mean that QD absorption would be highly impacted by the participation of higher energy quantum structures like QWIs, which we know is not the case from AFM investigation. In the end, the hypothesis of a hot carrier population seems valid. For the high-excitation laser regime, thanks

to our bandfilling study, we showed that the QDs are half-filled behaving as a metal-like intermediate band (IB). If we consider that the hot carrier hypothesis is valid we find a 140 meV energy separation between the QFL in the QDs and the QFL in the WL and host material. This would indicate that under high-excitation, there is a voltage recovery or at least a voltage separation in our QD-IBSC.

- Thanks to the two-color excitation PL characterization, we demonstrated a ΔPL quenching in the QDs and a slight gain in the WL and host material. This gain might induce a +1 meV gain on the V_{OC}. In theory, ΔPL quenching should have a higher impact on the ΔPL gain for the wide gap material. We see here again how the high level of non-radiative loss is detrimental for our QD-IBSC. We developed a simple steady-state rate equation model to investigate and compare the dynamic of the S-TPA in our cell with our experimental results. We noticed that increasing the QDs density decreases the ΔPL quenching effect while it is the opposite if we increase the absorptivity or the IR flux. It confirms our remarks in chapter 3 about the need to use more absorptive QD layers and light management technique and not rely so much on a direct increase of QDs density. We also noticed in our model that a variation of the recombination time for conduction band (CB) to intermediate band (IB) transition, τ_{CI} can be directly compensated by an inverse variation of the recombination time for CB to valence band (VB), τ_C. Indeed, both recombination times are channel losses for CB electrons. We were also able to estimate the radiative recombination time for the CB to VB (τ_{C-rad} = 200 µs) and IB to VB (τ_{I-rad} = 600 ns) transitions, which is just another way of giving the estimated radiative ratio discussed earlier.

- In the last part of this chapter, we showed that thermally activated IBSCs might be reconciliated with PV high-efficiency concepts for an operating regime where there is a hot carrier population in the IB as described in the concept of intermediate band assisted hot carrier solar cell (IB-HCSC). We tried to point out some empiric rules for such IB-HCSCs based on QDSCs: (1) temperature of hot carriers follows a constant increase with activation energy discussed earlier, (2) IB-CB QFLs splitting with a flat QFL in the IB and QFL from CB follows a conventional increase with concentration. These rules originate from the saturation effect observed in QDs. We believe that improvement on such QDSC could be obtained by increasing the quality of the material and pre-filling of QDs using for example capping and doping techniques. We also showed the advantage of a hot carrier population in comparison with a cold carrier population to preserve a subbandgap absorption. Finally, using simple hypothesis we predicted that a higher level of absorption for QDs is needed, at least between x20 and x40 compared to our present system. We will see in chapter 5 how we consider reaching this goal using light management techniques.

Chapter 5 Light management strategies applied to quantum-structured solar cells

In this chapter, we focus on the light management strategies that can be applied to quantum-structured solar cells. First, we present our work on multi-quantum well (MQW) solar cells. We discuss on the effect of a simple Fabry-Pérot (FP) cavity for very thin transferred solar cells compared to non-transferred as-grown solar cells. We also show the possibilities of adding more resonant effects by using nanopatterns as discussed in chapter 2. Second, we present our work on quantum dot (QD) solar cells and discuss the strategy that is devised specifically for the In(Ga)As/$Al_{0.2}$GaAs IBSC system.

5.1 Application to multi-quantum well solar cells

In this part, we investigate InGaAs/GaAsP strain-balanced multiple quantum wells (MQWs) in the intrinsic region of GaAs *p-i-n* solar cells as introduced in chapter 2. One drawback of these structures is the low light absorption of MQWs. It often necessitates numerous layers of MQWs to compensate. Simultaneously a thinner *i*-region and smaller number of layers are favorable for more efficient carrier transport [254]. Furthermore, a thinner stack is also favorable to reduce the dislocation and defect density. Quantum structures display high strain levels which often necessitate the use of elaborate strain balancing for each layer [72]. In this context, light management can be useful to increase light absorption in MQWs layers. Different approaches have been proposed using distributed Bragg reflectors [103] or diffractive gratings [104]–[108].

First, we discuss the effect of a simple FP cavity to enhance light absorption in the subbandgap spectral region where only MQWs are absorbing. In a second part, we show the possibility of adding more resonant effects by using nanopatterns either at the back or at the front surface.

5.1.1 Fabry-Pérot cavity effect on MQW solar cells

In this part, we demonstrate that the implementation of a FP cavity for MQW solar cells can have a positive effect in enhancing light absorption for the spectral region where only MQWs are absorbing. It is also possible to increase the enhancement ratio by optimizing the position of QW layers and/or tuning the surface reflectivity by adding dielectric layers.

5.1.1.1 Light absorption enhancement by vertical Fabry-Pérot resonance

A single junction of GaAs *p-i-n* structure with 10 pairs of $In_{0.18}Ga_{0.82}As/GaAs_{0.78}P_{0.22}$ MQWs in the *i*-region was grown by metal organic vapor phase epitaxy (MOVPE). The thicknesses of the InGaAs wells and the GaAsP barriers are 8.5 and 12.5 nm, respectively. The total MQW region is 210 nm-thick. It is sandwiched between two 40 nm-thick intrinsic GaAs layers, and 50 nm-thick *n*-GaAs emitter and *p*-GaAs base layers. The thicknesses of the *n*-InGaP window and the *p*-InGaP back surface field (BSF) layers are 20 nm-thick. Finally, the *n* and *p*-GaAs contact layers are 50 nm-thick.

Layers thicknesses and doping are detailed in Figure 5.1-1, and growth conditions have been described elsewhere [118].

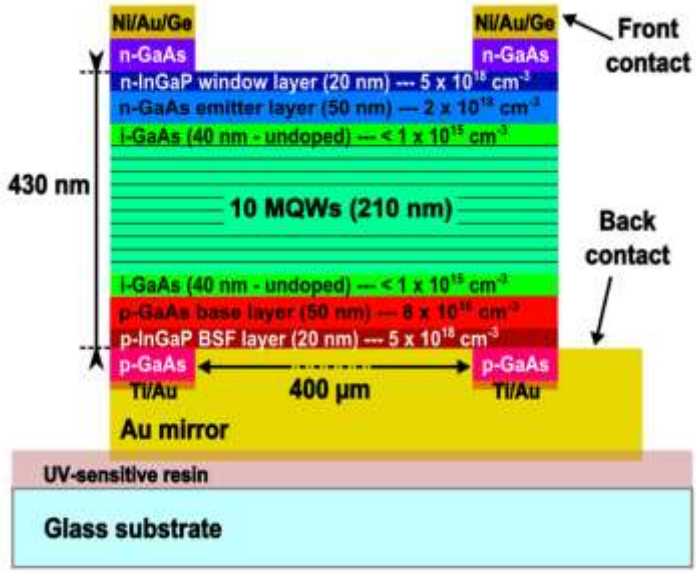

Figure 5.1-1: Sketch of the MQW solar cell transferred on a gold mirror. The *p-i-n* is inverted with *i*-region containing 10 pairs of MQWs. The *n*-GaAs and *p*-GaAs contact layers are doped at 2×10^{19} cm^{-3} and 1×10^{18} cm^{-3} respectively. The localized *n*-type ohmic contacts are regularly spaced every 400 µm.

Non-transferred *p-i-n* solar cells were fabricated as reference on the as-grown epitaxial structures and transferred *n-i-p* solar cells were fabricated with final structure schematically depicted in Figure 5.1-1. Metal alloys used for the *p*-type ohmic contacts of GaAs-based solar cells have poor optical properties leading to low reflectivity of the back mirror in transferred solar cells [255]. To avoid this disadvantage, we have first fabricated localized Ti/Au ohmic contacts regularly spaced on the p-contact layer (bar width: 10 µm, period: 400 µm), before subsequent deposition of a gold mirror by electron beam evaporation. Front contacts were processed by electron beam evaporation of Ni/Au/Ge on a highly-doped (2×10^{19} cm^{-3}) *n*-GaAs contact layer without annealing.

Table 5.1-1: Current-voltage measurements' parameters under AM 1.5 G illumination.

Sample	J_{SC} (mA/cm²)	V_{OC} (V)	FF	Efficiency (%)
Non-transferred	13.8	**0.891**	0.78	**9.6**
Transferred	16.2	**0.874**	0.74	**10.5**

Current-voltage (I-V) measurements were obtained under AM 1.5 G illumination with a solar simulator for transferred and non-transferred MQWs solar cells of 0.8 mm² surface area. Results are summarized in Table 5.1-1. We observe +18% increase in the J_{SC} for the transferred cells as compared to non-transferred cells, and a slight decrease of the V_{OC} from 0.891 V to 0.874 V. A decrease of fill factor (FF) from 0.78 to 0.74 is also observed but overall, the conversion efficiency is improved from 9.6% to 10.5%.

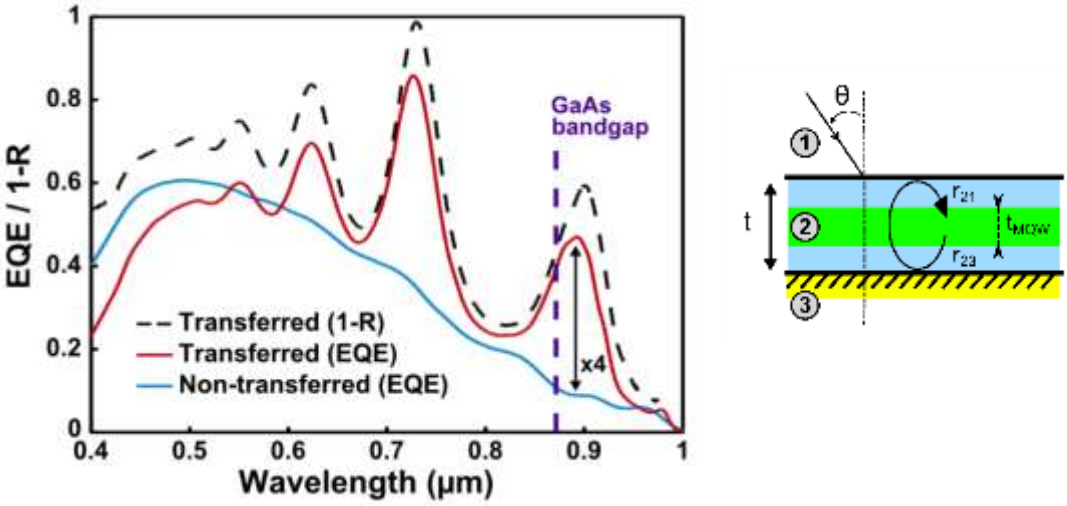

Figure 5.1-2: (Left figure): Optical reflection measurement 1-R (dashed black, transferred cells) and EQE measurements for transferred (red) and non-transferred cells (blue). The GaAs bandgap (vertical dashed line) and the absorption enhancement in the MQW region (arrow) are highlighted. (Right figure): Fabry-Pérot cavity model of the MQW solar cells is composed of a MQW region (green) sandwiched between GaAs/InGaP layers (blue).

The increase in the J_{SC} originates from resonances evidenced by the optical reflection measurement (1-R) and external quantum efficiency (EQE) measurements shown in Figure 5.1-2. These resonances occur in the 430 nm-thick solar cell transferred on a gold mirror that plays the role of a FP cavity. For wavelengths near resonant modes, light absorption is increased through multiple roundtrips. Around four-fold increase of the EQE below the GaAs bandgap demonstrates strong light absorption enhancement in the MQWs. We can distinguish MQWs energy levels around 915 nm and 970 nm on non-transferred EQE and transferred EQE (deformation of FP peak at 915 nm and deformation at 970 nm). Excitonic absorption peaks are not seen mainly because of the unsufficient EQE spectral resolution, as in reference [254]. In the spectral range where MQWs only are absorbing ($\Delta\lambda$=[870; 990] nm), the integrated J_{SC} amounts to 0.41 mA/cm² for non-transferred solar cells with 10 pairs of MQWs while it goes up to 1.45 mA/cm² for transferred solar cells.

The air/absorber/mirror FP cavity is schematically sketched in Figure 5.1-2 (on the right) for incoming light with an incident angle θ. r_{21} and r_{23} are the Fresnel reflection coefficients on the semiconductor/air and semiconductor/mirror interfaces, respectively: $r_{21} = |r_{21}|\exp(i\varphi_{21})$ and $r_{23} = |r_{23}|\exp(i\varphi_{23})$ with φ_{21} and φ_{23} the phases acquired upon reflection at each interface of the cavity. For θ= 0°, the resonance condition of the FP cavity can be written as in Equation 5.1-1 [256].

$$1 - r_{21}r_{23}\exp\left(-2i\frac{\widetilde{\omega}}{c}\langle\tilde{n}_2 t\rangle\right) = 0$$

Equation 5.1-1: Resonant condition of the FP cavity

The expression $\exp(-2i\frac{\widetilde{\omega}}{c}\langle\tilde{n}_2 t\rangle)$ represents a round-trip propagation in a cavity of thickness t, and $\tilde{n}_2 = n_2 + i\kappa_2$ the refractive index. $\langle\tilde{n}_2 t\rangle$, represents the spatial mean value of the product for the different layers forming the cavity. In Equation 5.1-1, weak reflections at the interfaces between the various semiconductor layers are neglected. The term $\widetilde{\omega} = \omega + i\gamma$ is the complex frequency of the incident light with γ expressing the total decay rate inversely proportional to a lifetime. In our case, we have moderate values of absorption, therefore the crossed term of the imaginary parts of

the frequency and refractive index ($\gamma \times \kappa_2$) can be neglected. The dispersion equation can then be separated in two equations describing the resonance position (phase condition) and the resonance amplitude (balance of losses), respectively. The resonant modes of order *m* are defined by the phase condition as in Equation 5.1-2.

$$2\frac{\omega}{c}\langle n_2 t\rangle + \varphi_{21} + \varphi_{23} = 2\pi m$$

Equation 5.1-2: Phase condition for *m* FP resonant modes

By using this condition in the 430 nm-thick FP cavity, the resonant peaks of Figure 5.1-2 can be identified to successive resonance orders *m* that were calculated using well-known optical data [257]. To model the MQW region we approximate an effective medium by averaging the optical index of the barriers and wells weighted by their thickness (effect of the quantum confinement is neglected). We found that *m*=3 at λ=906 nm, *m*=4 at λ=732 nm, *m*=5 at λ=626 nm and *m*=6 at λ=551 nm, which coincide very well with the FP resonances in Figure 5.1-2.

We are especially interested in the 3rd order FP resonance that is localized below the GaAs bandgap and enables a four-fold EQE enhancement in the ($\Delta\lambda$) spectral range where MQWs only are absorbing. This large enhancement is made possible because the broad resonance width is effective over the ($\Delta\lambda$) MQW absorbing domain. A broad resonance width is directly linked to the thickness of the FP cavity, and thus justifies the choice of a 430 nm-thick FP cavity in this study. Indeed, thicker quantum well solar cells (> 2 µm-thick with > 20 pairs of MQWs) that use distributed Bragg reflectors for enhancing light absorption [103] have demonstrated only a 1.4 enhancement ratio, because of very narrow resonant modes resulting in enhancement averaging between resonant and anti-resonant modes in $\Delta\lambda$ spectral region. Here, the peak is centered at λ=906 nm and the full width at half maximum is around 100 nm, which enables to cover most of $\Delta\lambda$. This also shows that the position of the resonance is important. Comparing with a relatively thin quantum well solar cell (≈800 nm-thick with 8 pairs of MQWs) with planar metal backside [108], where the FP resonance is centered at λ=860 nm, the MQWs does not benefit from the planar metal backside because the FP cavity is not tuned for the resonant peak in the $\Delta\lambda$ spectral region. This resulted in a low level of response of quantum-well device with planar metal at wavelengths from 900 to 1000 nm due to the absence of FP resonance in that region. In our case, the objective was to optimize the light trapping for enhancing light absorption in this region in particular.

5.1.1.2 Optimization possibilities for a FP cavity solar cell

We can optimize the light management strategy by keeping a simple FP cavity. The first possibility is to further adapt the MQW absorber to match the FP cavity electric field intensity enhancement in the vertical direction. A second possibility is to increase the light coupling by tuning the reflectivity of the front surface.

i). MQWs vertical position for maximum coupling with incident light

The *z*-position of MQWs in the cavity can be an important parameter to consider for better light management. To investigate this issue, the electric field intensity distribution ($|E|^2$) and the absorption spectra were calculated with a simple multilayer electromagnetic code. The calculated absorption spectrum (red curve in Figure 5.1-3) is in good agreement with our EQE measurements. The cross-section of the electric field intensity is plotted in Figure 5.1-3 for the 3rd order FP resonance at λ=906 nm. At this wavelength, the period of the mode of the electric field standing wave inside

the cavity along *z*-axis is given by $\lambda/(2n) \approx 130$ nm [256]. Therefore, the 210 nm-thick MQW region must be cautiously centered to maximize the absorption inside the MQWs. With respect to the fabricated *n-i-p* structure, the MQW region should be shifted by 20 nm closer to the *n*-region to maximize the absorption in Figure 5.1-3 (a). Simulations show that this shift results in +6% gain on the absorption in the $\Delta\lambda$ spectral region and +1% over all. Another way of making good use of this approach would be to split the MQW region into multiple sets of MQWs to cover only the maxima of the cavity while keeping the same total number of MQWs. For the 430 nm-thick FP cavity, the 3rd order FP results in a splitting of the MQW region in three parts as depicted in Figure 5.1-3 (b). This results in a +25% gain (from simulation) on the absorption in the $\Delta\lambda$ spectral region and +4% gain overall, as plotted in Figure 5.1-3 (c).

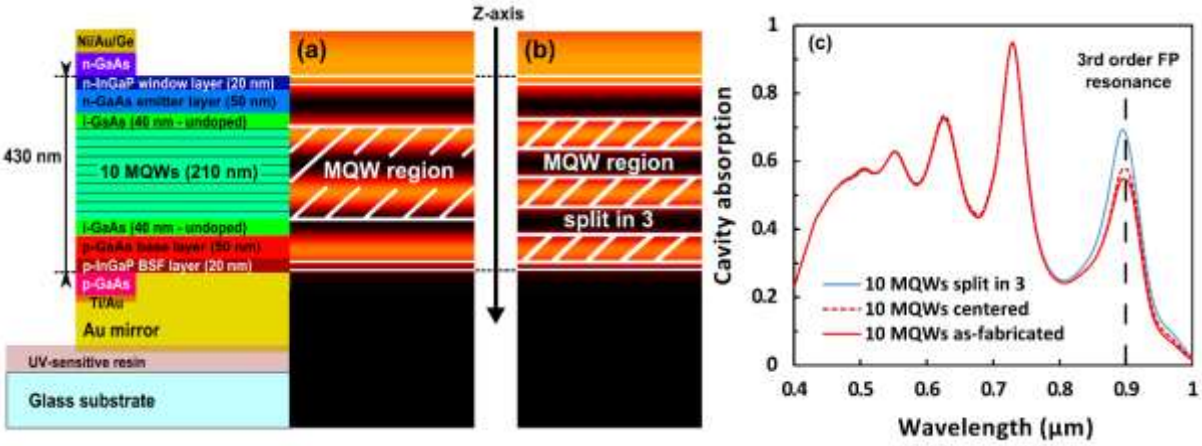

Figure 5.1-3: Cross-section of the electric field intensity $|E|^2$ at the 3rd order FP resonance for (a) the as-fabricated MQW structure, and (b) a cavity structure with a MQW region split to optimize the overlap with the three $|E|^2$ maxima. White lines mark interfaces between different materials. (c) Calculated absorption spectra for as-fabricated structure (red), a centered MQW region (red dashed) and the MQW split region (blue) without parasitic absorption from window layer, BSF layer and the gold mirror.

ii). Dielectric front multilayers for anti-reflection coating

The addition of dielectric front multilayers can be used for anti-reflection coating. For example, we studied the effect of a double layer anti-reflection coating (DLARC) on the MQWs solar cells. Albeit this might remove the FP resonance condition, we will show it actually does not. In Figure 5.1-4, we show numerical calculation of total absorption with and without a DLARC optimized differently for transferred and non-transferred MQW solar cells. By integrating the total absorption over the solar spectrum, we are able to predict a maximum of the J_{SC} collected by such solar cells. For non-transferred solar cells, we optimized the DLARC to have a maximum J_{SC} for the solar spectrum (MgF_2/TiO_2: 85/40 nm).

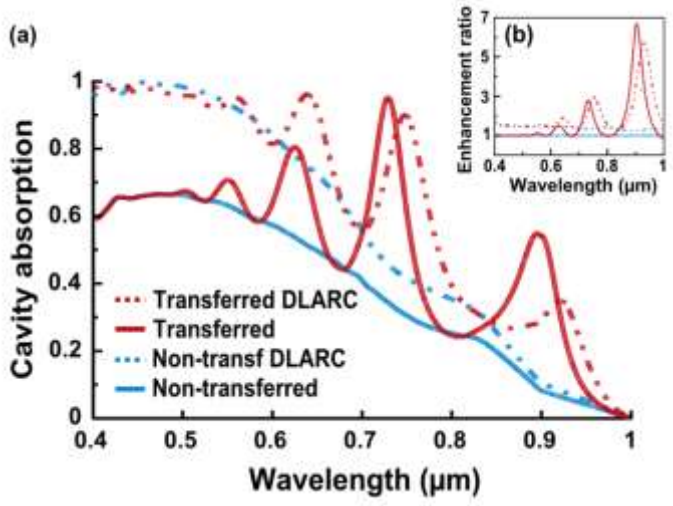

Figure 5.1-4: (a) Simulation of absorption in solar cells with 10 pairs of MQWs for transferred (red) and non-transferred (blue) structures without DLARC (solid lines) and with DLARC (dashed lines). (b) Wavelength-dependent enhancement ratio of the cavity absorption compared with non-transferred one without DLARC.

For transferred solar cells, we searched the best trade-off to reduce reflection loss in the bulk spectral region and at the same time keep a good FP enhancement in $\Delta\lambda$ spectral region (MgF_2/TiO_2: 65/20 nm). By estimating the ratio of the J_{SC}, we find that the deposition of a DLARC enables a gain of 45% on the J_{SC} for non-transferred cells, and 28% for transferred cells. In total, transfer and coating gives a 65% gain on the J_{SC}.

Moreover, we show that by using a DLARC it is possible to shift the wavelength of the FP resonant peaks. In Figure 5.1-4 (a), we can see on the *transferred DLARC* curve that the 3rd order FP resonance is shifted from λ=906 nm to λ=936 nm and is now better centered over the MQW absorbing spectral region $\Delta\lambda$. Even though the 3rd order resonant peak is now lower, Figure 5.1-4 (b) shows that the enhancement ratio is nearly the same (≈6) than the one without DLARC (≈7).

iii). Dielectric front multilayers for critical coupling

In order to obtain an optimal absorption for the resonances in our FP cavity, we see that Equation 5.1-1 provides also a relation between the total losses of the system (total decay rate $\gamma = 1/\tau$) and both reflection coefficients as expressed in Equation 5.1-3.

$$|r_{21}||r_{23}|e^{-\frac{2}{c}(\omega\langle\kappa_2 t\rangle+\gamma\langle n_2 t\rangle)} = 1 \quad \Leftrightarrow \quad \gamma = \frac{c}{2n_2 t}\ln|r_{21}| + \frac{c}{2n_2 t}\ln|r_{23}| - \frac{\kappa_2}{n_2}\omega$$

Equation 5.1-3: Resonant condition of the FP cavity expressed with the total decay rate $\gamma = 1/\tau$

The temporal coupled-mode theory (TCMT) provides a very powerful framework to determine analytically the absorptivity maximum [81]. In the vicinity of a resonance at frequency ω_0, the absorption spectrum in the cavity can be approximated by a Lorentzian function where $\gamma = \gamma_{21}+\gamma_{23}+\gamma_{nr}$ is the total decay rate of the resonant mode as expressed in Equation 5.1-4. γ_{nr} is the non-radiative decay rate (absorption in the cavity), while γ_{21} and γ_{23} are the radiative decay rates through the front and back interfaces, respectively that can be identified with the terms in Equation 5.1-3.

$$A_{cavity}(\omega) = \frac{4\gamma_{21}\gamma_{nr}}{(\omega - \omega_0)^2 + \gamma^2}$$

Equation 5.1-4: Near-resonant FP cavity absorptivity maximum from the TCMT

In the subbandgap spectral region, we make the approximation that $\kappa_2 \approx \kappa_{MQW}\, t_{MQW} / t$, and we suppose that the gold mirror reflection is perfect $|r_{23}| = 1$. At resonance frequency ω_0, absorption can be expressed as in Equation 5.1-5.

$$A_{cavity}(\omega_0) = \frac{2X}{\left(\frac{X}{2} + 1\right)^2} \; with\; X = \frac{-c\; ln(|r_{21}|)}{\omega_O \kappa_{MQW}\; t_{MQW}}$$

Equation 5.1-5: Near-resonant FP cavity absorptivity maximum in the subbandgap region

For critical coupling, at the resonant frequency, $A_{cavity}(\omega_O) = 1$, therefore we can calculate that $|r_{21}| = \exp(-2\omega_O \kappa_{MQW}\; t_{MQW}\; /c) = 0.93$ is necessary to achieve critical coupling. In other term, we see that we need to have a front interface with a high reflectivity R_{21}=0.86. To achieve this value of reflectivity with transparent dielectric layer it is possible to deposit multilayer coating to form a front distributed Bragg reflector (DBR).

In Figure 5.1-5, we notice that contrary to DLARC, the high-index layer will be preferentially at the top. Using well-known DBR's reflectivity formula [258], with TiO_2 and SiO_2 layers we calculate that we need at least two pairs of layers to achieve the critical coupling condition of R_{21}=0.86 in the MQW absorbing spectral region $\Delta\lambda$. In Figure 5.1-5, we show the front DBR structure for N=1 and N=2 pairs of layers. For N=2, critical coupling condition is achieved for the 3rd order FP resonance around 930 nm in wavelength. However, we notice that the increase of front reflectivity is at the expense of absorption in the bulk spectral region. The absorptivity is criticaly reduced in the 500-650 nm wavelength range where solar photon flux is at its maximum, therefore it is detrimental to PV applications.

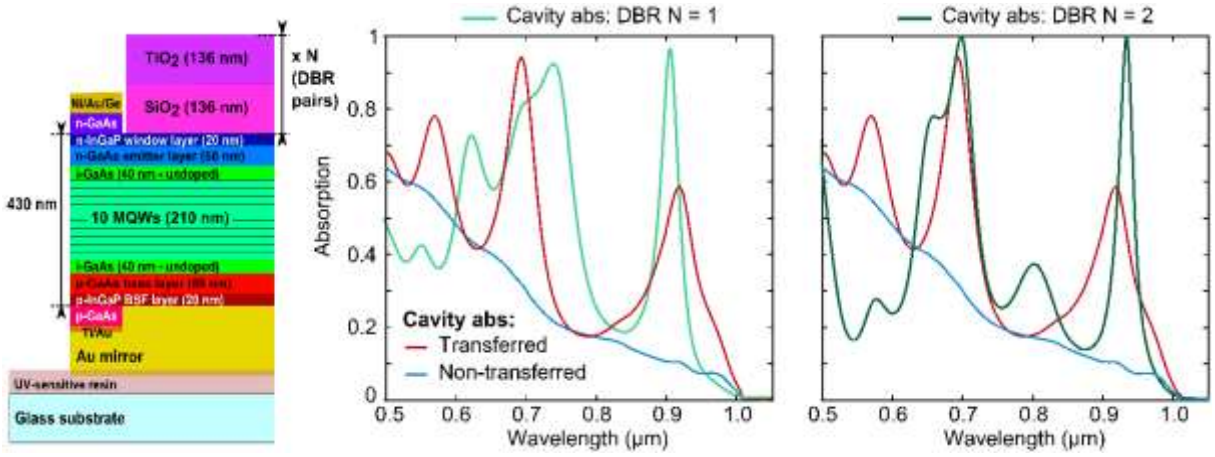

Figure 5.1-5: Front multilayer DBR to achieve critical coupling condition for FP resonances. Detailed schematic layer structure on the left represent the transferred MQW solar cell with N pairs of TiO_2/SiO_2 layers. Plotting of simulated FP cavity absorption spectrum for non-transferred (blue) and transferred (red) structures. Comparison with the front DBR structure for N=1 (light green) and N=2 (dark green).

Overall, we see that the enhancement of light intensity in the MQW spectral region often comes at the expense of a light absorption loss, as compared with a thicker GaAs solar cell that would absorb more light in the bulk spectral region. That is why, in the case of thin MQW solar cells, other strategies are developed to make use of a multitude of resonances for example using nanopatterning as it will be discussed next.

5.1.2 Nanopatterns effect on MQW solar cells

In this part, we show the possibility of adding more resonant effects by using nanopatterns either at the back or at the front surface. First, we evaluate the potential enhancement by simulation and then we present the experimental results that were obtained on the MQW solar cells.

5.1.2.1 Simulation for light management optimization

Numerical calculations for nanopatterns have been performed with the Reticolo software provided by Philippe Lalanne and Christophe Sauvan (Institut d'Optique, Palaiseau) [259], [260]. It is based on rigorous coupled wave analysis (RCWA) and performs an exact calculation of the electromagnetic field [82]. In our Reticolo model, we keep a relatively simple structure, which allow us to model 1D or 2D gratings (nanogrids or square-shaped nanopatterns).

i). Back and front nanostructured MQW solar cells transferred on gold mirrors

In order to investigate back and front nanostructures, we start with the schematic illustration in Figure 5.1-6. At least three parameters can be adjusted for the grating: the period (*p*), the diameter (*d*) and the height (*h*) of nanopatterns. The thickness of the absorbing layer is the same as in the case of the FP study but we can tune the FP cavity resonance by adding dielectric layers at the back or at the front as explained before. In both cases, we consider using TiO_2 for the nanostructures because TiO_2 material is a well-known dielectric that can be used in sol-gel solution for nanoimprint. It can also have a relatively high refractive index, which is an asset to develop resonant light-trapping solutions. In these simulations, we used high TiO_2 refractive index $n \approx 2.5$, from DeVore [261] and same parameters for other materials as in the FP study described previously.

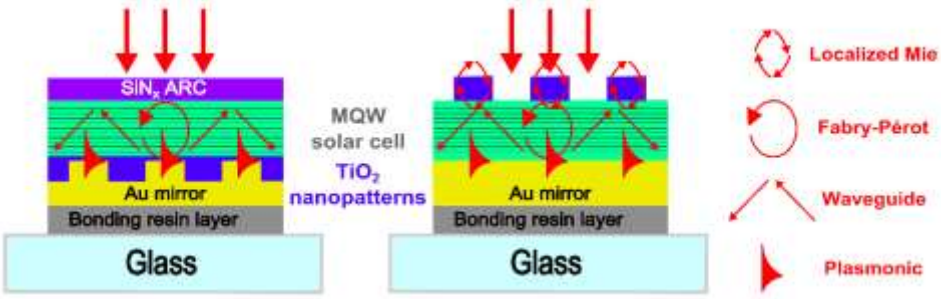

Figure 5.1-6: Schematic illustration of a back and front structured MQW solar cell with resonant effects as detailed in chapter 2.

In the case of the back-structured mirror solar cell, the nanoimprint residual or buffer layer at the back between the absorber and the nanopatterns is kept constant with 20 nm height. At the front, we choose to use a SiNx ARC with 70 nm height. It is an optimum value for broadband transmission of light into our structures. For the front-structured solar cell, we do not simulate the effect of adding an ARC layer so that we can keep a relatively simple structure. Anyhow, the front structuration in itself acts as an ARC. We compare both back and front structuration strategies by varying the same number of parameters.

ii). Varying nanopattern parameters

In order to explore and optimize our structure, we simulate a simple 1D grating using RCWA with 30 Fourier orders. The *d*/*p* ratio is fixed at one-half (fill factor: *ff*=1/2), therefore only two parameters are varied: height and diameter. Simulations are made for TM and TE polarizations in order to calculate the PV active absorption in each layer. In Figure 5.1-7 and Figure 5.1-8, we present the averaged results for TM and TE polarizations respectively for the back and front structuration. Theoretical short-circuit current are calculated by integrating the absorption in the semiconductor layers over the solar spectrum ($J_{SC\text{-}solar}$) and over the $\Delta\lambda$ spectral region where only MQWs are absorbing ($J_{SC\text{-}MQWs}$), as shown in Figure 5.1-7 (a,b) and Figure 5.1-8 (a,b) for varying diameters and heights. The analysis of these two-parameter J_{SC}-colormaps highlights optimum domains for PV light trapping: [*h*=50-150 nm; *d*=320-460 nm] and [*h*=100-300 nm; *d*=180-220 nm] respectively for back and front nanostructuration. In Figure 5.1-7 (c) and Figure 5.1-8 (c), we show the evolution of the active absorption spectrum with the variation of diameter for optimal heights: *h*=100 nm (back) and *h*=200 nm (front). Finally, in Figure 5.1-7 (d) and Figure 5.1-8 (d), we show active absorption spectra for optimum parameters with TM (dashed blue) and TE (dashed purple) curves plotted to identify the different resonant effect due to polarization. We also color in pink the $\Delta\lambda$ spectral region where only MQWs are absorbing to evidence the absorption gains.

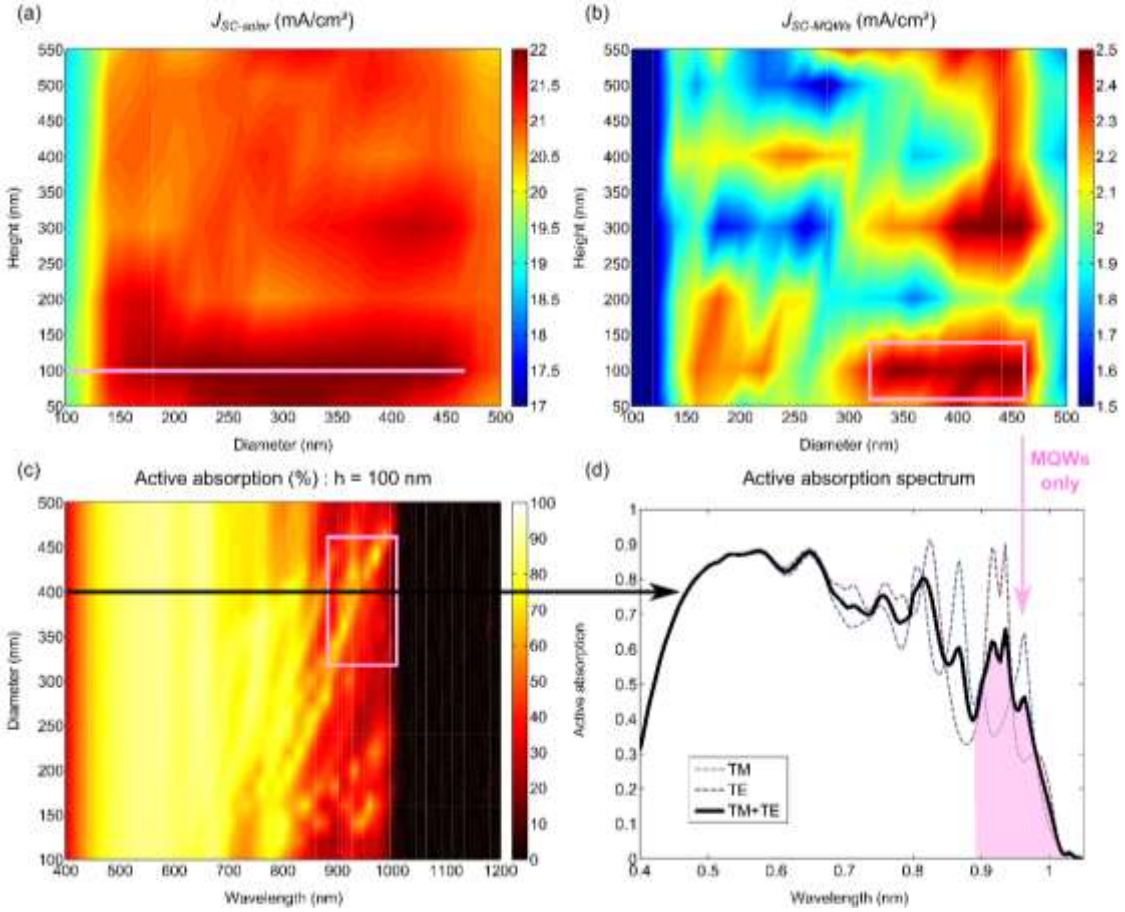

Figure 5.1-7: Optimization of a TiO_2 back structured gold mirror MQW solar cell with 70 nm SiNx ARC using RCWA simulation with 30 Fourier factors for a 1D grating. The grating parameters are varied as follow: *h*=50-550 nm, *d*=100-500 nm and *ff*=0.5. Theoretical short-circuit current are calculated by integrating the absorber absorption (active absorption) over the solar spectrum ($J_{SC\text{-}solar}$) as shown in figure (a) and over the $\Delta\lambda$ spectral region where only MQWs are absorbing ($J_{SC\text{-}MQWs}$) as shown in figure (b). Optimal values are found for *h*=100 nm and a colormap with active absorption spectrum versus diameters is shown in figure (c). An optimal configuration is found for *d*=400 nm as shown in figure (d) with TM (dashed blue) and TE (dashed purple) curves plotted to identify the different resonant effect due to polarization.

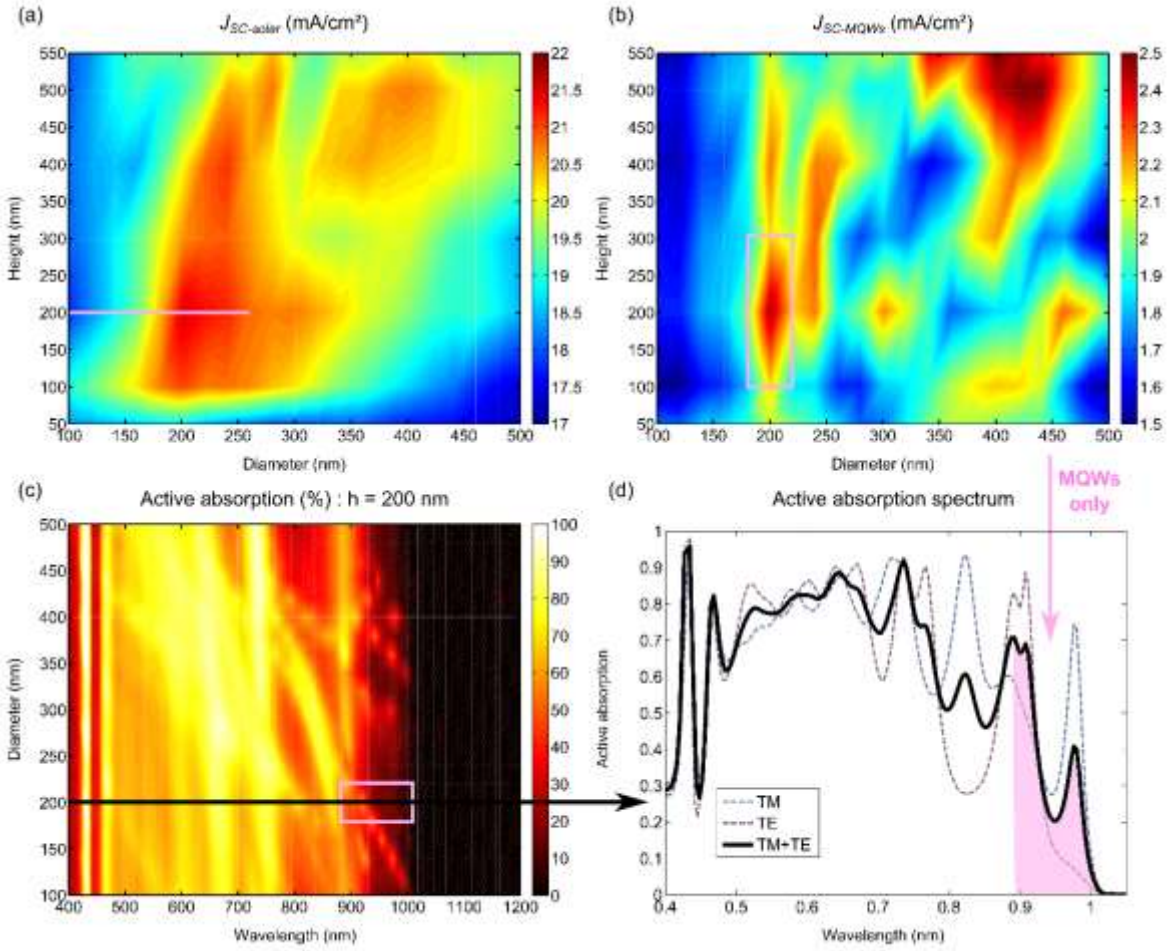

Figure 5.1-8: Optimization of a TiO_2 front structured MQW solar cell transferred on gold mirror using RCWA simulation with 30 Fourier factors for a 1D grating. The grating parameters are varied as follow: *h*=50-550 nm, *d*=100-500 nm and *ff*=0.5. Theoretical short-circuit current are calculated by integrating the absorber absorption (active absorption) over the solar spectrum ($J_{SC\text{-}solar}$) as shown in figure (a) and over the $\Delta\lambda$ spectral region where only MQWs are absorbing ($J_{SC\text{-}MQWs}$) as shown in figure (b). Optimal values are found for *h*=200 nm and a colormap with active absorption spectrum versus diameters is shown in figure (c). An optimal configuration is found for *d*=200 nm as shown in figure (d) with TM (dashed blue) and TE (dashed purple) curves plotted to identify the different resonant effect due to polarization.

iii). Multiresonant effect

In Figure 5.1-9, we compare the simulations of PV active absorption spectra in the optimal configurations for both nanostructurations. We also compare with PV active absorption in the non-transferred and transferred structures as discussed previously in the FP study. Contrary to Figure 5.1-4, in Figure 5.1-9, we consider only the PV active absorption, which excludes parasitic loss from gold mirror. For the bulk spectral region with high absorption, λ<700 nm, we are able to achieve the same level of absorption as in the case of a transferred structure with ARC. For λ>700 nm, we see that we keep the benefits of FP resonant effects at λ=732 nm and λ=906 nm but we also gain from other resonant effects in-between the FP resonances that were identified earlier. Collin's group at C2N laboratory has extensively studied this multiresonant effect for PV application in different PV materials [81]–[84]. Overall, we find that both back and front light-trapping solutions can offer about the same light absorption enhancement in their optimum configurations. However, it seems that the back structuration optimal domain is wider which make it easier for the fabrication.

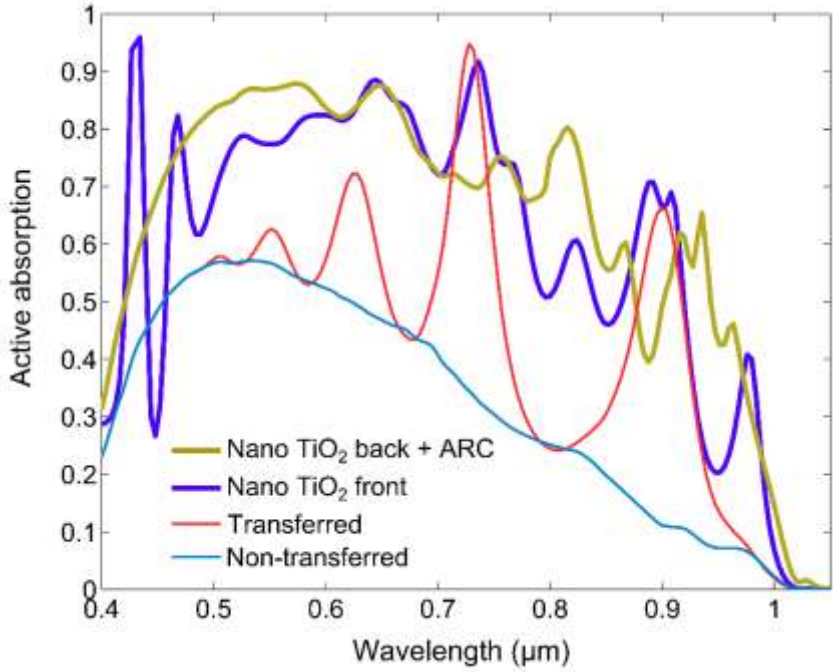

Figure 5.1-9: Comparison of RCWA simulations of active absorption for PV layers in the case of the proposed nanostructuration for the MQW solar cells fabricated in this study (from).

In Figure 5.1-10, we compare 1D and 2D back-structured mirror with sol-gel SiO_2 (refractive index n=1.45) instead of TiO_2 on MQW solar cells without ARC at the front. Height and fill factor parameters are fixed: h=200 nm and ff=1/2. The variation of the diameter parameter evidences the contribution of resonant effects in the PV active absorption. We can observe vertical bands enhancement of the active absorption at wavelength positions around λ=[500 nm; 560 nm; 630 nm; 720 nm; 800 nm; ≈900 nm]. They represent FP resonances, which as we can see are almost not impacted by the variation of the grating diameter especially for the shorter wavelength. For λ>700 nm, we start to see the contributions of other resonant effects that are impacted by the variation of the diameter grating. In the case of the 1D grating we can attribute this effect to diffraction from the 1D grating and waveguide modes inside PV layers. We see that between 1D and 2D gratings we have an increase of optical resonant modes especially for λ>900 nm. We can attribute this effect to the coupling of TM and TE modes by the 2D structuration and also the enhancement of other light-trapping effects like localized Mie resonance that can be found for nano-objects of geometrical size r in the Mie regime ($r \approx \lambda$).

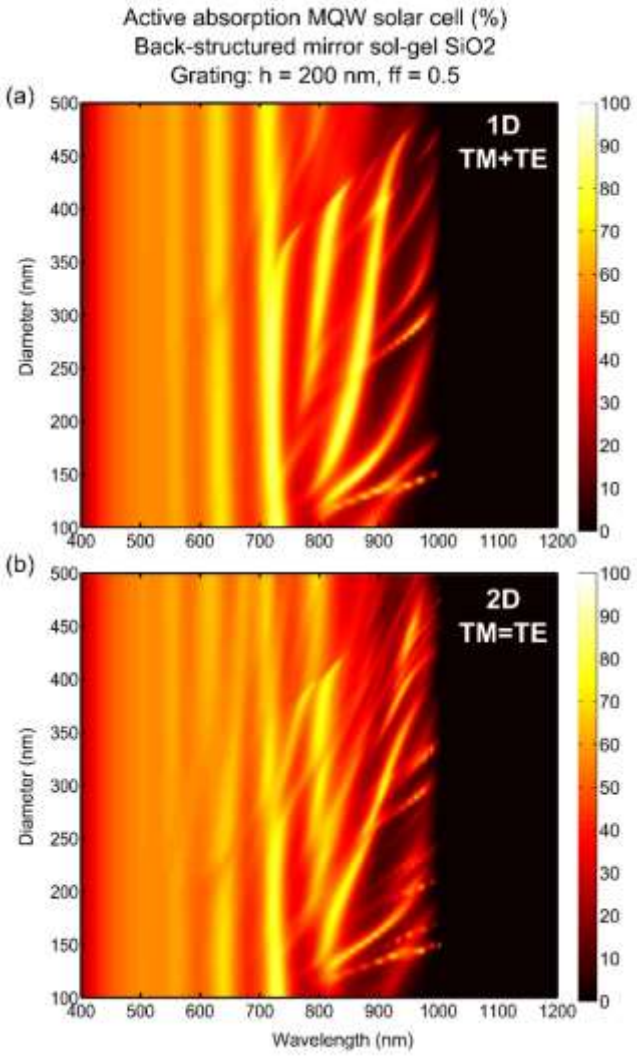

Figure 5.1-10 : Comparison of colormaps showing the variation of the active absorption of MQW solar cell with a back-structured mirror. Diameter parameter is changed for a 1D grating with averaging of TM and TE polarizations (top) and 2D grating (bottom). It reveals an increase of optical resonances for the longer wavelength region.

5.1.2.2 Experimental results after fabrication

In order to fabricate the nanostructuration at the back or at the front, we used the different processes described in chapter 2. We will talk in this part about the differences between what is expected from the simulation and the actual realization in the clean room. By careful investigation and simulation, we were able to understand its origin. We can consider it for future light management realization.

i). Back-structured mirror

We describe the results of our back structuration process. In Figure 5.1-11, we show the experimental results of fabricated MQW solar cells with back-structured mirror 2D grating with 5 different periods (p=[400 nm; 500 nm; 600 nm; 700 nm; 800 nm). Front and rear sides are shown and we choose to focus on extremal periods: 400 nm (solar cell #b16) and 800 nm (solar cell #b27). Investigation of SEM images allows us to check 2D grating parameters of the sol-gel TiO_2 nanogrid that was deposited by nanoimprint lithography. Total height with buffer layer is around 100 nm. The residual or buffer layer height (h_{buffer}) is almost equal to the nanogrid height ($h_{nanogrid}$), about 50 nm. Fill factors vary between 0.5 and 0.7 because the walls of the nanogrid are not perfectly abrupt. We

also notice that the holes are not strictly rectangular but a little round-shaped in the corner. We often encounter this issue when using sol-gel TiO_2. We suppose it is due to the viscosity and the effect change depending on the preparation of the sol-gel solution. It can be prevented by using another type of nanoimprint resist like Amonyl but the refractive index is then reduced to $n \approx 1.5$.

We measure a refractive index $n \approx 1.8$ by ellipsometry on a Si test sample after the deposition of a 163 nm-thick layer spin-coated with our preparation of sol-gel TiO_2. We notice that after 300°C annealing the refractive index increases up to 2.1 but the thickness is almost divided by 2 and we measured a higher imaginary index by ellipsometry measurement. It might indicate scattering loss due to a more dense material. In summary, it seems unlikely that we will be able to reach a high refractive index of 2.5 as in the case of our simulations. Annealing can help increase the index but the reduction of height has to be taken into account.

For the fitting of our experimental observations, we use the refractive index $n \approx 1.8$ that we measured with ellipsometry. In Figure 5.1-11 on the right, we show the comparison of reflectometry, EQE and calculation (1-R) using RCWA with nanogrid parameters: for b16 we use [p=390 nm, h_{buffer}=60 nm, $h_{nanogrid}$=40 nm, ff=0.64] and for b27 we use [p=775 nm, h_{buffer}=60 nm, $h_{nanogrid}$=40 nm, ff=0.64]. We find a good agreement between our simulations and experimental findings which seems to confirm the validity of the parameters that were considered.

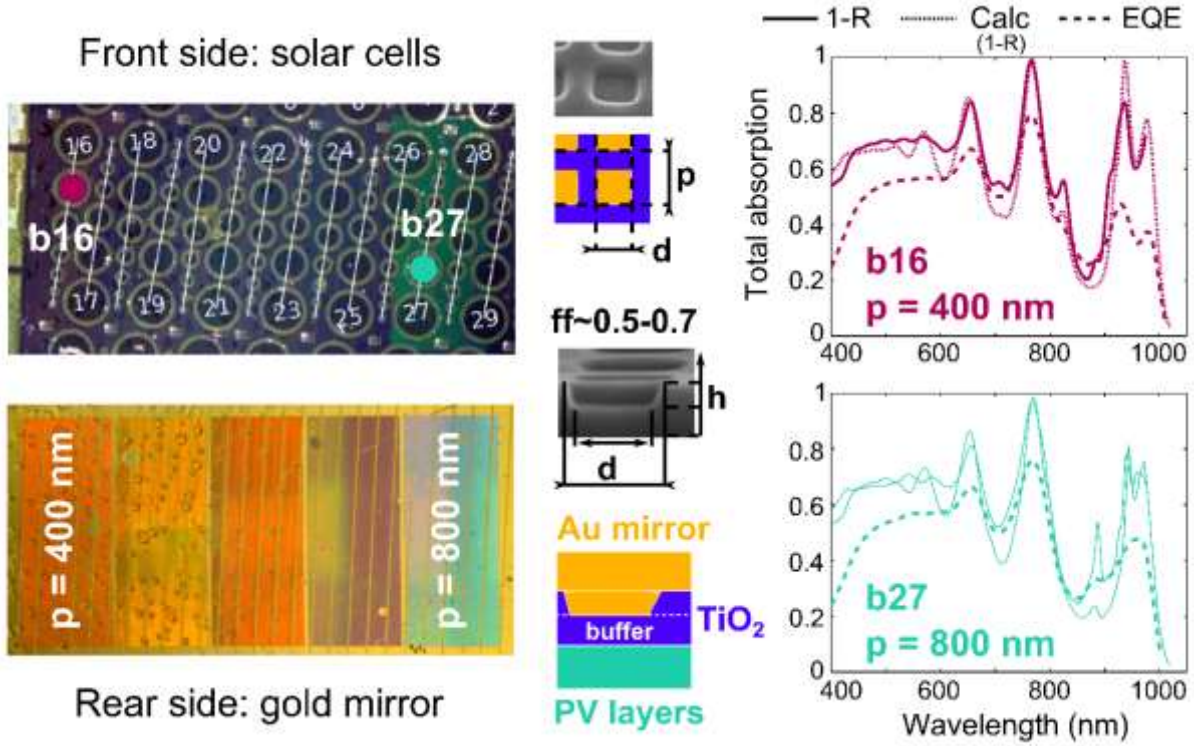

Figure 5.1-11: Experimental results of fabricated MQW solar cells with back-structured mirror 2D grating with 5 different periods (p=[400 nm; 500 nm; 600 nm; 700 nm; 800 nm). Front and rear sides are shown and we choose to focus on extrema periods: 400 nm (solar cell #b16) and 800 nm (solar cell #b27). Investigation of SEM images allows us to check 2D grating parameters of the sol-gel TiO_2 nanogrid. Total height with buffer layer is around 100 nm. Buffer layer height (h_{buffer}) is almost equal to the nanogrid height ($h_{nanogrid}$). Fill factor vary between 0.5 and 0.7 because the sides of the nanogrid are not flat. On the right, we show the comparison of reflectometry, EQE and calculation (1-R) using RCWA with nanogrid parameters: for b16 we use [p=390 nm, h_{buffer}=60 nm, $h_{nanogrid}$=40 nm, ff=0.64] and for b27 we use [p=775 nm, h_{buffer}=60 nm, $h_{nanogrid}$=40 nm, ff=0.64].

In Figure 5.1-12, we compare experimental EQE from five different solar cells. Two are taken from the FP study presented in the previous part: non-transferred (dashed blue) and transferred (dashed red). The three others come from the sol-gel TiO_2 nanogrid study presented in Figure 5.1-11: #b24 solar cell with *p*=700 nm (brown), #b27 solar cell with *p*=800 nm (green) and a flat (black) solar cell on the same sample with no back-structuration. This flat solar cell is like the transferred solar cell with a 100 nm-thick sol-gel TiO_2 buffer layer at the back in-between the PV layers and the gold mirror.

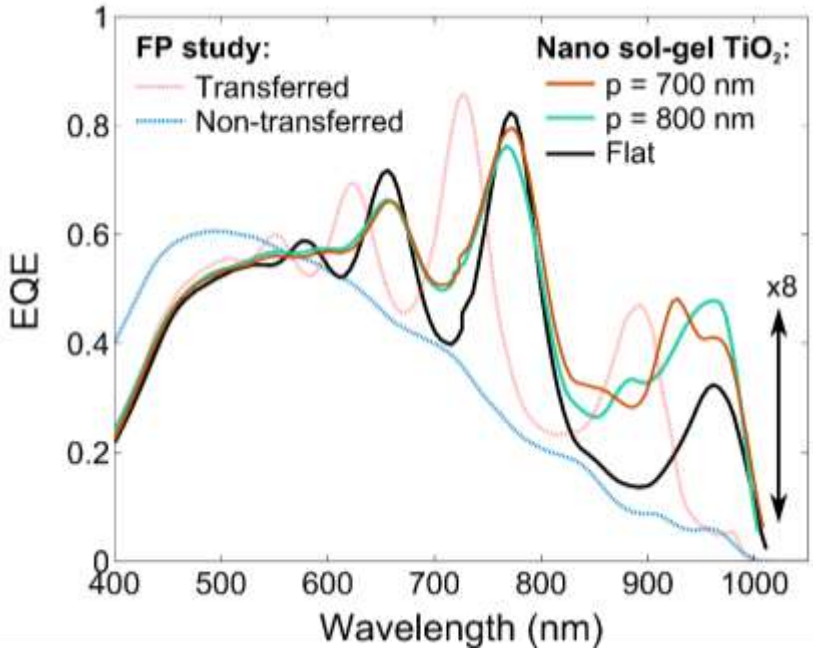

Figure 5.1-12: Comparison of EQE results from the FP study and from the back-structuration using 2D gratings presented in Figure for periods of 700 nm (b24) and 800 nm (b27). We find an EQE ratio enhancement of 8, twice the ratio of FP case.

In summary, compared to the non-transferred solar cell, we are able to reach a maximum of x8.5 EQE ratio enhancement at 965 nm in wavelength while the flat EQE indicates a maximum of x5.6 ratio enhancement for the same wavelength position. Therefore, the addition of the nanogrid at the back results in a maximum of x1.5 ratio enhancement. In Table 5.1-2, we summarize the short-circuit current (J_{SC}) taken by integrating EQE curves from Figure 5.1-12 over all spectrum or over the range of interest where only MQWs are absorbing. Over this range, in comparison with a non-transferred solar cell, FP transfer increase J_{SC} by a x3.5 ratio while nanostructuration increases by a x5.5 ratio.

Table 5.1-2: Short-circuit (J_{SC}) current taken by integrating EQE curves from Figure 5.1-12 over all spectrum or over the range of interest where only MQWs are absorbing.

Sample / J_{SC} (mA/cm²)	Non-transferred (FP study)	Transferred (FP study)	Flat	p = 700 nm	p = 800 nm
All: [400-1000 nm]	13.3	16.6	16.5	18.5	18.4
MQWs: [870-1000 nm]	0.41	1.44	1.24	2.21	2.28

In Figure 5.1-12, we also notice that the broadening of the FP resonance originated from the contribution of other resonant modes. We did not have time to explore more and deposit an ARC on

this sample. However, we know that we will not be able to achieve an optimal configuration because of the low refractive index and height of the nanogrid.

ii). Front structuration with TiO2 nanopatterns

We describe the results of our front structuration process. In Figure 5.1-13, we show experimental images of fabricated MQW solar cells before (Figure 5.1-13 (a)) and after (Figure 5.1-13 (b)) the deposition of 2D grating TiO_2 nanocylinders. In Figure 5.1-13 (c), we show a SEM image of the front nanostructuration (#7b solar cell). We notice at least 3 things that did not work as expected during the process:

(1) A part of the grating near the front contacts is not lifted. It might be due to the fact that front contacts are a hindrance for the nanoimprinting with the PDMS stamp.

(2) We see many cracks on the surface. These cracks are not from the nanoimprint step but from the TiO_2 deposition step. A 200 nm-thick TiO_2 layer is deposited by ion beam assisted deposition. We intend to have a high-refractive index, which means that we want a dense material. The process might induce strains that could result in cracks on the front surface. We measured the refractive index of the deposited TiO_2 by ellipsometry and we found a refractive index $n \approx 2.5$. We noticed a greenish color that does not seem to be caused by the 200 nm coating but might be due to parasitic absorption or other optical effects.

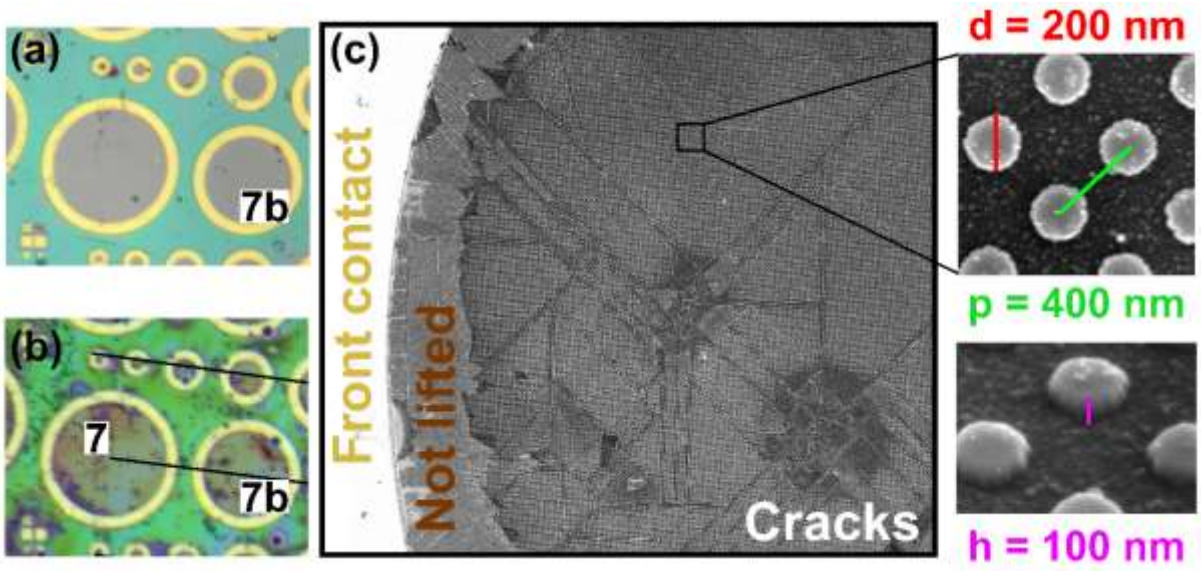

Figure 5.1-13: Experimental images of fabricated MQW solar cells with 2D TiO_2 front grating.

(3) On the SEM zoomed images of nanocylinders in Figure 5.1-13 (c) we find that the 2D grating has the following parameters: d=200 nm, ff=1/2 and h=100 nm. In the simulation and test samples we were expecting to get a 200 nm height as described in Figure 5.1-14.

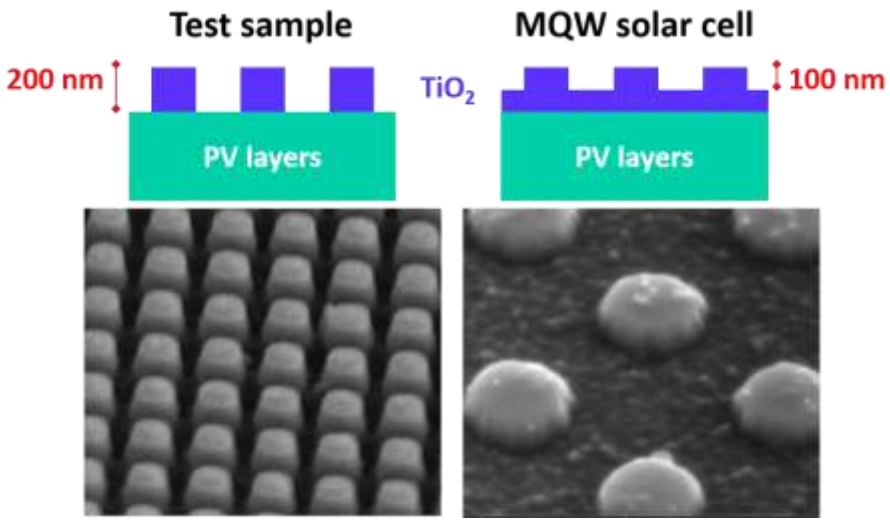

Figure 5.1-14: Difference of nanostructures height between the test sample and the target MQW solar cell.

After reflectometry fitting of our samples, we found that there is a remaining 100 nm TiO_2 layer beneath our nanocylinders. Therefore, we know that the light management will not be optimal as the structure is different from what we numerically found to be the best. In Figure 5.1-15, we compare the EQE and calculated PV absorption for the same transferred solar cell (#7b) without front nanostructuration (blue left) and in the case of front structuration presented in Figure 5.1-13 (red right). In the case of the transferred MQW solar cell without front TiO_2, we find a good agreement between the EQE and the calculated active absorption as described previously during the FP study. However, we see that when we add the front TiO_2 there is a homogeneous loss of about 30% between the EQE and our calculation. It is especially interesting to notice that FP resonances are small compared to the case without front TiO_2. This can only be explained by a global loss that can originate from electrical or optical losses.

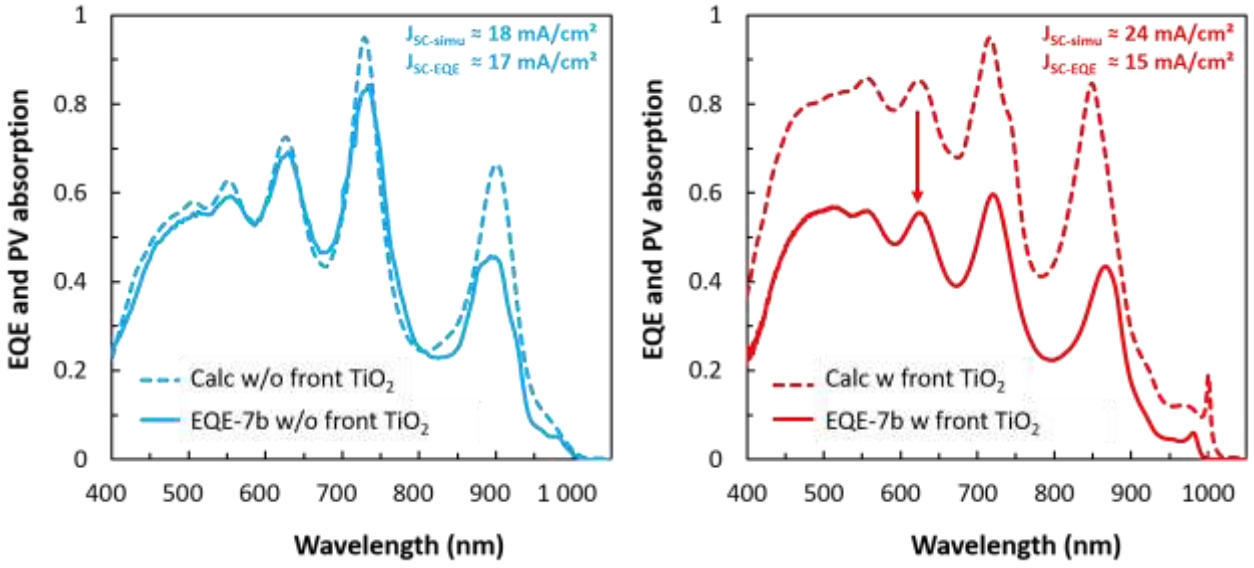

Figure 5.1-15:Comparison of EQE and calculated PV absorption for the same transferred solar cell (#7b) without front nanostructuration (blue left) and in the case of front structuration presented in Figure 5.1-13 (red right).

In Table 5.1-3, we present 1 sun I-V measurements performed before and after the deposition of the front TiO_2 nanocylinder coating. We also perform dark I-V analysis with two-diode model fitting. We notice a -10 mV degradation on the V_{OC} that we can relate with a x1.7 increase of dark current (n=2). We also notice a decrease of the fill factor (FF) from 0.72 to 0.64 that we can relate with a x3 increase on the serie resistance. We consider these electrical degradations to be relatively small if we think about the complexity of the process especially the cracks in the front TiO_2 layer. Therefore, we think the 30% loss between numerical and experimental EQE originates mostly from optical losses. We think that scattering loss or absorption loss in the TiO_2 layer might be responsible for this decrease.

Table 5.1-3: 1-sun I-V properties of #7b MQW solar cell without and with front TiO_2

MQW solar cell # 7b	J_{SC} (mA/cm²)	V_{OC} (V)	FF
Transferred w/o TiO_2	17	**0.86**	0.72
Transferred w TiO_2	15	**0.85**	0.64

In conclusion, for this part, we have shown that, using nanostructures, we are able to increase light absorption and at the same time keep FP resonant effects to enhance specific parts of the spectrum. We see that fabrication does not always go as planned but precise analysis can help to improve for future realizations.

5.2 Application to quantum dot solar cells

In this part, we investigate the application of light management strategies to Okd-3 type of quantum dot solar cell structure that was discussed in chapter 3 and 4. As in the case of MQWs, light management can be a great asset to increase light absorption in QD layers. As discussed in the previous chapter, their coefficient of absorption is very low even compared with MQW layers. It often necessitates numerous layers of QDs to compensate. Simultaneously a thinner *i*-region and thus a smaller number of layers is favorable for a more efficient carrier transport. Furthermore, a thinner stack is also favorable to reduce the dislocation and defects density. Different approaches have been proposed using scattering by metallic nanoparticles [262] or diffractive gratings [108].

In the case of IB-QDSCs, light management can also be used to enhance the photofilling of QDs and cautious light management positioned for inter-band transitions wavelength might have an impact on the dynamic of the IB. First, we discuss the effect of a simple FP cavity to enhance light absorption for the inter-band transitions. In a second part, we present an innovating strategy to enhance light absorption in QD-IBSCs using a front metallic nanogrid and discuss the problematic of low-absorbing material.

5.2.1 Fabry-Pérot effect on QDSCs

In this part, we present the FP cavity study of our QDSCs. First, we explain the design and fabrication of our samples. Second, we present the light absorption enhancement for the valence band (VB) to quantum states transition and then for the quantum states to conduction band (CB) transition.

5.2.1.1 Design and fabrication of Fabry-Pérot QDSCs

As discussed in chapter 2, on one side a precise design with optical simulation is needed to tune the thickness of the FP cavity and have resonances at strategic positions. On the other side, we have seen in chapter 3, that a precise knowledge of the QDSC system is needed to evaluate the effect of the FP cavity.

i). Light management strategy on QDSC system

In Figure 5.2-1, we show a schematic illustration of the light management strategy proposed for QDSCs using simple FP cavity. In Figure 5.2-1 (a), the In(Ga)As / $Al_{0.2}GaAs$ energy band system is reminded with different energy bandgaps that can be identified: $Al_{0.2}GaAs$ host material at 1.68 eV, InGaAs WL at 1.55 eV and In(Ga)As QDs around 1.2 eV. The transfer on a gold mirror of a 515 nm *p-i-n* junction with 10 layers of QDs sandwiched in the *i*-region enables the creation of a FP cavity as shown in Figure 5.2-1 (b). In Figure 5.2-1 (c), we present the calculation of total absorption spectrum inside the FP cavity. No absorption in the QD layers is considered in this simulation, the sub-bandgap FP resonances come from the absorption in the gold mirror. FP resonances are chosen to enhance VB to QDs transition (QDs PL), IR laser region and also possibly the QDs to CB transition that is supposed to have a higher absorption starting at 2.5 µm (0.5 eV). It is still not clear where FP resonances should be positioned in the case of IBSCs. Anyhow, we believe that this design is a first step for the realization of light management in the same way as for MQW solar cells when we used FP cavity as a cornerstone.

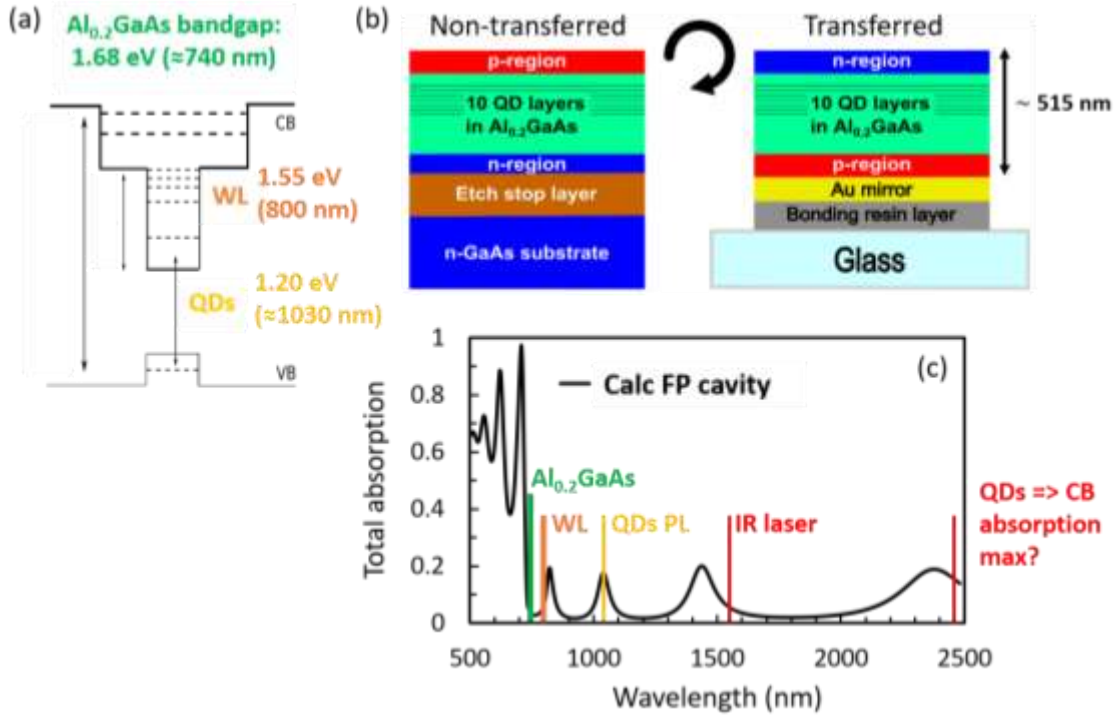

Figure 5.2-1: Schematic illustration of the light management strategy proposed for QDSCs using simple FP cavity. (a) In(Ga)As / $Al_{0.2}GaAs$ energy band system is reminded with different energy bandgaps that can be identified: $Al_{0.2}GaAs$ host material at 1.68 eV, InGaAs WL at 1.55 eV and In(Ga)As QDs around 1.2 eV. (b) The transfer on a gold mirror of a 515 nm *p-i-n* junction with 10 layers of QDs sandwiched in the *i*-region enables the creation of a FP cavity. (c) Calculation of total absorption spectrum inside the FP cavity is shown. FP resonances are chosen to enhance VB to QDs transition (QDs PL), IR laser region and also possibly the QDs to CB transition that is supposed to have a higher absorption starting at 2.5 µm (0.5 eV).

ii). Fabricated QDSC samples

In Figure 5.2-2, we give a detailed description of QDSC samples that are used to evaluate the effect of the FP cavity. In Figure 5.2-2 (a), transferred-on-mirror (M: Okd-3-0.2) and non-transferred (NT: Okd-3-1.4) 1x1 cm² samples are shown with solar cells specifically chosen (open red square: S3.2 and S2.4). A precise description of transferred samples is given in Chapter 2.

In Figure 5.2-2 (b), we show the results of PL mapping of Okd-3 3-inch wafer done with Horiba PL mapper before fabrication. The X-Y characterization step is of 2 mm (size of pixels on the color-maps). PL excitation is achieved with a 532 nm laser at low-intensity illumination (≈0.1 W/cm²). Colormaps are taken from chapter 3: Figure 3.2-16 and Figure 3.2-17. Colors indicate PL peak wavelength position in the top image (light blue: 1010 nm, light green: 1040 nm and light red: 1070 nm). In the bottom image, it indicates PL peak intensity in arbitrary units (light blue: 1, light green: 3 and light red: 5). 1x1 cm² samples positions are shown and written in white. Transferred (M) and non-transferred (NT) solar cells are chosen in order to be in the same QD zone in-between the middle (M) and edge (E) region identified in chapter 3: Figure 3.2-19. Both cells are about on the same circle indicated by the red arc. Therefore, PL peak position is the same for (1.2eV) but we find that intensity is about four times superior in the case of the transferred solar cell. We already discussed this asymmetry in chapter 3. We could not use other samples that were fabricated more in the center of the wafer (with higher and more uniform QD density) because of different schedule planifications between France and Japan fabrication and measurements campaigns.

We also show the position of two other NT solar cells that are used as references from sample 1.3: Okd-3-1.3-S2.2 (red triangle) and Okd-3-1.3-S4.4 (purple triangle). In Figure 5.2-2 (c), we reproduce Figure 3.3-5 taken from chapter 3. For three different wafer zones (C: Center, M: Middle, E: Edge) we show superposition of EQE measurements from solar cells in these zones and AFM measurements as previously studied in Figure 3.2-18. The transferred and NT solar cells are likely to have a QD distribution in-between M and E zones. For 1.2 eV PL peak position, if we compare M and E curves, we see a ratio of x10 for the EQE and a x4 ratio for the number of QDs per µm². We also find a x4 ratio between transferred and NT solar cells position on PL peak intensity map (b).

In Chapter 4, we investigated in detail the QDs electrofilling dynamic for different PL excitation regimes. In Figure 4.1-22, we noticed that at room temperature for low-excitation regime, large neighbouring QDs with low PL energy are filled first. In the case of the transferred and NT solar cells, it is possible that both cells have a bimodal M-like distribution with a peak close to 1.2 eV for "large QDs" which would explain the PL emission at 1.2 eV. However, the x4 ratio in PL intensity might indicate that the transferred QDSC has a higher number of "large QDs" compared to the NT QDSC that would be closer to an E-like distribution.

In summary, NT and transferred QDSCs are close but not strictly the same. This fact is important to interpret correctly any effect of the FP cavity.

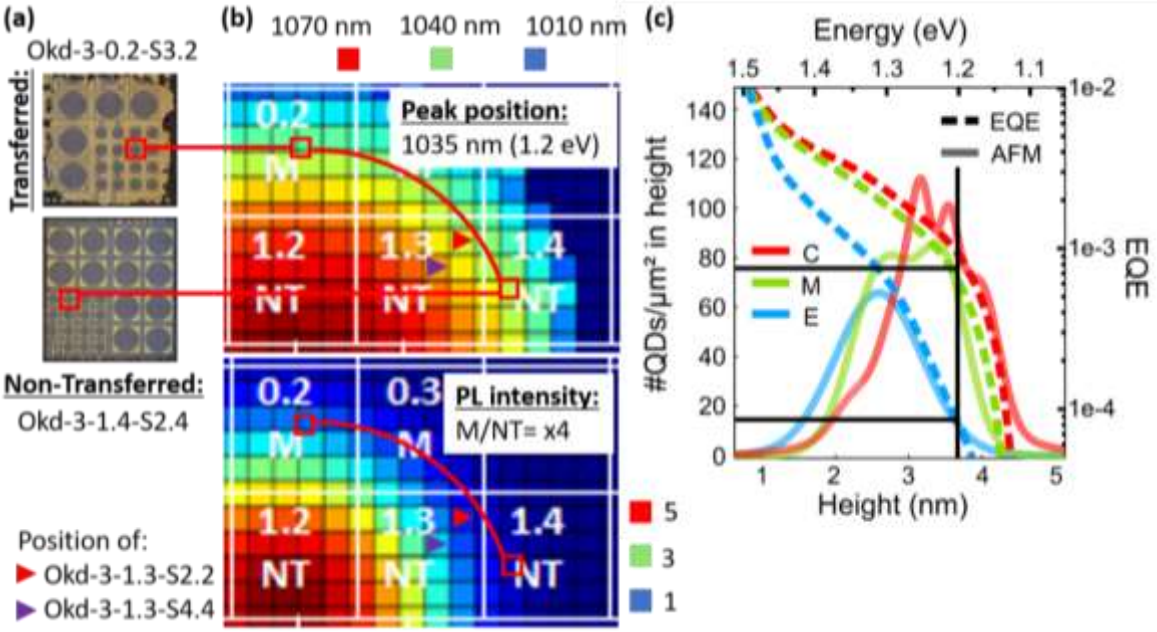

Figure 5.2-2: Description of QDSC samples used in order to evaluate the effect of the FP cavity. (a) Transferred-on-mirror (M: Okd-3-0.2) and non-transferred (NT: Okd-3-1.4) 1x1 cm² samples are shown with solar cells specifically chosen (open red square: S3.2 and S2.4). (b) PL mapping of Okd-3 wafer before fabrication done with Horiba PL mapper with 2 mm X-Y characterization step (pixels on the colormaps) at low-illumination (≈0.1 W/cm²) with 532 nm excitation is taken from chapter 3: Figure 3.2-16 and Figure 3.2-17. Colors indicate PL peak position in the top image (light blue: 1010 nm, light green: 1040 nm and light red: 1070 nm). In the bottom image, it indicates peak intensity in arbitrary units (light blue: 1, light green: 3 and light red: 5). 1x1 cm² samples positions are shown and written in white. Transferred (M) and non-transferred (NT) solar cells are chosen in order to be in the same QD zone in-between the middle (M) and edge (E) region identified in chapter 3 in Figure 3.2-19. PL peak position is the same (1.2eV) but intensity is about fourth time superior in the case of the transferred solar cell. We also show the position of two other NT solar cells that are used as references from sample 1.3: Okd-3-1.3-S2.2 (red triangle) and Okd-3-1.3-S4.4 (purple triangle). (c) Taken from chapter 3: Figure 3.3-5, superposition of EQE measurements characterization from samples in different wafer zone with AFM measurements as previously studied in Figure 3.2-18. The M and NT solar cells possibly have a QD distribution in-between M and E curves. For 1.2 eV PL peak, we see a ratio of 4 between M and E numbers of QDs per µm² which is about the same ratio as the PL intensity ratio between M and NT position on PL peak intensity map (b).

5.2.1.2 Enhancement for VB to QDs states

In this part, we focus on FP effects to enhance the VB to QDs states transition. First, we compare electrical results for transferred (M) and NT QDSCs and then we compare PL results to evaluate the influence on the IB dynamic using the same characterization method detailed in chapter 4.

i). Electrical study

In Figure 5.2-3, we present 1-sun I-V (left) and dark I-V (right) investigations for Okd-3-1.4-S2.4 non-transferred solar cell (blue) and Okd-3-0.2-S3.2 transferred solar cell (red). We also show a typical Al0.$_2$GaAs *p-i-n* solar cell grown in Okada laboratory with no QDs.

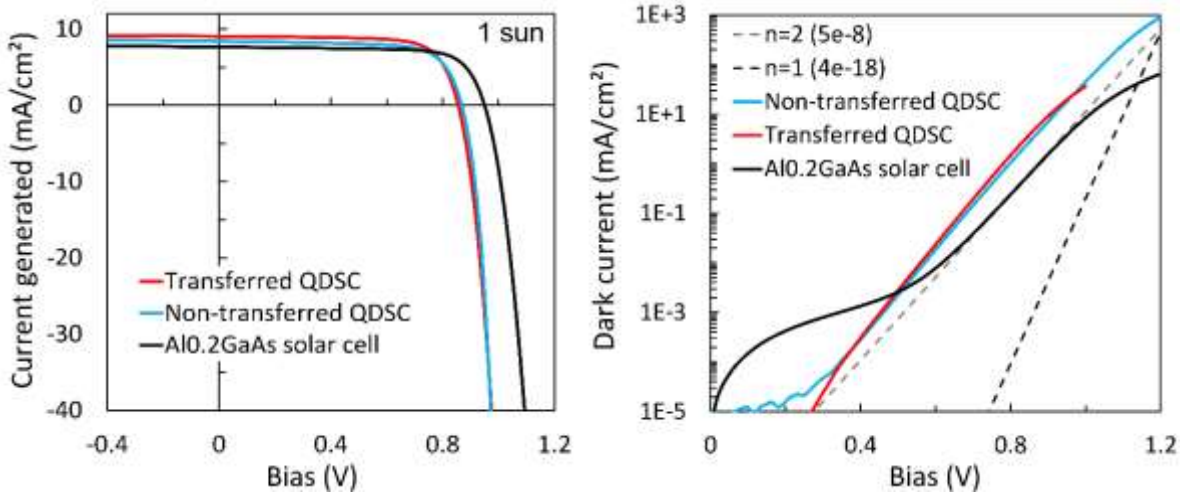

Figure 5.2-3: 1-sun I-V (left) and dark I-V (right) investigations for Okd-3-1.4-S2.4 non-transferred solar cell (blue) and Okd-3-0.2-S3.2 transferred solar cell (red). We also show a typical Al0.$_2$GaAs *p-i-n* solar cell grown in Okada laboratory with no QDs.

In Table 5.2-1, we summarize 1-sun I-V characterization results and two-diode model fitting parameters obtained by fitting the dark I-V. We notice that NT and M QDSCs have a lower V_{OC} compared with reference Al0.2GaAs without QDs. The difference is less than 100 mV. In theory, the difference could be higher because we have a ~500 meV difference between the host material energy bandgap and QDs PL emission. As discussed in Chapter 3 and 4, in the literature $Al_{0.2}GaAs$ *pn* solar cells have demonstrated V_{OC} record of 1.25 V [139]. We consider that our low temperature MBE grown $Al_{0.2}GaAs$ material has many defects, which holds back the V_{OC} performance of our $Al_{0.2}GaAs$-based solar cells.

Table 5.2-1: 1-sun I-V characterization results and two-diode model parameters for NT, M and $Al_{0.2}GaAs$ solar cell

Sample	J_{SC} (mA/cm²)	V_{OC} (V)	FF	Efficiency (%)	J_{dark} n=2 (mA/cm²)	Rs (Ω.cm²)
Al0.2GaAs solar cell	7.67	**0.949**	0.75	**5.46**	**4.3e-8**	**7.8e-2**
Non-transferred QDSC	8.42	**0.868**	0.72	**5.26**	**1.5e-7**	**1.6**
Transferred QDSC	9.07	**0.856**	0.74	**5.74**	**1.6e-7**	**4.0**

Overall, Figure 5.2-3 and Table 5.2-1 results show that the transfer process is well controlled and does not degrade the QDSC from an electrical point of view. Serie resistance is x2.5 higher for the transferred solar cell. We often observe this phenomenon for our transferred solar cells and we attribute it to the localized contacts that are fabricated before the deposition of the gold mirror. Especially in the case of QDSCs we did not use an optimal UV-mask to engineer localized back contacts. We also notice that the V_{OC} is 10 mV below and J_{dark} (n=2) increases slightly for M-QDSC compared with NT-QDSC. This decrease of the V_{OC} (and increase of J_{dark} (n=2)) might not be due to deg-

radation from the transfer process but maybe due to the difference in QD distribution as discussed previously.

Indeed, in Figure 5.2-4, we present a comparison of non-transferred (NT) and transferred-on-mirror (M) samples fabricated from Okd-3 3-inch wafer growth. PL mapping results are shown to indicate their positions as in Figure 5.2-2. On the left, we show PL peak position in wavelength done with Horiba PL mapper on Okd-3 wafer before fabrication and the indicative number for each sample. On the right, we show PL peak intensity and the average V_{OC} of characterized solar cells from each sample. First, looking only at non-transferred samples from the "off-beam" to the center zone as identified in Figure 3.2-19, we see that V_{OC} is decreasing from 0.88 V (1.5-NT) to 0.84 V (1.2-NT). This is explained by the fact that on sample 1.5-NT there is almost no QDs that are grown, only WL is present as explained previously in chapter 3: Figure 3.3-4. On the contrary, sample 1.2-NT in the center zone has larger QDs with lower PL energy that will reduce the V_{OC} compared to sample with WL only or even samples with smaller QDs like 1.3 and 1.4 samples.

We show that 1.1 transferred (M) sample and 1.3 non-transferred (NT) samples both have averaged V_{OC} of 0.85 V. They are at symmetric positions compared with the center of the wafer. Their PL mapping in peak position and peak intensity are also almost identical which means that they might have a similar QD distribution. Therefore it might indicate that the transfer process did not degrade sample 1.1-M (V_{OC} of 0.85 V). In comparison, QDSCs from sample 0.2-M have an average V_{OC} of 0.86 V in-between 1.4-NT (V_{OC} of 0.87 V) and 1.3-NT QDSCs (V_{OC} of 0.85 V). This might indicate that transferred QDSC from 0.2-M sample have a QD distribution in-between 1.4 and 1.3 solar cells.

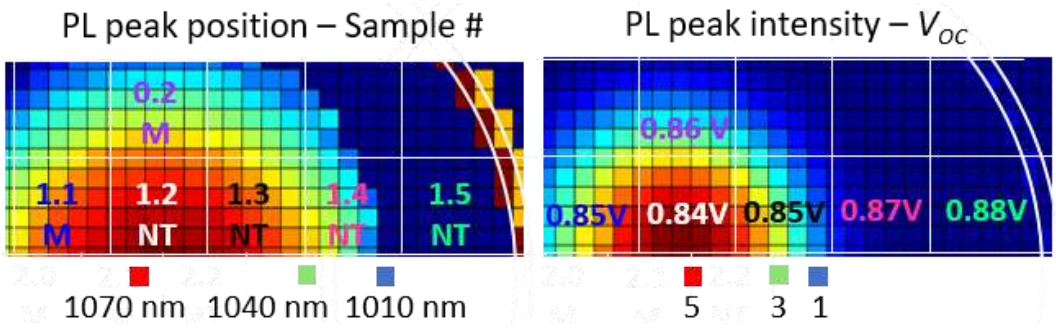

Figure 5.2-4: Comparison of non-transferred (NT) and transferred-on-mirror (M) samples fabricated from Okd-3 3-inch wafer growth. PL mapping results are shown to indicate their positions as in Figure 5.2-2. (left) PL peak position and sample indicative number. (right) PL peak intensity and averaged V_{OC} of characterized solar cells for each sample.

In Figure 5.2-5, we show a comparison of EQE for non-transferred and transferred solar cells with reflectometry measurements to evidence the FP resonances. A typical $Al_{0.2}GaAs$ *p-i-n* solar cell grown in Okada laboratory is shown to give an indication on the host material bandgap. On the right figure, we zoom on the WL and QD spectral region. WL bandgap is around 800 nm and QD bandgaps depend on the sample position as previously indicated in chapter 3: Figure 3.3-4. We estimate a x2 enhancement or x10 FP ratio enhancement depending if we compare transferred QDSCs from 0.2 or 1.1 samples with non-transferred QDSCs from 1.3 or 1.4 samples. Their positions are indicated in Figure 5.2-2. As discussed previously, we consider that samples 1.1 and 1.3 have about the same QD distribution. At Fabry-Pérot resonance wavelength (λ = 1040 nm), we observe a x5 ratio enhancement between the EQE from 1.1-M-S2.1 solar cell and the EQE from 1.3-NT QDSCs.

Using absorption coefficient that we found in Chapter 3 and Chapter 4 by different methods, we can simulate the expected FP absorption enhancement ratio from a NT-QDSC to a M-QDSC with the layer design represented in Figure 5.2-1. For the QDs spectral region, a maximum enhancement ratio of x6.8 is found at λ=1040 nm right on the FP resonance peak. The ratio enhancement is of x5 at λ=1020 nm which is higher than the x2 ratio enhancement of 0.2-M-S3.2 solar cell compared with 1.3-NT QDSCs. It amounts to x2.5 at λ=1000 nm which is lower than the x10 ratio enhancement of 0.2-M-S3.2 solar cell compared with 1.4-NT QDSC. Here again, it seems that the transferred QDSC from 0.2-M sample has a QD distribution in-between 1.4 and 1.3 solar cells.

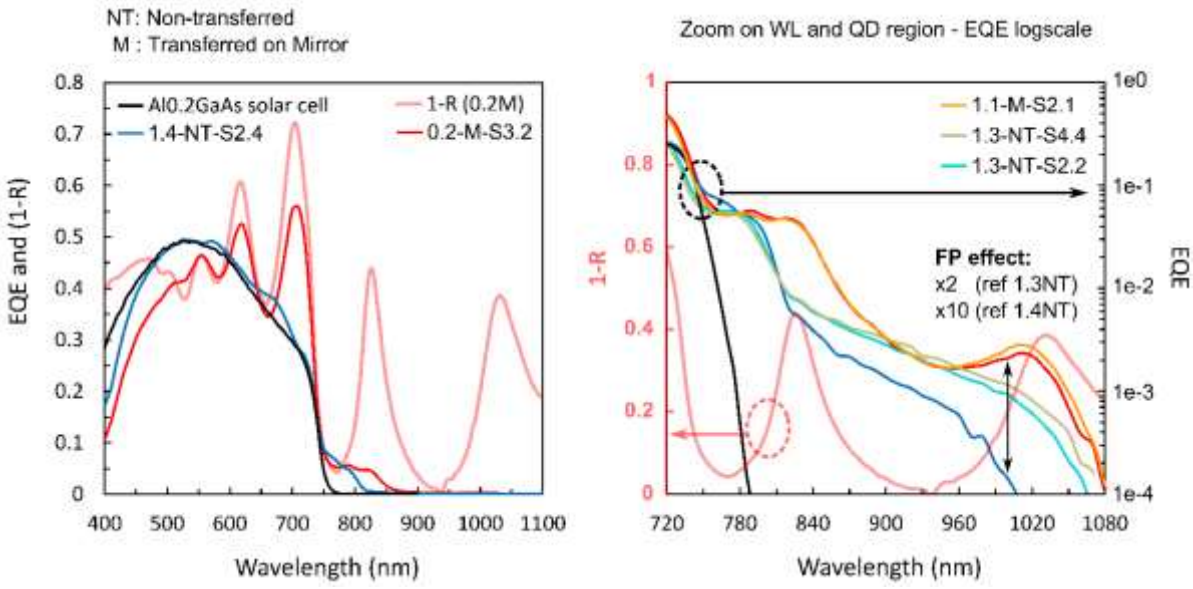

Figure 5.2-5: EQE comparison of non-transferred and transferred solar cells. Reflectometry measurements is shown as an indication of the FP cavity. A typical $Al_{0.2}GaAs$ *p-i-n* solar cell grown in Okada laboratory is shown which gives an indication on the host material bandgap. On the right figure, we zoom on the WL and QD spectral region. WL bandgap is around 800 nm and QD bandgaps depend on the sample position as previously indicated in chapter 3: Figure 3.3-4. We estimate a x2 or x10 FP ratio enhancement in comparison with non-transferred solar cells form 1.3 or 1.4 samples which positions are indicated in Figure 5.2-2.

ii). Photoluminescence study

In Figure 5.2-6, we compare PL characterization in the case of focused spots for Okd-3-1.4-S2.4 non-transferred (top line) and Okd-3-0.2-S3.2 transferred solar cell (bottom line). We use the same approach as in Chapter 4: Figure 4.1-12. We show the results for two extreme laser excitation regimes that were discussed in chapter 4: 0.01mW (low-excitation regime) and 1.6 mW (high-excitation regime). Images of integrated intensity are shown for integration over all the spectrum (left) and only the host material spectral region (right): [1.68-1.73 eV]. In the middle, we show PL spectrum in log scale taken from pixels in different spot zones defined by their ratio with maximum intensity pixel: 100% is the center zone, 10% is a middle zone and 0.5% is considered off-spot.

We notice that PL spot size from transferred sample is always smaller. We think it might come from our characterization setup. The difficulty with focused characterization is that we are not sure that both samples had the same focus conditions. Measurements were made at 1-day interval and focusing distance was modified when we changed the sample. Moreover, transferred samples are 500 µm thicker than non-transferred sample therefore the focal distance will necessarily need to be readjusted. Thus, it is difficult to compare PL intensity spectra because excitation conditions might not be the same.

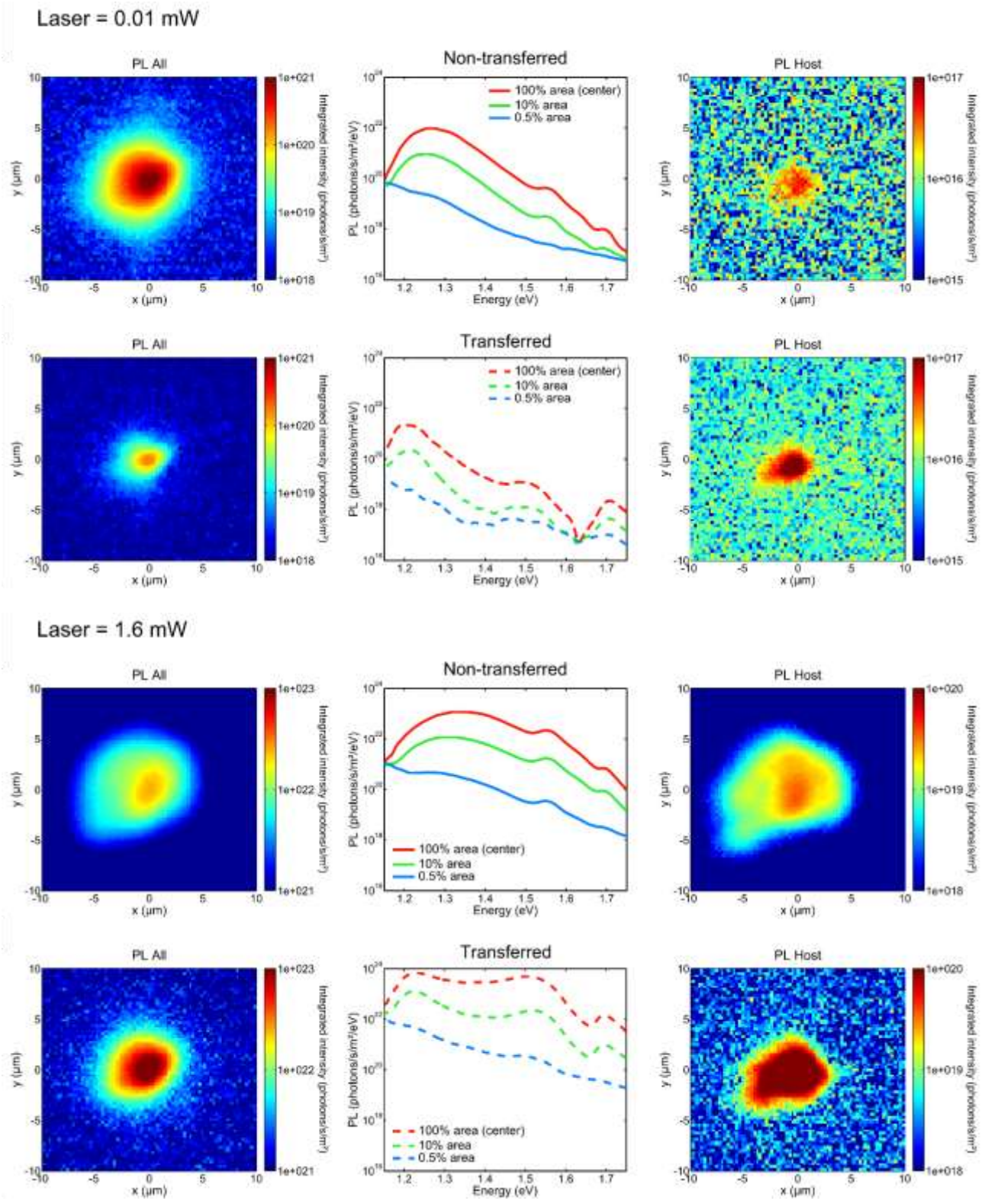

Figure 5.2-6: Comparison of PL characterization in the case of focused spots for Okd-3-1.4-S2.4 non-transferred (top line) and Okd-3-0.2-S3.2 transferred solar cell (bottom line). We use the same approach as in Chapter 4: Figure 4.1-12. Two extreme laser excitation regimes are shown as discussed in chapter 4: 0.01mW (low-excitation regime) and 1.6 mW (high-excitation regime). Images of integrated intensity are shown for integration over all the spectrum (left) and only the host material spectral region (right): [1.68-1.73 eV]. In the middle, we show PL spectrum in log scale taken from pixels in different spot zones defined by their ratio with maximum intensity pixel: 100% is the center zone, 10% is a middle zone and 0.5% is considered off-spot.

Nevertheless, if we just compare the evolution of PL spectrum, we see that PL intensity from transferred QDSC is lower than the non-transferred QDSC in the low-excitation regime but higher in the high-excitation regime. We believe that the difference of spot size may be responsible for the lower intensity.

In Figure 5.2-8, we compare calibrated PL spectra for Okd-3-1.4-S2.4 non-transferred (blue) and Okd-3-0.2-S3.2 transferred (red) QDSCs with defocused spot as shown in Figure 5.2-7. Three different levels of laser excitation are compared: [∼0.8 mW; ∼2 mW; ∼28 mW]. The levels are not strictly equal for NT and M solar cells but we will consider it is sufficient for the purpose of comparing the spectra. Reflectometry measurement (dashed black) for the transferred QDSC is shown to better identify the contribution of FP resonances. The characterization with defocused spot allows a more exact comparison of the two samples because both characterization were performed on the same day and the optical setup was untouched. As in chapter 4, for the defocused spot, we are in a low-excitation regime so we consider that there is no hot carrier effect in the QDs.

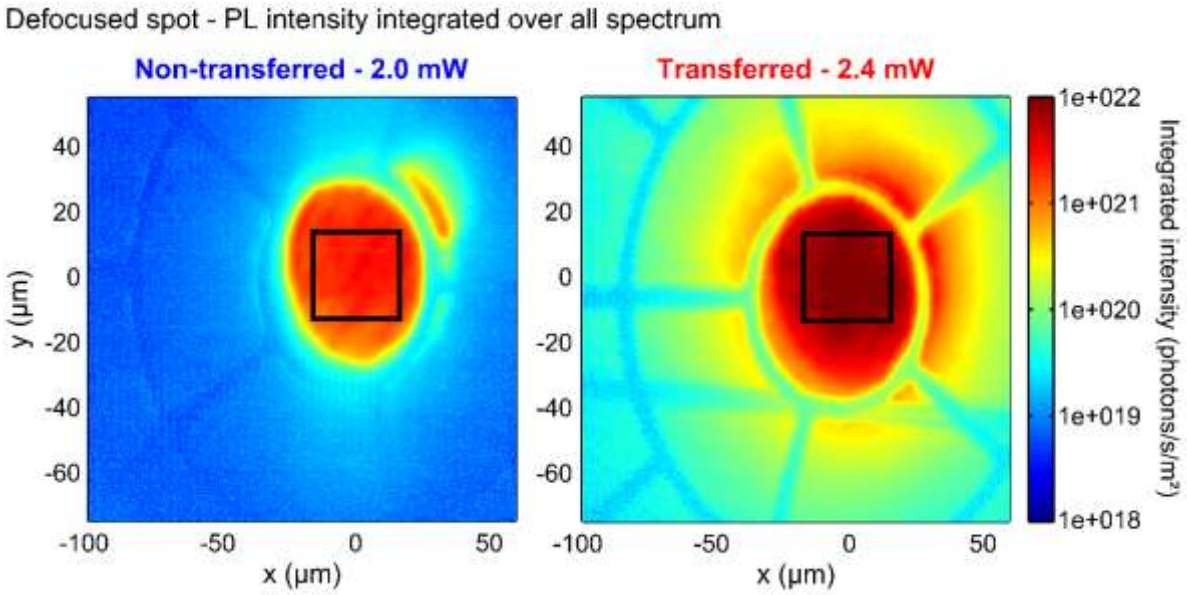

Figure 5.2-7: PL spot images of defocused spots for ∼2 mW laser excitation on Okd-3-1.4-S2.4 non-transferred (left) and Okd-3-0.2-S3.2 transferred (right) solar cells. Black square of 30x30 µm² are centered on the maximum point of the PL spots in both case. It shows the spatially integrated zone from which we extract PL spectrum presented in Figure 5.2-8.

Normalization of PL by E² and absorptivity (Abs) is shown using absorption coefficient values found by PL fitting (section 4.1.3.2) and plotted in Figure 5.2-9. PL normalization by E² and absorption enables to see that host material PL and therefore quasi-Fermi level splitting (QFLS) is the same for both samples while the level of QFLS in the QDs or WL is always lower for the transferred QDSC. For the ∼0.8 mW laser excitation, the difference in QFLS amount to about 60 meV ($k_B T ln[PL_{norm_{NT}}/PL_{norm_M}]$). This difference is quite high if we consider that both cells only have a 12 meV difference of V_{OC} under 1 sun illumination. We also notice that the transferred solar cell normalized PL is getting closer to the non-transferred level when we increase the laser excitation between ∼0.8 mW and ∼2 mW. These results confirm the focused characterization. We see again a different behavior in the filling of QDs between non-transferred and transferred solar cells. For the highest excitation condition at ∼28 mW, we see a redshift for the transferred QDSC that we attribute to laser heating. We know that transferred samples have a poor thermal conductivity compared with as-grown sam-

ples. Transferred samples are glued to glass substrate (thermal conductivity of polymer resist and glass < 1 W/K/m) which has a poorer thermal conductivity compared with GaAs material (50 W/K/m).

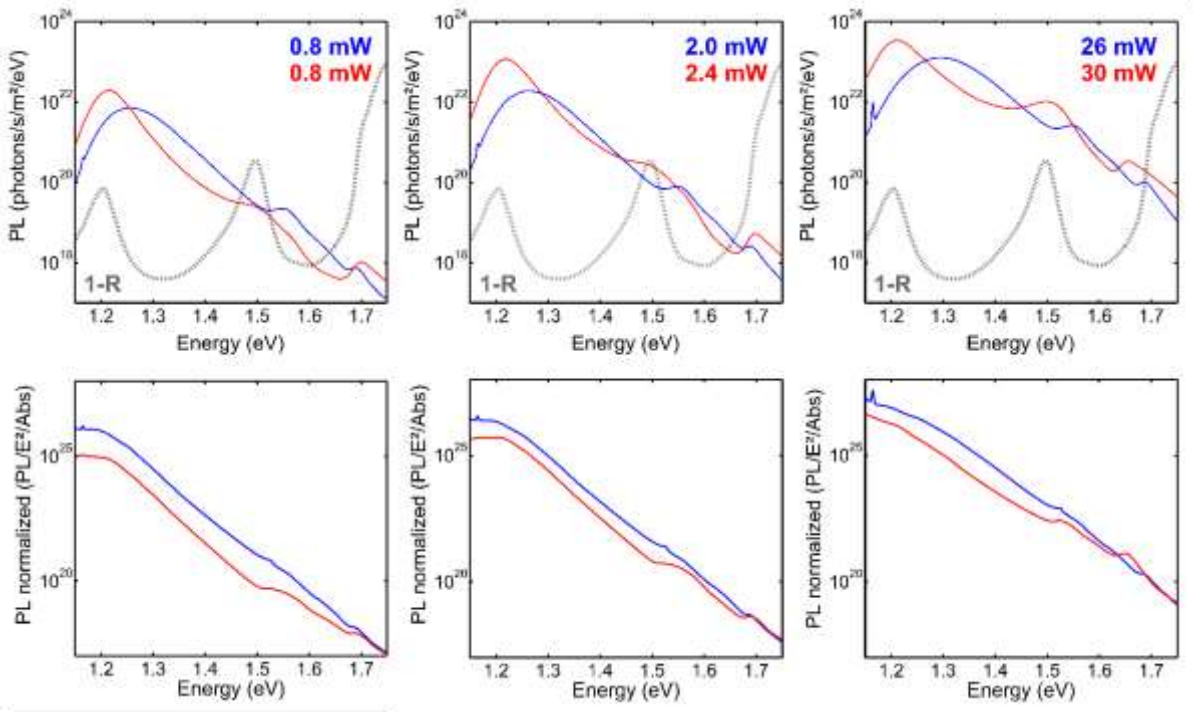

Figure 5.2-8: (top line) Comparison of calibrated PL spectrum for Okd-3-1.4-S2.4 non-transferred (blue) and Okd-3-0.2-S3.2 transferred (red) QDSCs with defocused spot as shown in Figure 5.2-7. Three different level of laser excitation are compared: [~0.8 mW; ~2 mW; ~28 mW]. The levels are not strictly equal for NT and M solar cells but still close for the purpose of comparing the spectrum. Reflectometry measurement (dashed black) for the transferred QDSC is shown to better identify the contribution of FP resonance. Normalization of PL by E^2 and absorptivity (Abs) is shown using absorption coefficient values found by PL fitting and represented in Figure 5.2-9.

There are two remarks that can be made from this study:

- First, it is difficult to evaluate the impact of the FP cavity on the transferred QDSC because both transferred and non-transferred solar cells does not have the same QDs distribution. However, if we were to consider that the difference in QDs distribution is negligible on the filling dynamic, we could say that the FP cavity has a slowing effect on the filling of QDs states.

  In term of intermediate band (IB) dynamics, we can refer to the model developed in chapter 4. We see that both an increase of the density of states of the IB (D_I) or a decrease of the QDs radiative recombination time (τ_I) can slow done the filling of the IB. From a QDSC point of view, an increase of the density of states would correspond to an increase of QDs and/or QD states (for example larger QDs). In our case, we suspect that the transferred solar cell (Okd-3-0.2-S3.2) has a higher QD distribution and larger QDs compared with the non-transferred QDSC (Okd-3-1.4-S2.4). It is also interesting to notice that we performed TRPL measurements on transferred and non-transferred samples for Okd-1 type of growth in the middle-center region of the wafer. We found a reduced recombination time at room temperature for the transferred sample ($\tau_{TRPL-transferred}$~2 ns) compared to non-transferred sample ($\tau_{TRPL-transferred}$~8 ns).

As we discussed in other parts of our study, the confinement of the electronic wave function in a quantum structure defines an intrinsic radiative lifetime for the excitons. It is theoretically possible to change the emission of a quantum structure by inserting it into an optical resonator. It was carried out for the first time in 1990 [263], for a quantum well inserted in a planar semiconductor microcavity and strong coupling was first observed in 1992 in Arakawa laboratory [264]. However, to achieve strong coupling, it is necessary to use resonances with high quality factor. In our study, the quality factor are always less than hundred and closer to a dozen. Therefore, light is weakly coupled and our FP cavity should have a negligible effect on recombination time.

- Second, we see that even though the QFLS for QDs and WL is different for transferred and non-transferred QDSCs, the QFLS for the host material is the same. It is not surprising in the sense that both solar cells have the same $Al_{0.2}GaAs$ host layers therefore the PL emission from both host material will be the same. In this defocused study, we are in a low-excitation regime with almost no hot carriers in the QD states. There is a chance that hot carrier will appear sooner in the non-transferred solar cell because of higher saturation and therefore the host material PL should increase faster, based on what we concluded in chapter 4.

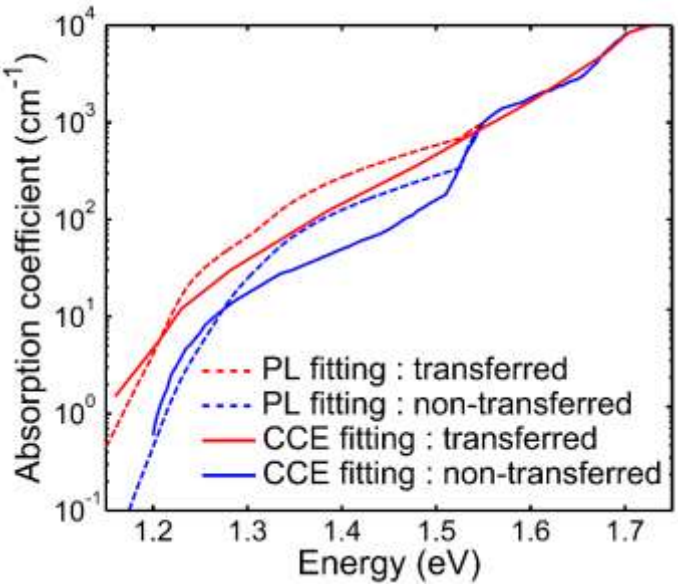

Figure 5.2-9: Absorption coefficients for Okd-3-1.4-S2.4 non-transferred (blue) and Okd-3-0.2-S3.2 transferred (red) QD solar cells. First using reverse bias EQE, fitting of CCE gives a first estimation of absorption coefficient as explained in Chapter 3: Figure 3.4-17. Then using PL fitting, we get another estimation as explained in Chapter 4: Figure 4.1-34.

5.2.1.3 Enhancement for QDs states to CB transition

In this part, we focus on FP effects to enhance QD states to CB transition. First, we compare electrical results for transferred (M) and NT QDSCs using ΔEQE measurements. Then we compare ΔPL results to evaluate the influence on the IB dynamic using the same characterization method detailed in chapter 4.

i). Two-step two-photon electrical generation

In order to detect an increase in the photocurrent as a direct result of optical transitions of electrons from QD states (or intermediate band: IB) to CB, we use the measurement system as illustrated in Figure 5.2-10 (a). Light from a Xe lamp, with an AM 1.5 filter placed at the exit, passes through

an appropriate set of filters that allows only the infrared (IR) region of λ>1400 nm (E<0.9 eV) to be transmitted. ΔEQE curves are measured at room temperature (RT) for short-circuit condition without and with continuous illumination of IR light. The alternating current (AC) signals is integrated and averaged using a standard lock-in technique.

There are two escape paths that can be caused by IR pumping as described in Figure 5.2-10 (b): (i) On one hand, high-energy electrons, from the absorption of photons of wavelength λ < 740 nm, can recombine in the QDs and escape again by the absorption of an IR photon. (ii) On the other hand electron can be promoted to the CB by sequential two-photon absorption (S-TPA), first with a photon of wavelength 740 nm < λ < 1100 nm to the IB and then by IR pumping to the CB.

In Figure 5.2-10 (c), we show EQE (solid light red line), ΔEQE (solid clear red line) and ΔEQE/EQE ratio (dashed red line) plotted on the same graph (left axis) for Okd-3-1.1-S1.2 transferred solar cell. Reflectometry measurement performed on Okd-3-1.1-S1.2 transferred solar cell is also represented (solid gray line) in order to evaluate the impact of FP resonances. The vertical dashed line in green indicates $Al_{0.2}GaAs$ host material bandgap at λ = 740 nm.

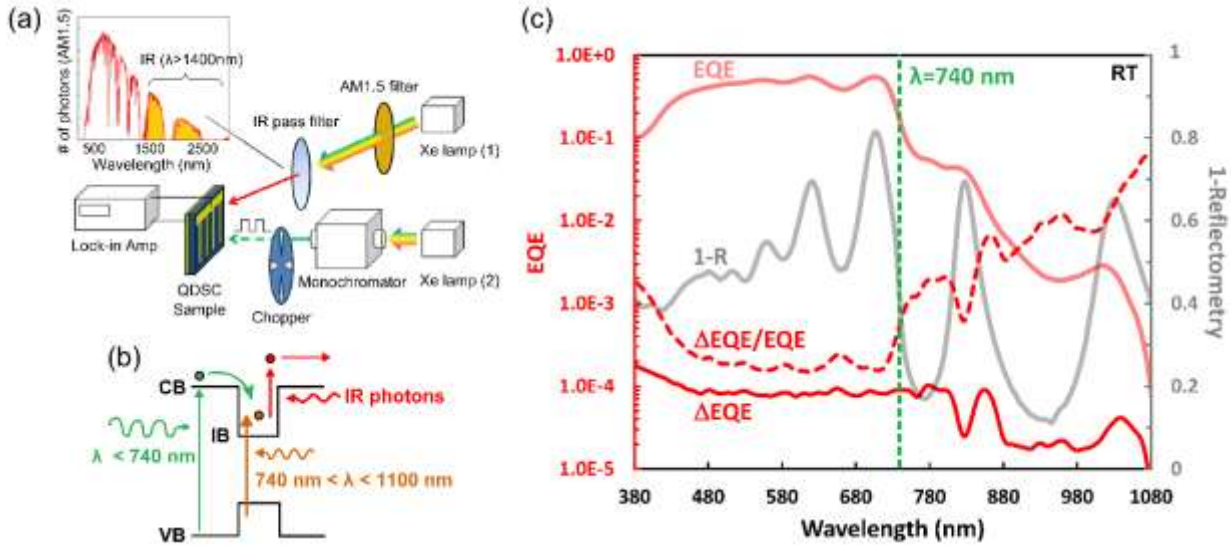

Figure 5.2-10: (a) Schematic measurement setup to characterize photocurrent production as a direct result of optical transitions of electrons from IB to CB. Light from Xe lamp with AM 1.5 filter placed at the exit passes through a set of filters that allows only IR photons of λ > 1400 nm to be transmitted. The illumination of low energy photons from this IR source can only pump electrons from IB to CB. Reproduced from [22]. (b) Schematic of electron escape by IR pumping: (i) High-energy electrons from the absorption of photons of wavelength λ < 740 nm can recombine in the QDs and escape again by the absorption of an IR photon. (ii) Electron can be promoted to the VB by sequential two-photon absorption (S-TPA) of a photon of wavelength 740 nm < λ < 1100 nm to the IB and then by IR pumping. (c) EQE (solid light line), ΔEQE (solid clear line) and ΔEQE/EQE ratio (dashed line) are ploted on the same graph (red lines, left axis) for Okd-3-1.1-S1.2 transferred solar cell characterization performed at room temperature (RT). Reflectometry measurement performed on Okd-3-1.1-S1.2 transferred solar cell is also shown in order to evaluate the impact of FP resonances. Vertical dashed line in green indicates the wavelength position of $Al_{0.2}GaAs$ host material bandgap at λ = 740 nm.

We could not detect any signal of ΔEQE for our Okd-3 non-tranferred samples, the signal level was noisy in-between 1e-6 and 1e-5. It is not surprising as it is usually difficult to detect ΔEQE at RT. The first photocurrent production due to sequential two-photon absorption (S-TPA) at RT was observed in 2011 by Okada laboratory using the same setup [22]. They obtained this result by characterizing a directly Si-doped InAs/GaAs QDSC (1Si/QD) with 25 layers and GaNAs strain-compensating layers grown by Dr. Yasushi Shoji. At that time, they could not detect a ΔEQE signal for their undoped

InAs/GaAs QDSCs. Since then, other groups have extensively discussed the sequential two-photon absorption (S-TPA) at room temperature focusing on a single quantum dot [265] and demonstrating a record S-TPA current of 0.6 mA/cm^{-2} under IR illumination (λ = 1300 nm and power density of 320 mW/cm^{-2}) [266].

In another study, Dr. Yasushi Shoji also fabricated non-transferred Si-doped InAs/$Al_{0.2}$GaAs QDSC (1Si/QD) with 20 QD layers but could not detect ΔEQE signal. In the literature, Tasco et al. have recently investigated ΔEQE characterization for an InAs/$Al_{0.17}$GaAs IBSC [179] that is close to the system we study. At room temperature, they find a negative ΔEQE that they attribute to the fact that carriers, which are extraced from QDs by IR pumping, may recombine non-radiatively in low-quality host material with a high defect density instead of being collected. This effect was first reported by Tex et al [165] and Dr. Ryo Tamaki from Okada laboratory [267] and negative-to-positive change seems to happen when for sufficient photocarrier generation that might saturate trap states.

In our case, it is quite remarkable that we could detect a ΔEQE signal at RT for our undoped InAs/$Al_{0.2}$GaAs transferred QDSC. The ΔEQE/EQE ratio indicate about +1% of S-TPA for the QD spectral region. We see a clear enhancement of ΔEQE at λ = 1040 nm that we attribute to the FP resonance. At λ = 800 nm, near the WL PL position, it seems that FP resonance induces a decrease of the ΔEQE. It could also be due to other effect like what we observed for the ΔPL if there is a peak shift due for example to heating. Anyhow, it seems that the FP cavity also contribute to the S-TPA effect. We will give an interpretation after we present the results from the comparison of non-transferred and transferred samples with two-color excitation.

ii). Two-color excitation

As described in chapter 4, we use the ΔPL setup characterization with defocused spot. In Figure 5.2-11, we show ΔPL ratio evolution with increasing the 532 nm laser excitation (G) for a fixed 1550 nm laser IR pump (P) on Okd-3-0.2-S3.2 transferred QDSC. On the left, the ratio is presented for PL raw data and on the right with a +4 meV shift correction on PL IR: ON that is attributed to IR laser heating. Grey bands are positioned at WL and host material PL peaks energy positions.

Looking at the shift-corrected spectrum on the right, we see a variation around -25% at maximum for QDs PL and of about +20% for WL and the host material PL. In Figure 5.2-12, we compare Okd-3-1.4-S2.4 non-transferred (blue) and Okd-3-0.2-S3.2 transferred (red) QDSCs for a defocused 532 nm laser excitation $\sim$2 mW and 48.6 mW IR laser excitation. We see a x2-3 decrease of the ΔPL ratio for QDs PL and x7-10 increase for WL and the host material PL in the case of the transferred QDSC compared with non-transferred QDSC.

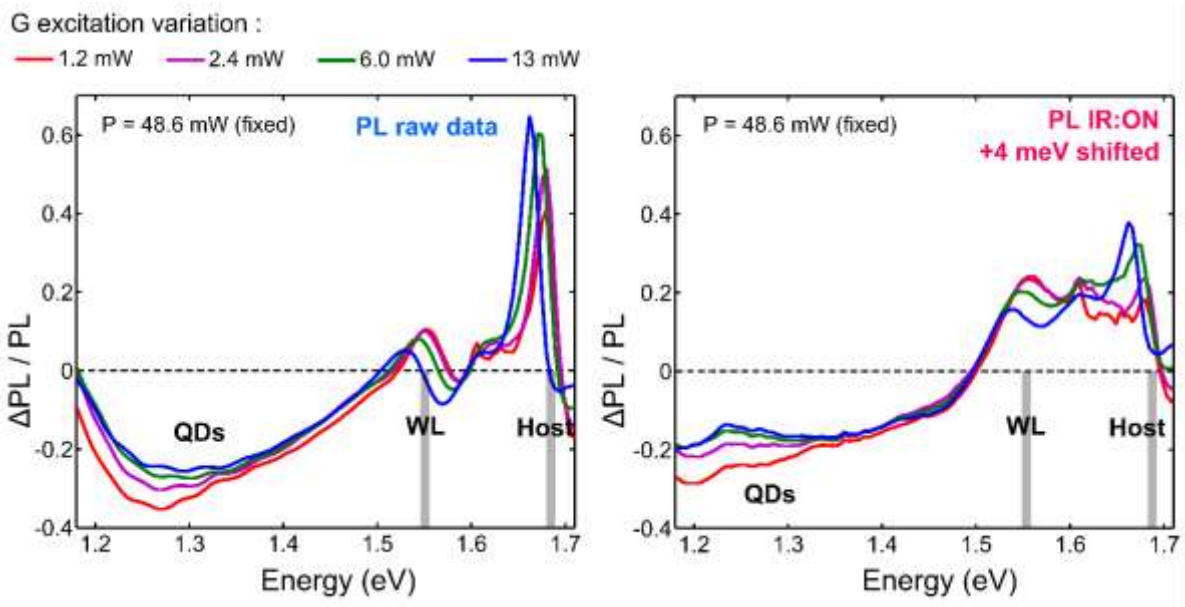

Figure 5.2-11: ΔPL ratio evolution with increasing the 532 nm laser excitation (G) for a fixed 1550 nm laser IR pump (P) on Okd-3-0.2-S3.2 transferred QDSC. On the left, the ratio is presented for PL raw data and on the right with a +4 meV shift correction on PL IR: ON that is attributed to IR laser heating. Grey bands are positioned at WL and host material PL peaks energy positions.

If we refer to the model developed in chapter 4, such a decrease of ΔPL ratio for QDs PL can be explained by a x2 increase of absorption of the IR pump (Abs_{1550nm}), a x2 decrease of the density of states (D_I) or also a x10 increase of the radiative recombination time from QDs states (τ_I). In our case, an increase of Abs_{1550nm} by at least x4 is expected from the simulation of the FP cavity. All these decreases of ΔPL ratio for QDs should lead to an increase of the ΔPL ratio for WL and the host material PL but not as much as what we observe experimentally. A decrease of the ratio between the capture time and recombination time from the CB (τ_{CI}/τ_C) could explain the significant increase in the ΔPL ratio for WL and the host material PL.

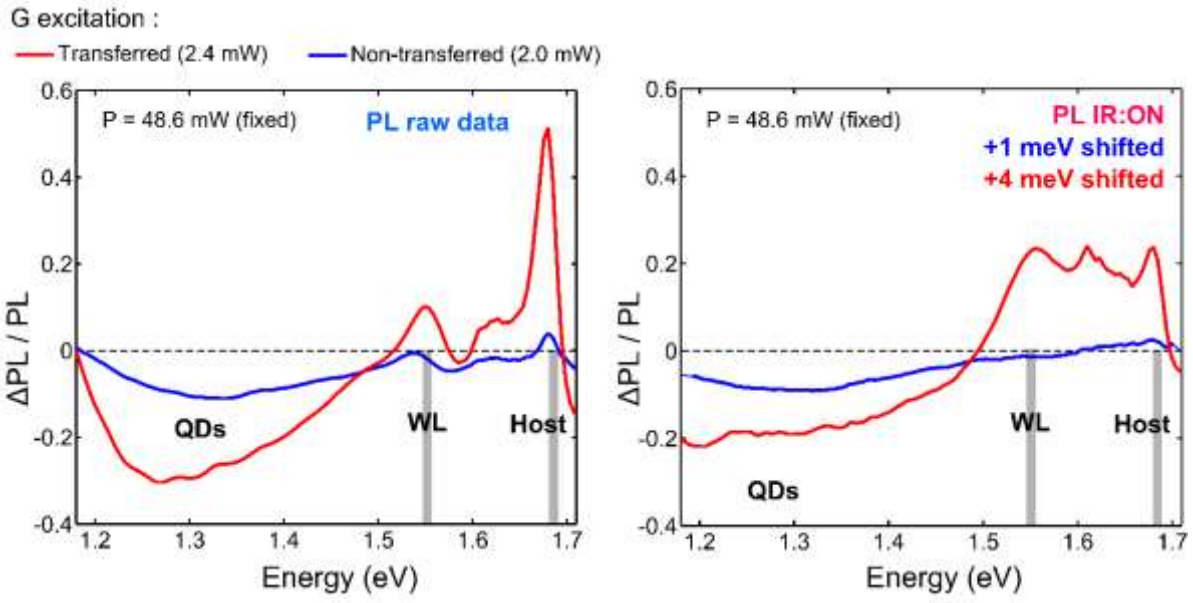

Figure 5.2-12: ΔPL ratio evolution for fixed excitations: 532 nm laser (G) 1550 nm laser IR pump (P) on Okd-3-1.4-S2.4 non-transferred (blue) and Okd-3-0.2-S3.2 transferred (red) QDSCs. On the left, the ratio is presented for PL raw data and

on the right with a +1 meV and a +4 meV shift correction respectively for the non-transferred and transferred QDSCs. Grey bands are positioned at WL and host material PL peaks energy positions.

In conclusion, both electrical and optical characterizations seem to indicate an enhancement effect of the transition from QDs states to the CB thanks to the FP cavity. It is difficult to quantify the importance of this effect because we have no ΔEQE for our non-transferred QDSC and ΔPL effect model indicates that different effect on the IB dynamic can be responsible for the enhancement effect.

5.2.2 Nanopatterns strategy for QDSCs

In this part, we present an innovating strategy to enhance light absorption in QD-IBSCs using a front metallic nanogrid and we discuss the problematic of low absorptive material.

5.2.2.1 Specific strategy for light absorption enhancement

i). Absorption consideration of a In(Ga)As / $Al_{0.2}GaAs$ QD-IBSC system

In an In(Ga)As / $Al_{0.2}GaAs$ QD-IBSC system, we identify three spectral domains, which are linked to the three transitions of interest in an IBSC. For domain (1): 0.4 µm < λ < 0.74 µm, absorption contribution comes mainly from the host material whose optical properties are well known in the literature. For domain (2): 0.74 µm < λ < 1 µm, absorption comes mainly from the VB to QD states transition, which has been studied in chapter 3 and 4. Finally, for the transition from QD states to the CB, k·p calculation from chapter 3 and experimental investigation from the literature indicate a maximum of absorption for domain (3): 3-5 µm in wavelength (250-400 meV in energy).

In Figure 5.2-14, we simulate the absorptivity of an as-grown (non-transferred) In(Ga)As / $Al_{0.2}GaAs$ QD-IBSC. We combine our knowledge of optical absorption over the different spectral domains, especially from the experimental measurements of the absorption coefficient of Okd-5 type of growth presented in chapter 3. We see that absorption in QD layers for spectral domains (2) and (3) are one or two orders of magnitude below absorption in spectral domain (1). Using light management strategies discussed previously, we wish to enhance absorption in these spectral domains. We reckon that domains (1-2) and domain (3) are quite distant from each other therefore we thought about an approach where both domains can be optimized differently.

ii). Metal-insulator-metal (MIM) nanostructure

In previous studies on metal-insulator-metal (MIM) nanostructures in our group [84], it was noticed that a vertical plasmonic resonance can originate from the vertical coupling of localized plasmon resonances between the top and the bottom metal layers in a MIM cavity as described in Figure 5.2-13. The resonance wavelength position depends almost only on the diameter of the metal nanopatterns but the coupling of near-field resonances can only arise for thin enought cavity. For domain (3), a strong MIM plasmonic resonance arise for silver nanopatterns of diameter around 320 nm. The plasmonic MIM coupling is decreasing with the increase of the cavity thickness and we consider 130 nm as a maximum value to benefit from this resonance. For domain (2), we used the same multi-resonant strategy described previously for MQW solar cells with a 2D grating.

For example, in Figure 5.2-13, we represent a nanogrid as previously investigated by our group for GaAs ultrathin absorber with an anti-reflection (ARC) coating SiN_x layer [83], [97]. For proper light management in the QD-IBSC spectral domain (3), we have a silver nanogrid with fixed diameter (*d*=320 nm) and the thickness of the MIM cavity is kept below 130 nm (*h*<130 nm). A maximum of 4

QD layers can be inserted with 20-25 nm spacer layer. Window and BSF layers are 5-20 nm-thick, the thinner the better. Other parameters are chosen to optimize the light trapping in the spectral domain (2).

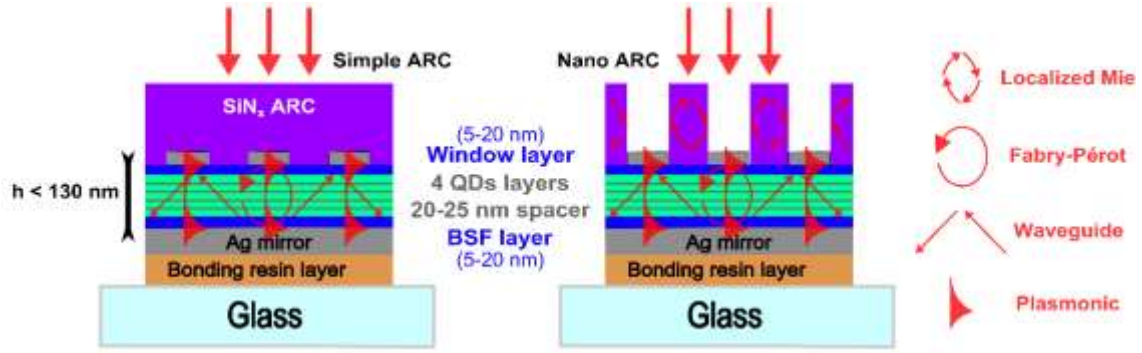

Figure 5.2-13: QDSCs transferred on a silver mirror with a silver nanogrid and SiN_x ARC. Total cavity thickness needs to be inferior to 130 nm to preserve plasmonic MIM coupling. Silver nanogrid diameter is fixed so that MIM resonance is in spectral domain (3). A maximum of 4 QD layers can be inserted with 20-25 nm spacer layer. Window and BSF layers are 5-20 nm-thick. On the right, we show a nanostructured ARC (nano-ARC) that can induce more resonant modes in the structure.

We find optimal values of calculated J_{SC} for silver nanogrid height of 20 nm, a fill factor of 0.5 and total ARC heights for two satisfaying conditions: 70 nm and 370 nm. In order to relax the constraint of the fixed diameter, we also propose to use a nanostructured ARC (nano-ARC) in-between the silver grid (right on Figure 5.2-13). In term of fabrication difficulty, this structure can be fabricated following the same step as the front nanostructured TiO_2 by depositing silver nanogrid before removing the aluminium masking the TiO_2 nanopatterned. We did not have time to fabricate such structure but we will see that the nano-ARC structure should improve the light-trapping.

iii). Light enhancement simulations

In Figure 5.2-14, we compare the simulations for QD-IBSC non-transferred (blue), transferred on a silver mirror (red) and in MIM configuration with a silver nanogrid and SiN_x ARC (purple) or nano-ARC (turquoise) as described in Figure 5.2-13. The simulation parameters are the following: [d=320 nm; ff=0.5; h_{cavity}=130 nm; h_{Ag}=20 nm; h_{ARC}=20+350 nm]. The cavity thickness is 130 nm; which includes 70 nm of QD absorber, 2x10 nm of $Al_{0.2}GaAs$ buffer layers and 2x20 nm of BSF and window layers. At the top, we show the active absorption inside the 70 nm-thick QD absorber layer only. At the bottom, we show the enhancement factor compared with the non-transferred calculation.

We notice a x3 to x30 enhancement by the MIM structure for domain (2) with a level of absorption almost reaching 10%. For domain (3) on the right graph, we see a quasi constant x10 enhancement factor that we attribute to the MIM plasmonic coupled resonance with an absorption close to 10% at resonant peaks. Overall, we see that the use of our light management strategy seems limited. Even though we are able to reach one order of magnitude enhancement, it is not enough for the realization of highly efficient QDSCs. In the next part we will see how low level of absorption might be an obstacle to the development of those cells.

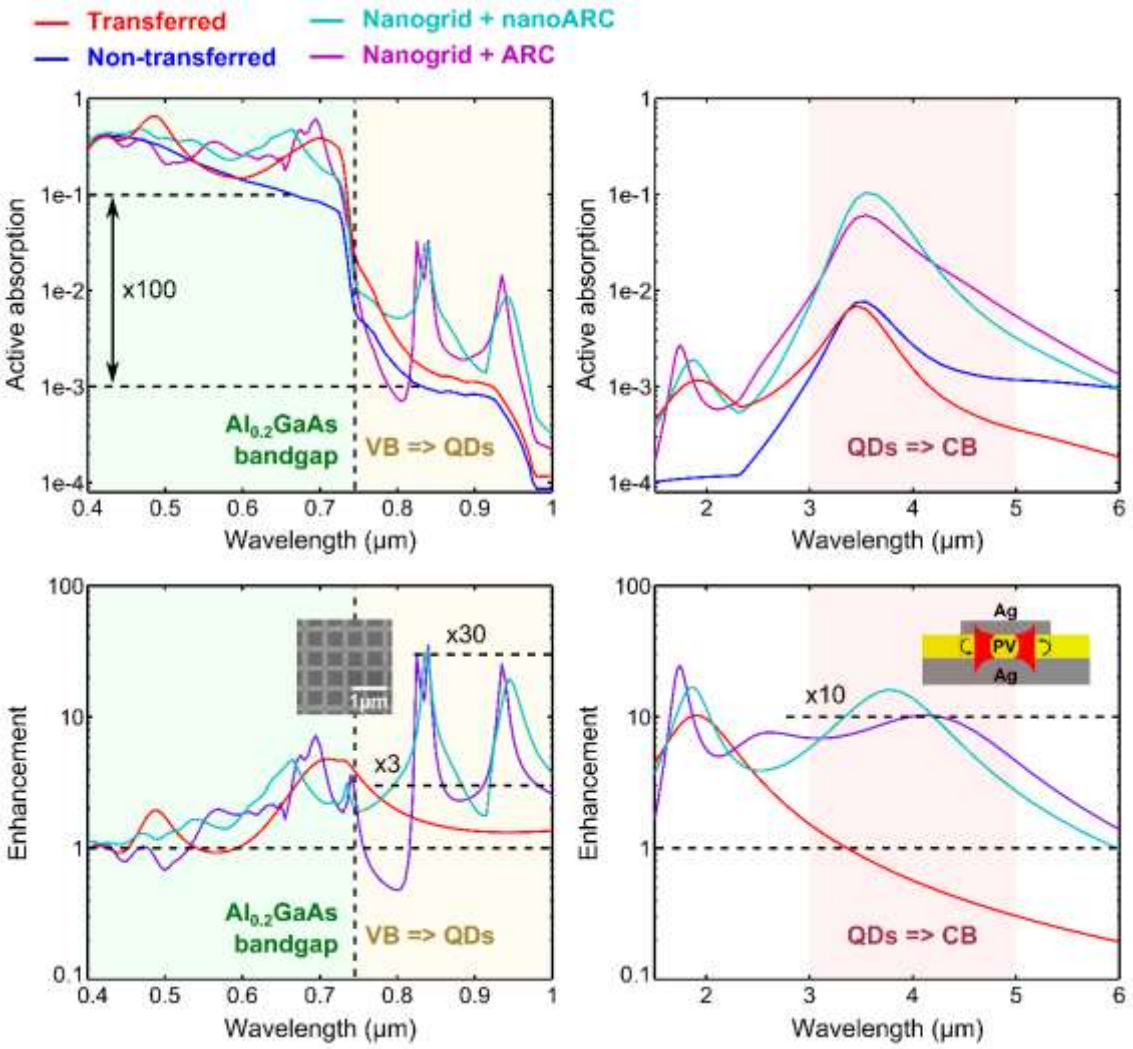

Figure 5.2-14: RCWA simulation with 16 Fourier factors for a 2D grating for QD-IBSC non-transferred (blue), transferred on a silver mirror (red) and in MIM configuration with a silver nanogrid and SiN_x ARC (purple) or nano-ARC (light blue) as described in Figure 5.2-13. The simulation parameters are the following: [d=320 nm; ff=0.5; h_{cavity}=130 nm; h_{ARC}=350 nm]. The cavity thickness is 130 nm; which includes 70 nm of QD absorber and 2x20 nm of BSF and window layers. The three spectral domains are shown in colors: (1) 0.4 µm < λ < 0.74 µm (green); (2) 0.74 µm < λ < 1 µm (yellow) and (3) 3 µm < λ < 5 µm (red). At the top, we show the active absorption inside the 70 nm-thick QD absorber layer only. At the bottom, we show the enhancement factor compared with the non-transferred calculation. We notice a x3-30 enhancement by the MIM structure for domain (2) and a quasi constant x10 enhancement factor in domain (3). In the inset we reproduce the SEM image top view of a fabricated silver nanogrid for the left graph [97] and in the right graph a side view to depict the role of the MIM plasmonic coupled resonance.

5.2.2.2 Limitation of low absorbtive quantum structured materials

In Figure 5.2-15, absorption coefficients for well known solar cell semiconductor absorbers like GaAs and Silicon are compared with Okd-5 In(Ga)As QD absorber. QDs have 2-3 nm heights and 20-25 nm for the spacer layers. We notice that Okd-5 QDs have about the same level of absorption or even less than Silicon material. We know that “very thin” for Silicon often means a “few microns” whereas “very thin” for GaAs often means a “few hundred nanometers”. We observe a x40 ratio difference between Okd-5 QDs and GaAs and we reckon that a x10 increase could be achieved for “closely stacked QDs”, for which the absorption coefficient is calculated considering QDs with 6 nm height and 8 nm spacer layer.

In order to determine if our light management strategy is good enough, we want to have a look from a theoretical point of view. As discussed in section 5.1, the temporal coupled-mode theory (TCMT) provides a powerful framework to determine analytically the absorptivity maximum of weak absorbers [81]. In the vicinity of a resonance at frequency ω_0, we remind the expression of the absorption as a function of radiative (γ_r) and non-radiative (γ_{nr}) decay rates in Equation 5.2-1. From that expression, the full width at half maximum (FWHM) of a resonant mode can be obtained.

$$A_{cavity}(\omega_0) = \frac{4\gamma_r\gamma_{nr}}{(\gamma_r+\gamma_{nr})^2} \; ; \quad FWHM = 2\,(\gamma_r+\gamma_{nr})$$

Equation 5.2-1: Absorption in the vicinity of a resonance at frequency ω_0 and the full width at half maximum (FWHM) of the resonant mode.

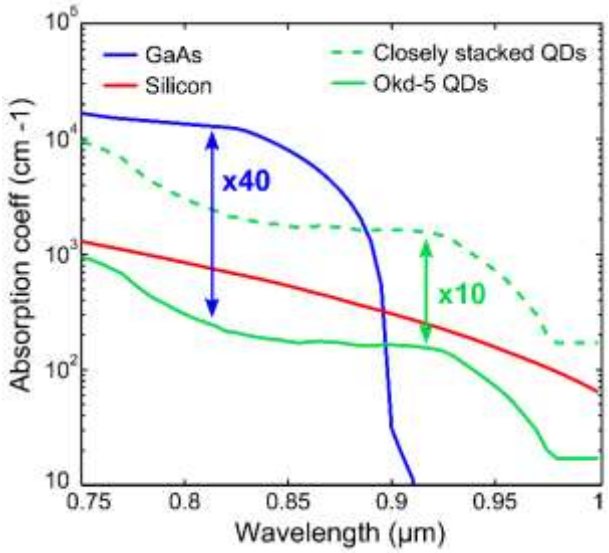

Figure 5.2-15: Absorption coefficients for well known solar cell semiconductor absorbers like GaAs and Silicon are compared with Okd-5 In(Ga)As QD absorber (QDs have 2-3 nm heights and 20-25 nm for the spacer layers). We indicate a x40 ratio difference between GaAs and a x10 with "closely stacked QDs", for which the absorption coefficient is calculated considering QDs with 6 nm height and 8 nm spacer layer.

100% absorption at resonance is achieved for a critical coupling condition when $\gamma_r = \gamma_{nr}$. In the case of a low-absorptive material like the QDs of Okd-3 or Okd-5 type of growth, we see that the absorption coefficient is about x40 less than in GaAs case. Therefore, we can write that $\gamma_{nr-QDs} = \gamma_{nr-GaAs}/40$. In Figure 5.2-13 and Figure 5.2-14, we use a strategy of multi-resonant light management which has shown high absorption enhancements for GaAs solar cells as demonstrated by Collin's group [82]–[84], [97]. If we use the same light management strategy on the QDs absorber, we can assume that the radiative decay rates for both cavities with QDs or with GaAs will be about the same ($\gamma_{r-QDs} \sim \gamma_{r-GaAs}$). The reason is that the radiative decay rates mostly depend on the reflection coefficients on the interfaces as discussed in section 5.1. These reflection coefficients will not be impacted by the change of absorption coefficient because for spectral domain (2) we are already in a low-absorption region for GaAs. Therefore, both in the case of GaAs and QDs absorbing cavity, we have the following condition at critical coupling: $\gamma_{r-GaAs} = \gamma_{nr-GaAs}$ and $\gamma_{r-QDs} \approx 40 \times \gamma_{nr-QDs}$. In Equation 5.2-2, we calculate the absorption and FWHM values for the QDs cavity compared with the GaAs case.

$$A_{cavity-QDs}(\omega_0) = \frac{4\gamma_{r-QDs}\gamma_{nr-QDs}}{\left(\gamma_{r-QDs}+\gamma_{nr-QDs}\right)^2} \sim \frac{4\gamma_{nr-QDs}}{\gamma_{r-QDs}} \sim 0.1$$

$$FWHM_{QDs} = 2\left(\gamma_r+\gamma_{nr}\right) \sim 2\gamma_r \sim \frac{FWHM_{GaAs}}{2}$$

Equation 5.2-2: Absorption and FWHM of a QDs cavity with the same optical design as a GaAs cavity at critical coupling condition but with a x40 less non-radiative decay rates which reduces the absorption level by a factor 10 and the FWHM by 2.

We see that we get 10% absorption instead of 100% and the FWHM is divided by two. If we want to get 100% absorption, we also need to have $\gamma_{r-QDs} = \gamma_{r-GaAs}/40$ for example by tuning the front interface as we did in the case of the MQW solar cell study. However, we see that in this case we will have a FWHM divided by 40. It means that to use the multi-resonant modes strategy we will have to find a way to increase the density of resonant modes by 40, which seems to be a difficult target at our level of study.

We recommend first to increase the absorption of QDs by one order of magnitude. For example, by using closely stacked QDs (8 nm spacer layer and 6 nm height), we should be able to increase QD layers absorptivity by 10 as illustrated in Figure 5.2-15. Such QDSC have proven to be feasible using InGaAs type of growth or QDs superlattices [73]. From this point, multi-resonant light management could be used to reach high absorption enhancement.

Conclusion

In this chapter, we have shown that simple light management strategies based on Fabry-Pérot (FP) cavity can be used to increase light trapping in quantum-structured materials. We also showed the possibility of using more advanced strategies working with other resonant effects. We would like to underline some points that seem important for our study and highlight our achievements:

- We achieved to increase EQE in quantum-structured materials like MQW solar cells (x4-6) or QD-IBSCs (x2-10) by light trapping using a simple FP cavity. For QD-IBSCs, we were not able to determine if the FP has an effect on the intermediate band (IB) dynamics, for example the QDs filling. However, we demonstrated an enhancement of the two transitions that are necessary for achieving sequential two-photon absorption (STPA). We have seen that the thickness of the non-quantum layer has to be minimized in proportion and that the vertical position of quantum layers can be optimized in the stacking design. Moreover, the addition of dielectric layers at the front can either be used as anti-reflection coating (ARC) to increase the broadband coupling of the cavity with the incident light or on the contrary as distributed Bragg reflector (DBR) to increase the reflection, in order to achieve a local maximum absorption.

- We also saw that multi-resonant optical designs can be achieved by fabricating nanostructured patterns at the front or at the back of a transferred solar cell. They enable a higher and more broadband light-trapping effect by adding resonant modes inside the cavity. However, the example of QD absorber shows the limitation of low absorptive materials for which other strategies might be needed where light management needs to be more local.

- In the future, we suggest to study three ways of increasing light absorption: (i) higher absorbing materials for example using closely stacked QDs [50], (ii) design with higher density of optical modes for example using asymmetric patterns [268] and (iii) highly doped QDs for electrofilling but also to be used as near-field plasmonic relays in-between QDs absorbing layer. We noticed that degenerately doped QDs with carrier concentration as high as 1e19 cm^{-3} might be achievable in our system and the literature [269]–[271] indicates that it might be possible for heavily doped InAs to induce plasmonic resonances in the spectral range of the QD to CB transiton (2-5 µm in wavelength).

Conclusion and perspectives

This thesis work illustrates the challenges and potentialities of working on the topic of advanced PV concepts in an international collaboration. On one hand, III-V quantum-structured solar cells originate from quantum electronics and its application to photovoltaics is not trivial. On the other hand, multiresonant light management strategies rely on nanophotonic concepts which have gained in popularity only recently in the PV community. Moreover, working in an international laboratory collaborating with two very different cultures is not always the shortest road and can be laborious. However, I believe that differences and hardships are unavoidable to grow and enrich one another whether it is about people or scientific communities. Taking a step back on my work, I identify three important topics that are linked with the three laboratories I have been working with and correspond to chapters 3, 4 and 5. (i) Material: Knowledge and control over properties of new PV materials fabricated at RCAST. (ii) Device: Understanding mechanisms of new PV devices and its operating conditions by specific characterization provided by IRDEP. (iii) Optics: Implementation of novel optical design to improve the whole PV system that we explored by simulation and nanofabrication at C2N. In the framework of my PhD, progress have been made on these three topics.

From a material point of view, we were able to improve our knowledge and control over the In(Ga)As / $Al_{0.2}Ga_{0.8}As$ quantum dot (QD) system. In chapter 3, we showed that these QDs are far from being ideal for an IBSC system. The main problems are the thermal activation of the QD states and the high density of defects. In Table I, we summarize some key points that seem important to us.

Table I: Issues concerning QD material fabrication for IBSC system

QD material fabrication	Consequences	Solutions
Universal relation on aspect ratio	Quasi-continuum of QD states	In(Ga)As closely stacked
Wetting layer, QWIs	Increased coupling with QD states	AlAs capping
High sensitivity to temperature and In flux	Inhomogeneity on a millimetre scale	As described in MBE version 2
InAs growth < 520°C	Low-quality host material	Higher temperature or annealing
High QD density	High trap density	Doping
QDs in intrinsic layer	Not optimal position	n+np/damping layer/junctionless

We understood that self-assembled In(Ga)As QDs might be limited by a universal relation on aspect ratio. We have seen that QDs ground states are generally determined by the smallest dimension, which is usually the height. In order to have at the same time QDs with a low-energy ground state and pseudo-discrete states, strategies using combinations of closely stacked In(Ga)As QDs or QD superlattices might be more suited to have an aspect ratio closer to unity with small size QDs. We also noticed the negative influence of the wetting layer (WL) or the quantum-well islands (QWIs) that are formed due to Stranski-Krastanov (S-K) QD growth. We suggest using AlAs capping layer in order to create an alloyed WL with energy levels localized in the $Al_{0.2}GaAs$ host material. From a macroscopic point of view, we noticed that QD growth is very

sensitive to temperature and Indium flux, which can creates great inhomogeneity of QD structures on a millimeter scale if not controlled properly. On another note, we considered the low-temperature growth of InAs to hinder the growth of a high-quality $Al_{0.2}GaAs$ system by inducing deep defects even for reference cell grown without QDs. We also reckoned that a high density of QDs might induce a high trap density and therefore the use of doping can help for the prefilling of QD states. Finally, the position of the QD layer in the intrinsic region might not be optimal and other layer architectures can be used like *n+np* junctions, damping layers or ultrathin junctionless solar cell.

From a device point of view, we were able to understand the dynamics of our device by working under different excitation conditions. In chapter 4, we showed that our system may work as an intermediate-band assisted hot carrier solar cell (IB-HCSC). The hyperspectral imager with focused and defocused excitation tends to demonstrate a distinct behavior for electrons and holes. We proved the existence of a IB-CB splitting of quasi-Fermi levels (QFLs) for a certain "hot" regime in the IB under high illumination conditions (>10k suns). At the same time, we evidenced the advantage of a "hot" population to maintain sub-bandgap absorption. In Figure 4.3-3, we hinted to the fact that the use of QD capping could increase the V_{OC} at 1-sun illumination (vertical axis), while the use of doping might help the prefilling in order to have a metal-like IB closer to 1-sun illumination (horizontal axis). Both material improvements could help to make an IB-HCSC to work under realistic illumination conditions e.g. high concentration photovoltaics (HCPV) around 1k sun. We also investigated the sequential two-photon absorption (S-TPA) in our system. For a high IR excitation regime, we were able to demonstrate a consequent out-pumping from quantum states to host material conduction band even evidencing a small gain in the QFL splitting in the host material. This gain would be a lot more important if the defect density in the host material was reduced.

From an optical point of view, we were able to discuss the absorptivity of quantum-structured solar cells and the possible gain that could be obtained using light management strategies. In chapter 3, we investigate the absorption of QD layers from a theoretical point of view with k·p calculation and compared it with different experimental methods. We specifically developed a novel characterization method based on Fabry-Pérot (FP) interferometry dedicated to the investigation of low absorption material. Then in chapter 5, we have shown that simple light management strategies based on FP cavity can be used to increase the light path in quantum-structured materials like multi-quantum well (MQW) solar cells (x4-6 on the EQE) or QD solar cells (x2-10 on the EQE). We could not conclude if the implementation of a FP cavity has an effect on the intermediate band (IB) dynamic for example on the QDs filling. However, we demonstrate an enhancement of the two transitions, necessary for achieving S-TPA. We have also noticed that the total proportion of layers without quantum structures has to be minimized and that the vertical position of quantum layers can be optimized in the stacking design to match the repartition of the electric field from the incident light. The addition of dielectric layers at the front can either be used as anti-reflection coating (ARC) to increase the broadband coupling of the cavity with the incident light or on the contrary as distributed Bragg reflector (DBR) increasing the reflection to achieve a local maximum absorption. Multi-resonant optical designs can be achieved by fabricating nanostructured patterns at the front or at the back of a transferred solar cell. They enable a higher and more broadband light-trapping effect by adding resonant modes inside the cavity. However, the example of QD absorber showed the limitation of low absorptive materials for which other strategies might be needed, for example by using more localized light management effects. In the future, we suggest to study three ways of increasing light absorption: (i) higher absorbing materials for example using closely stacked QDs, (ii) design with higher density of optical modes for example using

asymmetric patterns and (iii) highly doped QDs used as near-field plasmonic relays in-between QDs absorbing layer.

Overall, these three topics have a lot in common and allow us to identify three proposition of investigation in the future in term of QD growth: (i) QD solar cell with high quality host material, (ii) highly doped QDs, (iii) triplet or pair of closely stacked QDs. In term of device and optical realization, going towards junctionless solar cell with thin electron and hole selective contacts would be interesting in order to maximize the ratio of quantum-structured absorber over the total thickness of the epitaxial layers. In terms of light management, it would be interesting to fabricate the proposed structure with MIM configuration in order to investigate the effect on the IB to CB transition.

In the future, we believe that high-efficiency PV with flexible and lightweight thin-films will become more conventional and unlock novel applications. Recently, in this year, LG Electronics have exceeded the world record of a single-junction solar cell with an efficiency of 29.3 % under concentration (AM 1.5-direct, 50 suns). Using novel concepts with quantum structures and light management implementation, a target efficiency over 30 % for a single-junction solar cell seems to be a realistic goal for the next decade. In this regard, IB-HCSCs with a high-quality host material and a prefilled quantum-structured IB with proper light management seems to be a serious candidate and should receive more attention in the coming years.

Appendices

A. Fabrication protocols

A-1. Solar cell fabrication

Example of protocol used to process as-grown (non-transferred) MQW solar cells grown by MOVPE at Sugiyama Lab. on a 350 µm-thick n-doped GaAs substrate.

#	Step name	Remarks	Date
1	Wafer cutting	Size: 1 x 1 cm². - graze wafer edge with diamond probe. - cleave with needle as a lever.	Day 1
2	Front contact	p-doped	
2-1	UV lithography		Day 1
2-1-1	Spin coating	Gas gun to remove dust and check vacuum, 1.5 µm of AZ 5214 E photoresist, 4000 rpm.	
2-1-2	Annealing #1	125°C, 1 min: resist curing.	
2-1-3	UV curing - Align	Chrome mask with front contact patterns, 5 seconds UV curing.	
2-1-4	Annealing #2	125°C, 1 min: hardening for UV cured resist.	
2-1-5	UV curing - Flood	No mask, 30 seconds UV curing.	
2-1-6	Develop resist	Rince in MIF 826 for 30 to 50 seconds max.	
2-2	Metal deposition		Day 1
2-2-1	Deoxidation	5-10 minutes in HCl solution diluted in DI water (1/4). Need to be done just before sample is put in the metal evaporation machine.	
2-2-2	E-beam evaporation	Consecutives depositions Ti/Au (20/200 nm).	
2-3	Lift-off	Acetone for 5 min. Syringe and ultrasounds if needed.	
2-4	Chemical etching	Selective to etch GaAs and stop on InGaP window layer. $H_2O_2/H_3PO_4/H_20$ (1/3/80) for 2 min.	
3	Mesa		Day 2
3-1	UV lithography		
3-1-1	Spin coating	Gas gun to remove dust and check vacuum, 1.5 µm of AZ 5214 E photoresist, 4000 rpm.	
3-1-2	Annealing	125°C, 1 min: resist curing.	
3-1-3	UV curing - Align	Chrome mask with mesa patterns, 15 seconds UV curing.	
3-1-4	Develop resist	Rince in MIF 826 for 70 to 90 seconds.	
3-2	Chemical etching	- Selective to etch InGaP window layer: HCl non-diluted for 2 min. - Selective to etch GaAs layers at least up to the intrinsic region in order to isolate solar cells using $H_2O_2/H_3PO_4/H_20$ (1/3/80).	
4	Back contact	n-doped GaAs substrate rear side.	
4-1	Metal deposition		Day 2
4-1-1	E-beam evaporation	Ni/Au/Ge/Au/Ni/Au (4/10/60/110/10/100 nm).	
End			Day 3

A-2. Epitaxial transfer process

Example of protocol used for epitaxial transfer process of QD solar cells grown by MBE at Okada Lab on a 550 µm-thick n-doped GaAs substrate. A 300 nm-thick Al0.8Ga0.2As etch stop layer is grown but it does not stop the $NH_3/H_2O_2/H_2O$ (1/1/2) fast etching solution and therefore slower etching solution is used at the end.

#	Step name	Remarks	Date
1	Wafer cutting	Size: 1 x 1 cm². - graze wafer edge with diamond probe. - cleave with needle as a lever.	Day 1
2	Back contact	p-doped (front surface)	
2-1	UV lithography		Day 1
2-1-1	Spin coating	Gas gun to remove dust and check vacuum, 1.5 µm of AZ 5214 E photoresist, 4000 rpm.	
2-1-2	Annealing #1	125°C, 1 min: resist curing.	
2-1-3	UV curing - Align	Chrome mask with back contact patterns, 5 seconds UV curing.	
2-1-4	Annealing #2	125°C, 1 min: hardening for UV cured resist.	
2-1-5	UV curing - Flood	No mask, 30 seconds UV curing.	
2-1-6	Develop resist	Rince in MIF 826 for 30 to 50 seconds max.	
2-2	Metal deposition		Day 1
2-2-1	Deoxidation	5-10 minutes in HCl solution diluted in DI water (1/4). Need to be done just before sample is put in the metal evaporation machine.	
2-2-2	E-beam evaporation	Consecutives depositions Ti/Au (20/200 nm).	
2-3	Lift-off	Acetone for 5 min. Syringe and ultrasounds if needed.	
2-4	Chemical etching	Selective to etch GaAs and stop on $Al_{0.4}Ga_{0.6}As$ window layer. Citric acid based for 2 min.	
3	Mirror deposition		Day 2
3-1	Deoxidation	5-10 minutes in HCl solution diluted in DI water (1/4). Need to be done just before sample is put in the metal evaporation machine.	
3-2	E-beam evaporation	Depositions Au (200 nm).	
4	Glass bonding		Day 2
4-1	Glass cutting	1.5 x 1.5 cm² from microscope slide (soda lime glass).	
4.2	Surface cleaning	Acetone + Isopropanol + Ethanol baths.	
4.3	Annealing	Sample with gold mirror for 1 min, 100°C.	
4.4	Spin coating	ORMOSTAMP® on glass, 3 µm-thick, 2000 rpm.	
4.5	Bonding	Right after spin coating, deposit sample with Au mirror on glass. Flip sample and press carefully on the glass to remove air bubbles and ensure adhesion.	
4.6	UV curing	30 minutes throught glass.	
5	Substrate removal		Day 3
5.1	Polishing #1	Polish substrate by hand with sandpaper to remove about 30 µm in case top surface is not clean.	
5.2	Wax protection	Deposit red wax to protect sides, melting at 80°C.	
5.3	Chemical etching #1	Sample in vertical position in $NH_3/H_2O_2/H_2O$ (1/1/2) for 2h with stirring. Every 30 minutes turn sample (90° angle).	
5.4	Polishing #2	Remove wax in trichloroethylene (90°C) and polish about 30 µm to help homogeneous etching front. About 100 µm GaAs substrate should remain.	

5.5	Chemical etching #2	No red wax, in $NH_3/H_2O_2/H_2O$ (1/1/2) until see etch stop appearing at one edge of the sample and check for color change then STOP and remove sample from chemical bath.	
5.6	Chemical etching #3	Switch to citric acid for the remaining 40 µm and protect with red wax if the etch stop is getting attacked. End the process when all GaAs substrate has been removed.	
5.7	Chemical etching #4	Remove etch stop layer in HF diluted at 20% for 1 minute.	
End			Day 4

B. InGaAs QD growth issues

First test sample, Okd-4t1, was made with two capped layers of QDs stacked on each other with spacer for PL investigation and a third layer uncapped for AFM investigation as detailed in Figure B-1.

Material	Role	Thickness
InGaAs	QD 3	7 ML
$Al_{0.3}Ga_{0.7}As$	spacer 2.0	75 nm
AlAs	etch stop 2	15 nm
$Al_{0.3}Ga_{0.7}As$	spacer 1.2 (QD 2)	25 nm
InGaAs	QD 2	7 ML
$Al_{0.3}Ga_{0.7}As$	spacer 1.1 (QD 1)	25 nm
InGaAs	QD 1	7 ML
$Al_{0.3}Ga_{0.7}As$	spacer 1.0	75 nm
AlAs	etch stop 1	15 nm
GaAs	buffer	200 nm

Figure B-1: Okd-4t1 stacking structure

In Figure B-2 is summarized PL mapping and AFM investigation for this growth. We see a strong homogeneity issue revealing growth assymetry. PL maps exhibit two distinct oval shapes that overlap in the center. AFM scanning indicates another oval shape position for InGaAs QD 3 layer as shown in Figure B-2 (blue oval line circling AFM images). It seems that nucleation step for QD growth step is not taking place at the same position on the 3-inch wafer for the 3 different layers that are grown on top of each others. This problem arises from the fact that InGaAs QDs have a very short growth time. It takes 7 seconds from the moment when shutter is opened for InGaAs flux to deposit on the surface and the different steps to take place as seen earlier: nucleation, assembling, self-limitation. Before dissolving step takes place, the shutter is closed. At the same time, substrate rotation speed is of about 5 seconds per lap.

To overcome this issue we thought about having the same test structure grown with no rotation (Okd-4t2) and we found out that we were able to have homogeneous PL over a surface area of 1.5 cm^2 as confirmed by AFM scanning images. Nevertheless for the final Okd-4 growth with 3-inch and with 40 QDs layers, we could not have the same success as shown in Figure B-3.

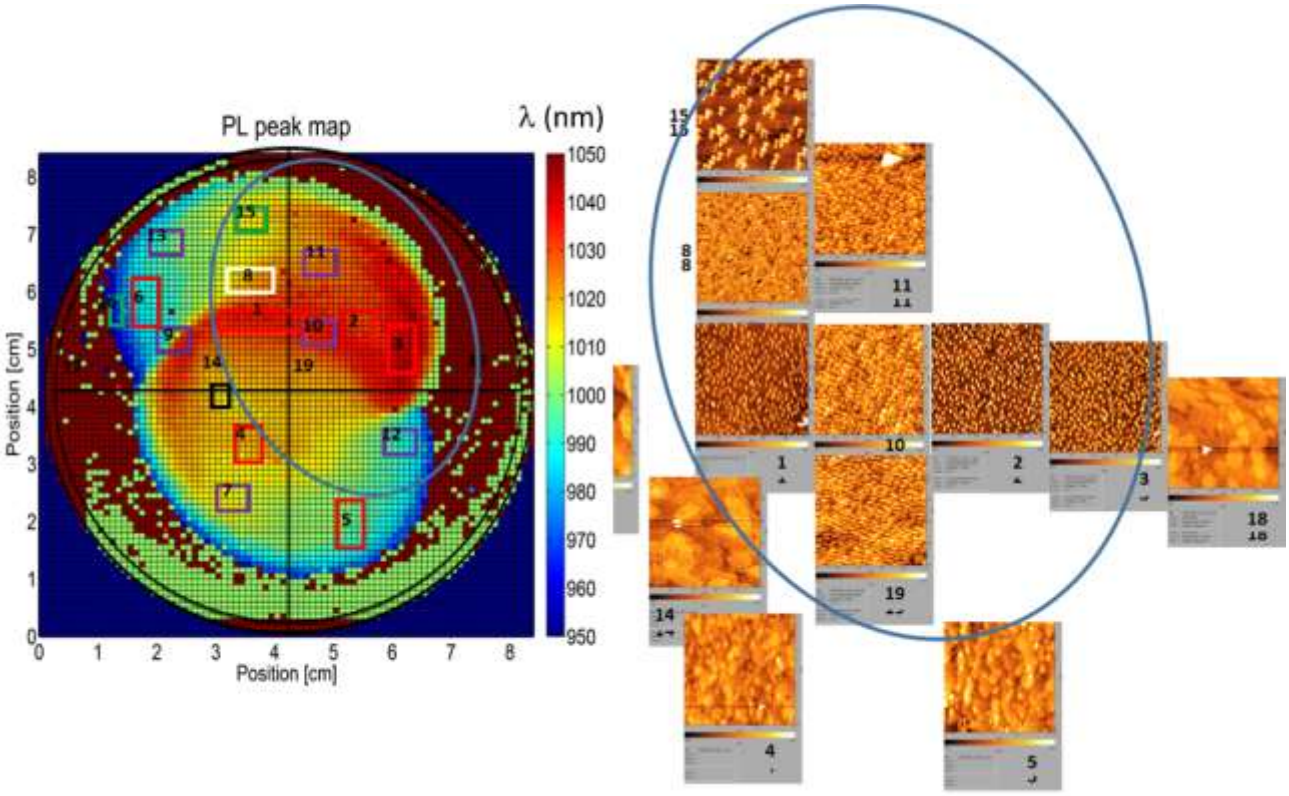

Figure B-2: Okd-4_test1 3-inch wafer PL peak wavelength mapping in colorscale and AFM scanning images for different samples (on the right side). The blue oval line indicates the presence of QDs detected by AFM investigations.

There are at least two important remarks that can be made from Figure B-3 analysis:

- High inhomogeneity.
- "Hole-zone" with no QDs.

In Figure B-3, for Okd-4 3-inch type of growth with no rotation, the two top PL map and the four spectrum graphs, show high inhomogeneity and multi-gaussian fitting of PL that are representative of the different kinds of growth for different layers as we showed before with the test sample. Nevertheless, 1-gaussiand fitting is not so bad (see r-square) and PL FWHM is still reasonably below 80 nm. Hence by approximation, it is possible to calculate 1-gaussian fitting version of peak position and peak intensity as shown in the two bottom PL map color maps in Figure B-3. We somehow see the same kind of representation as in Okd-3B and it reveals the strange impact of the "hole-zone" on the growth of QDs. This was also investigated in the purpose of MBE setup version 2 and we think it could be due to problems of effusion cell alignement, heater or strains. Wafer surface after growth was mirror-like but with some green-colored part of the wafer as shown in Figure B-4. This change in color might be the result of different concentrations of aluminium.

Anyway, these investigations show that it is possible to work with InGaAs QD growth but we need to keep in mind the difficulty to have homogeneous samples due to the very fast growth.

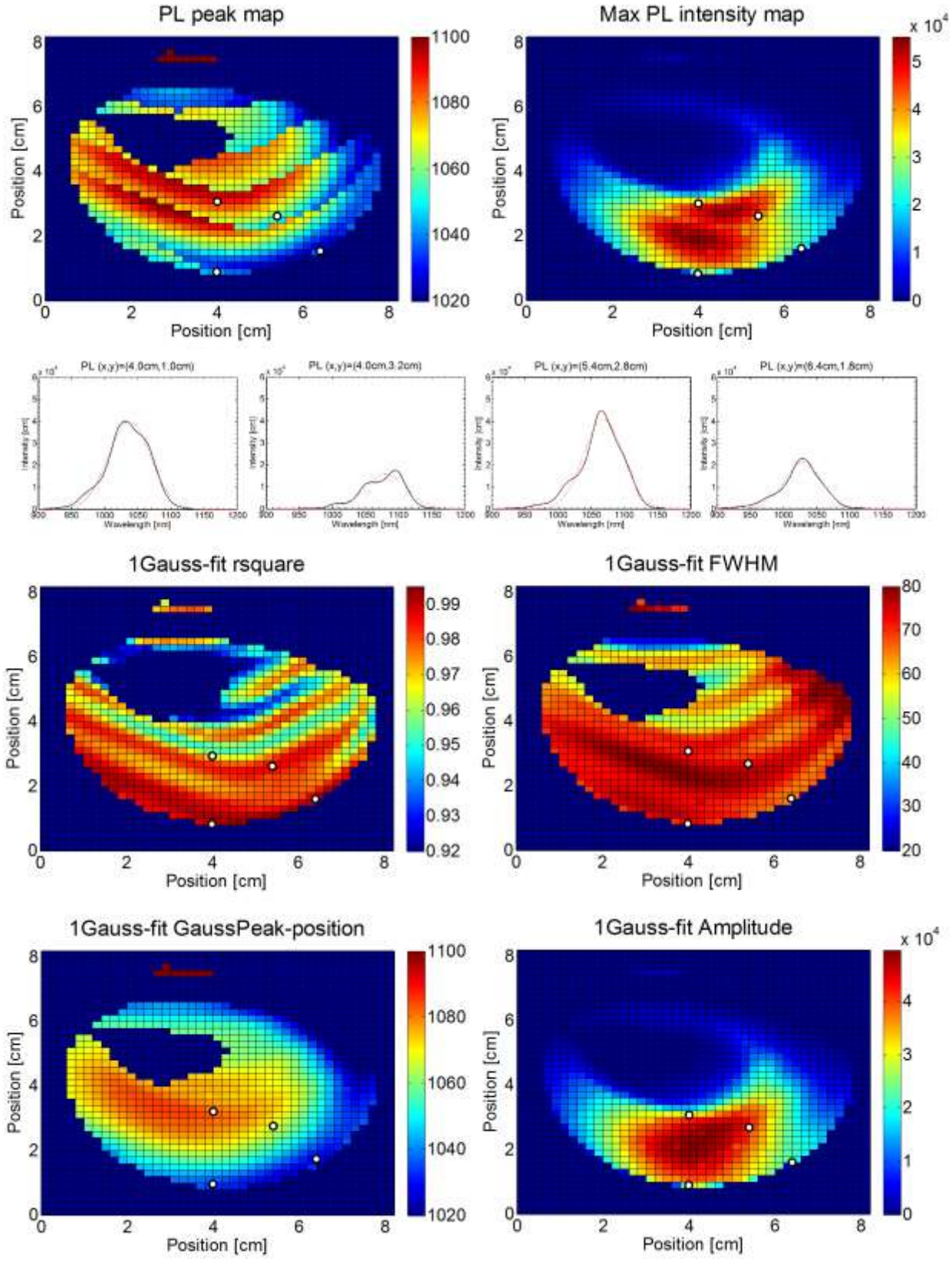

Figure B-3: Okd-4B PL mapping with single-gaussian fitting and PL graph shown at the different positions represented by a white spot.

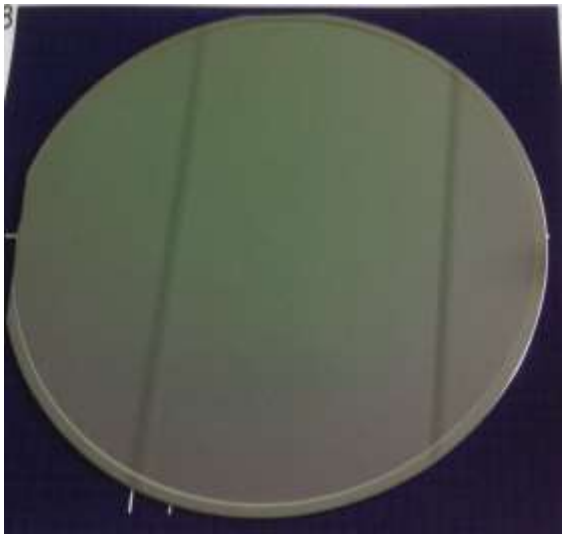

Figure B-4: Photo of Okd-4B growth with green-colored part. Lines are the reflection of the ceiling in the mirror-like wafer surface.

C. Method to fit the PL from a QD ensemble

In Figure C-1, we summarize how we consider the absorption coefficient from a group of QDs (QDs_i) in order to fit PL with the Generalized Planck's law.

Generalized Planck's law:

$$\phi_{PL}(E) = A(\alpha(E))\frac{2\pi}{h^3c^2}\frac{E^2}{\exp\left(\frac{E-\Delta\mu}{kT}\right)-1}$$

Absorption coeff with bandfilling factor:

$$\alpha(E) = \alpha_0(E) \times \left(1 - \frac{2}{\exp\left(\frac{E-\Delta\mu}{2kT}\right)+1}\right)$$

For a group of QDs (QDs_i), absorption coefficient can be fitted by $\alpha_{QDs_i}(E)$ with fixed parameters (for example if ground state (GS) of QDs at ~1.2 eV:

$$\sigma = 25\ meV \quad (FWHM = 60\ meV)$$

$$\frac{A_{quasi-continuum}}{A_{GS}} = 18$$

$$\gamma = 10\ meV$$

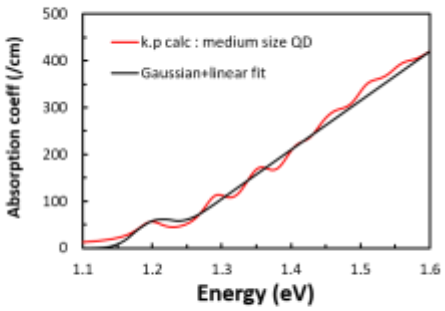

$$\alpha_0(E) = \alpha_{QDs_i}(E) = A_{QDs_i} \times [A_{GS} \times \exp\left(-\frac{(E-E_{GS_i})^2}{2\sigma^2}\right) + A_{quasi-continuum} \times \frac{E-E_{GS_i}}{1+\exp(-\frac{E-E_{GS_i}}{\gamma})}]$$

Figure C-1: Summary of how we consider the absorption coefficient from a group of QDs in order to fit PL with the Generalized Planck's law.

In the case of the PL fitting that we present in chapter 4, we consider six different groups of QDs in order to cover the energy spectral range between 1.18 eV and 1.48 eV. The ground states (GS) energy positions for each group of QDs are the following: E_{GS_1}=1.21 eV, E_{GS_2}=1.26 eV, E_{GS_3}=1.31 eV, E_{GS_4}=1.36 eV, E_{GS_5}=1.41 eV, E_{GS_6}=1.46 eV. The ground states of each groups are separated by 50 meV and FWHM of a QD group is of 60 meV. We consider this discretization of groups of QDs to be enough. PL of "large" QDs at low excitation (HORIBA Jobin Yvon PL mapper) has a FWHM of 90 meV as shown in chapter 3. Therefore taking into account temperature broadening a FWHM value of 60 meV for the Gaussian distribution of a group of QDs seems realistic. We do not wish to consider groups of QDs that would have lower GS energies because low-excitation PL is around 1.21 eV. We do not wish to consider groups of QDs that would have higher GS energies because wetting layer (WL) PL is around 1.55 eV and we believe it impact PL at least on a +/-50 meV scale.

Following these considerations, we can write the absorption coefficient as the sum of the absorption coefficients from the six groups of QDs considered:

$$\alpha_0(E) = \sum_{i=1}^{6} \alpha_{QDs_i}(E, A_{QDs_i}, E_{GS_i})$$

We see that for the PL fitting we have six variables that are the six prefactors, A_{QDs_i}, for each group of QDs. These variables are the same for any temperature T, or quasi-Fermi level splitting (QFLS) Δμ. In the generalized Planck's law, a precise value of absorption is especially important for energies in the range: $E - \Delta\mu < 2\ k_B T$. Therefore, when increasing the excitation, Δμ also increases and PL spectrum will give information on the absorption from QDs that have a higher GS energy. In other words, at low excitation starting at 0.01 mW, PL peak is around 1.26 eV. It means that absorption coefficient contributions from QDs6 (sixth group of QDs) with GS energy, E_(GS_6)=1.46 eV, will have a very low impact on the PL because their energies is

far from Δμ. For the highest excitation, PL peak is around 1.35 eV and the value of the absorption coefficient from this group will have a larger impact.

In order to fit the PL, we decide to use the following method as described in Figure C-2 using Matlab:

E=1.18:0.001:1.48; % Energy scale (eV) $A_{QDs_i} = x(i)$

```
fit = @(x) (log10(φ_PL(E,dmu1,T1, A_QDs1, A_QDs2, A_QDs3, A_QDs4, A_QDs5, A_QDs6,t))-log10(Data(:,1))).^2+...
           (log10(φ_PL(E,dmu6,T6,x(1),x(2),x(3),x(4),x(5),x(6),t))-log10(Data(:,6))).^2+...
           (log10(φ_PL(E,dmu10,T10,x(1),x(2),x(3),x(4),x(5),x(6),t))-log10(Data10)).^2;

options.Algorithm = 'levenberg-marquardt';
x0=[0.0035,0.05,0.25,0.7,0.7,0.25];
[x,resnorm]=lsqnonlin(fit,x0,[1,1,1,1,1,1]*1e-5,[1,1,1,1,1,1]*10,options);
```

Data1=low excitation
Data6=mid excitation
Data10= high excitation

We do loops for 5 parameters. Only T1 is kept constant.

T1 is fixed at 310 K	dmu1 =1.10:0.02:1.26; % eV
T6 = 310:20:470;	dmu6 =1.14:0.02:1.32; % eV
T10 = 310:20:690;	dmu10=1.20:0.02:1.40; % eV

```
Resnorm = sum of (fit)^2 = sum of errors between calc and experimental PL
```

Figure C-2: Method to fit PL data for three different excitations (low, medium, high) and different range for temperature and QFLS.

1/. We fit PL data on the energy spectral range [1.18 eV; 1.48 eV] for three different excitations: low (0.01 mW), medium (0.37 mW) and high excitation (2.71 mW). For example, in the fitting of PL data at low excitation, PL peak is around 1.26 eV, therefore the absorption coefficient prefactor values for QD groups 1 to 3 will impact much more the fitting than the values for QD groups 4 to 6.

2/. We see that fitting for different excitations gives a better accuracy to evaluate the absorption coefficient prefactors for QD groups. However, for each excitation there should be a different value of the temperature T, and quasi-Fermi level splitting (QFLS) Δμ. For the three different excitations, there will be three sets of two variables: $[T_{low};\ \Delta\mu_{low}]$, $[T_{medium};\ \Delta\mu_{medium}]$, and $[T_{high};\ \Delta\mu_{high}]$.

3/. For the fitting, we decide to fix T_{low} at 310K and we do five loops varying the remaining five parameters in range that are expected for our system:

- T_{medium} is varied between 310 K and 470 K with 20 K interval.
- T_{high} is varied between 310 K and 690 K with 20 K interval.
- $\Delta\mu_{low}$ is varied between 1.10 eV and 1.26 eV with 20 meV interval.
- $\Delta\mu_{medium}$ is varied between 1.14 eV and 1.32 eV with 20 meV interval.
- $\Delta\mu_{high}$ is varied between 1.20 eV and 1.40 eV with 20 meV interval.

4/. In outputs of the fitting, we get two different kind of information. First, we get “resnorm”, the sum of errors between the calculated fit and experimental data. Second we get the absorption coefficient prefactors for each group of QDs, which gives the global absorption coefficient for our QDs. In Figure C-3, we show all the “resnorm” values for each fit with respect to temperatures and QFLS. It enables us to reduce the interval to have better fit and more probabilities to find realistic values for all variables.

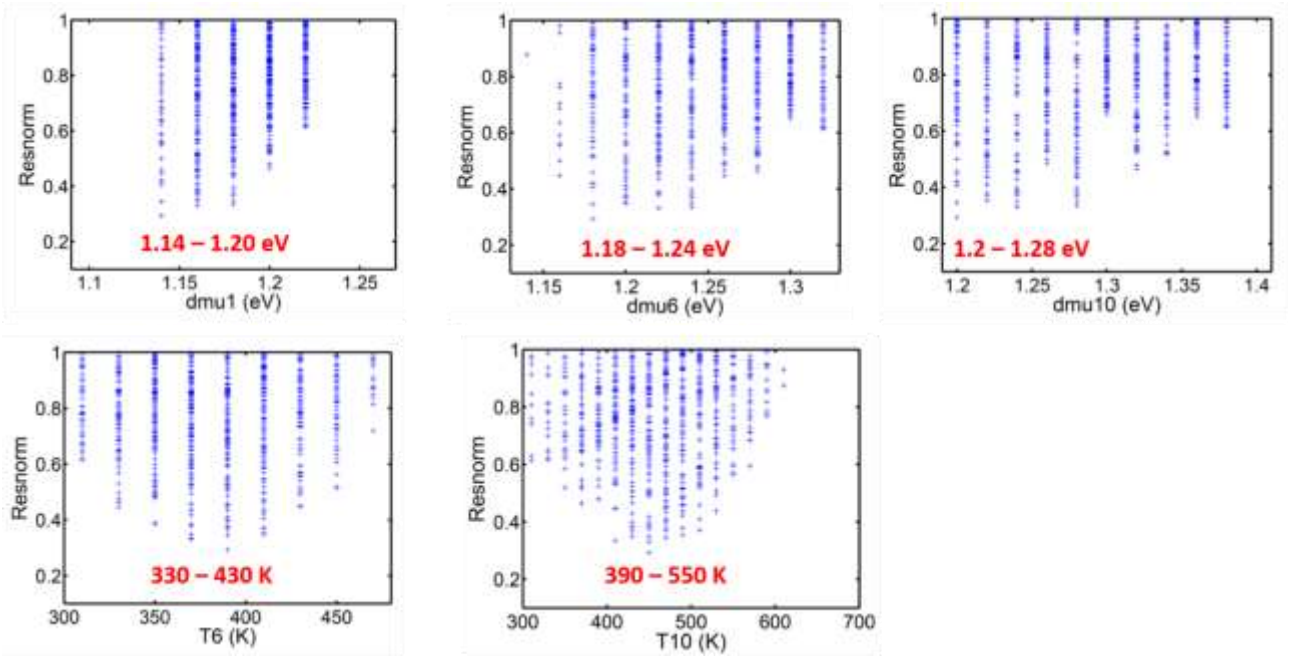

Figure C-3: Plot of goodness of PL fits with respect to temperatures and QFLS.

In Figure C-4, we show all the "resnorm" values for each fit with respect to the absorption coefficient prefactors for the six groups of QDs. We filter for resnorm=0.6 and we take the median values. It gives us a statistical information for the fitting that is not arbitrary. Therefore, we see that most probable values of prefactors in cm^{-1} follow a Gaussian distribution as we show in Figure 4.1-33. In chapter 4, we also show values of good fit for a high absorption coefficient and for fixed temperature at 310 K.

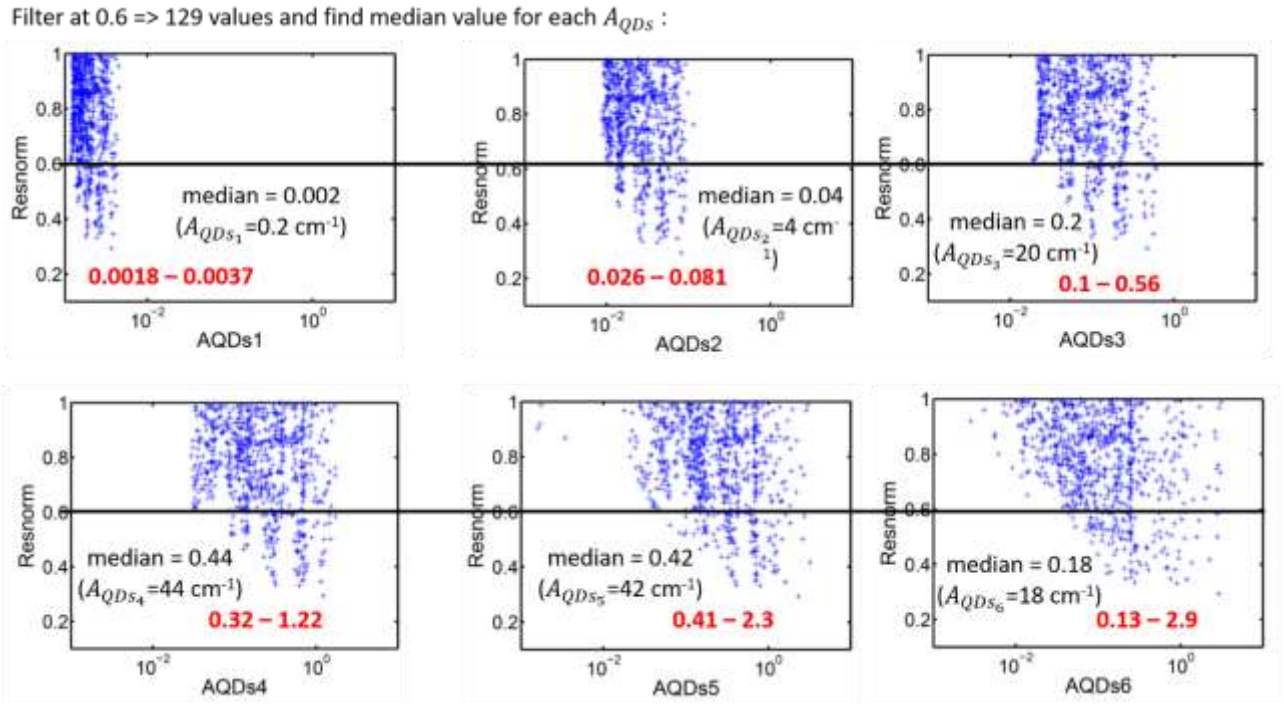

Figure C-4: Plot of goodness of PL fits with respect to the absorption coefficient prefactors for the six groups of QDs.

References

[1] E. Becquerel, “Mémoire sur les effets électriques produits sous l’influence des rayons solaires,” *Comptes Rendus des Séances Hebd.*, vol. 9, pp. 561–567, 1839.

[2] W. Shockley and H. J. Queisser, “Detailed Balance Limit of Efficiency of p-n Junction Solar Cells,” *J. Appl. Phys.*, vol. 32, no. 3, pp. 510–519, 1961.

[3] M. Wolf, “Limitations and Possibilities for Improvement of Photovoltaic Solar Energy Converters,” *Proc. IRE*, vol. 18, pp. 1246–1263, 1960.

[4] R. Scheer and H. W. Schock, *Chalcogenide photovoltaics: Physics, Technologies, and Thin Film Devices.* Weinheim: Wiley-VCH, 2011.

[5] M. A. Green, Y. Hishikawa, W. Warta, E. D. Dunlop, D. H. Levi, J. Hohl-Ebinger, and A. W. Y. Ho-Baillie, “Solar cell efficiency tables (version 50),” *Prog. Photovoltaics Res. Appl.*, vol. 25, no. May, pp. 668–676, 2017.

[6] M. A. Green and S. P. Bremner, “Energy conversion approaches and materials for high-efficiency photovoltaics,” *Nat. Mater.*, vol. 16, no. 1, pp. 23–34, 2016.

[7] M. A. Green, “Radiative efficiency of state-of-the-art photovoltaic cells,” *Prog. Photovolt Res. Appl.*, vol. 20, no. September 2011, pp. 472–476, 2011.

[8] M. A. Steiner, J. F. Geisz, I. Garcia, D. J. Friedman, A. Duda, W. J. Olavarria, M. Young, D. Kuciauskas, and S. R. Kurtz, “Effects of Internal Luminescence and Internal Optics on Voc and Jsc of III-V Solar Cells,” *IEEE J. Photovoltaics*, vol. 3, no. 4, pp. 1437–1442, 2013.

[9] O. D. Miller, E. Yablonovitch, and S. R. Kurtz, “Strong internal and external luminescence as solar cells approach the Shockley-Queisser limit,” *IEEE J. Photovoltaics*, vol. 2, no. 3, pp. 303–311, 2012.

[10] R. T. Ross, “Some Thermodynamics of Photochemical Systems,” *J. Chem. Phys.*, vol. 46, no. 12, pp. 4590–4593, 1967.

[11] A. Richter, S. W. Glunz, A. Richter, M. Hermle, and S. W. Glunz, “Crystalline Silicon Solar Cells Reassessment of the Limiting Efficiency for Crystalline Silicon Solar Cells,” *IEEE J. Photovoltaics*, vol. 3, no. 4, pp. 1184–1191, 2013.

[12] I. Schnitzer, E. Yablonovitch, C. Caneau, and T. J. Gmitter, “Ultrahigh spontaneous emission quantum efficiency, 99.7% internally and 72% externally, from AlGaAs/GaAs/AlGaAs double heterostructures,” *Appl. Phys. Lett.*, vol. 62, no. 2, pp. 131–133, 1993.

[13] G. Smestad, H. Ries, R. Winston, and E. Yablonovitch, “The thermodynamic limits of light concentrators,” *Sol. Energy Mater.*, vol. 21, no. 2–3, pp. 99–111, 1990.

[14] R. B. Wehrspohn, U. Rau, and A. Gombert, *Photon Management in Solar Cells*. Wiley-VCH, 2015.

[15] V. Ganapati, M. A. Steiner, and E. Yablonovitch, “The voltage boost enabled by luminescence extraction in solar cells,” *IEEE J. Photovoltaics*, vol. 6, no. 4, pp. 801–809, 2016.

[16] E. D. Kosten, B. K. Newman, J. V. Lloyd, A. Polman, and H. A. Atwater, “Limiting light escape angle in silicon photovoltaics: Ideal and realistic cells,” *IEEE J. Photovoltaics*, vol. 5, no. 1, pp. 61–69, 2015.

[17] E. D. Kosten, J. H. Atwater, J. Parsons, A. Polman, and H. A. Atwater, “Highly efficient GaAs solar cells by limiting light emission angle,” *Light Sci. Appl.*, vol. 2, no. e45, pp. 1–6, 2013.

[18] Y. Takeda and T. Motohiro, “Intermediate-band-assisted hot-carrier solar cells using indirect-bandgap absorbers,” *Prog. Photovolt Res. Appl.*, vol. 21, pp. 1308–1318, 2013.

[19] F. Dimroth, M. Grave, P. Beutel, U. Fiedeler, C. Karcher, T. N. D. Tibbits, E. Oliva, G. Siefer, M. Schachtner, A. Wekkeli, A. W. Bett, R. Krause, M. Piccin, N. Blanc, C. Drazek, E. Guiot, B. Ghyselen, T. Salvetat, A. Tauzin, T. Signamarcheix, A. Dobrich, T. Hannappel, and K. Schwarzburg, “Wafer bonded four-junction GaInP/GaAs//GaInAsP/GaInAs concentrator solar cells with 44.7% efficienc,” *Prog. Photovolt Res. Appl.*, vol. 22, pp. 277–282, 2014.

[20] A. Luque and A. Martí, “Increasing the Efficiency of Ideal Solar Cells by Photon Induced Transitions at Intermediate Levels,” *Phys. Rev. Lett.*, vol. 78, no. 26, pp. 5014–5017, 1997.

[21] A. Luque and A. Martí, “The intermediate band solar cell: Progress toward the realization of an attractive concept,” *Adv. Mater.*, vol. 22, no. 2, pp. 160–174, 2010.

[22] Y. Okada, T. Morioka, K. Yoshida, R. Oshima, Y. Shoji, T. Inoue, and T. Kita, “Increase in photocurrent by optical transitions via intermediate quantum states in direct-doped InAs/GaNAs strain-compensated quantum dot solar cell,” *J. Appl. Phys.*, vol. 109, no. 2, 2011.

[23] E. López, A. Datas, I. Ramiro, P. G. Linares, E. Antolín, I. Artacho, A. Martí, A. Luque, Y. Shoji, T. Sogabe, A. Ogura, and Y. Okada, “Demonstration of the operation principles of intermediate band solar cells at room temperature,” *Sol. Energy Mater. Sol. Cells*, vol. 149, pp. 15–18, 2016.

[24] T. Trupke, M. A. Green, and P. Würfel, “Improving solar cell efficiencies by up-conversion of sub-band-gap light,” *J. Appl. Phys.*, vol. 92, no. 7, pp. 4117–4122, 2002.

[25] S. Deb and H. Saha, “Secondary ionisation and its possible bearing on the performance of a solar cell,” *Solid State Electron.*, vol. 15, no. 12, pp. 1389–1391, 1972.

[26] A. J. Nozik, “Multiple exciton generation in semiconductor quantum dots,” *Chem. Phys. Lett.*, vol. 457, pp. 3–11, 2008.

[27] M. C. Beard, J. M. Luther, O. E. Semonin, and A. J. Nozik, “Third generation photovoltaics based on multiple exciton generation in quantum confined semiconductors,” *Acc. Chem. Res.*, vol. 46, no. 6, pp. 1252–1260, 2013.

[28] N. J. L. K. Davis, M. L. Böhm, M. Tabachnyk, F. Wisnivesky-Rocca-Rivarola, T. C. Jellicoe, C. Ducati, B. Ehrler, and N. C. Greenham, “Multiple-exciton generation in lead selenide nanorod solar cells with external quantum efficiencies exceeding 120%,” *Nat. Commun.*, vol. 6, no. 8259, pp. 1–7, 2015.

[29] Y. Takeda and T. Motohiro, “Requisites to realize high conversion efficiency of solar cells utilizing carrier multiplication,” *Sol. Energy Mater. Sol. Cells*, vol. 94, no. 8, pp. 1399–1405, 2010.

[30] T. Trupke, M. A. Green, and P. Würfel, “Improving solar cell efficiencies by down-conversion of high-energy photons,” *J. Appl. Phys.*, vol. 92, no. 3, pp. 1668–1674, 2002.

[31] R. T. Ross and A. J. Nozik, “Efficiency of hot-carrier solar energy converters,” *J. Appl. Phys.*, vol. 53, no. 5, pp. 3813–3818, 1982.

[32] P. Würfel, “Solar energy conversion with hot electrons from impact ionisation,” *Sol. Energy Mater. Sol. Cells*, vol. 46, no. 1, pp. 43–52, 1997.

[33] A. Luque and A. Martí, “Electron-phonon energy transfer in hot-carrier solar cells,” *Sol. Energy Mater. Sol. Cells*, vol. 94, no. 2, pp. 287–296, 2010.

[34] G. Conibeer, S. Shrestha, S. Huang, R. Patterson, H. Xia, Y. Feng, P. Zhang, N. Gupta, M. Tayebjee, S. Smyth, Y. Liao, S. Lin, P. Wang, X. Dai, and S. Chung, “Hot carrier solar cell absorber prerequisites and candidate material systems,” *Sol. Energy Mater. Sol. Cells*, vol. 135, pp. 124–129, 2015.

[35] G. Conibeer, N. Ekins-Daukes, J. F. Guillemoles, D. Konig, E. C. Cho, C. W. Jiang, S. Shrestha, and M. Green, “Progress on hot carrier cells,” *Sol. Energy Mater. Sol. Cells*, vol. 93, pp. 713–719, 2009.

[36] Y. Takeda and T. Motohiro, “Highly efficient solar cells using hot carriers generated by two-step excitation,” *Sol. Energy Mater. Sol. Cells*, vol. 95, pp. 2638–2644, 2011.

[37] Y. Takeda and T. Motohiro, “Hot-Carrier Extraction from Intermediate-Band Absorbers through Quantum-Well Energy-Selective Contacts,” *Jpn. J. Appl. Phys.*, vol. 51, no. 10ND03, pp. 1–6, 2012.

[38] S. Saeed, E. M. L. D. de Jong, K. Dohnalova, and T. Gregorkiewicz, “Efficient optical extraction of hot-carrier energy.,” *Nat. Commun.*, vol. 5, no. 4665, pp. 1–5, 2014.

[39] E. M. L. D. De Jong, S. Saeed, W. C. Sinke, and T. Gregorkiewicz, “Generation of hot carriers for photon management in future photovoltaics,” *Sol. Energy Mater. Sol. Cells*, vol. 135, pp. 67–71, 2015.

[40] G. Güttler and H. J. Queisser, “Impurity Photovoltaic Effect in Silicon,” *Energy Convers.*, vol. 10, pp. 51–55, 1970.

[41] K. W. J. Barnham and G. Duggan, “A new approach to high-efficiency multi-band-gap solar cells,” *J. Appl. Phys.*, vol. 67, no. 7, pp. 3490–3493, 1990.

[42] M. A. Green, “Multiple band and impurity photovoltaic solar cells: General theory and comparison to tandem cells,” *Prog. Photovoltaics Res. Appl.*, vol. 9, no. 2, pp. 137–144, 2001.

[43] A. S. Brown and M. A. Green, “Intermediate band solar cell with many bands: Ideal performance,” *J. Appl. Phys.*, vol. 94, no. 9, pp. 6150–6158, 2003.

[44] M. Yoshida, N. J. Ekins-Daukes, D. J. Farrell, and C. C. Phillips, “Photon ratchet intermediate band solar cells,” *Appl. Phys. Lett.*, vol. 100, no. 26, 2012.

[45] O. J. Curtin, M. Yoshida, A. Pusch, N. P. Hylton, N. J. Ekins-daukes, C. C. Phillips, and O. Hess, “Quantum cascade photon ratchets for intermediate-band solar cells,” *IEEE J. Photovoltaics*, vol. 6, no. 3, pp. 673–678, 2016.

[46] Y. Okada, S. Yagi, and R. Oshima, “High-efficiency solar cells based on quantum dot superlattice,” *OYO BUTURI*, vol. 79, no. 3, p. 206, 2010.

[47] M. J. Sher, C. B. Simmons, J. J. Krich, A. J. Akey, M. T. Winkler, D. Recht, T. Buonassisi, M. J. Aziz, and A. M. Lindenberg, “Picosecond carrier recombination dynamics in chalcogen-hyperdoped silicon,” *Appl. Phys. Lett.*, vol. 105, no. 5, 2014.

[48] J. T. Sullivan, C. B. Simmons, T. Buonassisi, and J. J. Krich, “Targeted Search for Effective Intermediate Band Solar Cell Materials,” *IEEE J. Photovoltaics*, vol. 5, no. 1, pp. 212–218, 2015.

[49] M. Yoshida, H. Amrania, D. J. Farrell, B. Browne, E. Yoxall, N. J. Ekins-Daukes, and C. C. Phillips, “Progress toward realizing an intermediate band solar cell-Sequential absorption of photons in a quantum well solar cell,” *IEEE J. Photovoltaics*, vol. 4, no. 2, pp. 634–638, 2014.

[50] Y. Okada, N. J. Ekins-Daukes, T. Kita, R. Tamaki, M. Yoshida, A. Pusch, O. Hess, C. C. Phillips, D. J. Farrell, K. Yoshida, N. Ahsan, Y. Shoji, T. Sogabe, and J.-F. Guillemoles, "Intermediate band solar cells: Recent progress and future directions," *Appl. Phys. Rev.*, vol. 2, no. 21302, pp. 1–48, 2015.

[51] W. Shan, W. Walukiewicz, J. W. Ager III, E. E. Haller, J. F. Geisz, D. J. Friedman, J. M. Olson, and S. R. Kurtz, "Band Anticrossing in GaInNAs Alloys," *Phys. Rev. Lett.*, vol. 82, no. 6, pp. 1221–1224, 1999.

[52] J. Wu, W. Shan, and W. Walukiewicz, "Band anticrossing in highly mismatched III – V semiconductor alloys," *Semicond. Sci. Technol.*, vol. 17, pp. 860–869, 2002.

[53] N. López, K. M. Yu, T. Tanaka, and W. Walukiewicz, "Multicolor Electroluminescence from Intermediate Band Solar Cell Structures," *Adv. Energy Mater.*, vol. 6, no. 1501820, pp. 1–5, 2015.

[54] N. Ahsan, N. Miyashita, K. M. Yu, W. Walukiewicz, and Y. Okada, "Multiband modification of III-V dilute nitrides for IBSC application," *Proc. SPIE*, vol. 10099. p. 8, 2017.

[55] I. Ramiro, A. Martı, E. Antolın, and A. Luque, "Review of experimental results related to the operation of intermediate band solar cells," *IEEE J. Photovoltaics*, vol. 4, no. 2, pp. 736–748, 2014.

[56] P. G. Linares, A. Marti, E. Antolin, C. D. Farmer, I. Ramiro, C. R. Stanley, and A. Luque, "Voltage recovery in intermediate band solar cells," *Sol. Energy Mater. Sol. Cells*, vol. 98, no. March, pp. 240–244, 2012.

[57] A. Luque, A. Martí, and L. Cuadra, "Thermodynamic consistency of sub-bandgap absorbing solar cell proposals," *IEEE Trans. Electron Devices*, vol. 48, no. 9, pp. 2118–2124, 2001.

[58] R. Tamaki, Y. Shoji, T. Sugaya, and Y. Okada, "Universal linear relationship on two-step photon absorption processes in In(Ga)As quantum dot solar cells," in *Photovoltaic Specialists Conference (PVSC), 2016 IEEE 43rd*, 2016, pp. 1–4.

[59] F. K. Tutu, P. Lam, J. Wu, N. Miyashita, Y. Okada, K. H. Lee, N. J. Ekins-Daukes, J. Wilson, and H. Liu, "InAs/GaAs quantum dot solar cell with an AlAs cap layer," *Appl. Phys. Lett.*, vol. 102, no. 163907, pp. 1–4, 2013.

[60] A. Varghese, M. Yakimov, V. Tokranov, V. Mitin, K. Sablon, A. Sergeev, and S. Oktyabrsky, "Complete voltage recovery in quantum dot solar cells due to suppression of electron capture," *Nanoscale*, vol. 8, pp. 7248–7256, 2016.

[61] X. Yang, K. Wang, Y. Gu, H. Ni, X. Wang, T. Yang, and Z. Wang, "Improved efficiency of InAs/GaAs quantum dots solar cells by Si-doping," *Sol. Energy Mater. Sol. Cells*, vol. 113, pp. 144–147, 2013.

[62] P. Lam, S. Hatch, J. Wu, M. Tang, V. G. Dorogan, Y. I. Mazur, G. J. Salamo, I. Ramiro, A. Seeds, and H. Liu, "Voltage recovery in charged InAs/GaAs quantum dot solar cells," *Nano Energy*, vol. 6, pp. 159–166, 2014.

[63] S. J. Polly, D. V. Forbes, K. Driscoll, S. Hellstrom, and S. M. Hubbard, "Delta-doping effects on quantum-dot solar cells," *IEEE J. Photovoltaics*, vol. 4, no. 4, pp. 1079–1085, 2014.

[64] F. Cappelluti, M. Gioannini, and A. Khalili, "Impact of doping on InAs/GaAs quantum-dot solar cells: A numerical study on photovoltaic and photoluminescence behavior," *Sol. Energy Mater. Sol. Cells*, vol. 157, pp. 209–220, 2016.

[65] M. Kaniewska, O. Engström, A. Barcz, and M. Pacholak-Cybulska, "Electrical activity of deep levels in the presence of InAs/GaAs quantum dots," *Mater. Sci. Semicond. Process.*, vol. 9, pp. 36–40, 2006.

[66] M. Kaniewska, O. Engström, A. Barcz, and M. Pacholak-Cybulska, “Deep levels induced by InAs/GaAs quantum dots,” *Mater. Sci. Eng. C*, vol. 26, pp. 871–875, 2006.

[67] J. S. Kim, E. K. Kim, S. J. Lee, and S. K. Noh, “Study on defects and confined energy level of InAs/GaAs quantum dot system,” *Phys. B Condens. Matter*, vol. 376–377, pp. 877–880, 2006.

[68] C. J. Park, H. B. Kim, Y. H. Lee, D. Y. Kim, T. W. Kang, C. Y. Hong, H. Y. Cho, and M. D. Kim, “Deep level defects of InAs quantum dots grown on GaAs by molecular beam epitaxy,” *J. Cryst. Growth*, vol. 227–228, pp. 1057–1061, 2001.

[69] S. V. Kondratenko, O. V. Vakulenko, Y. I.Mazur, V. G. Dorogan, E. Marega, M. Benamara, M. E.Ware, and J. Salamo, “Deep level centers and their role in photoconductivity transients of InGaAs/GaAs quantum dot chains,” *J. Appl. Phys.*, vol. 116, no. 193707, pp. 1–11, 2014.

[70] S. V Kondratenko, S. A. Iliash, O. V Vakulenko, Y. I. Mazur, M. Benamara, E. Marega, and G. J. Salamo, “Photoconductivity Relaxation Mechanisms of InGaAs / GaAs Quantum Dot Chain Structures,” *Nanoscale Res. Lett.*, vol. 12, no. 183, pp. 1–7, 2017.

[71] H. Fujii, K. Toprasertpong, K. Watanabe, M. Sugiyama, and Y. Nakano, “Evaluation of Carrier Collection Efficiency in Multiple Quantum Well Solar Cells,” *IEEE J. Photovoltaics*, vol. 4, no. 1, pp. 237–243, 2014.

[72] H. Sodabanlu, S. Ma, K. Watanabe, M. Sugiyama, and Y. Nakano, “Impact of strain accumulation on InGaAs/GaAsP multiple-quantum-well solar cells: direct correlation between in situ strain measurement and cell performances,” *Jpn. J. Appl. Phys.*, vol. 51, pp. 1–4, 2012.

[73] A. Takahashi, T. Ueda, Y. Bessho, Y. Harada, T. Kita, E. Taguchi, and H. Yasuda, “One-dimensional miniband formation in closely stacked InAs/GaAs quantum dots,” *Phys. Rev. B - Condens. Matter Mater. Phys.*, vol. 87, no. 23, pp. 1–6, 2013.

[74] M. Sugiyama, H. Fujii, T. Katoh, K. Toprasertpong, H. Sodabanlu, K. Watanabe, D. Alonso-Álvarez, N. J. Ekins-Daukes, and Y. Nakano, “Quantum wire-on-well (WoW) cell with long carrier lifetime for efficient carrier transport,” *Prog. Photovoltaics Res. Appl.*, vol. 24, no. 12, pp. 1606–1614, 2016.

[75] A. Luque and A. Martí, “A metallic intermediate band high efficiency solar cell,” *Prog. Photovoltaics Res. Appl.*, vol. 9, no. 2, pp. 73–86, 2001.

[76] R. Strandberg and T. W. Reenaas, “Photofilling of intermediate bands,” *J. Appl. Phys.*, vol. 105, no. 124512, pp. 1–8, 2009.

[77] A. Goetzberger, “Optical confinement in thin Si solar cells by diffuse back reflectors,” *Proc. 15th IEEE Photovolt. Spec. Conf.*, pp. 867–870, 1981.

[78] E. Yablonovitch, “Statistical ray optics,” *J. Opt. Soc. Am.*, vol. 72, pp. 899–907, 1982.

[79] M. A. Green, “Lambertian light trapping in textured solar cells and light-emitting diodes: Analytical solutions,” *Prog. Photovoltaics Res. Appl.*, vol. 10, no. 4, pp. 235–241, 2002.

[80] Z. Yu, A. Raman, and S. Fan, “Fundamental limit of nanophotonic light trapping in solar cells,” *Proc. Natl. Acad. Sci.*, vol. 107, no. 41, pp. 17491–17496, 2010.

[81] S. Collin, “Nanostructure arrays in free-space: optical properties and applications.,” *Rep. Prog. Phys.*, vol. 77, no. 126402, pp. 1–33, 2014.

[82] N. Vandamme, “Nanostructured ultrathin GaAs solar cells,” PhD these, Université Paris-Sud, 2016.

[83] I. Massiot, “Design and fabrication of nanostructures for light-trapping in ultra-thin solar cells,” PhD these, Université Paris-Sud, 2013.

[84] C. Colin, “Metallic nanostructures for light-trapping in ultra-thin GaAs and CIGS solar cells,” PhD these, Université Paris-Sud, 2013.

[85] P. Spinelli, V. E. Ferry, J. van de Groep, M. van Lare, M. A. Verschuuren, R. E. I. Schropp, H. A. Atwater, and A. Polman, “Plasmonic light trapping in thin-film Si solar cells,” *J. Opt.*, vol. 14, no. 24002, pp. 1–11, 2012.

[86] T. K. Chong, J. Wilson, S. Mokkapati, and K. R. Catchpole, “Optimal wavelength scale diffraction gratings for light trapping in solar cells,” *J. Opt.*, vol. 14, no. 24012, pp. 1–9, 2012.

[87] D. Liang, Y. Huo, Y. Kang, K. X. Wang, A. Gu, M. Tan, Z. Yu, S. Li, J. Jia, X. Bao, S. Wang, Y. Yao, H. S. P. Wong, S. Fan, Y. Cui, and J. S. Harris, “Optical absorption enhancement in freestanding GaAs thin film nanopyramid arrays,” *Adv. Energy Mater.*, vol. 2, no. 10, pp. 1254–1260, 2012.

[88] S. Sandhu, Z. Yu, and S. Fan, “Detailed balance analysis of nanophotonic solar cells,” *Opt. Express*, vol. 21, no. 1, pp. 1209–1217, 2013.

[89] J. Grandidier, D. M. Callahan, J. N. Munday, and H. a Atwater, “Enhancement using whispering gallery modes of dielectric nanospheres,” *IEEE J. Photovoltaics*, vol. 2, no. 2, pp. 123–128, 2012.

[90] H. A. Atwater and A. Polman, “Plasmonics for improved photovoltaic devices,” *Nat. Mater.*, vol. 9, no. March, pp. 205–213, 2010.

[91] M. Van Lare, F. Lenzmann, M. A. Verschuuren, and A. Polman, “Mode coupling by plasmonic surface scatterers in thin-film silicon solar cells,” *Appl. Phys. Lett.*, vol. 101, no. 22, 2012.

[92] M. L. Brongersma, Y. Cui, and S. Fan, “Light management for photovoltaics using high-index nanostructures,” *Nat. Mater.*, vol. 13, no. 5, pp. 451–60, 2014.

[93] S. Collin, J. Goffard, A. Cattoni, C. Colin, C. Sauvan, P. Lalanne, and J. F. Guillemoles, “Multi-resonant light trapping: New paradigm, new limits,” *2015 IEEE 42nd Photovolt. Spec. Conf. PVSC 2015*, pp. 1–3, 2015.

[94] D. M. Callahan, J. N. Munday, and H. A. Atwater, “Solar cell light trapping beyond the ray optic limit,” *Nano Lett.*, vol. 12, no. 1, pp. 214–218, 2012.

[95] E. A. Schiff, “Thermodynamic limit to photonic-plasmonic light-trapping in thin films on metals,” *J. Appl. Phys.*, vol. 110, no. 10, 2011.

[96] Z. Yu, A. Raman, and S. Fan, “Thermodynamic upper bound on broadband light coupling with photonic structures,” *Phys. Rev. Lett.*, vol. 109, no. 17, pp. 1–5, 2012.

[97] I. Massiot, N. Vandamme, N. Bardou, C. Dupuis, A. Lemaître, J. F. Guillemoles, and S. Collin, “Metal nanogrid for broadband multiresonant light-harvesting in ultrathin GaAs layers,” *ACS Photonics*, vol. 1, no. 9, pp. 878–884, 2014.

[98] S. Collin, F. Pardo, N. Bardou, A. Lemaître, S. Averin, and J.-L. Pelouard, “Harvesting light at the nanoscale by GaAs-gold nanowire arrays,” *Opt. Express*, vol. 19, no. 18, pp. 17293–17297, 2011.

[99] K. Tanabe, K. Watanabe, and Y. Arakawa, “Flexible thin-film InAs/GaAs quantum dot solar cells,” *Appl. Phys. Lett.*, vol. 100, no. 192102, pp. 1–4, 2012.

[100] M. F. Bennett, Z. S. Bittner, D. V Forbes, S. R. Tatavarti, S. P. Ahrenkiel, N. Pan, K. Chern, and S. M.

Hubbard, “Epitaxial lift-off of quantum dot enhanced GaAs single junction solar cells,” *Appl. Phys. Lett.*, vol. 103, no. 213902, pp. 1–4, 2013.

[101] B. Behaghel, P. Rale, Y. Shoji, R. Tamaki, N. Vandamme, L. Lombez, C. Dupuis, A. Cattoni, K. Watanabe, M. Sugiyama, Y. Okada, S. Collin, and J.-F. Guillemoles, “Strong absorption exaltation in ultrathin QDs and MQWs for intermediate band solar cells,” in *Proceedings of the 6th World Conference on Photovoltaic Energy Conversion (Kyoto)*, 2014.

[102] T. Sogabe, Y. Shoji, P. Mulder, J. Schermer, E. Tamayo, and Y. Okada, “Enhancement of current collection in epitaxial lift-off InAs/GaAs quantum dot thin film solar cell and concentrated photovoltaic study,” *2014 IEEE 40th Photovolt. Spec. Conf. PVSC 2014*, pp. 3485–3487, 2014.

[103] D. C. Johnson, I. Ballard, K. W. J. Barnham, D. B. Bishnell, J. P. Connolly, M. C. Lynch, T. N. D. Tibbits, N. J. Ekins-Daukes, M. Mazzer, R. Airey, G. Hill, and J. S. Roberts, “Advances in Bragg stack quantum well solar cells,” *Sol. Energy Mater. Sol. Cells*, vol. 87, no. 1–4, pp. 169–179, 2005.

[104] C. O. McPheeters, C. J. Hill, S. H. Lim, D. Derkacs, D. Z. Ting, and E. T. Yu, “Improved performance of In(Ga)As/GaAs quantum dot solar cells via light scattering by nanoparticles,” *J. Appl. Phys.*, vol. 106, no. 56101, pp. 1–3, 2009.

[105] X. H. Li, P. C. Li, D. Z. Hu, D. M. Schaadt, and E. T. Yu, “Light trapping in thin-film solar cells via scattering by nanostructured antireflection coatings,” *J. Appl. Phys.*, vol. 114, no. 44310, pp. 1–7, 2013.

[106] S. Turner, S. Mokkapati, G. Jolley, L. Fu, H. H. Tan, and C. Jagadish, “Periodic dielectric structures for light-trapping in InGaAs/GaAs quantum well solar cells,” *Opt. Express*, vol. 21, no. S3, pp. 324–335, 2013.

[107] K. Watanabe, B. Kim, T. Inoue, H. Sodabanlu, M. Sugiyama, M. Goto, S. Hayashi, K. Miyano, and Y. Nakano, “Thin-film InGaAs/GaAsP MQWs solar cell with backside nanoimprinted pattern for light trapping,” *IEEE J. Photovoltaics*, vol. 4, no. 4, pp. 1086–1090, 2014.

[108] C. O. McPheeters, D. Hu, D. M. Schaadt, and E. T. Yu, “Semiconductor heterostructures and optimization of light-trapping structures for efficient thin-film solar cells,” *J. Opt.*, vol. 14, no. 24007, pp. 1–11, 2012.

[109] D. Derkacs, W. V. Chen, P. M. Matheu, S. H. Lim, P. K. L. Yu, and E. T. Yu, “Nanoparticle-induced light scattering for improved performance of quantum-well solar cells,” *Appl. Phys. Lett.*, vol. 93, no. 9, pp. 10–13, 2008.

[110] B. L. Smith, M. A. Slocum, Z. S. Bittner, Y. Dai, G. T. Nelson, D. Staffan, R. Tatavarti, S. M. Hubbard, and M. Devices, “Inverted growth evaluation for epitaxial lift off (ELO) quantum dot solar cell and enhanced absorption by back surface texturing,” in *2016 IEEE 43rd Photovoltaic Specialists Conference (PVSC)*, 2016, pp. 1276–1281.

[111] K. Watanabe, T. Inoue, K. Toprasertpong, A. Delamarre, H. Sodabanlu, J. Guillemoles, M. Sugiyama, and Y. Nakano, “Optical analysis of the photon recycling effect in InGaAs / GaAsP multiple quantum well solar cell with light trapping structure,” in *2016 IEEE 43rd Photovoltaic Specialists Conference (PVSC)*, 2016, pp. 1268–1272.

[112] M. J. Mendes, A. Luque, I. Tobías, and A. Martí, “Plasmonic light enhancement in the near-field of metallic nanospheroids for application in intermediate band solar cells,” *Appl. Phys. Lett.*, vol. 95, no. 7, pp. 10–13, 2009.

[113] J. Wu, S. C. Mangham, V. R. Reddy, M. O. Manasreh, and B. D. Weaver, “Surface plasmon enhanced

intermediate band based quantum dots solar cell," *Sol. Energy Mater. Sol. Cells*, vol. 102, pp. 44–49, 2012.

[114] S. Foroutan and H. Baghban, "Theory of plasmonic quantum-dot-based intermediate band solar cells," *Appl. Opt.*, vol. 55, no. 13, p. 3405, 2016.

[115] F. Cappelluti, M. Gioannini, G. Ghione, and A. Khalili, "Numerical study of thin-film quantum-dot solar cells combining selective doping and light-trapping approaches," *Conf. Rec. IEEE Photovolt. Spec. Conf.*, vol. 2016–Novem, pp. 1282–1286, 2016.

[116] R. S. Ohl, "Light-sensitive electric device," US2402662A, 1946.

[117] S. Ma, H. Sodabanlu, K. Watanabe, M. Sugiyama, and Y. Nakano, "Strain-compensation measurement and simulation of InGaAs/GaAsP multiple quantum wells by metal organic vapor phase epitaxy using wafer-curvature," *J. Appl. Phys.*, vol. 110, no. 113501, pp. 1–5, 2011.

[118] M. Sugiyama, Y. Wang, H. Fujii, H. Sodabanlu, K. Watanabe, and Y. Nakano, "A superlattice solar cell for enhanced current output and minimized drop in open-circuit voltage under sunlight concentration," *J. Phys. D. Appl. Phys.*, vol. 46, no. 24001, pp. 1–11, 2013.

[119] D. B. Bushnell, N. J. Ekins-Daukes, K. W. J. Barnham, J. P. Connolly, J. S. Roberts, G. Hill, R. Airey, and M. Mazzer, "Short-circuit current enhancement in Bragg stack multi-quantum-well solar cells for multi-junction space cell applications," *Sol. Energy Mater. Sol. Cells*, vol. 75, no. 1–2, pp. 299–305, 2003.

[120] D. C. Johnson, I. M. Ballard, K. W. J. Barnham, J. P. Connolly, M. Mazzer, a. Bessìre, C. Calder, G. Hill, and J. S. Roberts, "Observation of photon recycling in strain-balanced quantum well solar cells," *Appl. Phys. Lett.*, vol. 90, no. 2007, pp. 10–13, 2007.

[121] G. C. DeSalvo, W. F. Tseng, and C. James, "Etch rates and selectivities of citric acid/Hydrogen peroxide on GaAs , Al0.3Ga0.7As , In0.2Ga0.8As , In0.53Ga0.47As , In0.52Al0.48As , and InP," *J. Electrochem. Soc.*, vol. 139, no. 3, pp. 831–835, 1992.

[122] C. Carter-Coman, R. Bicknell-Tassius, R. G. Benz, A. S. Brown, and N. M. Jokerst, "Analysis of GaAs substrate removal etching with citric acid:H202 and NH4OH:H202 for application to compliant substrates," *J. Electrochem. Soc.*, vol. 144, no. 2, pp. 29–31, 1997.

[123] A. R. Clawson, "Guide to references on III–V semiconductor chemical etching," *Mater. Sci. Eng.*, vol. 31, pp. 1–438, 2001.

[124] K. Tanabe, M. Nomura, D. Guimard, and Y. Arakawa, "Room temperature continuous wave operation of InAs / GaAs quantum dot photonic crystal nanocavity laser on silicon substrate," vol. 17, no. 9, pp. 7036–7042, 2009.

[125] X. Y. Lee, a. K. Verma, C. Q. Wu, M. Goertemiller, E. Yablonovitch, J. Eldredge, and D. Lillington, "Thin film GaAs solar cells on glass substrates by epitaxial liftoff," *Conf. Rec. Twenty Fifth IEEE Photovolt. Spec. Conf. - 1996*, pp. 53–55, 1996.

[126] J. J. Schermer, P. Mulder, G. J. Bauhuis, M. M. a J. Voncken, J. Van Deelen, E. Haverkamp, and P. K. Larsen, "Epitaxial Lift-Off for large area thin film III/V devices," *Phys. Status Solidi Appl. Mater. Sci.*, vol. 202, no. 4, pp. 501–508, 2005.

[127] C.-W. Cheng, K.-T. Shiu, N. Li, S.-J. Han, L. Shi, and D. K. Sadana, "Epitaxial lift-off process for gallium arsenide substrate reuse and flexible electronics.," *Nat. Commun.*, vol. 4, p. 1577, 2013.

[128] J. Adams, V. Elarde, A. Hains, C. Stender, F. Tuminello, C. Youtsey, A. Wibowo, and M. Osowski, “Demonstration of multiple substrate reuses for inverted metamorphic solar cells,” *IEEE J. Photovoltaics*, vol. 3, no. 2, pp. 899–903, 2013.

[129] N. Miyashita, B. Behaghel, J.-F. Guillemoles, and Y. Okada, “Enhancement of Photocurrent in Epitaxial Lift-Off Thin Film GaInNAsSb Solar Cells By The Light Confinement Structure,” in *PVSEC-26, Singapore*, 2016.

[130] A. Cattoni, J. Chen, D. Decanini, J. Shi, and A.-M. Haghiri-Gosnet, “Soft UV Nanoimprint Lithography: A Versatile Tool for Nanostructuration at the 20nm Scale,” in *Recent Advances in Nanofabrication Techniques and Applications*, InTech, 2011.

[131] P. Spinelli, M. A. Verschuuren, and A. Polman, “Broadband omnidirectional antireflection coating based on subwavelength surface Mie resonators,” *Nat. Commun.*, vol. 3, p. 692, 2012.

[132] Í. Ramiro, E. Antolın, M. J. Steer, P. G. Linares, E. Hernández, I. Artacho, E. López, T. Ben, J. M. Ripalda, S. I. Molina, F. Briones, C. R. Stanley, A. Martí, and A. Luque, “InAs / AlGaAs quantum dot intermediate band solar cells with enlarged sub-bandgaps,” in *Photovoltaic Specialists Conference (PVSC)*, 2012, pp. 652–656.

[133] H. M. Ji, B. Liang, P. J. Simmonds, B. C. Juang, T. Yang, R. J. Young, and D. L. Huffaker, “Hybrid type-I InAs/GaAs and type-II GaSb/GaAs quantum dot structure with enhanced photoluminescence,” *Appl. Phys. Lett.*, vol. 106, no. 103104, pp. 1–5, 2015.

[134] A. Lemaître, G. Patriarche, and F. Glas, “Composition profiling of InAs/GaAs quantum dots,” *Appl. Phys. Lett.*, vol. 85, no. 17, pp. 3717–3719, 2004.

[135] M. A. Migliorato, A. G. Cullis, M. Fearn, and J. H. Jefferson, “Atomistic simulation of strain relaxation in InxGa1-xAs/GaAs quantum dots with nonuniform composition,” *Phys. Rev. B*, vol. 65, no. 115316, pp. 1–5, 2002.

[136] K. Yamanaka, S. Naritsuka, K. Kanamoto, M. Mihara, and M. Ishii, “Electron traps in AlGaAs grown by molecular-beam epitaxy,” *J. Appl. Phys.*, vol. 61, no. 11, pp. 5062–5069, 1987.

[137] P. M. Mooney, “Deep donor levels (DX centers) in III-V semiconductors,” *J. Appl. Phys.*, vol. 67, no. 3, pp. 1–26, 1990.

[138] I. Vurgaftman, J. R. Meyer, and L. R. Ram-Mohan, “Band parameters for III–V compound semiconductors and their alloys,” *J. Appl. Phys.*, vol. 89, no. 11, pp. 5815–5875, 2001.

[139] S. Heckelmann, D. Lackner, C. Karcher, F. Dimroth, and A. W. Bett, “Investigations on AlGaAs Solar Cells Grown by MOVPE,” *IEEE J. Photovoltaics*, vol. 5, no. 1, pp. 446–453, 2015.

[140] D. M. Tex, K. Akahane, and Y. Kanemitsu, “Intrinsic Trade-off between Up-Conversion and Trapping Rates in InAs Quantum Dots for Intermediate-Band Solar Cells,” *Phys. Rev. Appl.*, vol. 6, no. 4, pp. 1–10, 2016.

[141] A. Pusch, M. Yoshida, N. P. Hylton, A. Mellor, A. Vaquero-steiner, C. C. Phillips, O. Hess, and N. J. Ekins-daukes, “The Purpose of a Photon Ratchet in Intermediate Band Solar Cells,” in *2016 IEEE 43rd Photovoltaic Specialists Conference (PVSC)*, 2016, pp. 9–12.

[142] J. Wu, B. Passmore, and M. O. Manasreh, “The impact of quantum dot filling on dual-band optical transitions via intermediate quantum states,” *J. Appl. Phys.*, vol. 118, no. 84501, pp. 1–6, 2015.

[143] K. S. Lee, D. U. Lee, E. K. Kim, and W. J. Choi, “Effect of space layer doping on photoelectric

conversion efficiency of InAs/GaAs quantum dot solar cells," *Appl. Phys. Lett.*, vol. 107, no. 203503, pp. 1–6, 2015.

[144] S. Naito, K. Yoshida, N. Miyashita, R. Tamaki, T. Hoshii, and Y. Okada, "Effect of Si doping and sunlight concentration on the performance of InAs / GaAs quantum dot solar cells," *J. Photonics Energy*, vol. 7, no. 2, pp. 1–9, 2017.

[145] T. Li, H. Lu, L. Fu, H. H. Tan, C. Jagadish, and M. Dagenais, "Enhanced carrier collection efficiency and reduced quantum state absorption by electron doping in self-assembled quantum dot solar cells," *Appl. Phys. Lett.*, vol. 106, no. 53902, pp. 1–5, 2015.

[146] D. Kim, M. Tang, J. Wu, S. Hatch, Y. Maidaniuk, V. Dorogan, Y. I. Mazur, G. J. Salamo, and H. Liu, "Si-Doped InAs / GaAs Quantum-Dot Solar Cell," *IEEE J. Photovoltaics*, vol. 6, no. 4, pp. 906–911, 2016.

[147] T. Inoue, S. Kido, K. Sasayama, T. Kita, and O. Wada, "Impurity doping in self-assembled InAs/GaAs quantum dots by selection of growth steps," *J. Appl. Phys.*, vol. 108, no. 63524, pp. 1–5, 2010.

[148] D. G. Sellers, E. Y. Chen, S. J. Polly, S. M. Hubbard, and M. F. Doty, "Effect of doping on room temperature carrier escape mechanisms in InAs/GaAs quantum dot p-i-n junction photovoltaic cells," *J. Appl. Phys.*, vol. 119, no. 194301, pp. 1–6, 2016.

[149] D. Zhou, P. E. Vullum, G. Sharma, S. F. Thomassen, R. Holmestad, T. W. Reenaas, and B. O. Fimland, "Positioning effects on quantum dot solar cells grown by molecular beam epitaxy," *Appl. Phys. Lett.*, vol. 96, no. 8, pp. 2010–2012, 2010.

[150] A. Kechiantz, A. Afanasev, and J.-L. Lazzari, "Impact of spatial separation of type-II GaSb quantum dots from the depletion region on the conversion efficiency limit of GaAs solar cells," *Prog. Photovolt Res. Appl.*, vol. 23, pp. 1003–1016, 2015.

[151] K. Driscoll, M. F. Bennett, S. J. Polly, D. V. Forbes, and S. M. Hubbard, "Effect of quantum dot position and background doping on the performance of quantum dot enhanced GaAs solar cells," *Appl. Phys. Lett.*, vol. 104, no. 23119, pp. 1–5, 2014.

[152] a. Martí, E. Antolín, E. Cánovas, N. López, P. G. Linares, a. Luque, C. R. Stanley, and C. D. Farmer, "Elements of the design and analysis of quantum-dot intermediate band solar cells," *Thin Solid Films*, vol. 516, pp. 6716–6722, 2008.

[153] J. Nelson, I. Ballard, K. Barnham, J. P. Connolly, J. S. Roberts, and M. Pate, "Effect of quantum well location on single quantum well p-i-n photodiode dark currents," *J. Appl. Phys.*, vol. 86, no. 10, pp. 5898–5905, 1999.

[154] Y. X. Gu, X. G. Yang, H. M. Ji, P. F. Xu, and T. Yang, "Theoretical study of the effects of InAs/GaAs quantum dot layer's position in i-region on current-voltage characteristic in intermediate band solar cells," *Appl. Phys. Lett.*, vol. 101, no. 81118, pp. 1–5, 2012.

[155] I. V. Markov, *Crystal Growth for Beginners: Fundamentals of Nucleation, Crystal Growth, and Epitaxy*, 2nd ed. World Scientific, 1995.

[156] I. N. Stranski and L. Krastanow, "Zur Theorie der orientierten Ausscheidung von Ionenkristallen aufeinander," *Abhandlungen der Math. Klasse IIb. Akad. der Wissenschaften Wien*, vol. 146, pp. 797–810, 1938.

[157] T. Kudo, T. Inoue, T. Kita, and O. Wada, "Real time analysis of self-assembled InAs/GaAs quantum dot growth by probing reflection high-energy electron diffraction chevron image," *J. Appl. Phys.*, vol. 104, no. 74305, pp. 1–5, 2008.

[158] M. C. Xu, Y. Temko, T. Suzuki, and K. Jacobi, “Shape transition of InAs quantum dots on GaAs(001),” *J. Appl. Phys.*, vol. 98, no. 83525, pp. 1–8, 2005.

[159] A. M. Andrews, M. Schramböck, T. Roch, W. Schrenk, E. Gornik, and G. Strasser, “Independent control of InAs quantum dot density and size on AlxGa1–xAs surfaces,” *J. Mater. Sci. Mater. Electron.*, vol. 19, no. 8–9, pp. 714–719, 2007.

[160] H. Z. Song, Y. Tanaka, T. Yamamoto, N. Yokoyama, M. Sugawara, and Y. Arakawa, “AlGaAs capping effect on InAs quantum dots self-assembled on GaAs,” *Phys. Lett. Sect. A Gen. At. Solid State Phys.*, vol. 375, no. 40, pp. 3517–3520, 2011.

[161] D. S. Sizov, Y. B. Samsonenko, G. E. Tsyrlin, N. K. Polyakov, V. a. Egorov, a. a. Tonkikh, a. E. Zhukov, S. S. Mikhrin, a. P. Vasil’ev, Y. G. Musikhin, a. F. Tsatsul’nikov, V. M. Ustinov, and N. N. Ledentsov, “Structural and optical properties of InAs quantum dots in AlGaAs matrix,” *Semiconductors*, vol. 37, no. 5, pp. 559–563, May 2003.

[162] Q. Gong, P. Offermans, R. Nötzel, P. M. Koenraad, and J. H. Wolter, “Capping process of InAs/GaAs quantum dots studied by cross-sectional scanning tunneling microscopy,” *Appl. Phys. Lett.*, vol. 85, no. 23, pp. 5697–5699, 2004.

[163] D. González, D. F. Reyes, A. D. Utrilla, T. Ben, V. Braza, A. Guzman, A. Hierro, and J. M. Ulloa, “General route for the decomposition of InAs quantum dots during the capping process,” *Nanotechnology*, vol. 27, no. 12, p. 125703, 2016.

[164] T. Kada, S. Asahi, T. Kaizu, Y. Harada, T. Kita, R. Tamaki, Y. Okada, and K. Miyano, “Two-step photon absorption in InAs/GaAs quantum-dot superlattice solar cells,” *Phys. Rev. B - Condens. Matter Mater. Phys.*, vol. 91, no. 201303(R), pp. 1–6, 2015.

[165] D. M. Tex, I. Kamiya, and Y. Kanemitsu, “Control of hot-carrier relaxation for realizing ideal quantum-dot intermediate-band solar cells.,” *Sci. Rep.*, vol. 4, no. 4125, pp. 1–6, 2014.

[166] D. M. Tex, I. Kamiya, and Y. Kanemitsu, “Efficient upconverted photocurrent through an Auger process in disklike InAs quantum structures for intermediate-band solar cells,” *Phys. Rev. B - Condens. Matter Mater. Phys.*, vol. 87, no. 245305, pp. 1–7, 2013.

[167] D. M. Tex, T. Ihara, I. Kamiya, and Y. Kanemitsu, “Temperature and light-intensity dependence of upconverted photocurrent generation in shallow InAs quantum structures Temperature and light-intensity dependence of upconverted photocurrent generation in shallow InAs quantum structures,” *Jpn. J. Appl. Phys.*, vol. 53, no. 05FV01, pp. 1–4, 2014.

[168] S. Adachi, *GaAs and Related Materials: Bulk Semiconducting and Superlattice Properties*. World Scientific, 1994.

[169] A. Polimeni, A. Patane, M. Henini, L. Eaves, and P. C. Main, “Temperature dependence of the optical properties of InAs / AlyGa1-yAs self-organized quantum dots,” *Phys. Rev. B*, vol. 59, no. 7, pp. 5064–5068, 1999.

[170] R. Heitz, I. Mukhametzhanov, a. Madhukar, a. Hoffmann, and D. Bimberg, “Temperature dependent optical properties of self-organized InAs/GaAs quantum dots,” *J. Electron. Mater.*, vol. 28, no. 5, pp. 520–527, 1999.

[171] S. Sanguinetti, M. Henini, M. Grassi Alessi, M. Capizzi, P. Frigeri, and S. Franchi, “Carrier thermal escape and retrapping in self-assembled quantum dots,” *Phys. Rev. B*, vol. 60, no. 11, pp. 8276–8283, 1999.

[172] G. Muñoz-Matutano, I. Suárez, J. Canet-Ferrer, B. Alén, D. Rivas, L. Seravalli, G. Trevisi, P. Frigeri, and J. Martínez-Pastor, "Size dependent carrier thermal escape and transfer in bimodally distributed self assembled InAs/GaAs quantum dots," *J. Appl. Phys.*, vol. 111, no. 123522, pp. 1–8, 2012.

[173] M. Kaniewska and O. Engström, "Deep traps at GaAs/GaAs interface grown by MBE-interruption growth technique," *Mater. Sci. Eng. C*, vol. 27, pp. 1069–1073, 2007.

[174] Y. P. Varshni, "Temperature dependence of the energy gap in semiconductors," *Physica*, vol. 34, no. 1, pp. 149–154, 1967.

[175] A. Cedola, F. Cappelluti, and M. Gioannini, "Dependence of quantum dot photocurrent on the carrier escape nature in InAs/GaAs quantum dot solar cells," *Semicond. Sci. Technol.*, vol. 31, no. 25018, pp. 1–12, 2016.

[176] S. Khatsevich, D. H. Rich, E. T. Kim, and A. Madhukar, "Cathodoluminescence imaging and spectroscopy of excited states in InAs self-assembled quantum dots," *J. Appl. Phys.*, vol. 97, no. 123520, pp. 1–8, 2005.

[177] Y. Dai, S. J. Polly, S. Hellstroem, M. A. Slocum, Z. S. Bittner, V. Forbes, P. J. Roland, R. J. Ellingson, and S. M. Hubbard, "Effect of electric field on carrier escape mechanisms in quantum dot intermediate band," *J. Appl. Phys.*, vol. 121, no. 13101, pp. 1–8, 2017.

[178] Y. Dai, M. A. Slocum, Z. Bittner, S. Hellstroem, D. V Forbes, and S. M. Hubbard, "Optimization in wide-band-gap quantum dot solar cells," in *Photovoltaic Specialists Conference (PVSC), 2016 IEEE 43rd*, 2016.

[179] V. Tasco, A. Cretì, A. Taurino, A. Cola, M. Catalano, A. Salhi, Z. Che, M. J. Kim, M. Lomascolo, and A. Passaseo, "Inter-level carrier dynamics and photocurrent generation in large band gap quantum dot solar cell by multistep growth," *Sol. Energy Mater. Sol. Cells*, vol. 171, no. July, pp. 142–147, 2017.

[180] S. M. Sze and K. K. Ng, *Physics of Semiconductor Devices*, 3rd ed. Wiley-VCH, 2007.

[181] O. Breitenstein, J. Bauer, A. Lotnyk, and J. M. Wagner, "Defect induced non-ideal dark I-V characteristics of solar cells," *Superlattices Microstruct.*, vol. 45, no. 4–5, pp. 182–189, 2009.

[182] H. Kim, M. H. Park, S. J. Park, H. S. Kim, J. D. Song, S. H. Kim, H. Kim, W. J. Choi, and D. W. Kim, "Influence of InAs quantum dots on the transport properties of GaAs-based solar cell devices," *Curr. Appl. Phys.*, vol. 14, no. 2, pp. 192–195, 2014.

[183] F. A. Padovani and R. Stratton, "Field and thermionic-field emission in schottky barriers," *Solid. State. Electron.*, vol. 9, pp. 695–707, 1966.

[184] Y. Dai, S. Polly, S. Hellstroem, D. V. Forbes, and S. M. Hubbard, "Electric field effect on carrier escape from InAs/GaAs quantum dots solar cells," *2014 IEEE 40th Photovolt. Spec. Conf.*, pp. 3492–3497, 2014.

[185] S. Hardikar, M. K. Hudait, P. Modak, S. B. Krupanidhi, and N. Padha, "Anomalous current transport in Au/low-doped n-GaAs Schottky barrier diodes at low temperatures," *Appl. Phys. A Mater. Sci. Process.*, vol. 68, no. 1, pp. 49–55, 1999.

[186] C. De Santi, M. Meneghini, M. La Grassa, B. Galler, R. Zeisel, M. Goano, S. Dominici, M. Mandurrino, F. Bertazzi, D. Robidas, G. Meneghesso, and E. Zanoni, "Role of defects in the thermal droop of InGaN-based light emitting diodes," *J. Appl. Phys.*, vol. 119, no. 94501, pp. 1–9, 2016.

[187] S. M. Willis, J. A. R. Dimmock, F. Tutu, H. Y. Liu, M. G. Peinado, H. E. Assender, A. A. R. Watt, and I. R.

Sellers, “Defect mediated extraction in InAs/GaAs quantum dot solar cells,” *Sol. Energy Mater. Sol. Cells*, vol. 102, pp. 142–147, 2012.

[188] Y. Cheng, M. Fukuda, V. R. Whiteside, M. C. Debnath, P. J. Vallely, T. D. Mishima, M. B. Santos, K. Hossain, S. Hatch, H. Y. Liu, and I. R. Sellers, “Investigation of InAs/GaAs1-xSbx quantum dots for applications in intermediate band solar cells,” *Sol. Energy Mater. Sol. Cells*, vol. 147, pp. 94–100, 2016.

[189] S. L. Chuang, *Physics of Optoelectronic Devices*. Wiley-VCH, 1995.

[190] S. Tomić, T. S. Jones, and N. M. Harrison, “Absorption characteristics of a quantum dot array induced intermediate band: Implications for solar cell design,” *Appl. Phys. Lett.*, vol. 93, no. 263105, pp. 1–3, 2008.

[191] S. Tomić, “Intermediate-band solar cells: Influence of band formation on dynamical processes in InAs/GaAs quantum dot arrays,” *Phys. Rev. B*, vol. 82, no. 195321, pp. 1–15, 2010.

[192] S. Tomić, A. Marti, E. Antolin, and A. Luque, “On inhibiting Auger intraband relaxation in InAs/GaAs quantum dot intermediate band solar cells,” *Appl. Phys. Lett.*, vol. 99, no. 53504, pp. 1–3, 2011.

[193] S. Tomic, T. Sogabe, and Y. Okada, “In-plane coupling effect on absorption coefficients of InAs/GaAs quantum dots arrays for intermediate band solar cell,” *Prog. Photovolt Res. Appl.*, vol. 23, no. February 2014, pp. 546–558, 2015.

[194] A. Luque, A. Marti, E. Antolin, and P. Garcia-Linares, “Intraband absorption for normal illumination in quantum dot intermediate band solar cells,” *Sol. Energy Mater. Sol. Cells*, vol. 94, no. 12, pp. 2032–2035, 2010.

[195] A. Luque, A. Martí, E. Antolín, P. G. Linares, I. Tobías, I. Ramiro, and E. Hernandez, “New Hamiltonian for a better understanding of the quantum dot intermediate band solar cells,” *Sol. Energy Mater. Sol. Cells*, vol. 95, no. 8, pp. 2095–2101, 2011.

[196] A. Luque, A. Mellor, I. Ramiro, E. Antolín, I. Tobías, and A. Martí, “Interband absorption of photons by extended states in intermediate band solar cells,” *Sol. Energy Mater. Sol. Cells*, vol. 115, pp. 138–144, 2013.

[197] A. Luque, A. Panchak, A. Vlasov, A. Martí, and V. Andreev, “Four-band Hamiltonian for fast calculations in intermediate-band solar cells,” *Phys. E Low-Dimensional Syst. Nanostructures*, vol. 76, pp. 127–134, 2016.

[198] T. Kotani, S. Birner, P. Lugli, and C. Hamaguchi, “A theoretical analysis of the optical absorption properties in one-dimensional InAs/GaAs quantum dot superlattices,” *J. Appl. Phys.*, vol. 115, no. 143501, pp. 1–15, 2014.

[199] A. Trellakis, T. Zibold, T. Andlauer, S. Birner, R. K. Smith, R. Morschl, and P. Vogl, “The 3D nanometer device project nextnano: Concepts, methods, results,” *J. Comput. Electron.*, vol. 5, no. 4, pp. 285–289, 2006.

[200] S. Birner, T. Zibold, T. Andlauer, T. Kubis, M. Sabathil, A. Trellakis, and P. Vogl, “Nextnano: General purpose 3-D simulations,” *IEEE Trans. Electron Devices*, vol. 54, no. 9, pp. 2137–2142, 2007.

[201] C. Pryor, “Eight-band calculations of strained InAs/GaAs quantum dots compared with one-, four-, and six-band approximations,” *Phys. Rev. B*, vol. 57, no. 12, pp. 7190–7195, 1998.

[202] T. Andlauer, “Optoelectronic and spin-related properties of semiconductor nanostructures in

magnetic fields," Technischen Universität München, 2009.

[203] M. Fox, *Optical Properties of Solids*. OUP Oxford, 2010.

[204] I. Vurgaftman, J. R. Meyer, and L. R. Ram-Mohan, "Band parameters for III-V compound semiconductors and their alloys," *J. Appl. Phys.*, vol. 89, no. 11, pp. 5815–5875, 2001.

[205] A. Luque, A. Martí, E. Antolín, P. G. Linares, I. Tobías, and I. Ramiro, "Radiative thermal escape in intermediate band solar cells," *AIP Adv.*, vol. 1, no. 22125, pp. 1–6, 2011.

[206] V. Popescu, G. Bester, and A. Zunger, "Strain-induced localized states within the matrix continuum of self-assembled quantum dots," *Appl. Phys. Lett.*, vol. 95, no. 23108, pp. 1–3, 2009.

[207] D. Watanabe, N. Kasamatsu, Y. Harada, and T. Kita, "Hot-carrier solar cells using low-dimensional quantum structures," *Appl. Phys. Lett.*, vol. 105, no. 171904, pp. 1–5, 2014.

[208] J. J. Olivero and R. L. Longbothum, "Empirical fits to the Voigt line width: a brief review," *J. Quant. Spectrosc. Radiat. Transf.*, vol. 17, pp. 233–236, 1977.

[209] G. D. Gillen and S. Guha, "Use of Michelson and Fabry-Perot interferometry for independent determination of the refractive index and physical thickness of wafers," *Appl. Opt.*, vol. 44, no. 3, pp. 344–347, Jan. 2005.

[210] H. J. Choi, H. H. Lim, H. S. Moon, T. B. Eom, J. J. Ju, and M. Cha, "Determination of refractive index of transparent plate by Fabry-Perot fringe analysis," in *Proc. SPIE*, 2010, vol. 7790, pp. 1–6.

[211] E. Steveler, M. Verdun, B. Portier, P. Chevalier, C. Dupuis, N. Bardou, J. B. Rodriguez, R. Haïdar, F. Pardo, and J. L. Pelouard, "Optical index measurement of InAs/GaSb type-II superlattice for mid-infrared photodetection at cryogenic temperatures," *Appl. Phys. Lett.*, vol. 105, no. 141103, pp. 1–5, 2014.

[212] A. Datas, E. López, I. Ramiro, E. Antolín, A. Martí, A. Luque, R. Tamaki, Y. Shoji, T. Sogabe, and Y. Okada, "Intermediate band solar cell with extreme broadband spectrum quantum efficiency," *Phys. Rev. Lett.*, vol. 114, no. 157701, pp. 1–4, 2015.

[213] P. Rale, "Multi-transitions solar cells with localised states," *PhD Thesis, Univ. Pierre Marie Curie*, 2015.

[214] M. Ito, "Theoretical and Experimental Investigation of Quantum Well Intermediate Band Solar Cells," Imperial College London, 2014.

[215] L. C. West and S. J. Eglash, "First observation of an extremely large-dipole infrared transition within the conduction band of a GaAs quantum well," *Appl. Phys. Lett.*, vol. 46, no. 12, pp. 1156–1158, 1985.

[216] P. Lecaruyer, E. Maillart, M. Canva, and J. Rolland, "Generalization of the Rouard method to an absorbing thin-film stack and application to surface plasmon resonance.," *Appl. Opt.*, vol. 45, no. 33, pp. 8419–8423, 2006.

[217] C. P. Michael, K. Srinivasan, T. J. Johnson, O. Painter, K. H. Lee, K. Hennessy, H. Kim, and E. Hu, "Wavelength- and material-dependent absorption in GaAs and AlGaAs microcavities," *Appl. Phys. Lett.*, vol. 90, no. 51108, pp. 1–4, 2007.

[218] A. Delamarre, "Développement de nouvelles méthodes de caractérisation optoélectroniques des cellules solaires," Université Pierre et Marie Curie, 2013.

[219] H.-L. Chen, “Characterization of Quantum-dot Intermediate Band Solar Cells by Photoluminescence,” Ecole Polytechnique - Université Paris-Saclay (Master Theses), 2015.

[220] T. Kita, T. Maeda, and Y. Harada, “Carrier dynamics of the intermediate state in InAs/GaAs quantum dots coupled in a photonic cavity under two-photon excitation,” *Phys. Rev. B - Condens. Matter Mater. Phys.*, vol. 86, no. 35301, pp. 1–7, 2012.

[221] T. Trupke, R. A. Bardos, M. D. Abbott, and J. E. Cotter, “Suns-photoluminescence: Contactless determination of current-voltage characteristics of silicon wafers,” *Appl. Phys. Lett.*, vol. 87, no. 9, pp. 7–10, 2005.

[222] T. Tran, “T. D. , High brightness InP micropillars grown on silicon with Fermi level splitting larger than 1 eV.,” *Nano Lett.*, vol. 14, pp. 3235–3240, 2014.

[223] R. A. Sinton and R. M. Swanson, “Recombination in highly injected silicon,” *IEEE Trans. Electron Devices*, vol. 34, no. 6, pp. 1380–1389, 1987.

[224] T. Kirchartz, B. E. Pieters, J. Kirkpatrick, U. Rau, and J. Nelson, “Recombination via tail states in polythiophene:fullerene solar cells,” *Phys. Rev. B - Condens. Matter Mater. Phys.*, vol. 83, no. 11, pp. 1–13, 2011.

[225] N. Vandamme, H. L. Chen, A. Gaucher, B. Behaghel, A. Lemaître, A. Cattoni, C. Dupuis, N. Bardou, J. F. Guillemoles, and S. Collin, “Ultrathin GaAs solar cells with a silver back mirror,” *IEEE J. Photovoltaics*, vol. 5, no. 2, pp. 565–570, 2015.

[226] A. Delamarre, L. Lombez, and J. F. Guillemoles, “Contactless mapping of saturation currents of solar cells by photoluminescence,” *Appl. Phys. Lett.*, vol. 100, no. 13, pp. 2012–2015, 2012.

[227] Y. Harada, T. Maeda, and T. Kita, “Intraband carrier dynamics in InAs/GaAs quantum dots stimulated by bound-to-continuum excitation,” *J. Appl. Phys.*, vol. 113, no. 223511, pp. 1–5, 2013.

[228] Z. Xu, Y. Zhang, and J. M. Hvam, “Long luminescence lifetime in self-assembled InGaAs/GaAs quantum dots at room temperature,” *Appl. Phys. Lett.*, vol. 93, no. 183116, pp. 1–3, 2008.

[229] O. Nasr, N. Chauvin, M. H. Hadj Alouane, H. Maaref, C. Bru-Chevallier, L. Sfaxi, and B. Ilahi, “Carrier dynamics of strain-engineered InAs quantum dots with (In)GaAs surrounding material,” *J. Opt.*, vol. 19, no. 25401, pp. 1–8, 2017.

[230] P. A. Dalgarno, J. M. Smith, J. McFarlane, B. D. Gerardot, K. Karrai, A. Badolato, P. M. Petroff, and R. J. Warburton, “Coulomb interactions in single charged self-assembled quantum dots: Radiative lifetime and recombination energy,” *Phys. Rev. B - Condens. Matter Mater. Phys.*, vol. 77, no. 245311, pp. 1–8, 2008.

[231] S. Asahi, H. Teranishi, N. Kasamatsu, T. Kada, T. Kaizu, and T. Kita, “Saturable Two-Step Photocurrent Generation in Intermediate-Band Solar Cells Including InAs Quantum Dots Embedded in Al0.3Ga0.7 As/GaAs Quantum Wells,” *IEEE J. Photovoltaics*, vol. 6, no. 2, pp. 465–472, 2016.

[232] P. D. Buckle, P. Dawson, S. A. Hall, X. Chen, M. J. Steer, D. J. Mowbray, M. S. Skolnick, and M. Hopkinson, “Photoluminescence decay time measurements from self-organized InAs/GaAs quantum dots,” *J. Appl. Phys.*, vol. 86, no. 5, pp. 2555–2561, 1999.

[233] A. J. Nozik, M. C. Beard, J. M. Luther, M. Law, R. J. Ellingson, and J. C. Johnson, “Semiconductor quantum dots and quantum dot arrays and applications of multiple exciton generation to third-generation photovoltaic solar cells,” *Chem. Rev.*, vol. 110, no. 11, pp. 6873–6890, 2010.

[234] P. Zhang, Y. Feng, X. Wen, W. Cao, R. Anthony, U. Kortshagen, G. Conibeer, and S. Huang, “Generation of hot carrier population in colloidal silicon quantum dots for high-efficiency photovoltaics,” *Sol. Energy Mater. Sol. Cells*, vol. 145, pp. 391–396, 2016.

[235] J. K. Katahara and H. W. Hillhouse, “Quasi-fermi level splitting and sub-bandgap absorptivity from semiconductor photoluminescence,” *J. Appl. Phys.*, vol. 116, no. 173504, pp. 1–12, 2014.

[236] T. N. Morgan, “Broadening of impurity bands in heavily doped semiconductors,” *Phys. Rev.*, vol. 139, no. 1A, pp. 343–348, 1965.

[237] E. M. Conwell, *High Field Transport in Semiconductors*. New York: Academic Press, 1967.

[238] U. Bockelmann and G. Bastard, “Phonon scattering and energy relaxation in two-, one-, and zero-dimensional electron gases,” *Phys. Rev. B*, vol. 42, no. 14, pp. 8947–8951, 1990.

[239] W. Cao, Z. Zhang, R. Patterson, Y. Lin, X. Wen, B. P. Veetil, P. Zhang, Q. Zhang, S. Shrestha, G. Conibeer, and H. Shujuan, “Quantification of hot carrier thermalization in PbS colloidal quantum dots by power and temperature dependent photoluminescence spectroscopy,” *RSC Adv.*, vol. 6, no. 93, pp. 90846–90855, 2016.

[240] J. Rodière, L. Lombez, A. Le Corre, O. Durand, and J. F. Guillemoles, “Experimental evidence of hot carriers solar cell operation in multi-quantum wells heterostructures,” *Appl. Phys. Lett.*, vol. 106, no. 183901, pp. 1–4, 2015.

[241] A. Le Bris, L. Lombez, S. Laribi, G. Boissier, P. Christol, and J.-F. Guillemoles, “Thermalisation rate study of GaSb-based heterostructures by continuous wave photoluminescence and their potential as hot carrier solar cell absorbers,” *Energy Environ. Sci.*, vol. 5, pp. 6225–6232, 2012.

[242] Y. Harada, N. Kasamatsu, D. Watanabe, and T. Kita, “Nanosecond-scale hot-carrier cooling dynamics in one-dimensional quantum dot superlattices,” *Phys. Rev. B - Condens. Matter Mater. Phys.*, vol. 93, no. 115303, pp. 1–5, 2016.

[243] S.-F. Ren, D. Lu, and G. Qin, “Phonon modes in InAs quantum dots,” *Phys. Rev. B*, vol. 63, no. 195315, pp. 1–9, 2001.

[244] I. Yeo, J. D. Song, and J. Lee, “Temperature-dependent energy band gap variation in self-organized InAs quantum dots,” vol. 99, no. 151909, pp. 1–3, 2011.

[245] A. Creti, V. Tasco, A. Cola, G. Montagna, I. Tarantini, A. Salhi, A. Al-Muhanna, A. Passaseo, and M. Lomascolo, “Role of charge separation on two-step two photon absorption in InAs/GaAs quantum dot intermediate band solar cells,” *Appl. Phys. Lett.*, vol. 108, no. 63901, pp. 1–5, 2016.

[246] P. Wurfel, “The chemical potential of radiation,” *J. Phys. C Solid State Phys.*, vol. 15, no. 18, pp. 3967–3985, 1982.

[247] U. Rau, “Reciprocity relation between photovoltaic quantum efficiency and electroluminescent emission of solar cells,” *Phys. Rev. B - Condens. Matter Mater. Phys.*, vol. 76, no. 85303, pp. 1–8, 2007.

[248] Y. Dai, C. G. Bailey, C. Kerestes, D. V Forbes, and S. M. Hubbard, “Investigation of carrier escape mechanism in InAs/GaAs quantum dot solar cells,” in *Photovoltaic Specialists Conference (PVSC), 38th IEEE*, 2012, pp. 39–44.

[249] V. van Roosbroeck and H. C. Casey, “Transport in relaxation semiconductors,” *Phys. Rev. B*, vol. 5, no. 6, pp. 2154–2174, 1972.

[250] N. M. Haegel, “Relaxation semiconductors : in theory and in practice,” *Appl. Phys. A*, vol. 53, pp. 1–7, 1991.

[251] B. Liao, E. Naja, H. Li, A. J. Minnich, and A. H. Zewail, “Photo-excited hot carrier dynamics in hydrogenated amorphous silicon imaged by 4D electron microscopy,” *Nat. Nanotechnol.*, vol. 12, no. 9, pp. 871–876, 2017.

[252] Y. Harada, T. Maeda, and T. Kita, “Intraband carrier dynamics in InAs/GaAs quantum dots stimulated by bound-to-continuum excitation,” *J. Appl. Phys.*, vol. 113, no. 22, pp. 11–16, 2013.

[253] T. Li and M. Dagenais, “High saturation intensity in InAs/GaAs quantum dot solar cells and impact on the realization of the intermediate band concept at room-temperature,” *Appl. Phys. Lett.*, vol. 110, no. 61107, pp. 1–5, 2017.

[254] H. Fujii, K. Watanabe, M. Sugiyama, and Y. Nakano, “Effect of quantum well on the efficiency of carrier collection in InGaAs/GaAsP multiple quantum well solar cells,” *Jpn. J. Appl. Phys.*, vol. 51, no. 10S, pp. 1–5, 2012.

[255] G. J. Bauhuis, P. Mulder, E. J. Haverkamp, J. C. C. M. Huijben, and J. J. Schermer, “26.1% thin-film GaAs solar cell using epitaxial lift-off,” *Sol. Energy Mater. Sol. Cells*, vol. 93, no. 9, pp. 1488–1491, 2009.

[256] B. E. A. Saleh and M. C. Teich, *Fundamentals of Photonics*, no. 2nd edition. Wiley-VCH, 2007.

[257] E. D. Palik, *Handbook of Optical Constants of Solids*. Academic Press, 1985.

[258] C. J. R. Sheppard, “Approximate calculation of the reflection coefficient from a stratified medium,” *Pure Appl. Opt. J. Eur. Opt. Soc. Part A*, vol. 4, no. 5, pp. 665–669, 1995.

[259] P. Lalanne and G. M. Morris, “Highly improved convergence of the coupled-wave method for TM polarization,” *J. Opt. Soc. Am. A*, vol. 13, no. 4, p. 779, 1996.

[260] P. Lalanne and M. P. Jurek, “Computation of the near-field pattern with the coupled-wave method for transverse magnetic polarization,” *J. Mod. Opt.*, vol. 45, no. 7, pp. 1357–1374, 1998.

[261] J. R. DeVore, “Refractive Indices of Rutile and Sphalerite,” *J. Opt. Soc. Am.*, vol. 41, no. 6, pp. 416–419, 1951.

[262] C. O. McPheeters, C. J. Hill, S. H. Lim, D. Derkacs, D. Z. Ting, and E. T. Yu, “Improved performance of In(Ga)As/GaAs quantum dot solar cells via light scattering by nanoparticles,” *J. Appl. Phys.*, vol. 106, no. 56101, pp. 48–51, 2009.

[263] S. D. Brorson, H. Yokoyama, and E. P. Ippen, “Spontaneous emission rate alteration in optical waveguide structures,” *IEEE J. Quantum Electron.*, vol. 26, no. 9, pp. 1492–1499, 1990.

[264] C. Weisbuch, M. Nishioka, A. Ishikawa, and Y. Arakawa, “Observation of the coupled exciton-photon mode splitting in a semiconductor quantum microcavity,” *Phys. Rev. Lett.*, vol. 69, no. 23, pp. 3314–3317, 1992.

[265] T. Nozawa, H. Takagi, K. Watanabe, and Y. Arakawa, “Direct observation of two-step photon absorption in an InAs/GaAs single quantum dot for the operation of intermediate-band solar cells,” *Nano Lett.*, vol. 15, pp. 4483–4487, 2015.

[266] S. Asahi, H. Teranishi, K. Kusaki, T. Kaizu, and T. Kita, “Two-step photon up-conversion solar cells,” *Nat. Commun.*, vol. 8, no. 14962, pp. 1–9, 2017.

[267] R. Tamaki, Y. Shoji, Y. Okada, K. Miyano, R. Tamaki, Y. Shoji, Y. Okada, and K. Miyano, “Spectrally resolved intraband transitions on two-step photon absorption in InGaAs/GaAs quantum dot solar cell,” *Appl. Phys. Lett.*, vol. 105, no. 73118, pp. 1–4, 2014.

[268] S. Mokkapati and K. R. Catchpole, “Nanophotonic light trapping in solar cells,” *J. Appl. Phys.*, vol. 112, no. 10, p. 101101, 2012.

[269] J. M. Luther, P. K. Jain, T. Ewers, and A. P. Alivisatos, “Localized surface plasmon resonances arising from free carriers in doped quantum dots,” *Nat. Mater.*, vol. 10, no. 5, pp. 361–366, 2011.

[270] D. Li and C. Z. Ning, “All-semiconductor active plasmonic system in mid-infrared wavelengths,” *Opt. Express*, vol. 19, no. 15, pp. 14594–14603, 2011.

[271] S. Law, D. C. Adams, A. M. Taylor, and D. Wasserman, “Mid-infrared designer metals,” *Opt. Express*, vol. 20, no. 11, pp. 12155–12165, 2012.